FLUID-DYNAMIC CHARACTERISTICS OF TWO-PHASE FLOW

AKIMI SERIZAWA

MARCH 1974

INSTITUTE OF ATOMIC ENERGY
KYOTO UNIVERSITY

FLUID-DYNAMIC CHARACTERISTICS OF TWO-PHASE FLOW

AKIMI SERIZAWA

MARCH 1974

INSTITUTE OF ATOMIC ENERGY
KYOTO UNIVERSITY

ACKNOWLEDGEMENTS

The author wishes to express his cordial gratitude to the many people who gave their aid and encouragement during the course of this investigation.

Special thanks are extended to Professor I. Michiyoshi, Department of Nuclear Engineering, Kyoto University, for the interest, guidance, and constructive criticisms given throughout the investigation. Grateful acknowledgements are expressed for the support of Professor A. Sakurai, Institute of Atomic Energy, Kyoto University.

The author also wishes to express his sincere appreciation to Assistant Professor H. Nishihara, Department of Nuclear Engineering, Kyoto University.

Thanks are also extended to Dr. M. Fukao for his useful suggestion in fabricating electronic instruments for measurements ; to Mr. K. Wada for his useful suggestion in utilizing a gas-chromatograph technique ; to Messrs. K. Ogino, K. Yoshida, and O. Takahashi for their encouragement ; and Mr. I. Kataoka for his aid in the operation of the experiments.

ABSTRACT

Phenomena of the gas-liquid mixture flowing in various geometries have been investigated. This thesis deals mainly with the experimental results on the general behavior of the hydrodynamics of the gas-liquid two-phase flows and the minute structure of air-water bubble flow in a pipe.

In PART I of this thesis, the general behaviors of the over-all parameters, such as the cross-sectional average void fraction and the frictional pressure drop, are described based upon the experimental findings obtained in steam-water, air-water, and argon-mercury two-phase flows in pipes, annuli, and in rod-bundles, with respect to the effects of the flow patterns, the superficial liquid velocity, the heat flux through the heating wall, the geometric configuration of the flow channel, the fluid properties, and the discrete surface roughness of the channel upon the void fraction and the frictional pressure drop.

Empirical correlations for predicting the void fraction and the frictional pressure drop are presented. Comparisons of the predicted void fractions and the frictional pressure drops with corresponding various available data obtained by the own and other investigators show a good agreement in a wide range of flow variables not only for ordinary non-metallic but also for metallic fluid two-phase flows.

The rate of rise of a single air bubble in channels of various shapes has been studied experimentally. Based upon this experimental result, a slug flow theory is used to predict the effect of the geometric configuration of the channel upon the average void fraction. The result indicated a fairly qualitative agreement with the void fraction data of the author.

An analytical model for droplet-dispersed annular flow is also presented to predict the rates of droplet deposition and entrainment, which considers the probability distribution functions of the residence

time for droplet to stay within the liquid film along the wall. The predicted result indicates a fairly good agreement with the experiments.

PART II of this thesis, the main objective of the present work, is devoted to studying and clarifying in detail and systematically the minute flow structure of air-water two-phase bubble flow in pipe through the measurements of the various local parameters and their turbulent characteristics, as many as possible, by using specially developed techniques.

Over a large portion of any flow cross section in fully-developed bubble flow region, the phase distribution was nearly uniform in radial direction, while in the wall region, a maximum void fraction was observed. The bubble velocity, the water velocity, and the local slip ratio showed fairly flat profiles in radial direction without any maxima near the wall. All these facts may support the validity for applying a homogeneous flow field to the present case. Spectra of the bubble velocity and the water velocity presented the Poisson distribution and the normal distribution functions, respectively. The experimental evidence indicated a trend for the turbulent intensity to decrease first with increasing the gas flow rate for constant water velocity and to increase again with a further increase in the gas flow rate. This phenomenon was more remarkable for a higher water velocity.

A study of heat and bubble transports in turbulent air-water bubble flow was carried out by means of a tracer technique. The data of the helium tracer bubble concentration and the temperature rise distributions were used to extract bubble and heat diffusivity information. The results indicated that the turbulent velocity components of the liquid phase play a predominantly important role in turbulent transport process of heat and bubbles. A systematic variation of the diffusivity of heat ε_H with the quality and the water velocity was observed with increasing tendencies. And an empirical correlation for the diffusivity ratio $\varepsilon_{H,TP}/\varepsilon_{H,SP}$ is presented. The Péclet number $u_c'\bar{d}/\phi$ for bubble dispersion can be approximated

2.0 independently of the quality and the water velocity. The bubble-to-heat diffusivity ratio ϕ/ε_H was observed to approach unity with increasing the quality and the water velocity.

TABLE OF CONTENTS

PART II

TURBULENCE STRUCTURE OF AIR-WATER TWO-PHASE BUBBLE FLOW FLOWING UPWARD IN CIRCULAR TUBE

INTRODUCTION

Phenomena of the gas-liquid mixture flowing in a pipe which is widely encountered in the petroleum industry, the chemical process industry, steam generation equipment, refrigerators, and nuclear reactor design have been studied extensively for several decades.

Although a significant amount of work has been done with many different gas-liquid to meet the needs of, especially, the design of the water-cooled reactors in which gas-liquid two-phase flow is often encountered, there still exist numerous anomalies and gaps in two-phase flow theories. This is mainly due to the thermohydrodynamic complexities accompanied by the continuously changing properties of the mixture.

It is well known from previous studies based upon the experimental findings that the various flow patterns exist, depending mainly on the flow rates of the liquid and the gas, their physical properties, and on the geometry of the flow channel. Since the thermodynamic characteristic, to say nothing of the hydrodynamic characteristic, of the two-phase flow is severely sensitive to the prevailing flow pattern, the existence of the various flow patterns surely makes problems associated with two-phase flow too complicated to be solved. Accurate and detailed information about the behavior of the various flow parameters, the flow structure, and the corresponding flow pattern is very importantly related to safety and behaviors of nuclear reactors which are usually operated at higher thermal load.

A great deal of experimantal work has been carried out of the over-all characteristics of the ordinary non-metallic two-phase flow, and has provided some amount of general information about flow pattern [1-8], and general behaviors of such over-all parameters as the cross-sectional average void fraction[9-32], and the pressure drop[33-57]. However despite these progresses, many uncertainties are still left to

be clarified, especially as to the effects of the physical properties of the fluids and the effects of the mass velocity of the fluid upon such over-all flow parameters.

Some theoretical models proposed to predict the cross-sectional average void fraction or slippage of the gas[58-63], and the frictional pressure drop[64-69] are generally confined to specific flow regimes or limited flow conditions, and cannot describe the true phenomena, since in these investigations the very complicated two-phase flow phenomena were usually described mistakenly by too simplified models due to the lack of the detailed information about the minute structure of two-phase flows.

In designing liquid metal-cooled fission reactors, fusion reactors, and MHD generators using liquid metal two-phase flow as working fluid, which are all desired to be successfully developed, the liquid metal two-phase flow phenomenon is one of the most important themes to be studied as to their performance characteristics. In order to provide the data required, a series of experimental works have been made, from various viewpoints, of the measurements of the cross-sectional average void fraction and frictional pressure drop for sodium[70-78], potassium[79-89], potassium-mercury amalgam[90,91], sodium-potassium[92,93], and mercury[94,95,96]. However, they cannot necessarily offer sufficiently reliable information because of the difficulties involved in their measuring techniques, especially, under high-temperature operations.

In consideration of the fact that the physical properties of liquid metals are greatly different from those of the ordinary non-metallic fluids, a doubt may arise as to whether the common knowledges obtained from the experimental results for various ordinary non-metallic fluid two-phase flows can be successfully applied for the liquid metal two-phase flows or not, even in respect to the general behaviors of the over-all parameters such as the void fraction and frictional pressure drop. Besides, the effects of the wettability between the fluid and the wall, and the effects of the magnetic field

strength upon the flow and heat transfer characteristics of the liquid metal two-phase flow appear one of the most interesting and important themes relating to the phenomena peculiar to the liquid metal two-phase flows.

In PART I of this thesis, the general behaviors of the over-all parameters, such as the cross-sectional average void fraction and the frictional pressure drop, are described based upon the experimental findings made by the author of this thesis, in steam-water, air-water, and argon-mercury two-phase flows in pipes, annuli, and also in rod-bundles. Empirical equations for predicting the void fraction and the frictional pressure drop in ordinary non-metallic fluids, and an analytical model for dispersed-annular flow are also presented.

On the other hand, as it were possible, accurate information about the minute structure of two-phase flow, in which we are now greatly interested, would surely provide an instructive answer to the problems concerning the general behaviors of the over-all parameters, and, hence, it would further offer some more useful bases for designing safety problems and thermohydrodynamic performance characteristics of a nuclear reactor.

At the present status, the studies of the minute structure of two-phase flow confine themselves unfortunately to the flow without heat addition. Because, in flows with heat addition, very complicated mechanisms of boiling heat transfer may affect the flow mechanism, and, therefore, an analysis may become more difficult. These studies are generally classified into three categories, i.e., the studies associated with bubble flow, slug flow, and dispersed-annular flow. A number of investigators confined their research to the study of the last category, but, more exactly speaking, only a few works were devoted to the study of the "minute" structure of the dispersed-annular flow. But they measured only all or part of the liquid velocity profile within the thin liquid film on the pipe wall, profiles of the gas velocity and liquid droplet entrainment in the center core region of the flow, droplet size distribution, and turbulent diffusivity of the liquid

droplet. On the other hand, as far as the author knows, a series of works by the author and his co-workers in air-water flow[97-101] are the only contributions to the systematic study associated with bubble flow which, the first stage of the flow pattern, is most popularly encountered but presents the most perplexing behaviors among various flow patterns.

Among a considerable amount of partial observation of the distributions of the phase, the liquid velocity, the bubble velocity, the bubble transit frequency, and bubble size (see REFERENCES in PART II), only a few are available to evaluate the characteristic flow structure of bubble flow. But, to have a correct and general physical picture of the flow, detailed information is severely required further not only for the distributions of the aforementioned variables but also for the followings : the bubble velocity spectrum, the liquid velocity spectrum, the turbulent intensity or the turbulent velocity components of the liquid phase, the turbulent diffusivities for bubble dispersion, momentum and heat transports, and the statistical nature of bubble behaviors. Correct measurements of these quantities are apparently very difficult because of the following reasons :

1) A considerable slippage exists between the velocities of the gas and the liquid phases in bubble flow (whereas, in dispersed-annular flow, small liquid droplets are usually entrained in the gas core at almost the same velocity as the ambient gas stream),
2) Large bubble size,
3) Perplexingly complicated interactions between bubbles, between bubbles and the ambient liquid, and between bubbles and the wall of the flow passage may influence reciprocally to determine the flow field.

The author and his co-workers have succeeded in developing special techniques for measuring all of those aforementioned variables specifying the flow structure of bubble flow[97-101].

The main objective of this thesis is devoted to studying and clarifying in detail and systematically the minute flow structure of

the gas-liquid two-phase bubble flow, exhibiting very intricated but very interesting turbulent flow characteristics, through the measurements of the various local parameters and their turbulent characteristics, as many as possible, by using specially developed techniques (PART II).

REFERENCES

[1] Baker, O.: Oil Gas J., 53, 185 (1954).

[2] Goldmann, K.: Trans. Am. Soc. Mech. Engrs., Ser.C, Vol.83,158 (1961).

[3] Griffith, P., Wallis, G.B.: ibid., Ser.C, Vol.83, 307 (1961).

[4] Wallis, G.B.: International Developments in Heat Transfer, Part II, Am. Soc. Mech. Engrs., (1961).

[5] Quandt, E.: 55th AIChE Annu. Meeting, Chicago (1962).

[6] Bergles, A.E., Suo, M.: Proc. 3rd Intn. Heat Transfer Conf., Chicago, (1966).

[7] Yanai, M.: Doctoral thesis, Kyoto Univ. (1971).

[8] Iida, Y., Wakao, N.: 10th Japan Heat Transfer Symp., A110, (1973).

[9] Cook, W.H.: ANL-5621 (1956).

[10] Hoglund, B.M., Weatherhead, R.J., Marchaterre, J.F.: ANL-5760.

[11] Lottes, P.A., Petrick, M., Marchaterre, J.F.: ANL-6063.

[12] Thie, J.A., Beidelman, J., Hoglund, B.M.: Nucl. Sci. Engrs., Vol.11, 1 (1961).

[13] Condon,R.A., Sher, N.C.: ibid., Vol.14, 327 (1962).

[14] Zuber, N.: Trans. Am. Soc. Mech. Engrs., Ser.C, Vol.82, 255 (1960).

[15] Lottes, P.A., Cook, W.H., Neusen, K.F., Wright, R.W., Zivi, S.M., Zuber, N.: Fluid Dynamics, Stability and Vapor-Liquid Slip in Boiling Reactor System, Session 1-11, p.230.

[16] Alia, P., Cravarolo, L., Hassid, A., Pedrocchi, E.: CISE-R-105 (1965).

[17] Egen, R.A., Dingee, D.A., Chastain, J.W.: BMI-1163 (1957).

[18] Larsen, H.C.: Ph.D. thesis, Univ. of Minnesota (1958).

[19] Sher, N.C.: M.S. thesis, Univ. of Minnesota (1955).

[20] William, H.V., Moulton, R.W.: Am. Inst. Chem. Engrs. J., 11 [6], 1114 (1965).

[21] Shirataki, K.: M.S. thesis, Kyoto Univ. (1965).

[22] Michiyoshi, I., Shirataki, K., Takitani, K.: Int. Chem. Eng., 7 [1], 159 (1967).

[23] Michiyoshi, I., Serizawa, A., Mitani, S.: J. At. Energy Soc. Japan, 10 [5], 238 (1968).

[24] Serizawa, A.: M.S. thesis, Kyoto Univ. (1968).

[25] Michiyoshi, I., Serizawa, A.: J. At. Energy Soc. Japan, 12 [6], 311 (1970).

[26] Smissaert, G.E.: ANL-6755 (1963).

[27] Petrick, M.: ANL-6581 (1962).

[28] Rouhani, S.Z.: AE-286 (1967).

[29] Chisholm, D., Laird, A.D.K.: Trans. Am. Soc. Mech. Engrs., Ser.C, Vol.80, 276 (1958).

[30] Ueda, T.: Trans. Japan Soc. Mech. Engrs., 33 [248], 601 (1967).

[31] Griffith, P., Clark, J.A., Rohsenow, W.M.: ASME Paper 58-HT-19, (1958).

[32] Marchaterre, J.F., Hoglund, B.M.: Nucleonics, 20 [8], 142 (1962).

[33] Martinelli, R.C., Boelter, L.M.K., Taylor, T.H.M., Thomsen, E.G., Morrin, E.M.: Trans. Am. Soc. Mech. Engrs., Vol.66, 139 (1944).

[34] Martinelli, R.C., Nelson, D.B., Schenectady, N.Y.: ibid., Vol.70, 695 (1948).

[35] Lockhart, R.W., Martinelli, R.C.: Chem. Eng. Prog., 45 [1], 39 (1949).

[36] Fried, L.: Chem. Eng. Progr. Symp. Ser., Vol.50, No.9, 47 (1954).

[37] Hoglund, B.M., Weatherhead, R.J., Epperson, T.R.: ANL-5760.

[38] Petrick, M.: ANL-5787 (1958).

[39] Anderson, G.H., Mantzouranis, B.G.: Chem. Eng. Sci., Vol.12, 109 (1960).

[40] Bennett, J.A.R., Thornton, J.D.: Trans. Instn. Chem. Engrs., Vol.39, 101 (1961).

[41] Akagawa, K.: Trans. Japan Soc. Mech. Engrs., 23 [128], 292 (1957).

[42] Katsuhara, T.: ibid., 24 [148], 1050 (1958).

[43] Gaspari, G.P., Lombardi, C., Peterlongo, G.: CISE-R-83 (1964).

[44] Thom, J.R.C.: Int. J. Heat Mass Transfer, Vol.7, 709 (1964).

[45] Huang, M.N., El-Wakil, M.M.: Nucl. Sci. Eng., Vol.28, 12 (1967).

[46] Geiger, G.E., Rohrer, W.M.: Trans. Am. Soc. Mech. Engrs., Ser.C, Vol.88, 1 (1966).

[47] Tarasova, N.V., Leontiev, A.I., Hlopuskin, V.I., Orlov, V.M.: Proc. 3rd Intern. Heat Transfer Conf., Chicago, Vol.4, 178 (1966).

[48] Shiba, S., Yamazaki, Y.: Trans. Japan Soc. Mech. Engrs., 32 [240], 1231 (1966).

[49] Bergles, A.E., Dormer, T.: Int. J. Heat Mass Transfer, Vol.12, 459 (1969).

[50] Milopol'skiy, Z.L., Shneyerova, R.I., Kalamysheva, A.I., Semin, E.T., Vinogradov, M.N.: ASME Heat Transfer-Soviet Research, Vol.1, No.1, 13 (1969).

[51] Hilding, W.E.: Proc. 3rd Intern. Heat Transfer Conf., Chicago, Vol.4, 167 (1966).

[52] Inoue, A.: Doctoral thesis, Tokyo Industrial College (19__).

[53] Inoue, A., Aoki, S.: Trans. Japan Soc. Mech. Engrs., 36 [288], 1358 (1970).

[54] Janssen, E., Kervinen, T.A.: GEAP-416 (1964).

[55] Moen, R.H.: Ph.D. thesis, Univ. of Minnesota (1956).

[56] Muscettola, M.: AEEW-R-284 (1963).

[57] Serizawa, A., Michiyoshi, I.: J. Nucl. Sci. Technol.,10 [7], 435 (1973).

[58] Levy, S.: Trans. Am. Soc. Mech. Engrs., Ser.C, Vol.80, 113 (1960).

[59] Zivi, S.M.: ibid., Vol.86, 247 (1964).

[60] Michiyoshi, I., Shirataki, K., Takitani, K.: J. At. Energy Soc. Japan, 8 [1], 16 (1966).

[61] Zuber, N., Findley, J.A.: Trans. Am. Soc. Mech. Engrs., Ser.C, Vol.87, 453 (1965).

[62] Polomik, E.E.: ibid., Vol.88, 10 (1966).

[63] Bankoff, S.G.: ibid., Vol.82, 265 (1960).

[64] Lottes, P.A., Flinn, W.S.: Nucl. Sci. Eng., Vol.1, 461 (1956).

[65] Levy, S.: Trans. Am. Soc. Mech. Engrs., Ser.C, Vol.82, 113 (1960).

[66] idem.: ibid., Vol.85, 137 (1963).

[67] Chisholm, D.: Int. J. Heat Mass Transfer, Vol.10, 1767 (1967).
[68] Hilding, W.E.: JSME 1967 Semi-Intern. Symp., 115 (1967).
[69] Sekoguchi, K.: Doctoral thesis, Osaka Univ. (1960).
[70] Lurie, H.: NAA-SR-11586 (1966).
[71] Noyes, R.C., Lurie, H.: 3rd Intern. Heat Transfer Conf., Vol.5 (1966).
[72] Fauske, H.K., Grolmes, M.A.: Winter Annu. Meeting Am. Soc. Mech. Engrs., New York, (1970).
[73] Fauske, H.K., Quinn, D.J., Jeans, W.C.: Trans. Am. Nucl. Soc., Vol.12, 305 (1969).
[74] Costa, J., Charlety, P.: Winter Annu. Meeting Am. Soc. Mech. Engrs., New York, (1970).
[75] Lewis, J.P., Groesbeck, D.E., Christenson, H.H.: NASA TN D-5323 (1969).
[76] Kuroyanagi, T., Ochiai, M., Furukawa, K.: 1969 Annu. Meeting At. Energy Soc. Japan, (1969).
[77] Ochiai, M., Kobayashi, K., Kuroyanagi, T., Furukawa, K.: 1970 Annu. Meeting At. Energy Soc. Japan, (1970).
[78] Takahashi, T., Kikuchi, Y., Haga, K., Ohkohchi, T., Hori, M.: 1972 Fall Meeting At. Energy Soc. Japan, (1972).
[79] Bernstein, E., Petrek, J.P., Rose, G.J., Horan, J.J.: PWAC-429 (1964).
[80] Baroczy, C.J.: Am. Inst. Chem. Engrs. J., 12 [5], 1028 (1966).
[81] Smith, L.R., Tek, M.R., Balzhiser, R.E.: ibid., 12 [1], 50 (1966).
[82] Balzhiser, R.E., Barry, R.E., Herman, M.Jr., Caswell, B.F., Andrew Padilla, Jr., Smith, L.R.: 05750-19-P, Univ. Michigan, (1965).
[83] Aladyev, I.T., Gavrilova, N.D., Dodovov, L.D.: ASME Heat Transfer-Soviet Research, 1 [4], 1 (1969). BNL-TR-267 (1969).
[84] Baroczy, C.J.: Chem. Eng. Progr. Symp. Ser., 64 [82], 12 (1968).
[85] Chen, J.C., Kalish, S.: 4th Intern. Heat Transfer Conf., Paris-Versailles, (1970).
[86] Balzhiser, R.E., et al.: AFAPL-TR-85 (1967).

[87] Prem, L.L., et al.: AI-68-117 (1968).
[88] Peterson, J.R.: NASA CR-842 (1967).
[89] Bond, J.A., Converse, G.L.: NASA CR-843 (1967).
[90] Smith, C.R., Tang, Y.S., Ross, P.T.: BNL-756.
[91] Tang, Y.S., Smith, C.R., Ross, P.T.: ORNL-3605, Vol.2.
[92] Thome, R.J.: ANL-6854 (1964).
[93] Milliot, B., Lazarus, J., Navarre, J.Ph.: Conference Internationale Sur La Surete Des Reacteurs a Neutrons Rapides, (1967).
[94] Neal, L.G.: ANL-6625 (1963).
[95] Smissaert, G.E.: ANL-6755 (L963).
[96] Tamao, S.: M.S. thesis, Kyoto Univ. (1970).
[97] Serizawa, A., Kataoka, I., Michiyoshi, I.: 1973 Annu. Meeting At. Energy Soc. Japan, E47 & E48, (1973).
[98] idem:: Bulletin Inst. Atomic Energy, Kyoto Univ., Vol.43, 56 (1973).
[99] idem : 1973 Fall meeting At. Energy Soc. Japan, B3, (1973).
[100] idem : Bulletin Inst. Atomic Energy, Kyoto Univ., Vol.44, 64 (1973)
[101] idem : ibid., Vol.45 (to be published).

PART I

OVER-ALL CHARACTERISTICS OF TWO-PHASE FLOW

I. INTRODUCTION

From a physical point of view, the main objective of the study of two-phase flow is to get some correct indication of a coupled thermo-hydrodynamic structure of a given flow, while, from an engineering viewpoint, emphases have been put on the determination of the heat transfer and pressure drop characteristics. For example, the nuclear design conditions are strongly bounded up with thermal design conditions.

The heat transfer and pressure drop characteristics of the flow depend strongly on the various independent variables of the flow, such as the volumetric gas fraction (void fraction) or the weight fraction of the gas (quality), the type of flow (flow pattern), the total flow rate of the fluid, the system pressure, the fluid properties, and on the geometry of the flow passage. Among these variables, the void fraction and the type of flow are the most important parameters which cannot be easily estimated directly from a given flow condition. However, the value of the over-all void fraction, a key quantity of interest defined as the fraction of the flow area filled by the gas phase, is not equal to that of the quality which can be estimated relatively easily, because the average linear velocities of the gas and the liquid phase are different due to the difference between the densities of the two phases. As pointed out elsewhere, the void fraction and the type of flow are closely related to the pressure drop in two-phase flow, and accurate information about them is therefore prerequisite for evaluation of the two-phase pressure drop.

The pressure drop, which may affect the heat transfer characteristics through causing a change in the hydrodynamics along the flow path, has been the most investigated item in two-phase flow from both the experimental and theoretical viewpoints. A desirable result is usually the total pressure drop over a given channel length. The measured total pressure drop is given by the sum of three different

terms corresponding respectively to the hydrostatic head due to the gravity force, to the acceleration loss due to the velocity variation along the flow direction, and to the frictional loss due to the resistance experienced by the fluid in its motion. The first and the second losses can be calculated from the void fraction data. On the contrary, the last term, the frictional loss, can never be uniquely determined by the void fraction.

Accordingly, in the study of two-phase flow, one must always take into account the average void fraction, the different type of flow, and the frictional pressure drop.

General descriptions of two-phase flow phenomena are summarized in detail in Refs.[1-6].

PART I of this thesis summarizes a series of the experimental works of the author on the average void fractions in steam-water, air-water, and argon-mercury two-phase flows flowing upward in a vertical pipe, concentric annuli, and in rod-bundles[7-10], on the frictional pressure drop in air-water flow under atmospheric pressure [9], and on some behaviors of a single bubble rise in upward and downward water flow in vertical and inclined pipes, annuli, and also in rod-bundles[11]. It also summarizes the empirical correlation recommended for predicting the average void fraction in a wide range of flow variables[7], and the pressure drop correlation for predicting the frictional pressure drop of the ordinary non-metallic and metallic fluid flows, which both take into consideration the mass velocity effects, the pressure level effects and the effects of the fluid properties[12,13,14].

In the last chapter of this PART, an analytical model for predicting some hydrodynamic characteristics of droplet-dispersed annular flow, such as the flow rates of the liquid film on the pipe wall and the entrained liquid droplets, the deposition rate of the droplets, and the deposition coefficient, is proposed by introducing a concept of a probability distribution function for the residence time of the liquid droplet in the thin liquid film on the wall[15].

REFERENCES

[1] Tong, L.S.: Boiling Heat Transfer and Two-Phase Flow, John Wiley & Sons, (1965).

[2] Silvestri, M.: Advances in Heat Transfer, Vol.1, 355 (1964).

[3] Akagawa, K.: Kikai-no-Kenkyu (in Japanese), Yokendo Ltd., 17 [8] — 18 [2], (1965-1966).

[4] Sekoguchi, K.: ibid., 21 [1], 140 (1969).

[5] Ueda, T.: Trans. Japan Soc. Mech. Engrs., 33 [248], 601 (1967).

[6] Govier, G.W., Aziz, K.: The Flow of Complex Mixtures in Pipes, Van Nostrand Reinhold Co., (1972).

[7] Michiyoshi, I., Serizawa, A., Mitani, S.: J. At. Energy Soc. Japan, 10 [5], 238 (1968).

[8] Michiyoshi, I., Serizawa, A.: ibid., 12 [6], 311 (1970).

[9] Serizawa, A.: M.S. thesis, Kyoto Univ. (1968).

[10] Tamao, S.: M.S. thesis, Kyoto Univ. (1970).

[11] Michiyoshi, I., Serizawa, A.: 1969 Fall Meeting At. Energy Soc. Japan, E29, (1969).

[12] Serizawa, A., Michiyoshi, I.: 1972 Annu. Meeting At. Energy Soc. Japan, F41, (1972).

[13] idem.: Bulletin Inst. Atomic Energy , Kyoto Univ., Vol.42, 11 (1972).

[14] idem.: J. Nucl. Sci. Technol., 10 [7], 435 (1973).

[15] Serizawa, A., Mishima, K., Michiyoshi, I.: 1971 Fall Meeting At. Energy Soc. Japan, D36, (1971).

II. GENERAL DESCRIPTION OF FLOW PATTERNS

Consideration of the type of flow (flow pattern or flow regime) is indeed necessary for understanding or full description of the two-phase flow phenomena.

Flow pattern charts have been usually traced starting mostly from qualitative visual inspections by eye or by photographic technique, which makes it very difficult to translate it in quantitative term. Therefore, the number of characteristic flow patterns and names used for specifying them vary somewhat from investigator to investigator, depending on the flow with or without heat addition, the flow geometry, and on other mechanical parameters. To increase clarity, four major characteristic flow patterns (bubble flow, slug flow, dispersed-annular flow, and mist flow) can be considered as basic descriptive terms identifying the various flow patterns.

These and the parasitic flow patterns in vertical upflow are described below in the order of increasing quality or gas flow rate. Each flow pattern is illustrated in Fig.2.1.

2.1 Bubble Flow

The gas phase is approximately uniformly dispersed as a suspension of small bubbles in the continuous liquid phase. The small gas bubbles, of which shape vary from spheres or spheroids to oblate spherical caps, move more or less independently of each other at velocities which depend upon their size, shape, and also upon their ambient flow field. This region is most stable in flows without heat addition or any large pressure gradient along the flow direction, and is the most popular type of flow. In water-cooled and moderated reactors and high pressure boilers, this type of flow is believed to play an important role in their performance characteristics.

2.2 Developing Slug Flow (Bubble-to-Slug Transition Flow)

With a further increase in gas flow rate at constant liquid flow rate, some of individual smaller bubbles may coalesce to form larger cap-shaped or bullet-shaped bubbles, so-called Taylor bubbles or slugs, of very nearly the same diameter as the pipe and many diameters long. In this region of flow, only over the downstream section of the flow path, these bubble coalesces become important, and the trailing short bubbles will rapidly overtake the leading bubbles and coalesce to form longer bubbles. This makes the transition to the next stable flow pattern, slug flow.

2.3 Slug Flow

Slug flow is characterized by alternately coming bullet-shaped bubbles which are surrounded by a thin liquid annulus, and separated by the slugs of liquid containing trailed small bubbles.

In this region, a large scale periodic flow instability may be induced correspondingly to every passage of the bullet-shaped bubbles.

2.4 Ripple Flow (Slug-to-Annular Transition Flow)

As the gas flow rate is further increased, the slug length increases until eventually the slugs touch to fill the core of the pipe with gas, and the liquid distributes itself between an upward moving wavy or ripply layer of liquid on the pipe wall and coarse droplets carried in the continuous gas phase. This region may be characterized as a developing film flow.

2.5 Dispersed-Annular Flow

At slightly higher gas velocities, the liquid film on the wall becomes relatively smooth as a result of attrition of liquid into the faster moving phase. A fraction of the liquid is continuous in an annulus around the solid boundary of the channel, and the remainder

flowing discontinuously in the form of small droplets entrained by the gas stream in the core of the annulus.

2.6 Mist Flow

At even higher gas flow rates, the liquid does not cover the wall of the pipe any longer. When the liquid film on the wall does not exist or is disrupted, the liquid deficient region is entered, where the complete liquid distributes itself as small droplets in the gaseous core. This type of flow is called mist flow.

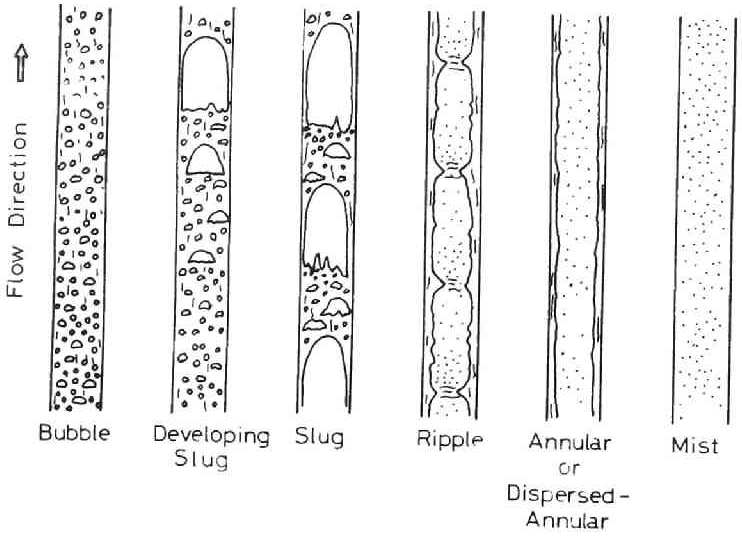

Fig. 2.1 Typical flow patterns in a vertical upflow

III. VOID FRACTION MEASUREMENT

3.1 General

The successful design and operation of boiling process systems and other sytems using a two-phase flow depend, to a large extent, upon the comprehensive predictions for void fraction.

Theoretical study of gas-liquid two-phase flow has been reported by a relatively limited number of papers. Levy[1] used a momentum exchange model to predict steam void fraction and pressure drop. But the results of the void fraction for steam-water are in general agreement but were consistently low, particularly at low pressures. Bankoff[2] used variable-density single-fluid model for two-phase flow by introducing power law variations for velocity and void fraction, with unity local slip ratio, to predict the average void fraction and the frictional pressure drop multiplier. Good agreement for steam voids was obtained for the cases shown in his paper. Houghton[3] used a bubble force balance, diffusion concept, and a volumetric balance, with assuming bubbles as free particles, and also assuming Markoff process for their motions, to obtain the simultaneous equations for the axial variations of the void fraction and temperature. Levy[4] applied the mixing length concept to the established two-phase flow, with assuming that the mixing length for momentum exchange was equal to that for the density. Zivi[5] used the principle of minimum entropy production, with assumptions of frictionless annular flow, to obtain the slip ratio. Zuber and Findley[6] took into account the effect of the local relative velocity between the two phases upon the void fraction, and obtained a linear relationship between the average absolute velocity of the gas phase and the mixture velocity with a slope of C_o and an intercept of V_{so}, where C_o and V_{so} are the distribution parameter and the terminal velocity of a bubble or a slug in stationary liquid. They obtained values C_o and V_{so} for several

different flow patterns. Polomik[7] used the principle of minimum total kinetic energy to obtain the expressions for the void fraction. Michiyoshi et al.[8] applied a bubble force balance for bubble flow which took into consideration the hydrodynamic effect of mutual interference between the bubbles, and they finally obtained the expression for the slip ratio or the void fraction which includes the effects of the liquid velocity upon them in an explicit mathematical form. The results are in good agreement with the experimental results of their own, Cook[9], and Egen et al.[10] for steam-water sytems.

However, most of the available information regarding the average void fraction or slip ratio between phases are based on the experimental studies, and numerous methods have been proposed for predicting such quantities. The correlations of Lockhart & Martinelli[11] for various fluids, Martinelli & Nelson[12] for steam-water under various pressure levels, Hughmark & Pressburg[13], Hughmark[14], Marchaterre & Hoglund[15], von Glahn[16], and Baroczy[17] are typical ones. Despite these progresses in the prediction of the void fraction, only a few works take into account the mass velocity effects on void fraction in mathematical or diagrammatical forms, which have been often observed to be significant.

It is the purpose of this chapter to summarize the results of a series of experimental studies of the author on the void fraction in steam-water flow, air-water flow, and argon-mercury flow in pipes, annuli, and in rod-bundles, and to clarify the effects of the mass velocity of the fluid, the heat flux through the heating wall, the fluid properties, and of the geometric configuration of the flow channel, based upon the experimental results.

The experiments described thereafter are one of a series that describes heat transfer and fluid flow studies performed at the Reactor Engineering Laboratory, Department of Nuclear Engineering, Kyoto University.

Measurements of the void fraction in pipe flow of steam-water mixture is described in detail in Ref.[8,18], and of argon-mercury

in Ref.[19].

3.2 Steam-Water Experiments

Measurements were carried out of the steam void fraction of a steam-water mixture flowing upward under atmospheric pressure in concentric annuli with inner and outer diameters respectively 9.5 mm and 21 mm, 9.5 mm and 55 mm, and 10 mm and 28.5 mm, and in 4-rod and 7-rod bundle geometries of triangular lattice with inner rod diameter and channel diameter respectively 9.5 mm and 55 mm, and with p/d ratio 1.37 and 1.79, which is defined as the ratio of the pitch to diameter of the rods arranged in triangular lattice.

The experiments were performed with use made of a capacitance-type void meter.

3.2.1 Experimental Equipment and Procedure

The general flow loop components are shown schematically in Fig.3.1. Details of these loop components, instrumentation and operation are given in Ref.[20].

The measuring test sections were made of transparent polycarbonate pipes in order to make visual observation of the flow patterns possible. The void fraction was measured by means of a capacitance-type void meter which is based, in principle, on the difference of the dielectric constant between liquid water and its vapor[18].

Test runs were made by fixing the flow rate of water (city water) and the heat flux through the electrically heated wall, and then increasing the inlet temperature of the water until the signal of the void meter indicated the presence of vapor.

Geometries of the test sections are summarized in Table 3.1 with some additional descriptions, and are illustrated of their cross sections in Fig.3.2.

3.2.2 Experimental Results in Annular Passage

Figures 3.4 and 3.5 show the effect of the superficial water velocity V_o on the relation between the steam void fraction α and the

steam weight fraction (quality) X obtained for different pipe diameters with smoothly surfaced heater rod, when the heat flux q is approximately 1.8×10^5 kcal/m^2·hr. As pointed out in Ref.[8], α increases usually with an increase in V_o. In these figures, values calculated by the correlation of Martinelli-Nelson[12] and those calculated by an empirical equation proposed by Nishino and Yamazaki[25]* are also given for atmospheric pressure. The solid lines in both figures will be mentioned later. The transition boundaries of the flow patterns are also shown in figures. When the flow changes from bubble flow to slug flow, the steam void fraction does not vary smoothly, i.e., it once decreases. But it smoothly changes from slug flow to annular flow. This is the same trend that was observed in pipe flow[8] (see Fig.3.6).

Figure 3.7 shows the effect of the heat flux upon the relation between α and X at V_o = 0.45 m/sec. For constant steam quality, the steam void fraction decreases with increasing the heat flux except in the bubble flow region where the steam quality is small. This trend is comparatively conspicuous in low velocity region, but it appears scarcely at higher velocities or when the heat flux is sufficiently large. This experimental evidence may account for why such effects cannot be found or inverse effect has been reported for higher-pressure saturated-boiling data[26,27].

Figures 3.8 and 3.9 indicate the effects of the velocity and heat flux upon the relation between the slip ratio S and the steam quality, where the over-all slip ratio is defined by

$$S = \frac{V_g}{V_l} = \frac{1 - \alpha}{\alpha} \frac{X}{1 - X} \frac{\rho_g}{\rho_l} \quad . \tag{3.1}$$

As indicated in these figures, the slip ratio increases in general

---

* $$\alpha = 1 - \left[\frac{(1 - X)\rho_g}{X\rho_l + (1 - X)\rho_g} \right]^{1/2}$$

with an increase in the steam quality for constant velocity and the heat flux. These figures also indicate, on the other hand, that the slip ratio decreases with increasing the velocity and with decreasing the heat flux for constant steam quality.

Figure 3.10 shows a comparison of the steam void fraction data obtained for smoothed and roughened surface heater rods, which indicates no significant effect of the surface roughness of the heater upon the void fraction.

3.2.3 Experimental Results in Rod-Bundle Geometries

Figure 3.11 demonstrates the effect of the superficial water velocity on the relation between the steam void fraction and the steam quality in 4-rod bundle geometry with the rod pitch p = 1.7 cm (p/d = 1.79). The tendency of this effect seen in this figure is well consistent with those shown in Fig.3.4 and in the experimental data obtained by other investigators in single flow passages of different shape such as pipes and rectangular ducts[9,10,28,29].

Figures 3.12 and 3.13 represent the effects of the distribution of the heat flux give independently to individual heater rods upon the steam void fraction (in both figures, "q_i" represents the heat flux through the surface of the i-th heater rod, of which number refers to that shown in Fig.3.2). In small quality region of the flow, the bubble flow region, the steam void fraction increases with increasing the steam quality, just like in pipe flows. However, these figures show that a larger discontinuity of the steam void fraction exists in rod-bundle geometries at the transition from bubble to slug flow than in other types of flow passage. This peaking of the steam void fraction in α-X diagram appears to depend greatly on the heat flux distribution over the cross-sectional area of the total flow channel. In some cases, there may be found two or three peaks. This interesting phenomenon may be accounted for by introducing a concept of thermohydrodynamically divided subchannels of the flow, and by recalling that a given flow pattern can take place independently within each individual subchannel (see Fig.3.14). Then, the peaking of the steam void frac-

tion averaged over the total flow area may happen at every transition from bubble to slug flow occurring in the individual subchannels. And the intensity of the peaking phenomenon or the difference between the maximum and the minimum values of the steam void fraction at the transition, is closely related to the difference in rising velocity or slip velocity between small bubbles and larger slugs. It may be also estimated, by referring to the study of Rowe & Angle[30] on the mixing rates between the adjacent subchannels in two-phase flow, that this peaking of the steam void fraction well corresponds to the peak in the mixing rate caused by the turbulent interchange.

Now, we will attend to the dependence of the general behavior of the steam void fraction upon the hydraulic equivalent diameter of the channel. In the case q = 0, the steam void fraction in the concentric annulus D_h = 11.5 mm (shown in Fig.3.7) is a little higher than that in the circular pipe of D_h = 13.8 mm shown in Ref.[8] for the same velocity V_o. This trend qualitatively agrees with the predicted one by Marchaterre-Hoglund correlation[15] for pipes and rectangular channels. However, any significant difference cannot be found between the experimental data in concentric annuli shown in Fig.3.4 (D_h = 11.5 mm) and in Fig.3.5 (D_h = 45.5 mm). On the other hand, in rod-bundle geometry, the steam void fraction is somewhat lower than that in the circular pipe and in the concentric annulus, especially in slug flow region. It is approximately 5 percents lower in 4-rod bundle geometry, and approximately 10 percents lower in 7-rod bundle geometry. As mentioned later, this difference may probably be ascribed partly to the shape and the rising velocity of slugs which strongly depend on the flow geometry.

3.2.4 Axial Void Fraction Profile

In order to deduce accurately the frictional pressure drop from the measured total pressure drop in boiling liquid two-phase flow systems, a need is strongly felt for a correct knowledge of the axially changing steam void fraction, since the terms, such as the average density of the fluid both in the subcooled boiling and the bulk boil-

ing regions, the frictional pressure drop in the subcooled boiling region, and the acceleration pressure drop, have to be evaluated from the axially distributed void fraction. In this calculating procedure, we usually assume some correlation between the steam void fraction and the steam quality under certain special conditions. But this procedure may be subjected to some errors.

Measurements were carried out of the axially changing steam void fraction for boiling water two-phase flow in a concentric annulus with use of a capacitance type void meter. 15 pairs of the copper electrodes (50 mm in length, 40 mm in width and 0.3 mm in thickness) were installed at every 10 cm distance in contact with the inside diameter of the measuring pipe (see Table 3.1). The hydraulic resistance of the flow channel with the electrodes in single-phase water flow agreed well with the Colebrook's expression for the friction factor vs. Reynolds number with the equivalent sand roughness $\varepsilon/D = 0.001$.

Typical distributions of the steam void fraction are represented in Fig.3.15 for some cases of the smoothed and the roughened heater rod. A characteristic S-shaped distribution is a very popular one[26]. This figure demonstrates no systematic effects of the surface roughness of the heater, and of the heat flux through the heating wall upon the axial variation of the steam void fraction within the range of flow variables covered in the present experiment.

The data of Rouhani[26] shown in Fig.3.16, for reference, indicate clearly that, for low mass velocities, a marked effect of the heat flux upon the steam void fraction can be seen in the subcooled boiling region where an increase in the heat flux increases the void fraction, and this effect in the subcooled boiling region may extend into the bulk boiling region but with a reducing tendency. While, for larger mass velocities of the order of magnitude 10^6 kg/m^2·hr, the tendency of this effect is reduced, i.e., the void fraction increases only slightly with an increase in the heat flux. This tendency does not always agree qualitatively with that observed in our experiment (see, for example, Fig.3.7).

Now, we will attempt to explain qualitatively the experimental results of the effect of the heat flux on the void fraction with an aid of the generally accepted knowledges of boiling heat transfer. In general, the steam void fraction depends strongly on the number of bubble nuclei distributed over the surface of the heated wall, the bubble frequency, the departure diameter of bubbles, the bubble shape, and the bubble rise velocity. The possible dominant parameters specifying these quantities are the volume of vapor generated per unit time per unit area of the heating surface, and the bubble rise velocity. If spherical bubbles are assumed, the volume of vapor produced per unit time over a given area and a given length of the heating surface, Q_v, is given by

$$Q_v = \frac{\pi}{6} A l \; d_b^3 \; nF \qquad (3.2)$$

where, A, l, d_b, n, and F are the heated area (cm^2), the heater length (cm), the bubble diameter (cm), the density of bubble nucleus ($1/cm^2$), and the bubble frequency per unit length of the heater (1/sec·cm).

(a) Subcooled boiling region ($X < 0$):

In the subcooled region, the bubbles are in an environment of subcooled water so that they slowly collapse as they are swept downstream. Therefore, the void fraction in this region depends mainly upon the vapor volume produced on the heating surface rather than upon the bubble rise velocity. According to a textbook on boiling heat transfer, for example, Ref.[43], the bubble diameter and the product Fd are not seriously affected by increasing the heat flux, while the density of the bubble nucleus increases with an increase in the heat flux. Accordingly, an increase in the heat flux increases the vapor volume production and hence the steam void fraction. This predicted trend agrees well with the experimental data of Rouhani (Fig.3.16).

(b) Bulk boiling region ($X > 0$):

Also according to Ref.[43], the bubble nucleus density n

increases in proportion to approximately h^3, where h is the heat transfer coefficient. If we assume $q \propto \Delta T_{sat}^{3}$ for fully-developed nucleate boiling, we have $n \propto q^2$. The experimental data of Nishikawa et al.[44] in pool boiling of water with using a 0.5 mm diam. platinum wire indicate that, for the heat flux range $q > 1 \times 10^5$ kcal/m^2·hr, so-called coalesced bubble region, d increases linearly with the heat flux, and F is approximately constant. Consequently, an increase in the heat flux increases the vapor volume Q_v defined by E_q.(3.2). This effect is a positive contribution to increasing the steam void fraction. On the other hand, an increase in bubble diameter means an increase in bubble rising velocity or the slippage between two phases[45], and hence a decrease in the void fraction. Therefore, the tendency of the effect of the heat flux upon the void fraction in bulk boiling region may be determined by the competition between these two effects, and therefore, it depends upon the experimental conditions, such as the state of the heating surface, the heat flux, the water velocity, the system pressure, the fluid temperature, the fluid properties, the flow geometry, and so on.

Among the suggested methods for predicting the axial variation of the steam void fraction both in the subcooled and the bulk boiling regions[31-38], Bowring's physical model[33] seems to be the most elaborate one. Comparisons of this model with a little modification[20] with the present data are given in Fig.3.17. Comparisons of Levy's theory[34] with the data are also demonstrated in Fig.3.18. These comparisons indicate a good agreement between the Bowring's model and the experimental data, but a large discrepancy between Levy's theory and the data.

3.3 Air-Water Experiments

An attempt was made for air-water flow in a vertical concentric annulus with and without discrete surface roughness of the flow passage

in order to study the effects of the fluid properties and of the surface roughness upon the void fraction, and also in order to improve the two-phase flow correlation proposed by the author et al.[22] for predicting the void fraction for steam-water flows at various pressure up to 2,000 psia (see the succeeding chapter).

3.3.1 Experimental Apparatus and Measuring Equipment

The experimental apparatus used for the measurement of the steam void fraction of steam-water two-phase flow schematically shown in Fig.3.1 was also available for this experiment in air-water flows.

The air supply was obtained from the 8-ata supply line in the laboratory, and the air was introduced into the mixing section & lower plenum through a series of 84 holes (1.5 mm diameter) spaced along the periphery of the $1^1/_4$-inch pipe, and its flow rate was measured by means of an orifice. The 150-mesh screen of stainless steel was placed between the outlet of the lower electromagnetic valve and the entrance to the test section in order to disperse any large air bubbles, and to give a uniform distribution and bubble size at the entrance.

The test section was a concentric annulus made of a 1848 mm long and 28.5 mm i.d. transparent polycarbonate pipe, and a 10 mm o.d. rod with and without discrete surface roughness made of wire rings (Fig.3.3).

The void fraction was measured by trapping the liquid in the test section by simultaneously shutting "quick-closing" electromagnetic valves at entry and exit, then measuring the trapped liquid.

3.3.2 Experimental Results and Discussions

Figure 3.19 represents the effect of the superficial water velocity upon the channel average void fraction in the case of a smooth surface, of which tendencey is in qualitative agreement with those shown in Figs.3.4, 3.5, 3.10, and 3.11, i.e., the void fraction increases as a rule with an increase in the water velocity. From this figure, it will be seen that the void fraction in air-water flow is somewhat a little higher than that in steam-water flow under nearly the same flow conditions. The data shown in this figure indicate no marked peaking of the void fraction at the transition from bubble flow to slug flow,

while, as mentioned earlier, a marked peaking was observed in steam-water flows. This difference in the peaking phenomenon may be perhaps due to the difference in the definition of the term "void fraction". Namely, the cross-sectional average value was used for steam-water data, while the channel average value for air-water data. In general, the transition from bubble flow to slug flow may take place first at a certain downstream position of the test channel, and then gradually extends over the whole section of the channel with an increase in the gas flow rate. Hence, the effect of the change of flow patterns locally occurring may be reduced by the averaging procedure in getting the void fraction over the whole channel length.

Figure 3.20 demonstrates the intensity of the effect of the surface roughness of the flow passage upon the channel average void fraction. It can be seen that this effect is negligibly small. This is a large discrepancy between the data of the present work and the work of Chisholm & Laird[39]. They measured the void fraction of air-water mixture in smooth and rough horizontal pipes also by means of the quick-closing mechnical cocks. They finally obtained an empirical void fraction correlation for 1.018-inch diameter galvanized pipe with sand uniformly distributed on its surface ($\varepsilon/D = 0.068$). Their correlation is given by

$$0.8/(1 - \alpha)^{1.75} = 1 + \frac{21}{\overline{X}} + \frac{1}{\overline{X}^2} \tag{3.3}$$

where

$$\overline{X} = \left(\frac{1 - X}{X}\right)^{0.875} \left(\frac{\mu_l}{\mu_g}\right)^{0.125} \left(\frac{\rho_g}{\rho_l}\right)^{0.5} \tag{3.4}$$

The equivalent sand roughness of the flow passages we tested was approximately 0, 0.02 ~ 0.03, and 0.04 ~ 0.06 (Fig.5.1). However the difference between the results of the author and Chisholm & Laird may be accounted for, to some extent, by taking into consideration the effects of the surface roughness upon the bubble rising velocity,

details are not yet clarified.

The solid lines in figures are predicted curves calculated from the authcr's correlation, Eq.(4.12).

3.4 Argon-Mercury Experiment

Since, in general, the density ratio ρ_l/ρ_g for liquid metal two-phase flow is much greater than that for ordinary non-metallic fluid two-phase flow, and slippage between the two phases seems to some extent to be dependent upon the surface tension of the liquid, two-phase flow characteristics are expected to be also different between them.

An advantage in utilizing two-phase flow as an accelerating device for MHD power generator using mercuy as a working fluid depends greatly upon the slippage between two phases. Therfore, it seems very fruitful to acquire the complete knowledge or the accurate experimental data on void fraction in gas-mercury two-phase flow systems.

An experimental study was carried out for upward argon-mercury two-phase flow in a vertical pipe of stainless steel with non-wetting property between the pipe and mercury.

Details of the experiment are described in Ref.[19].

3.4.1 Experimental Apparatus and Measuring Techniques

The mercury loop schematically shown in Fig.3.21 consists of two vertical legs known as the riser (test section) and downcomer. The mercury pumped up to the upper plenum by a diaphragm pump falls down through the downcomer and flows up through the test section by gravitational force. The accumlator was used to avoid the flow pulsation. The mercury and the argon gas were mixed in a special mixer sleeve at the bottom of the test section. The mercury circulation rate was measured by means of an electromagnetic flowmeter.

The test section was made of the untreated stainless steel pipe of 27 mm i.d. and 1,200 mm long. The mounting studs for probes were installed at the downstream distance of the entrance to the test section, Z = 350, 750, and 1,150 mm (corresponding Z/D = 13.0, 27.7, and

42.9, respectively).

The void fraction measurements were performed with an electrical resistivity probe very similar to that described later in detail in PART II. The cross-sectional average void fraction was deduced by integrating the local void fraction profile.

3.4.2 Experimental Results and Discussions

Typical profiles of the local void fraction are shown in Figs. 3.22 and 3.23. The general trend is that the profile changes, as a rule, from a uniform to a dome-shaped with a maximum at pipe center, as the quality increases. However, any accurate information could not be obtained about the relation between the shape of that profile and the flow patterns. An increase in the local void fraction towards the wall was observed in all experimental runs, and is expected to be the result of the non-wetting property between the mercury and the pipe wall.

A comparison of the profiles obtained at different axial positions for constant superficial mercury velocity V_o and constant quality X indicates the developing or accelerating characteristics of the flow due to the large pressure gradient along the flow direction.

Figure 3.24 demonstrates the dependence of the average void fraction upon the mercury velocity V_o. Despite some scatters of the data, it will be seen from this figure that the average void fraction increases significantly with increasing the mercury velocity for constant pressure and constant quality. It will be also seen that the void fraction for constant mercury velocity and constant quality decreases with an increase in pressure.

Smissaert[40] measured the void fraction of nitrogen-mercury flow by differential pressure method, backed up by γ-ray traversing technique, with utilizing the mercury-wetted test section of a stainless steel pipe (2-inch i.d.) plated with a 0.002-inch nickel coating after treatment by dilute hydrochloric acid. A comparison between the data of Neal[41] (nitrogen-mercury: non-wetted surface), the present work (argon-mercury: non-wetted surface), and of Smissaert (nitrogen-

mercury: wetted-surface, see Fig.3.25) appears to hold promising information about the effect of the wettability upon the void fraction, though it is premature to compare these data directly, since they were obtained with different measuring techniques under different flow conditions. These data appear to indicate a higher void fraction for non-wetted system than for the wetted. This may be closely related to the experimental evidence that large gas bubbles or slugs were apt to rise along the non-wetted wall. Further details are referred to Ref.[42].

3.5 Summary and Conclusions

The study was undertaken with the purpose of providing the void fraction data for steam-water, air-water, and argon-mercury two-phase flow systems. The effects of the flow patterns, the fluid properties, the superficial liquid velocity, heat flux through the heating surface, the flow geometry, and the surface roughness of the flow passage upon the void fraction have been summarized.

It was confirmed that, especially, the superficial liquid velocity and the fluid properties have significant influences on the void fraction or slippage in gas-liquid mixtures.

The effect of the flow patterns was found to be significant at the transition from bubble flow to slug flow. This follows the peaking in the void fraction-quality diagram, and the intensity of this effect was more markedly observed especially in rod-bundle geometries than in more simple shaped flow passages.

REFERENCES

[1] Levy, S.: Trans. Am. Soc. Mech. Engrs., Ser.C, Vol.82, 113 (1960).

[2] Bankoff, S.G.: ibid., Vol.82, 265 (1960).

[3] Houghton, G.: Nucl. Sci. Eng., Vol.11, 121 (1961).

[4] Levy, S.: Trans. Am. Soc. Mech. Engrs., Ser.C, Vol.85, 137 (1963).

[5] Zivi, S.: ibid., Vol.86, 247 (1964).

[6] Zuber, N., Findley, J.A.: ibid., Vol.87, 453 (1965).

[7] Polomik, E.E.: ibid., Vol.88, 10 (1966).

[8] Michiyoshi, I., Shirataki, K., Takitani, K.: Int. Chem. Eng., 7 [1], 159 (1967).

[9] Cook, W.H.: ANL-5621, (1965).

[10] Egen, R.A., Dingee, D.A., Chastain, J.W.: Battelle Memorial Inst., Rept. No. 1163, (1957).

[11] Lockhart, R.W., Martinelli, R.C.: Chem. Eng. Prog., 45 [1], 29 (1949).

[12] Martinelli, R.C., Nelson, D.B.: Trans. Am. Soc. Mech. Engrs., 70 [6], 39 (1948).

[13] Hughmark, G.A., Pressburg, B.S., Am. Inst. Chem. Engrs. J., Vol.7, 677 (1961).

[14] Hughmark, G.A.: Chem. Eng. Prog., 58 [4], 62 (1962).

[15] Marchaterre, J.F., Hoglund, B.M.: Nucleonics, 20 [8], 142 (1962).

[16] von Glahn, U.H.: NASA TN-D-1189, (1962).

[17] Baroczy, C.J.: Chem. Eng. Progr. Symp. Ser., 61 [57], 179 (1965).

[18] Shirataki, K.: M.S. thesis, Kyoto Univ., (1965).

[19] Tamao, S.: M.S. thesis, Kyoto Univ., (1970).

[20] Serizawa, A.: M.S. thesis, Kyoto Univ., (1968).

[21] idem.: B.S. thesis, Kyoto Univ., (1966).

[22] Michiyoshi, I., Serizawa, A., Mitani, S.: J. At. Energy Soc. Japan, 10 [5], 238 (1968).

[23] Kitagawa, K.: B.S. thesis, Kyoto Univ., (1967).

[24] Michiyoshi, I., Serizawa, A.: J. At. Enervy Soc. Japan, 12 [6], 311 (1970).

[25] Nishino, H., Yamazaki, Y.: ibid., 5 [1], 39 (1963).

[26] Rouhani, S.G.: Symposium on Two-Phase Flow, Univ. of Exeter, Exeter, (1965).

[27] Jordan, D.P., Leppert, G.: Int. J. Heat Mass Transfer, Vol.5, 751 (1962).

[28] Yanai, M.: Doctoral thesis, Kyoto Univ., (1971).

[29] Hoglund, B.M., Weatherhead, R.J., Epperson, T.R.: ANL-5760, (1961).

[30] Rowe, D.S., Angle, C.W.: BNWL-371, Pt.2, (1967).

[31] Griffith, P., Clark, I.A., Rohsenow, W.M.: Paper No.58-HT-19 presented at the ASME-AIChE Joint Heat Transfer Conf., Chicago, (1958).

[32] Mauer, G.W.: WAPD-BT-19, (1960).

[33] Bowring, R.W.: Institutt for Atomenergi, Halde, Norway, HPR-10, (1962).

[34] Levy, S.: Int. J. Heat Mass Transfer, Vol.10, 951 (1967).

[35] Rouhani, S.Z.: AE-286, (1967).

[36] Kroeger, P.G., Zuber, N.: Int, J. Heat Mass Transfer, Vol.11, 211 (1968).

[37] Staub, F.W.: Trans. Am. Soc. Mech. Engrs., Ser.C, Vol.90, 151 (1968).

[38] Larsen, P.S., Tong, L.S.: ibid., Vol.91, 471 (1969).

[39] Chisholm, D., Laird, A.D.K.: Trans. Am. Soc. Mech. Engrs., Ser.C, Vol.80, 276 (1958).

[40] Smissaert, G.E.: ANL-6755, (1963).

[41] Neal, L.G.: ANL-6625, (1963).

[42] Serizawa, A., Michiyoshi, I.: J. Nucl. Sci. Technol., 10 [7], 435 (1973).

[43] Futto-Netsu-Dentatsu (in Japanese): Japan Soc. Mech. Engrs., (1964).

[44] Nishikawa et al.: Technol. Rep. of Kyushu Univ., 33 [1], 24 (1960).

[45] Kiho-Ekiteki-Kogaku (in Japanese): Japan Soc. Chem. Engrs., p.5 (1969).

NOMENCLATURE

A	heated area
C_o	distribution parameter
d	rod diameter
d_b	bubble diameter
D	pipe diameter
D_h	hydraulic equivalent diameter of the flow passage
e	height of discrete surface roughness
F	bubble frequency per unit length of heater
g	gravitational constant
G	mass flow rate
h	heat transfer coefficient
l	heater length
n	bubble nucleus density, or number of wire rings
p	rod pitch or wire ring pitch
P	pressure
$P.D$	power density
q	heat flux
Q_v	volume of vapor production per unit time over a given area and length of the heating surface
r	radial position
R	pipe radius
S	over-all slip ratio
T_l	liquid temperature
T_s	saturation temperature
T_w	wall temperature
ΔT_{sat}	temperature difference ($= T_w - T_s$)
ΔT_{sub}	inlet subcooling ($= T_s - T_l$)
V_g	average phase velocity of gas
V_l	average phase velocity of liquid
V_o	superficial liquid velocity
V_{so}	terminal velocity of a single bubble in stationary water

X	quality
$\bar{X}$	flow modulus defined by Eq.(3.4)
Z	axial position
α	average void fraction
α_l	liquid fraction (= 1 - α)
α_{loc}	local void fraction
ε/D	equivalent sand roughness
μ_g	viscosity of gas
μ_l	viscosity of liquid
ξ	property index defined by $(\mu_l/\mu_g)^{0.2}/(\rho_l/\rho_g)$
ρ_g	density of gas
ρ_l	density of liquid

Table 3.1 Geometry of the test section

Geometry of the flow passage	Reference	Description of the test section	Range of flow variables	Remarks
Annulus	[21,22]	Inner diam. 9.5 mm$^{\phi}$ Outer diam. 21.0 mm$^{\phi}$ Length 850 mm	P ≃ 1 ata V_o = 0.15 ~ 1.0 m/sec q = 0 ~ 2.08 × 10^5 kcal/m^{2}h X = 0 ~ 0.08	Measurements were performed at the downstream distance Z = 700 mm from the entrance to the test section. Inner rod was a sheathed electrical heater with smooth surface.
Annulus	[23]	Inner diam. 9.5 mm$^{\phi}$ Outer diam. 55.0 mm$^{\phi}$ Length 1000 mm	P ≃ 1 ata V_o = 0.15, 0.23, 0.30 m/sec q = 1.5, 1.9 × 10^5 kcal/m^{2}h	500 mm long calming section was installed upstream of the test section. Measurements were performed at Z = 750 mm. Inner rod was a sheathed electrical heater with smooth surface.
Annulus	[20]	Inner diam. 10.0 mm$^{\phi}$ Outer diam. 28.5 mm$^{\phi}$ Length 1848 mm	P ≃ 1.2 ata G = 2.3, 3.4 × 10^6 kg/m^{2}h q = 0 ~ 5.5 × 10^4 kcal/m^{2}h X = 0 ~ 0.008	500 mm long calming section was installed upstream of the test section. This test section was used mainly for measurement of the axial variation of the void fraction along the flow direction. Inner rod was a sheathed electrical heater with and without discrete surface roughness, e/d = 0, 0.05, 0.10, and 0.15 (Fig.3.3).
4-rod bundle	[20,24]	Rod diam. 9.5 mm$^{\phi}$ Outer diam. 55.0 mm$^{\phi}$ Length 1000 mm Triangular lattice	P ≃ 1 ata V_o = 0.15 ~ 0.30 m/sec q = 0 ~ 8.6 × 10^4 kca/m^{2}h X = 0 ~ 0.03 p = 1.3, 1.7 cm	500 mm long calming section was installed upstream of the test section. Measurements were performed at Z = 750 mm, with giving various heat input to each heater rod independently.
7-rod bundle			P = 1 ata V_o = 0.2, 0.3 m/sec q = 0 ~ 4.5 × 10^4 kcal/m^{2}h X = 0 ~ 0.12 p = 1.7 cm	

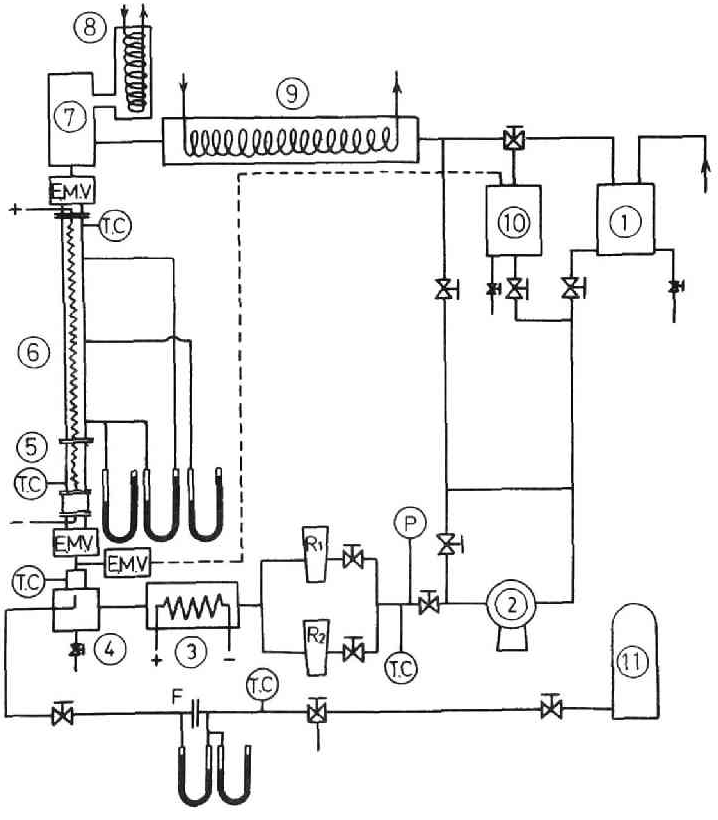

	Designation
①	Storage Tank & Boiler
②	Slurry Pump
③	Preheating Tank
④	Lower Plenum
⑤	Calming Section
⑥	Test Section
⑦	Upper Plenum
⑧	Condenser
⑨	Cooler
⑩	Auxiliary Tank
⑪	Air Compressor
E.M.V	Electromagnetic Valve
F	Orifice Flowmeter
R_1, R_2	Rotameter
P	Pressure Gauge
T.C	Thermocouple

Fig. 3.1 Schematic representation of water loop

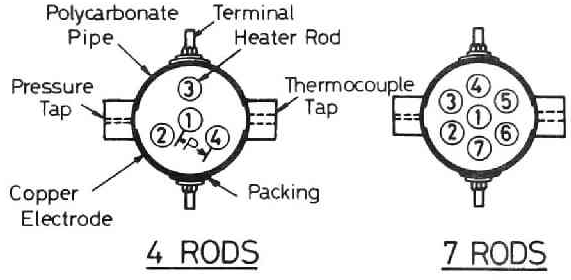

Fig. 3.2 Geometric configuration of flow channels

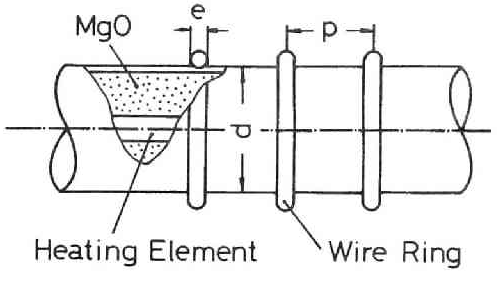

	e mm$^{\phi}$	p mm	n	e/d	ε/D
Smooth surface	0.0				0.0
Rough surface	0.5	5	300	0.05	0.02
Rough surface	1.0	10	150	0.10	0.04 ~ 0.06
Rough surface	1.5	15	100	0.15	0.04 ~ 0.06

d 10 mm$^{\phi}$

n : number of wire rings

ε/D : equivalent sand roughness

Fig. 3.3 Schematic of surface roughness of heater rods

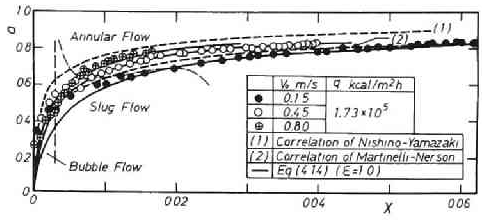

Fig. 3.4 Effect of water velocity upon the steam void fraction (D_p= 21 mm)

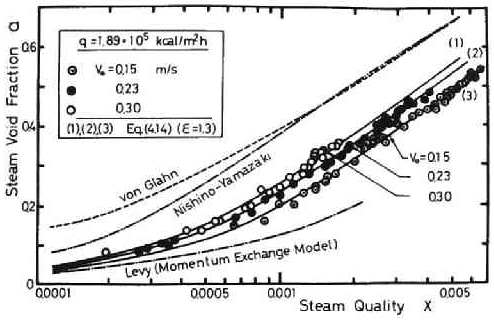

Fig. 3.5 Effect of water velocity upon the steam void fraction (D_p= 55 mm)

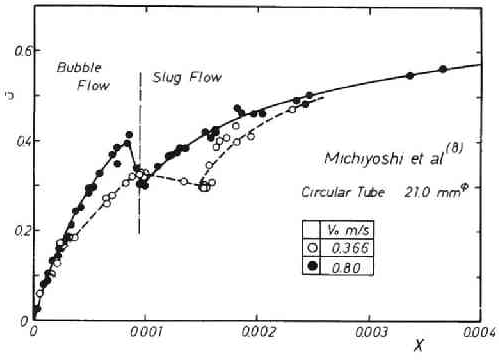

Fig. 3.6 Effect of flow pattern upon the steam void fraction (data of Michiyoshi et al.[8])

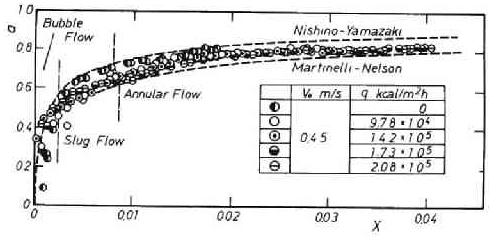

Fig. 3.7 Effect of heat flux upon the steam void fraction (D_p=21 mm)

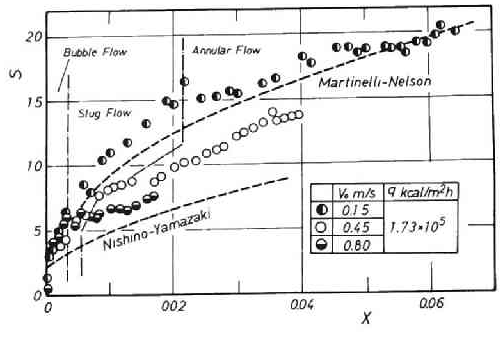

Fig. 3.8 Effect of water velocity upon slip ratio (D_p=21 mm)

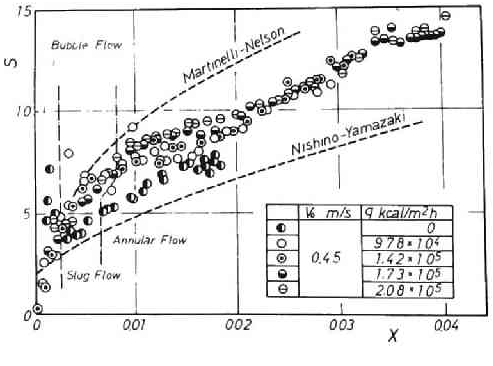

Fig. 3.9 Effect of heat flux upon slip ratio (D_p=21 mm)

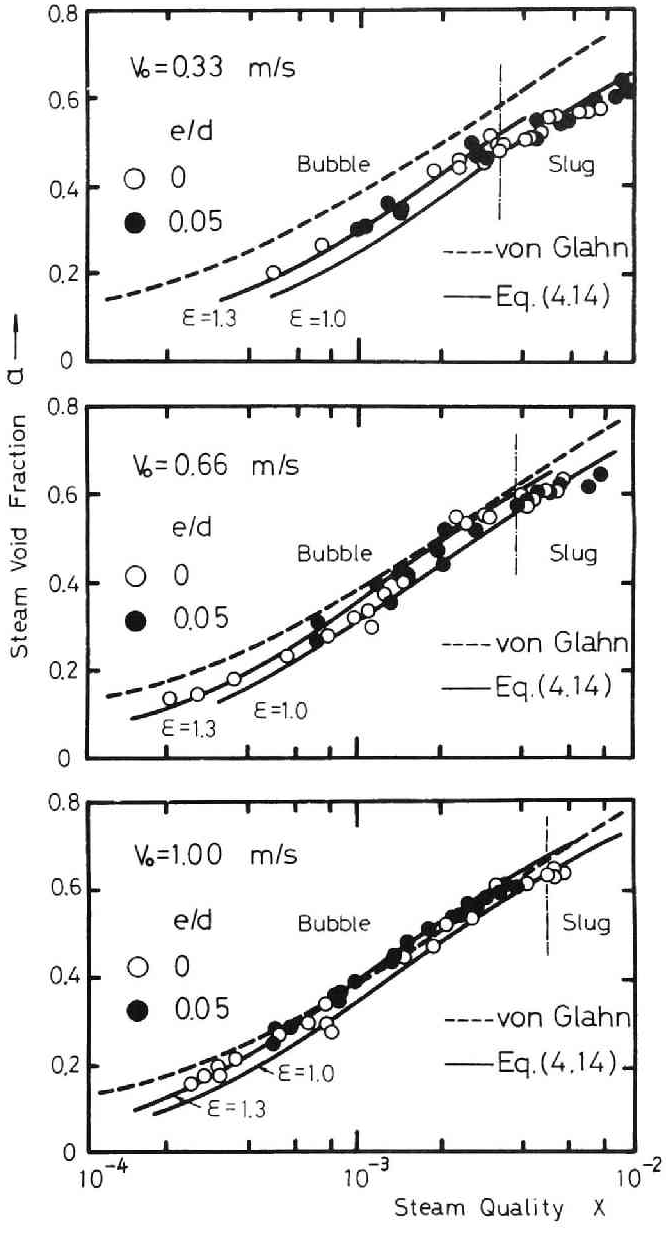

Fig. 3.10 Effect of surface roughness upon the steam void fraction (annulus : D_b=28.5 mm, D_s=10 mm)

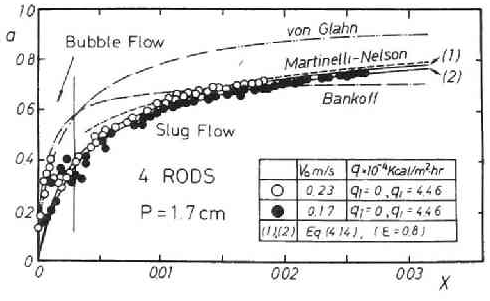

Fig. 3.11 Effect of water velocity upon the steam void fraction (4-rod-bundle)

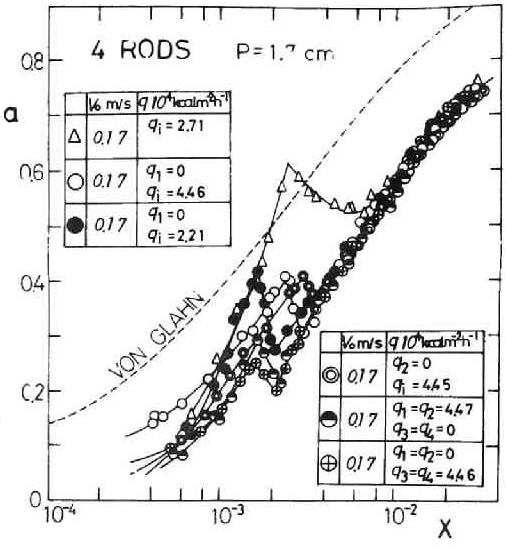

Fig. 3.12 Effect of heat flux upon the steam void fraction (4-rod-bundle)

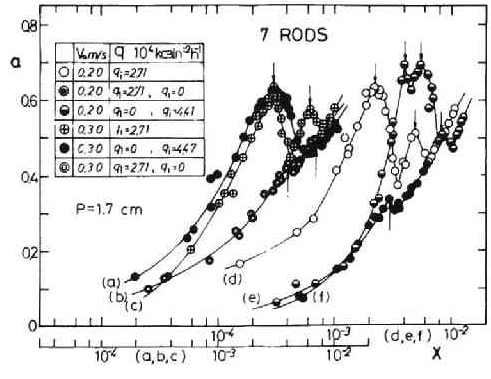

Fig. 3.13 Effect of heat flux upon the steam void fraction (7-rod-bundle)

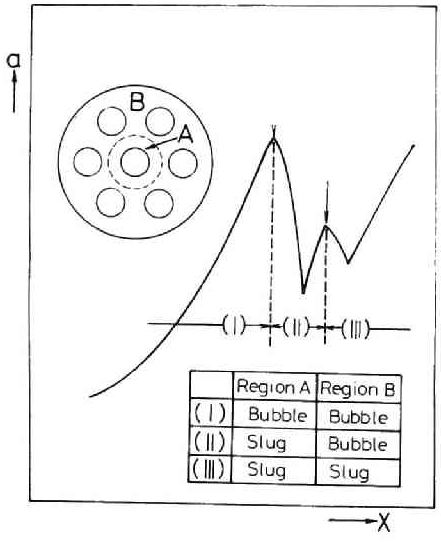

	Region A	Region B
(I)	Bubble	Bubble
(II)	Slug	Bubble
(III)	Slug	Slug

Fig. 3.14 Subchannels and flow patterns

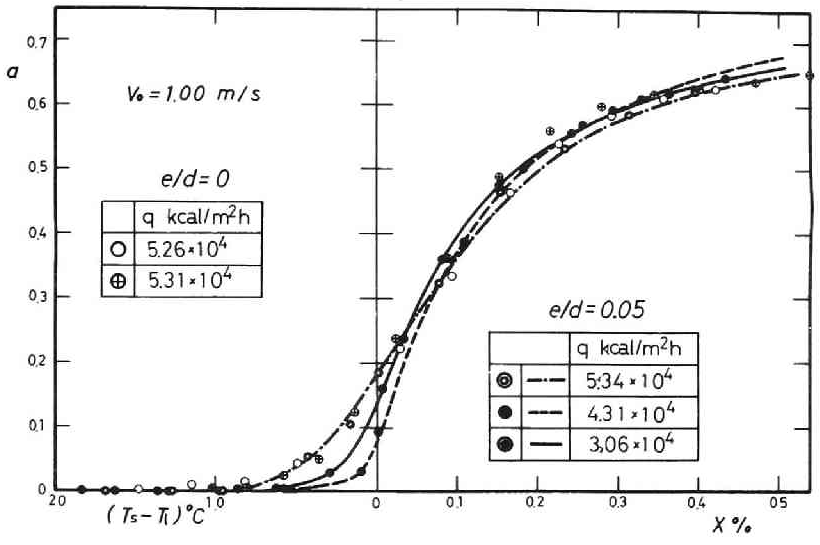

Fig. 3.15 Axial void fraction distribution in an annulus

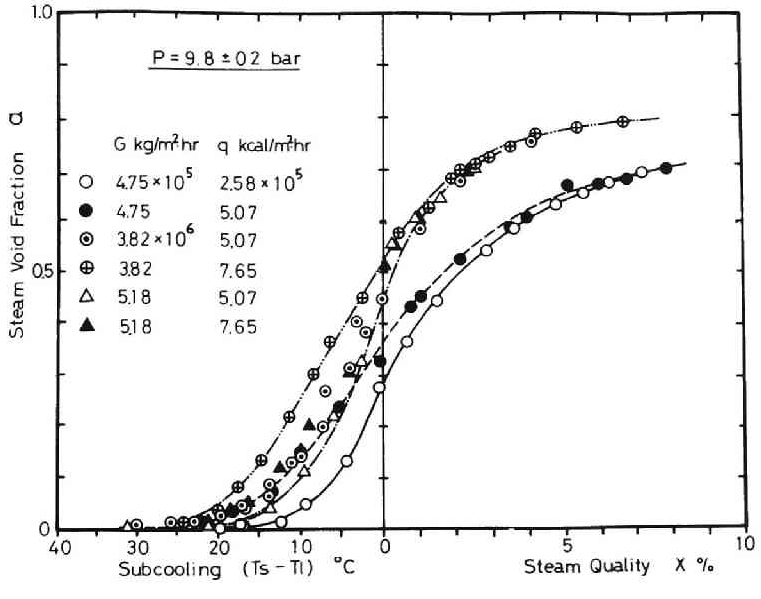

Fig. 3.16 Axial void fraction distribution obtained by Rouhani[26]

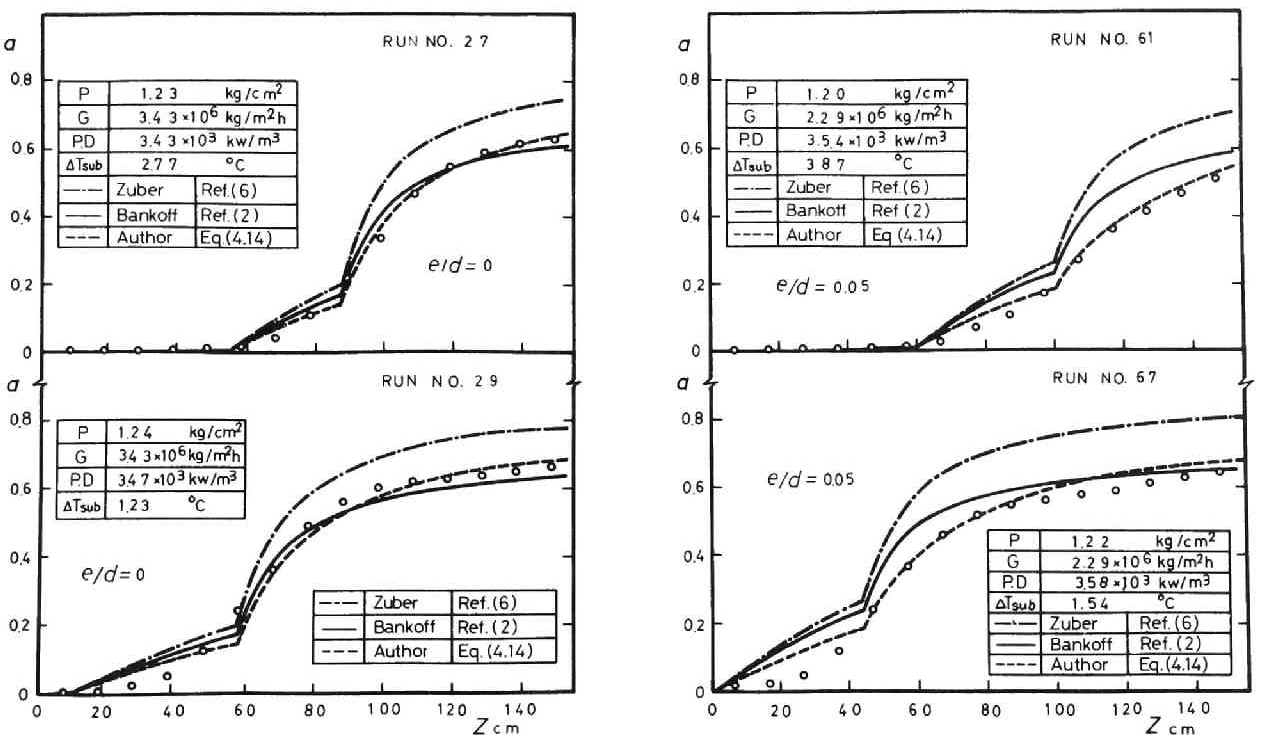

Fig. 3.17 Correlative representation of experimental void fraction distributions with Bowring's physical model

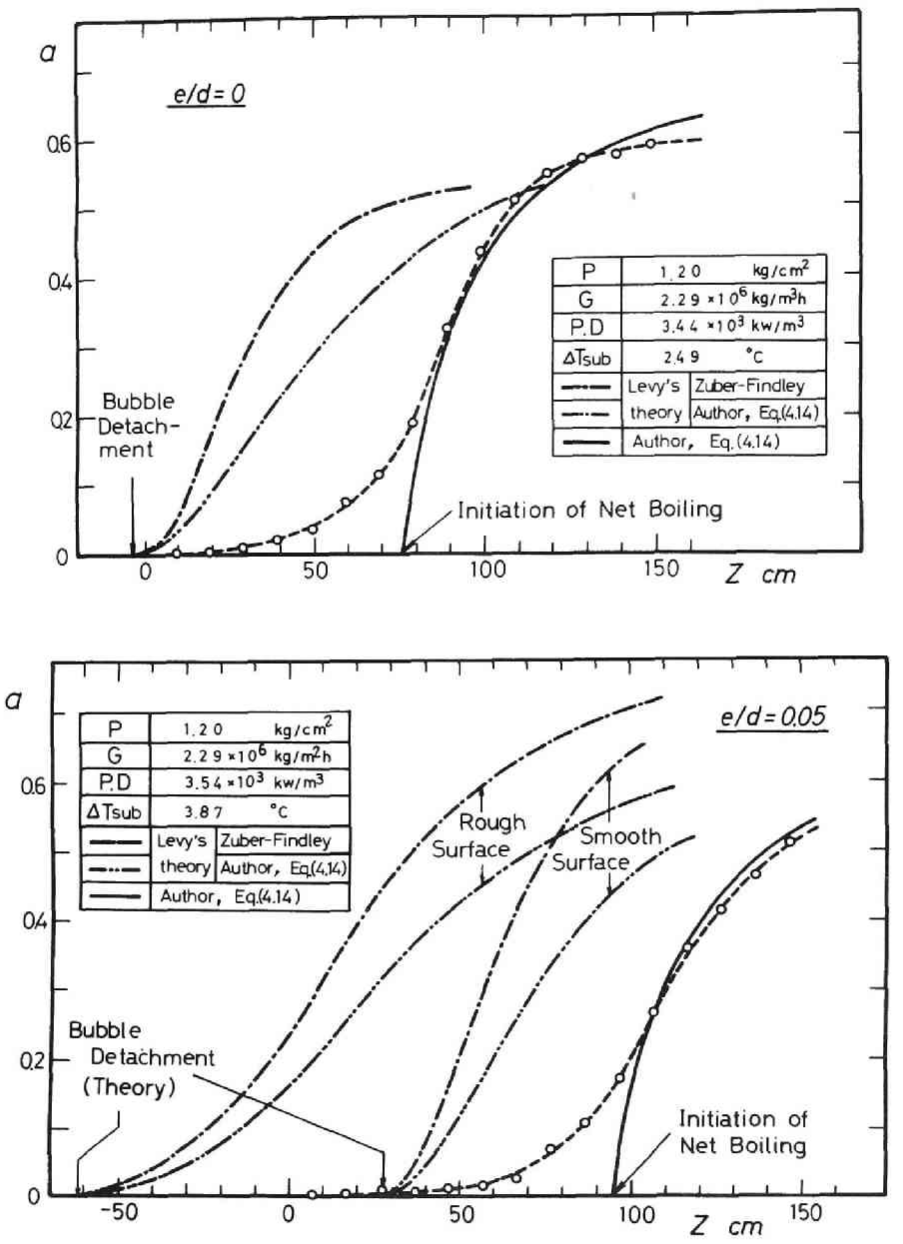

Fig. 3.18 Correlative representation of experimental void fraction distributions with Levy's theory

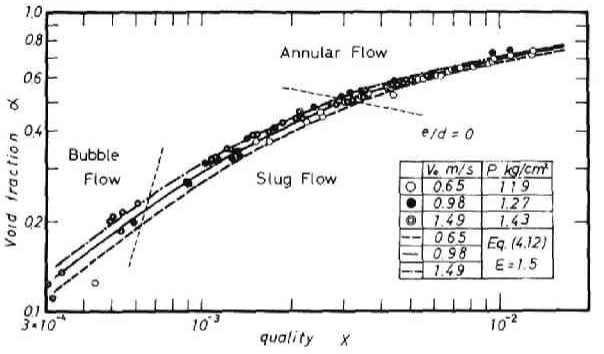

Fig. 3.19 Effect of water velocity upon the void fraction in air-water flow in a vertical smooth annulus

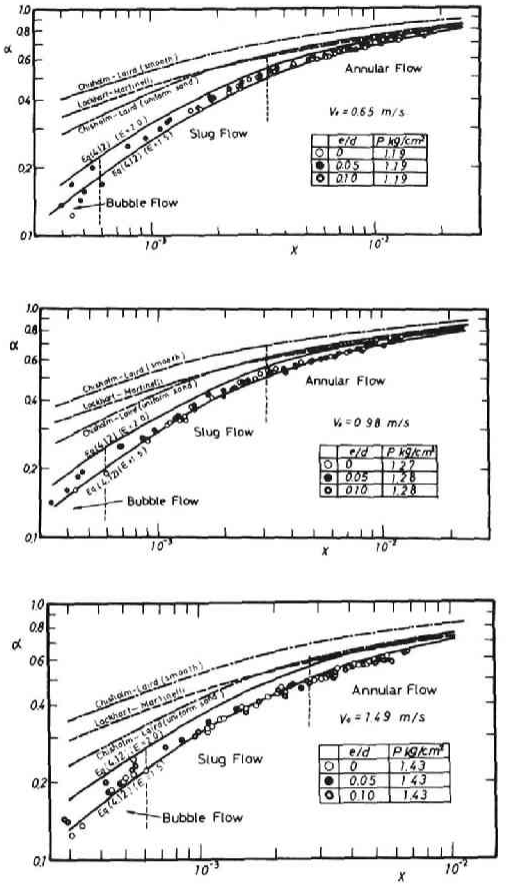

Fig. 3.20 Effect of surface roughness upon the void fraction in air-water flow in an annulus

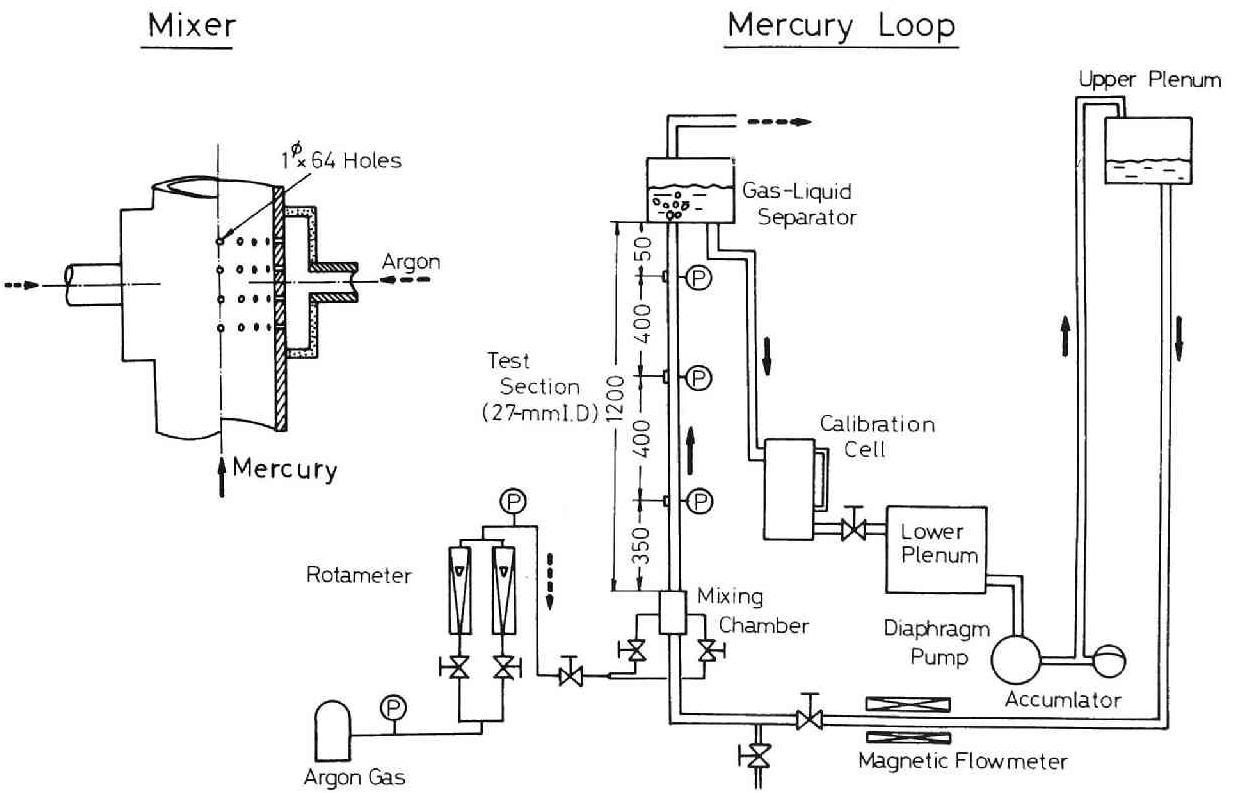

Fig. 3.21 Schematic representation of mercury loop

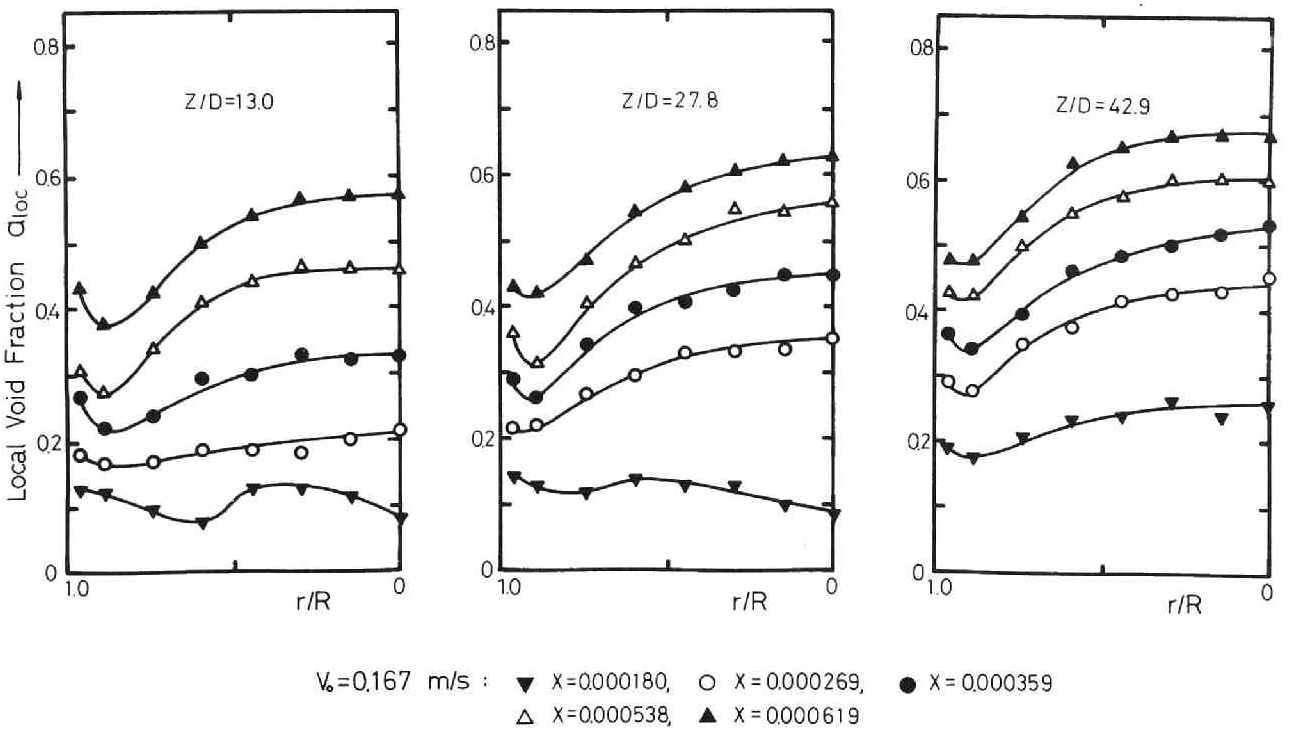

Fig. 3.22 Local void fraction in argon-mercury flow

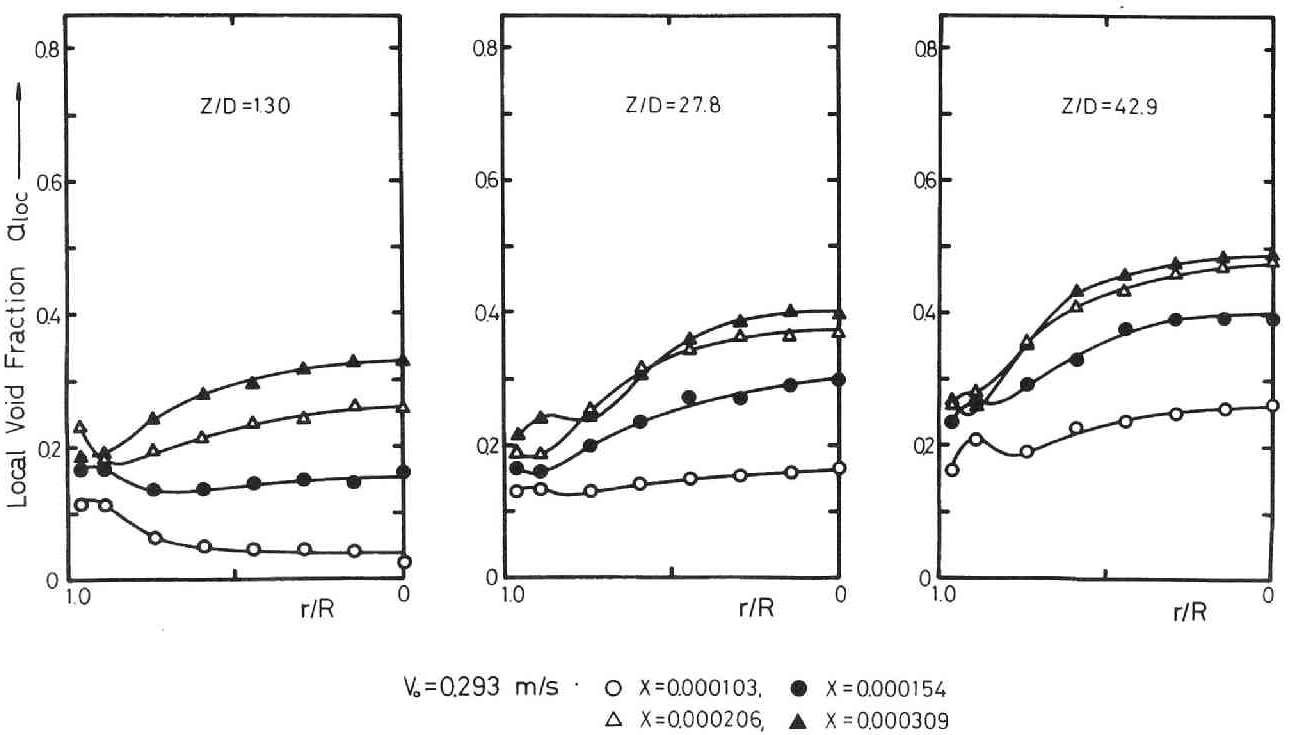

Fig. 3.23 Local void fraction in argon-mercury flow

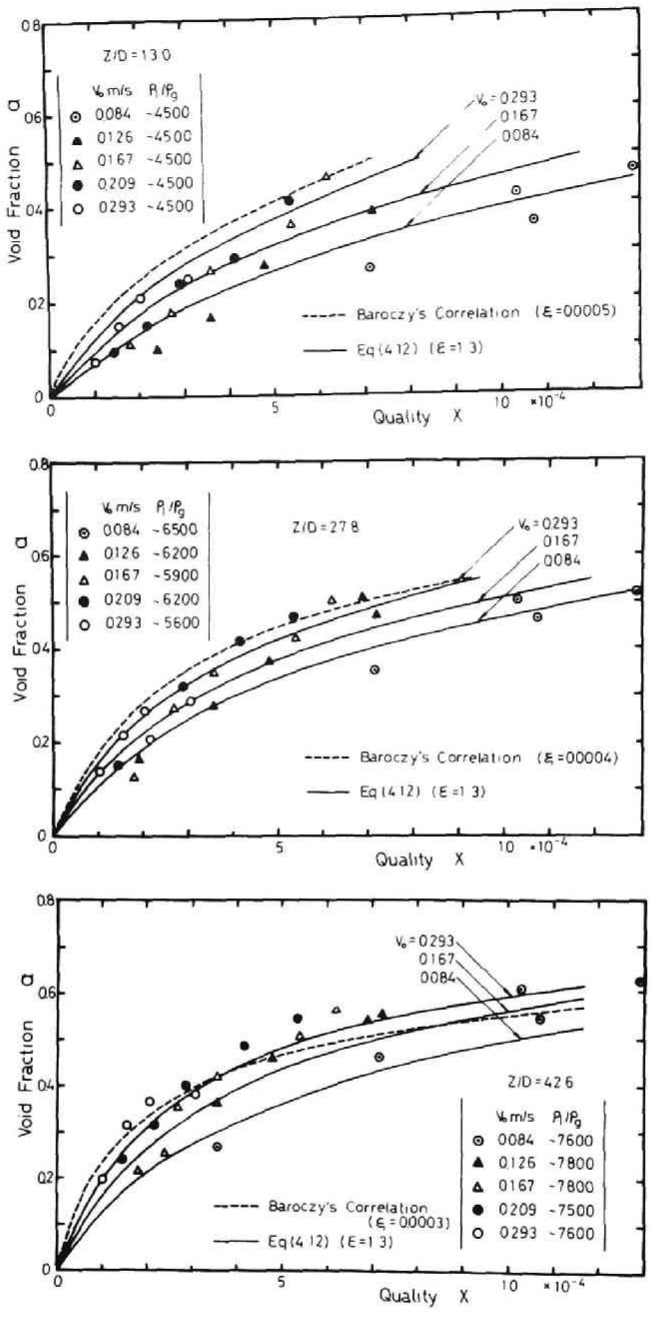

Fig. 3.24 Dependence of the void fraction upon mercury velocity

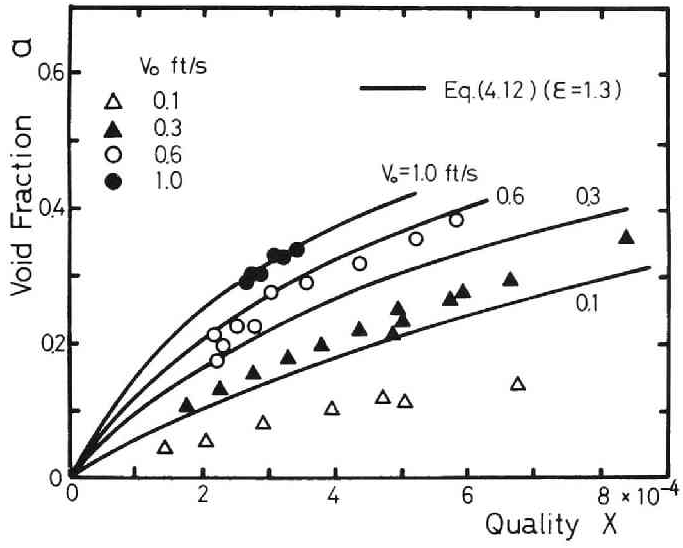

Fig. 3.25 Nitrogen-mercury void fraction data of Smissaert[40]

IV. VOID FRACTION CORRELATION

Among a considerable amount of correlations for predicting the void fraction, Baroczy's correlation[1], applicable to the liquid metal two-phase flows, has often been used for comparisons with experimental data, and similarly the Lockhart-Martinelli correlation[2]. But these correlations, as mentioned already, do not always agree well with measured data. And this may be attributable to the fact that the mass velocity effect is not at all taken into account, whose existence has been indicated by detailed surveys of experimenal data. The need is strongly felt for a more realistic correlation of void fraction applicable to the various conditions of two-phase flow.

This chapter summarizes an attempt to derive an empirical void fraction correlation from the aforementioned experimenal findings which is applicable for steam-water mixture flowing in a pipe, a concentric annulus, or in a rectangular duct extensively at various pressure levels up to 2,000 psia[3,4], and an attempt to identify the various flow geometries[5,6]. It also describes an attempt to extend the obtained correlation to be valid for various fluid two-phase flow systems[7,8].

The resulting void fraction correlation of the author incorporates the mass velocity effects, the effects of the fluid properties (or pressure level effects), and the effects of the flow geometry, which is valid not only for ordinary fluid two-phase flow but also for that of liquid metals within a wide range of flow variables, whether single or two-component.

4.1 Derivation of Void Fraction Correlation

The fluid enteres the test section in single liquid-phase at mass flow rate W and superficial velocity V_o. Assume that boiling occurs at a certain axial position z = 0, and at any point z = Z the fluid

flows in two-phase mixture at mass flow rate and cross-sectional average velocity W_l, V_l for liquid phase, and W_g, V_g for gas phase, respectively. (See Fig.4.1).

The increment of the kinetic energy flux in liquid phase between the two points, z = 0, and z = Z, is given by

$$\Delta E_{kl} = \frac{1}{2} (W_l V_l^2 - W V_o^2) \quad . \tag{4.1}$$

Here, from the equation of continuity for two phases, we have

$$\begin{aligned} W_l &= W (1 - X) \\ V_l &= V_o \frac{1 - X}{1 - \alpha} \end{aligned} \tag{4.2}$$

Substitute Eq.(4.2) into Eq.(4.1), and then

$$\Delta E_{kl} = \frac{1}{2} W V_o^2 \left[\frac{(1 - X)^3}{(1 - \alpha)^2} - 1 \right] \quad . \tag{4.3}$$

As shown in Fig.4.2, the increment of the dimensionless kinetic energy flux of the liquid $\Delta E_{kl} / (\frac{1}{2} W V_o^2)$ correlates neary proportionally with the steam quality X for given values of the heat flux q, the velocity V_o, and the operational pressure P. This experimental evidence gives the following approximation.

$$\frac{(1 - X)^3}{(1 - \alpha)^2} - 1 = KX \quad , \tag{4.4}$$

where K is a function of q, V_o, P, and probably the channel geometry (see Appendix I). (If we compare our data for V_o = 0.55 m/sec with Marchaterre's data for V_o = 0.51 ~ 0.56 m/sec and 115 psia in Fig.4.2, we can understand that the function K is greatly affected by the operational pressure.)

The function K was chosen to fit our experimental data obtained in a concentric annulus, and the data of Michiyoshi et al.[9] in a

pipe, and finally we obtained the following equation for predicting the void fraction with an application of the correlation for the steam-water systems at even higher pressure held in mind.

$$\alpha = 1 - \sqrt{\frac{(1 - X)^3}{1 + KX}} \tag{4.11}$$

$$K = \varepsilon \frac{\rho_l}{\rho_g} V_o^{0.5} \qquad (V_o: \text{ m/sec}) \tag{4.12}$$

$$\varepsilon = \begin{cases} 1.3 & \text{for bubble flow} \\ 1.0 & \text{for slug and annular flows} \end{cases} \tag{4.13}$$

In applying this correlation to the systems at nearly atmospheric pressure, the effect of the heat flux may well be taken into consideration by using the following equation instead of Eq.(4.12), though such an effect appears obscure in many published high pressure data.

$$K = \varepsilon \frac{\rho_l}{\rho_g} V_o^{0.5} \exp(-2 \times 10^{-6} q) \tag{4.14}$$

$$(q: \text{ kcal/m}^2 \cdot \text{hr})$$

At this stage, these equations are valid only for flows in geometrically simple flow passages such as pipes, concentric annuli, and rectangular ducts. In rod bundle geometries, as already stated in the foregoing chapter, the measured void fraction was a little lower than that in a pipe. A series of experiments on the rising velocity of a single air bubble, flowing upward in a cocurrent or countercurrent water flow in pipes, concentric annuli, and 4-rod and 7-rod bundle geometries, indicated the clear dependence of the slug velocity upon the flow geometry (see Chapter VII). Based upon this experimental finding, we determined the value ε for rod bundle geometry in terms of $(1 - D_h/D_b)$, where D_h and D_b are the hydraulic equivalent diameter of the flow passage and the inner diameter of the outer pipe. The results for slug and annular flows are represented in Fig.4.3 for velocity range $V_o \lesssim 0.5$ m/sec. For $V_o > 0.5$ m/sec, 0.8 is recommended for ε

for slug and annular flows in rod bundle geometry. On the other hand, for bubble flow, we may take 1.3 times value of ε given in Fig.4.3 (see Table 4.1).

4.2 Comparison of the Correlation with Experimental Data

Figures 4.4 to 4.12 represent comparisons of the predicted void fraction obtained with the present correlation using various experimental data by Michiyoshi et al.[9] (steam-water, pipe), Michiyoshi et al.[4] (steam-water, concentric annulus), Michiyoshi & Serizawa[6] (steam-water, 4-rod bundle), Marchaterre[10] (steam-water, rectangular duct), Hoglund et al.[11] (steam-water, rectangular duct), Egen et al.[12] (steam-water, rectangular duct), Alia et al.[13] (argon-water, and argon-ethyl alchol, pipe), and Staub & Zuber[14] (Freon, pipe), respectively. Other comparisons are shown in Chapter III with the data obtained in steam-water, air-water, argon-mercury, and nitrogen-mercury systems.

Generally speaking, these figures show good coincidence between the proposed correlation and experimental data for ordinary non-metallic fluid two-phase flows.

Other correlations for predicting void fraction used for comparisons are those of Martinelli & Nelson[15], Nishino & Yamazaki[16] (see footnote on page 20), von Glahn[17], Marchaterre & Hoglund[18], Baroczy[1], and CISE correlation[13]*.

---

* von Glahn's correlation:

$$1/X = 1 - (\rho_l/\rho_g)^{0.67} \left[1 - (1/\alpha)^{(\rho_l/\rho_g)^{0.1}}\right]$$

CISE correlation:

$$1 - \alpha = (1 - \beta) \left[1 + \frac{1.35\beta^{0.9+0.05\sigma}}{1 + 0.355G\sqrt{D/\sigma}} (1/\rho_g)^{1/4}\right]$$

4.3 Application of Proposed Correlation to Liquid Metal Two-Phase Flow Systems

It is well established that the void fraction in ordinary non-metallic fluid systems - such as steam-water or air-water - is influenced by the superficial liquid velocity V_o. This means that the void fraction α increases with the velocity V_o. But this effect is not very clearly revealed in experimental data of void fraction in such liquid metal two-phase flow systems as sodium and potassium.

Figure 4.13 shows a comparison between recent data on the sodium void fraction and the correlations by Lockhart-Martinelli[2] and Baroczy[1], in which the liquid fraction ($\alpha_1 = 1 - \alpha$) is plotted against the Martinelli modulus X_{tt}*. Figure 4.14 similarly represents recent data on the potassium void fraction. If the mass velocity effect is ignored, both the Lockhart-Martinelli and Baroczy correlations agree comparatively well with the recent data, but poorly with the earlier ones, as reported by Baroczy[19]. And these data on liquid metal void fraction reveal tendencies very similar to those for ordinary fluid two-phase flow. Potassium data would be expected to fall into the same region of α_1 vs. X_{tt} diagram as air-water two-phase data, since the hydrodynamic fluid properties of potassium are similar to those of water. Nevertheless, Baroczy[19] and Aladyev et al.[20] have reported that the mass velocity effect could not be appreciably observed in their experiments. Is this valid? Reviewing a number of representative experiments in liquid metal two-phase flow systems, we will attempt to clarify mainly the mass velocity effect on the liquid metal two-phase flow characteristics, and we will also discuss briefly applicability of the present author's correlation to liquid metal systems.

---

* $$X_{tt} = (W_l/W_g)^{0.9} \ (\rho_g/\rho_l)^{0.5} \ (\mu_l/\mu_g)^{0.2}$$

To compare various reported data for void fraction with Eq.(4.11), we can obtain the values $[K/(\rho_l/\rho_g)]$ for each data point as shown in Fig.4.15, in which $[K/(\rho_l/\rho_g)]$ is plotted against the superficial liquid velocity V_o. The solid and dotted lines represent Eq.(4.12) with letting $\varepsilon = 1.3$ and 1.4 respectively. This figure implies the existence of the mass velocity effect on void fraction explicitly in the liquid metal flow systems, with tendency qualitatively common with the case of ordinary non-metallic fluid systems.

Further assuming Eqs.(4.11) and (4.12), we can easily obtain the value ε for each data point. Figure 4.16 represents ε as a function of the property index $[(\mu_l/\mu_g)^{0.2}/(\rho_l/\rho_g)]$ proposed by Baroczy*. The data scatter around the value of 1.3 or 1.4. From these facts, it can be concluded that the mass velocity effect on void fraction for any single or two-component fluid can be determined from Eqs.(4.11) and (4.12) assuming 1.3 or 1.4 for ε.

Figure 4.17 shows a comparison of the correlating equations (4.11) and (4.12), - letting $\varepsilon = 1.3$ - with recent data on void fraction obtained by Aladyev et al.[20] and Baroczy[21] for potassium. The calculated values agree within ± 5%. Thus the author's void fraction correlation (Eqs.(4.11) and (4.12) with 1.3 for ε) is valid and can express very well the mass velocity effect not only for ordinary fluid flow but also for that of liquid metals, whether single or two-component.

In general, a correlation for predicting the void fraction in liquid metal two-phase flow systems is desired to take into consideration the effects of the magnetic field, the flow patterns, and wettability between the fluid and the wall as problems peculiar to the liqiud metals. But the contributions to these have been very scanty [22,23] (the effect of the last term has been discussed briefly in Chapter III), and so, details about such effects have not yet been

---

* Physical properties of the liquid metals used here were quoted from Ref.[31].

clarified. A brief comment will be seen in Ref.[8].

4.4 Conclusions

Empirical relations were developed to evaluate the void fraction as a function of the flow parameters such as the quality, the superficial liquid velocity, the heat flux through the heating surface, the flow patterns, the flow geometry, and the fluid properties. This correlation is also compared with published data of void fraction for non-metallic and metallic two-phase flow, and is found to predict satisfactorily the void fraction not only for ordinary non-metallic fluids but also for liquid metal two-phase flow in a wide range of flow variables.

The recommended void fraction correlation is summarized here again:

$$\alpha = 1 - \sqrt{\frac{(1 - X)^3}{1 + KX}}$$

$$K = \varepsilon \, (\rho_l/\rho_g) \, V_o^{0.5} \qquad (V_o: \text{ m/sec})$$

The value ε is given as represented in Table 4.1. If the effect of the heat flux is applied for steam-water flow under atmospheric pressure, the function K defined above should be corrected with being multiplied by the term $[\exp(-2.0 \times 10^{-6})]$ (q: kcal/m^2·hr).

REFERENCES

[1] Baroczy, C.J.: Chem. Eng. Progr. Symp. Ser., 61 [57], 179 (1965).

[2] Lockhart, R.W., Martinelli, R.C.: Chem. Eng. Progr., 45 [1], 39 (1949).

[3] Serizawa, A.: B.S. thesis, Kyoto Univ., (1966).

[4] Michiyoshi, I., Serizawa, A., Mitani, S.: J. At. Energy Soc. Japan, 10 [5], 238 (1968).

[5] Serizawa, A.: M.S. thesis, Kyoto Univ., (1968).

[6] Michiyoshi, I., Serizawa, A.: J. At. Energy Soc. Japan, 12 [6], 311 (1970).

[7] Serizawa, A.: Reactor Engineering Research, Reactor Engineering Laboratory, Dept. Nucl. Eng., Kyoto Univ., 6 [17], 7 (1971).

[8] Serizawa, A., Michiyoshi, I.: J. Nucl. Sci. Technol., 10 [7], 435 (1973).

[9] Michiyoshi, I., Shirataki, K., Takitani, K.: Int. Chem. Eng., 7 [1], 159 (1967).

[10] Marchaterre, J.F.: ANL-5522, (1956).

[11] Hoglund, B.M., Weatherhead, R.J., Epperson, T.R.: ANL-5760, (1961).

[12] Egen, R.A., Dingee, D.A., Chastain, J.W.: BMI-1163, (1957).

[13] Alia, P., Cravarolo, L., Hassid, A., Pedrocchi, E.: CISE-R-105, (1965).

[14] Staub, F.W., Zuber, N.: GEAP-4631, (1964).

[15] Martinelli, R.C., Nelson, D.B.: Trans. Amer. Soc. Mech. Engrs., 70 [6], 39 (1948).

[16] Nishino, H., Yamazaki, Y.: J. At. Energy Soc. Japan, 5 [1], 39 (1963).

[17] von Glahn, U.H.: NASA TN-D-1189, (1962).

[18] Marcharerre, J.F., Hoglund, B.M.: Nucleonics, 20 [8], 142 (1962).

[19] Baroczy, C.J.: AI-AEC-12804, (1970).

[20] Aladyev, I.T., et al.: BNL-TR-267, (1969).

[21] Baroczy, C.J.: Chem. Eng. Progr. Symp. Ser., 64 [82], 12 (1968).

[22] Thome, R.J.: ANL-6854, (1964).

[23] Smissaert, G.E.: ANL-6755, (1963).

[24] Fauske, H.K., et al.: Trans. Amer. Nucl. Soc., Vol.12, 305 (1969).

[25] Costa, J., Charlety, P.: Winter Annu. Meeting Amer. Soc. Mech. Engrs., New York, (1970).

[26] Balzhiser, R.E., et al.: AFAPL-TR-85, (1967).

[27] Chen, J.C., Kalish, S.: 4th Int. Heat Trans. Conf., Paris-Versailles, (1970).

[28] Prem, L.L., et al.: AI-68-117, (1968). (Quoted from Ref.[19]).

[29] Tamao, S.: M.S. thesis, Kyoto Univ., (1970).

[30] Neal, L.G.: ANL-6625, (1963).

[31] Burdi, G.F.: NAA-SR-8617, Vol.1 (1964).

NOMENCLATURE

D_b	pipe diameter for a pipe, and shroud diameter for an annulus and a rod-bundle
D_h	hydraulic equivalent diameter
ΔE_{kl}	increment of kinetic energy flux for liquid phase
g	gravitational constant
G	mass flow rate
J	mechanical equivalent of heat
K	flow parameter defined by Eq.(4.10)
L	latent heat of vaporization
P	pressure
q	heat flux
Q	heat input
Q_g	volumetric flow rate of gas
Q_l	volumetric flow rate of liquid
Q_o	axially-uniform heat input
V_g	average phase velocity of gas
V_l	average phase velocity of liquid
V_o	superficial liquid velocity
W	total flow rate
W_g	gas flow rate
W_l	liquid flow rate
X	quality
X_{tt}	flow modulus defined by $(W_l/W_g)^{0.9}(\rho_g/\rho_l)^{0.5}(\mu_l/\mu_g)^{0.2}$
ΔX	increment of quality
z	axial coordinate
Z	axial position
α	average void fraction
α_{calc}	void fraction calculated from Eqs.(4.11) and (4.12) with $\varepsilon = 1.3$
α_{exp}	void fraction obtained in experiment
α_l	liquid fraction (= $1 - \alpha$)
β	volumetric flow rate ratio (= $Q_g/(Q_g + Q_l)$)

$\partial\alpha/\partial X$ void fraction gradient in α-X diagram

ε parameter defined by Eq.(4.12) or (4.14)

μ_g viscosity of gas

μ_l viscosity of liquid

ρ_g density of gas

ρ_l density of liquid

σ surface tension

Table 4.1 Flow parameter ε

			$V_o \leq 0.5$ m/sec	$V_o > 0.5$ m/sec
Ordinary Fluid	Steam-Water	Pipe, Annulus, Rectangular channel	Bubble flow : 1.3 Slug and annular flow : 1.0	
		Rod-bundle	Bubble flow 1.3 times of the value given in Fig. 4.3 for slug and annular flow. Slug and annular flow : Given in Fig. 4.3.	Bubble flow : 1.0 Slug and annular flow . 0.8
	Others	Pipe, Annulus, Rectangular channel	1.3	
Liquid	Metals	Pipe, Annulus, Rectangular channel	1.3	

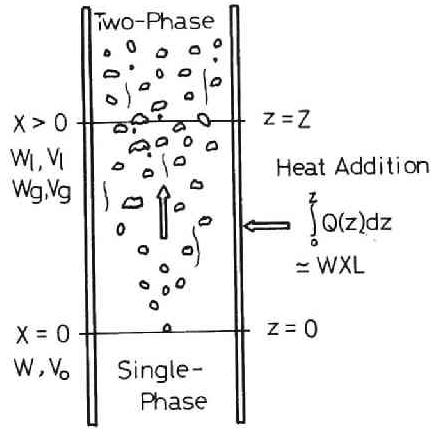

Fig. 4.1 Flow model

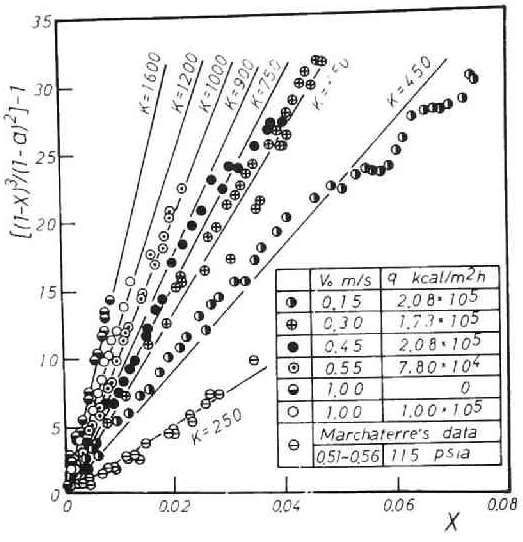

Fig. 4.2 Increment of kinetic energy flux vs. quality

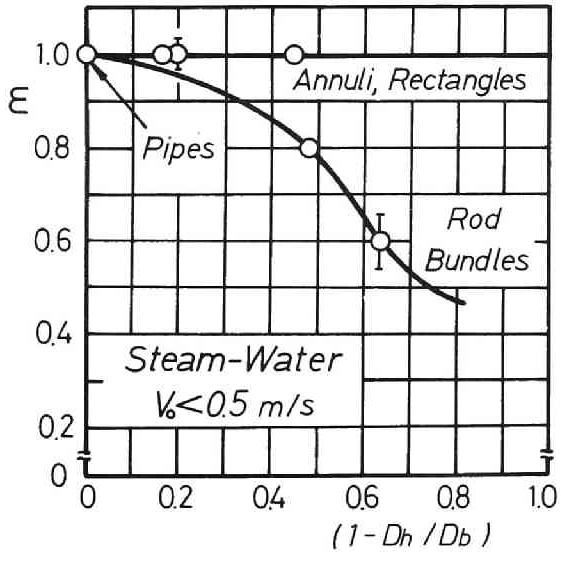

Fig. 4.3 Dependence of parameter ε upon channel geometry (V_o<0.5 m/sec)

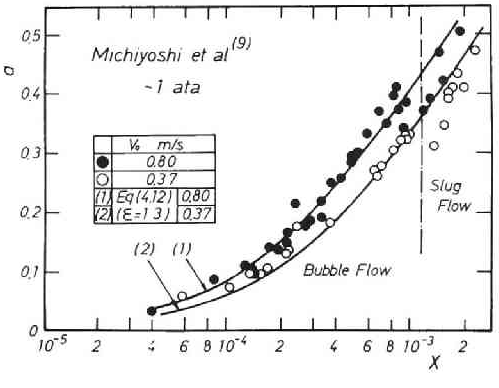

Fig. 4.4 Correlative representation of experimental void fraction for steam-water (bubble flow)

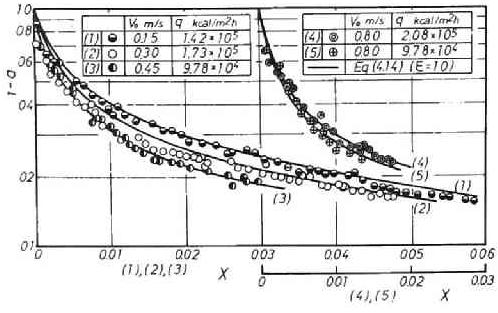

Fig. 4.5 Correlative representation of experimental void fraction for steam-water in an annulus (slug and annular flows)

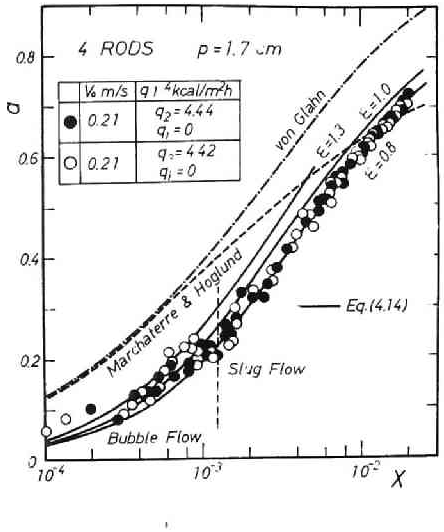

Fig. 4.6 Correlative representation of experimental void fraction for steam-water in 4 rod-bundle

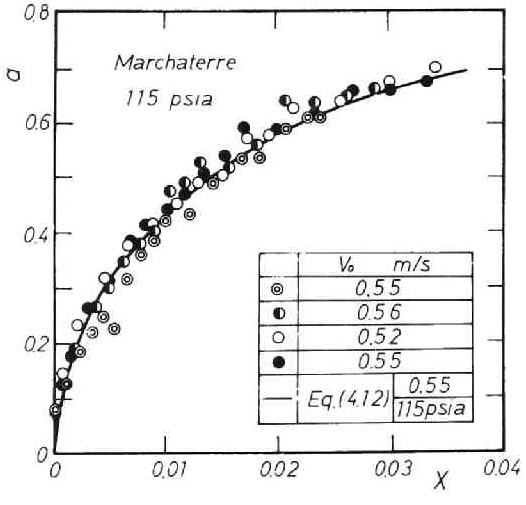

Fig. 4.7 Correlative representation of experimental void fraction for steam-water(bubble flow)

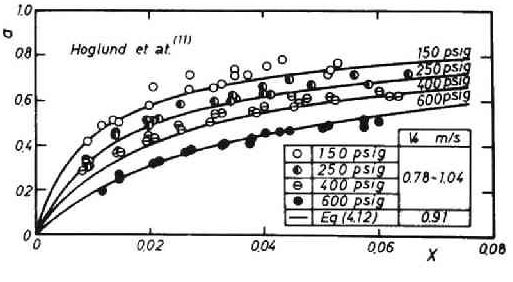

Fig. 4.8 Correlative representation of experimental void fraction for steam-water (bubble flow)

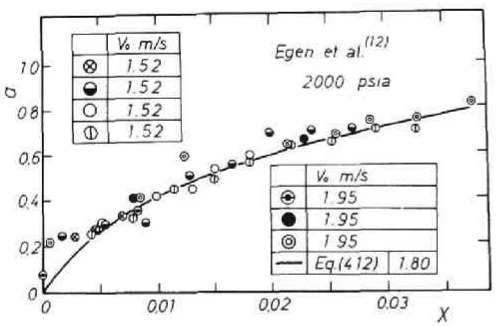

Fig. 4.9 Correlative representation of experimental void fraction for steam-water (bubble flow)

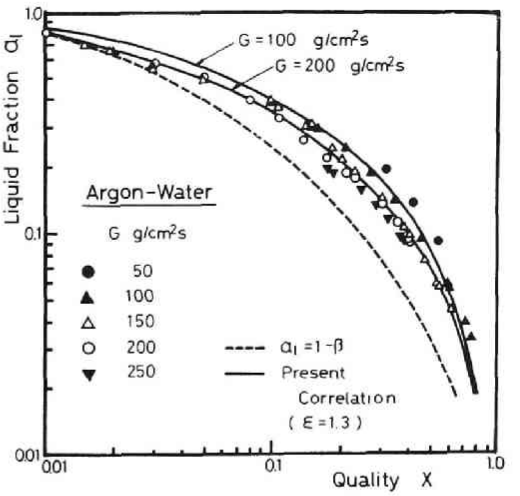

Fig. 4.10 Correlative representation of experimental void fraction for argon-water

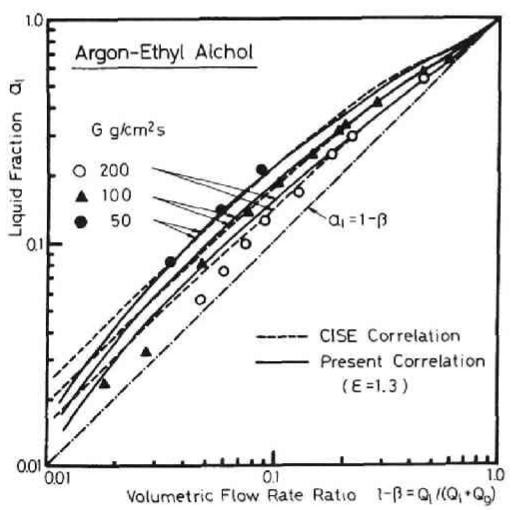

Fig. 4.11 Correlative representation of experimental void fraction for argon-ethyl alchol

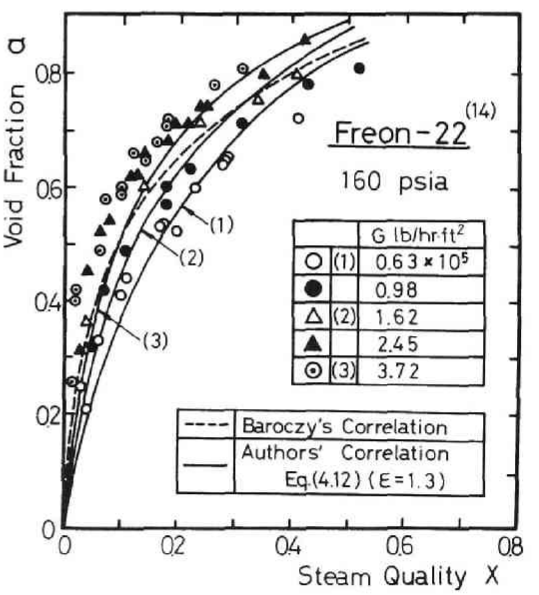

Fig. 4.12 Correlative representation of experimental void fraction for Freon-22

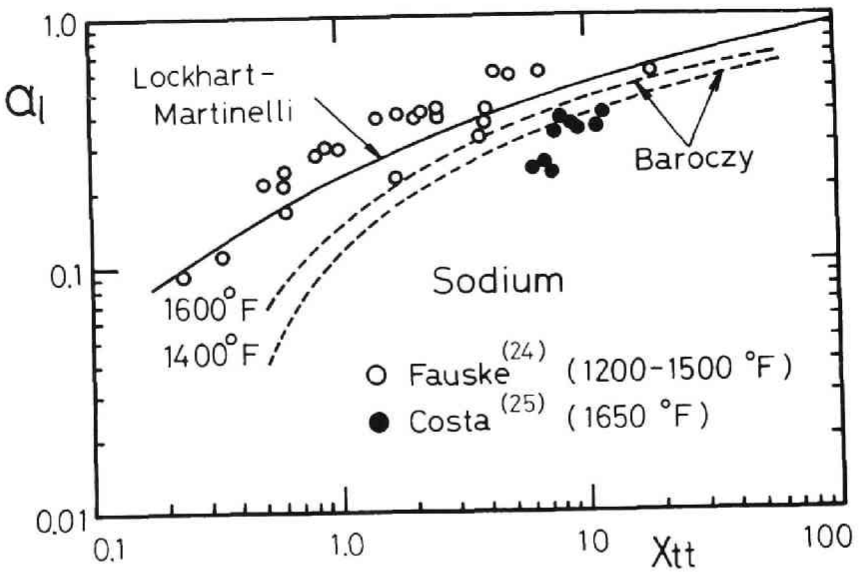

Fig. 4.13 Liquid fraction vs. X_{tt} for sodium

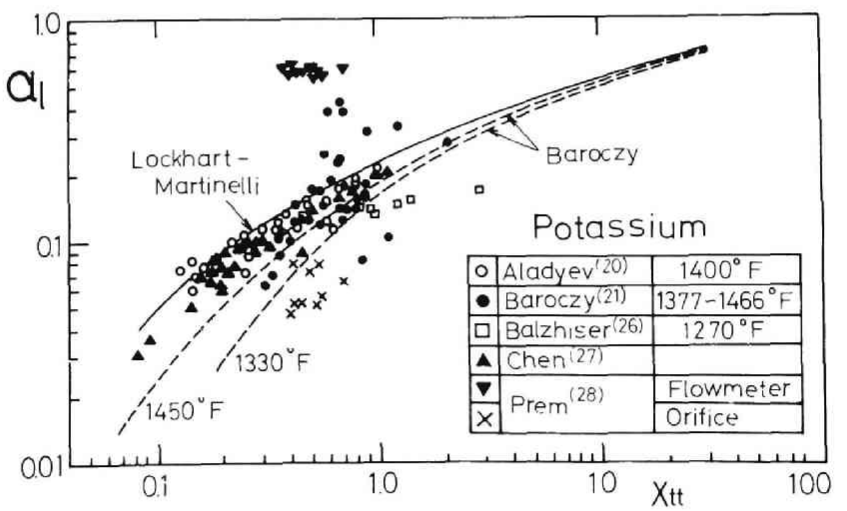

Fig. 4.14 Liquid fraction vs. X_{tt} for potassium

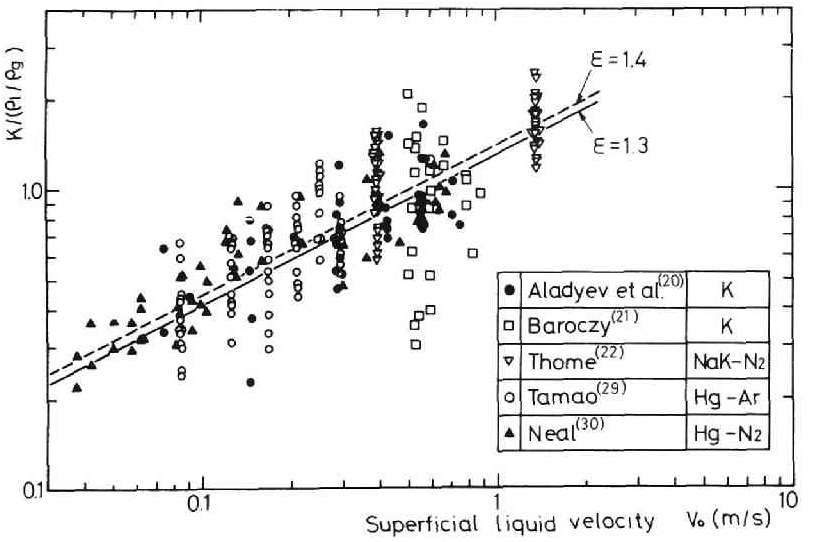

Fig. 4.15 Mass velocity effect on liquid metal void fraction ($K/(\rho_l/\rho_g)$ vs. V_o)

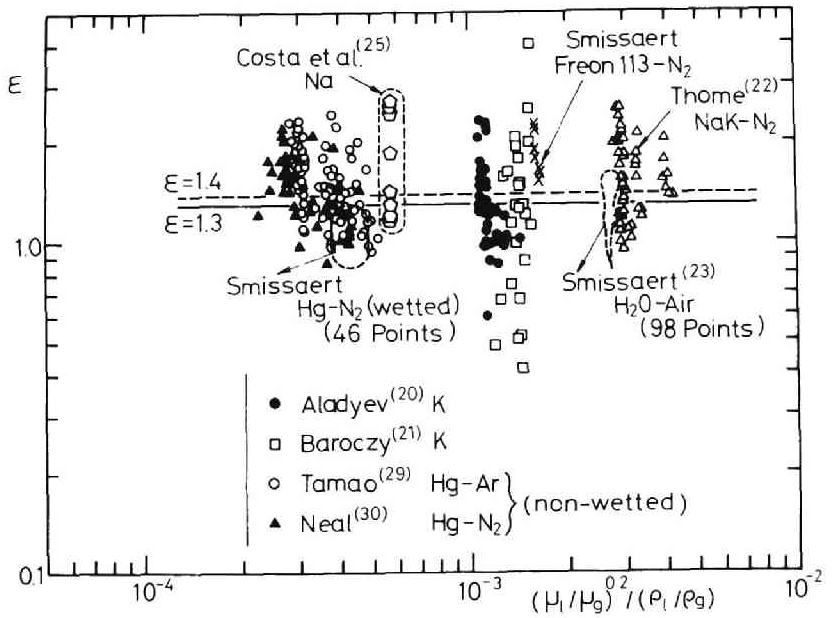

Fig. 4.16 Parameter ε vs. property index for various fluids

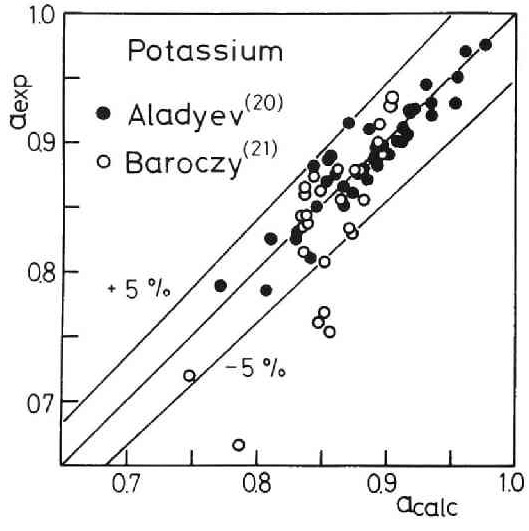

Fig. 4.17 Comparison between predicted and measured void fractions for potassium

V. PRESSURE DROP MEASUREMENT IN AIR-WATER FLOW

5.1 General

As stated earlier, in a number of engineering flow systems, it is an important problem to predict the pressure drop occurring during the forced circulation of boiling or non-boiling liquid, and so, much attention has been given to pressure drop investigations of gas-liquid mixtures flowing in channels of various forms.

Phenomenon of two-phase flow is so complicated that the attempts to solve theoretically the pressure drop problem have not yet led to desirable results due to their specific assumptions, and hence, the experimental testing have been needed.

Two principal types of theoretical flow models have appeared in analyses of two-phase pressure drops; one is the homogeneous model and the alternate the slip model or separated flow model. The former model, which is considered applicable for mist flow occurring at high quality (see Fig.2.1), considers the two phases as a single phase possessing certain mean properties defined from the properties of each phase. Variable density single-fluid model by Bankoff[1], and the mixing length theory by Levy[2] are the modified homogeneous flow models. The latter model, i.e., the slip model has been developed for an annular flow. This model considers only one continuous boundary between phases in a flow, and assumes that two phases are completely separated into two parts by the boundary and flow with a certain relative velocity. This model was first successfully developed by Lockhart & Martinelli[3] for arrangement of the experimental data obtained from horizontal flow of air and various liquids at atmospheric pressure. Martinelli & Nelson[4] modified this procedure for calculating the frictional pressure gradient to be applicable for high-pressure steam-water systems by taking the pressure level effect into consideration. Another modification, suggested by Levy[5], is based upon a

"Momentum Exchange Model". He postulated that momentum was exchanged between liquid and vapor, whenever X, α or ρ_l/ρ_g varies, and that this exchange tends to maintain the sum of the frictional and head losses equal for the two phases. Further modifications have been suggested by many other investigators.

A large amount of experimental work has been carried out on two-phase frictional pressure drop, and a great many reliable data and experimental correlations have been also proposed for predicting the pressure drops in ordinary non-metallic two-phase flows. Some of them may suggest very significant experimental results with respect to the understanding of systematic behavior of two-phase pressure drops[6-12].

Of the various pressure drop correlations, both the Lockhart-Martinelli and Baroczy[11] correlations are the most utilized ones. Especially, the latter was intended for application to the liquid metal systems, which incorporates the mass velocity effects on the frictional pressure drop. Serizawa and Michiyoshi[13] have recently proposed the generalized correlation available for predicting a two-phase frictional pressure drop of various fluids, irrespective of whether non-metallic or metallic. It incorporates both the effects of the pressure levels and the mass velocity.

Here, the pressure drop of a vertical two-phase flow consists of three components - frictional loss, acceleration loss (or momentum change), and hydrostatic head (or elevation loss) arising from the effect of the gravitational force field. Therefore, the total pressure drop for a two-phase flow is normally written as

$$\left(\frac{dP}{dz}\right)_t = \left(\frac{dP}{dz}\right)_f + \left(\frac{dP}{dz}\right)_a + \left(\frac{dP}{dz}\right)_h \quad . \tag{5.1}$$

The acceleration pressure drop can be evaluated by the following equation.

$$\left(\frac{dP}{dz}\right)_a = \frac{d}{dz}\left[\frac{1}{A}(W_l V_l + W_g V_g)\right]$$

$$= \frac{G^2}{\rho_l g} \frac{d}{dz} \left[\frac{(1 - X)^2}{1 - \alpha} + \frac{X^2}{\alpha} \frac{\rho_l}{\rho_g}\right] \quad , \tag{5.2}$$

where, A and G are the effective flow area and the mass flow rate of the total flow. While, the hydrostatic head can be deduced by applying the momentum equation to a differential length of a vertical channel with upward two-phase flow:

$$\left(\frac{dP}{dz}\right)_h = [\rho_l(1 - \alpha) + \rho_g \alpha] g \quad . \tag{5.3}$$

Hence, $\left(\frac{dP}{dz}\right)_a$ and $\left(\frac{dP}{dz}\right)_h$ can be evaluated if the relation between the cross-sectional average void fraction α and the quality X is given for a given flow condition. Then, only the frictional pressure drop term is left unknown. In experiment, this term may be deduced by subtracting the acceleration and hydrostatic terms from the measured total pressure drop. And experimental data on two-phase frictional pressure drop are usually presented in terms of the frictional pressure drop multiplier ϕ_{lo}^2 or ϕ_l^2, which are defined as the ratio of frictional pressure drop gradient between that for two-phase and for all-liquid flow, and that between two-phase and liquid single-phase flow, respectively.

The present study was initiated to clarify the influence of the surface roughness of the flow passage upon the pressure drop due to the friction in air-water two-phase mixture flowing upward in a vertical concentric annulus under nearly atmospheric pressure. The study of the flow phenomena in rough passages may give us a trace of understanding basic mechanisms of the wall turbulence or the development process of the boundary layer near the wall. Practically much attention has been paid to it from an engineering viewpoint that the surface roughness may promote the heat transfer characteristics between the heating wall and the fluid.

5.2 Experimental Apparatus and Procedures

The experimental apparatus and procedures were the same as have been already described in Paragraph 3.3.1.

Pressure difference was measured between two points (Z = 535 and 1,535 mm downstream of the entrance to the test section) by means of a carbon-tetrachloride manometer or a three-liquids-system manometer (water-kerosene-water). Three pressure taps were installed at every 120^{o} along the periphery of the pipe (28.5 mm i.d.) at a given axial position.

The surfaces of 10 mm o.d. inner rods tested had discrete roughness made of wire rings of different diameters welded separately on the surface of the rod with pitch-to-height ratio p/e = 10 (Fig.3.3)*.

5.3 Experimental Results and Discussions

5.3.1 Single-Phase Friction Factor

The channel friction factors f obtained from measured pressure drops during water flow are shown in Fig.5.1 as a function of the Reynolds number Rel, where

$$f = \left(\frac{dP}{dz}\right)_{sf} / \left(\frac{\rho_1 V_o^2}{2gD_h}\right) \quad , \tag{5.1}$$

$$Rel = V_o D_h / \nu_1 \quad . \tag{5.2}$$

From this figure, the equivalent sand roughness ε/D was determined for each flow passage, as shown in Fig.3.3, according to the Colebrook's expression[14] for friction factor in rough pipes (Eq.(5.3)).

---

* The study of boundary-layer turbulence promoter performance indicates that the optimum pitch-to-height ratio of discrete roughness elements can be made approximately equal to 10 for coupled heat transfer-flow resistance performance[19].

$$1/\sqrt{f} = -2.0 \log_{10} \left[\frac{1}{3.7}\frac{\varepsilon}{D} + \frac{2.51}{Re\sqrt{f}}\right] \qquad (5.3)$$

5.3.2 Effect of Flow Pattern

For smooth channel, as indicated in Fig.5.2, the frictional pressure drop multiplier ϕ_l^2 increases in the ϕ_l^2 vs. $(1 - \alpha)$ diagram with an increase in the void fraction in the bubble flow region, while it once decreases at the transition from bubble flow to slug flow, just like the void fraction*. This trend appears more remarkable for lower water velocities, and agrees qualitatively with that observed by Aoki et al.[15] in air-water flow. However, for rough channel with e/d = 0.05 or 0.10, it scarcely appears, and the multiplier ϕ_l^2 smoothly changes with the void fraction. Similar trends are found in the ϕ_l^2 - X diagram as illustrated, for example, in Fig.5.5.

A decrease in the multiplier occurring at the transition from bubble flow to slug flow may be attributable to the fact that, in slug flow, a considerable volume of the liquid is displaced from the front to the back of the large bubbles or slugs as they rise upward through their own diameter with a certain slip velocity, and the resultant backflow of the liquid may take place in a thin annular liquid layer along the wall. The effect of this backflow of the liquid with a reducing tendency of the frictional pressure loss is rationally expected to become smaller for a higher superficial liquid velocity.

5.3.3 Mass Velocity Effect

Figures 5.2 and 5.4 show the mass velocity effect on the frictional pressure drop multiplier ϕ_l^2, in the diagram ϕ_l^2 - $(1 - \alpha)$ and ϕ_l^2 - X, respectively. It will be seen that ϕ_l^2 tends to decrease with an increase in the velocity V_o regardless of whether the channel is smooth or not. This trend is in a qualitative agreement with that predicted by Baroczy's correlation[11] for air-water flow in a smooth channel within the range of flow variables tested in this experiment.

---

* See Chapter III.

5.3.4 Effect of Surface Roughness

As demonstrated in Figs.5.3 and 5.5, the effect of the surface roughness upon the friction multiplier ϕ_l^2 is very important as well as the mass velocity effect, i.e., ϕ_l^2 decreases linearly with increasing the surface roughness except at the transition from bubble flow to slug flow.

A linear relation between log ϕ_l^2 and log$(1 - \alpha)$ was first proposed by Akagawa[16] for smooth pipes in the following manner.

$$\phi_l^2 = (1 - \alpha)^{-m} \tag{5.4}$$

He obtained 1.75 for the exponent m theoretically, based upon the separated flow model. According to this procedure for data arrangement, Martinelli-Nelson correlation can be also approximated for steam-water mixture by putting[16]

$$m = 1.975 - 0.987 \times 10^{-3} P \quad (P: \text{ ata}). \tag{5.5}$$

A similar expression was obtained by Chisholm & Laird[17] from their own experimental results in horizontal air-water flow in a galvanized pipe ($\varepsilon/D = 0.0025$).

$$\phi_l^2 = 0.8 \ (1 - \alpha)^{-1.875} \tag{5.6}$$

A similar investigation was carried out systematically by Katsuhara[18] for air-water flow in vertical and inclined pipes with sand distributed uniformly on the inner surface ($\varepsilon/D = 0.004 \sim 0.0327$ in Nikuradse's expression). For vertical flows, he presented about $1.9 \sim 2.5$ for the exponent m, and concluded that the frictional pressure drop multiplier ϕ_l^2 increased with increasing the roughness, which is quite contradictory to our experimental result.

This discrepancy in the effect of the surface roughness between the experimental results of Katsuhara and those of the author may be

partly due to the difference in the type of roughness, i.e., the macroscopically continuous roughness of uniformly distributed sand and the discrete roughness of wire rings, and partly due to the difference in the flow geometry tested, i.e., pipes and concentric annuli. It seems rational that, in our experiment in a concentric annulus with discrete roughness, even large bubbles or slugs could slide into or out of the space between two adjacent wire rings without experiencing any large drag forces through their transfigurations, since their size is just the same order of magnitude as the pitch of discrete wire rings. Then, the resultant two-phase frictional pressure drop may only gradually increase relatively to the increase in the single-phase frictional pressure drop with increasing the roughness, and this follows a decrease in the friction multiplier ϕ_1^2 .

REFERENCES

[1] Bankoff, S.G.: Trans. Am. Soc. Mech. Engrs., Ser.C, Vol.82, 265 (1960).

[2] Levy, S.: ibid., Vol.85, 137 (1963).

[3] Lockhart, R.W., Martinelli, R.C.: Chem. Eng. Prog., 45 [1], 29 (1949).

[4] Martinelli, R.C., Nelson, D.B.: Trans. Am. Soc. Mech. Engrs., 70 [6], 39 (1948).

[5] Levy, S.: Trans. Am. Soc. Mech. Engrs., Ser.C, Vol.82, 113 (1960).

[6] Haywood, R.W., Knights, G.A.: Proc. Inst. Mech. Engrs., Vol.175, 13 (1961).

[7] Muscettola, M.: AEEW-R-284, (1963).

[8] Thom, J.R.C.: Int. J. Heat Mass Transfer, Vol.7, 709 (1964).

[9] Sekoguchi, K.: Doctoral thesis, Osaka Univ., (1967).

[10] Gaspari et al.: CISE-R-83, (1964).

[11] Baroczy, C.J.: Chem. Eng. Progr. Symp. Ser., 62 [74], 232 (1966).

[12] Inoue, A.: Doctoral thesis, Tokyo Industrial College,

[13] Serizawa, A., Michiyoshi, I.: J. Nucl. Sci. Technol., 10 [7], 435, (1973).

[14] Colebrook, C.F.: Proc. Inst. Civil Eng., Vol.11, 33 (1939).

[15] Aoki, S., Inoue, A.: 2nd. Japan Heat Transfer Symposium, (1965).

[16] Akagawa, K.: Trans. Japan Soc. Mech. Engrs., 23 [128], 292 (1957).

[17] Chisholm, D., Laird, A.D.K.: Trans. Am. Soc. Mech. Engrs., Ser.C, Vol.80, 276 (1958).

[18] Katsuhara, T.: Trans. Japan Soc. Mech. Engrs., 24 [148], 1050 (1958).

[19] Sutherland, W.A.: Int. Heat Mass Transfer, Vol.10, 1587 (1967).

NOMENCLATURE

A	flow area
d	rod diameter
D_h	hydraulic equivalent diameter
e	height of discrete surface roughness
f	friction factor
g	gravitational constant
G	mass flow rate
m	exponent
P	pressure
$(\frac{dP}{dz})_t$	total pressure drop
$(\frac{dP}{dz})_a$	acceleration pressure drop
$(\frac{dP}{dz})_f$	frictional pressure drop
$(\frac{dP}{dz})_h$	hydrostatic head
$(\frac{dP}{dz})_{sf}$	single-phase frictional pressure drop resulting from $G(1 - X)$
$(\frac{dP}{dz})_{sfo}$	single-phase frictional pressure drop resulting from G
$(\frac{dP}{dz})_{tf}$	two-phase frictional pressure drop

Re_l	liquid Reynolds numner ($=V_o D_h/\nu_l$)
V_o	superficial liquid velocity
W_g	gas flow rate
W_l	liquid flow rate
X	quality
z	axial coordinate
α	average void fraction
ε/D	equivalent sand roughness
ν_l	kinematic viscosity of liquid
ρ_g	density of gas
ρ_l	density of liquid
ϕ_l^2	frictional pressure drop multiplier $(=(\frac{dP}{dz})_{tf}/(\frac{dP}{dz})_{sf})$
ϕ_{lo}^2	frictional pressure drop multiplier $(=(\frac{dP}{dz})_{tf}/(\frac{dP}{dz})_{sfo})$

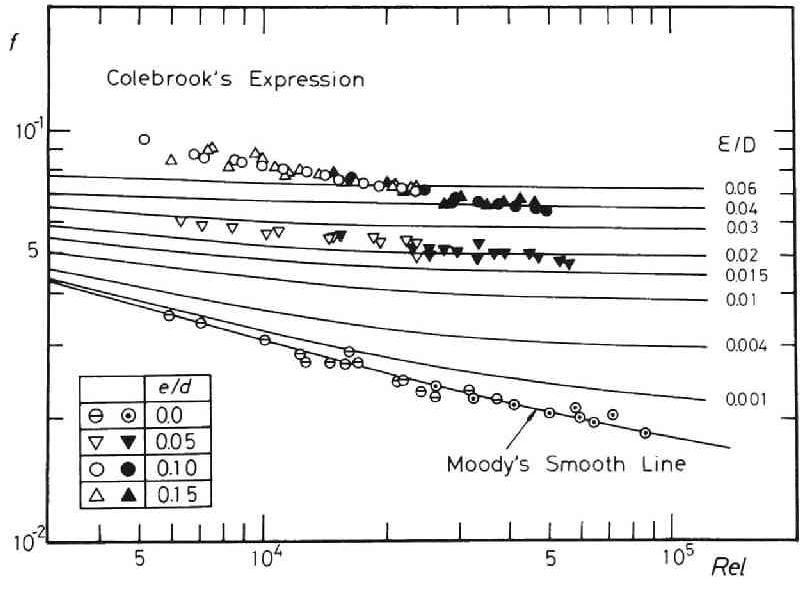

Fig. 5.1 Channel friction factor in water flow

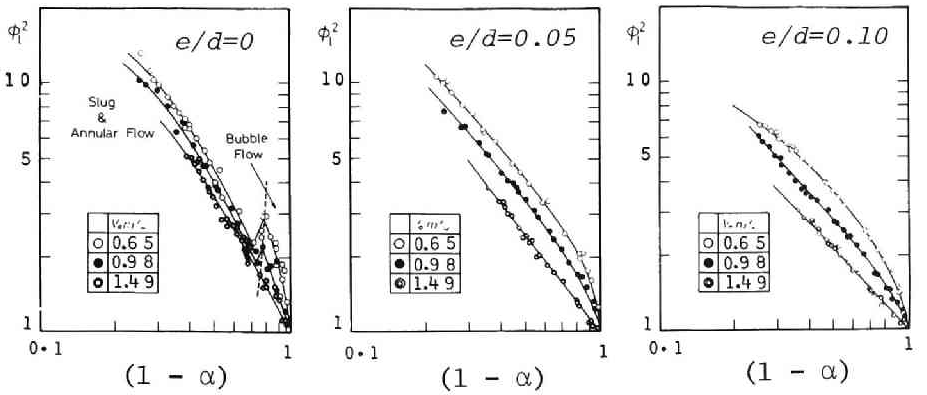

Fig. 5.2 Velocity effect upon friction multiplier

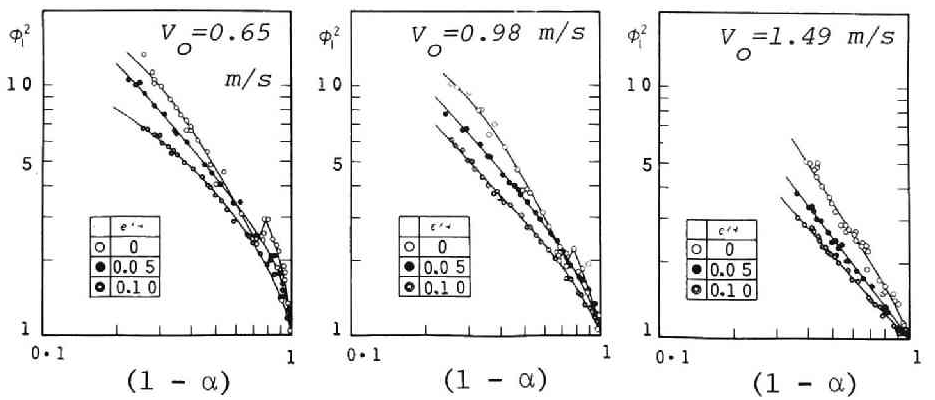

Fig. 5.3 Effect of surface roughness upon friction multiplier

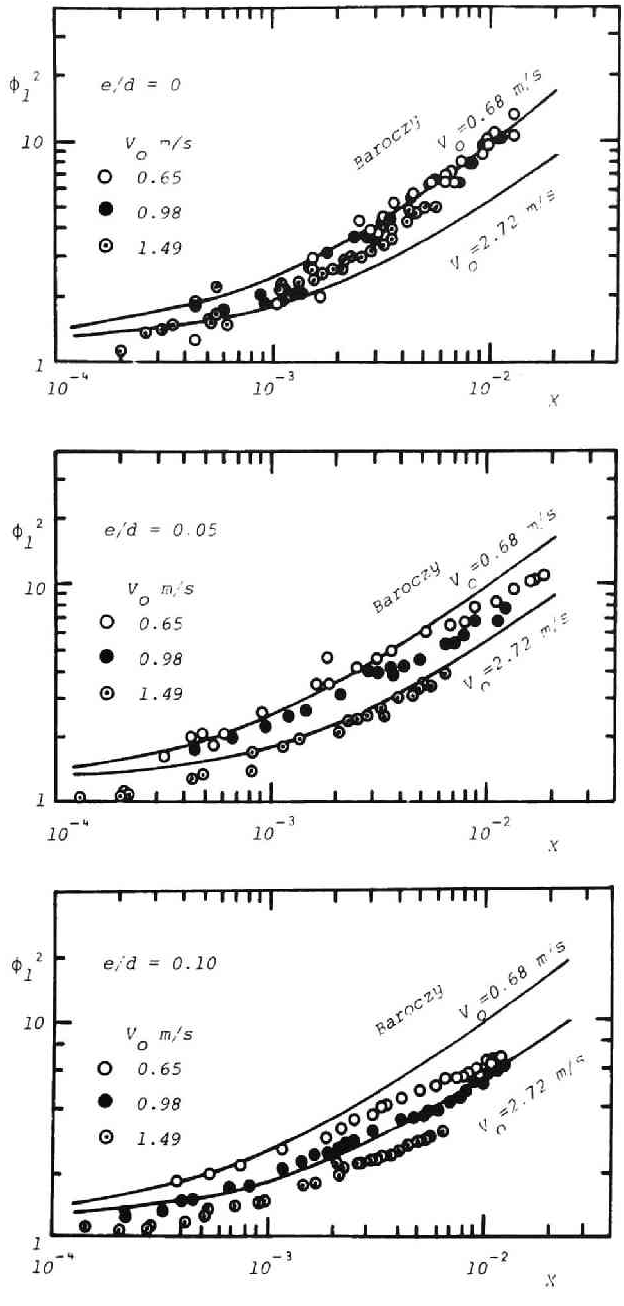

Fig. 5.4 Velocity effect upon friction multiplier

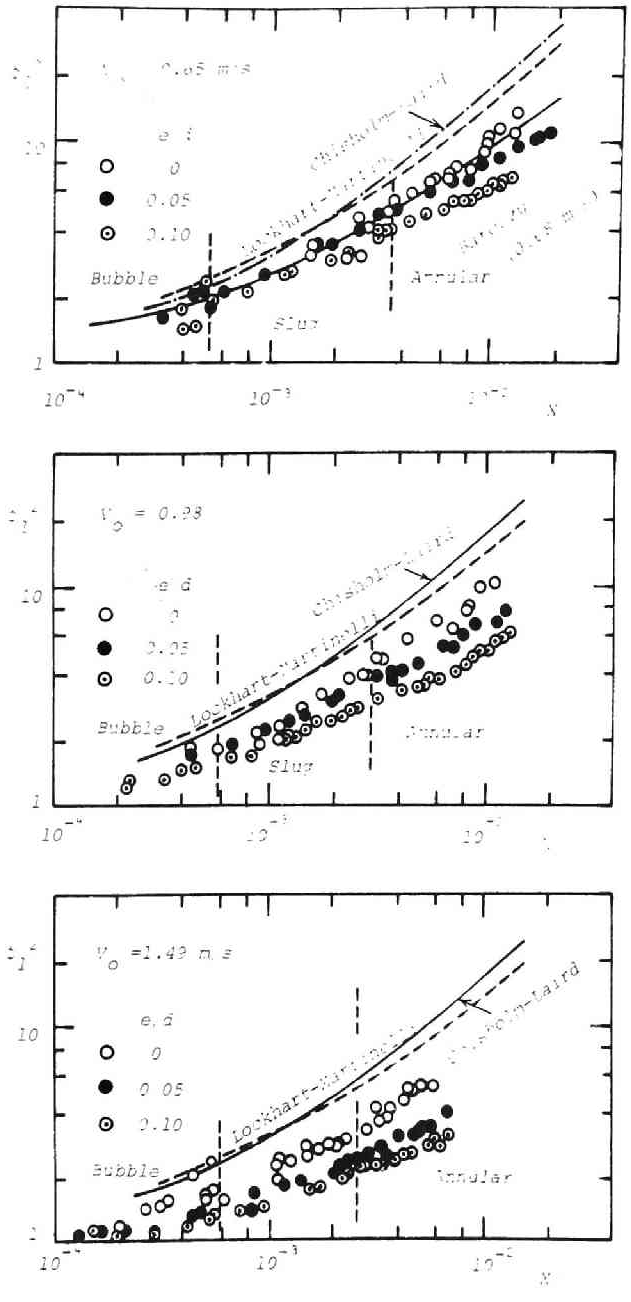

Fig. 5.5 Effect of surface roughness upon friction multiplier

VI. PRESSURE DROP CORRELATION

Of the various correlations possible relative to frictional pressure drop, both the Lockhart-Martinelli[1] and Baroczy[2] correlations are the most utilized, as stated elsewhere. It is to be recalled that the latter correlation in particular was obtained with application to liquid metals held in mind. The shortcomings of the Lockhart-Martinelli correlation for pressure drop are similar to those in the case of the liquid fraction correlation; the correlation does not take into account the mass velocity and pressure level effects. On the other hand, the Baroczy correlation incorporates these effects, and it has been intended for application to all fluids at various temperatures by embodying the property index $[(\mu_l/\mu_g)^{0.2}/(\rho_l/\rho_g)]$. This correlation provides for diagrammatical representation of both the two-phase friction multiplier ϕ_{lo}^2 (which is defined as the ratio of frictional pressure drop gradient between that for two-phase and that for all-liquid flow, and which is obtained as a function of the property index and the quality for a number of fluids with a constant mass velocity of 1×10^6 lb/hr·ft^2) and the mass velocity correction factors for the multipliers obtained above (as function of the property index and the quality at mass velocities of 0.25, 0.5, 2.0 and 3.0×10^6 lb/hr·ft^2).

Detailed survey of liquid metal two-phase frictional pressure drop data yields differences in the mass velocity effect between Baroczy's correlation and experimental data obtained at values of mass velocity in the range 0.2×10^6 to 1×10^6 lb/hr·ft^2: the experimental data reveal a trend, at constant quality, for the multiplier ϕ_{lo}^2 to increase with mass velocity G_o.

A generalized correlation proposed here for predicting two-phase frictional pressure drop is derived on the basis of an approximate expression of the Lockhart-Martinelli correlation by using the experimental data of Baroczy[3] and Aladyev et al.[4] for potassium,

Muscettola (CISE)[5] and Gaspari et al.[6] for steam-water, and Inoue [7] and Serizawa[8] for air-water.

6.1 Derivation of Pressure Drop Correlation

6.1.1 Approximate Mathematical Expression of Lockhart-Martinelli Correlation

The Lockhart-Martinelli pressure drop correlation agrees relatively well with the experimental data not only for ordinary non-metalic fluids but also for metalic fluids, but it has the shortcoming of not being expressed in the form of mathematical equations. Thus we will first try to derive its approximate expression.

The value ϕ_l, which is defined as the square root of the ratio of two-phase to liquid single-phase frictional pressure drop gradient, is tabulated in Ref.[1] for the Lockhart-Martinelli modulus X_{tt}, where

$$X_{tt} = \left(\frac{W_l}{W_g}\right)^{0.9} \left(\frac{\rho_g}{\rho_l}\right)^{0.5} \left(\frac{\mu_l}{\mu_g}\right)^{0.1} \quad . \tag{6.1}$$

From these tabulated values of ϕ_l, we have obtained the approximate formula

$$\log \phi_l = \frac{-z + \sqrt{z^2 + 9.2}}{4} \quad , \tag{6.2}$$

$$z = 2 \log X_{tt} + 0.176\, X_{tt} + 0.382 \quad . \tag{6.3}$$

Figure 6.1 represents a comparison between these equations (solid line), the Lockhart-Martinelli correlation curve (dotted line), and also the approximate eqation by Chisholm & Laird[7] (chain line)*.

---

* Pressure drop correlation of Chisholm & Laird is expressed in terms of the flow modulus $\overline{X}$ instead of X_{tt} in their original paper, where $\overline{X} = (W_l/W_g)^{0.875} (\rho_g/\rho_l)^{0.5} (\mu_l/\mu_g)^{0.125}$. However, the difference between X_{tt} and $\overline{X}$ is not so large, and then we can assume $\overline{X} = X_{tt}$, for comparison's sake, without any serious effect in Fig.6.1.

Equations (6.2) and (6.3) agree with the Lockhart-Martinelli curve within a few percents.

6.1.2 Derivation of Correlation

The variable ϕ_{lo}^2 appears more comprehensive and more convenient for practical use than ϕ_l^2. The relationship between ϕ_{lo}^2 and ϕ_l^2 is given as follows, provided that the single-phase friction factor f is known.

Assuming

$$f = c \cdot Re^{-n'} \quad , \tag{6.4}$$

we have

$$\phi_{lo}^2 = \phi_l^2 (1 - X)^{2-n'} \quad . \tag{6.5a}$$

When $n' = 0.2$,

$$\phi_{lo}^2 = \phi_l^2 (1 - X)^{1.8} \quad . \tag{6.5b}$$

And when the quality $X \longrightarrow 1$ (or $X_{tt} \longrightarrow 0$), $\phi_l^2 \longrightarrow +\infty$, and $\phi_{lo}^2 \longrightarrow 1/\xi$ (reciprocal of the property index at $n' = 0.2$).

In consideration of these facts and recalling Eqs.(6.2) and (6.3), we introduce the following formula for the two-phase friction multiplier ϕ_{lo}^2:

$$\log \phi_{lo} = \frac{-z + \sqrt{z^2 + 9.2}}{4} \quad , \tag{6.6a}$$

$$z = 2 \log X_{tt} + \frac{A}{X_{tt} + C} + B X_{tt} + D \quad . \tag{6.6b}$$

In the above equations, A, B, C and D are functions of the fluid properties, mass velocity G_o, the hydraulic diameter of the channel, etc. Here we determine their values as follows, based upon the experimental data listed in Table 6.1:

Function A: As shown in Fig.6.2, plotted against the product of Reynolds and Froude numbers (Re·Fr).

Function B: This function is rewritten

$$B = 10^{m} \, (Re \cdot Fr)^{n} \quad . \tag{6.6c}$$

The exponents m and n are given in Fig.6.3.

Function C: As shown in Fig.6.4, plotted against Re·Fr with the property index ξ as parameter, where

$$\xi = (\mu_l/\mu_g)^{0.2}/(\rho_l/\rho_g)$$

Function D: $D = 7.75 \, \xi^{0.536}$ (6.6d)

Since the first term on the right-hand side of Eq.(6.6b) becomes dominant for X_{tt} below a certain value, where the function z is negative, ϕ_{lo}^{2} rapidly increases in this range. In consequence, caution is required for applying Eqs.(6.6a), (6.6b), (6.6c), and (6.6d) to liquid metal two-phase flow systems where the property index is relatively small. The limiting value of X_{tt} for the applicability of these formulas may be estimated to be about 0.01 for potassium, subject to revision since, up to now, we have not yet obtained a sufficiently large number of pertinent experimental data for liquid metals. (This correlation cannot be defined at X = 1, since log X_{tt} is not defined at $X_{tt} = 0$.)

6.2 Comparison between Predicted and Experimental Pressure Drop

Figures 6.5 ~ 6.19 represent comparisons of the predicted two-phase friction multiplier obtained with the present correlation using various experimental data by Muscettola[5], Janssen & Kervinen[10], Moen[11], Gaspari et al.[6] for steam-water, Inoue[7] for

air-water*, Fauske et al.[12] for sodium*, Aladyev et al.[4] and Baroczy[3] for potassium, and Thome[13] for sodium-potassium-nitrogen* and Serizawa[8] for air-water*, respectively. In each figure, the solid or dotted lines represent the curves predicted for each flow condition by the set of Eqs.(6.6a ~ 6.6d). Generally speaking, these figures show good coincidence between the proposed correlation and experimental data.

For steam-water systems, the correlation seems to predict slightly higher values for the friction multiplier than the experimental data obtained in the range of mass velocity below 0.5×10^6 lb/hr·ft^2 and steam quality beyond 0.6. This tendency concurs with what is indicated directly from comparisons with the data shown in Figs.6.11 ~ 6.15. At higher mass velocities, better agreement is obtained than with the Baroczy correlation.

For liquid metal two-phase flow, overall agreement is satisfactory, and the trend shown by the predictions corresponds with the data. Both the experimental data of Aladyev et al. and of Baroczy for potassium and of Lurie[14] for sodium, which were restricted to a fairly small range of mass velocity, and the predicted values corresponding to these flow conditions reveal a trend for the two-phase friction multiplier ϕ_{lo}^2 to increase with mass velocity G_o. This corresponds to a negative value of exponent n for liquid metal, as shown in Fig.6.3, (positive, on the other hand, for most of ordinary fluids). This trend of mass velocity effect indicates a marked difference in behavior between liquid metal and ordinary fluid flows. Nevertheless, as mentioned later, at higher mass velocities of the order of 10^6 lb/hr·ft^2, this particular tendency gradually diminishes and reverses itself, and higher mass velocity is related to a lower friction multiplier ϕ_{lo}^2. The behavior thus becomes identical to that of ordinary fluid flow.

---

* In these cases, the conversion equation (6.5b) is used.

6.3 Pressure Level and Mass Velocity Effects on Liquid Metal Two-Phase Flow

In respect of the pressure level and mass velocity effects upon liquid metal two-phase frictional pressure drop, accurate information is hardly available. Baroczy's correlation appears the most valid, and it takes both effects into consideration by means of the property index and mass velocity correction factor, as described in detail earlier. But it cannot offer sufficient information for practical purposes. For this reason the two effects, as predicted by the present correlation, will be discussed briefly.

6.3.1 Pressure Level Effect

The effects of differences in temperature or pressure appear directly on the fluid properties such as the densities and viscosities of the two phases. One of the most possibly accurate and easily explainable parameters affecting the hydraulics of two-phase flow is the property index ξ $(= (\mu_l/\mu_g)^{0.2}/(\rho_l/\rho_g))$ proposed by Baroczy in Ref.[15].

The friction multipliers predicted by the present and Baroczy correlations at a mass velocity of 1×10^6 lb/hr·ft^2 and at temperatures of 1,200°, 1,300°, 1,400°, 1,500°, 1,600° and 1,700°F are represented for potassium in Fig.6.20, and for sodium in Fig.6.21. As a whole, the present correlation has a tendency to predict higher values of the friction multiplier compared with Baroczy's. In the former case, the friction multiplier decreases consistently with increasing system temperature in a wide quality or X_{tt} range, while in the latter case, the predicted curves cross each other in the range of X_{tt} from 0.03 to 0.2.

6.3.2 Mass Velocity Effect

This effect may be reduced to that based on the two-phase flow pattern. Careful examination of experimental data by Muscettola for steam-water at 70 kg/cm^2 and Inoue for air-water under atmospheric pressure reveals no significant systematic effect of channel diameter

or hydraulic-equivalent diameter upon the frictional pressure drop. This suggests that the proposed correlation should embody the mass velocity effect in the functions A, B and C as expressed by the parameter Re·Fr, and this product of the Reynolds and Froude numbers is proportional to G_o^3. Baroczy also takes this effect into consideration explicitly through incorporation of the mass velocity G_o.

The mass velocity effect predicted by the present correlation at a system temperature of 1,500°F and mass velocities of 0.25, 0.5, 1.0, 2.0, and 3.0×10^6 lb/hr·ft^2 is shown for potassium in Fig.6.22, and for sodium in Fig.6.23. In both figures, the predicted curves intersect each other in a complicated manner. These figures indicate the following two types of mass velocity effect according to the region of G_o and X_{tt}.

For $0.01 \lesssim X_{tt} \lesssim 0.5$

$G_o \lesssim 0.5 \times 10^6$ lb/hr·ft^2

The two-phase friction multiplier ϕ_{lo}^2 increases with the mass velocity G_o.

$G_o \gtrsim 0.5 \times 10^6$ lb/hr·ft^2

The two-phase friction multiplier ϕ_{lo}^2 decreases with increasing mass velocity G_o.

This predicted trend is attributed to the negative value of the exponent n in the function B, and to the minimum values of functions A and C at Re·Fr $\simeq 2.5 \times 10^5$ and 1×10^5 respectively. Actually the bulk of the data exhibits the same trend.

For $X_{tt} \gtrsim 0.5$, the prediction gives a large multiplier ϕ_{lo}^2 for higher mass velocity, since the third term on the right-hand side of Eq.(6.6b) overcomes the second term in this range of quality.

6.4 Conclusions

(1) Of various two-phase frictional pressure drop correlations, those of Lockhart-Martinelli and Baroczy give fairly good agreement with the experimental data irrespective of whether non-metallic or

metallic fluid, but they cannot always predict the mass velocity effect applicable to practical cases.

(2) Available data on liquid metal two-phase frictional pressure drop show a trend, in the range covered of the variables, for the friction multiplier to increase with the mass velocity. This trend is opposite to that seen in ordinary fluid systems.

(3) The present correlation, Eqs.(6.6a), (6.6b), (6.6c), and (6.6d), is proposed for predicting two-phase frictional pressure drop in various fluid systems, which takes account of the pressure level effect and the mass velocity effect by means of the property index and the factor Re·Fr. This correlation has results in good agreement with a wide variety of data obtained for sodium, potassium, sodium-potassium-nitrogen, steam-water and air-water systems. Figures 6.20 ~ 6.23 represent the friction multiplier ϕ_{lo}^2 for potassium and sodium predicted by the present correlation.

(4) Equations (6.2) and (6.3) are approximate expressions for the Lockhart-Martinelli pressure drop correlation.

REFERENCES

[1] Lockhart, R.W., Martinelli, R.C.: Chem. Eng. Progr., 45 [1], 39 (1949).

[2] Baroczy, C.J.: Chem. Eng. Progr. Symp. Ser., 62 [64], 232 (1966).

[3] idem.: ibid., 64 [82], 12 (1968).

[4] Aladyev, I.T., et al.: BNL-TR-267, (1969).

[5] Muscettola, M.: AEEW-R-284, (1963).

[6] Gaspari, G.P., et al.: CISE-R-83, (1964).

[7] Inoue, A.: Doctoral thesis, Tokyo Industrial College, (19__).

[8] Serzawa, A.: M.S. thesis, Kyoto Univ., (1968).

[9] Chisholm, D., Laird, A.D.K.: Trans. Am. Soc. Mech. Engrs., 80 [2], 276 (1958).

[10] Janssen, E., Kervinen, T.A.: GEAP-416, (1964), (Quoted from Ref. [2]).

[11] Moen, R.H.: Ph. D. these, Univ. Minnesota, (1956), (Quoted from Ref.[2]).

[12] Fauske, H.K., Grolmes, M.A.: Winter Annu. Meeting. Am. Soc. Mech. Engrs., New York, (1970).

[13] Thome, R.J.: ANL-6854, (1964).

[14] Lurie, H.: NAA-SR-11586, (1966).

[15] Baroczy, C.J.: Chem. Eng. Progr. Symp. Ser., 61 [57], 179 (1965).

NOMENCLATURE

A	a function defined by Eq.(6.6b) and given in Fig.6.2
B	a function defined by Eq.(6.6b) and given in Fig.6.3
C	a function defined by Eq.(6.6b) and given in Fig.6.4
D	a function defined by Eq.(6.6b) and given by Eq.(6.6d), or pipe diameter
D_h	hydraulic equivalent diameter
f	friction factor
Fr	Froude number ($= (G_o/\rho_l)^2/gD_h$)
g	gravitational constant
G_o	total mass flow rate or mass velocity
m	exponent
n	exponent
n'	exponent
P	pressure
$(\frac{dP}{dz})_{sf}$	single-phase frictional pressure drop resulting from $G_o(1 - X)$
$(\frac{dP}{dz})_{sfo}$	single-phase frictional pressure drop resulting from G_o
$(\frac{dP}{dz})_{tf}$	two-phase frictional pressure drop
Re	Reynolds number ($= (G_o/\rho_l)D_h/\nu_l$)
T	temperature
W_g	gas flow rate
W_l	liquid flow rate
X	quality
$\overline{X}$	flow modulus defined by $(W_l/W_g)^{0.875}(\rho_g/\rho_l)^{0.5}(\mu_l/\mu_g)^{0.125}$
X_{tt}	flow modulus defined by $(W_l/W_g)^{0.9}(\rho_g/\rho_l)^{0.5}(\mu_l/\mu_g)^{0.1}$
z	axial coordinate
z	a function defined by Eq.(6.3) or Eq.(6.6b)
ν_l	kinematic viscosity of liquid
μ_g	viscosity of gas
μ_l	viscosity of liquid
ξ	property index defined by $(\mu_l/\mu_g)^{0.2}/(\rho_l/\rho_g)$
ρ_g	density of gas

ρ_l density of liquid

ϕ_l^2 frictional pressure drop multiplier $(= (\frac{dP}{dz})_{tf} / (\frac{dP}{dz})_{sf})$

ϕ_{lo}^2 frictional pressure drop multiplier $(= (\frac{dP}{dz})_{tf} / (\frac{dP}{dz})_{sfo})$

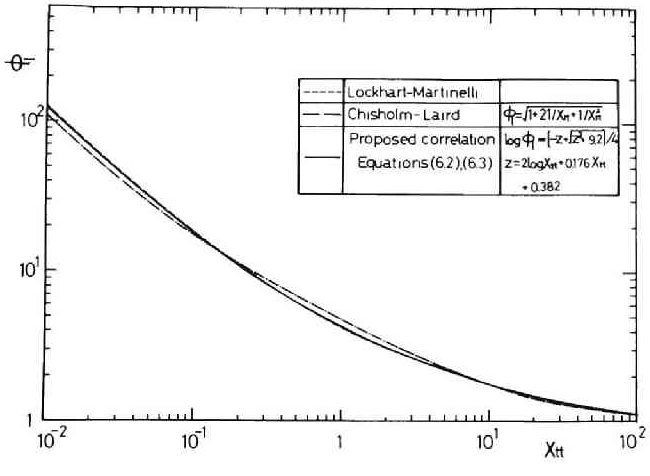

Fig. 6.1 Approximate equation of Lockhart-Martinelli pressure drop correlation

Table 6.1 Experimental data used to develop correlation

Author	System	Flow variables	Method of void fraction measurement
Aladyev et al.[4]	Potassium (adiabatic)	Vertical upflow Circular tubes (6.25, 6 mm$^{\Phi}$) T 1,028 ~ 1,109 °K G_o = 10.5 ~ 27.5 g/cm^2·sec X = 0.015 ~ 0.88	Electrical resistivity
Baroczy[3]	Potassium (adiabatic)	Horizontal flow Circular tube (0.62 in.$^{\Phi}$) T = 1,377 1,466 °F W_o = 225 940 lb/hr X = 0.01 ~ 0.094	Orifice
Muscettola[5]	Steam-water	Vertical upflow Circular tubes (5.2, 8.2, 10.1 mm$^{\Phi}$) P = 55.6, 70, ~ 84.3 kg/cm^2 G_o = 107 ~ 401 g/cm^2·sec X = 0.04 0.75	Calculated by momentum exchange model
Gaspari et al.[6]	Steam-water	Vertical upflow Circular tube (15.2 mm$^{\Phi}$) P = 51.5, 71.3, 91 kg/cm^2 G_o = 50, 75, 100, 125, 150 g/cm^2·sec X 0.03 0.97	Unmeasured (CISE homogeneous flow model)
Inoue[7]	Air-water	Vertical upflow Circular tubes (5, 9, 19, 28.8 mm$^{\Phi}$) Annulus (21 mm O.D., 28.8 mm I.D.) Rectangular duct (28.5 × 14.2 mm) Atmospheric pressure V_l = 0.19 2.68 m/sec X = 0.008 ~ 0.126	Quick-shut technique (with mechanical ball-valves)
Serizawa[8]	Air-water	Vertical upflow Annulus (10 mm O.D., 28.5 mm I.D.) P 1.05 ~ 1.2 kg/cm^2 V_l = 0.6 1.5 m/sec X 0.0014 ~ 0.013	Quick-shut technique (with electro-magnetic valves)

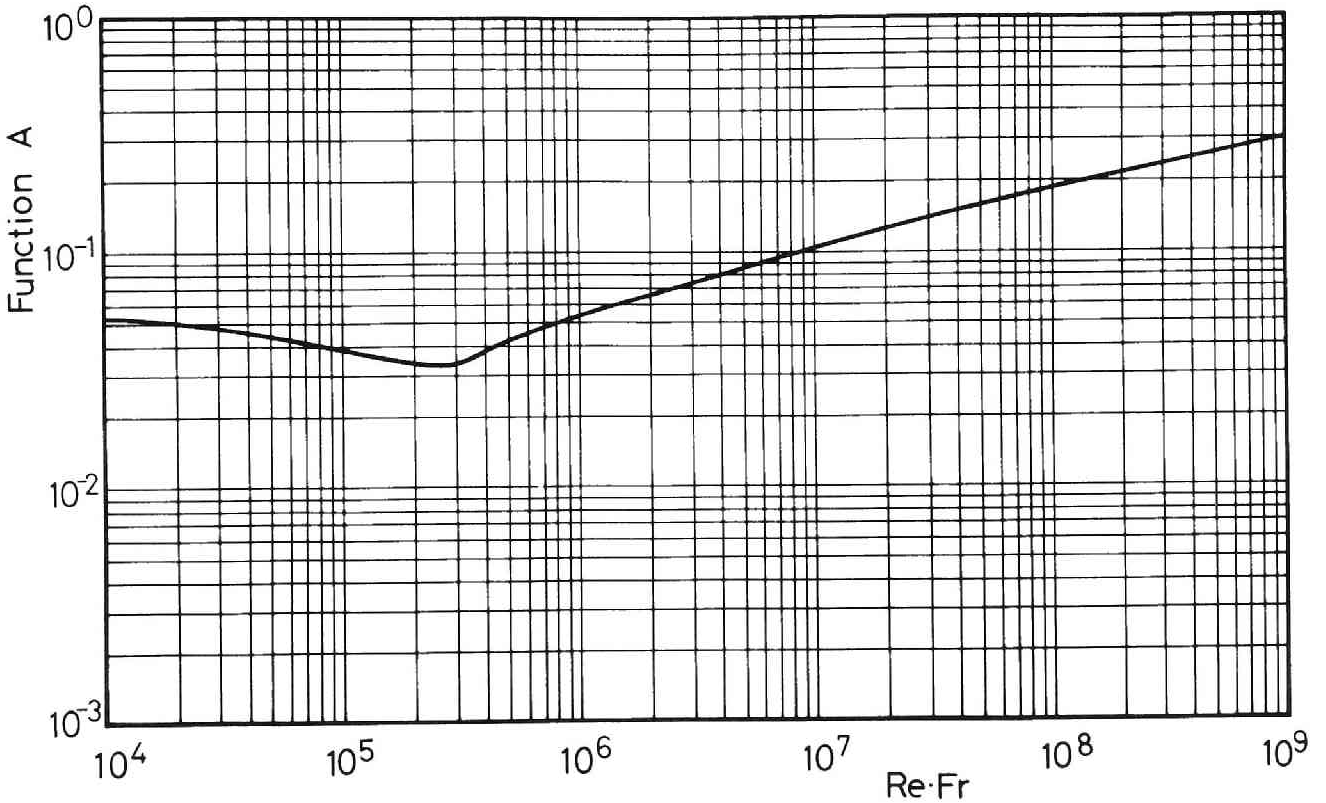

Fig. 6.2 Proposed pressure drop correlation (Function A)

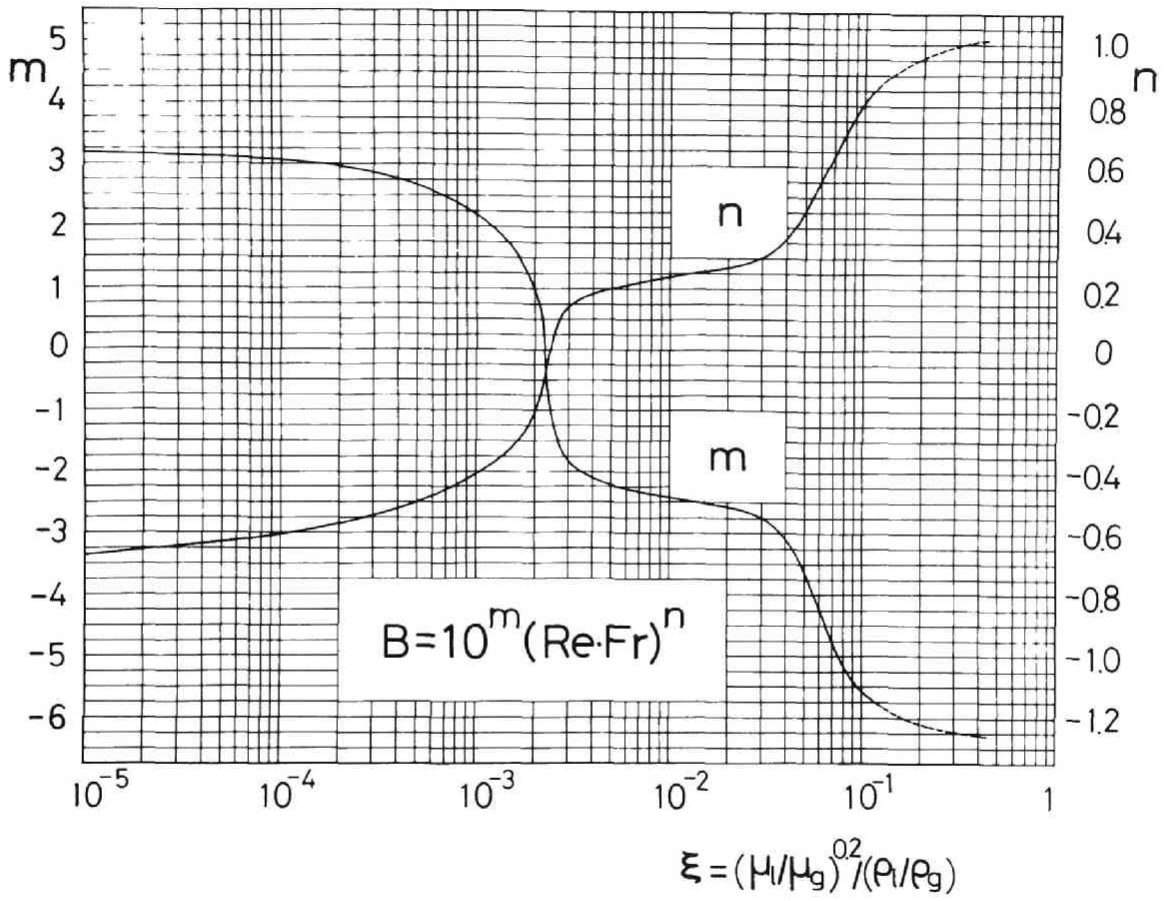

Fig. 6.3 Proposed pressure drop correlation (Function B)

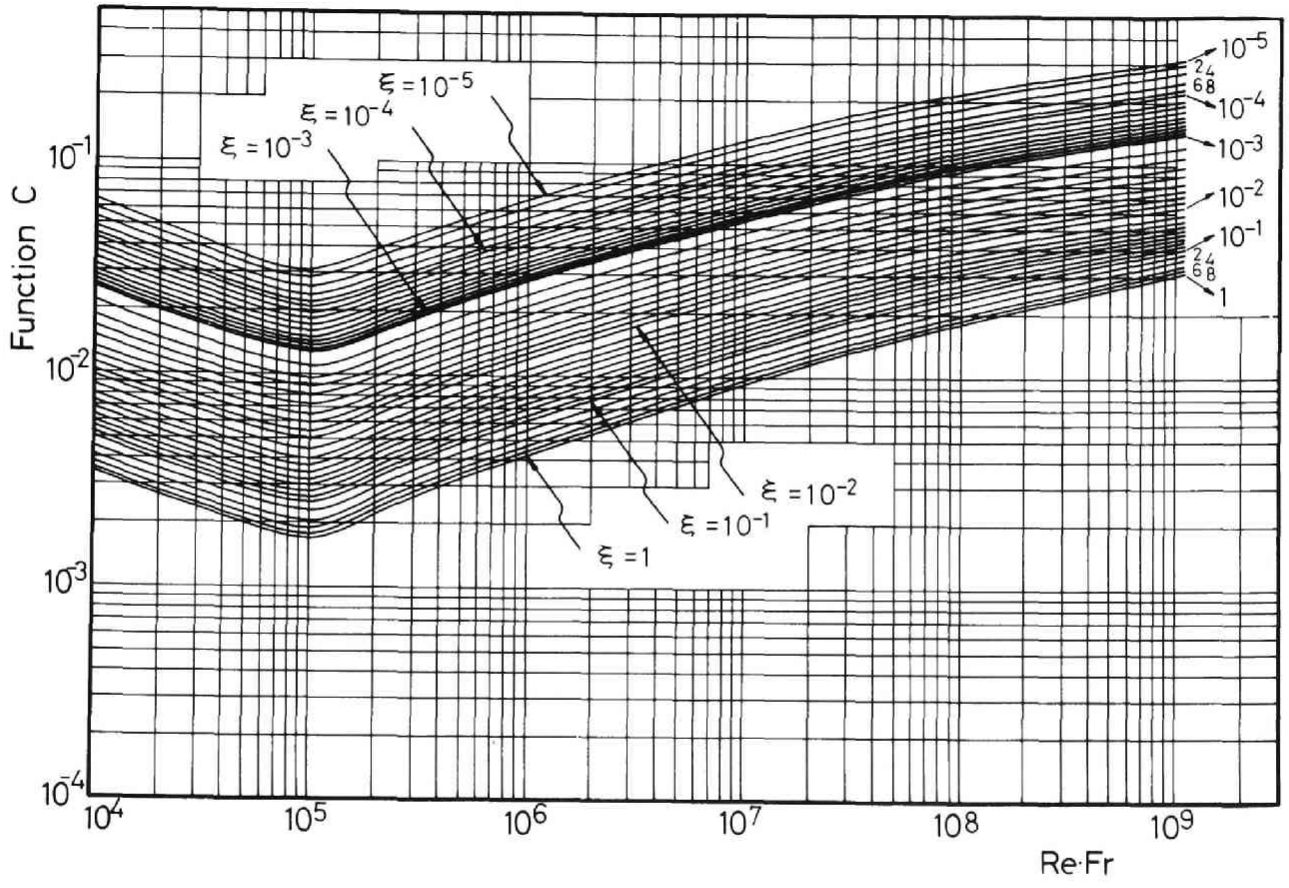

Fig. 6.4 Proposed pressure drop correlation (Function C)

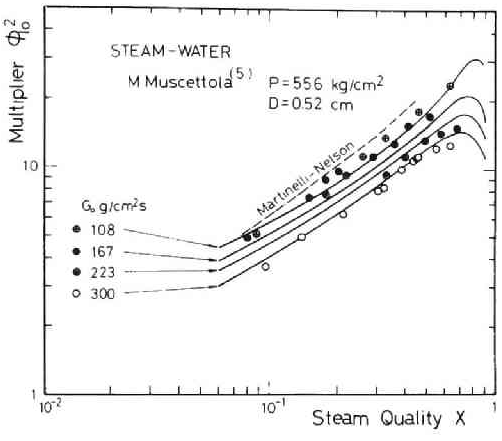

Fig. 6.5 Correlative representation of experimental pressure drop data for steam-water

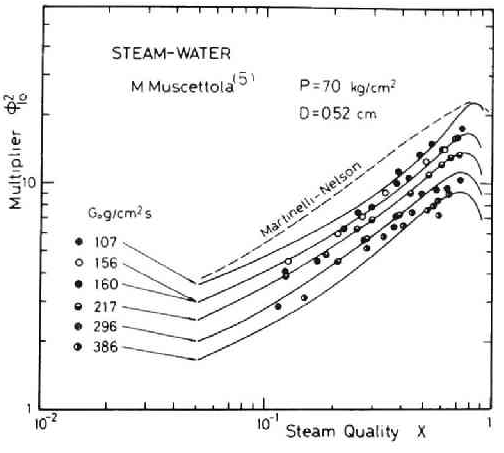

Fig. 6.6 Correlative representation of experimental pressure drop data of steam-water

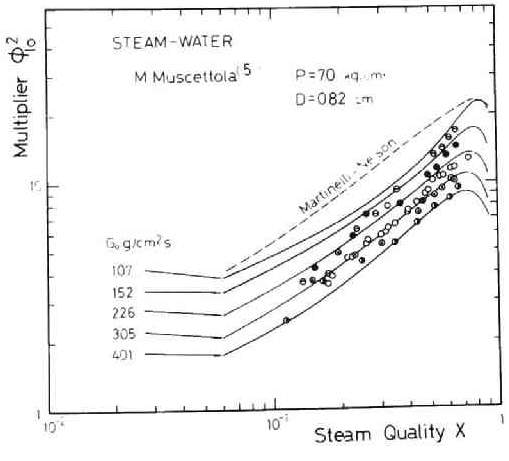

Fig. 6.7 Correlative representation of experimental pressure drop data for steam-water

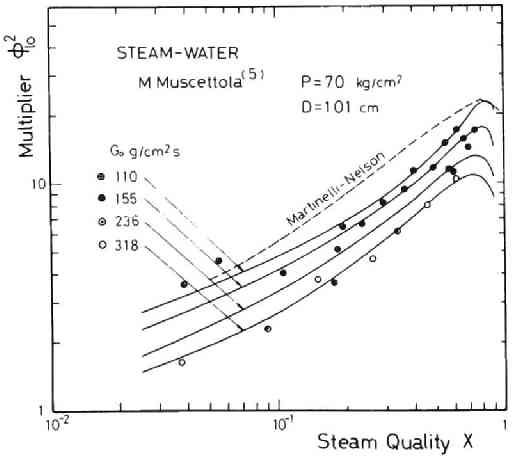

Fig. 6.8 Correlative representation of experimental pressure drop data for steam-water

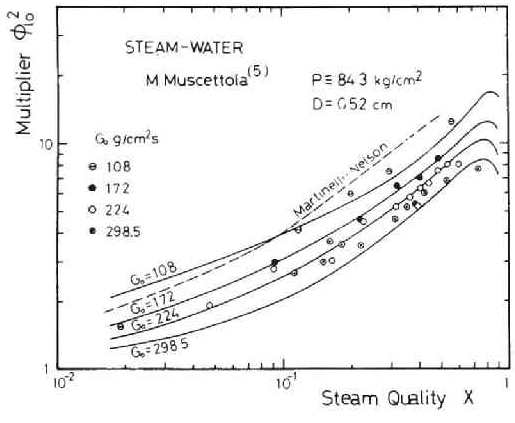

Fig. 6.9 Correlative representation of experimental pressure drop data for steam-water

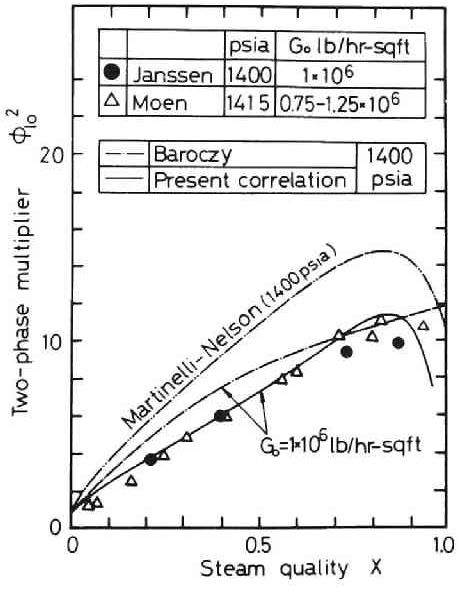

Fig. 6.10 Correlative representation of experimental pressure drop data for steam-water

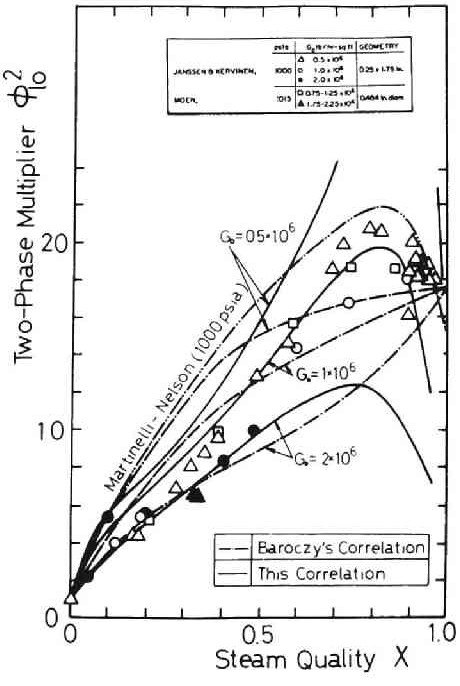

Fig. 6.11 Correlative representation of experimental pressure drop data for steam-water

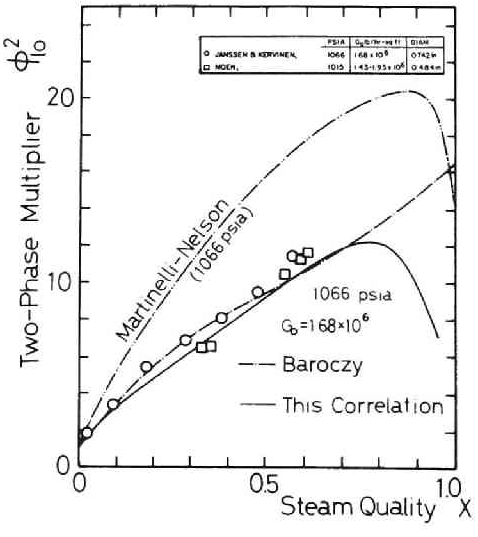

Fig. 6.12 Correlative representation of experimental pressure drop data for steam-water

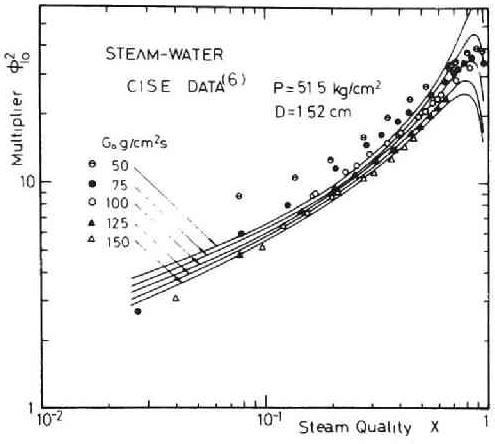

Fig. 6.13 Correlative representation of experimental pressure drop data for steam-water

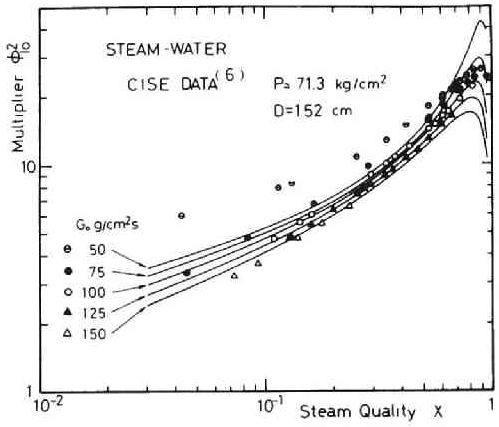

Fig. 6.14 Correlative representation of experimental pressure drop data for steam-water

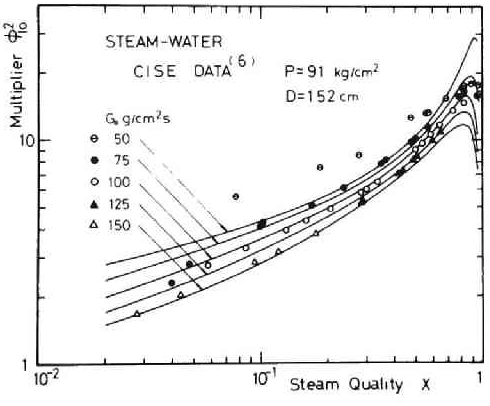

Fig. 6.15 Correlative representation of experimental pressure drop data for steam-water

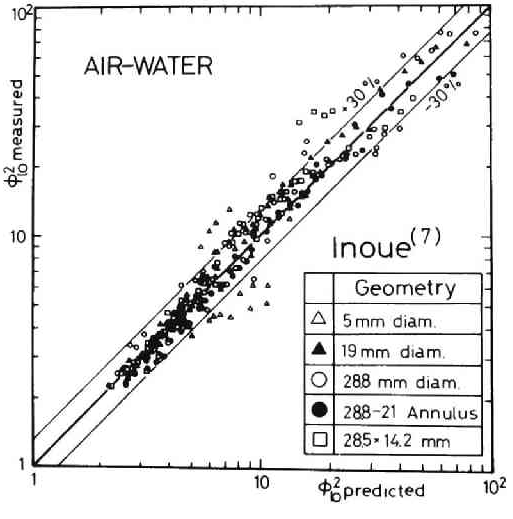

Fig. 6.16 Correlative representation of experimental pressure drop data for air-water

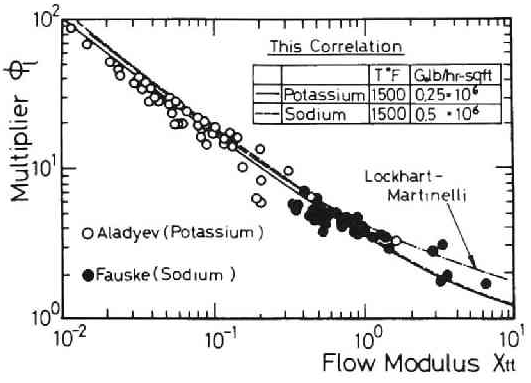

Fig. 6.17 Correlative representation of experimental pressure drop data for sodium

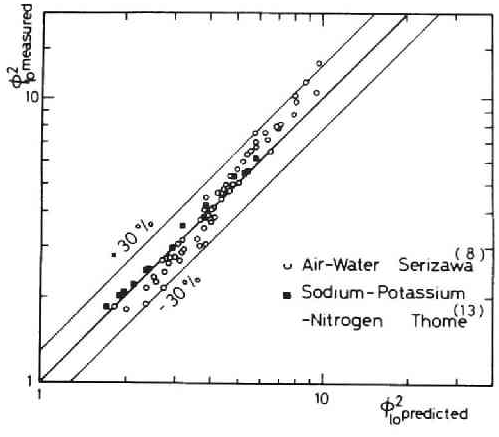

Fig. 6.19 Correlative representation of experimental pressure-drop data for sodium-potassium nitrogen and air-water

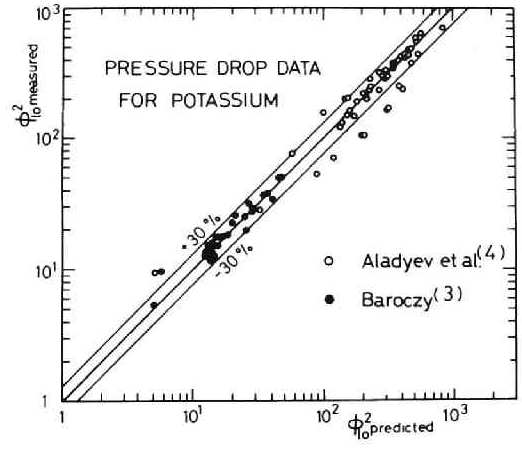

Fig. 6.18 Correlative representation of experimental pressure drop data for potassium

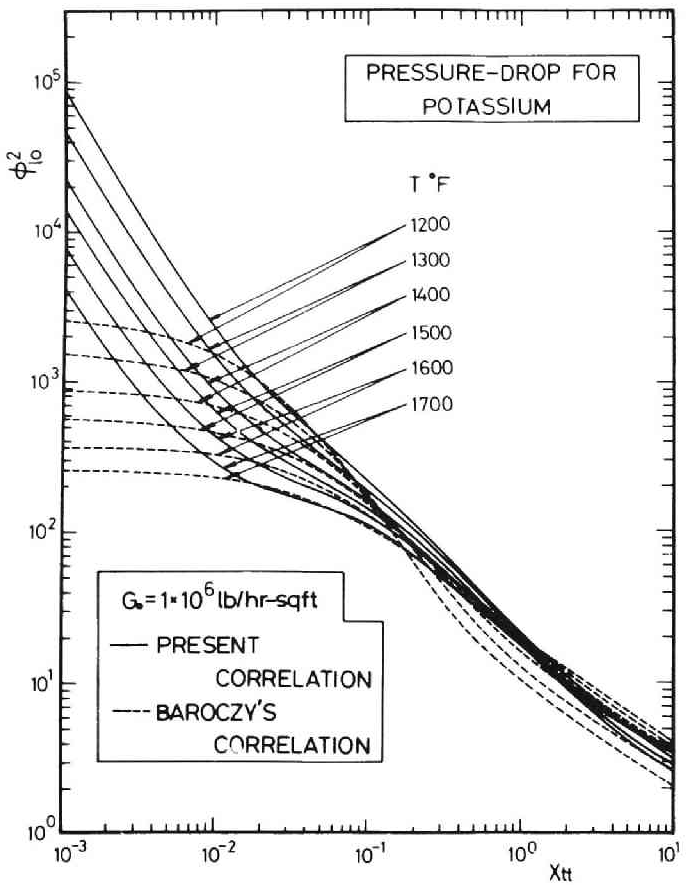

Fig. 6.20 Pressure level and temperature effects for potassium at $G_o = 1 \times 10^6$ lb/hr·ft^2

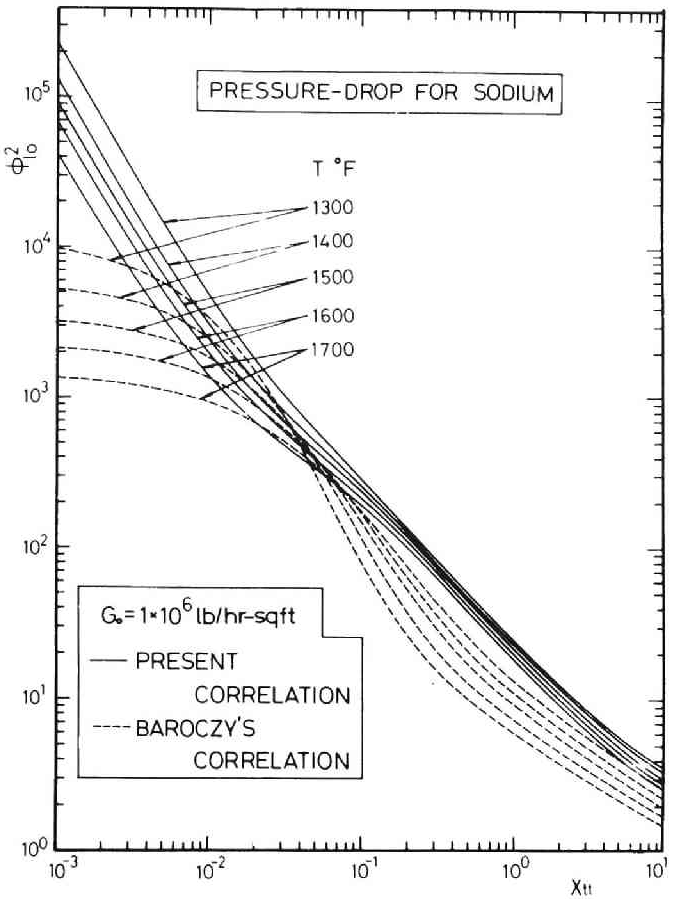

Fig. 6.21 Pressure level and temperature effects for sodium at $G_o = 1 \times 10^6$ lb/hr·ft^2

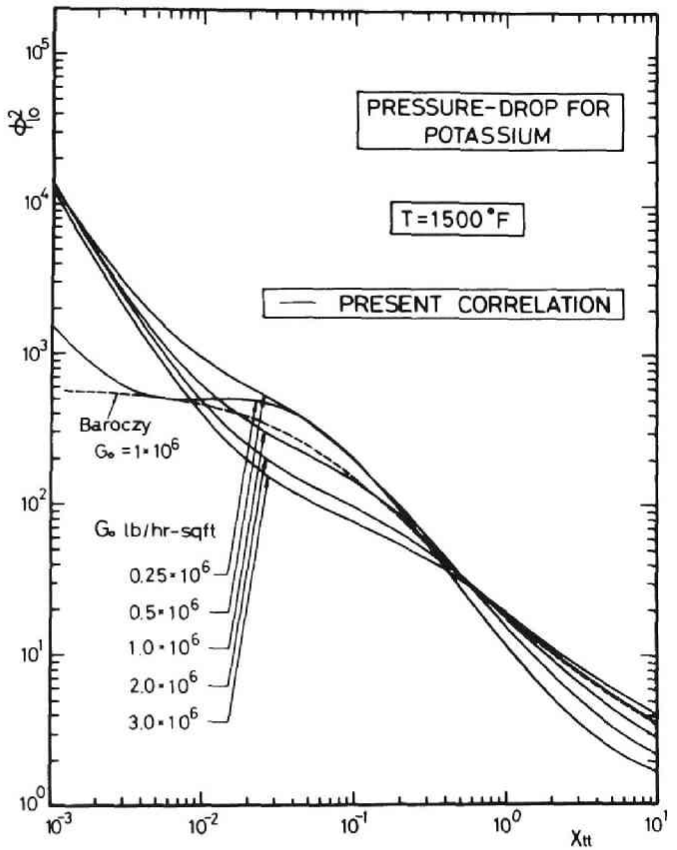

Fig. 6.22 Mass velocity effect for potassium at T=1,500°F

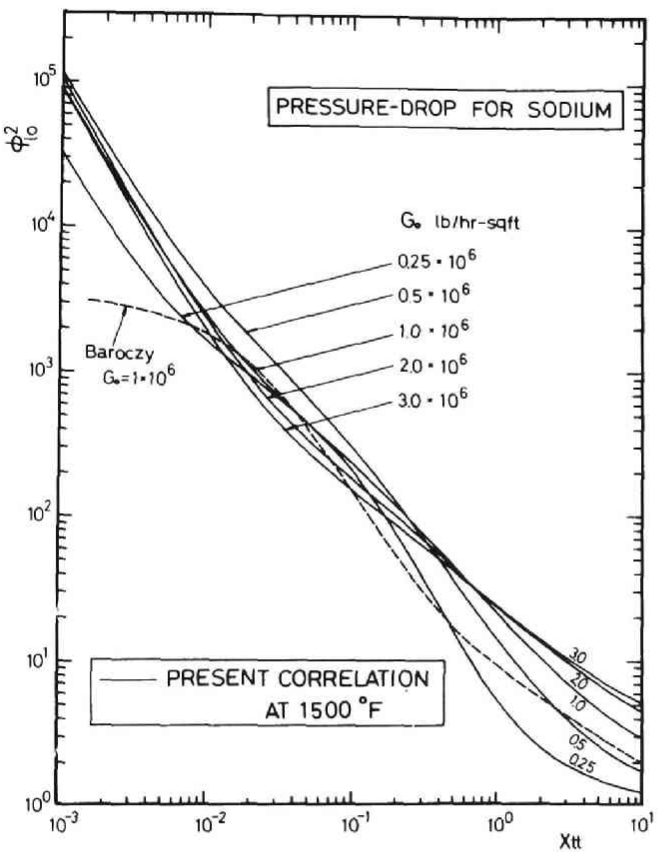

Fig. 6.23 Mass velocity effect for sodium at T=1,500°F

VII. EXPERIMENTS ON SINGLE SLUG BEHAVIOR

7.1 General

One may find it very difficult to predict correctly the steam void fraction in boiling two-phase flow systems due to perplexingly coupled thermohydrodynamics of the flow which is strongly affected by the type of flow, fluid properties, flow rates of the two phases, system pressure and temperature, heat flux through the heating wall, and geometric configuration of the flow channel.

Nevertheless, it is naive to expect that the void fraction can be evaluated for slug flow, which is characterized by large bubbles separated by slugs of liquid with filling almost the channel, on the basis of the slug flow model developed by Griffith & Wallis[1], Nicklin et al.[2], and Griffith[3], if we know correctly the velocity of those large bubbles.

In subsequent sections, descriptions will be presented of the observations made in an upward downward water flow of the dependence of the bubble rise velocity and shape upon the water velocity, the geometrical configuration and inclination of the flow channel, the bubble volume, and also upon the bubble expansion along the axial direction of the flow. Then, a comparison will be made between the experimental steam void fractions and the values predicted from a slug flow model. This experimental study was also intended to find, on the basis of the slug flow model, any explainable reason for the experimental finding that the steam void fraction obtained in rod-bundle geometry is somewhat lower than that in other geometries.

7.2 Experimental Apparatus and Measuring Equipments

Figure 7.1 represents a schematic drawing of the experimental apparatus. The test sections used in this experiment were made of a

3,000 mm long Lucite pipe (22.0, 28.5, 41.0, and 55.0 mm i.d.) and rods of three different sizes (3 mm or 6 mm o.d. stainless steel rods, or 8 mm o.d. glass rods). A summary of the test section dimensions and geometric configurations is presented in Table 7.1.

In upward water flow experiment, the water was circulated by a pump from a storage tank through the test channel, while in downward water flow experiment, the flow was circulated by gravitaional force from the upper plenum. The mean water flow rate was determined by measuring the volume of the water flow per unit time with using a measuring cylinder. The bubble volume was measured at the upper plenum by means of the underwater substitution technique.

First, the water velocity was set at a desired value by means of a valve, and then a single air bubble was introduced at the bottom of the test section by rapid action of the air supply valve (electro-magnetic valve). A camera lifted upward by means of a motor drive at nearly the same velocity as the slugs photographed the slug, an illuminated scale, and the reflection of stop-watch moving together with the camera mounted on the same platform, over a length of about 2,500 mm long. This method gives the temporarily varying bubble velocity and length. The bubble velocity and length were measured also by an electrical resistivity method with using pairs of electrodes closely contact inside the channel placed at 700, 1,700, and 2,700 mm downs-tream of the entrance to the test section. The bubble length measured by these two different methods were in good agreemant with each other.

7.3 Shape of Slugs

Representative shapes of large bubbles observed in this experiment are illustrated in Fig.7.2 for vertical flow. Most bubbles were the bullet-shaped with their nose rounded and the tail generally flat, but their cross sections were different correspondingly to the geometric configuration of the flow channel (Fig.7.2):

Circular pipe: A bubble almost fills the pipe with nearly circular

cross section.

Annulus : For a slender inner rod, a bubble was usually doughnut-shaped, whereas a thick one, sometimes cashewnut-shaped.

Rod-bundle : Various types of the cross section were observed, depending upon the bubble length, diameters of the inner rods and outer pipe, the clearance between them, the water velocity and the initial condition for introducing the bubbles into the test channel.

The bubble shape is also affected by the inclination of the channel and the direction of the flow (see Fig.7.3). In particular, the situation is more complicated with downflows, because the rising bubbles become unsymmetrical and quiver in trying to avoid the fast-moving water in the center of the pipe.

As for the relationship between the volume Q_b and the length L_s of bubbles, Griffith & Wallis[1] obtained an empirical formula, given by

$$Q_b = A\ D\ (mL_s - nD) \quad , \tag{7.1}$$

where, A, D, m, and n are the pipe cross section area, pipe diameter, and experimentally determined constants. For the particular case of potential flow around the bubble, the constants m and n are given by them as follows:

$$m = 0.913$$
$$n = 0.526 \qquad \text{for } L_s/D < 20 \quad .$$

Another semi-empirical equation has been recently suggested by Sugawara et al.[4].

Figures 7.4 ~ 7.6 represent the effects of the geometric configuration of the flow channel (for vertical case), the water velocity (for inclined pipe), and of the inclination of the test channel (for stationary water in pipe) upon the relation between Q_b and L_s, respectively. The general tendency of the effect of the channel inclination

coincides qualitatively with the illustrations shown in Fig.7.3.

7.4 Relation between Velocity and Length of Slugs

Dumitrescu[5] and Davis & Taylor[6] studied the rate of the bubble rise. Based on the assumption of a potential flow, i.e., the pressure over the front of the bubble is the same as that in ideal hydrodynamic flow round a sphere, they showed both theoretically and experimentally that the rising velocity of such a bubble V_{so} is related to the radius of curvature R, in the region of the vertex, by the equation $V_{so} = (2/3)\sqrt{gR}$. Then, the rising velocity of a slug in stationary liquid in a pipe of diameter D is given by

$$V_{so} = 0.35\sqrt{gD} \quad . \tag{7.2}$$

Equation (7.2) indicates that the rising velocity of a slug in stationary liquid should be determined uniquely by the pipe diameter alone. On the other hand, the experimental work of Laird & Chisholm [7] indicated that, in open system, the bubble velocity increased linearly in proportion to an increase in the bubble length. However, Nicklin et al.[2] showed experimentally that the slug velocity was independent of the slug length for non-expanding slugs in stationary liquid (closed system).

In the present work, prior to the measurements, the effects of the bubble expansion upon the rising velocity were examined for controlled conditions with using two cocks at the upper and the lower ends of the test channel. The arrangements tested were:

(a) Completely closed system (both cocks closed),

(b) Half-closed system (the upper cock closed, and the lower open),

(c) Half-closed system (the upper cock open, and the lower closed),

(d) Completely open system (both cocks open).

The experimental result indicated no dependence of the rising velocity on the type of arrangement, contradictorily to that obtained by Nicklin et al. Therefore, all the subsequent experiments were performed under the upper-open condition.

Figures 7.7 and 7.8 are the typical plots of the rising velocity of the slugs as a function of their length with the inner rod diameter as a parameter, and the channel inclination as a parameter, respectively. Thus, the approximate linear relations with increasing or decreasing tendency were observed in all experimental runs. The extrapolated values at $L_s = 0$ in the $V_s - L_s$ diagram thus obtained were applied for later analysis.

7.5 Rising Velocity of Single Slugs

Griffith & Wallis[1] made an attempt to realize the constant in Eq.(7.2) of Taylor and Dumitrescu for rising velocity of a slug flowing upward in stationary liquid in a pipe. They split it up into two parts, C_1 and C_2. The governing coefficient C_1 and the alternate C_2 are given both diagrammatically.

$$V_{so} = C_1 C_2 \sqrt{gD} \tag{7.3}$$

Nicklin et al.[2] proposed an empirical correlation given by Eq. (7.4) for predicting the velocity of slug in a moving liquid stream in a pipe.

$$V_s = 0.35\sqrt{gD} + 1.2 \left(\frac{Q_l + Q_g}{A}\right) , \tag{7.4}$$

where, Q_l, Q_g, and A are the flow rates of the liquid and the gas, and the cross-sectional area of the pipe.

Griffith[3] extended Eq.(7.4) to be valid for channels of various shapes, depending upon the experimental findings. The result is presented by the following equation.

$$V_s = K_1 K_3 \sqrt{gD_b} + (K_2 + 1)\left(\frac{Q_1 + Q_g}{A}\right) \quad , \qquad (7.5)$$

where, K_1 and K_2 are diagrammatically given as a function of the geometric parameter for various types of sections for $Re(= \left(\frac{Q_1 + Q_g}{A}\right)\frac{D_h}{\nu_1}) \geq 8{,}000$ (Fig.7.9). The other function K_3 is given as follows:

For a section with heat addition: $K_3 = 1.6$

For fully developed slug flow without heat addition: $K_3 = 1.0$.

In Fig.7.9, the abscissa D_s/D_b is for annuli and rectangles, and $(1 - D_h/D_b)$ is for rod-bundles, where D_s, D_h, and D_b and defined below.

D_s: insert diameter for an annulus, and small dimension for a rectangle,

D_h: hydraulic equivalent diameter,

D_b: pipe diameter for a pipe, large dimension for a rectangle, and shroud diameter for an annulus and a rod-bundle.

7.5.1 Experimental Determination of Flow Parameters K_1 and K_2

An expression identical to Eq.(7.5) appears more convenient for the arrangement of the experimental data on the rising velocity of a slug flowing upward in a moving liquid stream in a channel of various geometric configurations.

Typical plots of the flow parameter K_1 obtained in the present experiment are presented in Figs.7.10 and 7.11 in terms of the geometric parameters for pipes, and annuli and rod-bundles, respectively*. These figures indicate that almost all points show a small scatter with respect to the regressions (solid lines in the figures), of which trends are quite different from those shown in Fig.7.9.

Figure 7.12 represents the influence of the water velocity V_o upon another flow parameter K_2 obtained with using thus determined values of K_1*. The general trend of K_2 shown in Fig.7.12 is quite consistent both qualitatively and quantitatively with that obtained

---

* K_3 is chosen to be unity in these calculating procedures.

by Nicklin et al.[2]. A large value of K_2 for small upflows seen in the same figure may be attributable to a strong dependence of K_2 upon the slug length (see, for example, Fig.7.7), while, for the region of V_o exceeding nearly 0.5 m/sec, the value K_2 is nearly constant independently of the water velocity.

Figures 7.13 and 7.14 are the rearrangements of the experimental values of K_2 given in Fig.7.12 for the water velocity range $V_o \geq 0.5$ m/sec, and $V_o \leq 0.5$ m/sec, respectively.

Then, the rising velocity of a slug flowing through a vertical channel can be estimated from Eq.(7.4) with using the predicted values of K_1 and K_2, given in Figs.7.10 (for pipes) or 7.11 (for annuli, rectangles, and rod-bundles), and in Figs.7.10 (for pipes) or 7.13 ($V_o \geq 0.5$ m/sec) and 7.14 ($V_o \leq 0.5$ m/sec) (for annuli, rectangles, and rod-bundles), respectively.

7.5.2 Effect of the Channel Inclination

Figure 7.15 represents the effect of the channel inclination upon the relation between the rising velocity of slugs and the water velocity. This figure suggests two characteristic behaviors of the slugs. The first is that the rising velocity of the slugs increases with a decrease in the channel inclination Θ. This may be attributable to the fact that, as illustrated in Fig.7.3, a decrease in the channel inclination follows the eccentric transfiguration of a slug on one side, which will result in reducing the hydrodynamic resistance between the slug and the ambient water due to the resultant change in the stream velocity profile. The second is related to the minimum or the inflexion point found at nearly $V_o = -6$ cm/sec in the $V_s - V_o$ diagram. As the downflow water velocity was increased, a point was reached at which the stable character of the slug suddenly changed, i.e., the nose of the slug began to distort, or to become alternately eccentric on one side or another, and to lean over to one side of the pipe. Finally, as downflow water velocity was further increased, the unsymmetrical shape became dominant and the motion became steady again. This transition point corresponds to that minimum or the inflexion

point in that diagram. However, as the channel inclination varied from vertical to horizontal, the above mentioned unsteady character of the slug was reduced by the same reason as described just before.

Figure 7.16 shows the normalized flow parameters K_1^+, and K_2^+ for the velocity range $V_o \geq 0.3$ m/sec, where

$$K_1^+ = [K_1]_\Theta / [K_1]_{\Theta=90^o}$$

$$K_2^+ = [K_2 + 1]_\Theta / [K_2 + 1]_{\Theta=90^o}$$

A strong dependence of K_1^+ and K_2^+ upon the channel inclination, and a weak dependence upon the pipe diameter was observed.

The plots of $(K_2 + 1)$ similar to those shown in Fig.7.12 are presented in Fig.7.17, in which the solid line shows the present experimental curve, the dotted the one obtained by Nicklin et al.[2], the one-point-dotted chain line by Sugawara et al.[4], and the two-point-dotted chain line the predicted curve with the expanding equation of Nicklin et al. (Eq.(7.6)).

7.5.3 Effect of the Volume Expansion of Slugs

With respect to the dependence of the bubble rise velocity upon its length, Nicklin et al. reported that, as already described, the rising velocity generally increases with slug length dependently upon the absolute pressure of the system, and this increase is related to some character of expanding slugs, that is, the rate of expansion of the slug above which the liquid is taken off. They finally proposed for rising velocity of the slug in stationary liquid the following formula with an addition of the effect of expanding slug:

$$V_{so} = 0.35\sqrt{gD} + 1.48\ \Delta V_o \qquad (7.6)$$

where ΔV_o is the mean velocity of the liquid across any section in front of the slug caused by the volume expansion of the slug.

In the present experiment, the additional term ΔV_o can be calcu-

lated from the temporally varying slug length photographed by a camera, if we assume that the size and shape of the slug nose do not change during its travelling, and that the bubble expansion will cause equally both an upflow of the liquid above its nose and a downflow behind its tail. Then, we have

$$\Delta V_o = \frac{1}{2A}\frac{dQ_b}{dt} = \frac{1}{2A}\frac{dL_s}{dt} \tag{7.7}$$

Figure 7.18 represents the additional flow of the liquid ΔV_o as a function of the slug length. Comparisons of the experimental results with the predicted by Eq.(7.6) are also presented in Fig.7.19. From these figures it may be concluded that the effect of the expanding slug is only negligible, and the correlation of Nicklin et al. is not always valid. Figure 7.20, in which the relative expansion of the slug during its 1 m-long travel ($\Delta L_s/L_s$) is plotted against its length L_s, indicates that the experimental data of the bubble expansion well correspond to the predicted values from the static pressure drop data, with applying the ideal gas assumption to the air bubbles.

7.6 Void Fraction Predicted with Slug Flow Model

According to a plausible argument of two-phase flow in a pipe of diameter D made by Zuber & Findley[8], the weighted mean velocity of the gas phase V_g can be cast in the following form with the average volumetric flux density of the mixture $\bar{j}$ (= $(Q_l + Q_g)/A$), the drift velocity of bubbles or slugs V_{br}, and the distribution parameter C_o.

$$V_g = C_o \bar{j} + V_{br} \tag{7.8}$$

The drift velocity V_{br} is usually given as follows:

$$V_{br} = \begin{cases} 1.53[\sigma g(\rho_l - \rho_g)/\rho_l^2]^{1/4} & \text{for bubble flow} \\ 0.35[g(\rho_l - \rho_g)D/\rho_l]^{1/2} & \text{for slug flow} \end{cases}$$

The distribution parameter C_o depends, as a rule, upon the conditions of the flow. For fully-established axisymmetric two-phase flow, this value may range from about $C_o = 1.5$ to $C_o = 1.0$ correspondingly to the pronounced parabolic concentration profile, and to the flat one, respectively.

When $V_{br} = V_{so} = 0.35\sqrt{gD_b}$, and $C_o = 1.2$, Eq.(7.8) becomes equal to Eq.(7.4), since, for slug flow, the rising velocity of slugs V_s can be approximately replaced by the mean velocity of the gas phase V_g[9]. As a consequence, it may be expected that Eq.(7.5) becomes the most generalized one if it takes into account the dependence of the flow parameter K_2 upon the condition of the flow.

Moissis & Griffith[10] studied the velocity of a bubble rising behind a series of other bubbles in slug flow in a pipe. The rising velocity of such a bubble is expressed by the following equation as a function of the separation distance L_o from the bubble ahead of it, that is,

$$\frac{V_s - \bar{j}}{V_{s\infty} - \bar{j}} = 1 + 8\exp(-1.06\, L_o/D) \equiv \eta \qquad (7.9)$$

Here, it is assumed that Eq.(7.9) can be consistently applied for the various types of the flow channel. Then, replacing V_s by $V_{s\infty}$, the velocity of a single slug at $L_o = \infty$, in Eq.(7.5), and the substitution of the result into Eq.(7.9) yields

$$V_s = (1 + K_2\eta)\,\bar{j} + \eta K_1 K_3\sqrt{gD_b} \qquad (7.10)$$

Figures 7.21 and 7.22 show comparisons between the experimental results and the values predicted with correlating equations (7.10) (with letting $V_s = V_g$ and $K_3 = 1.6$), using the values of K_1 and K_2

given diagrammatically by Griffith in Fig.7.9 and also by the present author in Figs.7.11 and 7.14. These figures indicate that Eq.(7.10) with K_1 and K_2 given by us predicts fairly well the mean gas velocity in steam-water slug flow.

Next, we will derive the void fraction correlation, using this slug flow model. The mean gas velocity V_g and the volumetric flow rates of the two phases are given by

$$V_g = V_o \frac{X}{\alpha} \frac{\rho_1}{\rho_g} \quad , \quad W = A\, \rho_1\, V_o$$
$$Q_1 = W\,(1 - X)/\rho_1 \quad , \quad Q_g = W\, X/\rho_g \tag{7.11}$$

Since $V_g \simeq V_s$, we can easily obtain the following equation by substituting Eq.(7.11) into Eq.(7.10).

$$\alpha = \frac{\rho_1}{\rho_g} \frac{X}{(1 + K_2\eta)[(1 - X) + (\frac{\rho_1}{\rho_g})X] + \eta K_1 K_3/\sqrt{Fr}} \tag{7.12}$$

where Fr is a Froude number defined as $V_o^{\,2}/gD_b$.

Figure 7.23 represents comparisons between the experimental void fractions obtained in rod-bundles with the values predicted by Eq. (7.12) (solid lines) and also by Griffith's correlation Eq.(7.5) (dotted lines), with an aid of Figs.7.11 and 7.14 (the values L_o/D_b were chosen 3.0 for 4-rod bundle data, and 1.8 for 7-rod bundle data, however L_o/D_b varied in accordance with a change in conditions of the flow, that is, with an increase in the steam quality).

It may be thus evaluated that, according to the slug flow model, the dependence of the steam void fraction upon the geometric configuration of the channel is tightly subjected to the dependence of the bubble rise upon it, i.e., the slug flow model shows a lower void fraction for rod-bundles than for annuli in the range of flow variables covered in the present experimental work.

7.7 Conclusions

The conclusions of the experimental study on the behavior of single slugs may be summarized as follows:

(1) It is confirmed that Eq.(7.5) is valid for predicting the rising velocity of a single slug in both stationary and moving liquid stream in a vertical channel of various types, e.g., a pipe, an annulus, a rectangle, and a rod-bundle. Constants K_1 and K_2 chosen to fit our data are

K_1: shown in Fig.7.11,

K_2: shown in Fig.7.13 (for $V_o \geq 0.5$ m/sec) and in Fig.7.14 (for $V_o \leq 0.5$ m/sec),

and

K_3: 1.6 for a section with heat addition,
1.0 for fully-established slug flow without heat addition.

(2) Eq.(7.5) is also valid for bubble rise in the liquid in an inclined pipe. In this case, the constants K_1 and K_2 are given diagrammatically in Fig.7.16.

(3) Effect of the bubble expansion upon the rising velocity of the bubble was negligibly small in the present experiment.

(4) Dependence of the steam void fraction upon the geometric configuration of the flow channel in the slug flow region can be qualitatively accounted for by Eq.(7.12) derived on the basis of the slug flow model, but not necessarily quantitatively.

REFERENCES

[1] Griffith, P., Wallis, G.B.: Trans. Am. Soc. Mech. Engrs., Ser.C, Vol.83, 307 (1961).

[2] Nicklin, D.J., Wilkes, M.A., Davidson, M.A.: Trans. Instn. Chem. Engrs., Vol.40, 61 (1962).

[3] Griffith, P.: Trans. Am. Soc. Mech. Engrs., Ser.C, Vol.86, 327 (1964).

[4] Sugawara, S., Katsuta, T., Yamauchi, K.: 43th Western Japan Regular Meeting, Japan Soc. Mech. Engrs., 17 (1968).

[5] Dumitrescu, D.T.: Z. angew. Math. Mech., Vol.23, No.3, 139 (1943).

[6] Davies, R.M., Taylor, Sir Geoffrey: Proc. Roy. Soc. (London) 200A, 1062 (1950).

[7] Laird, A.D.K., Chisholm, D.: Ind. Eng. Chem., 48 [8], 1361 (1956).

[8] Zuber, N., Findley, J.A.: Trans. Am. Soc. Mech. Engrs., Ser.C, Vol.87, 453 (1965).

[9] Shirataki, K.: M.S. thesis, Kyoto Univ., (1965).

[10] Moissis, R. Griffith, P.: Trans. Am. Soc. Mech. Engrs., Ser.C, Vol.84, 29 (1962).

[11] Michiyoshi, I., Serizawa, A., Mitani, S.: J. At. Energy Soc. Japan, 10 [5], 238 (1968).

NOMENCLATURE

A	flow area
C_1	flow parameter defined by Eq.(7.3)
C_2	flow parameter defined by Eq.(7.3)
C_o	distribution parameter defined by Eq.(7.8)
D	pipe diameter
D_b	pipe diameter for a pipe, large dimension for a rectangle, and shroud diameter for an annulus and a rod-bundle
D_h	hydraulic equivalent diameter
D_s	insert diameter for an annulus and a rod-bundle, and small dimension for a rectangle
Fr	Froude number ($= V_o^2/gD_b$)
g	gravitational constant
$\bar{j}$	average volumetric flux density of the mixture
K_1	flow parameter defined by Eq.(7.5)
K_{1+}	dimensionless flow parameter
K_2	flow parameter defined by Eq.(7.5)
K_{2+}	dimensionless flow parameter
K_3	flow parameter defined by Eq.(7.5)
L	axial distance
L_o	separation distance between adjacent bubbles
L_s	bubble length
m	exponent
n	exponent
Q_b	bubble volume
Q_g	volumetric gas flow rate
Q_l	volumetric liquid flow rate
R	pipe radius
Re	Reynolds number ($(Q_g + Q_l)D_h/A\nu_l$)
t	time
V_{br}	drift velocity of a bubble
V_g	weighted mean velocity of gas phase
ΔL_s	bubble expansion in axial direction per unit length

V_o superficial liquid velocity

ΔV_o mean velocity of the liquid caused by the volume expansion of a bubble

V_s rising velocity of a single bubble

V_{so} rising velocity of a single bubble in stationary liquid

V_s rising velocity of a bubble at $L_o = \infty$

W total flow rate of the mixture

X quality

α average void fraction

η a function defined by Eq.(7.9)

Θ inclination angle

ν_l kinematic viscosity of liquid

ρ_g density of gas

ρ_l density of liquid

σ surface tension

Table 7.1 Geometric configuration and dimensions of the test section

Shroud Diameter (mm^{ϕ}) \ Insert Diameter (mm^{ϕ})	0	3.0	6.0	8.0
22.0	A	A,B,C,D		
28.5	A	A,B,C,D	A,B,C,D	A,B,C,D
41.0	A		A,B,C,D	
55.0	A			

Rod pitch = 9 mm

A : Circular pipe tested

B : Annulus tested

C : 4-Rod bundle tested

D : 7-Rod bundle tested

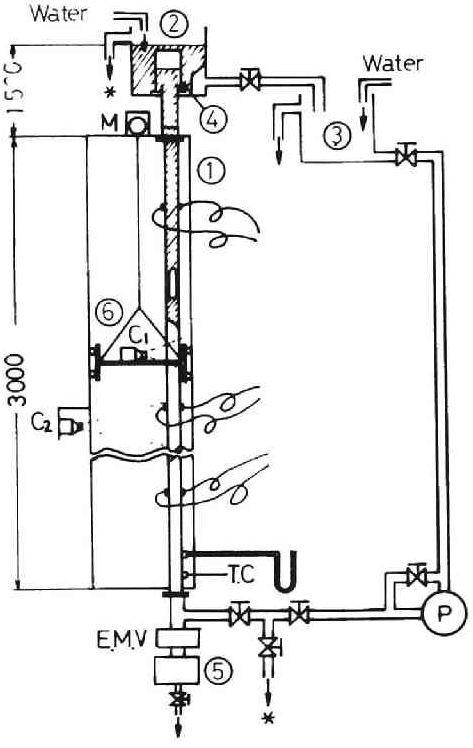

	Designation
①	Test Section
②	Separator
③	Storage Tank
④	Measuring Cylinder
⑤	Air Storage
⑥	Movable Platform
C_1, C_2	Camera
EMV	Electromagnetic Valve
M	Motor
P	Pump
T.C	Thermocouple
	Electrodes

* Flow Rate Measurement

Fig. 7.1 Schematic of experimental apparatus

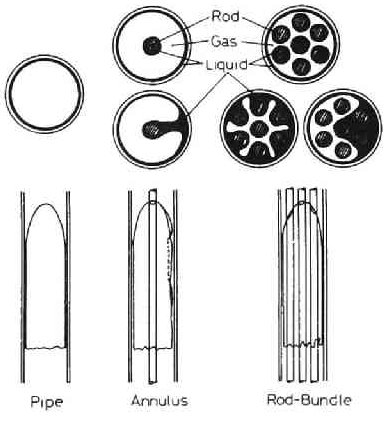

Fig. 7.2 Illustration of slug shape

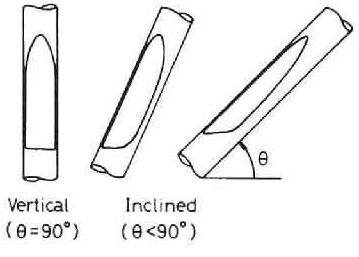

Fig. 7.3 Illustration of slug shape

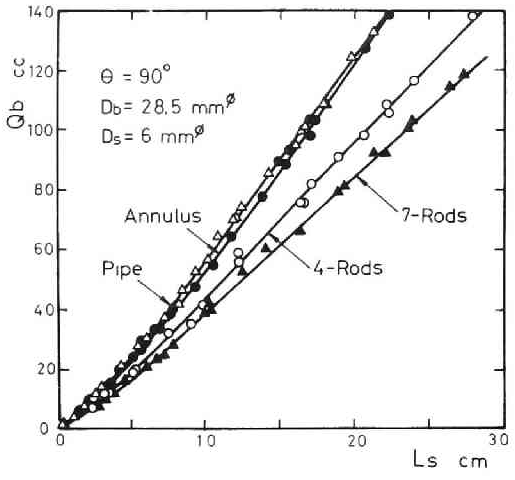

Fig. 7.4 Effect of geometric configuration of flow channel upon Q_b vs. L_s (D_b=28.5 mm)

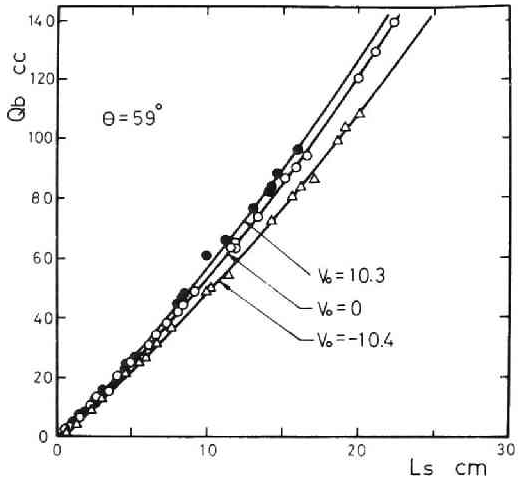

Fig. 7.5 Effect of water velocity upon Q_b vs. L_s (D_b=28.5 mm)

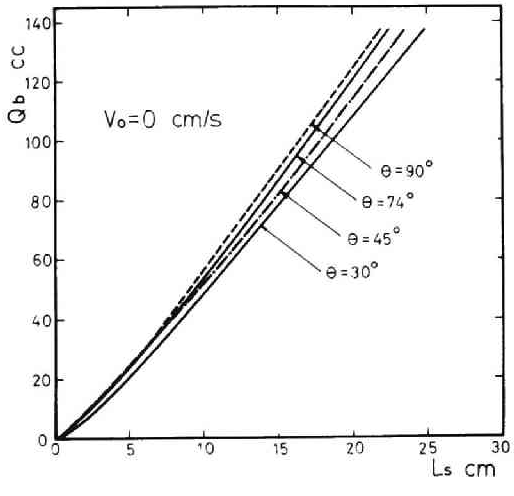

Fig. 7.6 Effect of channel inclination upon Q_b vs. L_s (D_b=28.5 mm)

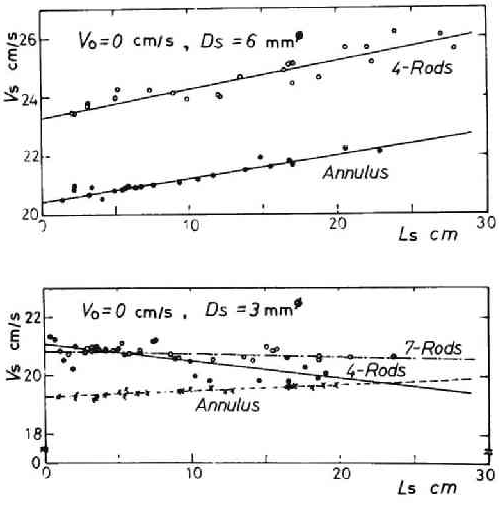

Fig. 7.7 Bubble rise velocity vs. length (D_b=28.5 mm)

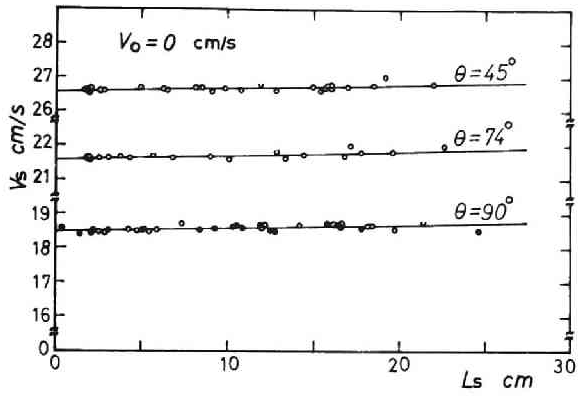

Fig. 7.8 Effect of channel inclination upon bubble rise velocity (D_b=28.5 mm)

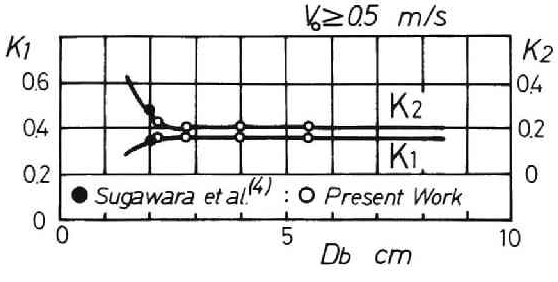

Fig. 7.10 Flow parameter K_1 vs. pipe diameter

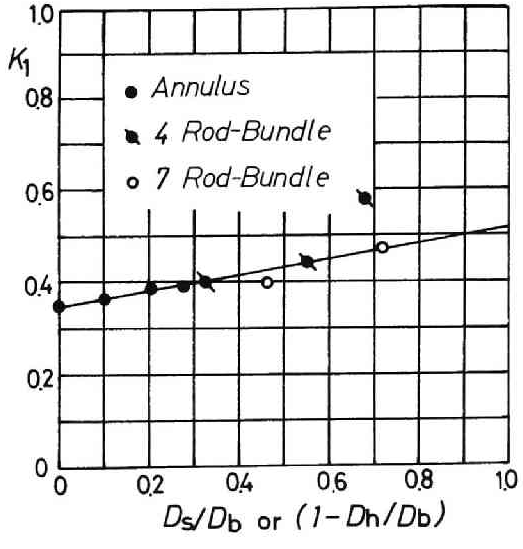

Fig 7.11 Flow parameter K_1 for various types of flow channel

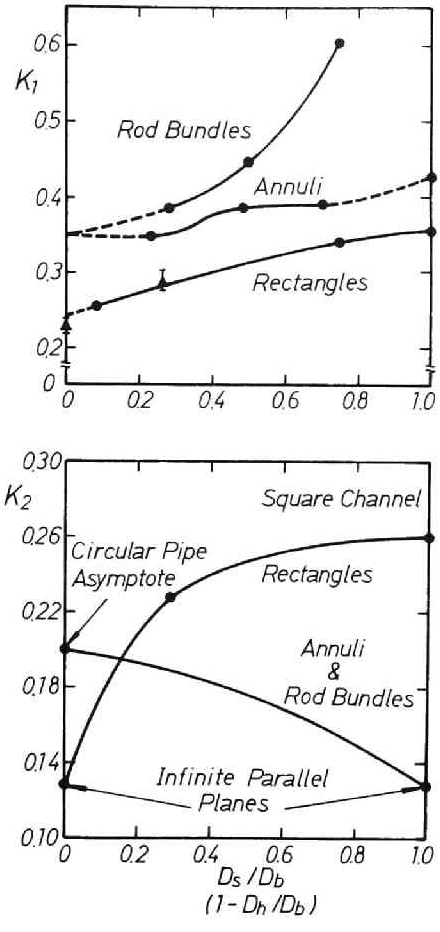

Fig. 7.9 Representation of flow parameters (by Griffith[3])

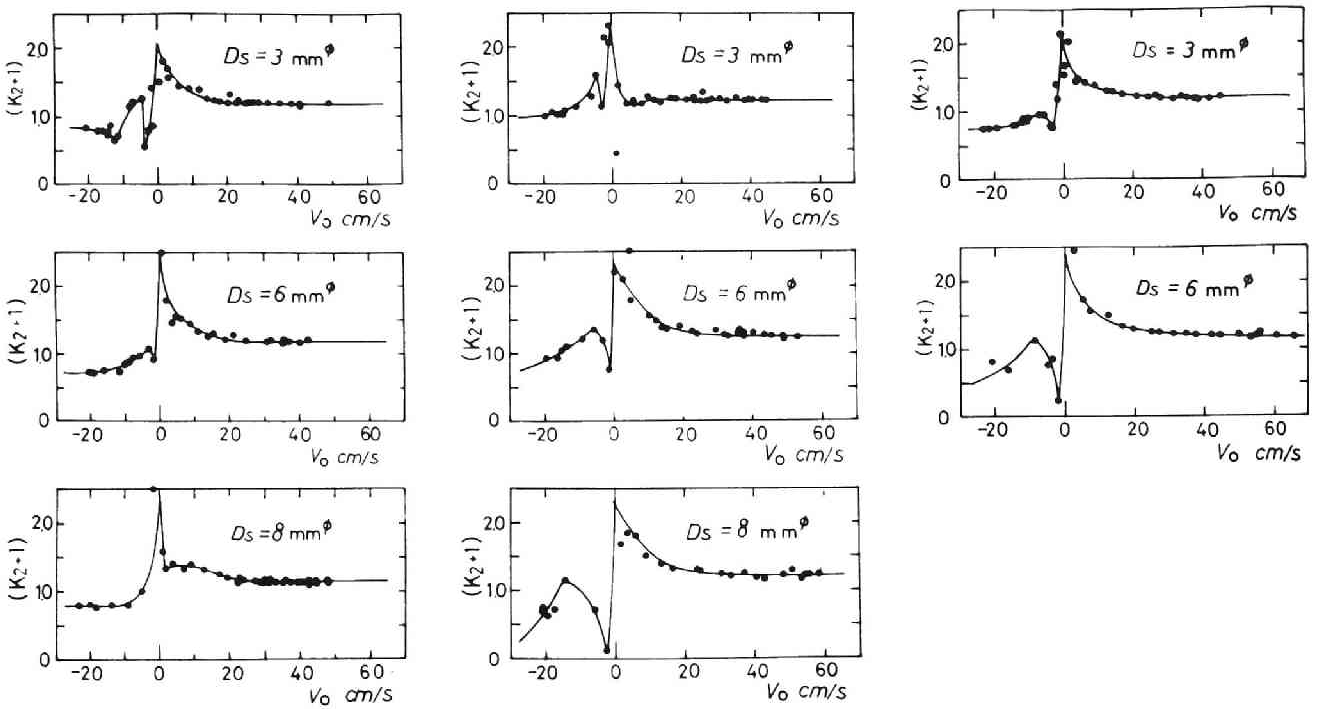

Fig. 7.12 Variation of (K_2+1) with water velocity and channel geometry

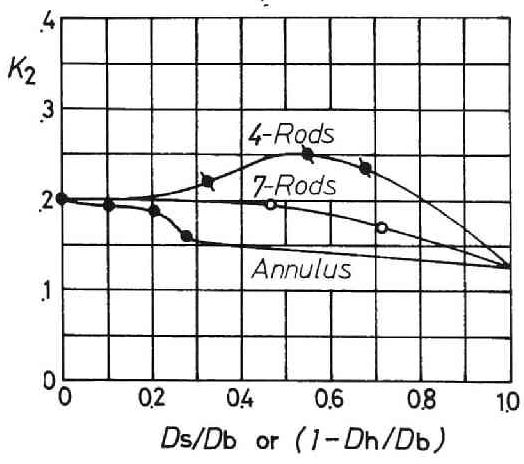

Fig. 7. 13 Flow parameter K_2 for various types of flow channel ($V_o \geq 0.5$ m/sec)

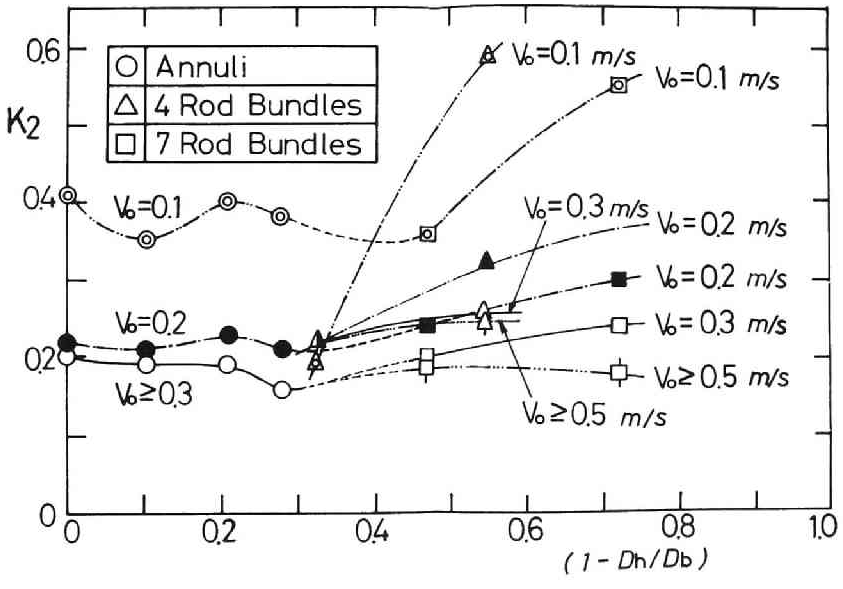

Fig. 7.14 Flow parameter K_2 for various water velocity and types of flow channel ($V_o < 0.5$ m/sec)

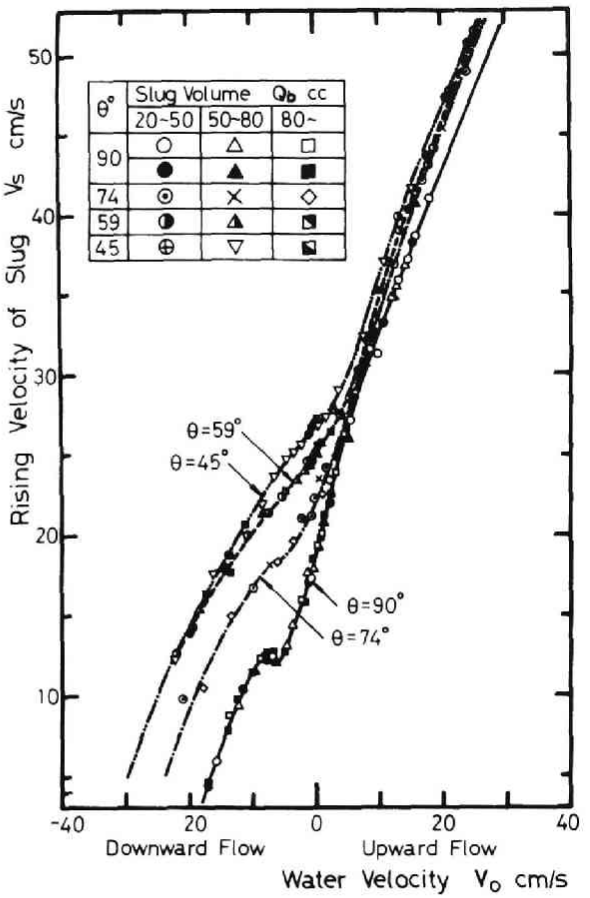

Fig. 7.15 Rising velocity of slugs vs. water velocity in terms of channel inclination (circular pipe : D_b=28.5 mm)

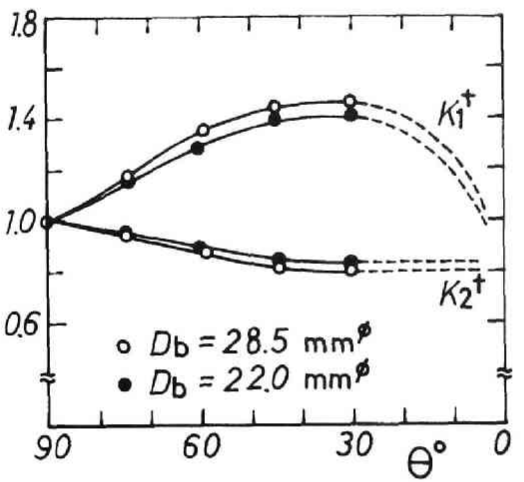

Fig. 7.16 Effect of channel inclination upon K_1 and K_2 for pipes ($V_o \geq 0.3$ m/sec)

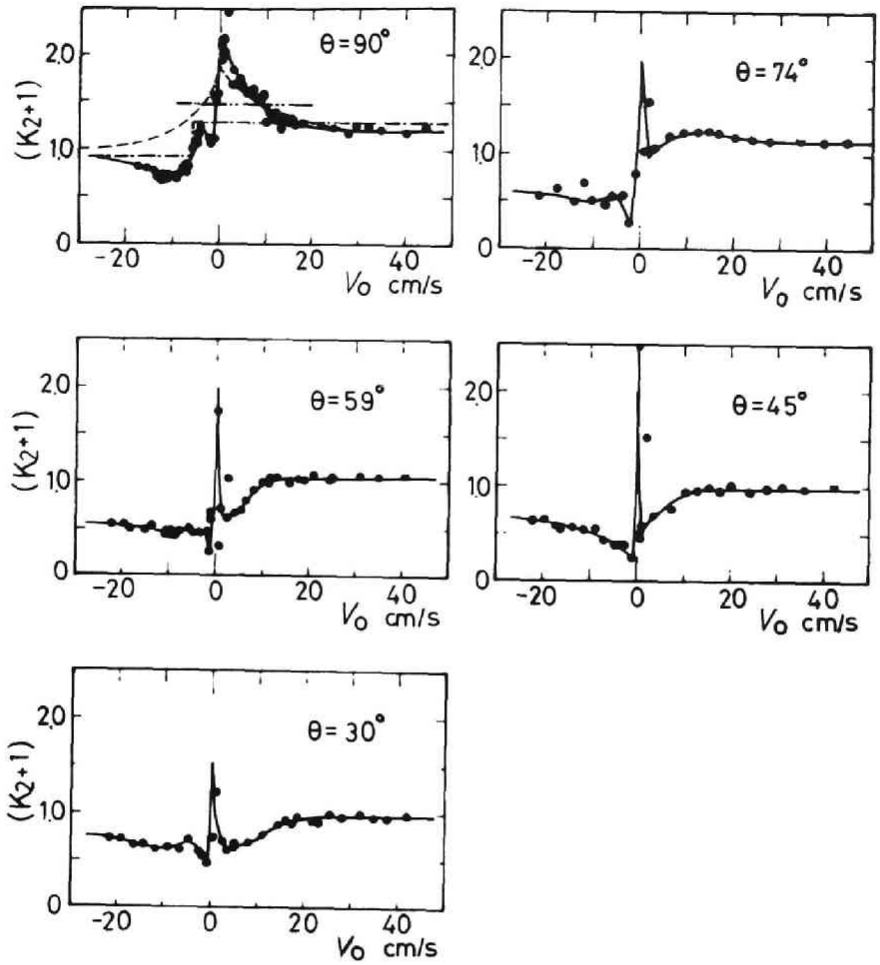

Fig. 7.17 Effect of channel inclination upon K_2 vs. V_o diagram (circular pipe : D_b=28.5 mm)

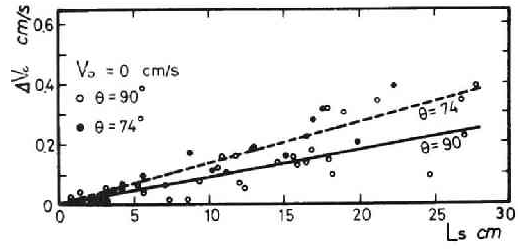

Fig. 7.18 Water flow caused by bubble expansion

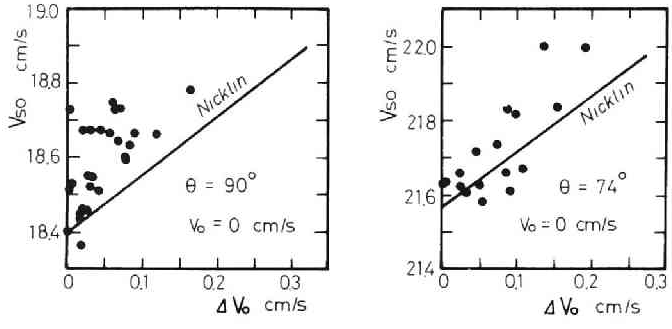

Fig. 7.19 Correlative representation of water flow caused by bubble expansion

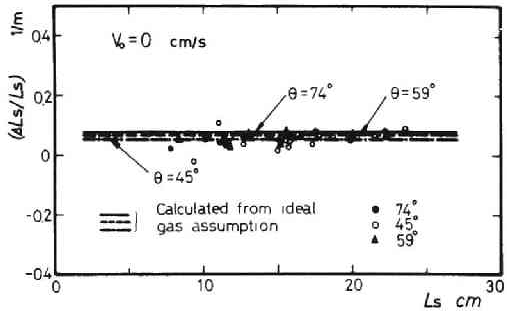

Fig. 7.20 Bubble expansion vs. length

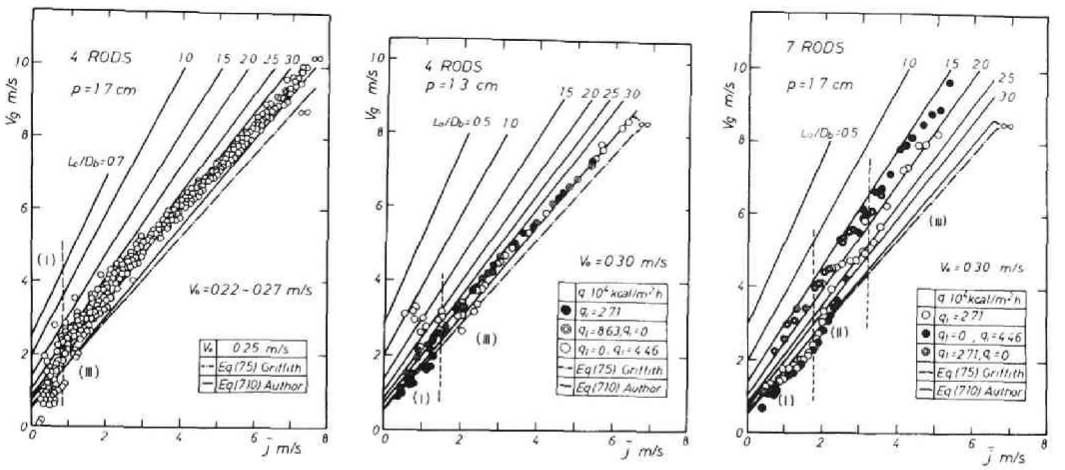

Fig. 7.21 Comparison of slug flow model with experimental mean gas velocity (I:Bubble flow, II:Slug flow, III:Annular flow)

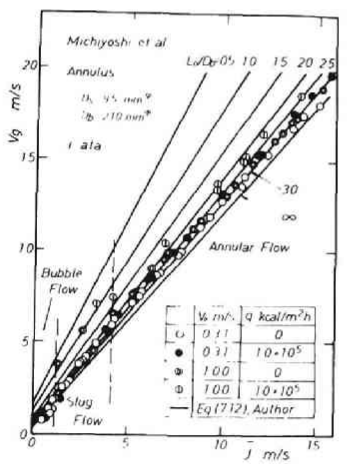

Fig. 7.22 Comparison of slug flow model with experimental mean gas velocity in pipe flow obtained by Michiyoshi et al.[11]

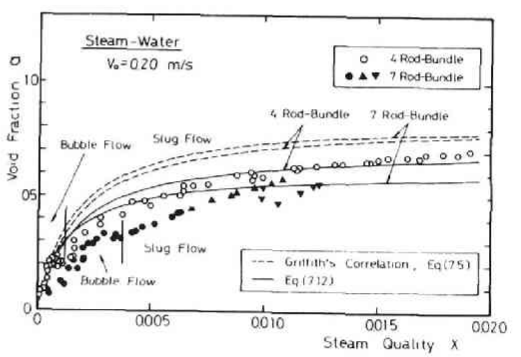

Fig. 7.23 Comparison between experimental and theoretical void fraction for steam-water in rod-bundles

VIII. AN ANALYTICAL MODEL FOR DROPLET-DISPERSED ANNULAR FLOW

8.1 General

Annular flow with liquid entrainment in the stream core and the liquid film along the periphery of the wall occurs in a wide variety of two-phase flow systems. In such flows with heat addition, burnout (i.e., slow burnout or wall temperature excursion) may occur when the flow of the liquid film tends smoothly to zero along the heated channel.

For an accurate prediction of such burnout or liquid film dryout point are needed particular knowledges not only of the mechanism of heat transfer between the liquid film and the heating wall but also of the hydrodynamic mechanism or mass transfer mechanism of the liquid droplet deposition from the stream core onto the thin liquid film and the droplet supply (droplet entrainment) into the stream. However, both mechanisms are closely coupled, and therefore the situation becomes more complicated.

A particular important case of the droplet motions, such as the deposition or the entrainment of droplets, has not yet been completely clarified even for the systems without heat addition, though a large amount of ivestigations have been devoted to this objective both theoretically and experimentally. This may be perhaps due to the rate of deposition of droplets onto the film, the rate of entrainment of droplets from the wave on the film surface, and the turbulent diffusivity of the droplets usually depend strongly upon the conditions of the flow, such as the fluid properties, flow rates of the liquid droplets in the core region, the liquid film and of the gas stream, droplet size, pressure gradient along the channel, system pressure and temperature, the state of the wall surface, the channel geometry, the channel inclination, diabatic or adiabatic system, heat flux through the heating surface, and also upon the initial conditions for creating gas-droplet mixture.

Most of the theoretical works concerning the initiation or entrainment of droplets from the liquid film are based upon the theory of the hydrodynamics of the wave (for example, Ref.[1-5]). But the results are not necessarily in satisfactory agreement with the experimental results. Theoretical study of Kondic[6] on the trajectory of a liquid droplet cannot be applied directly to the droplet-dispersed annular flow systems.

A series of experimental works on annular two-phase flow has been systematically and extensively carried out according to the programs at both Atomic Energy Research Establishment, Harwell, England, and Centro Informazioni Studi Esperienze, Italy. A considerable amount of experimental findings has been already published in AERE-reports and CISE-reports.

In this chapter, a prediction of the flow parameters, such as the axially varying flow rates of the entrained droplets and the liquid film, the liquid film thickness, the rates of the deposition and the entrainment of droplets, and the deposition coefficient will be made, based on an analytical model which takes into consideration the probability distribution functions for droplet residence time within the liquid film. Finally the entrance effect upon the development process of the flow will be evaluated.

8.2 Formulation of the Model

8.2.1 Basic Concept

Schematic diagram of the basis for the present model is presented in Fig.8.1.

This model assumes that the liquid droplet, which has once deposited by some reason onto the film from the core, travels as a marked lump of the liquid within the liquid film, and after a certain time Θ, it will be blown off again into the core as a suspension from the film

surface*.

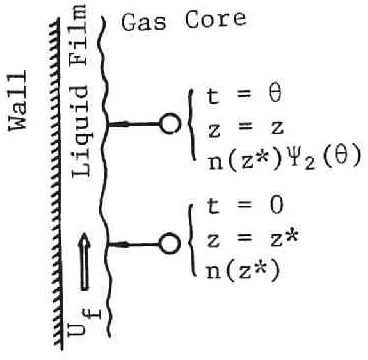

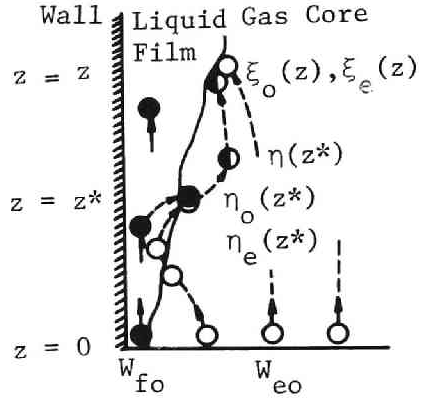

Fig. 8.1 Basic concept *Fig. 8.2 Basic flow model*

Now, let $\Psi_2(\Theta)d\Theta$ be the probability for that the above mentioned residence time of droplets within the liquid film is between θ and $\Theta + d\Theta$. Consider that, at time t = 0, n(z*) droplets deposit at the axial position z = z* on the liquid film flowing with constant velocity U_f. Then the number of the droplets entrained again into the gas stream at time $t = \Theta$ (i.e., at the position $z = z^* + U_f\Theta$) is

$$n(z^*)\ \Psi_2\left(\frac{z - z^*}{U_f}\right)\ d\Theta \qquad \text{(droplets/cm·sec)}. \tag{8.1}$$

---

* Strictly speaking, the travelling time or residence time Θ of the droplets within the film should be considered as a time lag between the deposition of a droplet onto the film and the first subsequent entrainment of a droplet from the film, since we cannot distinguish the marked droplet from the liquid film itself once it has deposited. However, the conventional residence time concept does not contradict seriously to the time-lag concept, except in their physical interpretations.

Therefore, the total number of the droplets entrained at z = z, N(z), is given by integrating Eq.(8.1) over z* = 0 ~ z.

$$N(z) = \int_0^z n(z^*)\ \Psi_2\left(\frac{z - z^*}{U_f}\right)\ \frac{dz^*}{U_f} \quad \text{(droplets/sec)}. \tag{8.2}$$

Here, it seems more convenient to use the deposition rate or entrainment rate (g/cm·sec) instead of the droplet number n (droplets/cm·sec), when the size of droplets is assumed uniform over the whole section of the channel.

The physical picture of the droplet-dispersed annular flow is presented in Fig.8.2. The terms used here are:

$W_e(z)$: Flow rate of the entrainment at any position z (g/sec),

W_{eo} : Flow rate of the entrainment at z = 0 (i.e., at the entrance to the channel) (○-marked component in Fig.8.2) (g/sec),

$W_f(z)$: Flow rate of the liquid film at any position z (g/sec),

W_{fo} : Flow rate of the liquid film at z = 0 (● -marked component in Fig.8.2) (g/sec),

$\xi(z)$: Total imaginary deposition rate at any position z (g/cm·sec),

$\xi_o(z)$: Deposition rate at z = z, resulting from the initial droplets W_{eo} which have not experienced any deposition during their travels (contribution from ○ -marked component in Fig.8.2) (g/cm·sec),

$\xi_e(z)$: Deposition rate at z = z, resulting from the entrained droplets which have been once entrained into the gas stream from the liquid film in their flight histories (◐ -marked component in Fig.8.2) (g/cm·sec),

$\eta(z)$: Total imaginary entrainment rate at any position z (g/sec),

$\eta_o(z)$: Entrainment rate at z = z, resulting from the droplets within the film which have not experienced any flight within the gas core in their travelling histories

(contribution from ● -marked component in Fig.8.2) (g/cm·sec),

$\eta_e(z)$: Entrainment rate at z = z, resulting from the droplets within the film which have once experienced at least one flight within the gas core as droplet suspensions (contribution from ○ and ◐ -marked component in Fig.8.2) (g/cm·sec),

$U_f(z)$: Mean axial velocity of the film flow at any position z (cm/sec),

$\delta_f(z)$: Mean film thickness at any position z (cm).

Thus, the (total imaginary) deposition rate $\xi(z)$ consists of two contributions $\xi_o(z)$ and $\xi_e(z)$, and also the (total imaginary) entrainment rate $\eta(z)$ of $\eta_o(z)$ and $\eta_e(z)$. The true deposition rate of droplets at any position z is therefore given by $[\xi(z) - \eta(z)]$.

8.2.2 Basic Equations

In the present analysis, the following assumptions are made for simplicity:

(1) Mean axial velocity of the liquid film U_f is constant independently of the axial position z,

(2) Droplet size distribution is uniform, and its spectral hardening is therefore ignored*.

(3) Deposition coefficient is constant*.

(4) Acceleration of the droplets due to the pressure gradient along the flow direction is neglected,

(5) The total deposition rate $\xi(z)$ and the total entrainment rate $\eta(z)$ consists of the two contributions, $\xi_o(z)$ and $\xi_e(z)$, and $\eta_o(z)$ and $\eta_e(z)$, respectively,

---

* Experimental results obtained by Farmer et al.[7] indicated λd = const., where λ and d are the droplet deposition coefficient and the mean droplet size. In the present case, the assumption of the constant droplet size may lead to the constant deposition coefficient.

(6) Minimum value W_{fc} is assumed for the flow rate of the inlet film flow from which droplet entrainment occurs. Then, the contribution $\eta_o(z)$ will become effective only when the inlet film flow rate exceeds the limiting value W_{fc}.

Then, the flow parameters are given as follows, respectively.

Deposition rate

$$\xi(z) = \xi_o(z) + \xi_e(z) \tag{8.3}$$

Entrainment rate

$$\eta(z) = \eta_o(z) + \eta_e(z) \tag{8.4}$$

Flow rate of the entrained droplets

$$W_e(z) = W_{eo} + \int_0^z [\eta(z) - \xi(z)]dz \tag{8.5}$$

Liquid film flow rate

$$W_f(z) = W_{fo} + \int_0^z [\xi(z) - \eta(z)]dz \tag{8.6}$$

$$W_e(z) + W_f(z) = W_{eo} + W_{fo} = W_l \quad (= \text{const.}) \tag{8.7}$$

Mean liquid film thickness (for a circular pipe of diameter D_p)

$$\delta_f(z) = W_f(z)/[\pi D_p \rho_l U_f] \tag{8.8}$$

According to the experimental work of Farmer et al.[7] on the liquid droplet deposition, the deposition rate $\xi_o(z)$ resulting from the initial droplet component W_{eo} is given by

$$\xi_o(z) = \lambda W_{eo} \exp(-\lambda z) \tag{8.9}$$

where, λ is the deposition coefficient (1/cm).

While, the deposition rate $\xi_e(z, z^*)$ at any position z resulting from a droplet entrainment rate $\eta(z^*)$ of droplets which were entrained at position z^* between 0 and z is given by Eq.(8.10) according to a similar discussion.

$$\xi_e(z, z^*) = \lambda \eta(z^*) \exp[-\lambda(z - z^*)] \tag{8.10}$$

Hence, the deposition rate $\xi_e(z)$ is obtained by integrating the above equation over $z^* = 0 \sim z$, that is

$$\xi_e(z) = \int_0^z \xi_e(z, z^*)dz^* = \lambda \int_0^z \eta(z^*) \exp[-\lambda(z - z^*)]dz^* \tag{8.11}$$

Next, we will consider the entrainment rate $\eta_o(z)$ resulting from the initial film flow W_{fo}. In general, possibility of the occurrence of the droplet entrainment is strongly governed by the type of the wave formed on the surface of the liquid film on the wall, and if the velocity of the film flow is below a certain value determined hydrodynamically for a given gas velocity, the roll waves can never be formed which act key roles in the process of the droplet entrainment[8-10]. Therefore, the droplet entrainment resulting from the initial film flow W_{fo} cannot take place either, unless W_{fo} exceeds a certain value. Let W_{fc} the limiting value of W_{fo} for the initiation of the droplet entrainment, and further assume that the entrainment rate $\eta_o(z)$ depends upon the effective initial film flow rate W_{fo}^* defined below.

$$\begin{aligned} W_{fo}^* &= W_{fo} - W_{fc} \qquad (\text{for } W_{fo} \geq W_{fc}) \\ &= 0 \qquad\qquad\quad (\text{for } W_{fo} \leq W_{fc}) \end{aligned} \tag{8.12}$$

Then, the contribution $\eta_o(z)$ is given by

$$\eta_o(z)dz = W_{fo}^* \Psi_1(\Theta)d\Theta \quad ,$$

and hence

$$\eta_o(z) = W_{fo}^* \Psi_1(\Theta) \frac{d\Theta}{dz} = \frac{W_{fo}^*}{U_f} \Psi_1(\frac{z}{U_f}) \quad , \tag{8.13}$$

where, $\Psi_1(\Theta)d\Theta$ is the probability for that the droplet entrainment occurs at the time between Θ and $\Theta + d\Theta$ as a result of the effective initial film flow W_{fo}^* (this quantity may correspond to the imaginary deposition of droplets at $t = 0$ and $z = 0$).

Let $\Psi_2(\Theta)d\Theta$ be the probability for that the residence time for the stay of the droplets within the liquid film, which deposited onto the film at the position z^* between 0 and z, is Θ and $\Theta + d\Theta$. Then,

similarly to Eq.(8.13), we have*

$$\eta_e(z) = \int_0^z \xi(z^*)\ \Psi_2(\Theta)d\Theta$$
$$= \frac{1}{U_f}\int_0^z \xi(z^*)\ \Psi_2\left(\frac{z - z^*}{U_f}\right)dz^* \qquad (8.14)$$

Finally, from Eqs.(8.3), (8.4), (8.9), (8.11), (8.13), and (8.14), we obtain the following relations between $\xi(z)$ and $\eta(z)$.

$$\xi(z) = \lambda\ e^{-\lambda z}\ [W_{eo} + \int_0^z \eta(z^*)\ e^{\lambda z^*}dz^*] \qquad (8.15)$$

$$\eta(z) = \frac{1}{U_f}\ [W_{fo}^*\ \Psi_1\left(\frac{z}{U_f}\right) + \int_0^z \xi(z^*)\ \Psi_2\left(\frac{z - z^*}{U_f}\right)dz^*] \qquad (8.16)$$

Equation (8.15) can be rewritten in more simplified form by differentiation.

$$\xi(z) - \eta(z) = -\frac{1}{\lambda}\frac{d}{dz}\xi(z) \qquad (8.17)$$

If $\Psi_1(\Theta)$ and $\Psi_2(\Theta)$ are given, $\xi(z)$ and $\eta(z)$ can be deduced from Eqs. (8.16) and (8.17).

While, the flow rates of the entrained droplets $W_e(z)$ and the liquid film $W_f(z)$ will become as follows from a set of equations (8.5) and (8.17), and (8.6) and (8.17), respectively.

$$W_e(z) = W_{eo} + [\xi(z) - \xi(0)]/\lambda \qquad (8.18)$$

$$W_f(z) = W_{fo} - [\xi(z) - \xi(0)]/\lambda \qquad (8.19)$$

---

* For this case, it is natural to expect that the droplet entrainment should occur even for $W_f(z) \lesssim W_{fc}$, since any droplet deposition is assumed here to be accompanied by the corresponding droplet entrainment after a certain stochastic time lag characterized by $\Psi_2(\Theta)d\Theta$.

8.3 Probability Distribution Functions and Solutions

Solutions have been performed for a number of cases. Typical probability distribution functions $\Psi_1(\Theta)$ and $\Psi_2(\Theta)$ tested are tabulated in Table 8.1. For these cases, analytical solutions to Eqs. (8.16) and (8.17) are usually given in considerably tedious expressions, and, hence, some of them will be presented here as occasion demands.

Representative solutions for several cases are shown in Fig.8.3 for values W_{fc} = 10.4 lb/hr, λ = 0.01149 1/inch, and $\lambda_c (=1/U_f\Theta_c)$ = 0.003868 1/inch (these values correspond to the experimental data of Cousins et al.[8], W_1 = 150 lb/hr and W_g = 60 lb/hr).

A detailed survey of comparisons of the predicted curves with the entrainment data of Cousins et al.[8, 11] (vertical air-water flow), and Hoogendoorn et al.[12] (horizontal air-mineral oil flow) has revealed that the CASE (A) is most practical. In this case, CASE (A), both $\Psi_1(\Theta)$ and $\Psi_2(\Theta)$ have their maximum point at Θ = 0. This may be interpreted as follows. It is natural that the droplet entrainment $\eta_o(z)$ resulting from the initial film flow may occur most probably at the inlet to the test section, since the flow turbulence due to the flow obstruction caused at the inlet is, of course, most intensified there, in particular when the gas-droplet mixture is created by entraining from a liquid film injected around the periphery of the pipe. This argument follows the maximum probability of $\Psi_1(\Theta)$ at z = 0, that is, Θ = 0. While, as for $\Psi_2(\Theta)$, it may be reasonable to expect that, at the moment of the deposition of a liquid droplet onto the film from the core, another droplet is possibly entrained into the core from the film at a different point of the same axial position z. Hence, $\Psi_2(\Theta)$ may well have its maximum at Θ = 0.

Various flow parameters are given below for CASE (A) with $\Theta_{c1} = \Theta_{c2}$ $(= \Theta_c)$.

Deposition rate

$$\xi(z) = \frac{\lambda\lambda_c}{\lambda_m}[W_{eo}(1 + \frac{\lambda}{\lambda_c} e^{-\lambda_m z}) + W_{fo}^*(1 - e^{-\lambda_m z})] \tag{8.20}$$

Entrainment rate

$$\eta(z) = \frac{\lambda\lambda_c}{\lambda_m}[W_{eo}(1 - e^{-\lambda_m z}) + W_{fo}^*(1 + \frac{\lambda_c}{\lambda} e^{-\lambda_m z})] \tag{8.21}$$

Flow rate of the entrained droplets

$$W_e(z) = W_{eo}[1 - \frac{\lambda}{\lambda_m}(1 - e^{-\lambda_m z})] + \frac{\lambda_c}{\lambda_m} W_{fo}(1 - e^{-\lambda_m z}) \tag{8.22}$$

Liquid film flow rate

$$W_f(z) = W_{fo} + \frac{1}{\lambda_m}(\lambda W_{eo} - \lambda_c W_{fo}^*)\ (1 - e^{-\lambda_m z}) \tag{8.23}$$

Liquid film thickness

$$\delta_f(z) = W_f(z)/[\pi D_p \rho_l U_f] \tag{8.8}$$

where,

$$\begin{aligned} W_{fo}^* &= W_{fo} - W_{fc} \qquad (W_{fo} \geq W_{fc}) \\ &= 0 \qquad\qquad\ (W_{fo} \leq W_{fc}) \end{aligned} \tag{8.12}$$

$$\begin{aligned} \lambda_c &= 1/U_f\Theta_c \\ \lambda_m &= \lambda + \lambda_c \end{aligned} \tag{8.24}$$

Equations (8.20) and (8.21) indicate that the deposition rate $\xi(z)$ becomes equal to the entrainment rate $\eta(z)$ at a sufficiently large z, which means that the flow is fully established there.

A prediction of the film thickness with using Eq.(8.8) requires a knowledge of the mean film velocity U_f. Provided that the pressure

gradient along the channel direction is constant, and that the frictional pressure drop is determined by U_f, we have

$$\phi_1^2 = \frac{(dP/dz)_{tf}}{(dP/dz)_{sf}} = [f_T \frac{U_f^2}{2gD_p}]/[f_S \frac{V_o^2}{2gD_p}]$$

$$= (f_T/f_S)\ (U_f/V_o)^2 \qquad (8.25)$$

If we further assume the following form of equation for friction factors f_T, and f_S.

$$f = C \cdot Re^{-n} \qquad (8.26)$$

Then, Eq.(8.25) becomes

$$\phi_1^2 = (\frac{U_f}{V_o})^2\ (\frac{U_f D_p}{\nu_1})^{-n} / (\frac{V_o D_p}{\nu_1})^{-n} = (\frac{U_f}{V_o})^{2-n} \quad ,$$

and, therefore

$$U_f = V_o[\phi_1]^{\frac{2}{2-n}} \quad .$$

When n = 0.25, we have

$$U_f = V_o[\phi_1]^{8/7} \quad . \qquad (8.27)$$

Thus, U_f can be determined by Eq.(8.27) for a given flow condition, since two-phase frictional pressure drop multiplier ϕ_1 is calculated from a well-known two-phase pressure drop correlation.

8.4 Deposition Coefficient of Droplets

It is extremely difficult to determine the values of the deposition coefficient λ and the entrainment coefficient λ_c (= $1/U_f\Theta_c$) from theoretical basis. Therefore, we applied the results of the CASE (A) to the experimental data of Cousins et al.[8] on the axial distribu-

tions of the flow rates of the entrained droplets and the liquid film, and then determined the coefficients λ and λ_c by least squares fitting*.

Figure 8.4 represents the plots of the deposition coefficient λ thus obtained as a function of the total liquid flow rate W_l. It will be seen from this figure that a large deposition coefficient is related to a small liquid flow rate for constant gas flow and to a large gas flow rate for constant liquid flow. Particularly for higher liquid flow rates, λ becomes nearly constant independent of the liquid flow rate but dependent upon the gas flow rate. This trend is qualitatively consistent with that observed by Farmer et al.[7].

Figure 8.5 represents λ_c/λ_m deduced from the same data in terms of W_g/W_l, of which value is closely related to the deposition rate or the entrainment rate in the fully-established flow region.

Almost all points in Figs.8.4 and 8.5 present a relatively small scatter with respect to the regressions which are represented by the equations

$$\lambda = A\, e^{-BW_l} + C$$

$$A = 0.0372 \times 10^{-0.00438 W_g}$$

$$B = 0.00361 \times 10^{0.0161 W_g} \qquad (8.28)$$

$$C = 0.0829 \times W_g^{-1.06} \quad ,$$

---

* The data of Cousins et al. used here were obtained in air-water annular flow in a 0.375-inch bore tube at inlet column pressure of 40 psia. The mixture was created by introducing the liquid phase through a porous sinter along the periphery of the tube after the gas velocity profile became established.

$$\lambda_c/\lambda_m = 3.13 \times 10^{-7}\ W_l^{0.363}\ W_g^{2.90} \qquad (8.29)$$

W_l, W_g: lb/hr

λ, λ_c, λ_m: 1/inch .

Figures 8.6 and 8.7 show the curves for λ_c and λ_m predicted by Eqs. (8.28) and (8.29). However, validity for applying the empirical formulas, Eqs.(8.28) and (8.29), to various flow conditions seems very doubtful, since they are not expressed in generalized forms.

A simple dimensional analysis of the situation may lead that λ_c/λ_m is a function of the dimensionless groups such as Rel (= $V_o D_p/\nu_l$: liquid Reynolds number), Reg (= $V_{go} D_p/\nu_g$: gas Reynolds number), Weg (= $\rho_g V_{go}^2 D_p/\sigma$: gas Weber number), d/D_p (diameter ratio of the droplet to the pipe), ρ_l/ρ_g (density ratio), and μ_l/μ_g (viscosity ratio), where V_{go} is the superficial gas velocity defined as $[W_g/(\pi/4)D_p^2\rho_g]$. Figure 8.8 represents the values of λ_c/λ_m, obtained by applying the present model CASE (A) to the aforementioned experimental data of Cousins et al. and Hoogendoorn et al., poltted against the volumetric flow rate ratio of the liquid with a parameter of a dimensionless magnitude Γ allowing for the principal physical properties influencing the droplet deposition or entrainment. Here, the dimensionless magnitude is given by

$$\Gamma = (\rho_l/\rho_g)(\mu_g/\mu_l)\ \text{Weg} \quad . \qquad (8.30)$$

The chain lines in Fig.8.8 represent the empirical formula, Eq.(8.29).

8.5 Comparison between Predicted and Experimental Values of Droplet Entrainment

Figures 8.9 ~ 8.11 show comparisons of the droplet entrainment predicted by the present model, using various experimental data by Cousins et al.[8, 11] for air-water flow in a circular pipe (W_{eo} = 0,

and $W_{fo} = 0$) and Hoogendoorn et al.[12] for air-mineral oil flow in a horizontal perspex pipe of 2-inch diameter ($W_{eo} = 0$). In each figure, the solid lines represent the curves drawn by least squares fitting with using Eq.(8.22). It may be concluded that the present audacious model can be thus successfully applied to the various flow conditions whenever we know the values λ and λ_c beforehand by some means.

8.6 Entrance Effect on Axial Entrainment Profile

Hydrodynamic characteristics of the flow with or without heat addition depend strongly upon whether the flow is fully established or not. Therefore, it is of importance to get an indication of the process of the flow development. Here, we will consider the entrance effect or the effect of the initial conditions for creating a gas-droplet mixture upon the axial profile of the entrainment flow rate.

Figure 8.12 indicates the general trend of this effect. The curves shown in the figure are predicted by Eq.(8.23) with $k = W_{eo}/W_{fo}$ as a parameter representing the initial condition of the flow ($k = 0$ corresponds to the case when all the liquid enters the channel in liquid film on the wall, while $k = \infty$, the case when all the liquid enters in liquid droplets, respectively)*. Thus, the result indicates that it takes as long as nearly 250 inch, for this case, for the flow establishment, and that the effect of the initial condition upon $W_e(z)/W_1$ may be considerable for $z < 200$ inch. (A discrepancy in the value $W_e(z)/W_1$ at infinite z between those for $k = \infty$ and $k = 5$, as shown in Fig.8.12, may follow from the definition of the effective initial film flow rate, i.e., Eq.(8.12).)

---

* The deposition coefficient λ, the entrainment coefficient λ_c, and the limiting initial film flow rate W_{fc} were chosen 0.01149 (1/inch), 0.003868 (1/inch), and 10.4 (lb/hr), respectively.

Figure 8.13 represents a comparison of the model with the experimental data on the liquid film flow rate obtained by Mishima[10] in air-water annular flow in a horizontal rectangular duct (16 mm × 40 mm) under nearly atmospheric pressure.

Thus, the initial condition may have an important effect upon the flow establishment even at a considerably downstream position from the entrance to the test section.

8.7 Conclusions

A simple analytical annular flow model was presented. Recommended probability distribution functions $\Psi_1(\Theta)$ and $\Psi_2(\Theta)$ for droplet residence time Θ within the liquid film are

$$\Psi_1(\Theta) = \Psi_2(\Theta) = (1/\Theta_c) \exp(-\Theta/\Theta_c) \quad .$$

The flow rates of the liquid droplets entrained in the core stream of the gas and of the liquid film on the wall, and other important flow parameters are given by Eqs.(8.20) ~ (8.24).

The results well coincide with the general trends of the experimental entrainment data. However, further experimental work will be needed for determining the deposition coefficient λ, and the entrainment coefficient λ_c.

An application of the present model to diabatic systems is one of the problems to be solved.

REFERENCES

[1] Hanratty, T.J., Egen, J.M.: Am. Inst. Chem. Engrs. J., 3 [3], 299 (1957).

[2] Hanratty, T.J., Hersham, A.: ibid., 7 [3], 488 (1961).

[3] Miles, J.W.: J. Fluid Mech., 8 [4], 593 (1960).

[4] Woodmansee, D.E., Hanratty, T.J.: Chem. Eng. Sci., Vol.24, 299 (1969).

[5] Yanai, M.: Doctoral thesis, Kyoto Univ., (1971).

[6] Kondic, N.N.: Trans Am. Soc. Mech. Engrs., Ser.C, Vol.92, 418 (1970).

[7] Farmer, R., Griffith, P., Rohsenow, W.M.: Trans. Am. Soc. Mech. Engrs., Ser.C, Vol.92, 587 (1970).

[8] Cousins, L.B., Denton, W.H., Hewitt, G.F.: AERE-R 4926, (1965).

[9] Pushkina, O.L., Sorokin, Yu.L.: ASME Heat Transfer-Soviet Research, 1 [5], 56 (1969).

[10] Mishima, K.: Private communication.

[11] Cousins, L.B., Hewitt, G.F.: AERE-R 5657, (1968).

[12] Hoogendoorn, C.J., Welling, W.A.: Symp. on Two Phase Flow, Exeter, (1965).

Table 8.1 Probability distribution functions

case	$\Psi_1(\theta)$	$\Psi_2(\theta)$	boundary condition
case A	$(1/\theta_{c_1})\exp(-\theta/\theta_{c_1})$	$(1/\theta_{c_2})\exp(-\theta/\theta_{c_2})$	$\eta(0) = \lambda_{c_1} W_{fo}^*$ $\xi(0) = \lambda W_{eo}$
case B	$(1/\theta_{c_1})\exp(-\theta/\theta_{c_1})$	$(\theta/\theta_{c_2}^2)\exp(-\theta/\theta_{c_2})$	$\eta(0) = \lambda_{c_1} W_{fo}^*$ $\xi(0) = \lambda W_{eo}$ $\eta'(0) = 0$
case C	$(\theta/\theta_{c_1}^2)\exp(-\theta/\theta_{c_1})$	$(\theta/\theta_{c_2}^2)\exp(-\theta/\theta_{c_2})$	$\eta(0) = 0$ $\xi(0) = \lambda W_{eo}$ $\eta'(0) = 0$
case D	$1/\theta_{c_1}$ (constant) $(U_f\theta_{c_1} > Z_{channel})$	$1/\theta_{c_2}$ (constant) $(U_f\theta_{c_2} > Z_{channel})$	$W_e(Z)$; finite at $Z \to \infty$
case E	$2(\theta/\theta_{c_1})\exp[-(\theta/\theta_{c_1})^2]$	$2(\theta/\theta_{c_2})\exp[-(\theta/\theta_{c_2})^2]$	$\eta(0)$ 0 $\xi(0)$ 0

NOMENCLATURE

C	constant
d	mean droplet size
D_p	pipe diameter
f	friction factor
f_S	single-phase friction factor
f_T	two-phase friction factor
g	gravitational constant
k	flow parameter ($= W_{eo}/W_{fo}$)
n	exponent
n	number of droplet deposition at $z = z$ and $t = t$
$N(z)$	number of droplet entrained at $z = z$
Re_g	gas Reynolds number ($= V_{go} D_p/\nu_g$)
Re_l	liquid Reynolds number ($V_o D_p/\nu_l$)
$(\frac{dP}{dz})_{tf}$	two-phase frictional pressure drop
$(\frac{dP}{dz})_{sf}$	single-phase frictional pressure drop
t	temporal coordinate
U_f	mean velocity of liquid film
V_{go}	superficial gas velocity
V_o	superficial liquid velocity
W_e	entrained droplet flow rate
W_{eo}	initial droplet flow rate
W_f	film flow rate
W_{fc}	minimum value of initial film flow effective for droplet entrainment
W_{fo}	initial film flow rate
W_{fo}^*	effective initial film flow rate defined by Eq.(8.12)
W_g	gas flow rate
W_l	liquid flow rate ($= W_e + W_f$)
We_g	Weber number ($=\rho_g V_{go}^2 D_p/\sigma$)

z axial coordinate

z^* axial position

Z axial position

Γ dimensionless magnitude defined by Eq.(8.30)

δ_f mean film thickness

$\eta(z)$ entrainment rate at $z = z$

$\eta_e(z)$ entrainment rate at $z = z$, resulting from the droplet within the film which have once experienced at least one flight within the gas core as droplet suspensions

$\eta_o(z)$ entrainment rate at $z = z$, resulting from W_{fo}^*

Θ residence time

Θ_c constant residence time

λ deposition coefficient

λ_c entrainment coefficient $(= 1/U_f\Theta_c)$

λ_m defined as $(\lambda + \lambda_c)$

μ_g viscosity of gas

μ_l viscosity of liquid

ν_g kinematic viscosity of gas

ν_l kinematic viscosity of liquid

$\xi(z)$ deposition rate at $z = z$

$\xi_e(z)$ deposition rate at $z = z$, resulting from the entrained droplets which have been once entrained into the gas stream from the liquid film in their flight histories

ρ_g density of gas

ρ_l density of liquid

σ surface tension

ϕ_l^2 frictional pressure drop multiplier $(= (\frac{dP}{dz})_{tf}/(\frac{dP}{dz})_{sf})$

$\Psi_1(\Theta)$ probability distribution function

$\Psi_2(\Theta)$ probability distribution function

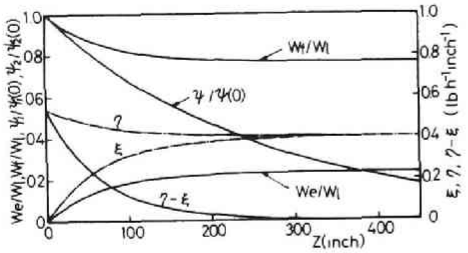

CASE (A) (W_{eo}=0)

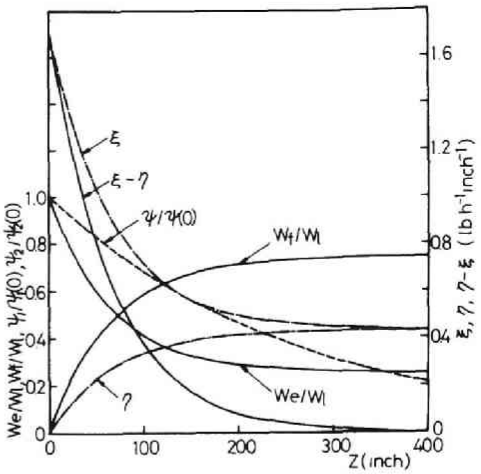

CASE (A) (W_{fo}=0)

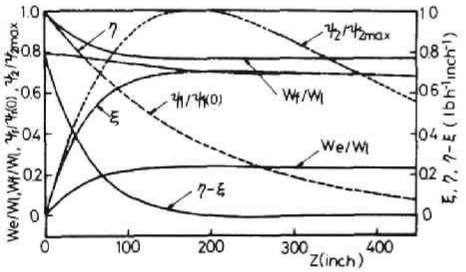

CASE (B) ($\lambda<4\lambda_c$: W_{eo}=0)

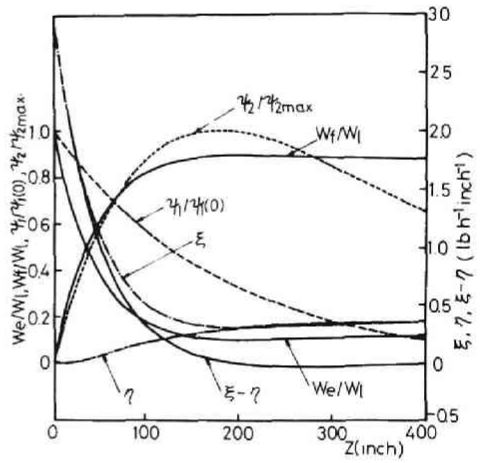

CASE (B) ($\lambda<4\lambda_c$: W_{fo}=0)

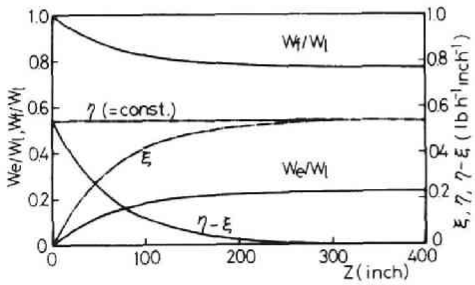

CASE (C) ($\lambda<4\lambda_c$: W_{eo}=0)

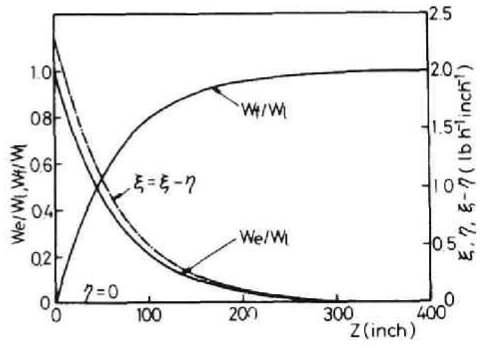

CASE (D) (W_{fo}=0)

Fig. 8.3 Solutions for several cases

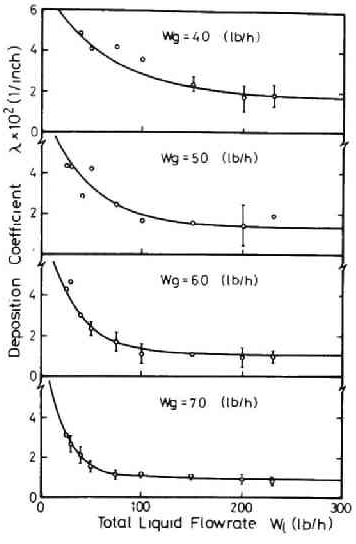

Fig. 8.4 Deposition coefficient calculated from data of Cousins et al.[8]

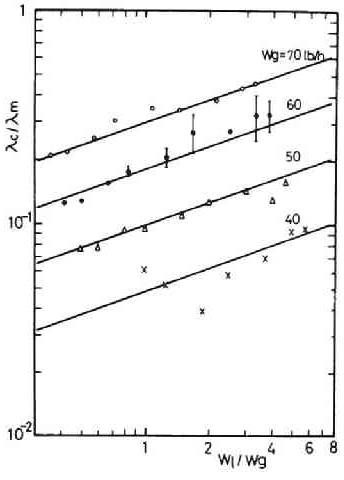

Fig. 8.5 Entrainment coefficient calculated from data of Cousins et al.[8]

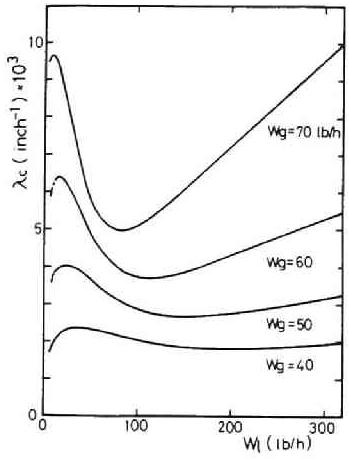

Fig. 8.6 Predicted entrainment coefficient

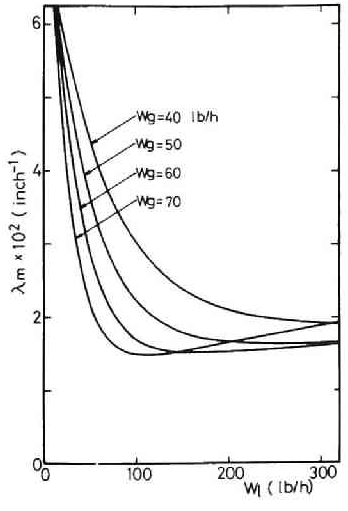

Fig. 8.7 Predicted values for λ_m

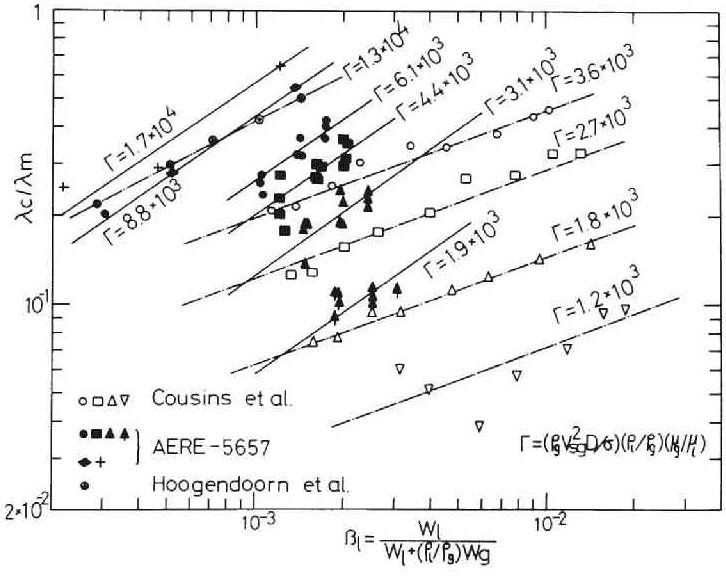

Fig. 8.8 Correlative representation of experimental λ_c/λ_m

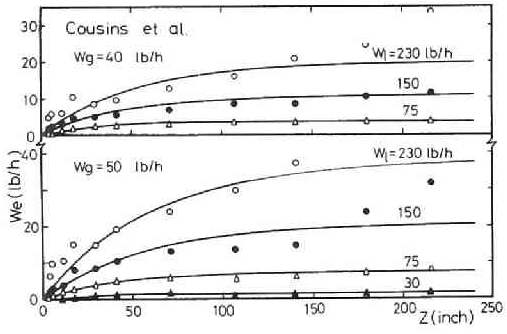

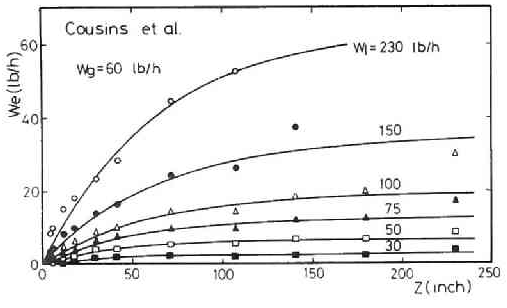

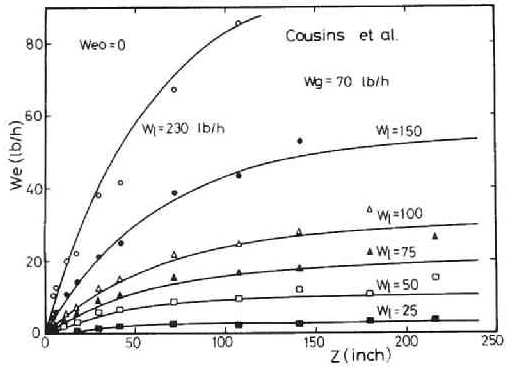

Fig. 8.9 Comparison between predicted and experimental entrainment (data of Cousins et al.[8])

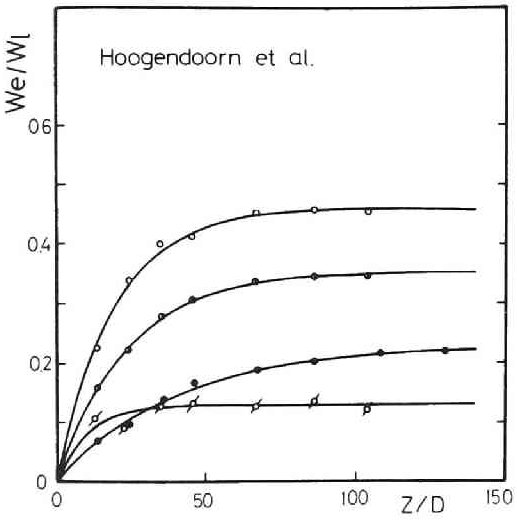

Fig. 8.10 Comparison between predicted and experimental entrainment (data of Hoogendoorn et al.[12])

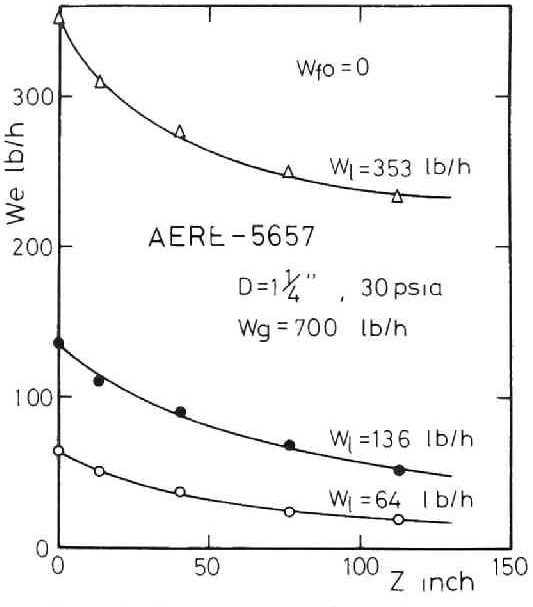

Fig. 8.11 Comparison between predicted and experimental entrainment (data of Cousin & Hewitt[11])

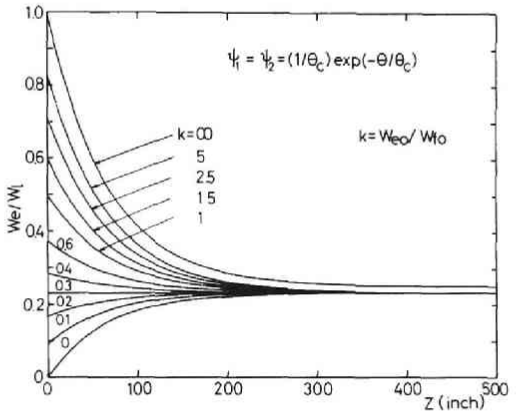

Fig. 8.12 Predicted entrance effect upon flow development

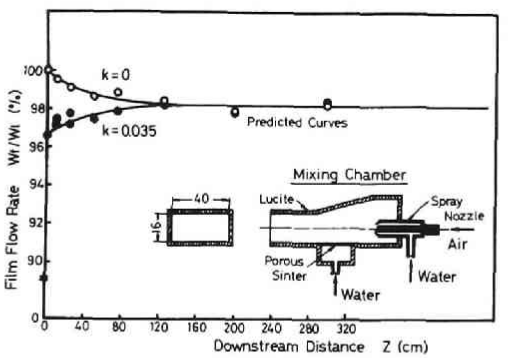

Fig. 8.13 Comparison between predicted and experimental film flow rate (data of Mishima[10])

IX. SUMMARY AND CONCLUSIONS

Over-all characteristics of gas-liquid two-phase flows were studied experimentally in upward steam-water flow in a vertical concentric annulus and 4-rod or 7-rod bundle of triangular lattice, upward air-water flow in a vertical concentric annulus, and argon-mercury flow in a vertical circular pipe.

The void fraction and the frictional pressure drop data confirm that they are strongly affected by the mass velocity of the two-phase mixture. With increasing the liquid velocity for constant quality, the former increasing remarkably, while the latter decrease irrespective of whether single or two-component flow. The effect of the heat flux through the heating wall upon the steam void fraction was also observed to have a trend for the void fraction to decrease with an increase in the heat flux for constant quality, which may contradict to the published data obtained by other investigators. However, this effect seems very obscure in small quality region.

In the slug flow and annular flow regions with large disturbance waves, 4-rod bundle data on the void fraction were 5 % lower than those in circular pipe and concentric annulus, and 7-rod bundle data 10 % lower.

The peaking phenomenon of the void fraction was observed at the transition from bubble flow to slug flow. This phenomenon may be attributable to the difference in slip velocity between the small bubbles in bubble flow and larger bubbles or slugs in slug flow. This phenomenon was more remarkable in rod-bundles with being supplied various heat input into each rod heater than in concentric annuli. This can be explained, to some extent, by introducing a concept of thermohydrodynamically divided subchannels.

New correlations for predicting the void fraction and the two-phase frictional pressure drop multiplier are presented. ~~These correlations for predicting the void fraction and the two-phase friction-~~

~~al pressure drop multiplier are presented.~~ These correlations take into consideration the mass velocity effect, the pressure level effect, and the effects of the geometric configuration of flow channel. They predict satisfactorily the void fraction and the frictional pressure drop not only for ordinary non-metallic fluids but also for liquid metal two-phase flow in a wide range of flow variables.

Single slug behavior was studied. The effects of the channel geometry, the channel inclination, and the water velocity upon bubble rise have been clarified, based upon the experimental results.

Finally, an analytical model was proposed for droplet-dispersed annular flow, which considers two probability distribution functions for residence time for a droplet having deposited onto the liquid film from the core stream to stay within the liquid film. This model can predict the general trends of droplet entrainment and droplet deposition. Further discussions are needed on its applicability to diabatic systems.

PART II

TURBULENCE STRUCTURE OF AIR-WATER TWO-PHASE BUBBLE FLOW FLOWING UPWARD IN CIRCULAR TUBE

I. INTRODUCTION

A complete knowledge of the turbulence structure of air-water two-phase bubble flow, characterized by small gas bubbles suspended in liquid phase, is of fundamental importance for understanding the complex phenomena of two-phase flow (for example, heat transfer characteristics and fluid-dynamics in two-phase flow), and also in a variety of engineering applications.

But, up to now, such systematic investigations in this domain have been very scanty either in experiment or in theory. And thus, even the basic knowledge about or insight into the mechanism of this complicated flow is still very limited, although gas bubbles in liquid are a very familiar sight. This is partly due to the difficulties involved in measuring local parameters, such as void fraction, liquid velocity and its fluctuating terms, bubble velocity and its spectrum, bubble impaction rate, the rate of turbulent diffusion of mass, momentum or heat, shear stress and so on, and is partly due to the statistically-random fluid motions induced by bubbles moving in random manner.

The particular regime of interest here is characterized, as mentioned above, by dispersed flowing mixture of gas bubbles and liquid. In such a flow, complicated interactions between adjacent bubbles or between bubbles and their surrounding liquid affect the local conditions of the flow field, and the resultant variation of the flow field may induce the change of bubble motion. This may result ultimately in more violent fluctuation or heterogeneity of the flow. For this reason, it seems impossible to describe these phenomena in distinct mathematical formulas. Hence, some analytical models, for example, the mixing length theory proposed by Levy[1], may be confined to be rather hypothetical than phenomenological because of these difficulties in formulating the phenomena and for lack of detailed information about the local parameters which strongly govern the local conditions

of the flow. Consequently, it must be realized that the validity of such models should be still very questionable, and that they could be applied only to well defined or strictly limited flow conditions.

On the other hand, however many efforts have been put on the development of instruments for measuring local parameters, they have been seldom accompanied with concurrent systematic and pertinent experimental studies of the phenomena. As a consequence, we must also realize that the experimental results on local parameters already reported show only the tendencies of the individual parameters within the range of flow variables tested, and that they could not give any generalized and significant correlative functions between the flow parameters.

The present work is an experimental study on air-water two-phase flow phenomena in the vertical bubble flow regime. Emphases are put on the following :

1) Development of the measuring techniques for local flow parameters.
2) To confirm the validity of the phenomenological bubble-diffusion model (or bubble-transport model) from a viewpoint of random bubble motion or the diffusing-particle characteristics of bubbles.
3) Measurement of local parameters, such as the void fraction, the bubble impaction rate, the liquid velocity and its fluctuating terms, the bubble velocity and its spectrum, the shear stress, the rate of the turbulent transport of momentum and heat, and other statistical characteristics of the flow.
4) To find generalized correlations between those parameters.
5) To obtain the basic information about the turbulent transport processes in air-water bubble flow.
6) Application of these experimental results to steam-water system.

II. MEASURING TECHNIQUES

2.1 General

In the study of problems associated with two-phase flow conditions, there is a strong need for instruments which will measure the detailed distribution of such local parameters as mentioned in previous chapter. Nevertheless, two-phase flow instrumentation has not yet reached the point where all of the desired measurements can be made.

Of those local parameters, the void fraction is the most important quantity for practical uses in engineerings, for example, for the design of nuclear reactors, steam boilers, evaporating equipments, refrigerating equipments and etc. Accordingly, during the past 15 years, extensive emphasis has been put on the measurement of the local void fraction. Due to the statistical nature of two-phase flow, all successful methods are based on length or time averaging, giving the local averaged void fraction. Gamma-ray traversing technique[2] belongs to the former treatment and isokinetic sampling method[3,4,5], the electrical resistivity probe method[6,7], hot-film anemometer technique[8,9] and optical-fiber probe method[10] are all subjected to the latter. Among all of these methods, the electrical resistivity probe method is most fitted to the present work because of its easy treatment and wide applicability. The principle of this method will be described in Paragraph 2.2.2 and in Appendix II.

From a viewpoint of studying the turbulence structure of two-phase flow, particularly in the bubble flow regime of much interest here, the experimental determination of the velocity profiles of the two phases is strongly called for, as well as the local void fraction profile. However, it has been more difficult to measure accurately these quantities than the local void fraction.

For measurement of the liquid velocity, impact probe method was

proposed first by Neal[6]. But this method seems very obscure, because we cannot find any theoretical validity in the concept that the impact pressure in two-phase flow should consist of those of the two phases individually weighted by the local void (or liquid) fraction. Recently Delhaye[11] proposed the hot-film anemometer technique, and with the aid of multi-channel pulse height analyzer he treated the output signal of the anemometer probe which fluctuates in correspondence to the liquid velocity and phase change. With careful treatment, this method gives us accurate information about time-averaged local liquid velocity and the turbulent intensity in reward for time-consuming work in data reduction.

The bubble velocity distribution across the tube was measured by Malnes[12] in steam-water system and also by Lackme[13] in air-water system by calculating cross-correlation function between the output signals of the two probe-sensors, with a use of double-probe or double-sonde similar to the above mentioned electrical resistivity probe for void fraction measurement. In calculating cross-correlation function, Malnes used an analog computer, and Lackme used a correlator. The use of this cross-correlation technique is suited to obtain the local mean bubble velocity* averaged over the all bubbles passing over the measuring point. Double-probe method was also reported by Kitayama et al.[14] and Aoki et al.[15]. They measured the time lag between a pair of start-stop signals by an electronic circuit or by photograph. But these treatments have a shortcoming in their averaging procedures, and therefore they could not always give reliable information of bubble velocity profile.

In the present study of the turbulence structure of the upward air-water bubble flow, a new instrument is presented for measurements of the local void fraction, the bubble impaction rate, the bubble

---

* Actually, this value is slightly different from the true mean velocity. Discussions on this problem will be mentioned later in Section 2.4.

velocity and its spectrum. This instrument consists of a double-probe (two electrical resistivity probes), a newly developed electronic circuit, a digital counter and a multi-channel pulse height analyzer. In order to clarify the usefulness and to examine the accuracy of cross-correlation technique, we also used a correlator.

In the measurements of liquid velocity and turbulent intensity, hot-film anemometer technique was used. And further, from a viewpoint of applicability to the measurements in steam-water system, tracer technique (salt water or hot water tracer) is also presented.

All of these instruments, as well as the method for other parameters, are described in detail in the following three sections.

2.2 Principles of Measurements and Electronic Instruments

Difficulties involved in measuring local parameters have been emphasized previously. In this section, we will present the principle of measurements for local parameters, such as the bubble impaction rate, the void fraction, the bubble velocity and its spectrum, the liquid velocity and turbulent intensity, the rate of turbulent diffusion of heat in liquid phase and the turbulent dispersion coefficient of bubbles, and further present and describe briefly the electronic circuits newly developed for the present purposes.

Figure 2.1 shows a block-diagram of the principles of measurements, and Fig. 2.2 electronic circuits. Details are described later in the following related paragraphs.

2.2.1 Measurement of Local Void Fraction

Resistivity probe method is based on the difference in electrical resistivity between the liquid and the gas phases. This method was first proposed by Neal[6] for mercury-nitrogen flow. But, up to now, the ratio of the periods while the probe tip is in contact with gas phase to the total sampling time has not yet been proved theoretically to be the local void fraction. Proof for this problem will be shown

in Appendix II, and it should be noticed that the resistivity probe method, as well as other probe method, finds its validity only in the case when the sampling (or measuring) time is long enough to allow the statistical treatment of bubbles.

Now, when the electrical probe tip is in contact with gas phase, the resistance between the probe and ground is infinite, whereas when the probe is in contact with water, the resistance is about 50,000 ohms. This corresponds with the fact that the voltage drop between the probe and the ground will change from 9 volts (line voltage) at gas-contact to about 3 volts at water-contact. When the effect of wettability between the probe and water can be neglected, this change of voltage drop will form a square wave of irregular frequency. However, in the system under study, water, which wets the probe, is the continuous phase, and this means that the change in resistance from 50,000 ohms to infinity or vice versa is gradual and not sharp enough to obtain square waves. Therefore, in order to apply the gate control circuit shown in Fig.2.2(a), the probe signal response has to be altered to a square-wave response. Schmitt trigger circuit in "Detecting Circuit" in Fig.2.2(a) is for this purpose. Thus modified waves are added with 10 kHz-pulse from pulse generator and are fed to a digital counter, passing through the gate control circuit. This modification of the probe signals is in common for measurements of the bubble velocity and the water velocity (by tracer technique). The outline of this modification is presented in Fig.2.3. Fabrication of the probe will be mentioned in Section 2.3*.

In experiment, the sampling time was 1 ~ 3 minutes. This is so

---

* In the case of the probe used here and flow systems, the decay time of the unmodified waves is extremely small compared with the rise time. This means that we can easily set the discriminator level at a slightly higher level than that of water in order to obtain an accurate local void fraction.

long that the number of bubbles piercing through the probe is statistically large enough for measurement. Then, the local void fraction $\alpha_{loc}(r)$ will be given as the ratio of the summation of each individual gas-contact period to the total sampling time T.

$$\alpha_{loc}(r) = \sum_i t_{gi}/T \tag{2.1}$$

2.2.2 Measurement of Bubble Impaction Rate

The bubble impaction rate was measured also by the resistivity probe method, with utilizing only START signal of a double-probe, as well as in measurement of the local void fraction. Namely, the number of the modified signals (output signals of the Schmitt trigger circuit) from START probe (see Paragraph 2.2.3), which corresponds to the number of bubbles arriving at the position of measurement for a given time duration, is to be counted by a digital counter.

2.2.3 Measurement of Bubble Velocity and Spectrum

In general, the bubble velocity can be determined by detecting the velocity of displacement of the interface between the gas and the liquid. Hence, the bubble velocity distribution across the tube can be measured by means of the double-probe method mentioned above. For this purpose, the two identical electronic circuits (detecting circuits shown in Fig.2.2(a), each of which contains a discriminator, a Schmitt trigger circuit, a differentiator and an amplifier) were needed for the two probes.

When a bubble flowing upward at a velocity V_b hits the START probe, as shown in Fig.2.3, electric signal of shape represented by the curve ⓐ is obtained. Presently, the same bubble hits the STOP probe situated a little apart from the START probe, and a signal (curve ⓐ' in Fig.2.3) similar to that from the START probe is obtained. If we know the time lag between these two signals, we can

obtain the bubble velocity as follows :

$$V_b = \Delta z/\tau_0 \tag{2.2}$$

where Δz and τ_0 are the distance between the two probes and the time lag between the two output signals (a) and (a') .

The time lag τ_0 of the bubble travelling can be obtained by the following two methods : one is the so-called multi-channel technique [17,18], and the other cross-correlation technique. With an aid of the former method, the time lag for each bubble can be obtained in a form of spectrum, whereas with the latter, the average time lag of bubbles*. In the present experiment, the distance Δz from one probe to the other was determined by photographic method.

2.2.3.1 Cross-Correlation Technique

When x(t) and y(t) are the START and the STOP signals from the two probes respectively, then the cross-correlation function $F_{xy}(\tau)$ can be calculated as follows.

$$F_{xy}(\tau) = \lim_{T\to\infty} \frac{1}{T} \int_0^T x(t-\tau)\ y(t)\ dt \tag{2.3}$$

A correlator (Model SAI-42, Signal Analysis Industries Corporation, U.S.A.) was available to this computing procedure with linear mode, and plotted automatically $F_{xy}(\tau)$ as a function of time lag τ via X-Y recorder. From this cross-correlation function $F_{xy}(\tau)$, it was then possible to find the "most probable", not "average", time lag τ_0 of bubbles travelling the distance from one probe to the other as the maximum point of the function $F_{xy}(\tau)$.

Now, let x(t) and y(t) be two ideal square-wave-signals of the pulse width $\Delta\tau_1$ and $\Delta\tau_2$ respectively, and then we will consider the

---

* In a strict sense, it is not the "average" but the time lag of which occurrence is most probable.

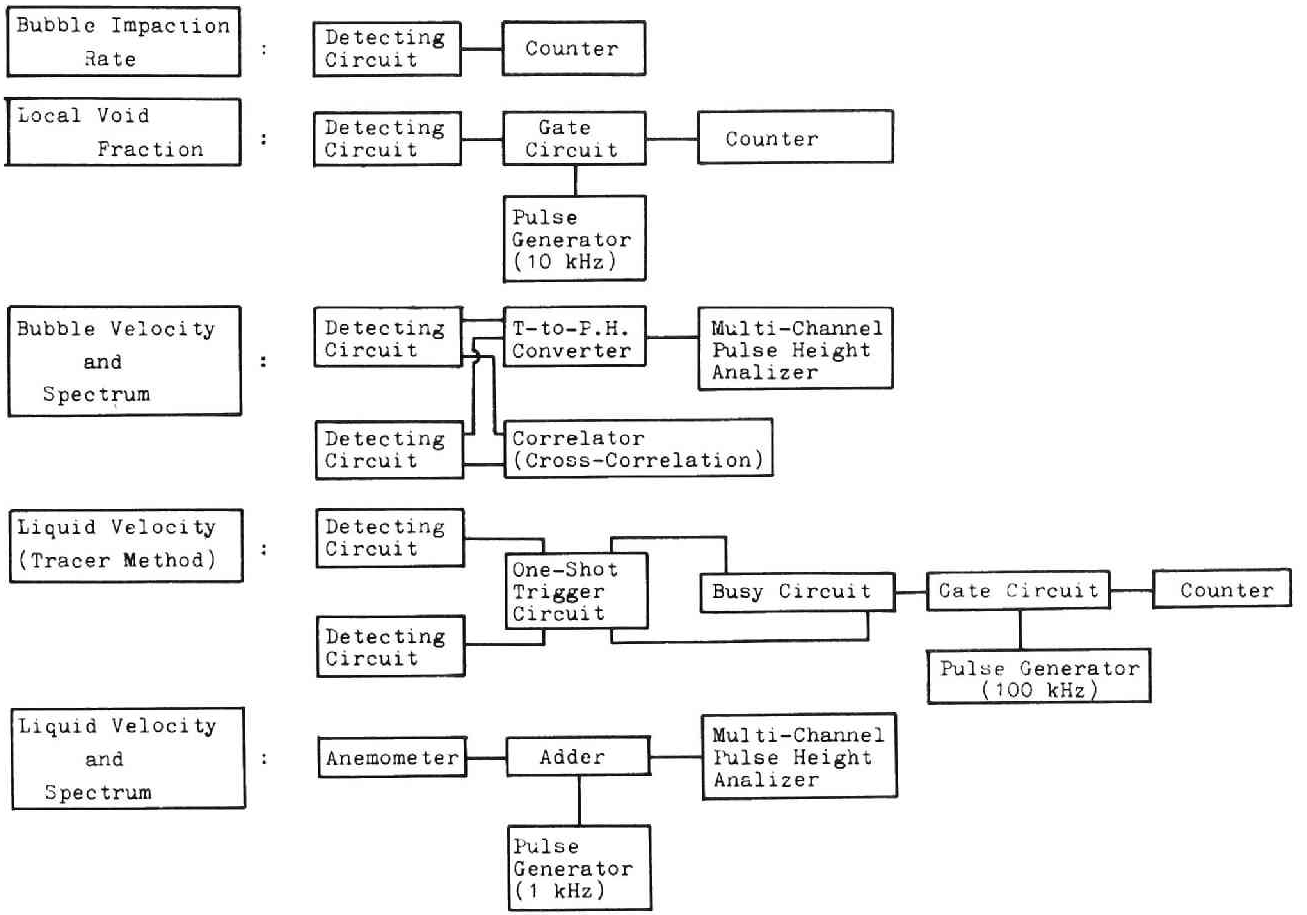

Fig. 2.1 Block-diagram of the principles of measurements

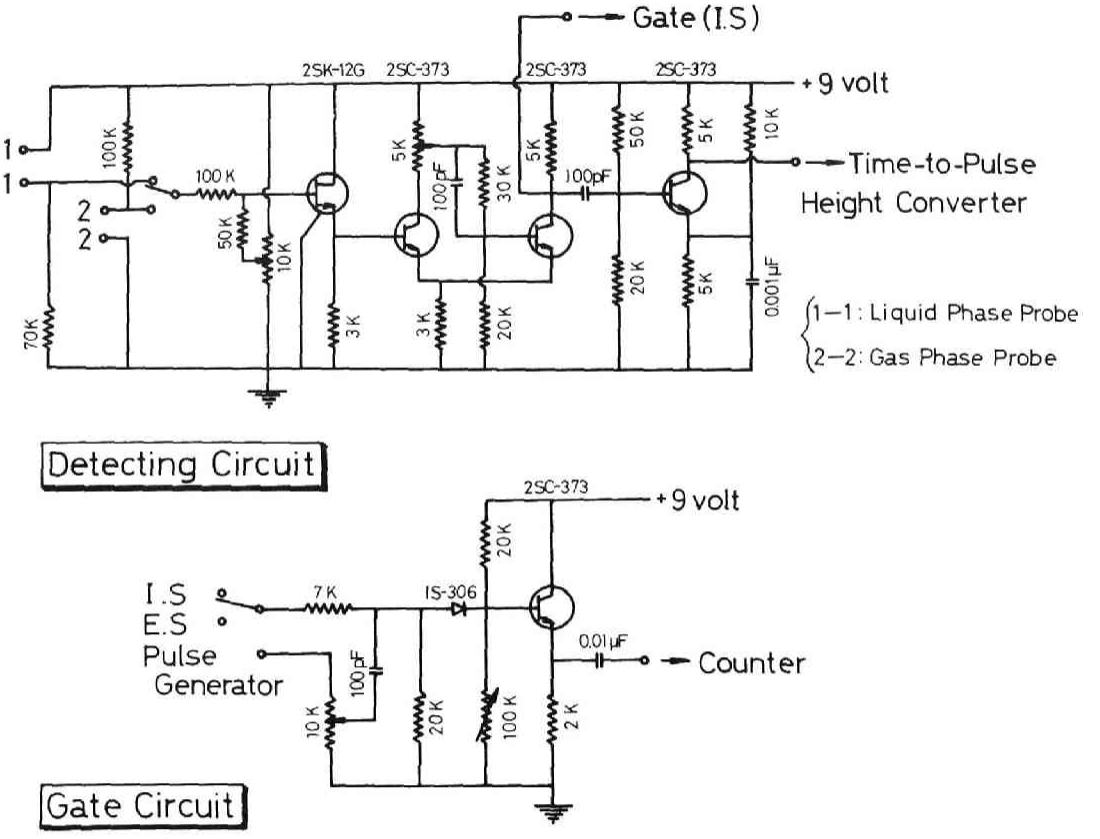

Fig. 2.2(a) Wiring diagram of electronic circuit

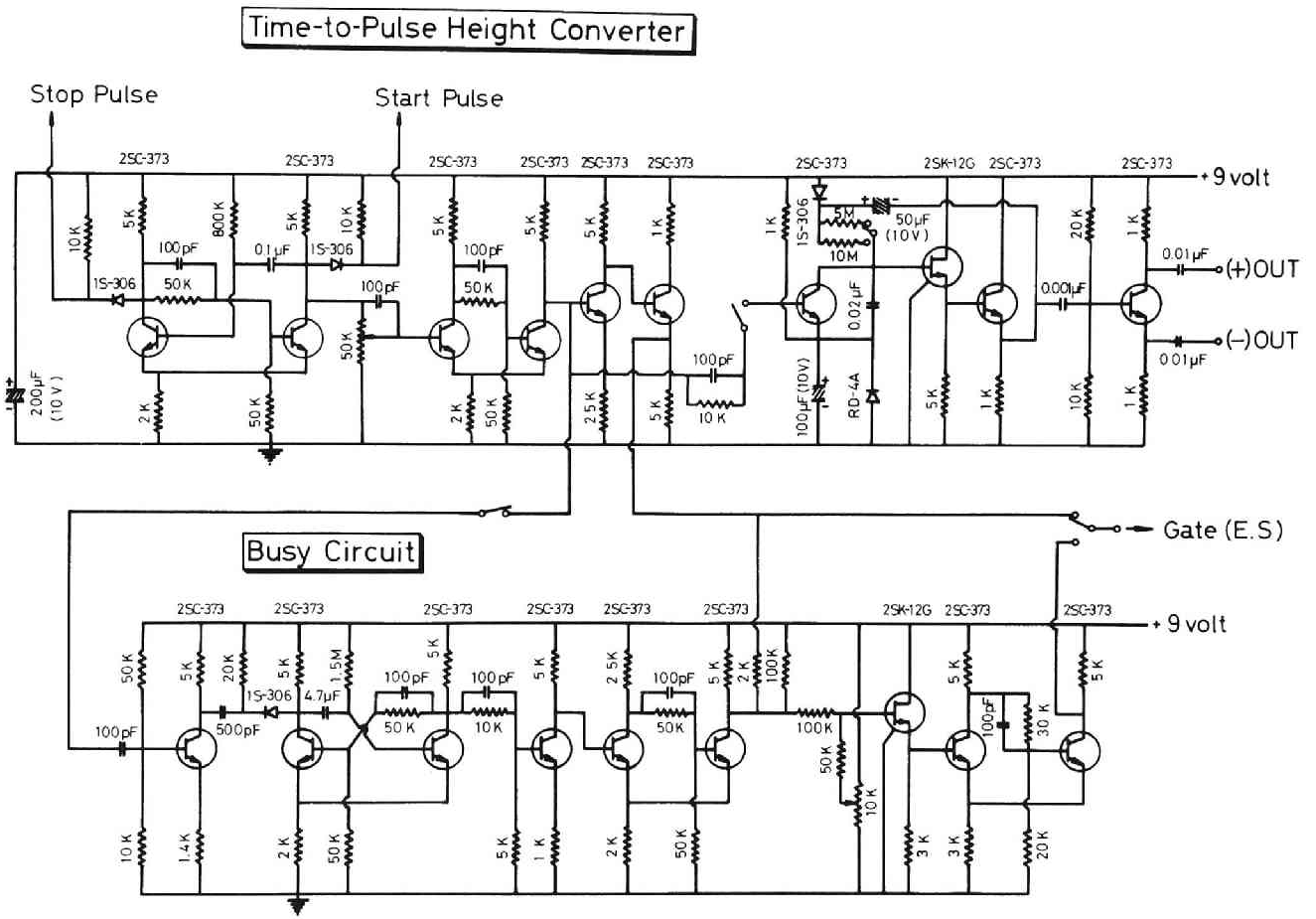

Fig. 2.2(b) Wiring diagram of electronic circuit

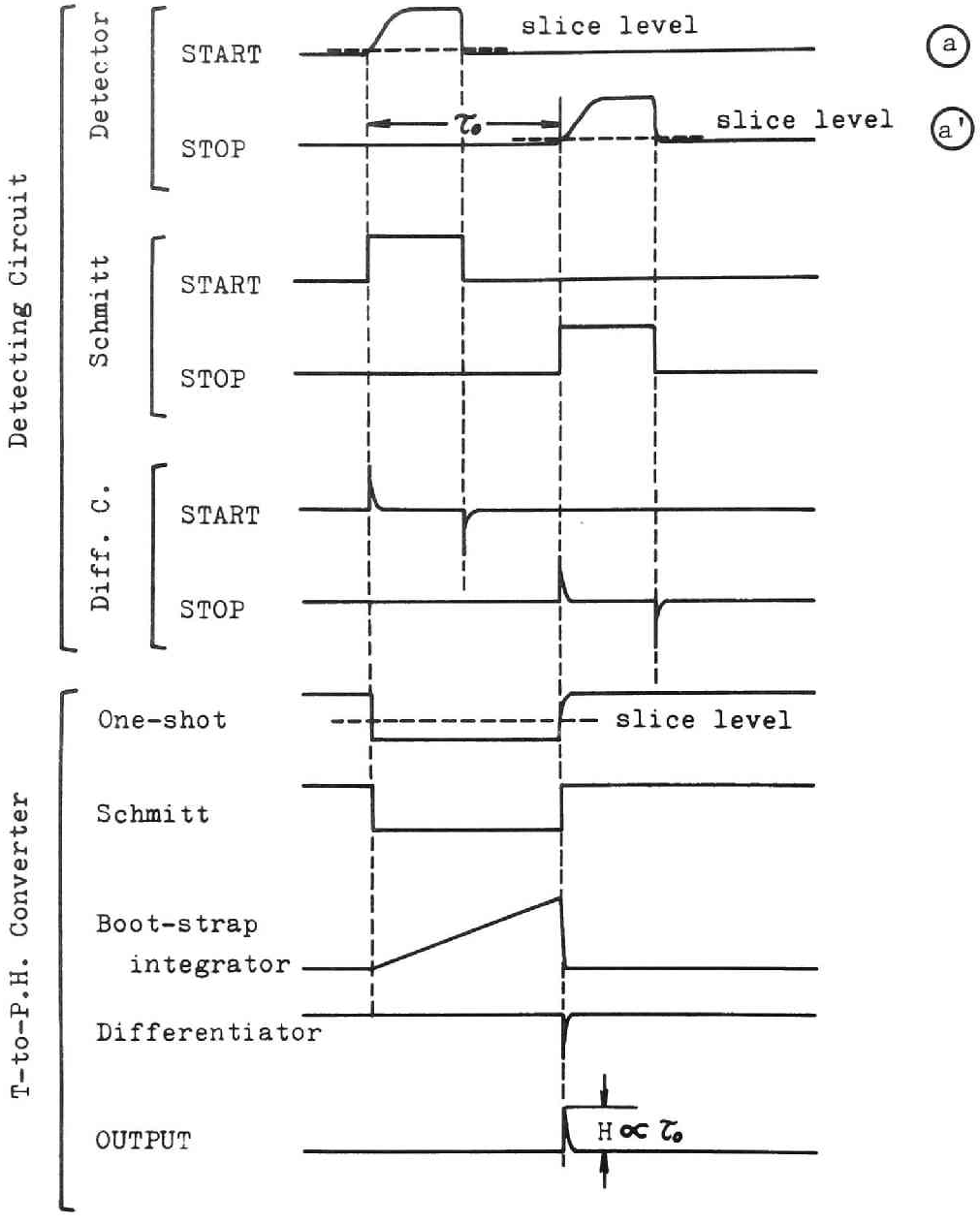

Fig. 2.3 Signal processing in multi-channel technique for bubble velocity measurement

cross-correlation function between x(t) and y(t). As shown in Fig.2.4, next two cases are possible in experiments.

(a) $\Delta\tau_1 = \Delta\tau_2$

The time lag τ_{max}, which corresponds to the maximum value of the cross-correlation function $F_{xy}(\tau)$, is just equal to τ_0.

(b) $\Delta\tau_1 \leq \Delta\tau_2$

In this case, τ_{max} is greater than τ_0 by $(\Delta\tau_2 - \Delta\tau_1)/2$.

Experiments indicated that the case (b) was more probable than case (a), because bubbles were apt to be exerted on with larger hydraulic resistance when penetrating the STOP probe than when penetrating the START probe (see the configuration of double-probe in Fig.2.13). This fact suggests that the bubble velocity measured by cross-correlation technique tends to be a little lower than actual velocity. An advantage of this method is in the capability of prompt measurement (about 30 seconds) and in easiness in data reduction.

2.2.3.2 Multi-Channel Technique

Time-to-pulse height converter shown in Fig.2.2 was employed in order to obtain, for each bubble, a pulse of which amplitude, denoted H, was proportional to the time lag τ_0. This electronic instrument consists of a one-shot trigger circuit, a Schmitt trigger circuit, a phase inverter, a boot-strap integrator and a differentiator. The signal processings by these circuits are illustrated in Fig.2.3.

When a statistical treatment of bubbles is wanted, thus obtained pulses of various amplitudes and of irregular frequency are fed to a multi-channel pulse height analyzer (Victreen PIP 400AA) and are analyzed and stored there. Data are printed out in digital manner by a printer. This method gives us the information of the local "mean" velocity of bubbles and further of the bubble velocity spectrum, however it requires time-consuming labors in their data deduction process. The statistical errors inherent to this technique will be mentioned later in Section 2.4.

If we want to know the velocity of a particularly interested

single bubble, connect the output terminal of the Schmitt trigger circuit in "Time-to-Pulse Height Converter" to the "Busy Circuit", and also the other end terminal of the busy circuit to the "E.S" terminal in "Gate Circuit". Then the velocity of the single bubble will be readily obtained in digital manner with use of a digital counter and a pulse generator (100 kHz). Signal processing in this busy circuit will be described later in Paragraph 2.2.4.2.

Figure 2.5 indicates an example of the characteristic curve in which the time lag τ is plotted against the channel address of the multi-channel pulse height analyzer. In Fig.2.6 is shown an example of the untreated results of the bubble velocity obtained both by multi-channel technique and by cross-correlation technique.

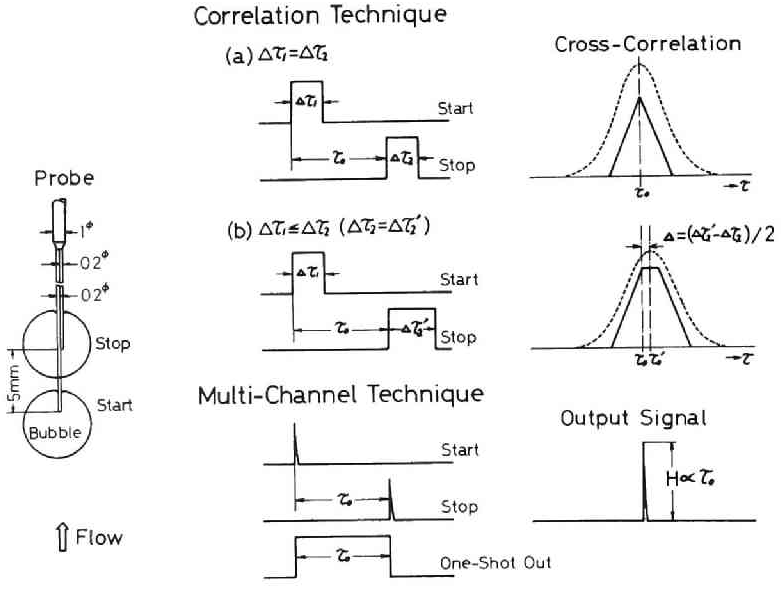

Fig. 2.4 Correlative representation between correlation technique and multi-channel technique

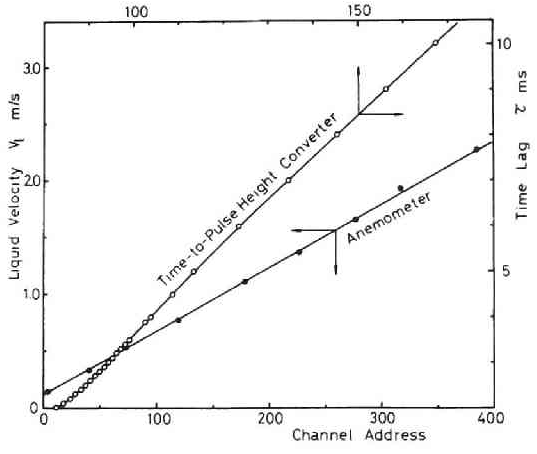

Fig. 2.5 Characteristic curves

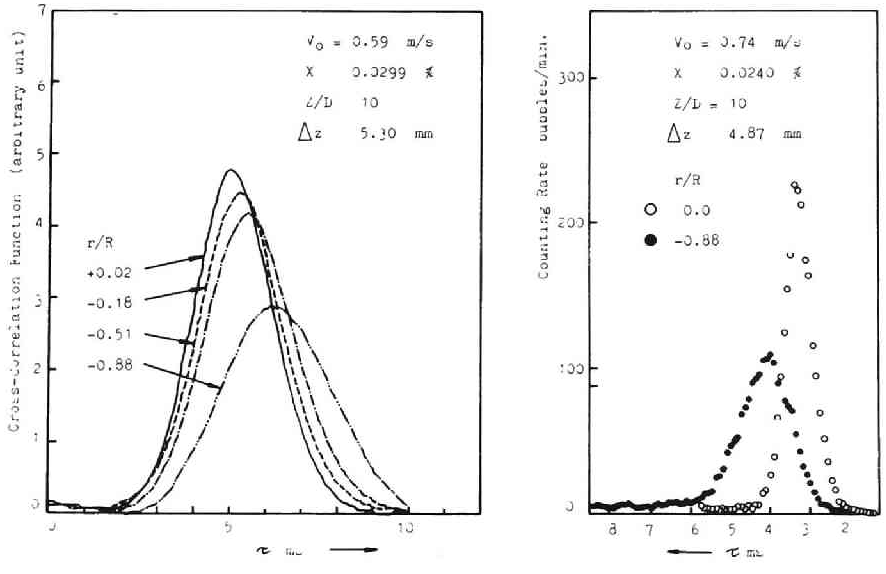

Fig. 2.6 Correlative representation between correlation technique and multi-channel technique

2.2.4 Measurement of Liquid Velocity and Spectrum

The experimental determination of the liquid velocity is so difficult that progresses in developing the available instruments have been suppressed in past 15 years, as already mentioned in Section 2.1. The impact probe (or Pitot tube) method seems inadequate in its application to two-phase flow systems. Semi-conductance pressure transducers with fast response time, small size, and mechanical and thermal firmness could give available and significant information about the liquid velocity. But such pressure transducers are not obtainable at the present status. Hot-film anemometer method proposed by Delhaye [11] appears most reliable, however many problems will arise from its applicability for two-phase flow system.

In the present work, we also employed hot-film anemometer method in order to confirm its applicability for air-water bubble flow and to obtain accurate information about the liquid velocity and its fluctuating characteristics. Furthermore, we presented tracer technique[17,18] (salt water or hot water tracer) with its application for steam-water system held in mind. (The hot-film anemometer method cannot be employed in such flow systems where the temperature gradient or the temperature fluctuation of the flow field may occur.)

2.2.4.1 Anemometer Method

The detecting element of a hot-film anemometry consists of a very fine short metal wire or film coated by quartz, which is heated by an electric current. The wire is cooled by the flowing fluid, causing the temperature to drop and, consequently, the electric resistance of the wire diminish. The degree of cooling of the wire sensor is a unique function of the flow velocity. Theories on the hot-wire anemometer in single-phase flow systems are described in detail by Hinze[19].

The constant-temperature method has basic advantages over the constant-current method with respect to accuracy of measurements. The former method requires the electronic feedback system for keeping the wire resistance and temperature constant. In this method, bridge-

top voltage is a unique function of the flow velocity.

The arrangement of the electronic instruments in the present work in air-water bubble flow are schematically shown in Fig.2.7. In all experimental runs, the overheating ratio of the hot-film anemometer probe was chosen 0.03*. This value of the overheating ratio has been recommended by Delhaye in Ref.[9]. Prior to each experimental run, the calibration of the anemometer unit was performed in upward water flow in the same test section with a back-up by a calibrated Pitot tube. One of the typical characteristic curves is presented in Fig.2.5 where the water velocity V_1 (m/sec) is plotted against the channel address of the multi-channel pulse height analyzer.

The passage of a single air bubble past the conical probe and the corresponding output signal of the anemometer are shown diagramatically in Fig.2.8(a), and in Fig.2.8(b) a velocity histgram for an air-water flow, where $E_s(t)$ is the output signal of the anemometer, V_1 the liquid velocity (a function of E_s), and the vertical abscissa of the histgram $N(E_s)$ is a function of E_s.

Up to the moment t_c, the sensitive element is in the liquid. When the bubble arrives near the probe, the value E_s increases up to point C, since the water ahead of bubble ascends at that bubble velocity which is slightly higher than mean velocity of the water, and where the alternation in phase takes place. E_s diminishes to the value of point D approximately lineally . At point E, the liquid comes in contact with the probe again and E_s instantaneously assumes a value slightly higher than its mean value in the liquid. This higher value of E_s at point F is due to the velocity of the liquid in the wake of the proceeding bubble.

---

* Overheating ratio "a" is defined as follows.

$$a = (R - R_o)/R_o$$

where R_o and R are the cold resistance and the operating resistance of the wire sensor of the hot-film probe. Too high value of this parameter may result in the formation of bubbles through nucleate boiling.

According to the data processing method proposed by Delhaye, we make the following assumptions :

1) the drop CD in the signal is linear ;
2) the rate of drop dE_s/dt between C and D is the same for all bubbles ;
3) the rise is instantaneous ;
4) the sensitive element of the probe is in the gas between the moment t_c and t_d.

With these assumptions, the average velocity of the liquid $\bar{V}_l$ and the turbulent intensity $\sqrt{\overline{u^2}}$ are calculated from the equations :

$$\bar{V}_l = \frac{\Sigma_i \, V_{li} \, (N_i - N_{oi})}{\Sigma_i \, (N_i - N_{oi})} \quad , \tag{2.4}$$

$$\sqrt{\overline{u^2}} = \sqrt{\frac{\Sigma_i \, (V_{li} - \bar{V})^2 (N_i - N_{oi})}{\Sigma_i \, (N_i - N_{oi})}} \quad , \tag{2.5}$$

where N_o is the contribution by bubbles to the $N - V_l$ histgram, and it functions as a background in the calculating procedures (the hatched part in Fig.2.8(b)).

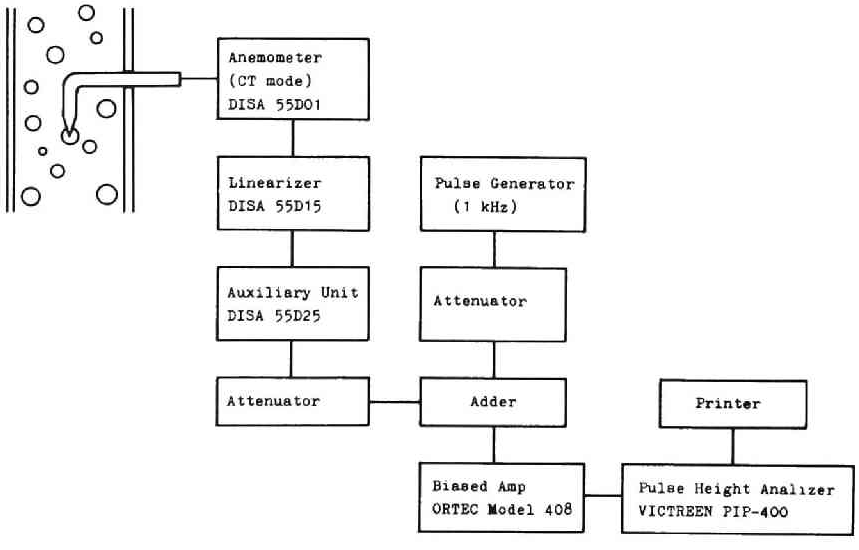

Fig. 2.7 Schematic of anemometer method

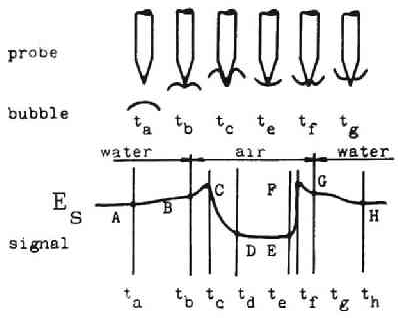

Fig. 2.8(a) Passage of a single air bubble past the conical hot-film probe

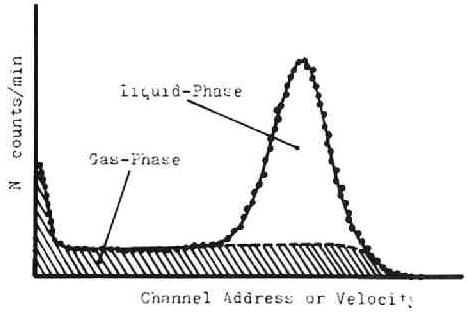

Fig. 2.8(b) Velocity histgram obtained by hot-film anemometer

2.2.4.2 Tracer Technique

In this method, the water velocity can be determined by detecting the velocity at which the lump of tracer (salt water or hot water) flows. When the tracer is salt water (nearly saturated solution at room temperature), the detecting sensors are the two impedance-probes (double-impedance-probe) shown in Fig.2.15, whereas with employing hot-water as the tracer, two alumel-chromel thermocouples of 0.3 mm in diameter.

The principle of this method is very similar to that of the aforementioned technique for measuring the velocity of a single bubble. When the salt water passes between a pair of opposite electrodes (symbol "1 - 1" in the "Detecting Circuit" shown in Fig.2.2), the impedance between both electrodes is about 30,000 ohms, whereas when the water, about 200,000 ohms. This follows the fact that the electric potential of one electrode is about 6 volts while salt water passing (the other electrode is always 9 volts — line voltage), and about 2.5 volts while water (working fluid) passing. On the other hand, when a bubble passes between the electrodes, the potential of that electrode falls down to the ground level. Therefore, it is possible to eliminate the signals caused by bubbles with setting the slice level at a little higher than that of water (see Fig.2.9(a)).

If we want to measure the water velocity in digital manner by the tracer method, the difficulties in injecting the tracer in single-pulse mode require the electronic instrument of special purpose, such a busy circuit as represented in Fig.2.2(b), which generates a busy signal (a square wave of about 5 seconds pulse width) instantaneously at the end of the impulsive square wave resulting from the first pair of START-STOP signals of the probe as the output signal of the one-shot circuit. This busy signal closes the gate control circuit for about 5 seconds long, and therefore the signals following after the first impulsive square wave are prevented from passing through the gate. The first-passing square wave of interest here, of which width is proportional to the time lag for the lump of tracer to flow the distance between the two probes located about 5 mm apart, is added with 100 kHz-pulse, and thereafter is counted by a digital counter the number of pulses of 100 kHz frequency involved within the width of the marked square wave (see Fig.2.9(b)).

The backmixing of the tracer into the ambient fluid flow was negligibly small relative to the convective term in axial direction.

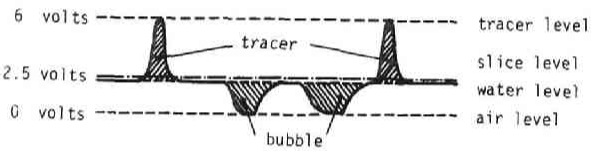

Fig. 2.9(a) Probe signal and slice level in tracer technique

2.2.5 Measurement of Turbulent Diffusivity of Heat in Liquid Phase

Radial turbulent diffusivity of heat in air-water bubble flow can be determined by measuring both radial and axial temperature distributions from a line heat source located perpendicular to the flow direction. Assuming the diffusivity of heat uniform in radial direction, the diffusion equation, similar to the equation of transient heat conduction in solid, can be applied. If the radial variation of the diffusivity is taken into consideration, the equation of

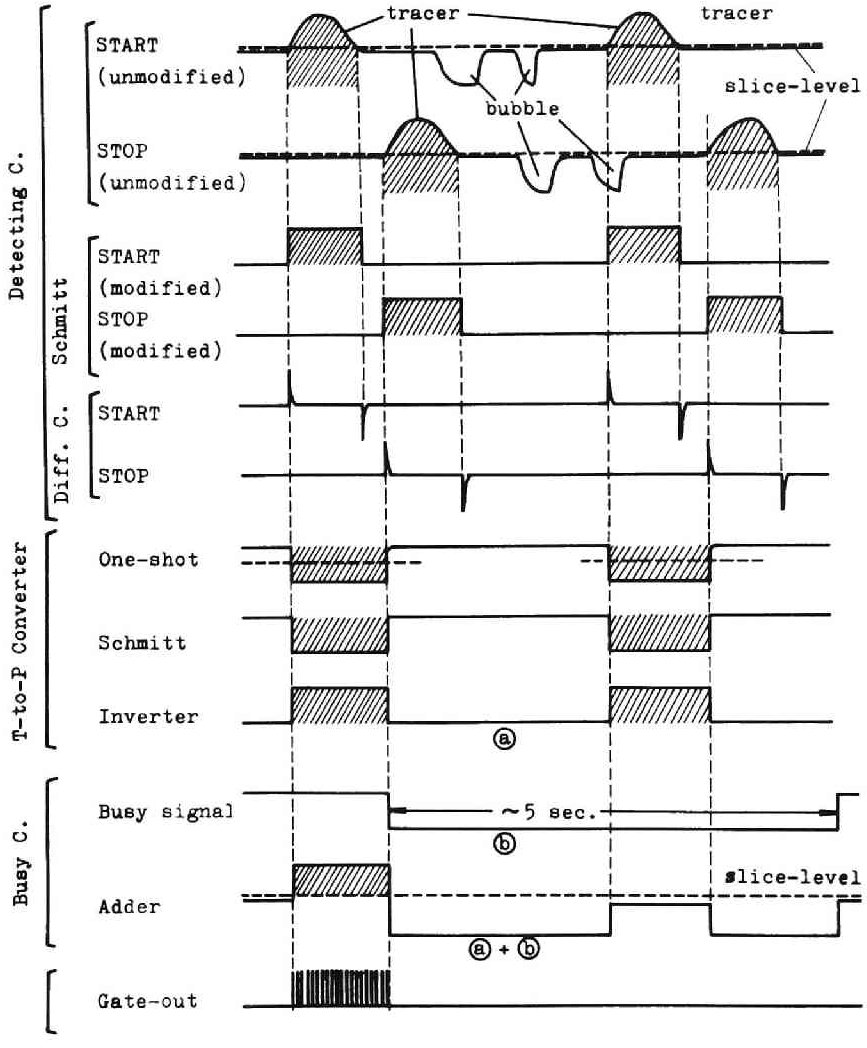

Fig. 2.9(b) *Signal processing of tracer technique for water velocity measurement*

heat balance must be analyzed. These theoretical treatments will be described in Chapter V.

In measurement of the rate of turbulent diffusion of heat, grounded alumel-chromel thermocouples of 0.65 mm in sheath diameter were used. Five thermocouples were utilized for measuring the radial and axial temperature distributions, and the one for reference temperature which was located upstream of the line source of heat. The line source was a nickel-chrome wire of 0.2 mm in diameter, and it was heated by about 25 volts-DC source (about 100 ~ 150 watts).

In order to measure the rise of the fluid temperature induced by the heater wire, the differential method was applied between two thermocouples. S/N ratio was comparatively small because the reference temperature of the fluid upstream of the heater fluctuated with a large amplitute and with an irregular high frequency, and therefore the following procedures were needed :

1) Temporal operation of the source. The nickel-chrome wire was impressed with DC voltage temporally only during the temperature measurement.
2) Integral (or low-pass filter) circuit (R-C circuit) for smoothing the fluctuating signal. The time constant was chosen 1 second and 10 seconds. The block-diagram of this method is indicated in Fig.2.10.

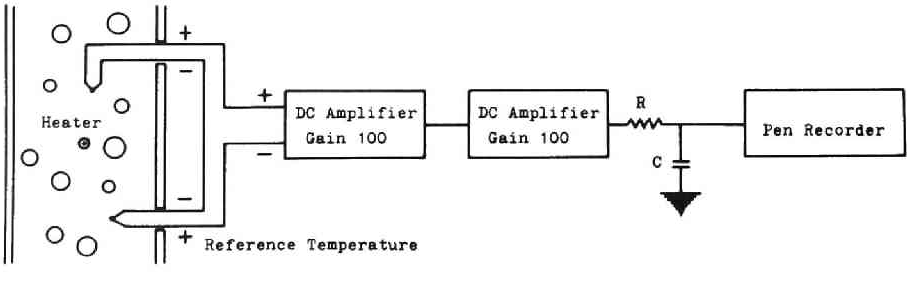

Fig. 2.10 Schematic for measurement of turbulent diffusion of heat in liquid phase

2.2.6 Measurement of Turbulent Dispersion Coefficient of Bubbles

Measurement of the turbulent dispersion coefficient of bubbles was conducted in two cases :

1) turbulent dispersion of air and argon bubbles in single-phase (water) flow and in stagnant water both in pool and in pipe,
2) turbulent dispersion of helium (tracer) bubbles in air-water bubble flow in pipe.

Descriptions about the first case will be found in Chapter III. Here, we will mention the second case, i.e., the turbulent dispersion of tracer gas bubbles (helium bubbles) in air-water bubble flow.

In this experiment was used an isokinetic sampling probe through which a two-phase sample was withdrawn at such a rate that the pressure just inside the probe orifice is equal to the local static pressure in the stream.

Of many published reports relating to the isokinetic sampling method, so far as the author knows, only the report by Shires and Riley[5] has described an attempt to develop an isokinetic sampling probe for use over a wide range of flow regimes (including the bubble flow regime). They have clarified in their report the two concepts for isokinetic sampling. It is very useful to introduce their concept here.

Figure 2.11 represents the quality probe. In this case, it is assumed that the probe presents no resistance to the flow of either phase, nor is there any interaction between them as they pass the probe orifice. The ratio of the sampling volume rate of two phases is given as follows :

$$\frac{q_g}{q_l} = \frac{V_{bs}^*}{V_{ls}^*} = \frac{V_b^*}{V_l^*} = \frac{V_b\,\alpha}{V_l\,(1-\alpha)} = S\,\frac{\alpha}{1-\alpha} \qquad (2.6)$$

where V_{bs}^* and V_{ls}^* are the superficial velocities in the probe orifice,

V_b^* and V_l^* the superficial velocities in the stream, V_b and V_l are the true velocities of the gas and the liquid, and α and S denote the local void fraction and the slip ratio, respectively.

The alternate concept, the voidage probe, is also represented in Fig.2.11. In this case, the two phases on entering the probe interact and their velocities are equalized, both becoming equal V. Therefore, the volume of each phase obtained over a given time interval is proportional to the time interval of contact with the probe, and hence to the percentage volume of the phase which is present at the sampling point. In this case,

$$\frac{q_g}{q_l} = \frac{\alpha}{1 - \alpha} \quad . \tag{2.7}$$

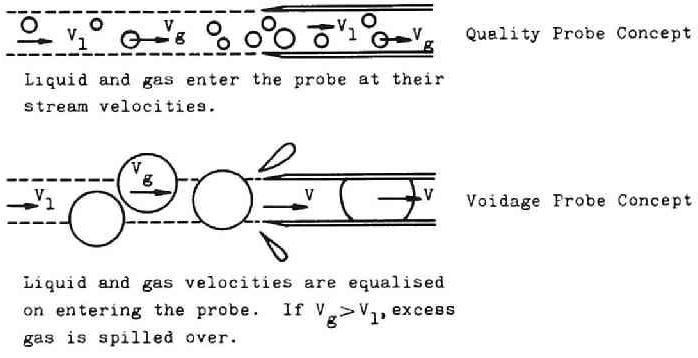

Fig. 2.11 Two concepts of two-phase flow sampling

Within the quality range of our experiments, the instrument would function as a voidage probe. Thus, the probe samples the two phases consecutively and penetrates the phase boundaries between them.

What is new in the present work with using a sampling probe is in obtaining the turbulent dispersion coefficient of bubbles by analyzing the mass concentration of tracer gas bubbles involved in the unit volume of the withdrawn air-water flow by gas-chromatograph in the following manner.

First, helium tracer bubbles, injected into the stream of air-water flow at constant volumetric flow rate from bubble injector of

0.88-mm inside diameter located at the pipe center, are withdrawn by the isokinetic sampling probe, together with the liquid and air bubbles involved in the stream. Next, the gas phase including the helium and the air thus withdrawn is separated from the liquid phase by separator and further dehydrated by cold-trap. Thereafter, the moler concentration of the helium involved in the unit volume of the withdrawn and dehydrated-gas phase is to be analyzed by a gas-chromatograph (Shimadze, TYPE GC-2A) (see Fig.2.12).

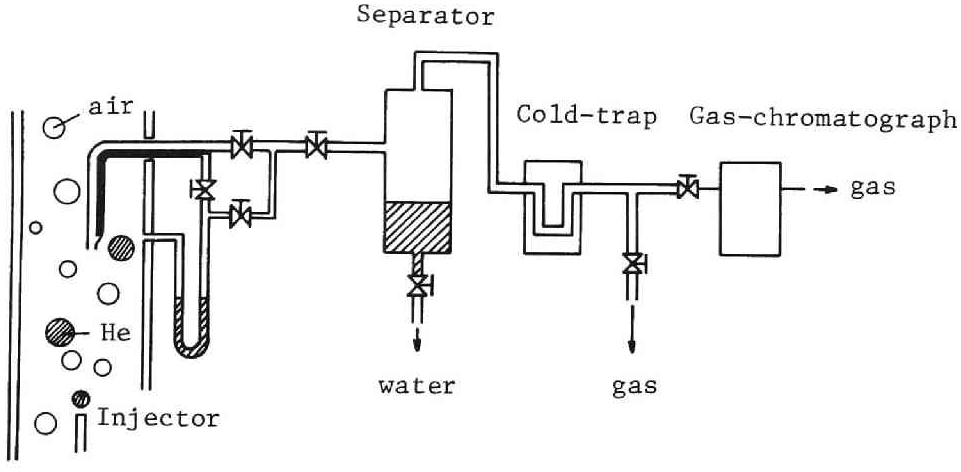

Fig. 2.12 Schematic of isokinetic sampling

In the present experiment, the argon gas was used as a carrier gas in order to increase the resolving power of the instrument. The output of the instrument was recorded by a pen recorder (typical results are represented in Fig.5.8). By reading the peak values of the output for the helium and the nitrogen we can easily get an indication of the helium mass concentration in two-phase flow in the following manner.

Let C_R and C_R' the apparent and the true moler ratio between the helium tracer gas and the nitrogen involved in the unit volume of the withdrawn mixture of air and helium, respectively (C_R is the ratio of the direct reading of the recorded peak value for the helium to

that for the nitrogen* — see the illustration), and then we have

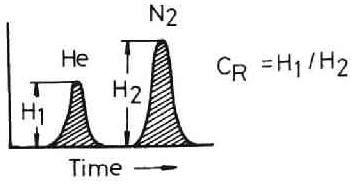

$$C_R' = k_1 C_R \qquad (2.8)$$

where

k_1 : Correction factor for the difference in the degree of ionization at a given ionization current between the helium and the nitrogen.

Assume $C_R' << 1$, and then the mass concentration of the helium contained within the unit volume of the gas phase of air-water flow, C_g, can be approximated by

$$C_g = k_1 C_R' \frac{M_{He}}{M_{N_2}} = kC_R \quad , \qquad (2.9)$$

$$k = k_1 k_2 \frac{M_{He}}{M_{N_2}} \quad , \qquad (2.10)$$

where

M_{He}, M_{N_2} : Molecular weight of the helium and the nitrogen, respectively,

k_2 : Mass concentration of the nitrogen within the unit volume of the air at system temperature and pressure.

Provided that the helium flow rate has no serious influence upon the local void fraction, the local mass concentration of the helium involved within the unit volume of air-water two-phase flow, C(r), can

---

* Strictly speaking, the integrated values of the output signals corresponding to the helium and the nitrogen (hatched parts in the above illustration) should be applied instead of their peak values.

be ultimately expressed by the following equation.

$$C(r) = C_g(r) \frac{\rho_g \alpha(r)}{\rho_g \alpha(r) + \rho_l \{1 - \alpha(r)\}} \tag{2.11}$$

$$\simeq kC_R \frac{\alpha(r)}{1 - \alpha(r)} \frac{\rho_g}{\rho_l}$$

or

$$\frac{C(r)}{C(0)} = \left\{ \frac{\alpha(r)}{1 - \alpha(r)} \Big/ \frac{\alpha(0)}{1 - \alpha(0)} \right\} \frac{C_g(r)}{C_g(0)} \quad . \tag{2.12}$$

The turbulent dispersion coefficient of bubbles (in a strict sense, that of helium bubbles) can be then calculated, in the same manner as will be described in Chapter III, from the experimental radial profiles of the relative mass concentration of the helium C(r)/C(0) measured at several different axial positions downstream of the bubble injector. In measurements, sampling was performed at five positions. Instruments are shown in Fig.2.12.

2.2.7 Measurement of Bubble Radius

Photographic method was used for this purpose. Bubbles were not all spherical in experiments. The spheroidal bubbles were observed in the experiments of bubble dispersion in single-phase flow, especially at higher flow rate of argon, and then the concept of the equivalent-spherical-diameter of bubble was introduced. The equivalent diameter is defined

$$d = \sqrt[3]{a^2 b} \quad . \tag{2.13.a}$$

In two-phase flow experiments, an alternate equivalent diameter is defined

$$d' = \sqrt{ab} \quad , \tag{2.13.b}$$

where a and b are the semimajor and the semiminor axes of the spheroidal bubble.

The equivalent diameter defined by Eq.(2.13.a) is based on the bubble volume, whereas that defined by Eq.(2.13.b) the cross-sectional area of bubble photographed in pictures. From Eqs.(2.13.a) and (2.13.b) we get

$$d/d' = (a/b)^{1/6} \quad . \tag{2.14}$$

The ratio a/b was not so large (at the biggest case, a/b = 2.5, as represented in Fig.3.32, and this value of the ratio corresponds to d/d' = 1.16) that d/d' becomes nearly equal to unity.

In taking photographs of bubbles, a caution was paid to the following two problems :

1) A water box filled with water was needed for avoiding an optical effect (lens-effect) due to the curvature of a pipe,
2) A stroboscopic illumination was also needed in order to avoid the photographs of bubbles out of focus, of which luminant time was of the order 1/10,000 second, since bubbles migrated fast at the velocity of 1 ~ 2 m/sec.

2.3 Detail Descriptions of Detectors and Accesories

2.3.1 Electrical Resistivity Probe (Double-Probe)

The double-probe consists of two identical electrical resistivity probes (or needles), whose tips are apart about 5 mm distance from each other (see Fig.2.13). In this thesis, the one of the two probes or needles which is located upstream is often called "START" probe, and the other "STOP" probe.

Each needle is made of a plastic-coated stainless steel wire of 0.2 mm diameter with the outer diameter of the plastic coating 0.45 mm. The steel wires were stripped off about 35 mm long of their plastic coating, and these stripped parts of wires except for tips, having been plated with a commercial resin varnish at about 120 °C after the treatment with carbon-tetrachloride, were encased together in a stainless steel tube of 1 mm diameter, and the gap between these wires and the tube or any other connections between the tubes were all glued and sealed over with a cementing material "THREE LOY". Except the needle tips, the needles are insulated electrically from the tubes.

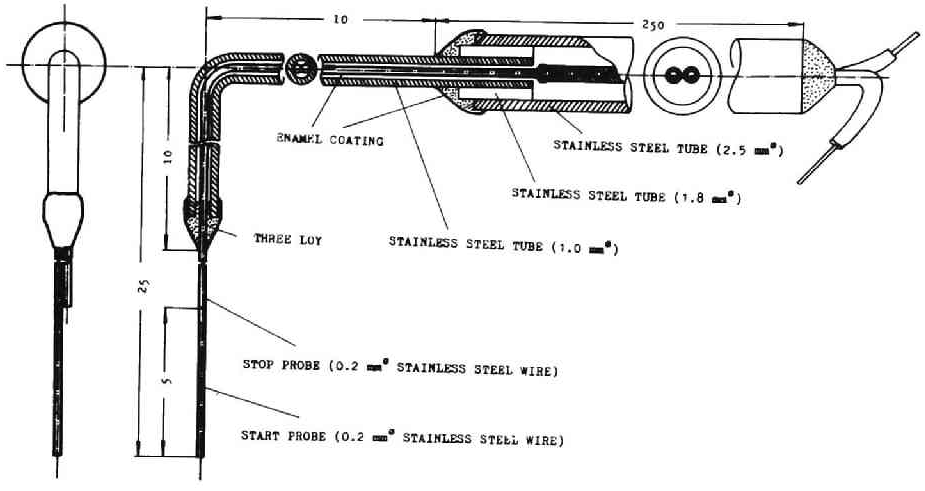

Fig. 2.13 Double-probe

2.3.2 Hot-Film Anemometer Probe

The choice of a probe configuration is very important in applying it for the two-phase flow experiments. A probe is desired to satisfy the following specifications as possible :

1) A probe should be fit to the operation in water.
2) The probe should not disturbe the flow field.
3) The probe should penetrate all the bubbles passing the measuring

station.

4) A sensitivity to phase change should be as high as possible, but nucleate boiling should be prevented to occur on the probe.
5) A sensitivity to the velocity fluctuation should be as high as possible, but the effect of the lateral velocity components of the flow should be eliminated.
6) A sensitivity to the temperature fluctuation of the flow field should be as low as possible.
7) Small air-bubbles or dirts in water should not attach the sensing element of the probe.
8) The probe should allow the measurements even in the vicinity of a pipe wall.
9) Mechanical firmness of the probe.

The hot-film probe, supplied by the Thermo-Systems Inc. (U.S.A.), is a tapered (or conical-shaped) probe (right-angled probe) with a fine film of platinum covered by a fine film of quartz (0.8 μ) electrically insulating the sensing element of platinum film from the ambient fluid (see Fig.2.14).

We used the MODEL-55D01 Anemometer, MODEL-55D15 Linearizer, and MODEL-55D25 Auxiliary Unit manufactured by DISA Elektronik A/S (Herlev, Denmark).

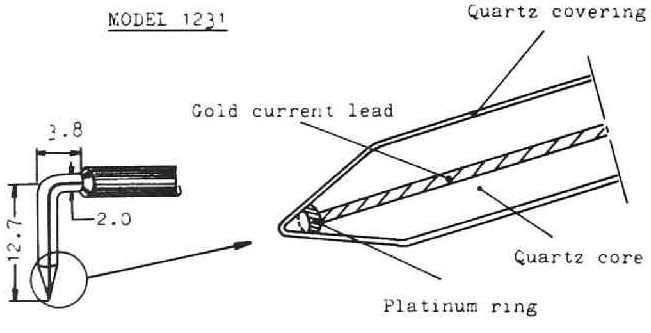

Fig. 2.14 Anemometer probe

2.3.3 Double-Impedance-Probe (Tracer Technique)

The double-impedance-probe consists of two identical pair-elec-

trodes which are apart about 5 mm distance from each other in the flow direction. Each electrode was fabricated in just the same manner as the electrical resistivity probe. A pair of electrodes, coated by a resin insulator except for the sensing tips, run parallel with each other in axial direction (Fig.2.15).

L-C circuit between the probe and the source-line of the electronic circuit (detecting circuit in Fig.2.2(a)) is necessary to eliminate the noise pulse on the source-line induced by the STOP signal. If this noise pulse could not be eliminated, it would prevent the busy circuit from the normal operation.

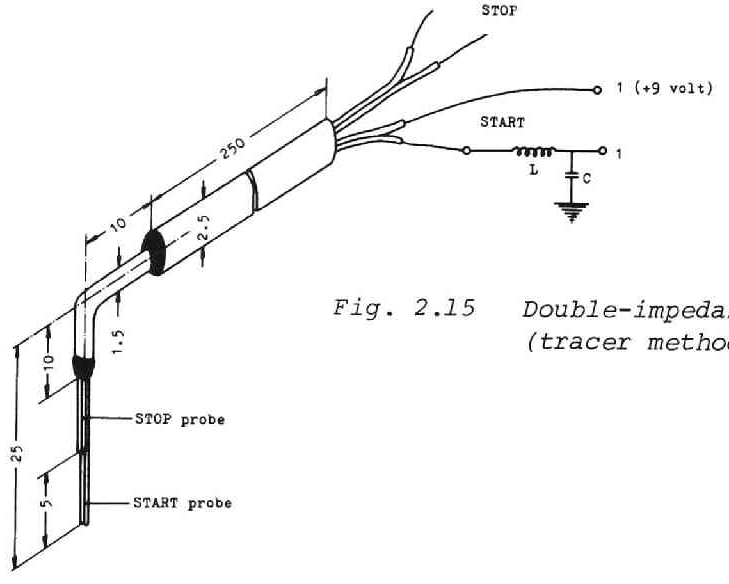

Fig. 2.15 Double-impedance-probe (tracer method)

2.3.4 Isokinetic Sampling Probe

The probe opening was selected in such a way that its diameter was small compared with the probable bubble diameter and that the probe would act as a voidage probe. Schematic of the isokinetic sampling probe is given in Fig.2.16.

2.4 Some Discussions on Accuracies of Measurements

In Section 2.2 were explained the principles of measurements for

various parameters in relation to the present study of bubble flow.

Accuracy of each measuring method or instrument plays an important role in interpreting the experimental results.

Some brief discussions or comments will be presented here about a few significant methods of measurements.

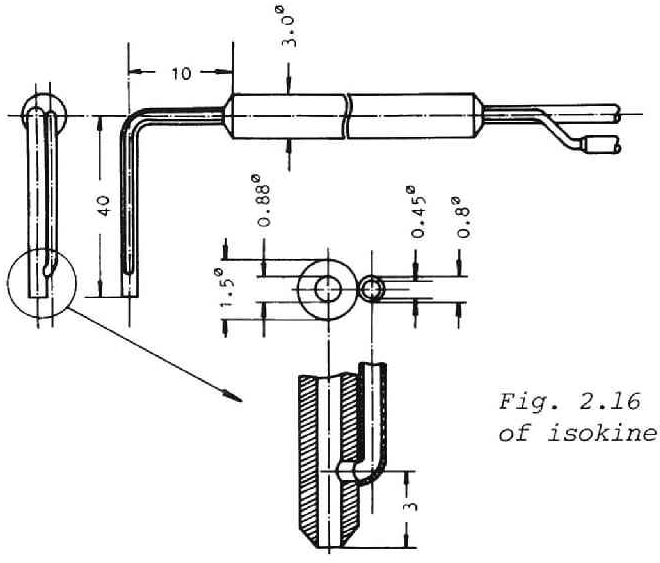

Fig. 2.16 Schematic drawing of isokinetic sampling probe

2.4.1 Measurement of Local Void Fraction

As already mentioned, the local void fraction was measured by utilizing the START probe (electrical resistivity probe) of the double-probe. The problems inherent to this method are :

1) Is it valid that the ratio of the sum of the periods of gas-contact to the total sampling time should be the true local void fraction ?
2) The effects of the probe geometry upon the bubble motion.
3) Where should the slice level (or discrimination level) be set in processing the modification of signals ?

The first problem is solved in Appendix II. The second is related to the wettability between the probe and the liquid.

The configuration of the probe and a single bubble, and corresponding signal of the probe are illustrated in Fig.2.17.

But for the wettability effect or the transfiguration of the

bubble, at point A, a bubble comes into contact with the probe tip, and at point D, it would detach from the probe tip. Therefore, the curve ABCD should be considered as a true bubble-contact period with the probe. The boundary-contact period, denoted by "t_c" in Fig.2.17, which is defined as a period while the boundary between the bubble and the liquid remains at the probe tip, cannot be distinguished even by means of the electronic instruments, since the probe signal is at water level during this period. Hence, in the resistivity probe method, the boundary-contact period has a negative effect on the local void fraction, because we cannot but take, for convenience sake, the apparent bubble-contact period, namely the bubble-penetration period, t_{gi}', instead of the true bubble-contact period t_{gi}. Sekoguchi et al. [20] have reported that the boundary-contact period was about 100 ~ 200 μsec in their experimental arrangement. (This value may correspond to nearly 5 ~ 10 percent error in void fraction, provided that the bubble velocity and the diameter are 2 m/sec, and 4 mm respectively.)

The existence of this boundary-contact period is due to the wettability between the probe tip and the liquid, and hence to the bubble transfiguration by the probe. On the other hand, it tends to decrease the bubble velocity, and hence it has a positive effect on the void fraction. The experimental study of Iida et al.[21] has indicated that the bubble transfiguration by the probe would be approximately 5 percents

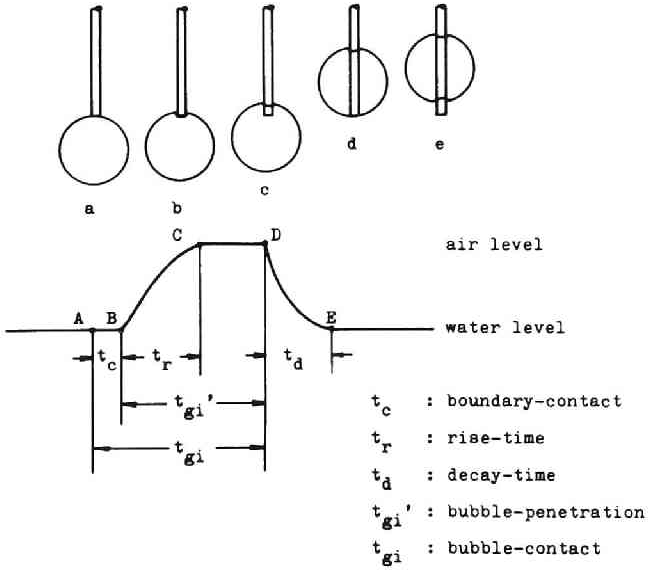

Fig. 2.17 Passage of a single air bubble past the resistivity probe

of the bubble diameter and the change of bubble velocity 1 percent at most in the present experimental arrangement, with an assumption of 4-mm bubble diameter. As a whole, both the negative and the positive effects of the boundary-contact period upon the void fraction measurement by the probe method may cancel each other, and therefore these effects due to the bubble transfiguration may introduce substantially only a few percents error, at most, in void fraction for the present experimental arrangement. (The experiment showed that the 0.2-mm probe was able to penetrate about 4-mm bubbles even near the bubble edge without forcing the bubble aside. This fact is quite similar to that observed by Malnes[12].)

In relation to the last problem, since the probe fabricated for this experiment indicated, fortunately, the very small decay time for the signal (of the order of 10 μsec), no significant errors were introduced in the measurements, by setting the slice level at such a little higher level than that of the liquid that the noise signal caused by fluctuating liquid level could be completely eliminated (practically, this adjustment for the level and sensitivity was made by observing the trigger input and the output signals by means of an oscilloscope).

2.4.2 Measurement of Bubble Velocity

The second and the third problems in the proceeding paragraph are the cases with the bubble velocity measurement.

In multi-channel technique exists one more problem related to the uniform statistical error which is independent of the bubble velocity. This error may result from the fact that one STOP signal does not always correspond with one START signal. The following three cases may be possibly encountered :

a) The case where no other bubbles hit the STOP probe within the time duration between the START and the STOP signals generated by the same bubble. This case is the normal operation.

b) A bubble, having penetrated the START probe, does not hit the STOP probe. In this case, the START signal produces a unique

pulse as the output of the time-to-pulse height converter, of which amplitude is proportional to the constant time delay determined by the "time constant" (RC = 80 msec) of one-shot circuit shown in Fig.2.2. (This time constant of 80 msec corresponds to the constant time delay of about 56 msec.)

c) Before a bubble, having penetrated the START probe, reaches the STOP probe, another bubble hits the STOP.

The last two cases, (b) and (c), are the missoperation. The above mentioned error may be considered statistically uniform with respect to time, and hence they function as a uniform background in the bubble velocity spectrum obtained by experiment (see Fig.2.19).

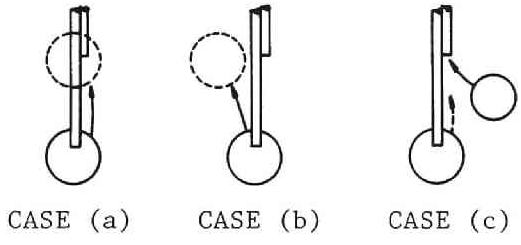

Fig. 2.18 Three possible cases encountered in double-probe method

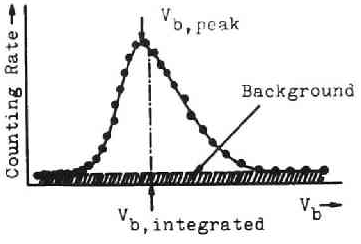

Fig. 2.19 Uniform background in bubble velocity spectrum

The experimental results indicate that the average (or in a more exact expression, the most probable) velocity of bubbles measured by cross-correlation technique is about 5 percents smaller in the bubble flow region than the averaged velocity (weighted with corresponding bubble numbers) measured by multi-channel technique (Fig.2.20).

Two reasons are possible for this difference. One of them is that already discussed in Paragraph 2.2.3.1. The alternate is related to the bubble velocity spectrum. The experimental results obtained by multi-channel technique indicate that the velocity spectrum of bubbles passing a certain point in the stream can be well approximated by Poisson probability distribution function (see Fig.4.59). Referring

to the sketch (Fig.2.19) and Fig.2.21, we can understand that the peak velocity in the spectrum, designated $V_{b,peak}$, — the most probable velocity of bubbles measured by multi-channel technique, and within the experimental accuracy this value is equal to the above mentioned most probable velocity of bubbles measured by cross-correlation technique — is lower than the average (number-averaged) velocity of bubbles, denoted $V_{b,integrated}$, by 5 ~ 10 percents in the bubble flow region and by 10 ~ 20 percents in the transition (or developing slug) flow and the slug flow regions.

2.4.3 Measurement of Liquid Velocity

Hinze[19] has already pointed out in detail the limitations for applying the anemometer method to the flow field where the relative turbulent intensity is large.

In the present work, when applying the hot-film anemometer technique to the air-water bubble flow region, some questions arose, in relation to the interpretation of its calibration procedure, from a viewpoint that the flow field in the air-water bubble flow system would be rationally different, to a large extent, from that in single-phase flow of water, and that the mechanism of heat transfer from the sensing wire of the hot-film probe would therefore vary in both cases. Inspection of our experimental results obtained by hot-film probe, however, suggests that, within the range of flow variables covered in the present experiment, the turbulent intensity in the bubble flow is of the same order as in water flow, as will be represented in Figs. 4.92 ~ 4.96 in Chapter IV. It also suggests that the characteristic curves for the anemometer system performed in water flow is capable of being applied to bubble flow with the assumptions of constant temperature of the ambient fluid and of constant overheating ratio of the heating element.

Total liquid flow rate, calculated by integrating over the whole cross-sectional area of the flow the experimental radial profiles both of the water velocity measured by the hot-film anemometer method and

of the void fraction by resistivity probe, showed a good coincidence with less than a few percent error with that measured directly by the turbine-flowmeter. (Measurements were conducted in the air-water experimental loop shown in Fig.3.2.)

In spite of the effect of heat removal by lateral velocity components upon the operation of the conical-type hot-film probe, and notwithstanding the differences both in the degree of turbulence and in heat transfer mechanism between the two-phase and the single-phase flows, the hot-film anemometer method facilitated us to obtain some significant information about turbulent characteristics of the liquid phase in air-water bubble flow in pipe.

On the other hand, the tracer method is of course more inaccurate than the anemometer method. This disadvantage is quite essential, because the velocity measured by the tracer method is an instantaneous value, whereas the time-averaged value by the anemometer method. Inaccuracy inherent to the tracer method is thus ascribed to the fluctuating character of the liquid velocity. Hence, the error involved in this method may be the same order of the relative turbulent intensity, if a number of sampling are performed (in our experiments, relative turbulent intensity was about 0.04 ~ 0.1, although it varied accordingly to the flow rates of the gas and the liquid). This method will surely serve as one of the most convenient and low-price methods for us to know the mean flow distribution. (When the lump of hot water is used as a tracer, the response time of each thermocouples are needed to have been examined beforehand.)

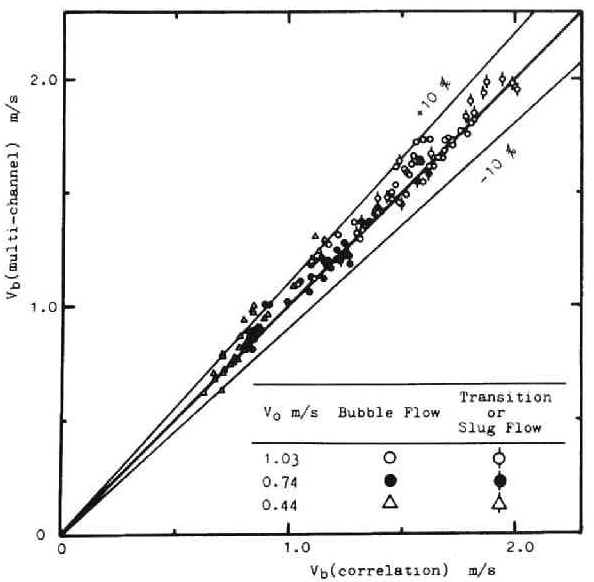

Fig. 2.20 Comparison between bubble velocities measured by cross-correlation technique and by multi-channel technique

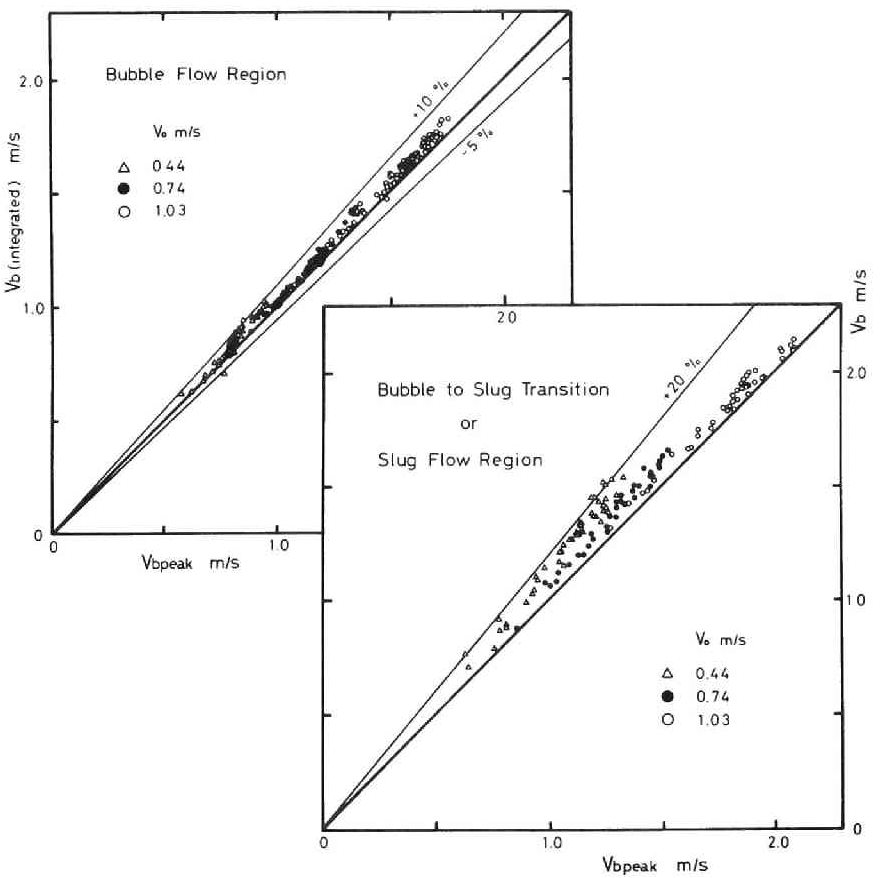

Fig. 2.21 Comparisons between the average and the most probable velocities measured by multi-channel technique

REFERENCES

[1] Levy, S.: Trans. Am. Soc. Mech. Engrs., Ser.C, 85 [2], 137 (1963).

[2] Petrick, M.: ANL-5787 (1958).

[3] Gill, L.E., Hewitt, G.F., Hitchen, J.W.: AERE-R-3954.

[4] Schraub, F.A.: ASME Paper 67-WA/FE28 (1967).

[5] Shires, G.L., Riley, P.J.: AEEW-M650.

[6] Neal, L.G.: ANL-6625 (1963).

[7] Nassos, P.G.: ANL-6738 (1963).

[8] Hyu, Y.Y., AL : Winter Annu. Meeting Am. Soc. Mech. Engrs., Philadelphia, (1963).

[9] Delhaye, J.M.: CEA-R-3465 (1968).

[10] Miller, N., Mitchie, R.E.: Two-Phase Flow Instrumentation, p.82, 11th Nat. ASME/AIChE Heat Transfer Conf., Minneapolis, Minnesota, (1969).

[11] Delhaye, J.M.: ibid., p.58.

[12] Malnes, D.: KR-110 (1966).

[13] Lackme, C.: CEA-R-3203 (1967).

[14] Kitayama, Y.: J. Nucl. Sci. Tech., 9 [10], 45 (1972).

[15] Aoki, S., Inoue, A., Yaegaki, H.: 6th Japan Heat Transfer Symp., p.241, (1965).

[16] Akagawa, K.: Trans. Japan Soc. Mech. Engrs., 29 [201], 924 (1963).

[17] Serizawa, A., Kataoka, I., Michiyoshi, I.: Annu. Meeting At. Energy Soc. Japan, (1973).

[18] idem : Bulletin of Inst. Atom. Energy, Kyoto Univ., Vol.43, 56 (1973).

[19] Hinze, J.O.: Turbulence, Mcgraw-Hill, (1959).

[20] Sekoguchi, K., Fukui, H., Matsuoka, T., Nishikawa, K.: 9th Japan Heat Transfer Symp., p.435 (1972).

[21] Iida, Y., Kobayashi, K., Kumagai, S.: J. At. Energy Soc. Japan, 9 [1], 2 (1967).

NOMENCLATURE

a	semimajor axis of spheroidal bubble
a	overheating ratio $(=(R-R_o/R_o)$
b	semiminor axis of spheroidal bubble
C	mass concentration of helium in two-phase mixture
C_g	mass concentration of helium in withdrawn mixture of air and helium
C_R	apparent moler ratio between helium and nitrogen
$C_{R'}$	true moler ratio between helium and nitrogen
d	equivalent-spherical diameter of bubbles defined by Eq.(2.13a)
d'	equivalent-spherical diameter of bubbles defined by Eq.(2.13b)
D	pipe diameter
E_s	anemometer output signal
F_{xy}	cross-correlation function between x(t) and y(t)
H	pulse height
k_1	constant
k_2	constant
k_3	constant
M_{He}	moler weight of helium gas
M_{N_2}	moler weight of nitrogen gas
N	counting rate
N_o	counting rate resulting from bubble passages
q_g	sampling volume rate of gas
q_l	sampling volume rate of liquid
r	radial coordinate
R	pipe radius
R	operational resistance of hot-film probe
R_o	cold resistance of hot-film probe
S	local slip ratio $(=V_b/V_l)$
t	time
u	turbulent velocity component of liquid in axial direction
$\sqrt{\overline{u^2}}$	turbulent intensity

t_c boundary-contact time

t_d decay-time

t_g gas-contact time

t_l liquid-contact time

t_r rise-time

V velocity

V_b bubble velocity

V_b^* superficial bubble velocity in the stream

V_{bs}^* superficial bubble velocity in the sampling probe orifice

V_l liquid velocity

V_l^* superficial liquid velocity in the stream

V_{ls}^* superficial liquid velocity in the sampling probe orifice

V_o superficial liquid velocity

$x(t)$ START-probe signal

X quality

$y(t)$ STOP-probe signal

z axial coordinate

Δz distance between START and STOP-probe tips

Z axial position

α_{loc} local void fraction

τ time lag

τ_o time lag

τ_{max} time lag corresponding to a maximum in $F_{xy}(\tau)$

$\Delta\tau$ pulse width

III. DISPERSION OF BUBBLES IN STAGNANT WATER AND IN THE CORE OF FULLY-DEVELOPED TURBULENT PIPE FLOW

3.1 General

One of the most predominant parameters relating to the turbulence structure of air-water two-phase bubble flow is a behavior of air bubbles moving in the turbulent flow field.

Many attempts have been performed experimentally in relation to the motion of a single air bubble in water and other liquids. Datta et al.[1], and Peebles & Garber[2] have described briefly many of these experiments, and further experiments have been carried out by Haberman & Morton[3]. The attempt by Saffman[4], concerning with the motion in water of air bubbles whose equivalent spherical radii were in the range 0.5 ~ 4.0 mm, is very instructive in order to know the systematic behaviors of bubbles. According to his detailed description of the motion of air bubbles, not spherical but oblate spheroids, the bubbles may rise steadily in a vertical straight line, or along a zig-zag path or in a uniform spiral, depending upon the bubble radius or other various factors. The reported experimental evidence indicates that the rectilinear motion occurs when the radius is less than about 1.3 mm, and that bubbles of larger radius (but below about 5 mm) either zig-zag or spiral depending upon the contaminants involved in water. The motion of air bubbles, of which radii are between about 3 ~ 4 mm, also depends significantly upon the initial conditions of bubble generation.

A single bubble motion can be determined theoretically, in principle, by solving the equations of motion, for example the equation of Navier-Stokes or Bernoulli's equation for steady motion, with some appropriate boundary conditions[4]. But in the two-phase bubble flow region, the complicated interactions between adjacent bubbles make such theoretical treatments of bubble motion impossible.

Another approach to the motion of bubbles lies in the statistical treatment of the phenomena. A number of experimental studies have been carried out in such a manner in relation to the turbulent diffusion of matter, small particles or small liquid droplets[5-9], but very scanty in relation to the gas bubbles.

Houghton[10,11] applied the statistical concept to the bubble motion in heated channels in order to estimate the cross-sectional average vapor void profile and the bulk temperature profile in the flow direction. According to the modern theory of the Brownian motion of a free particle[12], in this case a bubble, he obtained fundamental flux vectors for the diffusion of bubbles in heated channels by considering bubble motion in a turbulent liquid as a Markoff process. With several assumptions, these flux vectors lead to a following nonlinear partial differential equation representing the void fraction:

$$\frac{\partial C}{\partial t} = - \text{div} \left(- \varepsilon_B \text{ grad } C + \frac{\vec{V}_l \, C}{1 - C} + \vec{V}_s \, C\right) + p + q \qquad (3.1)$$

Similar equation representing heat transfer to the liquid phase is,

$$\frac{\partial T}{\partial t} = - \text{div} \left(- \varepsilon_L \text{ grad } T + \frac{\vec{V}_l \, C}{1 - C} - \vec{V}_s \, CT\right) - \frac{\rho_g \, \lambda}{\rho_l \, c_p} (p + q) \qquad (3.2)*$$

In the case of two-dimensional steady-state flow, Eqs.(3.1) and (3.2) are rewritten

$$\left[\frac{V_{lz}(y)}{(1 - C)^2} + V_s\right] \frac{\partial C}{\partial z} = \frac{\partial}{\partial y} \left(\varepsilon_B \frac{\partial C}{\partial y}\right) + p + q \quad , \qquad (3.3)$$

---

* The backflow of liquid $\vec{V}_s \, C$ in the parenthesis on the right hand side of this equation, representing the volume of liquid displaced from the front to the back of the bubbles as they rise upward through their own diameter, opposes the forward motion of the liquid.

$$\frac{\partial}{\partial z}\left[\left(\frac{V_{lz}(y)}{(1-C)} - V_s\, C\right) T\right] = \frac{\partial}{\partial y}\left(\varepsilon_L \frac{\partial T}{\partial y}\right) - \frac{\rho_g\, \lambda}{\rho_l\, c_p}(p + q) \tag{3.4}$$

where C, T, V_{lz}, V_s, p, q, ε_B, ε_L, ρ_g, ρ_l, c_p, and λ are the local void fraction, local temperature of liquid, the axial velocity of the liquid entering the channel, a weighted slip velocity of bubbles due to buoyancy, a weighted nucleation rate, a weighted bubble growth rate, a bubble diffusivity, a turbulent diffusivity of liquid, the densities of vapor and liquid, heat capacity at constant pressure, and latent heat of vaporization, respectively. (C and T are the functions of the coordinates y and z.) The first term in the parenthesis on the right hand side of Eq.(3.1) denotes the turbulent transport (or diffusion) of bubbles, and the sum of the second and the third in the parenthesis the transport of bubbles by convection.

This analysis by Houghton is quite interesting, but he didn't discuss the validity of such a diffusion model, at all, on its applying for two-phase flow systems. The attempts to apply diffusion theory to the analysis of the bubble movements raise serious doubts regarding the legitimacy of employing the known information about eddy diffusivities for particles, as small as 1 μ in mean size, since for such larger particles as bubbles eddy turbulence is believed to provide the dominant mechanism at the present stage of investigation.

Here, in this chapter, depending upon the experimental results on the movements of air and argon bubbles in water, we will discuss the validity of "a bubble diffusion model" or a concept that bubbles would move at random in the flow field, just like discrete dispersion matter or small diffusing particles in flow, provided that the phenomena should have statistical meanings both in their spatial and time dependences.

The purpose of this chapter is to clarify the following questions:

1) How is the spatial distribution of bubbles (more exactly speaking, the spatial distribution of the number of bubbles

which will pass one after another over the measuring point for a given sufficiently large time duration) which are introduced into the stream at a fixed point source? And does it obey such a certain statistical law as seen in the concentration distribution of the normal diffusing matter?

2) Is the bubble arrival at a certain point in space random in time?
3) How is the relation between the bubble dispersion time and the mean square of the lateral displacement of bubbles $\overline{y^2}$?
4) How large is the bubble dispersion coefficient, when assuming bubbles as diffusing particles?
5) How large are the Eulerian scales of turbulent motion of bubbles?
6) Is it possible to conclude the diffusing characteristics of bubbles in turbulent liquid flow?

3.2 Experimental Apparatus and Procedures

A study of gas bubble transport was carried out both in stagnant water in pool and in turbulent pipe flow. Stagnant water experiment was preliminary step to the other. In the former experiment, air and argon bubbles were introduced, whereas in the latter, mainly argon bubbles. Experimental procedures were common to both cases in many points. Details are described below.

3.2.1 Experiments in Stagnant Water

Figure 3.1 shows the schematic diagram of the experimental apparatus and the measuring equipments. Bubbles were generated by means of nozzle atomization (bubble injector - 0.88 mm inside diameter), and were introduced into the stagnant water in a glass-basin of 300 × 260 × 200 mm in size.

Lateral distributions of the bubble rise velocity and the bubble

impaction rate were measured at 4 ~ 13 different positions in vertical direction by the aforementioned techniques, i.e., double-probe (electrical resistivity probes) method with use of cross-correlation technique for bubble velocity.

3.2.2 Experiments in Pipe Flow

The experimental facility used in this study is shown schematically in Fig.3.2. This forced-convection loop, designed for operation with air-water at nearly atmospheric pressure, consists of the water and the air lines. The test section (1) in Fig.3.2 is divided into three parts, and each part, composed of 60-mm inside diameter Lucite pipe and Lucite chamber as represented in Fig.3.3, has five pressure taps (two of them are not shown in Fig.3.3) and eight taps for probes, bubble injector or heater wire.

In the experiment of interest here, the water (city water), degased at the lower tank (5), enters the test section in single-phase flow. Experiment was conducted about at Z/D = 20, after having confirmed that the flow was fully developed there. Details of the experimental arrangement are shown schematically in Fig.3.4.

Bubbles were introduced into the water from bubble injector (stainless steel tube of 0.88-mm inside diameter), located at the center of the pipe through the tap M1, and were carried away downstream with spreading towards the pipe wall. At various different superficial liquid velocities and different volumetric gas flow rates*, the radial distributions of the local average velocity of bubbles**, and impaction rate were measured by resistivity-probe method (using cross-correlation technique in the case of bubble velocity measurement), at three different measuring points located at about 3, 8, and 13.5 cm downstream from the exit of bubble injector respectively.

---

* The term "volumetric gas flow rate" means, in this chapter, the reduced value due to the pressure at the exit of bubble injector.

** See footnote on page 155.

(Probes, inserted into the flow field through the taps M4, M5, and M6, were run arbitrarily in radial direction with the traversing equipment. While a measurement was being conducted at a certain point, other two probes were necessarily placed near the wall so that the flow might not be disturbed by them.) Concurrently photographs of bubbles were taken to know their radii. (Water box for photographing is 80 × 66 mm in length and width respectively and is located at Z/D = 22.5.) Probe positioner runs with an accuracy of 1/100 mm.

3.3 Test for Fully-Developed Pipe Flow

Main purposes of this chapter are to find turbulent characteristics of bubble motions and to discuss the legitimacy of employing diffusion theory for bubble behaviors. As a consequence, verification of the following terms is strongly called for in an analysis of the experimental results obtained and also in discussing their practical meanings:

1) Fully-developed turbulent flow,
2) Axial-symmetric flow,
3) Smooth circular passage.

The first problem is satisfied, since the velocity range covered in the present experiment in pipe flow corresponds to the one where liquid Reynolds number is between $0.9 \sim 4.4 \times 10^4$. Remaining terms will be discussed below.

3.3.1 Radial Profile of Water Velocity

The mean (time-averaged) flow velocity profiles were surveyed with a Pitot tube at three different axial positions Z/D = 10, 20, and 30.

The most direct test for the existence of fully-developed flow is an unchanging velocity profile for increasing axial distance. If the mean velocity profiles at a given flow rate do not change over some distance of the test section, then it follows that nearly fully-developed flow is attained there. Figure 3.5 shows that, at the three

flow rates, this criterion was well satisfied at the stations Z/D = 20 and 30, and that the entrance effect was yet seen at Z/D = 10.

A slight asymmetry is evident in some profiles, which show higher velocities for $0 < r/R < +1.0$, but the deviation from symmetry is small. Hence, the flow field was postulated nearly symmetric during experiments.

3.3.2 Friction Factor

To complete the picture of bubble behaviors, single-phase pressure drops were measured in fully-developed turbulent flow region over 100 cm distance of the test section.

The resulting friction factors f, defined by Eq.(3.5), were plotted against liquid Reynolds number in Fig.3.6, and approximated by Eq.(3.6).

$$\left(\frac{\Delta P}{\Delta z}\right)_f = f \frac{\rho_l V_o^2}{2 gD} \tag{3.5}$$

$$f = 0.229 \, Re_l^{-0.219} \tag{3.6}$$

One can see that the experimental values of f agree very satisfactorily with Moody smooth curve below a certain value of Re_l, above which they become very slightly higher value than the predicted. This behavior may be the result of a wall roughness characterized by wall irregularities. According to the Colebrook's expression (Eq.(3.7)) for rough ducts, mean wall irregulality corresponds to about 10 microns in height. This follows that the inner wall of the test section may be postulated smooth enough in the present experiment.

$$1/\sqrt{f} = -2 \log_{10} \left[(1/3.7)\left(\frac{\varepsilon}{D}\right) + 2.51/(Re_l \cdot \sqrt{f})\right] \tag{3.7}$$

where ε is the equivalent sand roughness.

3.4 Definition of Bubble Dispersion Coefficient and Basic Equations

In this chapter, the major objective of the experimental investigation is, as already mentioned, to test the validity of the diffusion theory of bubble transport, and to determine a diffusion parameter, namely bubble dispersion coefficient, from a statistical description of bubble behaviors measured by semi-fixed probes.

In this section, the conservation equation of mass is applied for description of bubble transport in turbulent pipe flow. Quite similar approach has been performed recently by Ginsberg[8] for turbulent diffusion of liquid droplets in pipe.

3.4.1 Mass Conservation Equation and Bubble Dispersion Coefficient

In the case of no bubble source or sink in the flow field, the mass conservation equation for bubbles ascending in a fluid with convective velocity $\vec{V}$ may be written

$$\frac{\partial C^*}{\partial t} + \vec{V}\cdot\nabla C^* = 0 \qquad (3.8)^*$$

where C^* is the local mass concentration of bubbles.

---

* According to Houghton's analysis[10], the local mean bubble velocity $\vec{V}_b$ is given by $\left(\frac{\vec{V}_l}{1-C} + \vec{V}_s\right)$.
If we put p = q = 0 in Eq.(3.1), it will become

$$\partial C/\partial t = -\ \mathrm{div}\ (-\varepsilon_B\ \mathrm{grad}\ C + \vec{V}_b C).$$

When the bubble diffusivity ε_B can be further assumed to be a result of the turbulent motions of bubbles and fluid, that is, the turbulent dispersion coefficient of bubbles, we have

$$\mathrm{div}\ (-\varepsilon_B\ \mathrm{grad}\ C + \vec{V}_b C) = \vec{V}\cdot\nabla C \quad (\text{see Eqs.(3.9) and (3.10)}).$$

Hence, substitution of this equation into the foregoing one yields

$$\partial C/\partial t + \vec{V}\cdot\nabla C = 0 \quad ,$$

which is very similar to Eq.(3.8).

For the flow of bubbles in a turbulent water, let

$$C^* = C + c \tag{3.9}$$

$$\vec{V} = \vec{V}_b + \vec{v} \quad , \tag{3.10}$$

where C and $\vec{V}_b$ are the time-averaged bubble concentration and convective velocity of bubbles, respectively, and c and $\vec{v}$ the corresponding fluctuating quantities.

Inserting Eqs.(3.9) and (3.10) into Eq.(3.8), and time-averaging the result, we obtain the following equation for stationary-state case.

$$\vec{V}_b \cdot \nabla C + \nabla \cdot \overline{\vec{v}c} = 0 \tag{3.11}$$

The quantity $\overline{\vec{v}c}$ represents the turbulent flux of bubbles in the three coordinate directions. The over-bar denotes a time-average.

From a viewpoint of bubble diffusion concept, the turbulent bubble dispersion coefficient ϕ is defined by the following equation, relating to the turbulent flux of bubbles.

$$\overline{\vec{v}c} = - \phi \nabla C \tag{3.12}$$

Consider the flow of bubbles in fully-developed turbulent flow in pipe, and assume that the bubble concentration distribution and bubble velocity distribution are azimuthally symmetric, and that axial diffusion is negligible. Then, the bubble transport equation in cylindrical coordinate is give below.

$$V_b \frac{\partial C}{\partial z} = \frac{1}{r} \frac{\partial}{\partial r} \left(r \phi \frac{\partial C}{\partial r} \right) \quad , \tag{3.13}$$

where V_b is the local velocity of bubbles (scalar quantity) in axial direction.

Assuming that V_b and ϕ are independent of r*, then

$$\frac{\partial z}{\partial t} = V_b \quad , \tag{3.14}**$$

and

$$\frac{\partial C}{\partial t} = \phi \frac{1}{r} \frac{\partial}{\partial r} \left(r \frac{\partial C}{\partial r} \right) \quad . \tag{3.15}$$

Equation (3.15) is recognized as the classical diffusion equation, with constant value of ϕ. The use of the classical diffusion equation, the Fick's law differential equation, implicitly involves the assumption that the diffusion characteristics of particles contained in a differential volume are independent of their previous history, i.e., the length of time they have been in the field. This independence is not encountered in turbulent diffusion.

Taking a time-dependence of the bubble dispersion coefficient into consideration, we will rewrite Eq.(3.15) as below.

$$\frac{\partial C}{\partial t} = \phi(t) \frac{1}{r} \frac{\partial}{\partial r} \left(r \frac{\partial C}{\partial r} \right) \tag{3.16}$$

Thus, Eq.(3.15) has become a similar equation to that of one dimensional heat conduction from a fixed point source located at the origin of coordinate in the place $Z = \int_0^t V_b \, dt$.

---

* The assumption that V_b is independent of r is fairly satisfied over a large portion of the core region of the flow field, whereas not always in the vicinity of the pipe wall. This fact was verified by the experimental evidence, as is shown later.

** In Eq.(3.14), "t" represents the bubble dispersion time for bubbles to travel from a fixed source located in the stream, and is different from that used in Eq.(3.8). Hereafter, we mean the bubble dispersion time by the notation "t".

For a point source of bubbles of strength S_o at the origin, the solution to Eq.(3.16) is the Gaussian in the case of no wall effect.

$$C(r, t) = \frac{S_o}{2\pi[\int_0^t 2\phi(t)\, dt]} \exp\left[-\frac{r^2}{2\int_0^t 2\phi(t)\, dt}\right] , \tag{3.17}$$

with initial condition

$$C(r, 0) = \frac{S_o}{2\pi r}\, \delta(r) \quad . \tag{3.18}$$

In this case, the bubble dispersion coefficient $\phi(t)$ is rewritten by

$$\phi(t) = \frac{1}{2}\frac{d}{dt}\overline{y(t)^2} \quad , \tag{3.19}$$

where the mean square of bubble displacement $\overline{y(t)^2}$ is give by

$$\overline{y(t)^2} = \frac{\int_0^\infty r^3 C(r, t)\, dr}{\int_0^\infty r\, C(r, t)\, dr} \quad . \tag{3.20}$$

3.4.2 Bubble Impaction Rate

In the foregoing formulations, mass concentration distribution of bubbles was used, but virtually it is very troublesome and difficult to measure this quantity directly. Provided that the aforementioned assumption of the uniform bubble velocity in radial direction is satisfied, mass concentration C(r, t) can be replaced approximately by bubble impaction rate N(r, t) at that point. Verification will be presented below.

First of all, some assumptions are made:

1) a large number of bubbles permissible for statistical treatment,
2) uniform bubble velocity in radial direction,
3) mean diameter of bubbles passing the probe at a certain

position is uniform in radial direction under the assumption (1),

4) mean eccentricity between the probe tip and the bubble center is uniform in radial direction under the assumption (1).

Referring to Fig.3.7, one can easily obtain the following equation.

$$V_b\, C(r, t)\, dA = \rho_g \left(\sum_{i=1}^{N} l_i \right) dA \tag{3.21}$$

where

$$l_i = 2\sqrt{(d_i/2)^2 - e_i^2} \tag{3.22}$$

and dA, N, d_i, and e_i are effective cross-sectional area of the probe tip, bubble impaction rate, diameter of i-th bubble, and degree of eccentricity between the probe tip and the center of i-th bubble, respectively.

Let

$$\sum_{i=1}^{N} l_i = \bar{l}\, N(r, t) \quad , \tag{3.23}$$

then, Eq.(3.21) becomes

$$V_b\, C(r, t)\, dA = \rho_g\, \bar{l}\, N(r, t)\, dA \tag{3.24}$$

By virtue of the ssumptions, V_b and $\bar{l}$ become independent of r, and hence, the following relation between C(r, t) and N(r, t) can be obtained from Eq.(3.24).

$$C(r, t) \propto N(r, t) \tag{3.25}$$

Then, the time-dependent bubble dispersion coefficient $\phi(t)$ is to be calculated from measured distribution of bubble impaction rate with

using Eq.(3.19), when Eq.(3.17) is satisfied.

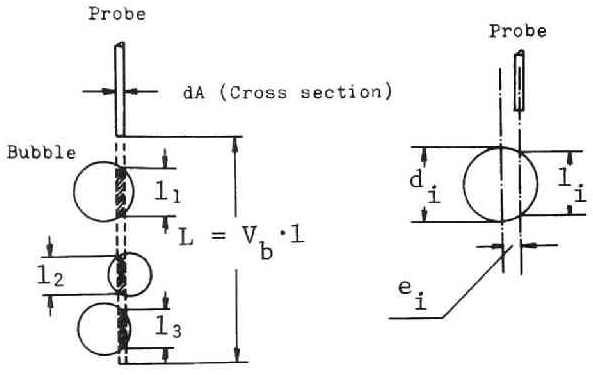

Fig. 3.7 Conceptual probe eccentricity

3.5 Measurement of Bubble Dispersion in Stagnant Water

Preliminary tests for lateral transport of bubbles were conducted in stagnant water in pool at nearly room temperature within the range of volumetric gas flow rate at injector outlet pressure of 150 ~ 700 cc/min for argon bubbles and 100 ~ 700 cc/min for air bubbles.

3.5.1 Radial Profile of Bubble Impaction Rate

Typical profiles of bubble impaction rate for air bubbles appear in Figs.3.8 and 3.9, and those for argon bubbles in Figs.3.10 and 3.11, where Z' is the downstream distance from bubble injector. Solid lines in these figures represent normal distribution curves (Gaussian) given by

$$\frac{N(r, Z')}{N_{max}(0, Z')} = \exp[-\frac{r^2}{2\overline{y^2}}] \quad . \qquad (3.26)^*$$

---

* This equation is obtained from Eq.(3.17) by replacing N(r, Z') for C(r, t). In Figs.3.9 and 3.10, λ_h in horizontal abscissa is half-width of the profile of impaction rate.

These figures indicate, perhaps surprisingly at a glance, that, even in the region of a small downstream from injector, gas bubbles of mean size as large as 2 ~ 7 mm exhibit a diffusivity that is familiar to the motions of the very small molecules.

An analytical result in the preceeding section dealt with a bubble behavior in turbulent water flow according to the bubble diffusion model. Whereas in stagnant water experiment, no turbulent flow of bulk water exists at all except for small-scale secondary flows of water induced by bubble motions. This fact implies:

1) A diffusivity of bubbles, inherent to the clouds of bubbles, is due to the interactions between bubbles and also due to a slight heterogeneity of the medium such as secondary flows induced around each bubble, and is not due to a violent turbulent flow or motion of bulk water,
2) A violent motion of bulk flow may make a contribution only to increasing the diffusivity of bubbles.

A brief comment to these will be discussed later in next section.

3.5.2 Bubble Dispersion Coefficient

The displacement variances $\overline{y^2}$ of lateral bubble dispersion in water are represented in terms of the transit time (or dispersion time) t between bubble injector and probes for air bubbles in Fig.3.12 (a) and for argon bubbles in Fig.3.12(b). These figures show that, in every case, $\overline{y^2}$ has a convex trend towards horizontal axis below a certain value of t, and that above which value it tends to increase proportionally with t. The variance curves shaped as shown in the above figures are slightly different in their tendencies from those for lateral particle or molecule diffusion in isotropic turbulence. According to a textbook of turbulence, for example, the textbook by Hinze[14], $\overline{y^2}$ increases first proportionally with t^2 and finally proportionally with t and has no points of contra-flexure in $\overline{y^2}$ - t diagram in such particle diffusion phenomena. This difference is partly because of the effects of bubble injector and partly because

the measured distributions of bubble impaction rate deviate from Gaussian in the region of small t or Z'.

Time-dependent bubble dispersion coefficients $\phi(t)$ are given in Figs.3.13 and 3.14 which are obtained by graphical differentiation of the $\overline{y^2}$ - t diagrams in accordance with Eq.(3.19). The results yield that $\phi(t)$ has a maximim value at $t \simeq 0.1$ sec, and that, at a large t, it tends to converge to a certain value determined by the volumetric gas flow rate and other factors. The maximim value of $\phi(t)$ or contra-flexure point in $\overline{y^2}$ - t diagram may be attributable to the following two reasons:

1') Effects of bubble injector upon bubble motions, i.e., the effects resulting from a variation in shape of the lateral distribution of bubble impaction rate or bubble rise velocity,

2') The bubble dispersion coefficient defined by Eq.(3.19) cannot be applied for small dispersion times.

In experiments, it was visually observed that, for small dispersion times, bubbles generated at injector ascended in a bubble-column along a zig-zag path or in a uniform spiral over a certain small distance, and, at this stage, bubbles scarcely dispersed laterally into the water. Temporal criterion of this bubble motion is nearly 0.1 sec of dispersion time in stagnant water, irrespective of air or argon bubbles.

Figure 3.15, representing (a discrepancy between) the measured distributions of bubble impaction rate (and corresponding Gaussians) at small downstream distances from the injector, indicates the validity of the above arguments, namely, the experimental fact that bubbles didn't move in lateral direction but rose in a uniform spiral of nearly 2-mm diameter.

Figure 3.16 shows one example representing the injector effect upon the rising velocity of bubbles, which indicates the bubble rise velocity increases exponentially with time t up to a certain constant terminal velocity due to buoyancy. This entrance effect upon bubble

velocity may affect a diffusivity of bubbles.*

Now, we will discuss the second reason. As already mentioned, time-dependent dispersion coefficient $\phi(t)$ defined by Eq.(3.19) has its meaning only for the two cases:

a) long dispersion times,

b) dispersions capable of being expressed by Eq.(3.16).

Both cases do not hold true within the region of small downstream distance from the injector as is shown in Fig.3.15.

Hence, the existence of maximum values of $\phi(t)$ seen in Figs.3.13 and 3.14 are somewhat doubtful, and they don't appear essential to bubble dispersion phenomena.

Our interest is devoted to the asymptotic characteristic of $\phi(t)$ and therefore to its asymtotic value, because one of the most direct tests for verifying the bubble diffusion model is to find experimental evidences for such characteristics. From this viewpoint, the obtained experimental results may have revealed such evidences.

Asymtotic values of $\phi(t)$ (cm^2/sec) are presented by Curves (A) and (B) in Fig.3.23 as a function of the volumetric gas flow rate Q_g (cc/min). Bubble dispersion coefficient ϕ at large dispersion times can be specified as follows in compliance with the value of Q_g:

a) In the range $Q_g \lesssim 200$ cc/min, ϕ increases rapidly with increasing Q_g. This may be a result of rapid increases both in bubble diameter (see Fig.3.31) and in bubble density, and also of an increase in fluctuating liquid velocity of secondary flows locally induced by bubble motions.

b) In the range $200 \lesssim Q_g \lesssim 500$ cc/min, ϕ is nearly at constant value, of which trend well corresponds to that observed in bubble size distribution shown in Fig.3.31. In this range of Q_g, an increase in the displacement variance of lateral transport of bubbles may be, perhaps, determined by the com-

---

* Theoretical estimation of this entrance region for bubble motion is performed in Appendix III.

petition among the rate of increase in bubble-bubble or bubble-liquid interactions (positive effect upon ϕ), the rate of the resulting relative decrease in bubble density (negative effect), and the rate of increase in bubble velocity which is related to a gradual increase in bubble diameter (positive effect).

c) In the range $Q_g \gtrsim 500$ cc/min, ϕ increases rapidly again with Q_g. This is perhaps due to a change in bubble shape from spheroid to mushroom shape with spherical cap, and is also due to a violent circulation of bulk water.

Figure 3.23 also indicates no significant differences in ϕ except in the range $Q_g \gtrsim 500$ cc/min between those in the two cases for air bubbles and for argon bubbles. This fact encouraged us to utilize helium gas bubbles as tracer in the measurement of bubble dispersion characteristics in air-water two-phase bubble flow system, whose results will be described later in Chapter V.

3.6 Measurement of Bubble Dispersion in Pipe Flow

In previous section, the diffusion model has been revealed to describe successfully the transport of bubbles in stagnant water. In this section, the effects of the turbulent flow field upon the bubble transport characteristics are to be pursued experimentally.

Experiments were conducted in turbulent flow in pipe at superficial liquid velocity range V_o = 0.15 ~ 0.74 m/sec and volumetric flow rate of argon Q_g = 100 ~ 500 cc/min.

3.6.1 Radial Profile of Bubble Impaction Rate

The results of the bubble impaction rate are represented in Figs.3.17 to 3.20, where bubble impaction data, for each set of bubble and liquid flow rate parameters, are fitted to the normal distribution given by Eq.(3.26)*. These correlative representations of bubble impaction rate show a satisfactory agreement between the bubble transport concept and obtained data. No such entrance effects as shown in Fig.3.15 of bubble injection upon bubble impaction data were encountered in all experimental runs.

3.6.2 Bubble Dispersion Coefficient

With respect to the relation between the mean squares of bubble displacement $\overline{y^2}$ and dispersion time t, good linearity was obtained except at V_o = 0.15 m/sec. This means a constant rate of lateral bubble transport prevailing in the region more than 3 cm downstream from injector. In other words, induction period[14] in turbulent transport process was already attained and no entrance effect upon $\overline{y^2}$ - t diagram was seen there. The most important thing implied by the above experimental results is that the bubble diffusion model

---

* A least squares procedure was used to fit the bubble impaction data to Eq.(3.26) with an aid of the calculated variance $\overline{y^2}$ of measured data.

can be also successfully applied for describing statistical characteristics of bubbles suspended in the core of fully-developed turbulent flow of water where turbulence is considered nearly uniform and isotropic.

Figures 3.21 and 3.22 are the representations of displacement variance at V_o = 0.15 m/sec in terms of dispersion time, and corresponding time-dependent values of bubble dispersion coefficients. Similar effects to those observed in stagnant water experiment appear to have remained for the exceptional case V_o = 0.15 m/sec, where corresponding liquid Reynolds number was as small as 9,000 and turbulence was not yet highly established. This consideration may support the hypothetic arguments in Paragraph 3.5.1 (p.202) about the role of the flow turbulence in lateral transport of bubbles, that is, a view that an extensive turbulent motion of bulk flow may promote a development of diffusion process and may increase a diffusivity of bubbles.

Figure 3.23 summarizes asymtotic values of bubble dispersion coefficient obtained by least squares fitting for V_o = 0.30, 0.44 and 0.74 m/sec, and by graphical differentiation for V_o = 0.15 m/sec. Notable remarks about the tendencies of ϕ are:

1) ϕ is an increasing function of liquid velocity V_o,
2) ϕ at constant liquid velocities is not a simple function of the volumetric gas flow rate Q_g,
3) ϕ is of order 1 cm^2/sec if V_o and Q_g-dependences are ignored.

Some brief comments will be made about characteristic behavior of dispersion coefficient.

a) Effect of Liquid Velocity

As cited earlier in this section, bubble dispersion coefficient at large dispersion times remarkably increases with increasing liquid velocity. This is a rational conclusion with recalling the aforementioned hypothetic arguments and in consideration of the fact that the turbulent intensity of the flow field gives a higher value for a higher liquid velocity. And furthermore, this is quite consistent with

the experimental results in single-phase water flow, as shown in Fig.4.91, which indicate that, at the pipe center, the turbulent (or fluctuating) water velocity $u' = \sqrt{\overline{u^2}}$ for V_o = 0.74 m/sec is nearly 1.8 times larger than that for V_o = 0.44 m/sec, whereas in Fig.3.23 the ratio $[\phi]_{V_o=0.74}/[\phi]_{V_o=0.44}$ lies between 1.5 to 2. This appears to be closely related to the experimental fact that bubble migration is more active for bubbles of smaller diameter which corresponds to a higher water velocity (see Fig.3.31).

b) Effect of the Volumetric Gas Flow Rate

As a rule, bubble dispersion coefficient tends to decrease gradually in turbulent pipe flow with an increase of the volumetric gas flow rate, whereas, in contradiction to this, it has been shown to have a positive Q_g-dependence in stagnant water. The difference in Q_g-dependence of the dispersion coefficient between the two cases may be attributable to the Q_g-dependence of turbulent intensity of the flow field; in the latter case, the turbulent intensity* may increase with increasing gas flow rate owing to an agitation effect by bubbles. On the other hand, in the former case, flow turbulence is not affected seriously by introducing a small quantity of bubbles into the stream (refer to Section 4.8.3). This concept would lead to no Q_g-dependence in ϕ - Q_g diagram for pipe flow contradictorily to experimental results. Discrepancy between above concept and experimental results can be, perhaps, ascribed qualitatively to the effects of bubble diameter. As shown in Fig.3.31, a higher gas flow rate appears to have been generally accompanied with larger bubbles. Hence, in consideration of the fact that larger bubbles are exerted on with larger hydrodynamic resistance forces when they move either in axial or in radial direc-

---

* For the case of stagnant water experiment, we may well chose, in a strict sense, a term "degree of agitation of the field caused by bubbles" in stead of the term "turbulent intensity", because so-called turbulence never exists there.

tions, it can be rationally realized that large values of ϕ correspond to small values of Q_g at constant liquid velocity curves.

Another most important and distinct feature in Fig.3.23 is characterized by the minimum values of ϕ existing at $Q_g \simeq 250$ cc/min for each constant liquid velocity curve, and this appears to be related to the mechanism of bubble dispersion itself. Namely, the value Q_g of nearly 250 cc/min is to be assumed a criterion which indicates whether bubble diffusion model can be applied for within the range of Q_g below that value or not.

For Q_g below that assumed critical value, intrinsic and periodic bubble motions such as zig-zag or spiral motions will become to play important roles together with flow turbulence in lateral transport of bubbles without being disturbed seriously by other adjacent bubbles, since low bubble density may well be attended there with only weak interactions or collisions between bubbles. And this may result in an additional increase in the apparent displacement variance of bubble number distributions. On the other hand, it seems possible that the flow turbulence should be reduced in the core of pipe flow with a certain quantity of bubbles suspended rather than in single-phase water flow, owing to a similar effect to that observed in experiment on the turbulent intensity in two-phase air-water bubble flow, as will be shown in Section 4.8.3. Hence, the existence of minimum values of ϕ at $Q_g \simeq 250$ cc/min may be thus a result of the intrinsic periodic bubble motions and relative decrease in flow turbulence there.

In other words, two mechanisma are implied for bubble transport process; one is due to the above mentioned intrinsic zig-zag or spiral motions of bubbles, and the other due to the flow turbulence or agitated liquid characteristics. According to this deduction about bubble transport mechanism, $\phi - Q_g$ diagram will be divided phenomenologically into the following three regions:

1) For very small Q_g: zig-zag or spiral motions are predominant,
2) For (approx. $100 \lesssim$) $Q_g \lesssim 300$: transition region where zig-zag or spiral motions and relatively reduced flow turbulence or

random walks of bubbles are coexistent,

3) For $Q_g \gtrsim 300$: bubble diffusion process predominant region where the flow turbulence or random walks of bubbles are prevailing.

In general, a higher bubble density or a higher flow turbulence or heterogeneity of the field may suppress periodic zig-zag or spiral motions of bubbles, and may contradictorily accelerate their random motions. This random walk or characteristics of a bubble is the essence of a bubble diffusivity itself.

3.6.3 Rising Velocity and Diameter of Bubbles

3.6.3.1 Bubble Velocity

A knowledge of axial bubble velocity distribution is necessary to calculate bubble dispersion time t at any traversing position Z' according to an equation

$$t = \int_0^{Z'} \frac{dz}{V_b(z)} \quad , \tag{3.27}$$

where V_b is the mean axial velocity of bubbles defined by

$$V_b(Z') = \frac{\sum_r N(r, Z')\, V_b(r, Z')}{\sum_r N(r, Z')} \quad . \tag{3.28}*$$

Figure 3.24 shows experimental axial distributions of mean bubble velocity defined by Eq.(3.28).

Generally speaking, a bubble generated at injector is introduced into the stream with zero or a certain initial velocity, and is accelerated up to a certain constant terminal velocity due to buoyancy. Consequently, it takes some entrance length for the bubble to attain

---

* $V_b(r, Z')$ is a local average velocity of bubbles at r = r and z = Z'. Figures 3.33 and 3.34 show that $V_b(r, Z')$ is nearly constant over the range of radial direction tested in the present study.

to the terminal velocity. Figure 3.24 indicates that, in some cases especially at high liquid velocities and at high gas flow rates (or for large gas bubbles), the terminal bubble velocity seems not to have been yet attained even at the most downstream measuring point $Z' \simeq$ 13.5 cm, but it seems to have had no significant effects upon bubble dispersion coefficient for those cases. Preliminary theoretical analysis for entrance region shows a similar trend as shown later in Fig.3.36 (see Appendix III).

Figure 3.25 represents slip velocities of bubbles plotted against the superficial liquid velocity with use of the extrapolated terminal velocities of bubbles. From this figure, one can see that bubble slip velocity increases with liquid velocity very gradually first at low liquid velocities and abruptly at $V_o \simeq 0.5$ m/sec, and that it is not affected by the volumetric gas flow rate.

A reported experimental correlation for slip velocity of a single bubble is give by[15]

$$V_b = V_{so} + 1.2\ (V_o + V_{sg}) \quad , \tag{3.29}$$

$$V_{so} = 1.53\left[\frac{\sigma g(\rho_l - \rho_g)}{\rho_l^2}\right]^{1/4} \quad , \tag{3.30}$$

where V_{so} is the drift velocity of a single bubble in stagnant water, V_{sg} the superficial gas velocity in the stream and σ the surface tension of water. The experimental slip velocities obtained in the present work were nearly twice as large as the predicted by Eq.(3.30), and moreover, slip velocities in pipe flow increased with liquid velocity not lineally but rather exponentially, which tendency is different from that predicted by Eq.(3.29). However a correction for the wake effect is applied for continuously rising bubbles with multiplying Eq.(3.29) by a factor $[1 + 8\ \exp(-1.06\ L_o/D)]$ proposed by Moissis & Griffith[16], these discrepancies between the present experimental data and those correlations cannot be accounted for at all*. Contaminants in water may affect bubble rise, but this effect

---

* See footnote on next page.

is not so large[17].

3.6.3.2 Bubble Diameter

Figures 3.26 to 3.30 are histgrams of the equivalent spherical diameter of bubbles defined by Eq.(2.13.a), from which no accurate information could be obtained about bubble diameter distributions for the sake of poor counting statistics of bubbles.

Figure 3.31 is a representation of mean bubble diameter deduced from the above histgram in terms of the volumetric gas flow rate, which indicates that the mean bubble diameter $\bar{d}$, defined as $\sum_i n_i d_i / \sum_i n_i$ (n_i is the number of sampled bubbles of diameter d_i), increases linearly with gas flow rate at constant liquid velocity and decreases, on the other hand, with liquid velocity at constant gas flow rate. This trend is consistent with the experimental value of ϕ as already described.

Experimental variation of a/b ratio (a: ratio between semimajor and seminor axes of the spheroidal bubbles) is compared with various corresponding correlations by Kubota et al.[18], Tsuge[19], Saffman[4], and Siemes[20]. As shown in Fig.3.32, a dotted line represents a theoretical analysis, and chain lines and solid lines experimental correlations for bubbles in purified and non-purified water respectively. Experimental result of the present work yields that most bubbles were of equivalent diameter 3 ~ 6 mm and a/b ratio 1.1 ~ 2 regardless of the liquid velocity and the gas flow rate, and that, in spite of its large scatter, a/b ratio seems, as a whole, to increase roughly with increasing equivalent diameter up to nearly 7 mm above which plane bubbles existed predominantly.

---

* L_o and D are the distance between the neighboring two bubbles, and diameter of a pipe, respectively.

3.7 Discussions

In previous sections, the diffusion model was proposed to describe the transport of bubbles in the central core region of turbulent pipe flow, and the values of bubble dispersion coefficient represented in Fig.3.23 were obtained as a result of fitting the bubble impaction rate data to the point source solution of diffusion equation with a few assumptions (see Paragraph 3.4.2).

In this section, some discussions will be made about the validity of these assumptions used for employing the diffusion equation and about the diffusivity results.

a) Radially-uniform bubble velocity:

Figures 3.33 and 3.34 show the radial profiles of bubble velocity (lumped-average value obtained by cross-correlation technique) plotted for each experimental condition and each measuring station. These figures give a fairly good experimental evidence to the validity for assuming the radially-uniform bubble velocity distribution at any axial position, although a considerable scatter of data exists for higher liquid velocity, especially for V_o = 0.74 m/sec. This fact implies the existence of a fairly uniform turbulent field in the central core region of pipe flow.

b) Negligibly small axial diffusion of bubbles:

If the flow is an isotropic and homogeneous turbulence, then both the axial and the radial turbulent dispersion coefficients of bubbles become equal to each other in the case of no wall effect and no entrance effects.

Provided that bubbles would diffuse isotropically into the water from a point source, the spread of spherical boundary formed with diffusing bubbles is given

$$L^* = \sqrt{\frac{1}{4\pi} \int_0^t \phi \, dt} \quad . \tag{3.31}$$

Hence, the ratio of axial diffusion rate to the axial convection rate in bubble transport becomes

$$\frac{L^*}{V_b t} = \frac{1}{V_b}\sqrt{\frac{1}{4\pi t^2}\int_0^t \phi \, dt} \quad . \tag{3.32}$$

Let ϕ = 1 cm^2/sec and V_b = 0.5 m/sec, then $L^*/V_b t$ becomes approximately 0.018 and 0.014 for t = 0.1 and 0.2 sec, respectively. These values are negligibly small. Since an isotropic diffusion characteristic is not always established in actual shear flow, above approximate treatment should be confined virtually to the central core region of pipe flow, but it will not give a signifficant error. Hence, within the range of parameters of the present experiment, the axial diffusion may well be neglected relatively to the convection term.

c) Radially-uniform bubble dispersion coefficient:

As described earlier, one of the objectives of the present work is to determine whether the turbulent diffusion model, with constant diffusivity, can be used to predict the bubble impaction rate at any position downstream from a point source of bubbles in the central core region of fully-developed turbulent pipe flow.

Radially-uniform bubble dispersion coefficient may be supported by the uniform turbulent characteristics of the flow field in radial direction.

If we consider radial variation of bubble dispersion coefficient, this coefficient can be deduced from bubble impaction rate distributions obtained at various axial positions downstream of the point of bubble injection by the following equation

$$\phi(r, z) = \frac{\int_0^r V_b \frac{\partial N}{\partial z} r dr}{r \frac{\partial N}{\partial r}} \quad . \tag{3.33}$$

Figure 3.35 shows a typical radially-dependent bubble dispersion coefficient $\phi(r, z)$ deduced by virtue of Eq.(3.33), which confirmed the validity for employing the assumption of radially-uniform

dispersion coefficient*.

Cousins & Hewitt[21] obtained, in this manner, the effective diffusivity of the liquid droplets entrained in the gas core of the air-water annular two-phase flow from the experimental concentration profiles of dyestuff measured at various axial positions with use of isokinetic sampling probe method.

However, in general, this data processing may often render the resultant diffusivity inaccurate in determining, in particular, the term $\frac{\partial N}{\partial z}$ by graphical differentiation.

d) Effects of the bubble injector and point source approximation:

It was expected that the point source solution might not always hold true for the present case, since bubbles were accelerated or decelerated to their steady-state terminal velocity after they detached from bubble injector. In addition, close to the source, the injector perturbation was expected to be relatively large, and the apparent displacement variance of bubbles was never zero at the exit of the injector, $Z' = 0$ cm. The last problem was not so significant in deducing the bubble dispersion coefficient from the impaction data, because such a defect of point source approximation was succesfully reduced to be negligibly small by graphical differentiation procedure in obtaining the value ϕ from time-dependent displacement variance of bubbles.

Temperature of bubbles generated at the injector is usually diffrent from the fluid temperature at the instance of their detachment from the injector, and therefore bubbles will contract or expand during their travels. At last they will come into the thermal-equilibrium condition with the environment. This thermodynamic process may affect the bubble acceleration.

---

* Difference between the values of ϕ deduced from Eq.(3.19) combined to Eq.(3.16) and those from Eq.(3.33) is mainly due to the inaccuracy involved in the procedure of graphical differentiation $\partial N/\partial z$.

It is an advantage to know the bubble acceleration due to the entrance injector effects including the above thermodynamic effect. A theoretical analysis is given in Appendix III. A typical result of the bubble velocity acceleration is presented in Fig.3.36 for 3 mm and 5 mm diameter bubbles at the ambient fluid temperature $T_l = 20^oC$, the initial bubble temperature at its departure from the injector $T_o = 50^oC$, the initial bubble velocity $V_{bo} = 0$ m/sec, and the average void fraction $\alpha = 0.05$. Figure 3.37 represents the effect of initial bubble temperature upon the bubble acceleration and diameter, and Fig.3.38 the effect of initial bubble velocity (it will be evaluated from Eq.(3) in Appendix III that the effect of the physical property, particularly the density of the gas bubble, is negligible). These theoretical results indicate that the bubble acceleration varies, to some extent, accordingly to bubble diameter, i.e., a shorter entrance length is related to a smaller bubble, and that bubbles are apt to come into the thermal-equilibrium condition with the ambient fluid instantaneously at their detachment from the injector. Other effects are negligibly small. (Analytical trends in bubble acceleration agree well with those observed in the experiment as shown in Fig.3.24.)

e) Values of ϕ:

As shown in Fig.3.23, the bubble dispersion coefficient ϕ, varying dependently upon the liquid velocity and the gas flow rate, is of the order 0.2 ~ 1.5 cm^2/sec. Okamoto et al.[22] have reported that the radial number distribution of hydrogen bubbles of about 0.05 mm diameter generated by electrolysis of water was characterized also by Gaussian curves in turbulent pipe flow of water, and they got 0.52 and 0.47 cm^2/sec for ϕ at $V_o = 1.15$ and 0.73 m/sec respectively, under the assumption of the radially uniform dispersion coefficient*. These values are quite consistent with our experimental results, though this fact may contradict the intuitive notion that small bubbles diffuse

---

* See footnote on next page.

readily than large ones. Both these experimental results indicate again that the bubble diffusion mechanism is strongly related to the flow turbulence and hence a bubble diffusivity is of the same magnitude as eddy diffisivity of momentum in liquid phase**.

f) Dimensional analysis of ϕ:

The independent variables which were believed to affect the bubble dispersion coefficient were the superficial liquid velocity V_l, the bubble rise velocity V_b, the gas flow rate $W_g (= \rho_g Q_g)$, the mean diameter of bubbles $\bar{d}$, the densities of the liquid and the gas ρ_l and ρ_g, the viscosity of liquid μ_l, the surface tension of liquid σ, and the gravitational constant g.

Any product of the above-listed variables has the following form,

$$\pi = (\phi)^{k_1}(V_l)^{k_2}(V_b)^{k_3}(W_g)^{k_4}(\bar{d})^{k_5}(\rho_l)^{k_6}(\rho_g)^{k_7}(\mu_l)^{k_8}(\sigma)^{k_9}(g)^{k_{10}} \tag{3.34}$$

If the appropriate dimensions are inserted, the condition that the exponent of every dimension is zero gives three equations with ten unknowns, which yield the following results with an additional assumption $k_6 + k_7 = 0$:

$$k_3 = -3k_1 - k_2 - k_4 - 2k_5 + k_8$$

$$k_7 = -k_6$$

$$k_9 = -k_4 - k_8$$

$$k_{10} = k_1 + k_4 + k_5 \quad .$$

---

* Ginsberg[8] and Cousins & Hewitt[22] have revealed that the turbulent diffusivity of liquid droplets travelling in air flow and in air-water annular-dispersed flow was of 0.2 ~ 10 cm^2/sec (for Re_g = 2.5 ~ 10 × 10^4) and of 4.6 ~ 19 cm^2/sec, respectively.

** Kinematic viscossty of water is nearly 0.01 cm^2/sec at room termperature[23].

Substitution of these variables into Eq.(3.34) and grouping the terms according to common exponent give

$$\frac{V_b \bar{d}}{\phi} = \text{Function of } [(\rho_l/\rho_g),\ Re_b,\ Fr_b,\ We_b,\ (V_l/V_b),\ (Q_g/V_b\bar{d}^2)] \quad , \tag{3.35}$$

where $Re_b (= V_b\bar{d}/\nu_l)$, $Fr_b (= V_b^2/g\bar{d})$, and $We_b (= \rho_l V_b^2 \bar{d}/\sigma)$ are the bubble Reynolds number, the bubble Froude number, and the bubble Weber number, respectively.

It is left to determine the functional relation between the Péclet number $V_b\bar{d}/\phi$ and the dimensionless groups of Eq.(3.35). But it is quite difficult to obtain such a functional relation from the present experimental data on bubble dispersion coefficient for the lack of data. In practice, any significant systematic effects of these dimensionless groups upon the bubble dispersion coefficient were not formulated.

3.8 Conclusions

The following main conclusions can be drawn from the experimental work on bubble dispersion for air and argon bubbles in stagnant water and for argon bubbles in the central core region of vertical upflow in pipe.

(1) Experiment has been carried out in which air or argon bubbles were injected both into stagnant water in pool and into the central core region of vertical upflow in pipe where fully-developed turbulence has been established. Measurements of bubble impaction rate at various axial positions indicate that, for the conditions tested, bubbles become statistically distributed throughout the field, i.e., lateral profiles of bubble impaction rate at given axial positions downstream of bubble injector are well approximated by normal distribution curves.

(2) The result indicates that a diffusion model with a radially uniform diffusivity can be well defined for applying it to the description of bubble transport in turbulent flow with point source approximation.

(3) The bubble impaction data deduction was carried out to determine the bubble dispersion coefficient as a function of the superficial liquid velocity and the volumetric gas flow rate. The value of dispersion coefficient varied from 0.2 to 1.5 cm^2/sec, with a tendency for the bubble dispersion coefficient to be a strong increasing function of the superficial liquid velocity and a weak decreasing function of the volumetric gas flow rate. But no systematic variation of ϕ with many other parameters was observed.

(4) The experimental result suggested two mechanisms for lateral bubble transport. For low bubble density, the intrinsic periodic bubble motions, such as zig-zag or spiral motions are predominant mechanisms, and for higher bubble density, the flow turbulence or the bubble agitation, where radial bubble motion is caused mainly by the interaction of bubbles with the turbulence or by bubbles having imparted upon themselves a finite radial velocity during their travels downstream from the bubble injector. For intermediate bubble density region, the above two mechanisms (the intrinsic bubble motions and the flow turbulence) are co-existent.

REFERENCES

[1] Datta, R.L., Napier, D.H., Newitt, D.M.: Trans. Intn. Chem. Engrs., Vol.28, p.14 (1950).

[2] Peebles, F.N., Garber, H.J.: Chem. Eng. Prog., Vol.49, 88 (1953).

[3] Harberman, W.L., Morton, R.K.: David Taylor Model Basin, Rep. no. 802, (1953).

[4] Saffman, P.G.: J. Fluid Mech., Vol.1, 249 (1956).

[5] Hanratty, T.J., Latinen, G., Wilhelm, R.H.: J. Am. Inst. Chem. Engrs., 2[3], 372 (1956).

[6] Briller, R., Robinson, M.: ibid., 15[5], 733 (1969).

[7] Atesman, K.M., Baldwin, L.V., Haberstroh, R.D.: Trans. Am. Soc. Mech. Engrs., Ser.C, Vol.93, 461 (1971).

[8] Ginsberg, T.: ANL-7694, (1971).

[9] Goldschmit, V.W., Householder, M.K., Ahmadi, G., Chuang, S.C.: Progress in Heat and Mass Transfer, Vol.6, 487 (1972).

[10] Houghton, G.: Nucl. Sci. Eng., Vol.11, 121 (1961).

[11] idem.: ibid., Vol.12, 390 (1962).

[12] Chandrasekhar, S.: Revs. Modern Phys., Vol.15, 1 (1943).

[13] Einstein, A.: Ann. Physik, Vol.17, 549 (1905).

[14] Hinze, J.O.: Turbulence, Macgraw-Hill.

[15] Nicklin, D.J., Wilkes, J.O., Davidson, J.F.: Trans. Inst. Chem. Engrs., Vol.40, 61 (1962).

[16] Moissos, R., Griffith, P.: Trans. Am. Soc. Mech. Engrs., Ser.C, Vol.84, 29 (1962).

[17] Ivey, H.J.: Int. J. Heat Mass Transfer, Vol.10, 1023 (1967).

[18] Kubota, ., Akehata, ., Shirai, .: Chem. Eng., (in Japanese), Vol.31, 1074 (1969).

[19] Tsuge, .: unpublished.

[20] Siemes, W.: Chem. Ing. Tech., Vol.26, 614 (1954).

[21] Cousins, L.B., Hewitt, G.F.: AERE-R 5693, (1968).

[22] Okamoto, Y., Hanawa, H., Kameoka, T.: Trans. Japan Soc. Mech. Engrs., 37[294], 305 (1971).

[23] Technical Handbook on Heat Transfer (Dennetsu Kogaku Shiryo): Japan Soc. Mech. Engrs., 2nd Eddition, 260 (1966).

NOMENCLATURE

a	semimajor axis of spheroidal bubbles
dA	effective cross sectional area of the probe tip
b	semiminor axis of spheroidal bubbles
c	fluctuating component of bubble concentration
c_p	specific heat at constant pressure
C	time-averaged mass concentration
C^*	local mass concentration of bubbles
d	bubble diameter
$\bar{d}$	mean bubble diameter
d_o	initial bubble diameter at its departure from bubble injector
d^*	dimensionless bubble diameter ($= d/d_o$)
D	pipe diameter
e	probe eccentricity from bubble center
f	friction factor
Fr_b	bubble Froude number ($= V_b^2/g\bar{d}$)
g	gravitational constant
l	reduced bubble length defined by Eq.(3.22)
$\bar{l}$	mean bubble length defined by Eq.(3.23)
L	length
L^*	spread of spherical boundary formed with bubbles diffusing isotropically into the medium from a point source
N	bubble impaction rate
N^*	dimensionless bubbles impaction rate ($= N/N_{max}$)
N_{max}	maximum bubble impaction rate
p	nucleation rate

$(\frac{\Delta P}{\Delta z})_f$	frictional pressure drop gradient
q	bubble growth rate
Q_g	volumetric flow rate of air or argon bubbles
r	radial coordinate
r^*	dimensionless radius (= r/λ_h)
R	pipe radius
Re_b	bubble Reynolds number (= $V_b\bar{d}/\nu_l$)
Re_l	liquid Reynolds number (= $V_o D/\nu_l$)
S_o	strength of a point source of bubbles
t	time
T	local temperature of liquid
T_l	liquid temperature
T_o	initial bubble temperature
u	turbulent velocity component of liquid in axial direction
u'	longitudial turbulent intensity (=$\sqrt{\overline{u^2}}$)
$\vec{v}$	fluctuating velocity (vector)
$\vec{V}$	convective velocity of bubbles (vector)
$\vec{V}_b$	time-averaged bubble velocity (vector)
V_b	time-averaged bubble velocity
V_{bo}	initial velocity of a single bubble injected from bubble injector
V_b^*	dimensionless bubble velocity (= $(V_l - V_b)/V_l$)
$\vec{V}_l$	liquid velocity (vector)
V_{lmax}	maximum velocity of liquid in axial direction
V_{lz}	axial velocity of liquid
V_o	superficial liquid velocity
$\vec{V}_s$	bubble slip velocity (vector)
V_s	bubble slip velocity
V_{so}	drift velocity of a single bubble in stationary liquid
We_b	Weber number (= $\rho_l V_b^2 \bar{d}/\sigma$)
W_g	gas flow rate
y	lateral coordinate
$\overline{y^2}$	displacement variance

z	axial coordinate
Z'	downstream distance from bubble injector
α	void fraction
δ	Dirac's delta function
ε_B	bubble diffusivity
ε_L	turbulent diffusivity of liquid
ε	equivalent sand roughness
λ	latent heat of vaporization
λ_h	half-width of the profile of bubble impaction rate
μ_l	viscosity of liquid
ν_l	kinematic viscosity of liquid
ρ_g	density of gas
ρ_l	density of liquid
σ	surface tension
ϕ	bubble dispersion coefficient

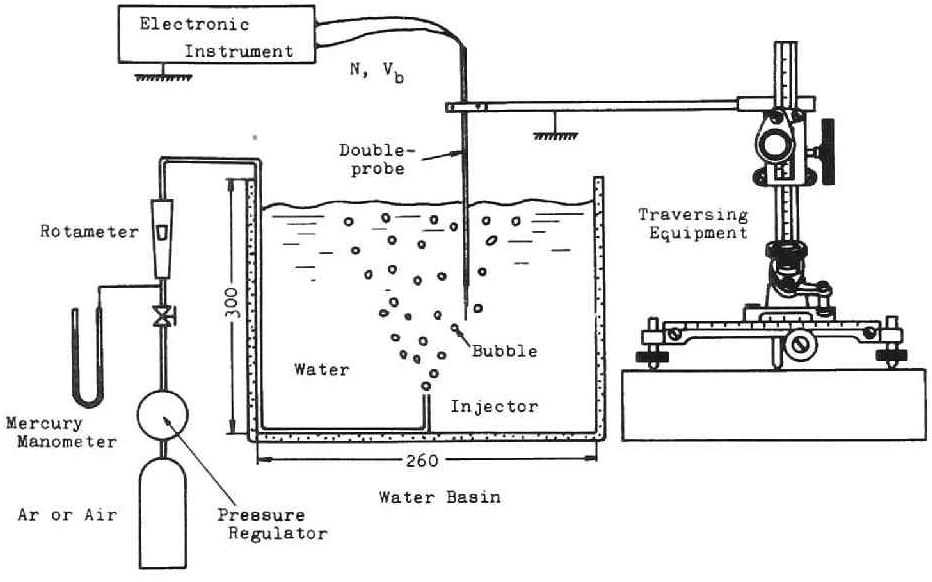

Fig. 3.1 Experimental apparatus (in pool)

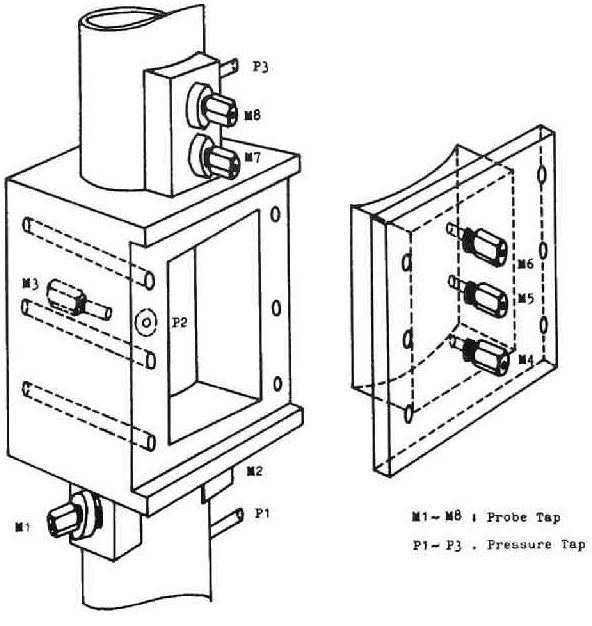

Fig. 3.3 Schematic drawing of the chamber

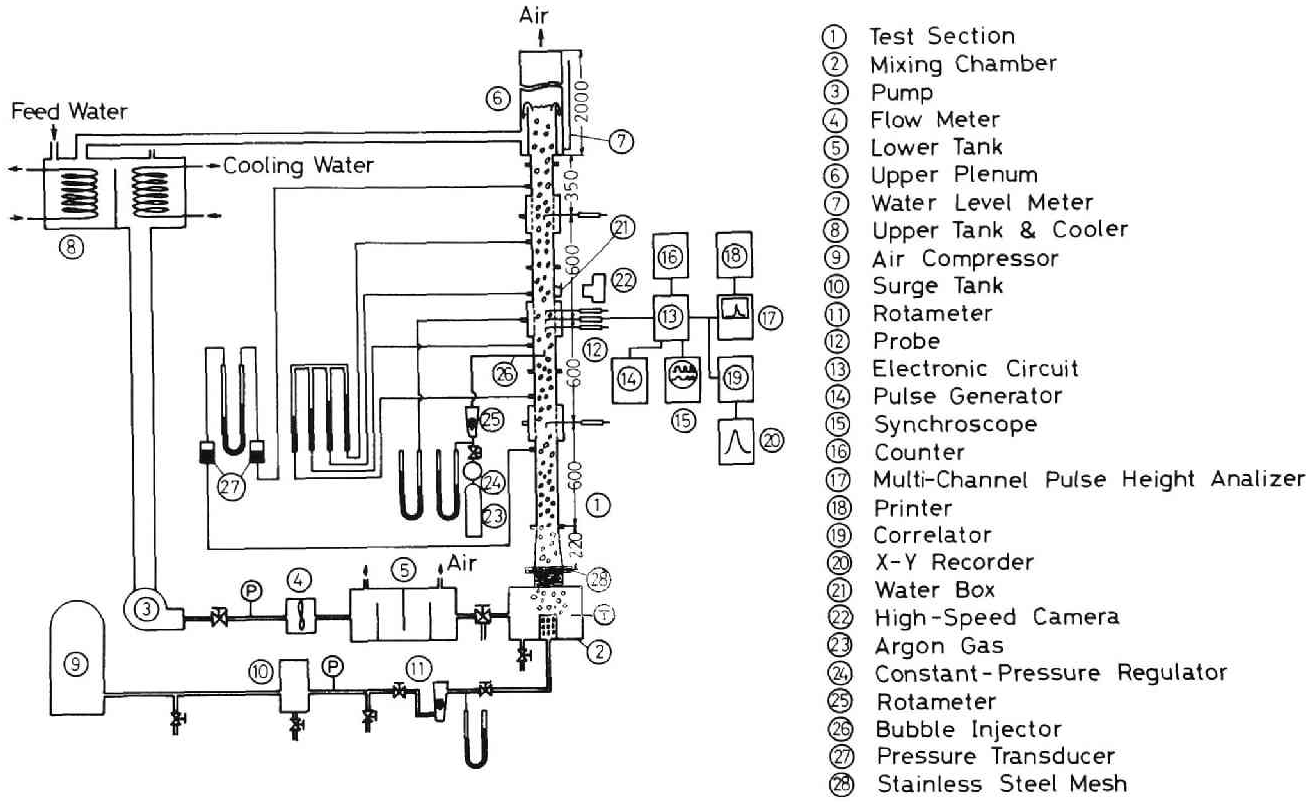

Fig. 3.2 Schematic diagram of the facility

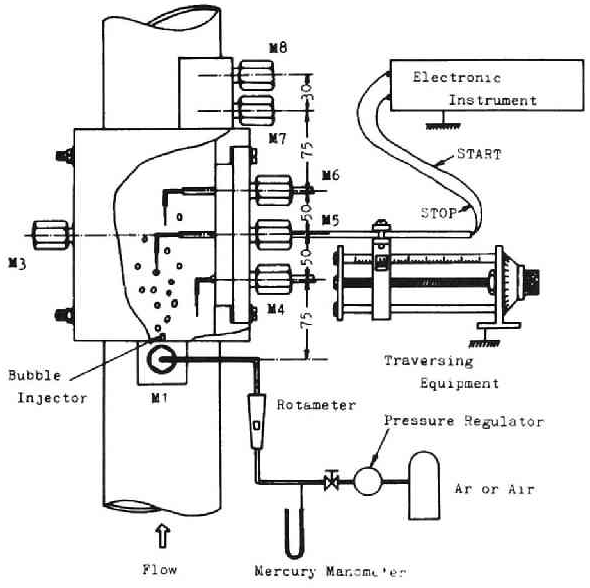

Fig. 3.4 Details of the experimental arrangement

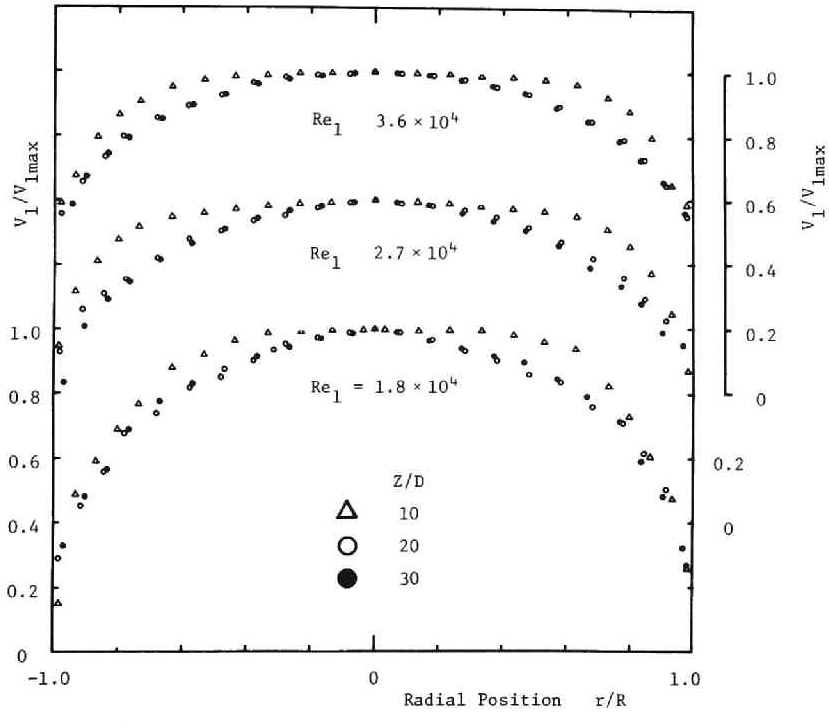

Fig. 3.5 Water velocity profile (single-phase flow)

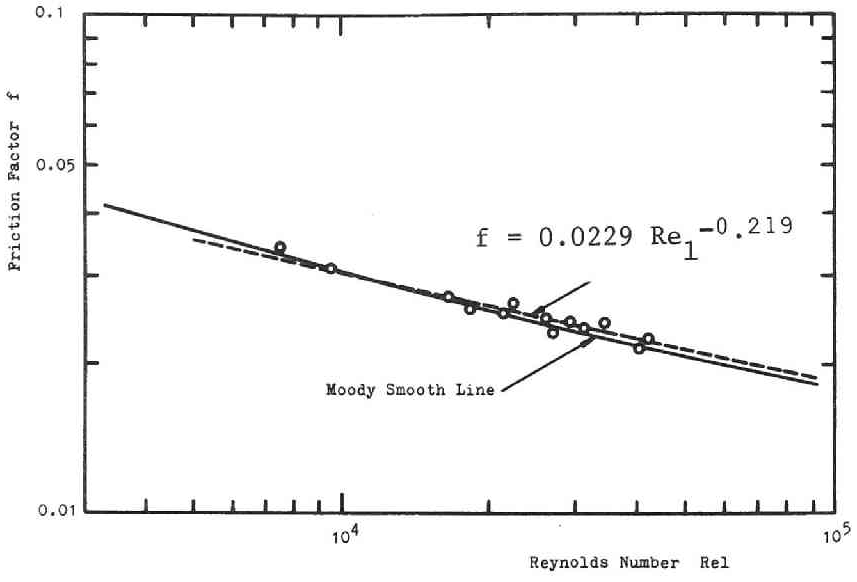

Fig. 3.6 Single-phase friction factor

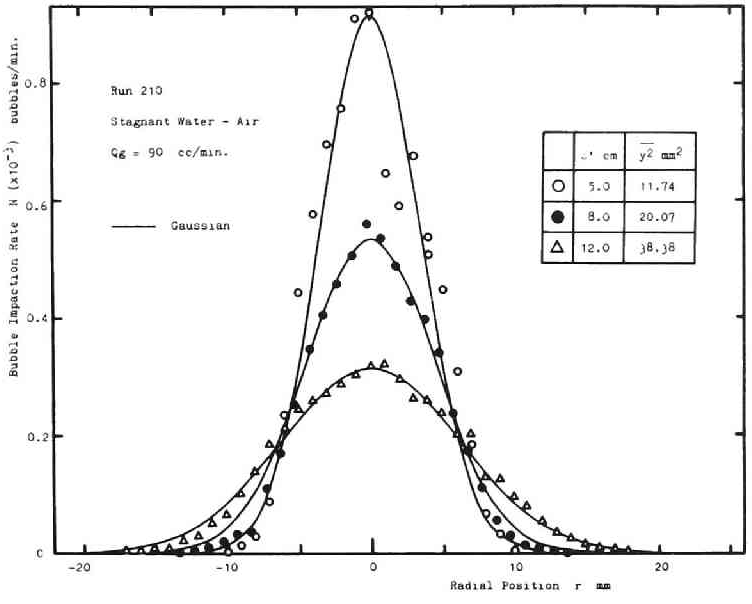

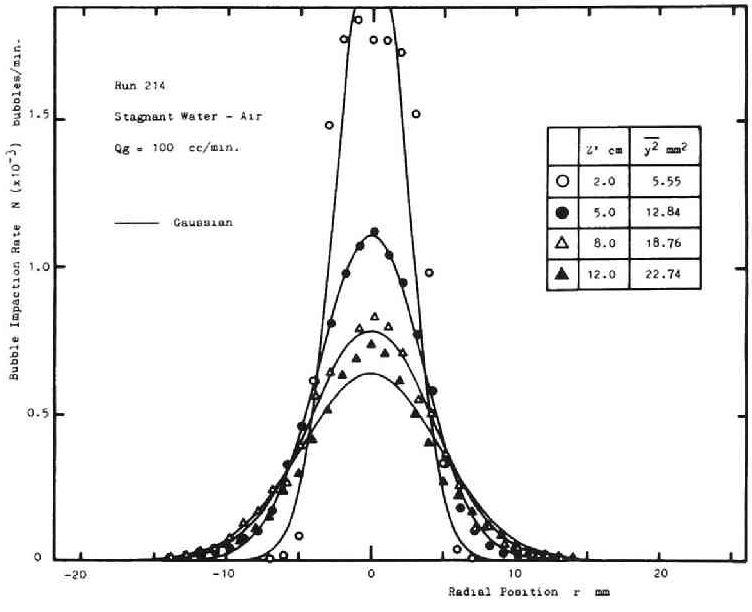

Fig. 3.8 Bubble impaction rate in stagnant water

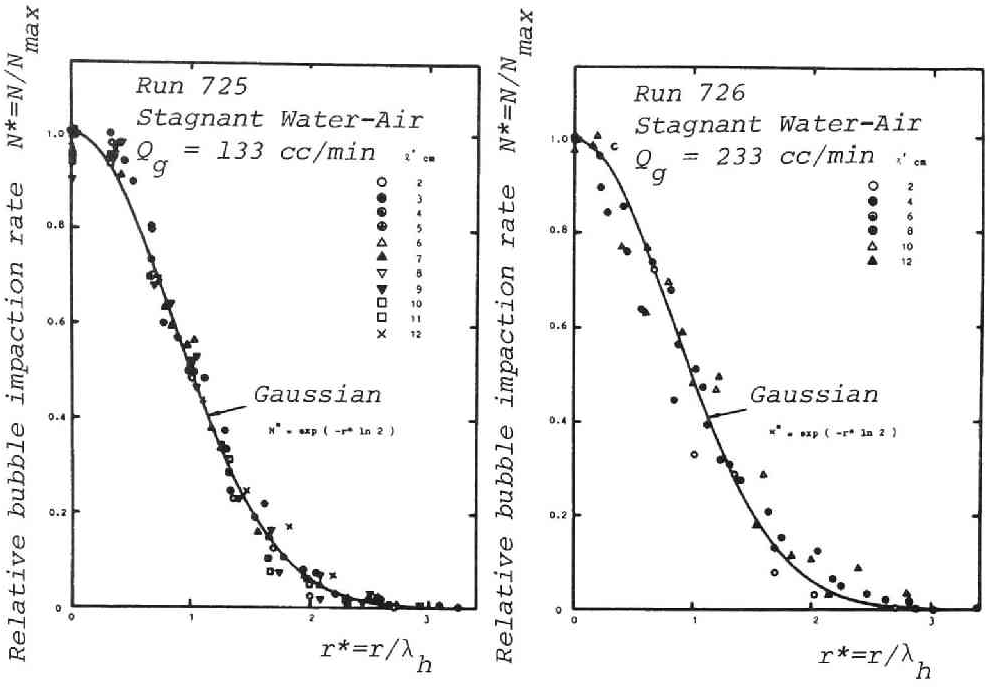

Fig. 3.9 Bubble impaction rate in stagnant water

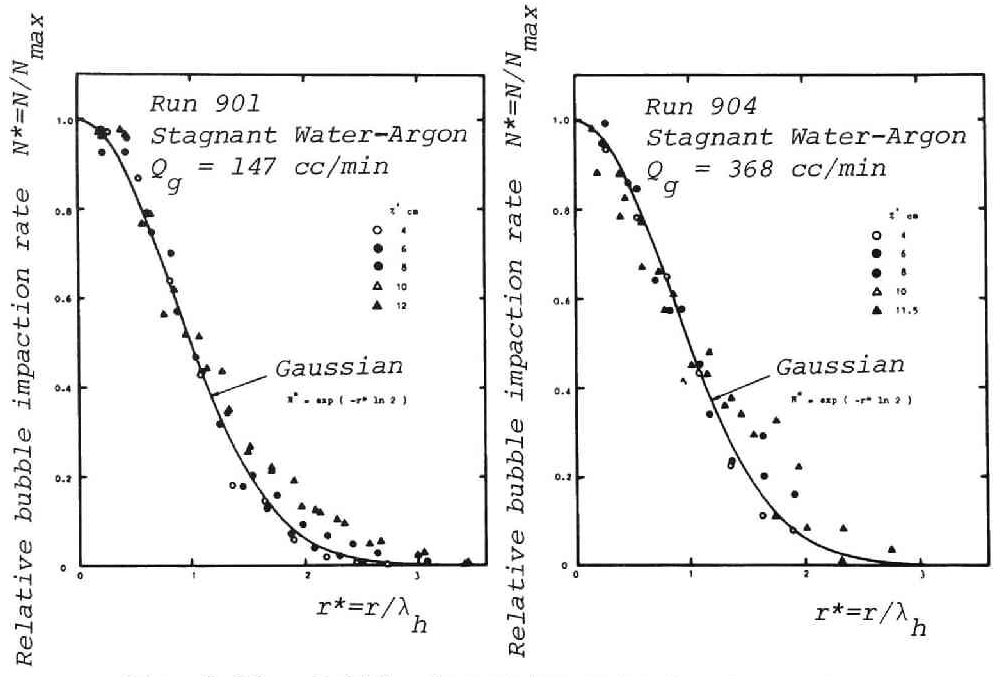

Fig. 3.10 Bubble impaction rate in stagnant water

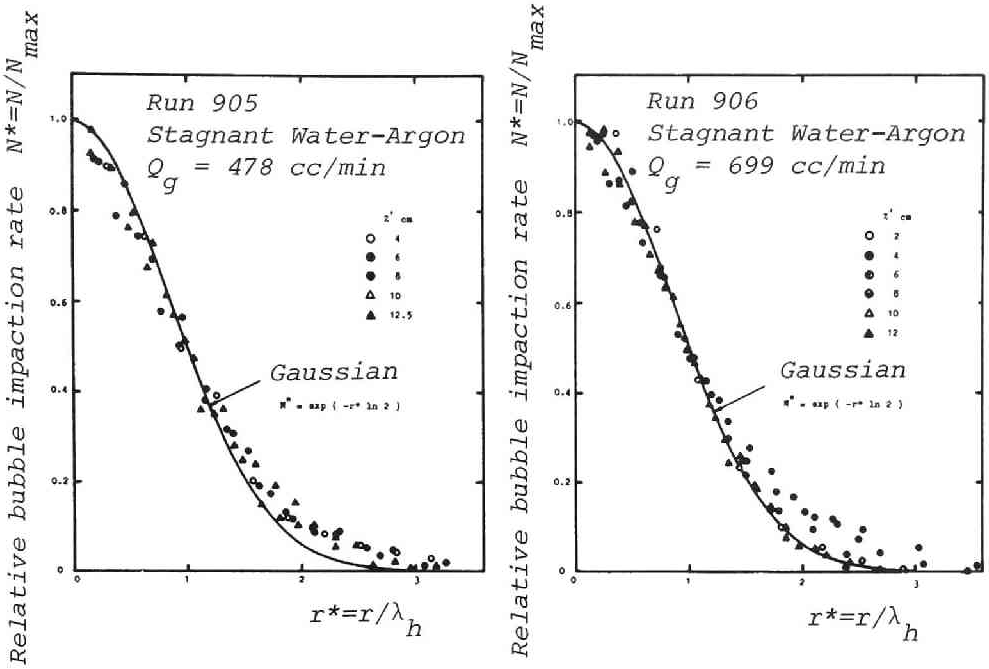

Fig. 3.11 Bubble impaction rate in stagnant water

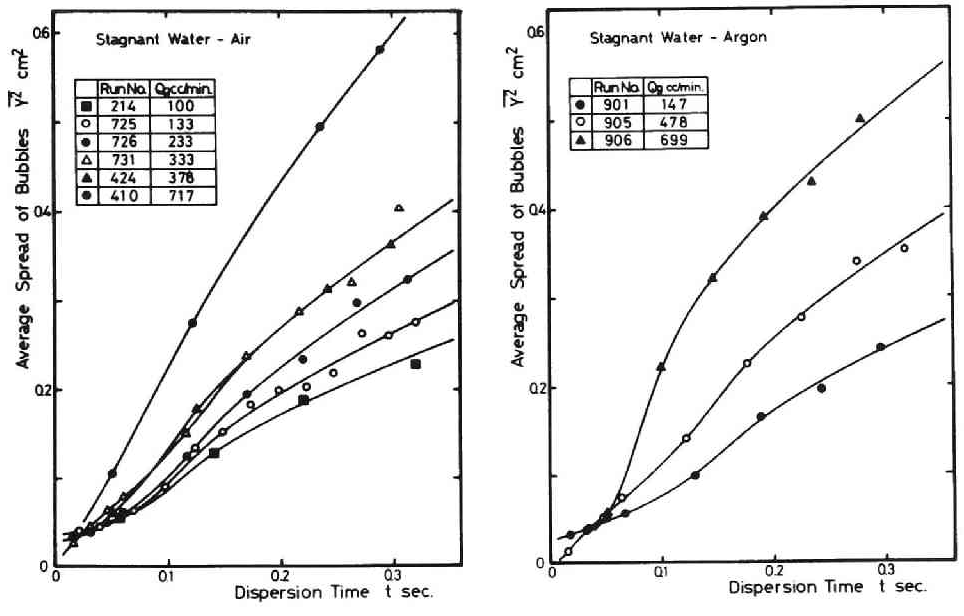

Fig. 3.12 Displacement variance $\overline{y^2}$ vs. dispersion time

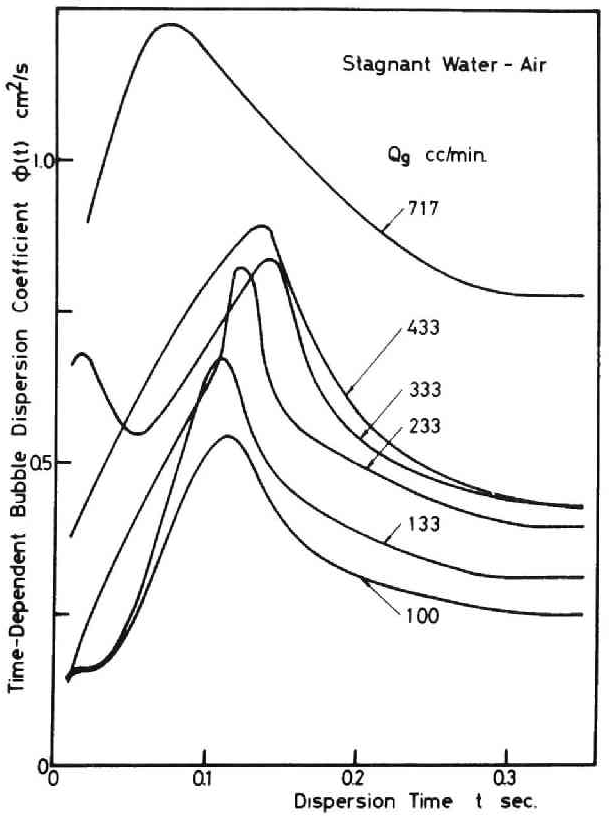

Fig. 3.13 Time-dependent bubble dispersion coefficient for air bubbles

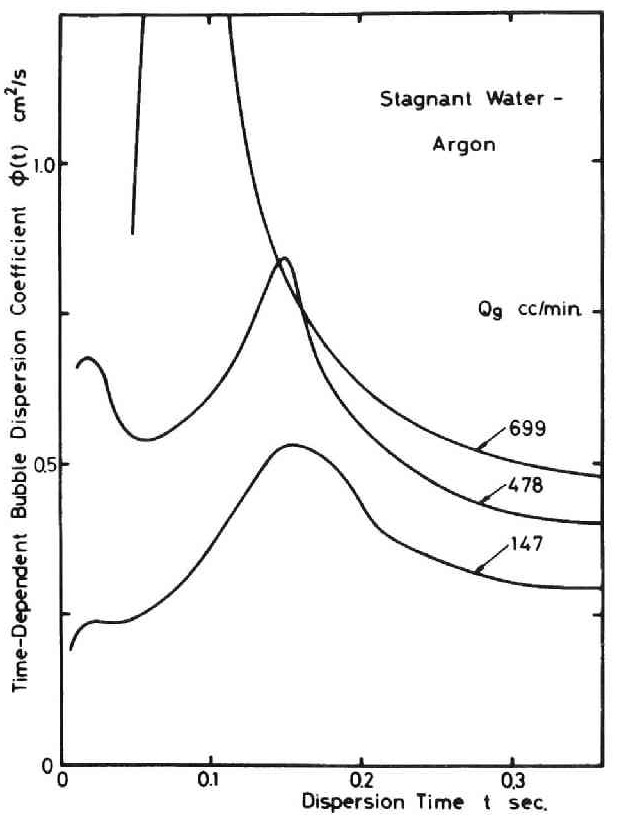

Fig. 3.14 Time-dependent bubble dispersion coefficient for argon bubbles

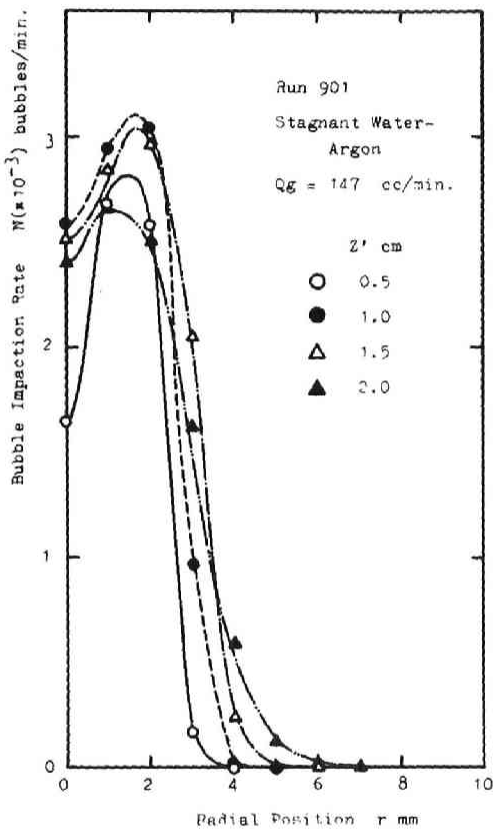

Fig. 3.15 Entrance effect upon the profile of bubble impaction rate

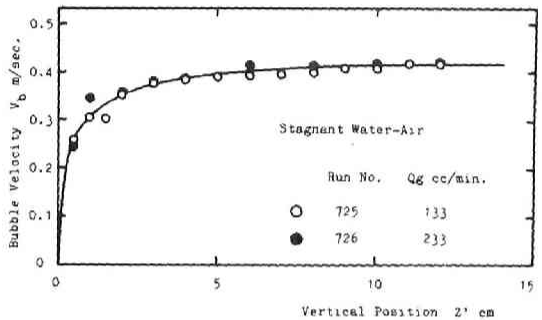

Fig. 3.16 Entrance (injector) effect upon rising velocity of bubbles

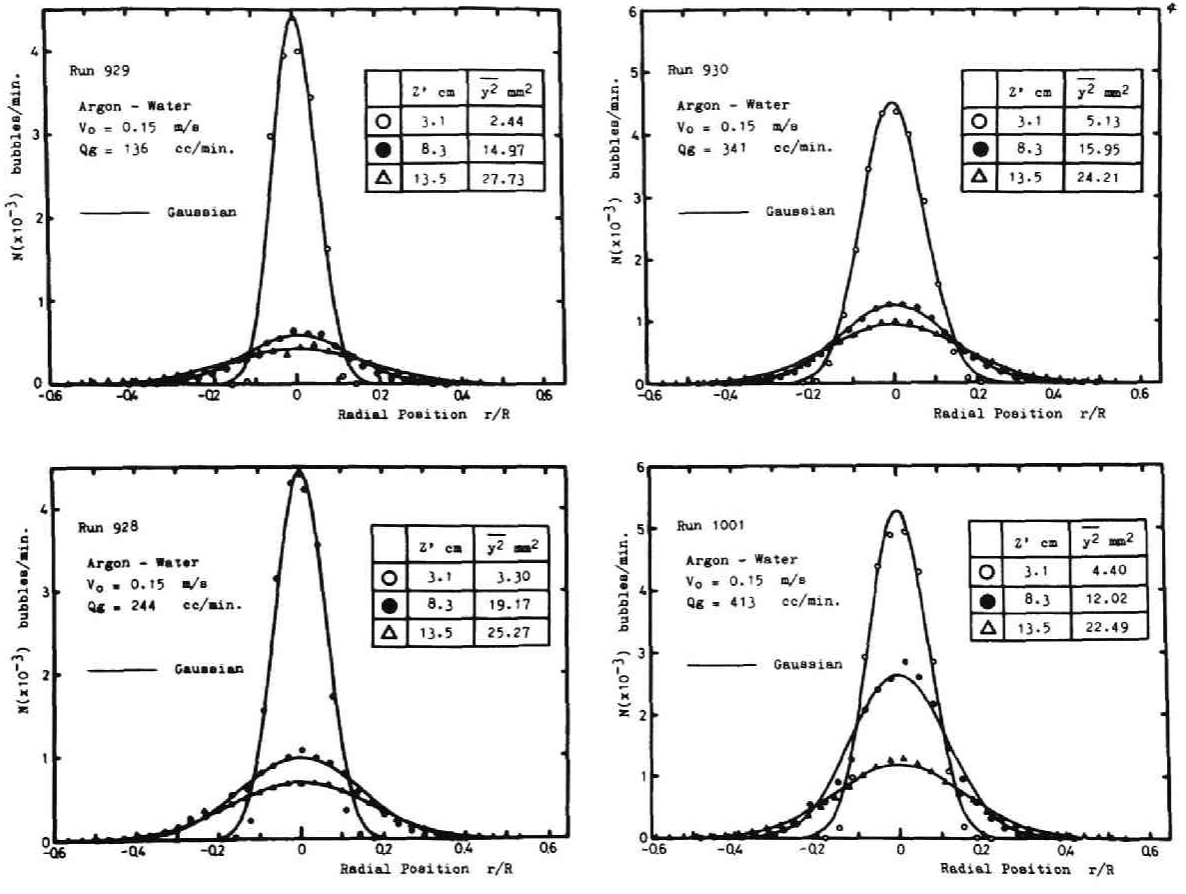

Fig. 3.17 Radial profile of bubble impaction rate in pipe flow (V_o=0.15 m/sec)

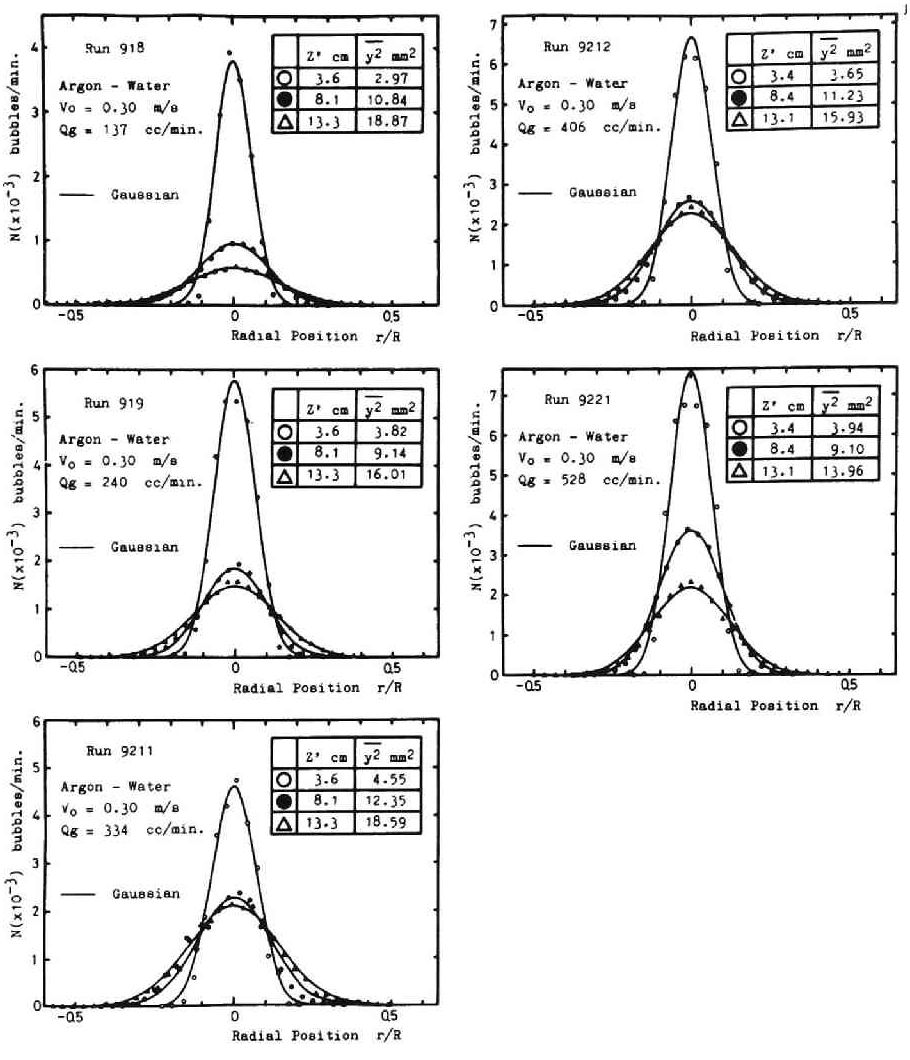

Fig. 3.18 Radial profile of bubble impaction rate in pipe flow (V_o=0.30 m/sec)

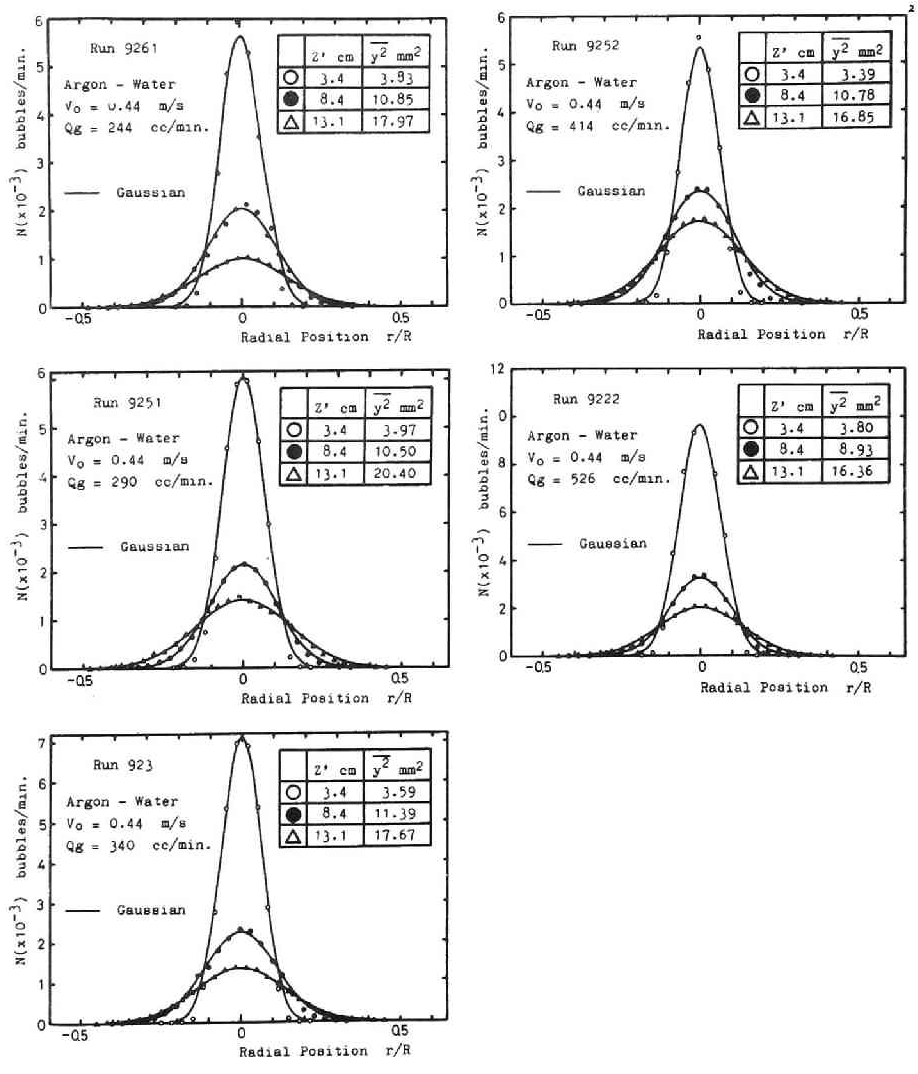

Fig. 3.19 Radial profile of bubble impaction rate in pipe flow (V_o=0.44 m/sec)

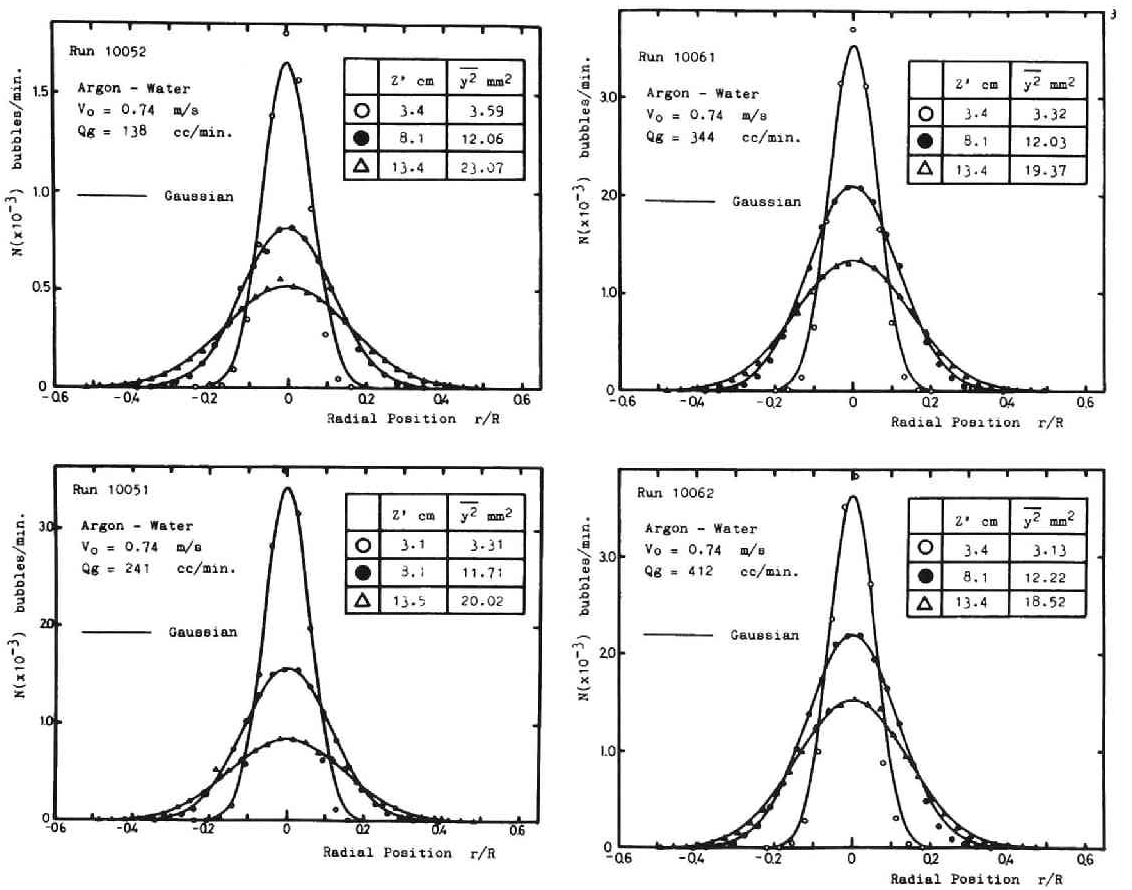

Fig. 3.20 Radial profile of bubble impaction rate in pipe flow (V_o=0.74 m/sec)

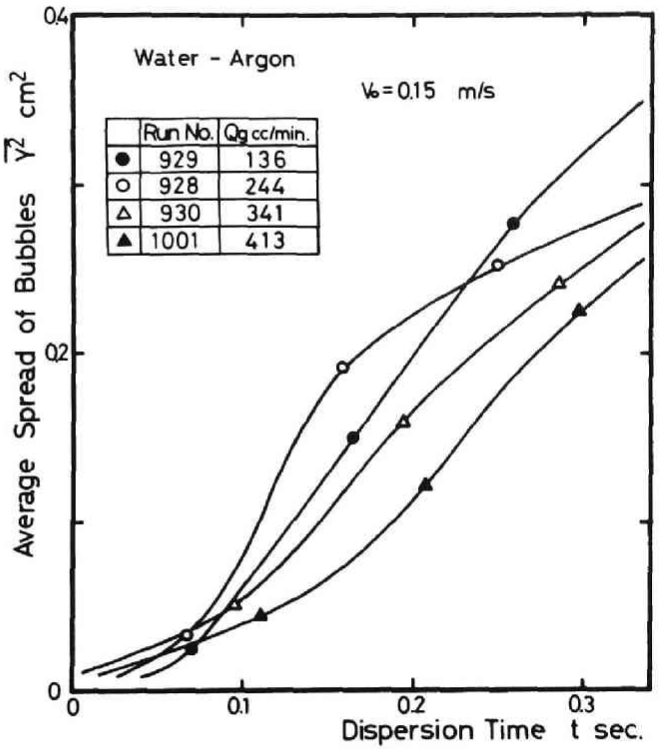

Fig. 3.21 Displacement variance $\overline{y^2}$ vs. dispersion time t

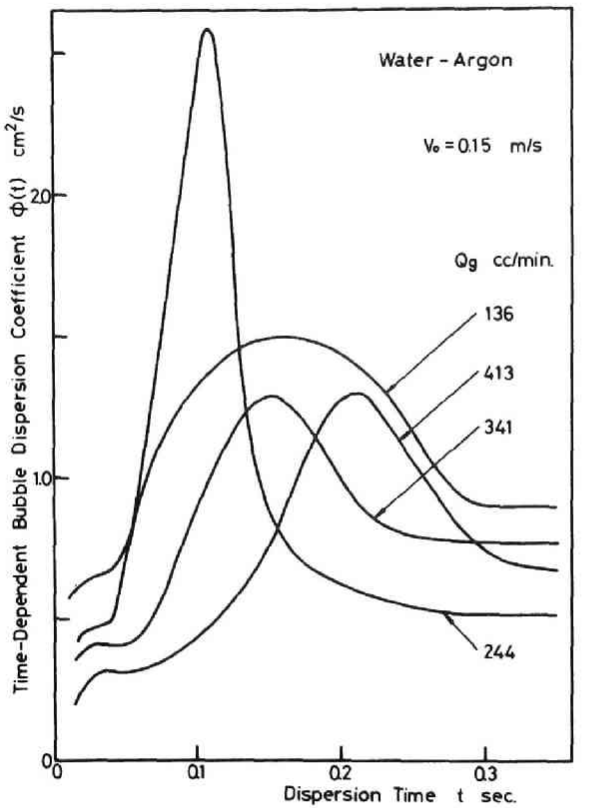

Fig. 3.22 Time-dependent bubble dispersion coefficient

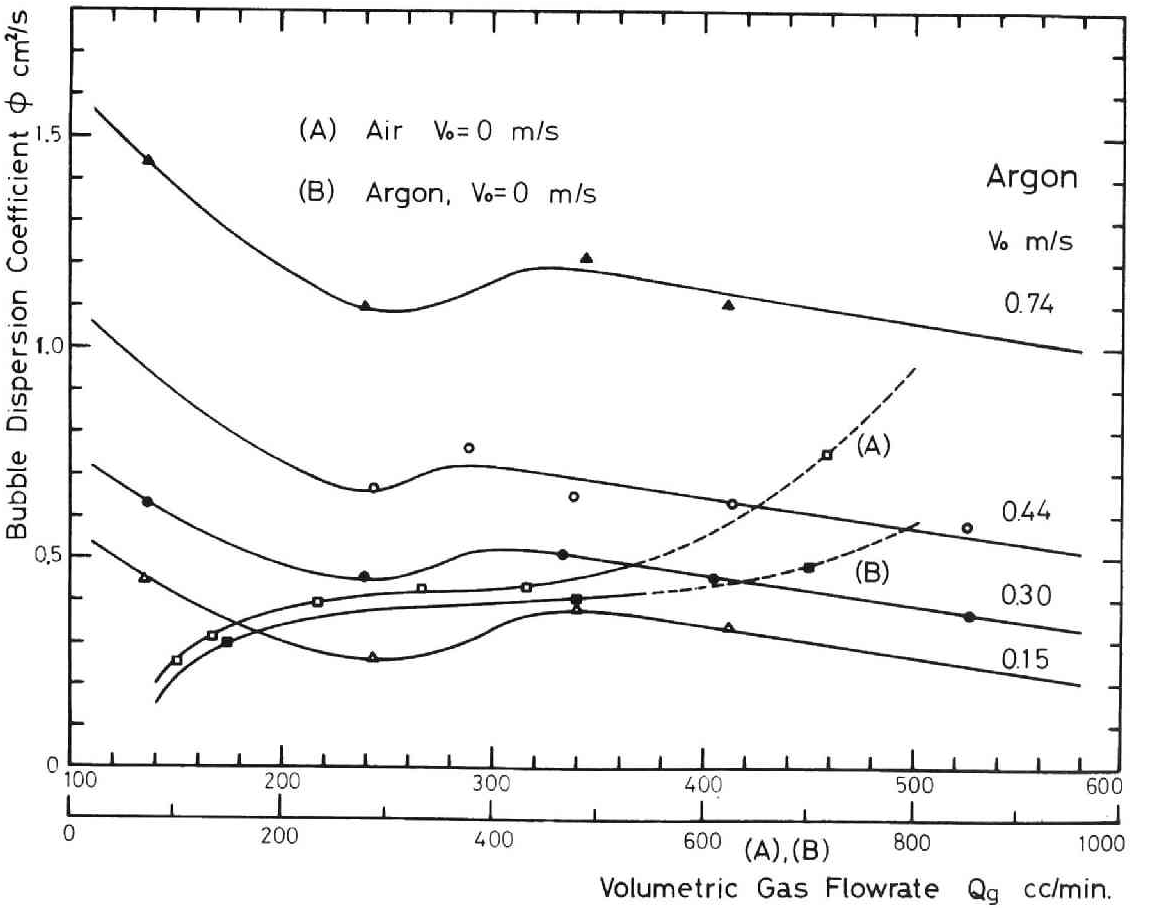

Fig. 3.23 Variation of bubble dispersion coefficient

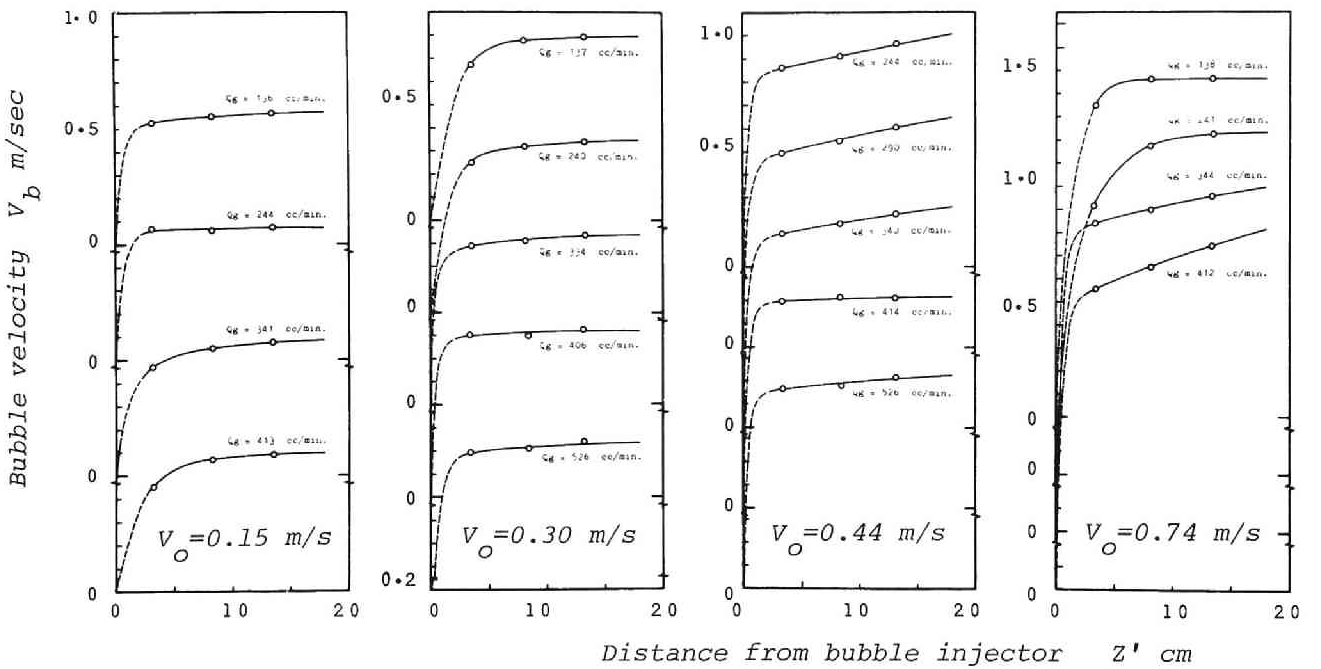

Fig. 3.24 Axial distribution of bubble rise velocity in pipe flow

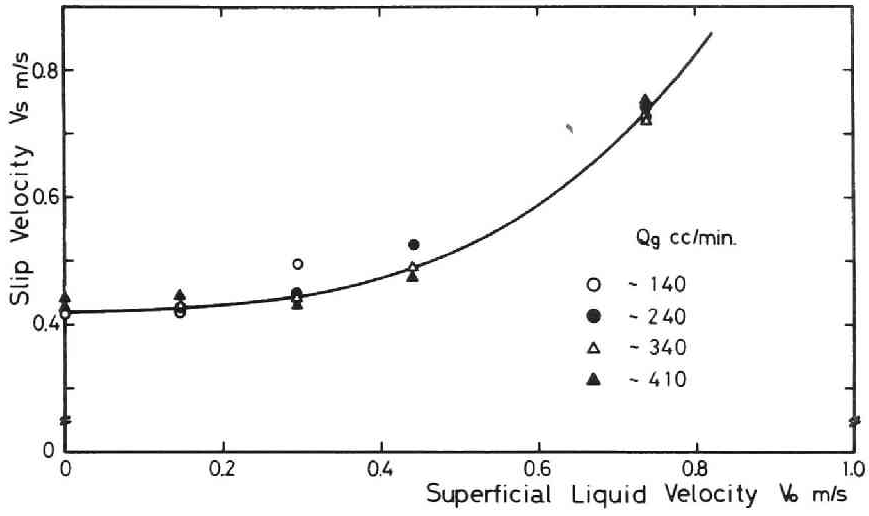

Fig. 3.25 Slip velocity vs. superficial liquid velocity

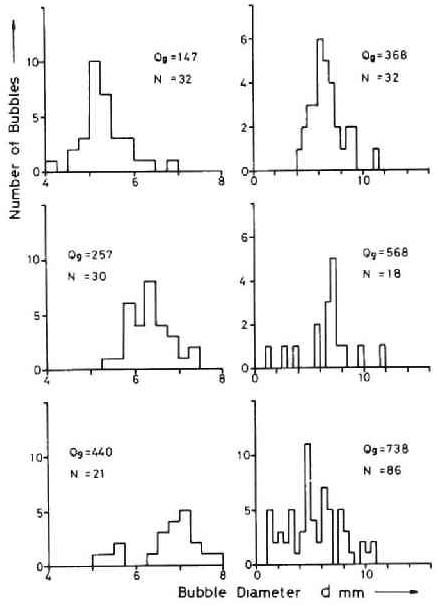

Fig. 3.26 Histgram of equivalent-spherical-diameter of bubbles (V_o=0 m/sec)

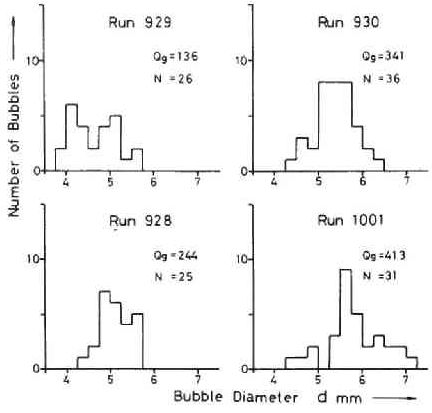

Fig. 3.27 Histgram of equivalent-spherical-diameter of bubbles (V_o=0.15 m/sec)

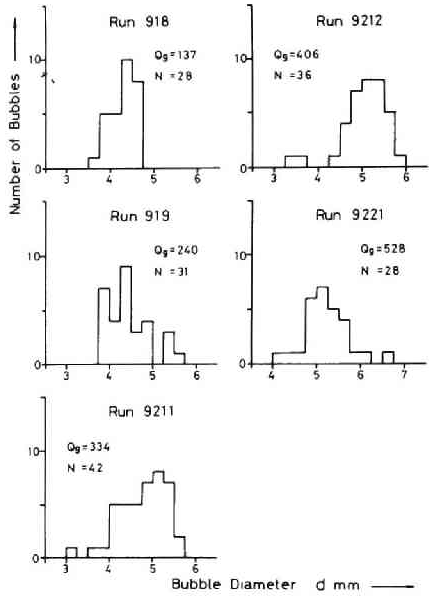

Fig. 3.28 Histgram of equivalent-spherical-diameter of bubbles (V_o=0.30 m/sec)

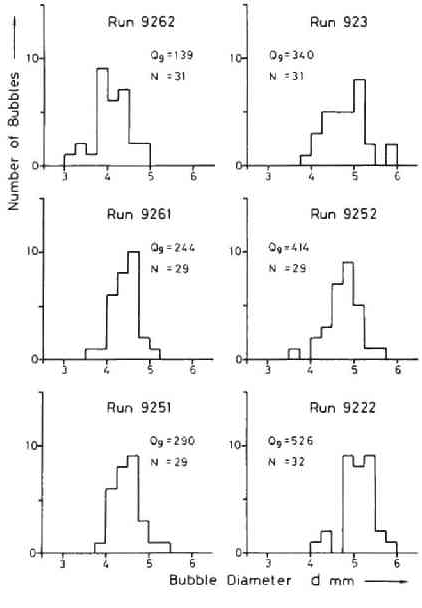

Fig. 3.29 Histgram of equivalent-spherical-diameter of bubbles (V_o=0.44 m/sec)

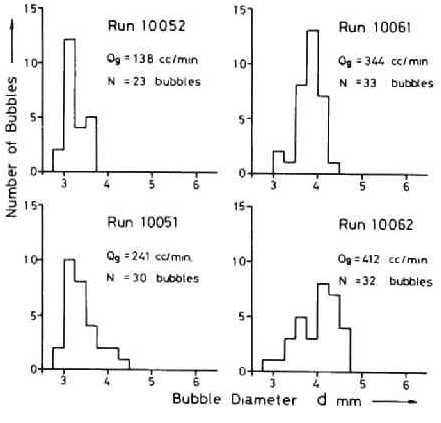

Fig. 3.30 Histgram of equivalent-spherical-diameter of bubbles (V_o=0.74 m/sec)

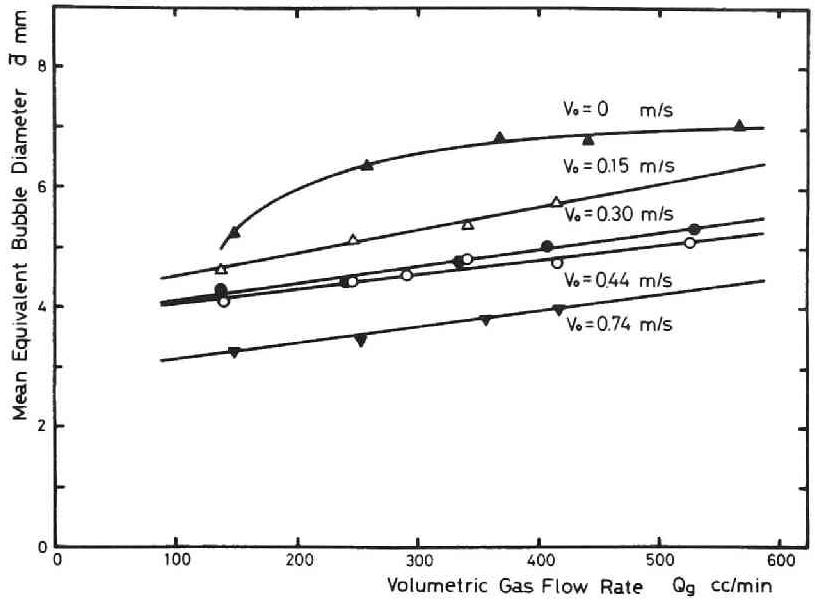

Fig. 3.31 Mean bubble diameter vs. volumetric gas flow rate

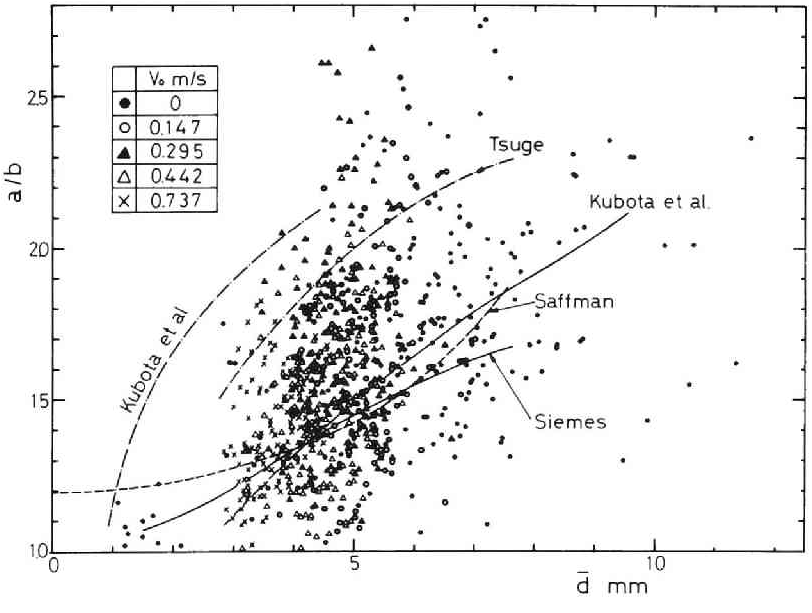

Fig. 3.32 Variation of a/b ratio of spherical bubbles

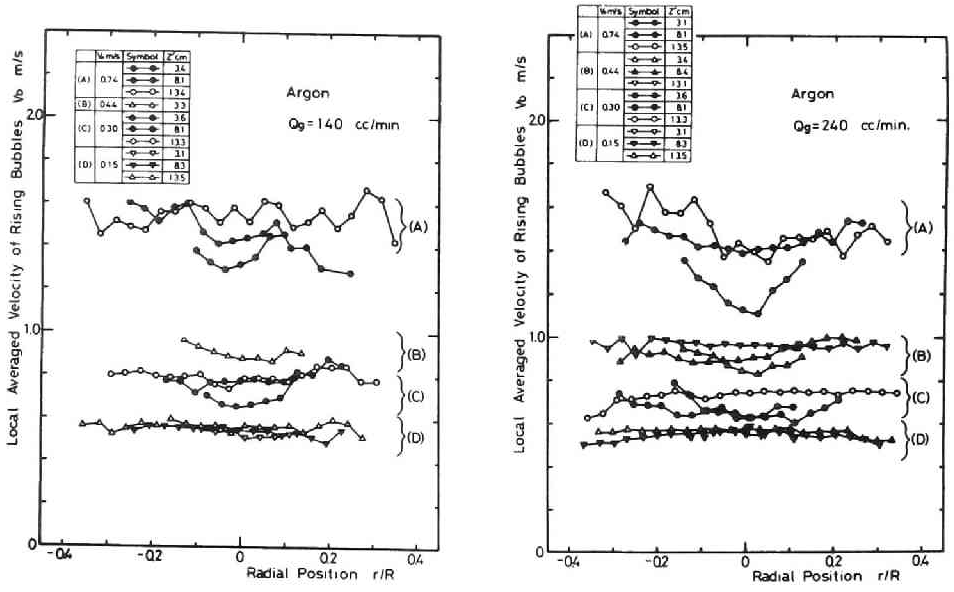

Fig. 3.33 Radial profiles of bubble velocity (cross-correlation technique)

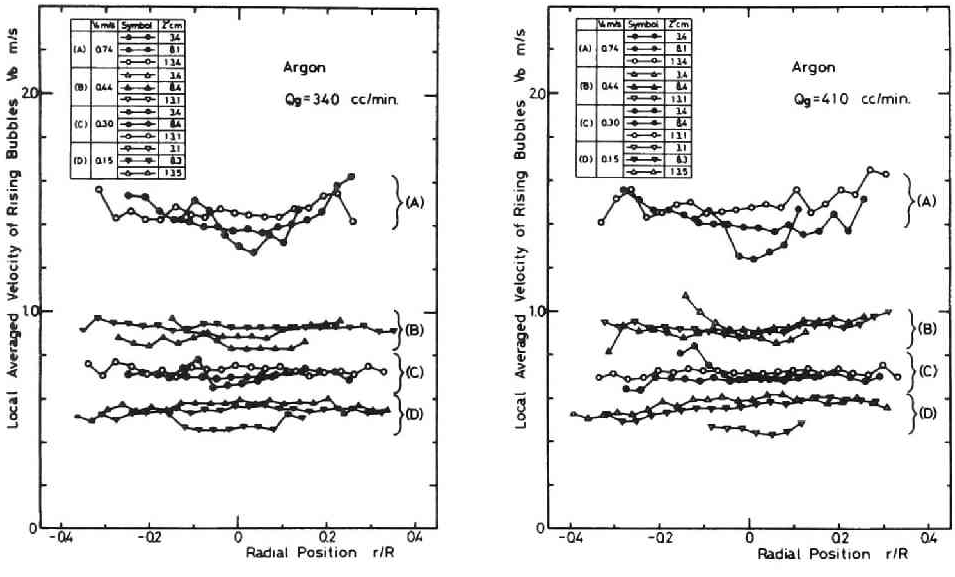

Fig. 3.34 Radial profiles of bubble velocity (cross-correlation technique)

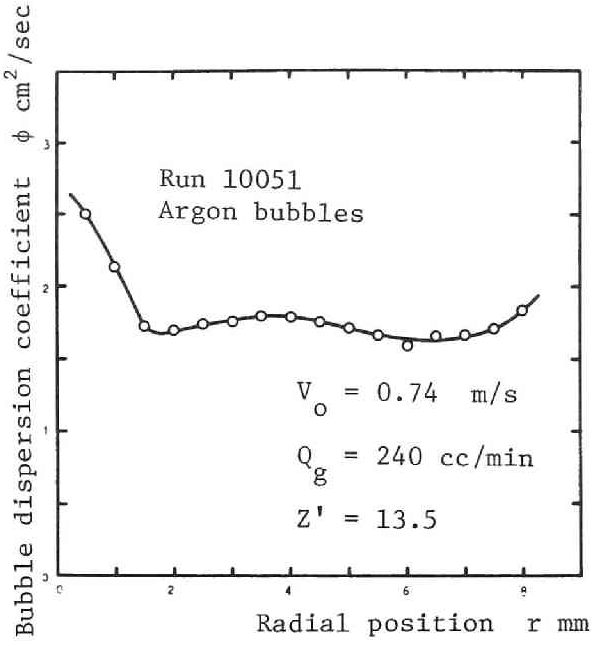

Fig. 3.35 Radial variation of bubble dispersion coefficient calculated by Eq.(3.33)

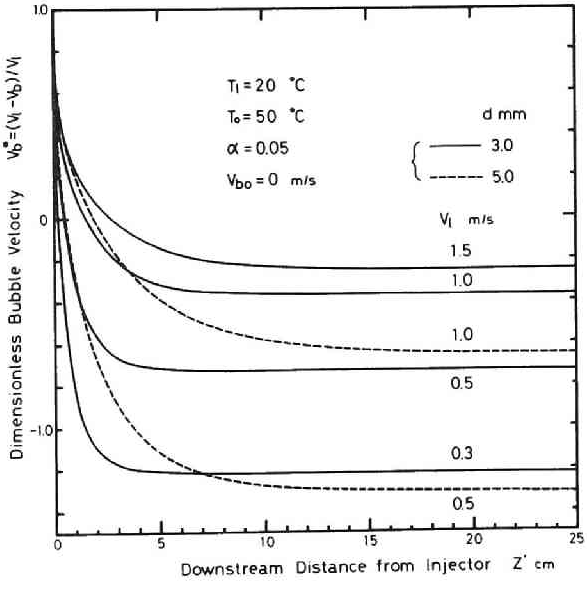

Fig. 3.36 Effect of bubble size upon bubble acceleration

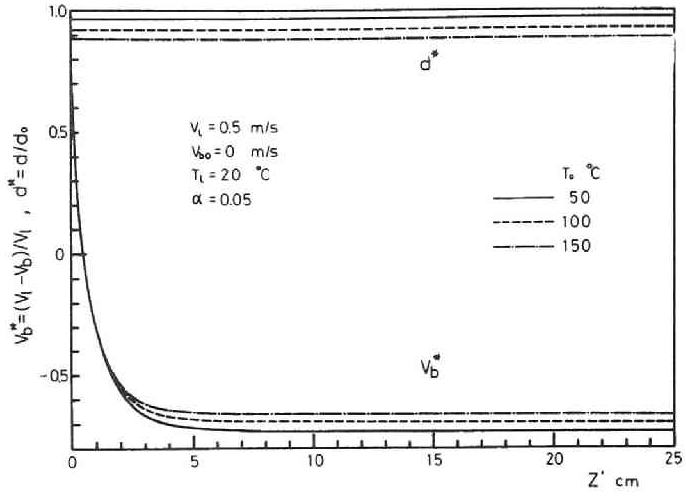

Fig. 3.37 Effect of initial bubble temperature upon bubble acceleration and contraction

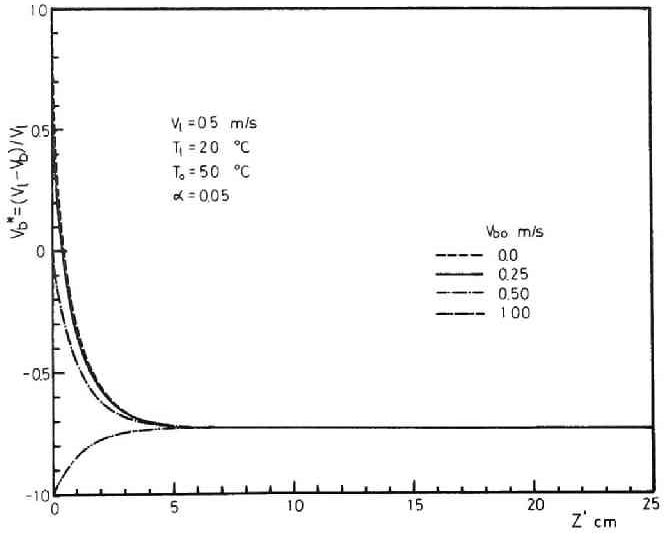

Fig. 3.38 Effect of initial bubble velocity upon bubble acceleration

IV. MEASUREMENT OF TURBULENT CHARACTERISTICS AND LOCAL PARAMETERS OF AIR-WATER TWO-PHASE FLOW IN PIPE

4.1 General

As cited earlier in Part I, when a liquid and a gaseous phase flow cocurrently or concurrently through a vertical pipe, the phases distribute themselves in one of several flow patterns depending mainly upon the mass flow rates of each phase, the physical properties of each phase, the interphase forces, and the geometrical configuration of flow passage. Various flow regimes can be distinguished. When the gas flow rate is small relative to the liquid flow rate, the gas appears as a suspension of small bubbles. The bubbles move more or less independently of each other at different velocities. As is known, this regime is called bubble flow and is the most basic and familiar flow pattern of practical importance for various industrial equipments.

Although a relatively large amount of experimental and theoretical work has been performed as to the structure of the bubble flow for air-water[1-11], for steam-water[12,13], for nitrogen-mercury[14], for argon-mercury[15], and etc, there still exist numerous anomalies and experimental gaps between the theories and experimental results.

The greatly simplified momentum and energy equations derived for special cases cannot represent the flow situation as it actually exists. This is also the case, more or less, with the recent more realistic approaches by Vohr[16], or by Lamb[17]. The differential equations of continuity, momentum, and energy for dispersed two-phase flow presented by Van Deemter[18] have a shortcoming of requiring the dependence of velocity and void fraction on position in order to evaluate these equations.

The analysis of Brawn and Kranich[8] for dispersed bubbles marks a significant advance in our understanding of bubble flow, but their assumption of no local slip in axial direction is not realistic.

On the other hand, comparisons between the results of many studies in literatures listed above provide little in the way of common basic information which presents an insight into the physical phenomena involved, since such studies were confined to the measurements of only one or two of various important local parameters, and, to make the matters worse, under different flow conditions.

In the study of this basic flow pattern, the bubble flow regime, some of the most significant and essential parameters of interest are, at least, the distribution and configuration of gas and liquid phase, bubble velocity and its spectrum, liquid velocity and its fluctuating term, bubble-size distribution, and bubble frequency. These variables are able to describe the local flow conditions of the steady-state bubble flow, both qualitatively and quantitatively, and hence accurate information on such flow variables and the generalized relationships between themselves are quite necessary for us to understand the complex phenomena of the two-phase bubble flow as it is, and further to derive a more realistic and strict bubble flow model.

In addition, generally speaking, bubbles suspended in liquid undergo, during their travels, various phenomena too complicated and too difficult for mathematical formulation, such as fluctuations in static pressure and in velocity, a violent turbulent motion of the liquid induced by their own random motions, interactions or collisions or coalescences among themselves, interactions between them and the pipe wall, and their transfiguration. All these phenomena occur statistically at random. The present knowledge in the domain of two-phase bubble flow dynamics is very scanty[5,6,19,20,21], and therefore the need is strongly felt for more systematic studies of the statistical nature or turbulent characteristics of bubble flow, regardless of whether single- or two-component flow.

This chapter deals with an experimental study of various local parameters and some of the turbulent aspects for the cocurrent two-phase bubble flow of air-water flowing upward in a vertical circular tube of 60 mm inside diameter.

To summarize, the purpose of this chapter may be stated as follws :

1) Present additional data and information on the phase distribution.
2) Present result of bubble velocity profile and its fluctuating characteristics measured by double-probe method with using multi-channel technique.
3) Present result of water velocity profile and its turbulent fluctuating characteristics with use of hot-film anemometer method.
4) Present result of bubble slip-velocity profile.
5) Clarify the entrance effect upon the phase distribution and bubble velocity.
6) Describe some statistical characteristics of air-water bubble flow.
7) Discuss the systematic relationships between the various important local parameters.
8) Develop an appropriate model based upon a diffusive character of bubbles suspended in turbulent pipe flow.

4.2 Experimental Apparatus and Procedure

The experiments were conducted in a forced-convection loop designed for operation with air-water (or steam-water) at nearly atmospheric pressure. As is shown schematically in Fig.3.2, the loop is basically composed of a pump for water, a lower tank for degas of water, a mixing chamber for two phases, the test section, an upper plenum & separator, an upper tank & cooler, an air compressor, a surge tank for air, measuring facilities for air, water and two-phase flow, and pressure and temperature instruments.

Tap water used in the experimental program was circulated from the upper tank through the loop by means of a slurry pump with being degased at the lower plenum, and the flow rate of water was controlled by a valve and measured by a turbine-flowmeter. In the tap water runs, temperature was kept constant by continuously introducing a certain amount of water in a heat exchager (two spiral copper tubes of 10 mm × 40,000 mm in diameter and in length respectively contained in the upper

tank & cooler).

The air supply was obtained from the 8-ata supply line in the laboratory. The air flow was measured by means of a rotameter. The prassure immediately downstream of the meter was kept constant at 1,390 mm Hg absolute by means of two valves in series with the aid of mercury manometer.

The 2,100 mm long vertical test section was divided into three parts which were made of 60 mm inside diameter Lucite tubing with a Lucite chamber, pressure taps and mounting studs for probes, and two of them were 600 mm in length and the remaining 900 mm. A Lucite chamber, containing pressure taps in the middle and mounting studs for the probe equipment as is shown in Fig.3.3, was for the convenience of the probe installation.

A 220 mm long Lucite calming section was used for visual observation between the mixer and the test section whose upstream inside diamter was 104 mm and downstream inside diameter 60mm.

The mixer section is shown schematically in Fig.4.1. The air entered through the 1/2 - inch pipe at the bottom and merged with the water stream through a series of 84 holes (1.5 mm diameter), spaced along the periphery of the $1^1/_4$ - inch pipe. The 150 - mesh screen of stainless steel between the flanges of the mixing chamber and the calming section served to disperse any large air bubbles which might tend to form due to coalescence and was intended to give a uniform gas distribution and bubble size at the entrace to the test section.

Thus the metered streams of air and water were fed to the bottom of the test section, and the resulting two-phase mixture (bubble flow) flowed up through the test section and into the separator where the air was liberated to the atmosphere and the water was returned to the upper tank.

The water temperature was measured with a sheathed alumel-chromel thermocouple of 1-mm diameter inserted into the mixing chamber.

The system pressure was measured at the station Z/D = 20 downstream of the entrance to the test section by means of mercury manometer.

The probe measurements were performed at three axial positions Z/D = 10, 20 and 30 downstream of the inlet of the test section, and probes were radially traversed every 1 or 2 mm from r/R = -0.98 to r/R = 0.98 by means of the traversing equipment shown in Fig.3.4 (values r/R = 1.0 and r/R = -1.0 represent the positions on the surface of the pipe wall this side and that side of the mounting studs for probes, respectively).

The ranges of the flow variables covered in this experimental study were :

superficial water velocity V_o = 0.30 ~ 1.03 m/sec,

quality X = 0.0085 ~ 0.0900 %,

water temperature T_1 = 18 ~ 22 °C,

system pressure P = 1.08 ~ 1.11 kg/cm^2 absolute.

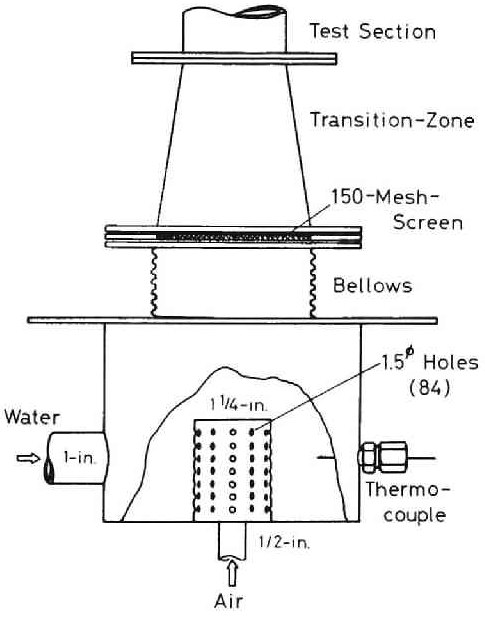

Fig. 4.1 Schematic diagram of mixing chamber

4.3 Flow Pattern Map

In the present work, emphasis is put on the study of turbulence structure of air-water two-phase bubble flow, and hence, information about the flow pattern map for the range of the flow variables covered in this experiment is necessary prior to the measurements.

Flow patterns were determined here by the visual observation and the recorded signals (output signals of the Schmitt trigger circuits) of three resistivity probes placed at the center of the flow through the mounting studs at Z/D = 10, 20 and 30.

In this chapter, the following three types of flow pattern were defined for convenience sake :

1) Bubble flow ;
   No slugs are found anywhere and small bubbles are suspended in the flow,
2) Developing slug (or bubble-to-slug transition) flow ;
   No slugs are found at Z/D = 10 or 20, but the small bubbles having been observed at the upstream section coalesce after some travels to form larger bubbles with a diameter nearly equal to the tube diameter (60 mm),
3) Slug flow ;
   Slugs are found at Z/D = 10, 20 and 30.

Figure 4.2 shows the flow pattern map thus obtained which is indicated in the form of the superficial liquid velocity versus quality diagram.

Typical recorded signals are presented in Figs. 4.3 ~ 4.5 for bubble flow, transition flow, and slug flow respectively. The length-scale given for each recorded data represents the reduced bubble length which was deduced from the experimental mean bubble velocity at the pipe center and the chart speed (25 cm/sec) of the linear pen-recorder. The process of the bubble coalescence in transition flow can be seen very clearly in Fig. 4.4.

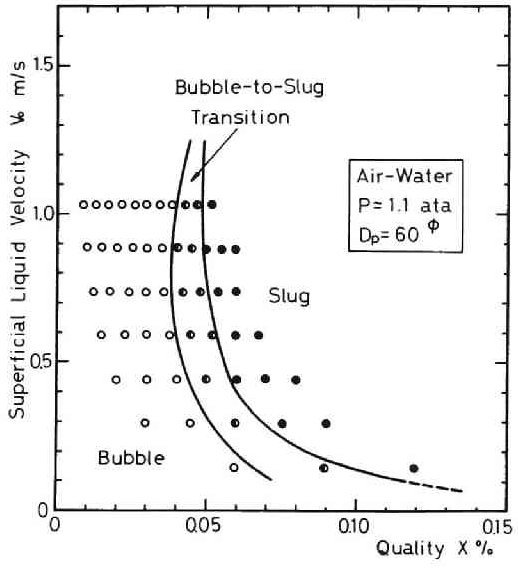

Fig. 4.2 Flow pattern map for vertical air-water flow

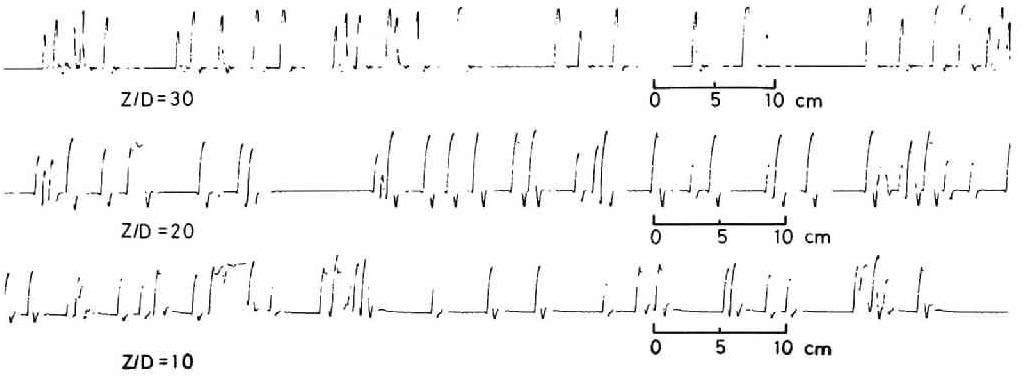

Fig. 4.3 Signals of the void probe (bubble flow)

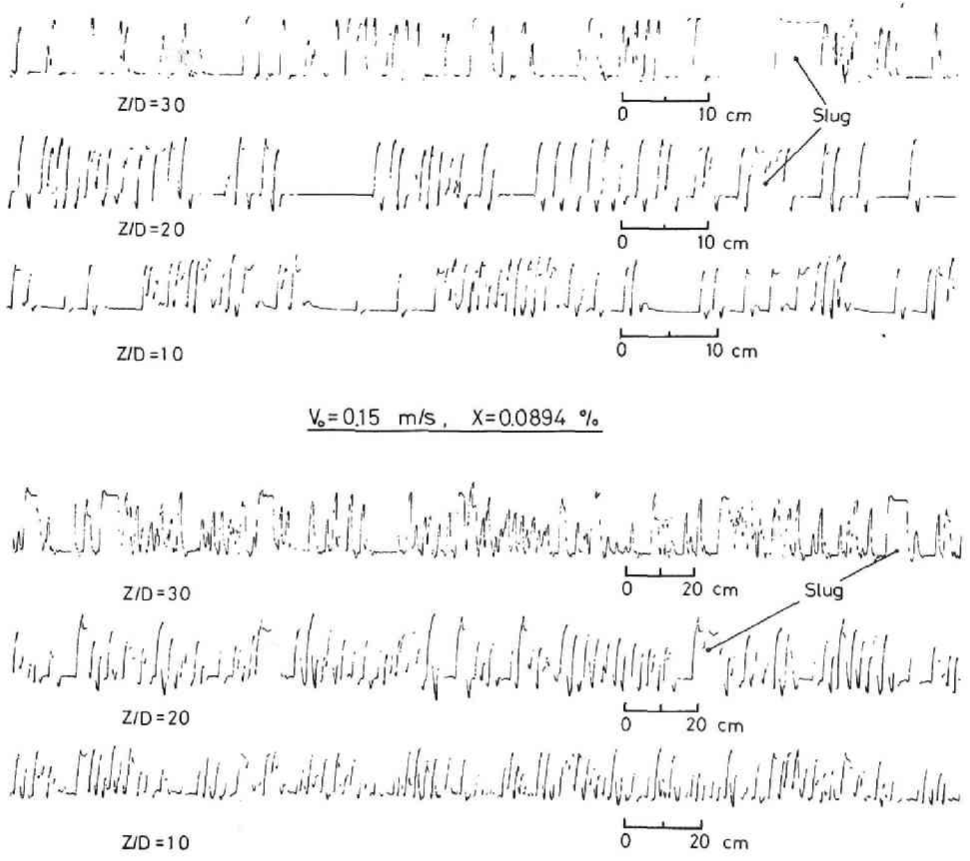

Fig. 4.4 Signals of the void probe (transition flow)

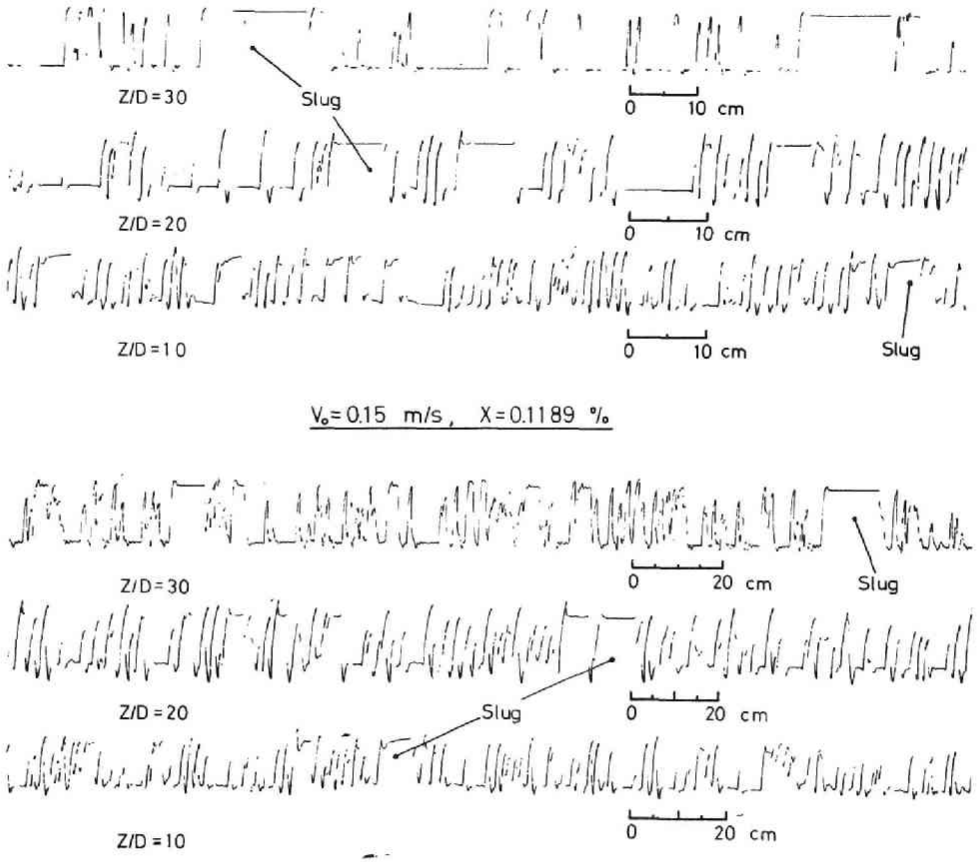

Fig. 4.5 Signals of the void probe (slug flow)

4.4 Entrance Effects on Development of Two-Phase Flow

In analyzing the experimental data on the turbulent flow characteristics and on the local parameters, it becomes imperative to predict the effects of a sudden geometry change of flow area or the entrance effect on two-phase flow development. But a search of the literature reveals a complete lack of such information for two-phase flow systems[22] whether single- or two-component two-phase flow with or without heat addition.

Therefore, the experimental program was undertaken to provide sufficient information to evaluate the entrance effect on the development of a bubble flow and to provide universality for physical interpretations of the present measured data on turbulence structure of air-water bubble flow.

Accurate measurements of the changing profiles of local void fraction, local mean bubble velocity and standard deviation of bubble velocity spectrum for increasing axial distance are one of the problems inherent to the evaluation of the entrance effect upon the flow development, and hence, were surveyed at three different axial positions Z/D = 10, 20 and 30.

4.4.1 Radial Profiles of Local Void Fraction and Bubble Velocity

Axially changing profiles were measured by the electrical resistivity probe method for local void fraction and mean bubble velocity (the latter was obtained by cross-correlation technique).

Typical results are represented for V_o = 1.03 m/sec in Figs.4.6 ~ 4.8, for V_o = 0.74 m/sec in Figs.4.9 ~ 4.11, for V_o = 0.59 m/sec in Figs.4.12 ~ 4.15(a), for V_o = 0.44 m/sec in Figs.4.16 ~ 4.18, and for V_o = 0.30 m/sec in Figs.4.15(b), 4.19, and 4.20. In these figures, the separated lines represent profiles taken simultaneously at each position and the spread between them is indicative of the time variation in both profiles of the local void fraction and the bubble velocity, which indicate that, as a whole, the void fraction is

increasing along the tube due to expantion though there are few exceptions. From these figures, it can be concluded that the profiles are clearly changing as the flow enters the test section, and that the azimuth-symmetry in both profiles is very poor at Z/D = 10, comparatively good at Z/D = 20, and was reasonably satisfied at the station Z/D = 30. This fact may follow that the fully-developed bubble flow has been already established at Z/D = 30 (a similar trend is more remarkable in the slug flow region).

In entrance region, bubbles initially seperated tend to collide, adhere, and coalesce with each other and furthermore to be accelerated or decelerated, depending upon their size, relative velocities, and initial flow conditions. And lastly we expect that they approach a regular arrangement and show reasonably symmetric profiles.

It is also interesting to note that some of those traverses, for example Fig. 4.14(a), show a slight but definite maximum void fraction at the pipe center with increasing downstream distance. Visual observation indicates that this is perhaps the result of agglomeration of small bubbles suspended in the flow into large slugs (slugging). This fact is consistent substantially with the recorded data, for example, shown in Fig.4.4.

4.4.2 Standard Deviation of Bubble Velocity Spectrum

Relative standard deviation of bubble velocity spectrum was deduced from bubble velocity spectrum measured across the tube by means of the double-(electrical resistivity)-probe and a multi-channel pulse-height analyzer.

Results are represented in Fig. 4.21 and 4.22. The general features indicated by these figures are :

1) Bubble flow region ;

   Relative standard deviation is nearly uniform across the tube (s/V_b = 0.1 ~ 0.2), and is lower for a larger downstream distance. This implies that the flow perturbation generated at the entrance

to the test section has not yet been weakened by the flow turbulence and still remains at Z/D =20, whereas, at Z/D = 30, bubbles may mostly exhibit a fairly uniform steady-state turbulent motion.

2) Transition and slug flow region ;
Relative standard deviation shows a larger value (s/V_b = 0.2 ~ 0.3) than that in the bubble flow region, and its profiles present a trend of higher values in the center core region of the tube and, whereas, lower values in the vicinity of the wall. And it is likely that the initial conditions of the flow has no longer significant effects upon the axial change of the profiles, since the flow turbulence is overwhelmingly large throughout the test section.

All these experimental trends agree satisfactorily with the results of the entrance effects upon the local void fraction and bubble velocity as already described in Paragragh 4.4.1.

4.4.3 Summary and Discussions

The existence of the fully-developed bubble flow or the entrance effects were evaluated from unchanging profiles of the local void fraction, the bubble velocity and its relative standard of deviation for increasing axial distance.

This survey reveals :

1) Nearly fully-developed flow is attained at Z/D = 30 for bubble flow, whereas in the transition and the slug flow region the entrance length is less than 30 D. This may be attributed to the competition between the intrinsic turbulent characteristics of of the flow and the flow perturbation occurring at the entrance to the test section. Since, in the bubble flow region, the latter effect overcomes the former, the entrance effect upon the flow arrangement and hence the skewness of the flow remains more or less over the downstream section even close to the station Z/D = 30. On the other hand, both in transition and slug flows,

large-scale mixing actions of the flow may precipitate the flow arrangement.

2) Relative standard deviation of bubble velocity spectrum shows a reasonably uniform profile for bubble flow, whereas an inflated one at the tube center for transition and slug flows. Especially in the bubble flow region, it gives a higher value for a smaller downstream distance from the entrance to the test section. These facts indicate an experimental evidence for the validity of arguments on the flow arrangement stated above.

A doubt arises, however, as to the entrance length for the single-phase water flow and for the air-water bubble flow. As stated earlier in the previous chapter, fully-developed flow is nearly established at Z/D = 20 for single-phase flow, whereas at Z/D = 30 for two-phase bubble flow. This elongation of the entrance length in two-phase flow can be accounted for neither by a concept of slightly changed (in some cases decreased) turbulent intensity of the flow field which is indicated later in Figs. 4.91 ~ 4.96, nor by a concept of uniform flow arrangement in fully-developed bubble flow region.

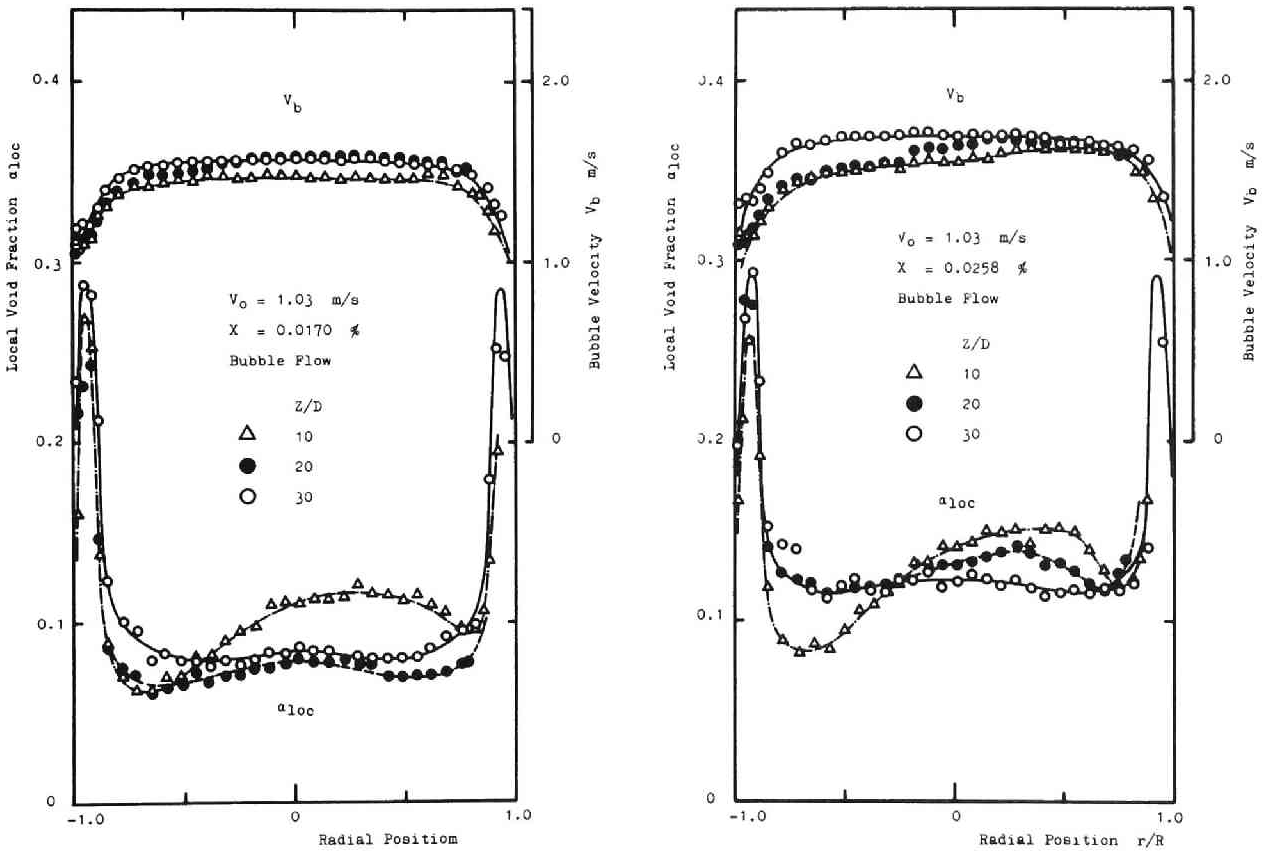

Fig. 4.6 Entrance effect upon flow arrangement

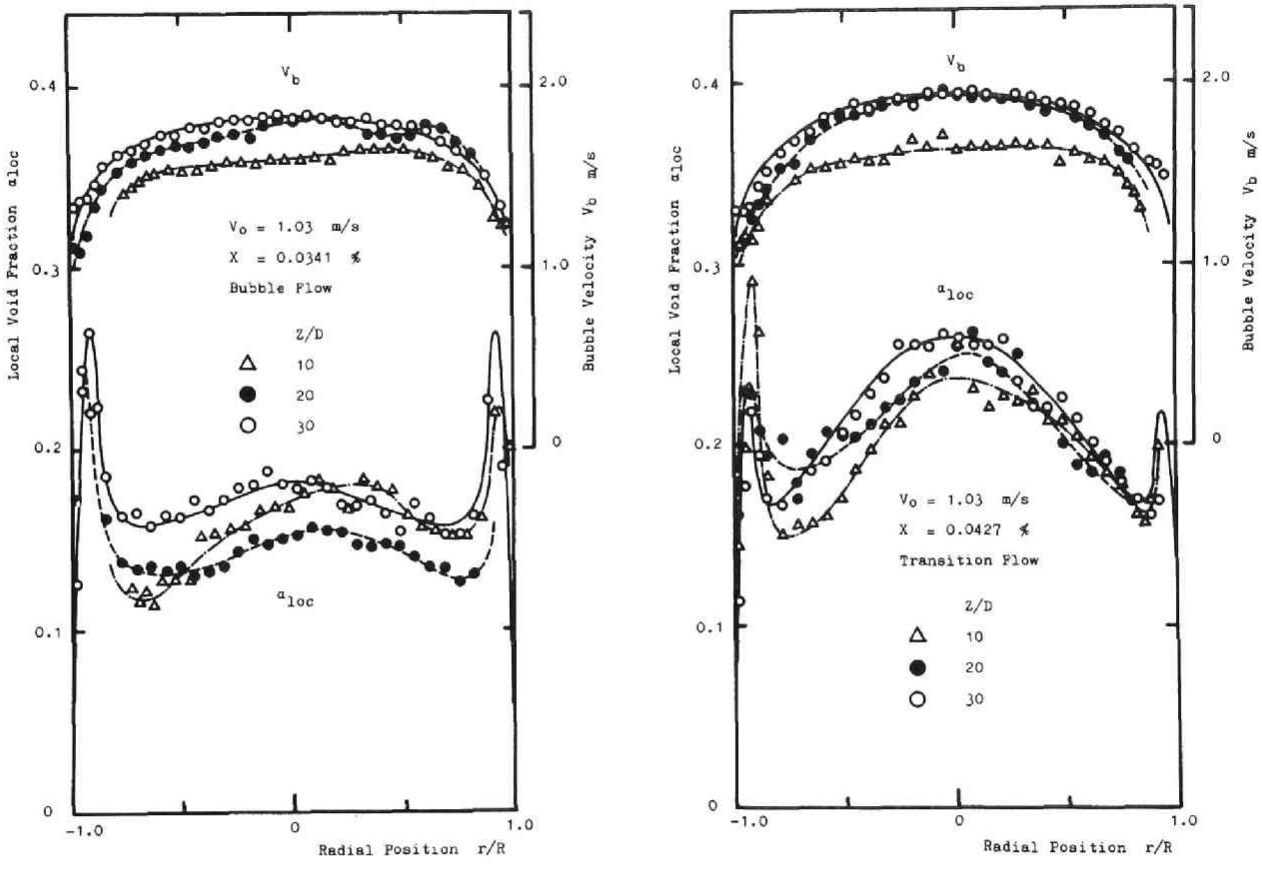

Fig. 4.7 Entrance effect upon flow arrangement

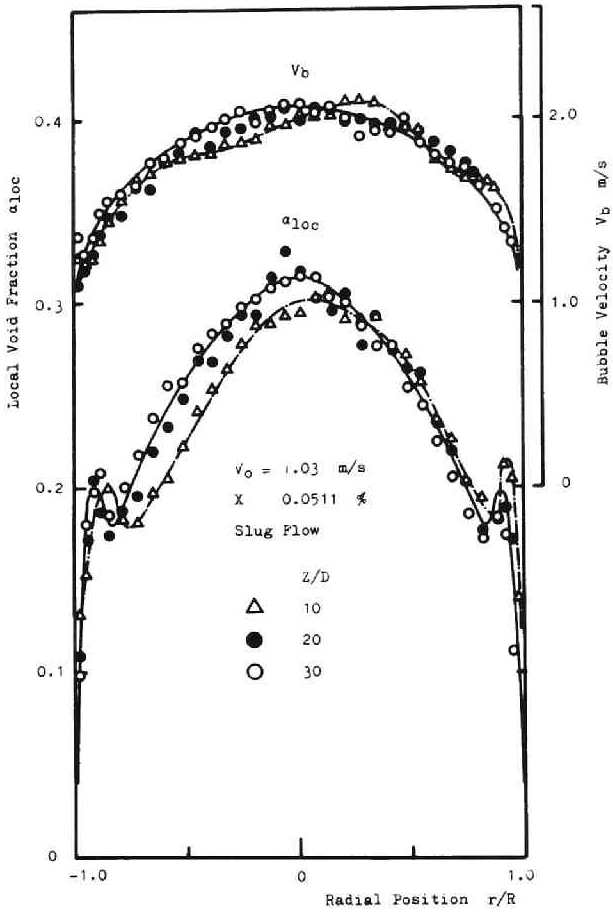

Fig. 4.8 Entrance effect upon flow arrangement

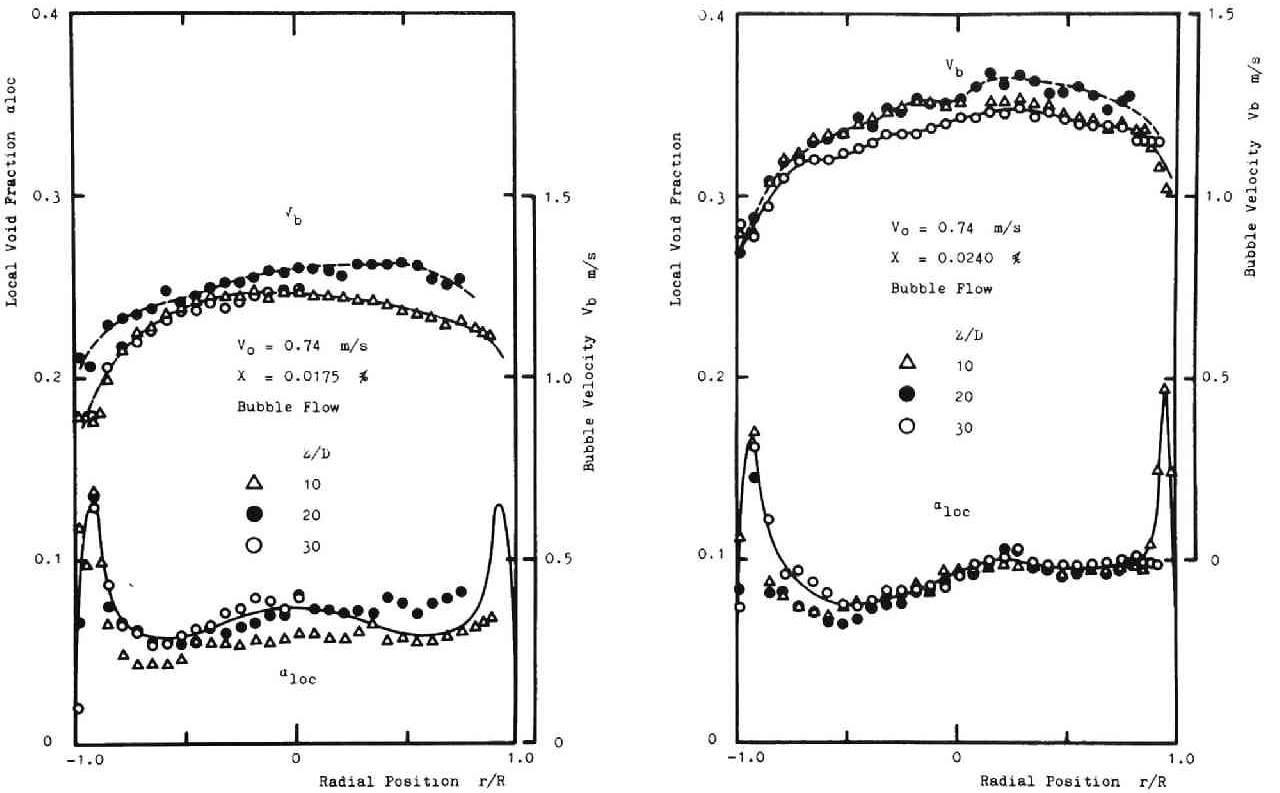

Fig. 4.9 Entrance effect upon flow arrangement

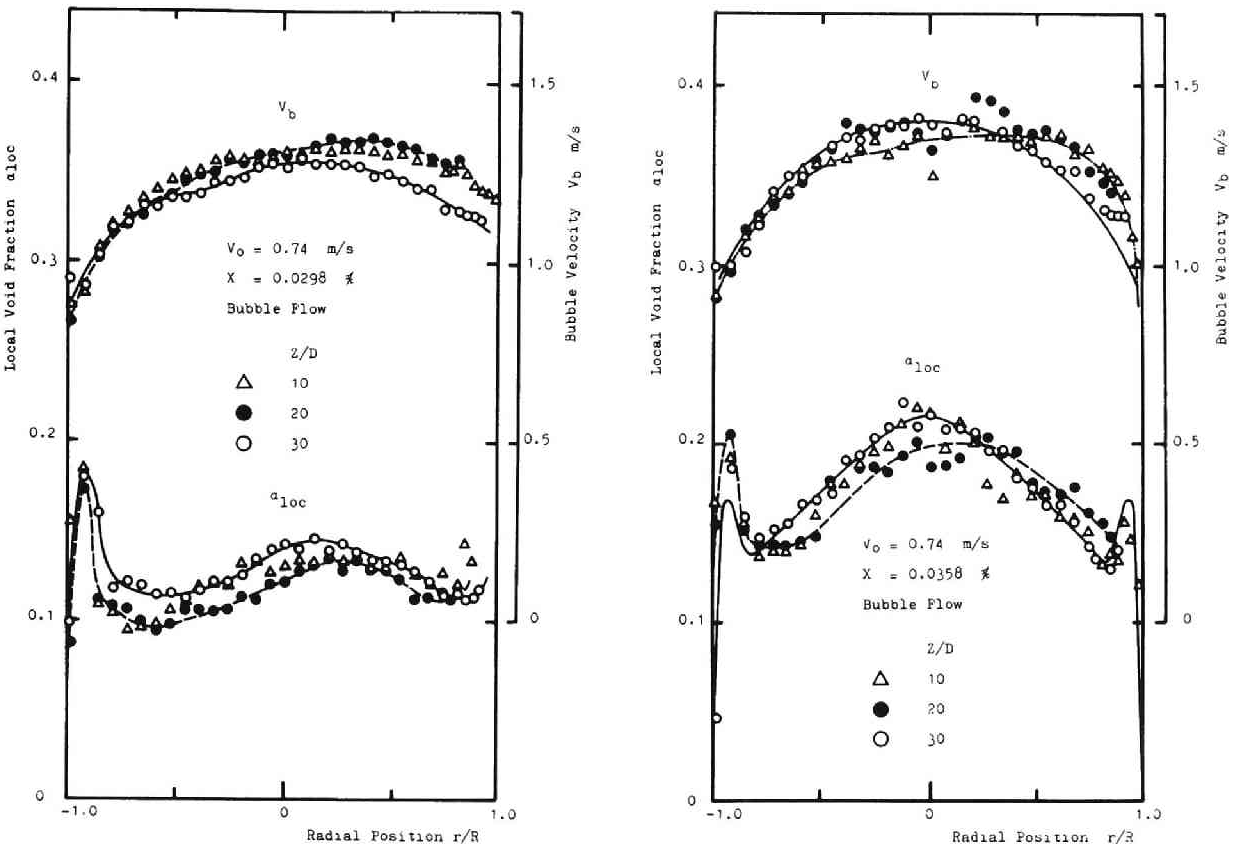

Fig. 4.10 Entrance effect upon flow arrangement

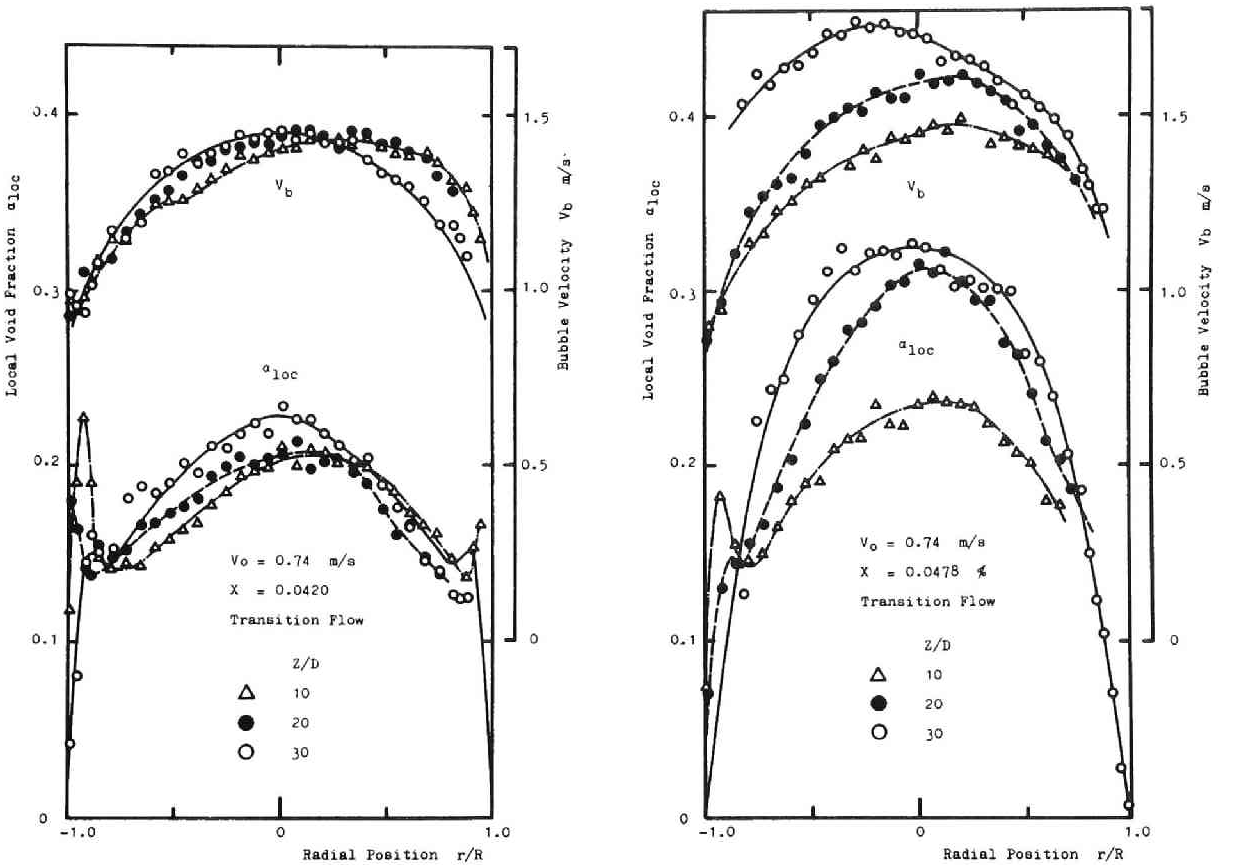

Fig. 4.11 Entrance effect upon flow arrangement

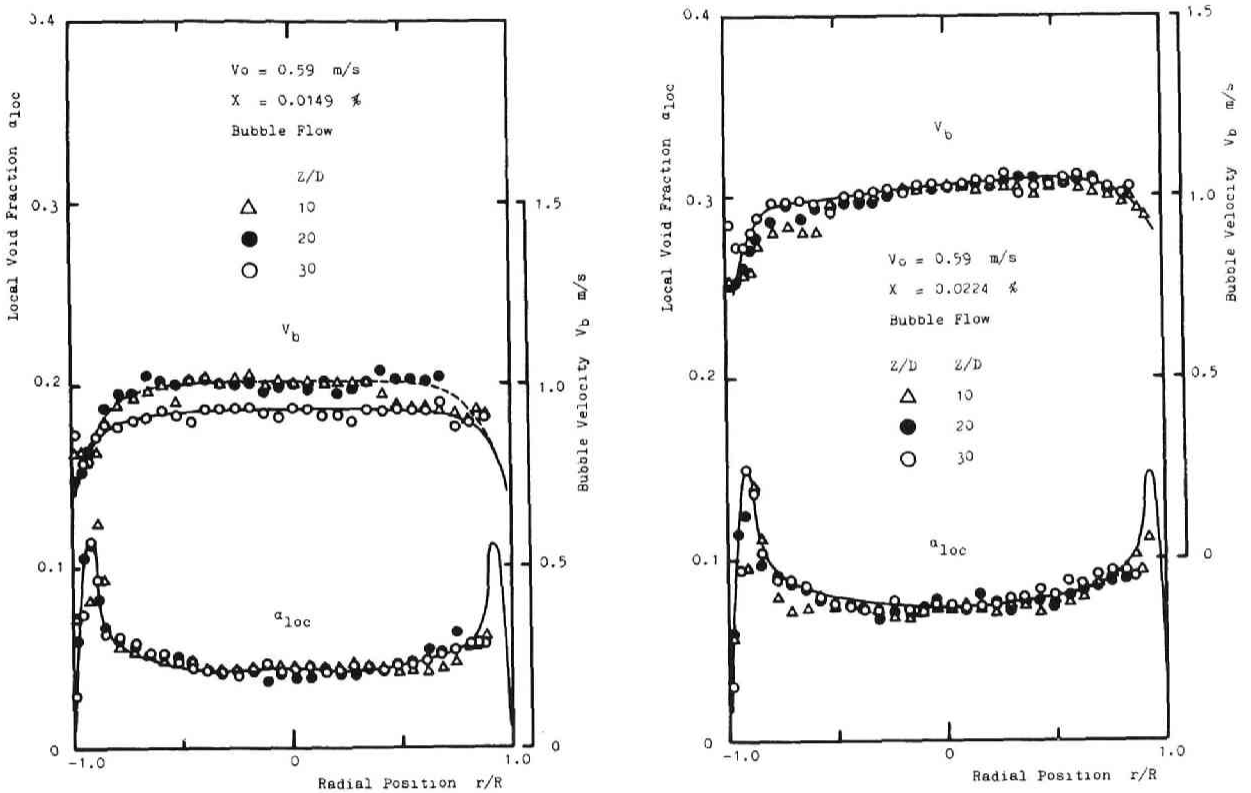

Fig. 4.12 Entrance effect upon flow arrangement

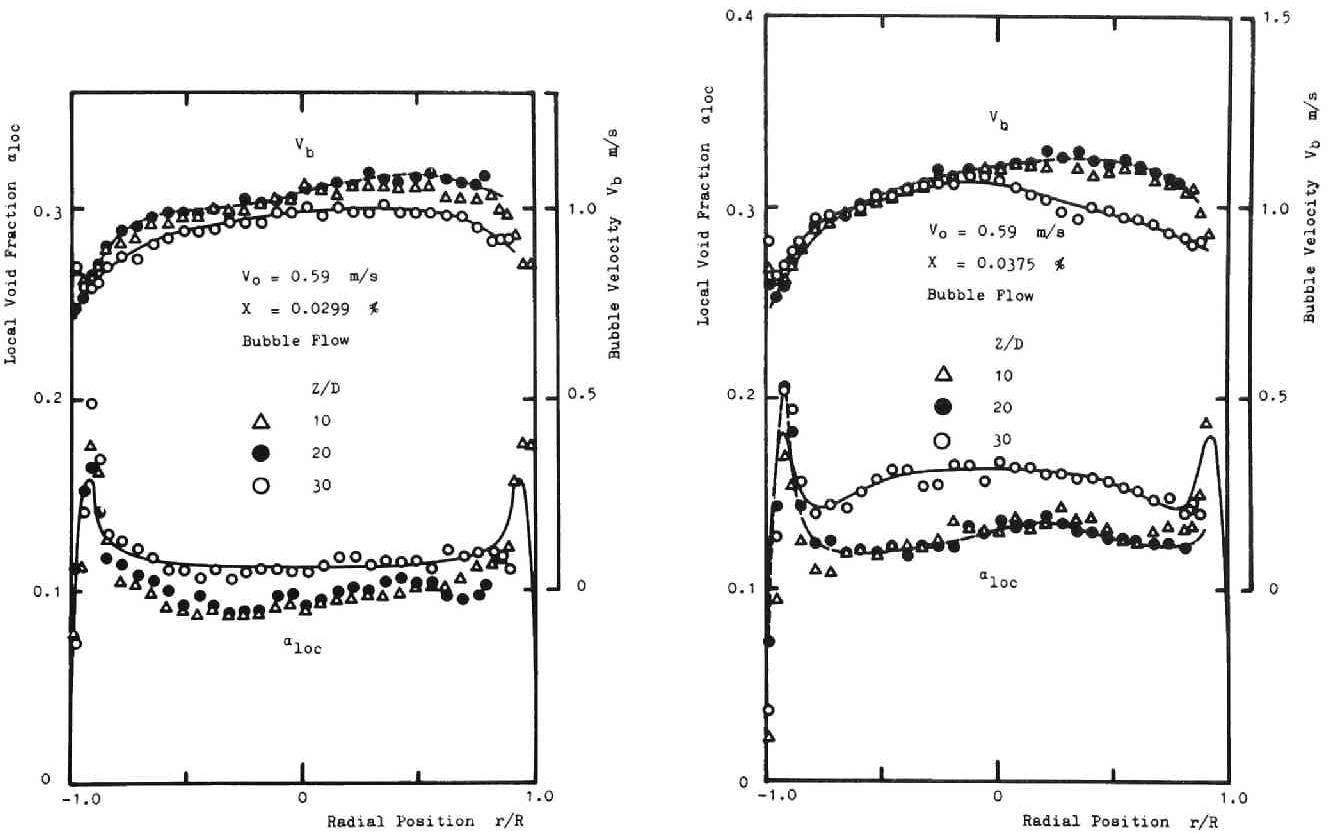

Fig. 4.13 Entrance effect upon flow arrangement

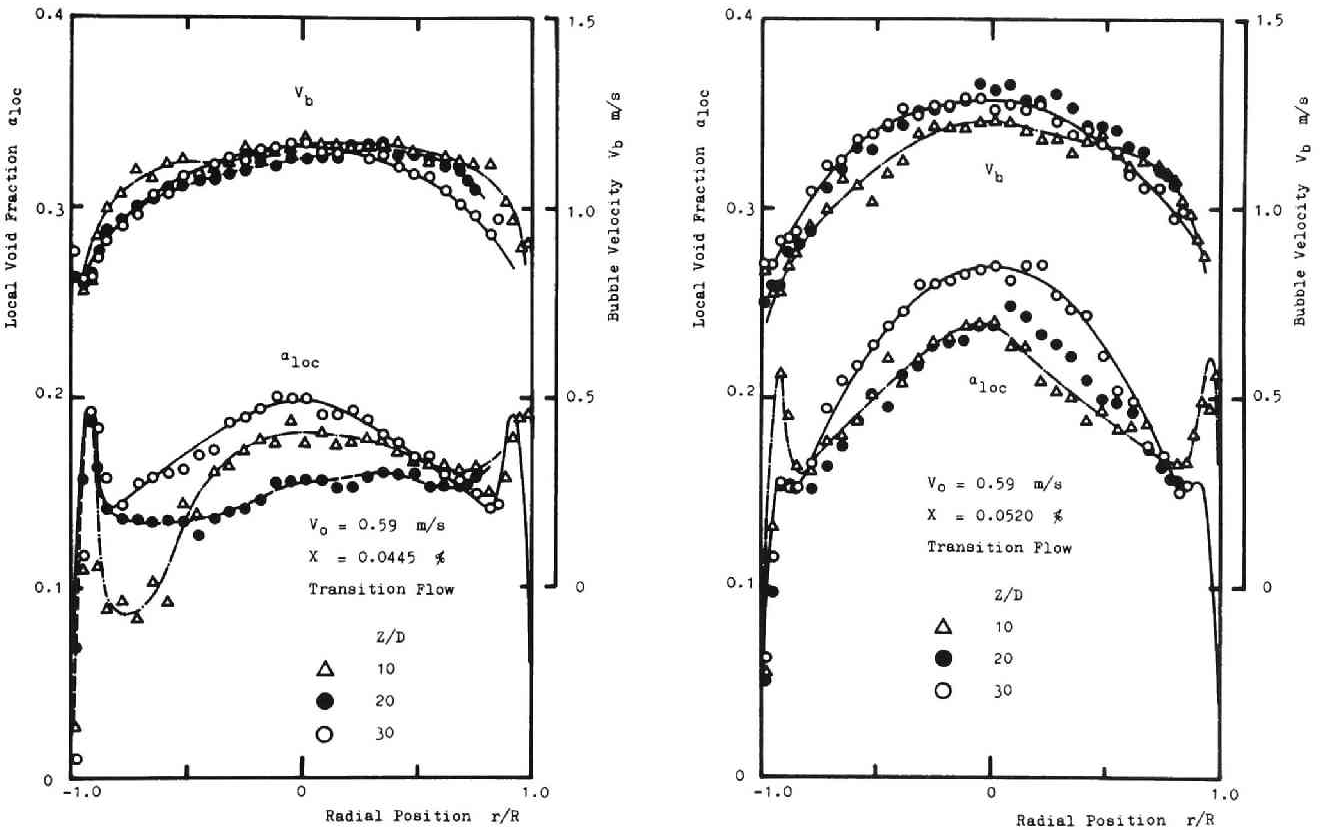

Fig. 4.14 Entrance effect upon flow arrangement

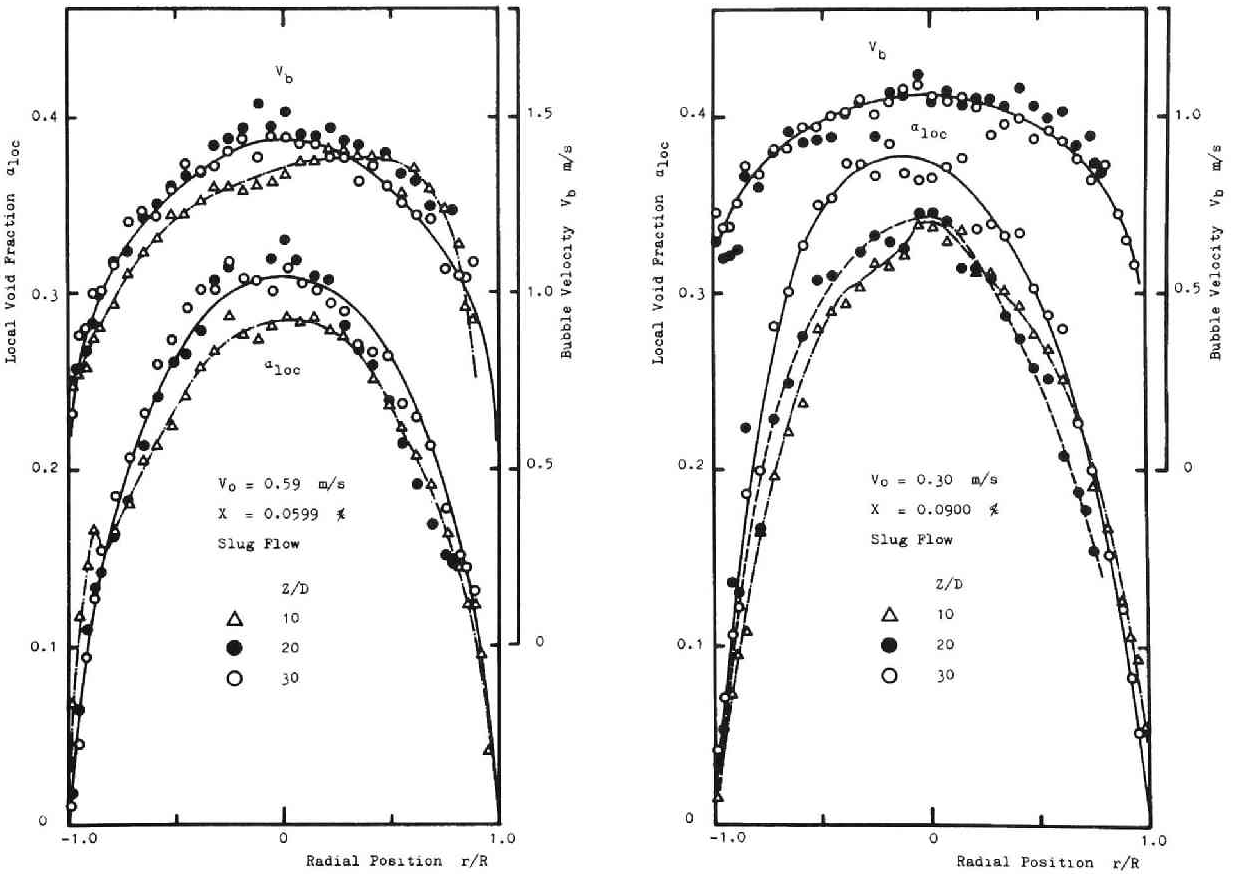

Fig. 4.15 Entrance effect upon flow arrangement

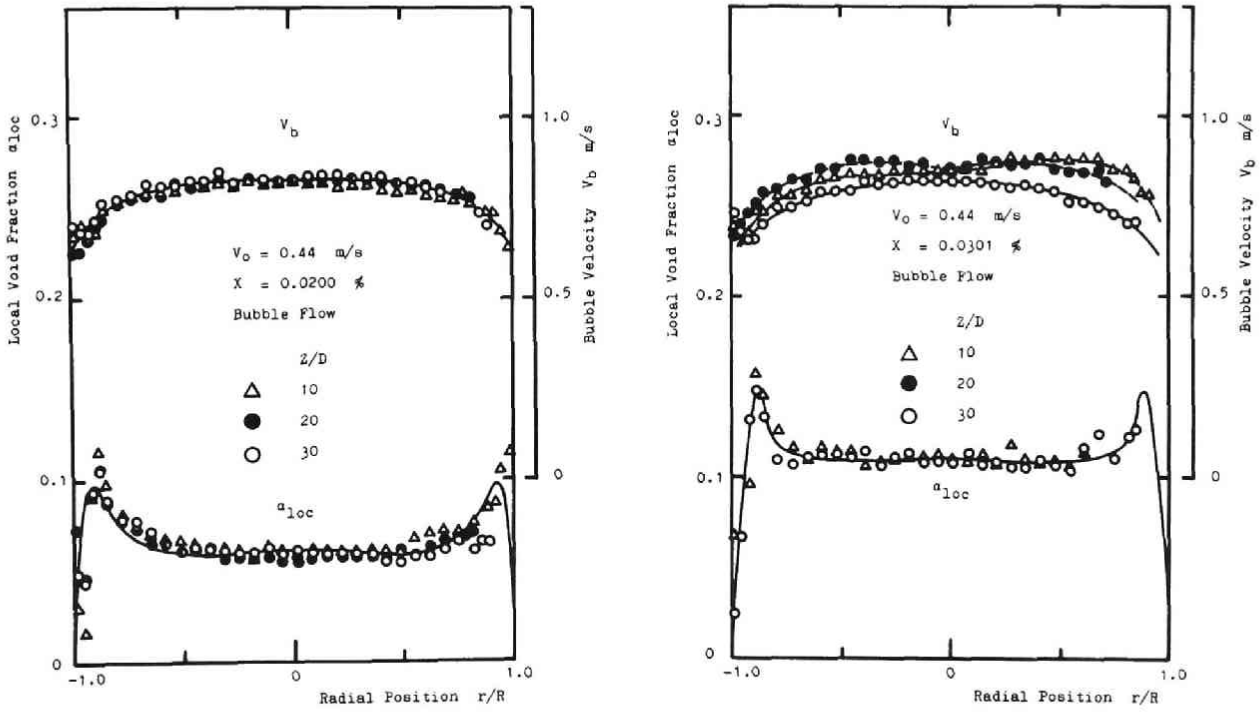

Fig. 4.16 Entrance effect upon flow arrangement

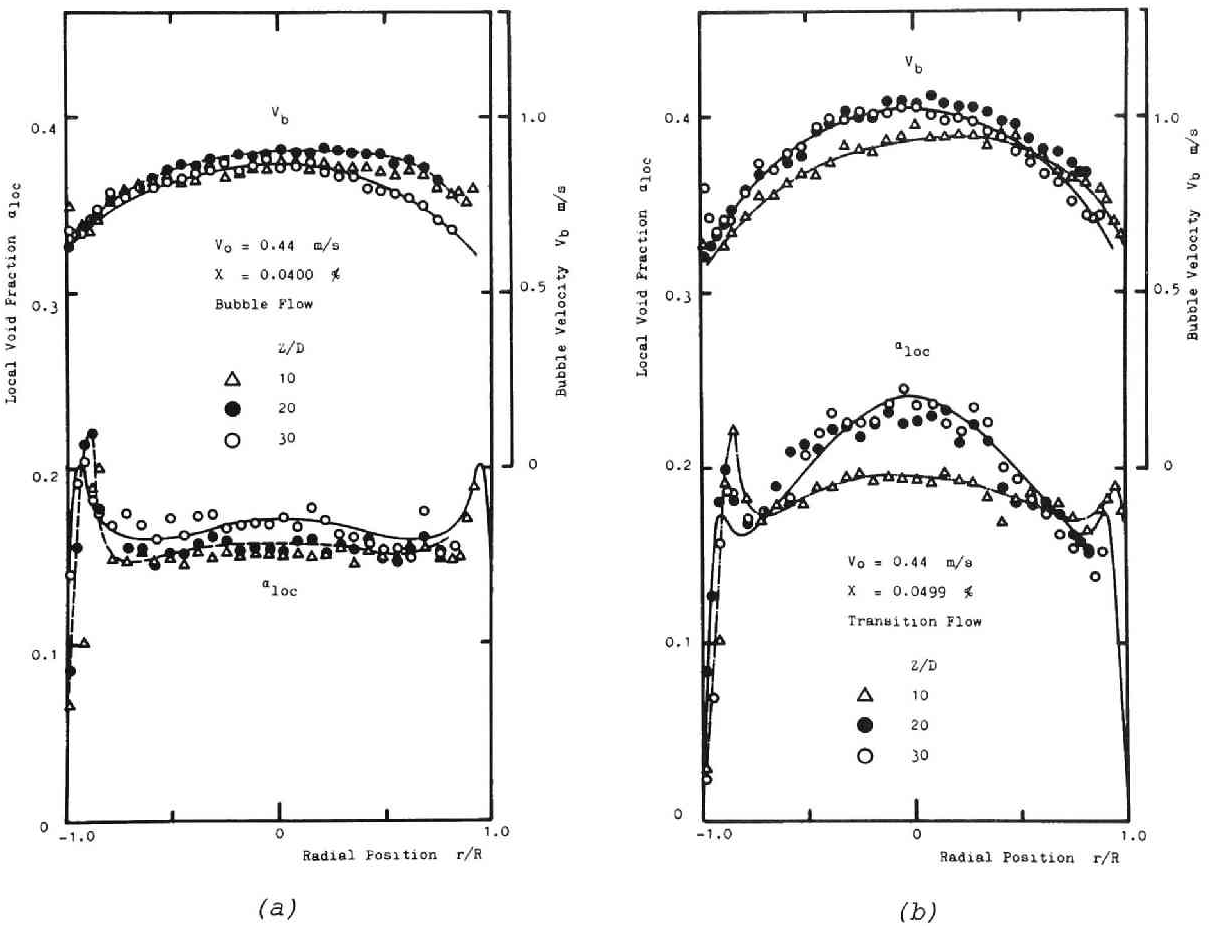

Fig. 4.17 Entrance effect upon flow arrangement

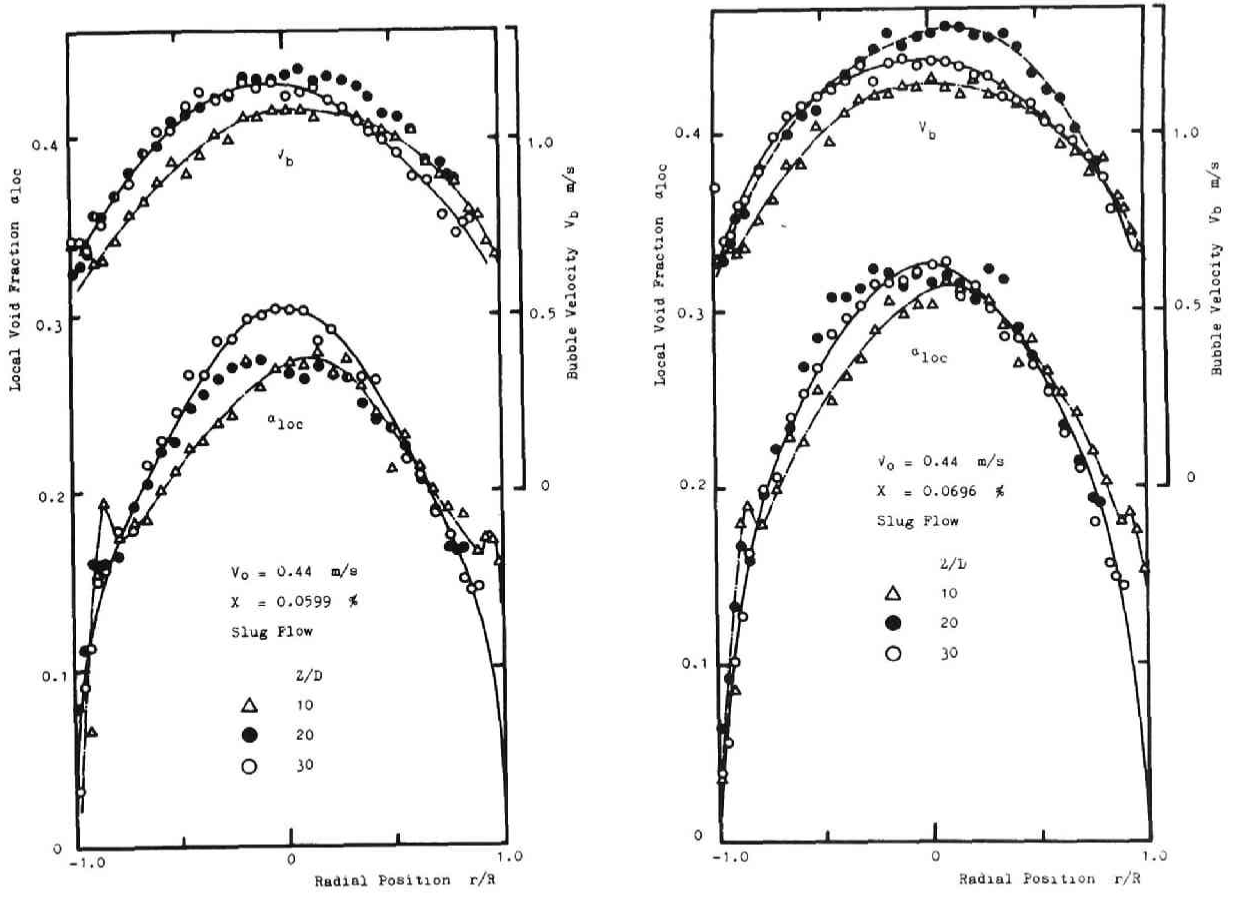

Fig. 4.18 Entrance effect upon flow arrangement

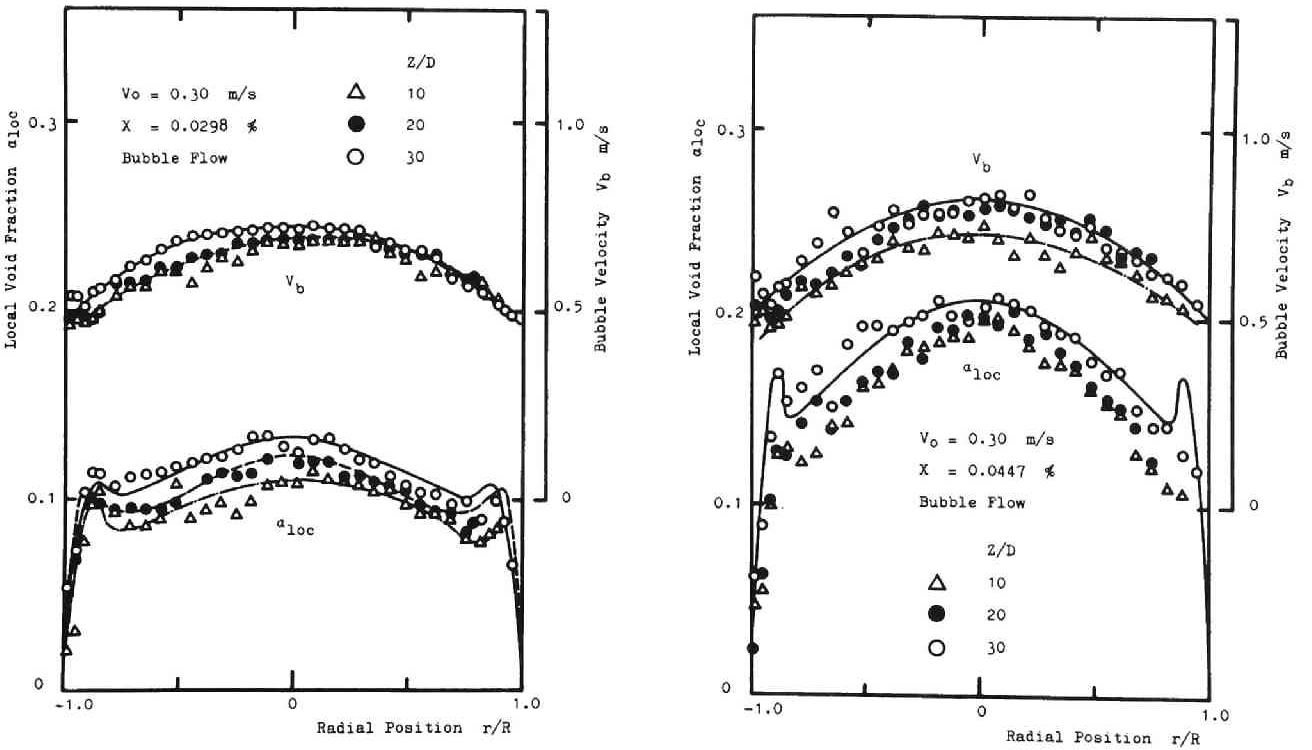

Fig. 4.19 Entrance effect upon flow arrangement

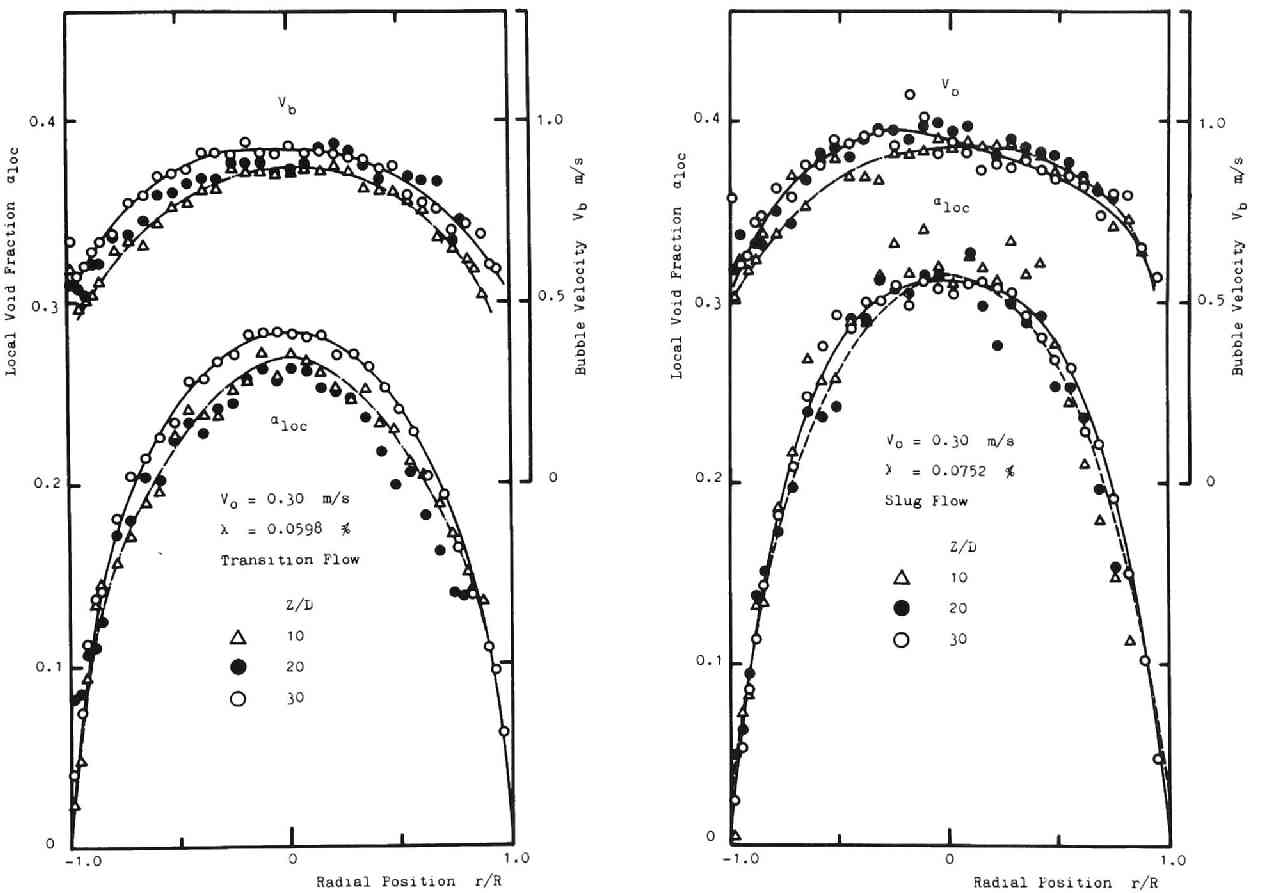

Fig. 4.20 Entrance effect upon flow arrangement

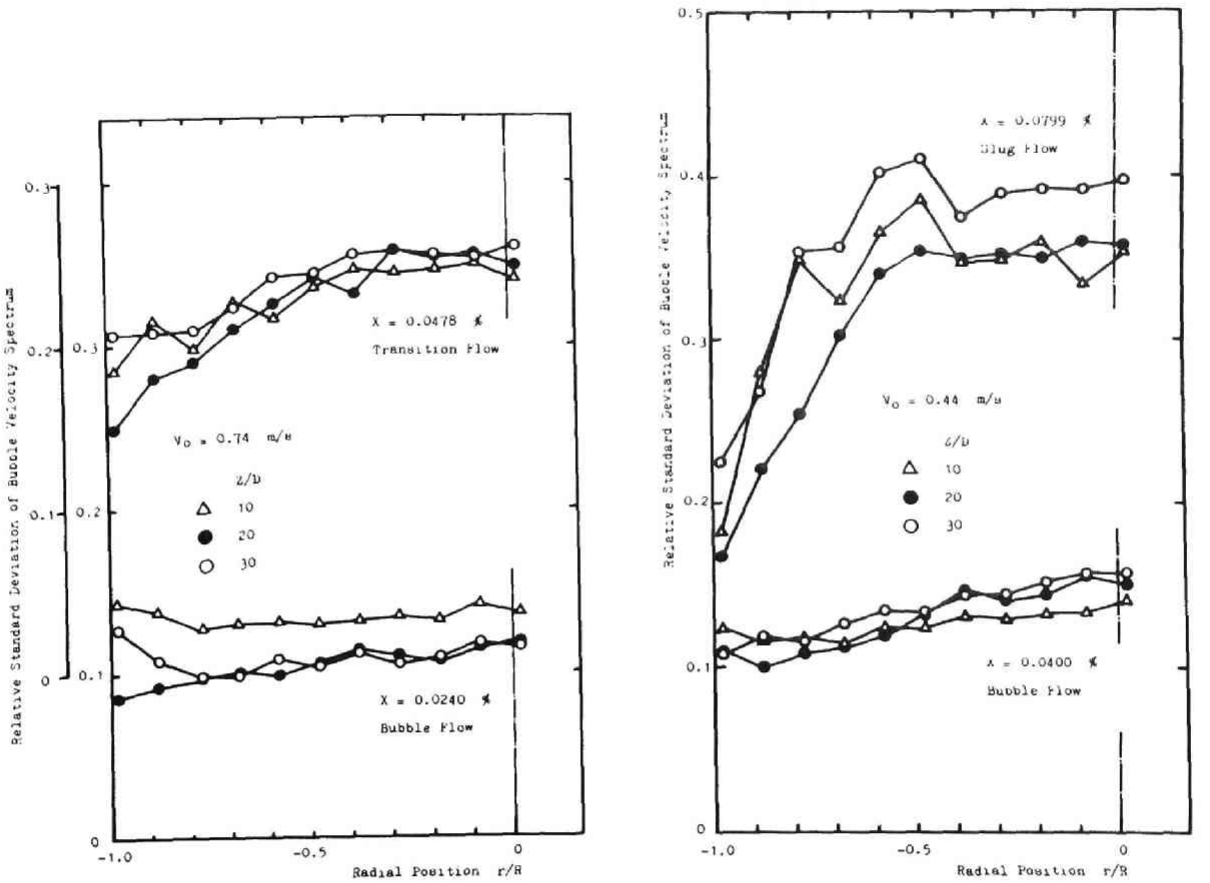

Fig. 4.21 Entrance effect upon flow arrangement

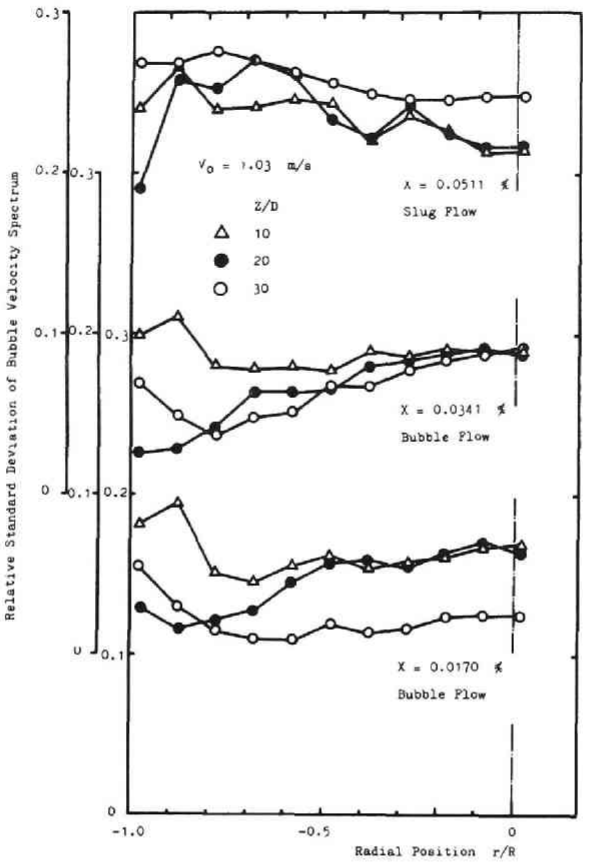

Fig. 4.22 Entrance effect upon flow arrangement

4.5 Some Statistical Aspects of Bubble Behavior

In the previous chapter, it has been indicated that bubbles suspended in water flow present some statistical behaviors as if they were ordinary diffusing particles. We might well expect such a diffusivity should be the case with bubbles travelling in air-water two-phase bubble flow.

Generally speaking, gas-liquid two-phase flow systems, where two phases are not uniformly mixed but are flowing alternately as discrete lumps of certain sizes, are usually accompanied with many unknown fluid-dynamically oscillating phenomena concerning closely the statistical characteristics of bubbles. At the present status, it is very difficult to state clearly these complicated oscillations, characterizing the flow itself, in mathematical or fluid-dynamical expressions. For such cases, statistical analysis appears more reasonable and is expected to give us some useful suggestions or insights into the flow structure.

To date, many attempts have been undertaken with respect to the statistical analysis of the fluctuating quantities such as water velocity, wall pressure or flow density of two-phase flow.

Adachi & Segawa[23] obtained the power spectral density distribution of the cross-sectional average water velocity fluctuation for upward nitrogen-water flow in pipe by means of an electromagnetic flowmeter. They reported that the spectral distributions were relatively flat in the bubble flow region, but, in transition flow, the contribution of low frequency component to the power spectral density became greater, and that in slug flow the distributions had periodic peaks at $f = (V_b/L)(n + 1/2)$, where f is frequency, V_b rising velocity of slugs, L length of the flow passage, and $n = 0,1,2....$

Kinoshita & Murazaki[24] analyzed the fluctuation of the dynamic pressure measured at various positions with a Pitot tube for air-water flow in a vertical tube. Their experimental results indicate that the distributions of amplitude and frequency of the dynamic pressure fluctuation can be approximated by Gaussian distribution and by Rayleigh

distribution, respectively. Further, they succeeded in obtaining theoretically the same results for both quantities.

Nishikawa et al.[25,26] studied the oscillating characteristics of wall pressure (such as power spectral density, probability density function, and coefficient of cross-correlation between two fluctuating signals at different axial positions) for air-water two-phase flow flowing upward in pipe. They revealed, for bubble flow, Gaussian distribution for probability density function, and smaller values both for the amplitude and for the intensity of the fluctuating quantity. They concluded that, although bubbles are distributed irregularly throughout the flow field, fairly regularly distributed bubble clouds, affecting the wall pressure fluctuation, gave periodic components to that pressure oscillation.

A number of attempts have been carried out in order to predict and characterize flow regimes in two-phase flow from their statistical natures. Hubbard & Dukler[27] studied wall pressure fluctuation for horizontal air-water flow in pipe with an aim of classifying and characterizing flow regimes. They presented, in their report, a new method to characterize flow regimes, i.e., the measurement and analysis of the spectral distribution of the wall pressure fluctuations, and they pointed out that those spectra were shown to uniquely characterize flow regimes.

The analyses of the power spectral density of flow density fluctuation (fluctuation in cross-sectional average void fraction) have been also performed as a diagnostic tool to develop insight into flow mechanisms or to detect at an early stage coolant boiling anomalies in nuclear reactors, by Terano et al.[28,29], Nishihara & Michiyoshi[30], Nakano[31], and Yamaguchi[32] in their boiling loops for steam-water using a capacitance type void meter. (Eurola[33] measured the power spectral density of water velocity variations in an electrically heated boiling loop which was directly related to the void content fluctuation.)

However, in most of these works above mentioned, emphases were put mainly on the study of the fluctuating characteristic itself of the two-phase fluctuation, and mere measurement of the power spectral density of such fluctuating quantities (density, flow rate, and other pertinent quantities of the mixture) does not give any direct information to understand the minute flow structure of the mixture, since the statistical nature of individual bubbles (or bubble clouds) and lumps of liquid induce very sensitively the fluctuations of the mixture. Therefore an extensive investigation of the statistical characteristics of bubbles suspended in the flow is much desired. Independent variables concerning such statistical nature of bubbles are the bubble radius, bubble velocity, time or length interval between bubble arrivals, and other quantities. In this section, we will describe the bubble radius, time interval between bubble arrivals (or bubble frequency distribution), and the statistical aspect of the resultant phase change or density fluctuation of the air-water mixture. (Discussions on bubble velocity will be given in Section 4.7.)

4.5.1 Auto-Correlation Function of Density Fluctuation

To inquire the statistical nature of the bubble motion from the viewpoint of considering bubbles as discrete deffusing particles (with random motions), a series of measurement of the auto-correlation function of the void probe signal (modified square waves of amplitude 1 or 0 correspondingly when the probe tip was in a gas or liquid - this variation of the signal level is closely related to the time-dependent variation of the local flow density of the mixture when the flow is assumed a continuous mixture and the probe tip in point manner) were carried out for three flow regimes (bubble flow, transition flow, and slug flow), using a correlator.

The Eulerian auto-correlation function $F_{xx}(\tau)$ is defined

$$F_{xx}(\tau) = \lim_{T\to\infty} \frac{1}{T} \int_0^T x(t)\ x(t-\tau)\ dt \quad , \qquad (4.1)$$

where x(t) and τ are the void probe output signal and time lag respectively.

a) Entrance effect: Figure 4.23 shows typical results representing this effect upon the auto-correlation functions for bubble flow measured at various radial positions for Z/D = 10, 20, and 30. No significant entrance effect can be seen from this figure, although this effect on the flow arrangement is considerable as already shown in Section 4.4. This fact indicates that, in the bubble flow region, the statistical aspect of the local density variation with time is independent of the process of flow arrangement.

b) Mass velocity effect: Figure 4.24 shows, as a function of quality, the mass velocity effect upon the auto-correlation functions measured at the pipe center in fully-developed flow region of bubble flow, transition flow*, and slug flow. For the complete set of measurements, no significant effects are expected from this figure, except for the fact that the auto-correlation function at constant quality tends to have rationally its component at smaller values of time lag with increasing the superficial water velocity.

c) Effect of flow pattern: The effect of the flow pattern or of increasing the quality upon the auto-correlation function of the density fluctuation is represented for V_o = 0.44 m/sec in Fig.4.25, for V_o = 0.74 m/sec in Fig.4.26, and for V_o = 1.03 m/sec in Figs. 4.27 and 4.28.

The results agree with intuitive picture of the phenomena, and are classified into two regions according to the flow pattern.

In the bubble flow region, the auto-correlation function fell down exponentially with increasing the time lag τ, without regard to the radial position (this trend may become more distinct when the function is normalized). No accurate information can be ob-

---

* By transition flow we mean the existence of slug flow, at least, at the station Z/D = 30.

tained as to the bubble shape or motions directly from the measured auto-correlation function of the density fluctuation, since this function is a result of the very complicated combination of the distributions of bubble radius, probe eccentricity from bubble center and of time interval between bubble arrivals. But, an audacious interpretation may lead to some special distribution functions, such as Gaussian or Poisson distribution, for bubble radius and time interval between the arrivals of neighboring two bubbles at the probe tip. This estimation is to be judged true from more direct measurements on both quantities as shown later in Figs.4.29 and 4.30.

In the transition* and the slug flow region, the shape of that function is different from that in the bubble flow region. When the individual smaller bubbles become to coalesce to form larger bubbles with a diameter nearly equal to the pipe diameter and those bubbles are formed continuously, the auto-correlation function incurs naturally, as shown clearly in Figs.4.25 ~ 4.28, an increase at large values of τ due to the slugs periodically flowing up through the test section with a low frequency. The effect of these periodically coming slugs is, thus, to deviate the auto-correlation function from an exponential shape. This characteristic deviation in the auto-correlation function of the density fluctuation may serve as a means for detecting the prevailing flow pattern or distinguishing bubble flow from slug flow. It is also very interesting that, in the vicinity of the pipe wall, afforementioned deviation is very small and the function is almost exponential even in slug flow. This follows from the fact that, in slug flow, slugs tend to ascend in the central core region of the flow passage and small bubbles are distributed throughout any cross section of the flow.

---

* See footnote on pase 280.

4.5.2 Time Interval between Bubble Impingements on Void Probe

A large difference in momentum of the motion between individual bubbles and lumps of water due to the difference in densities plays a key role in the fluctuation process of the local flow condition, and, therefore, the fluctuating characteristics of the flow system may be affected seriously by the spatial distribution of the transiting bubbles or time intervals between the transits of neighboring two bubbles at a given point of pipe cross section. On the other hand, as stated earlier, the temporal distribution of the bubble transit is closely related to the auto-correlation function of the local density fluctuation. Consequently, from this viewpoint, it is desirable to investigate the temporal and spatial distributions of the transit frequency of bubbles continuously flowing up through the test section.

Figure 4.29 indicates typical histgrams of the bubble transit frequency at r/R = 0 for bubble flows obtained from the recorded void probe signals (such as shown in Fig.4.3) which represent the bubble impingements on the probe tip (the ordinate of this figure represents the number of bubbles picked up from the recorded data of a given length).

From this figure, it may be concluded that the temporal distribution of the bubble transit in the bubble flow region is well approximated by Poisson distribution function (dotted line in each diagram)*, i.e., the bubble impingement on probe tip takes place at random in a statistical sense. This fact will support the conceptional bubble diffusivity based on the random bubble motions similar to the Brownian

---

* Owing to the theoretical analysis by Kinoshita & Murazaki[24], the distribution of the bubble transit frequency is characterized by the exponential function for bubble flow and by Rayleigh distribution for slug flow. Lackme[34] has shown that the distribution of bubble arrival time changed from Engangian type (i.e., exponential distribution) to Poisson type with increasing the gas flow rate.

motion of free particles. (The spatial distribution of the mean bubble frequency will be shown later in Paragraph 4.6.2.)

4.5.3 Equivalent Bubble Radius

As already shown in Chapter III, the bubble dispersion coefficient in single-phase flow generally depends on the radii of bubbles. This should hold true with bubbles in two-phase bubble flow. Hence, a knowledge of the bubble radius and bubble shape is very important to analyze the dynamic or steady-state flow characteristics.

A typical histgram of the equivalent-spherical-diameter of bubbles (defined by Eq.(2.13b)) is presented for bubble flow in Fig.4.30, which is obtained from bubble photographs with using a planimeter. (Photographs show most bubbles are nearly spherical or oblate and spheroidal in bubble flow, as is shown, for instance, in Photo.4.1.)

Mean equivalent-spherical-bubble diameter $\overline{d_v}$ is defined by the following equation, based upon the relationship between the total gas flow rate and the volume of individual bubbles.*

$$\frac{\pi}{6}(\overline{d_v})^3 = \{\sum_i \frac{\pi}{6} d_i^3 n_i\}/\{\sum_i n_i\} \quad , \tag{4.2}$$

where d_i and n_i are the equivalent-spherical-bubble diameter and the number of bubbles whose diameter are between $d_i - \Delta \sim d_i + \Delta$ ($\Delta = \frac{1}{2}(d_{i+1} - d_i)$).

Figure 4.30 indicates nearly normal distribution for bubble diameter distribution in the bubble flow region, and this trend agrees with the assumption used in the analysis by Sekoguchi et al.[35,36]. On the other hand, Petrick obtained the Poisson distribution for bubble size in his study on vapor carryunder phenomena[1]. This discrepancy

---

* Petrick[1] used the mean bubble size determined by $\sum_i d_i n_i / \sum_i n_i$. But this definition seems impractical as to the relationship between the total gas flow rate and the sum of the volume of individual bubbles.

in bubble size distribution between the experimental results by Petrick and by the author does not appear so significant and it is perhaps fruitless to speculate on its reason, because such difference may arise from that in the methods of producing bubbles between them.

In all experimental runs in the bubble flow region, mean bubble size was between nearly 3.5 ~ 4 mm regardless of the superficial water velocity and the quality.

4.5.4 Summary and Conclusions

A statistical nature of bubbles was studied for air-water bubble flow flowing upward in a vertical pipe.

The following conclusions are obtained.

1) No entrance effect and mass velocity effects were observed upon the auto-correlation function of density fluctuation.
2) The auto-correlation function of density fluctuation is a strong function of the flow pattern. In bubble flow, it falls exponentially with increasing the time lag, whereas, in transition and slug flow, it tends to deviate from such an exponential shape. From this, prevailing flow pattern can be distinguished.
3) Bubble transit frequency distribution is approximated by Poisson distribution.
4) Equivalent-spherical-bubble diameter is approximated by normal distribution.

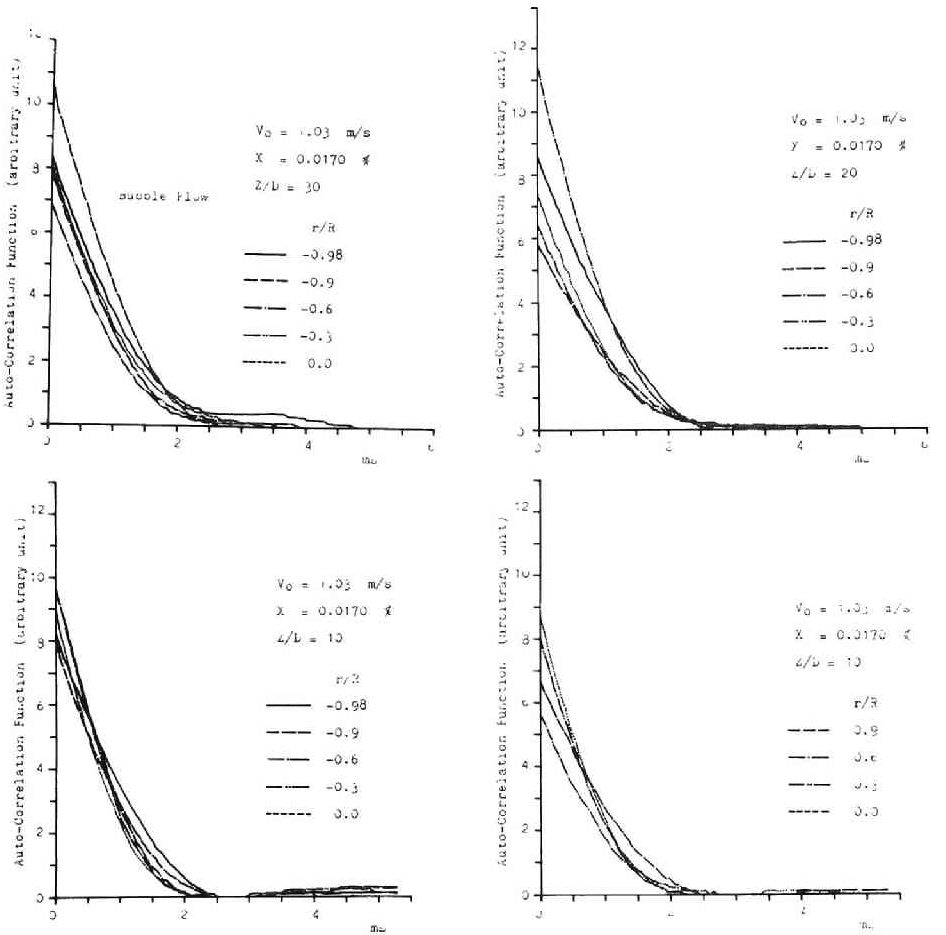

Fig. 4.23 Auto-correlation function of density fluctuation (entrance effect : V_o=1.03 m/sec)

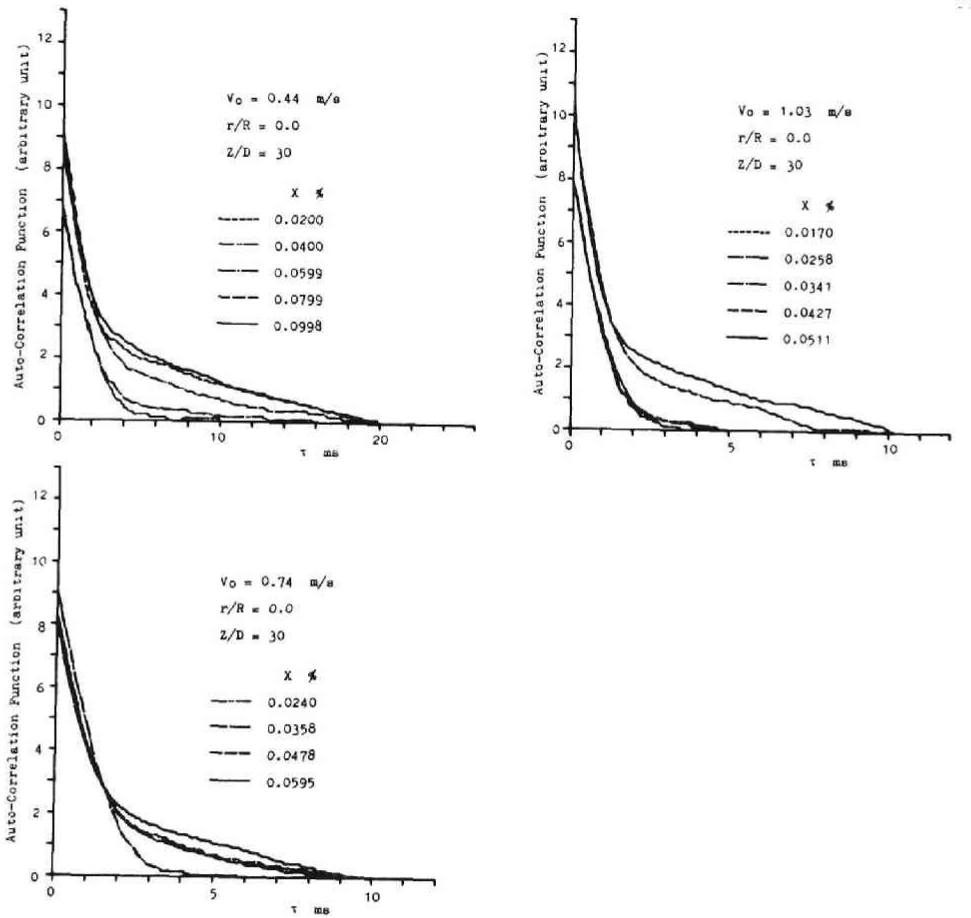

Fig. 4.24 Auto-correlation function of density fluctuation (effect of water velocity : r/R=0)

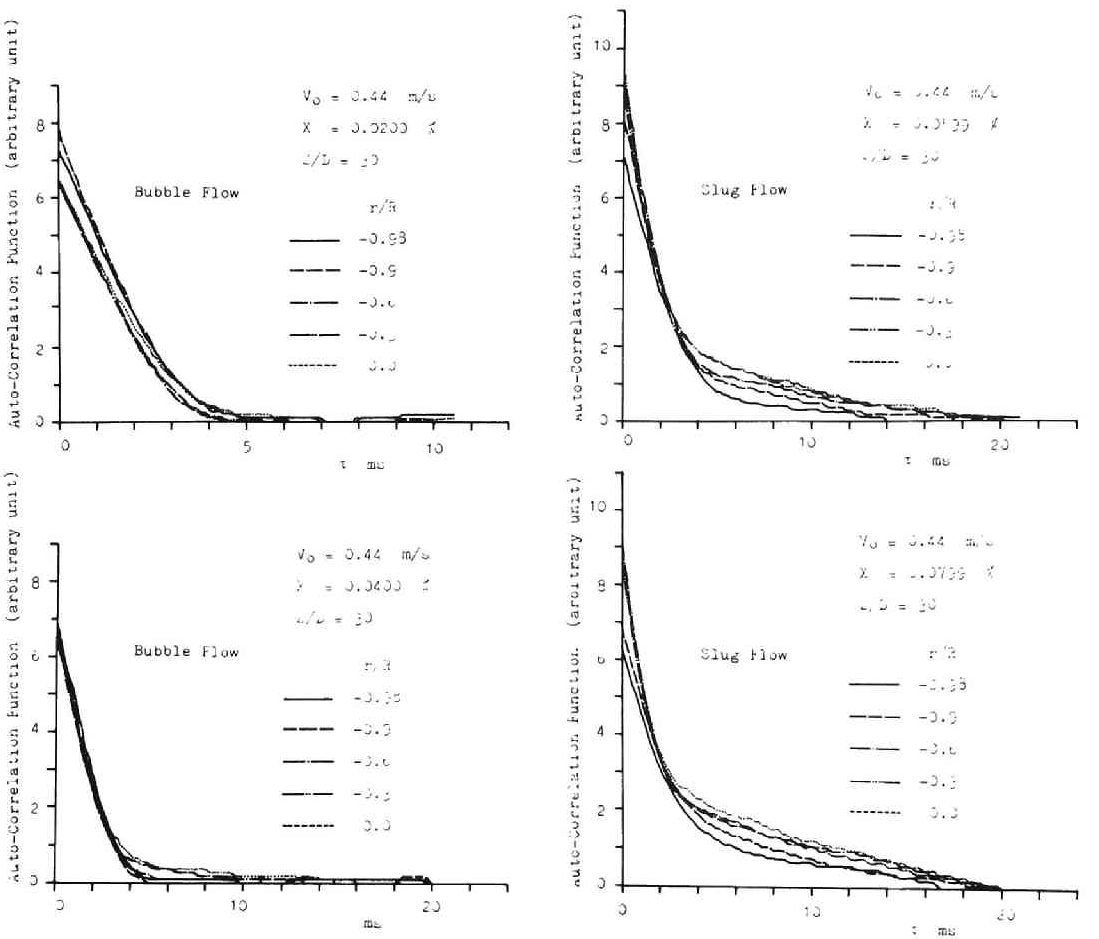

Fig. 4.25 Auto-correlation function of density fluctuation (effect of flow pattern : V_o=0.44 m/sec)

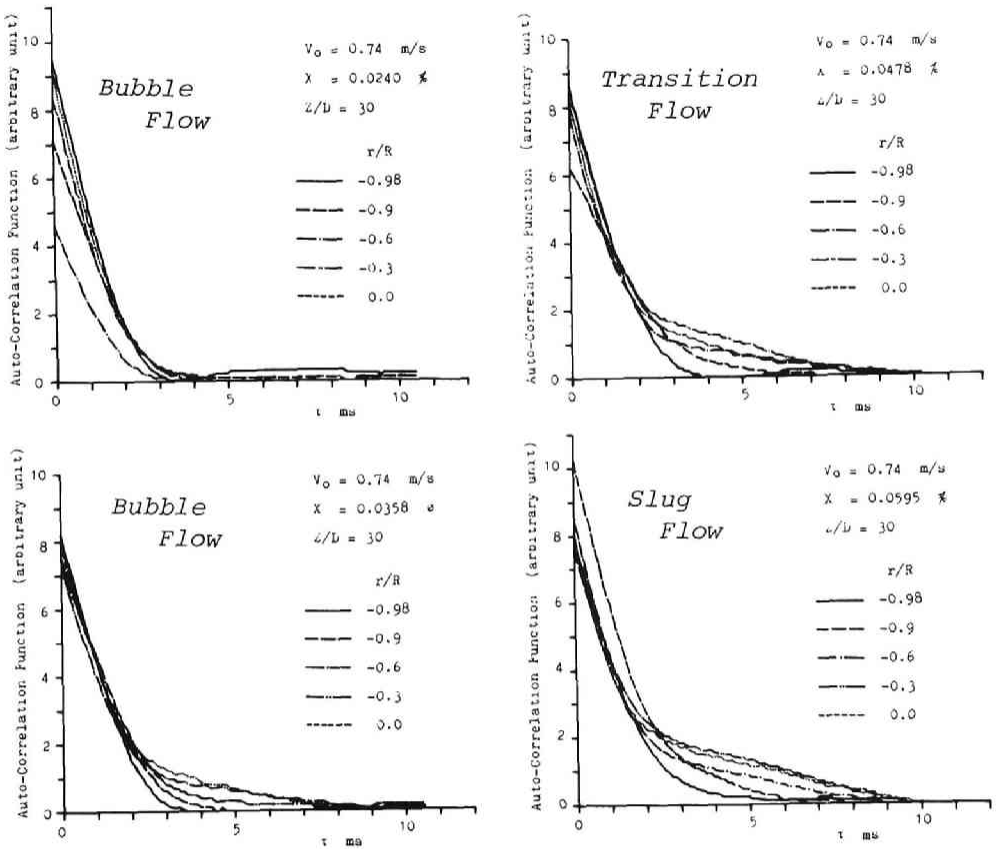

Fig. 4.26 Auto-correlation function of density fluctuation (effect of flow pattern : V_o=0.74 m/sec)

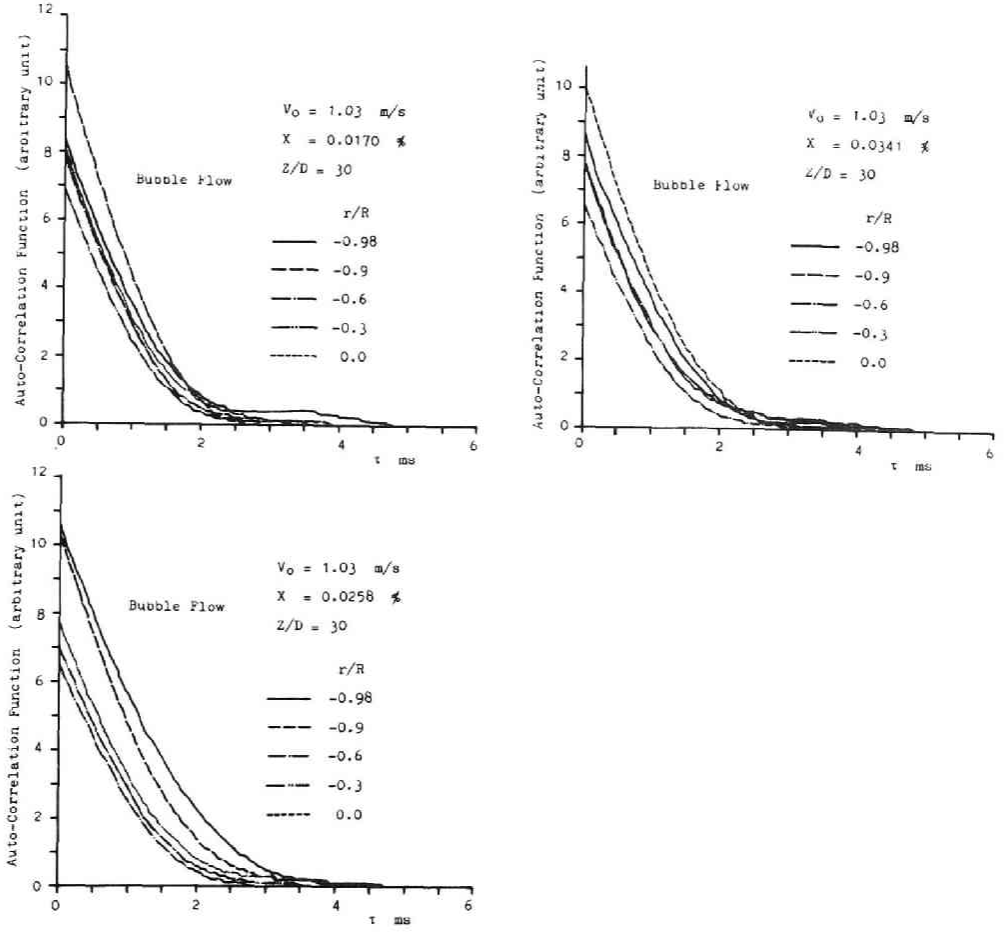

Fig. 4.27 Auto-correlation function of density fluctuation (effect of flow pattern : V_o=1.03 m/sec)

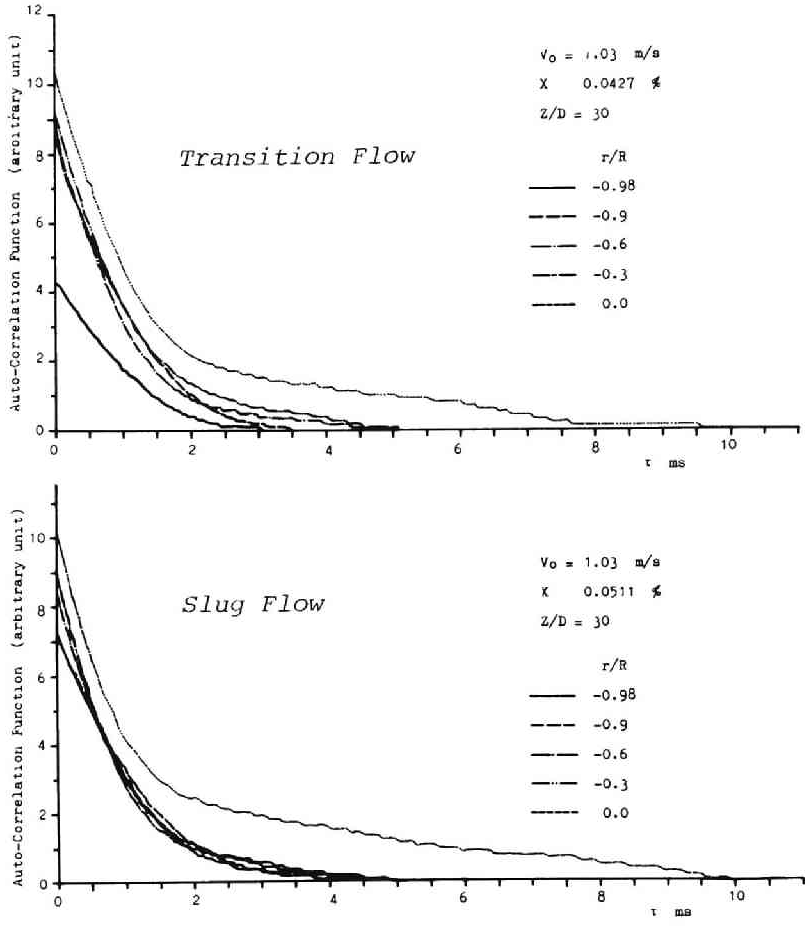

Fig. 4.28 Auto-correlation function of density fluctuation (effect of flow pattern : V_O=1.03 m/sec)

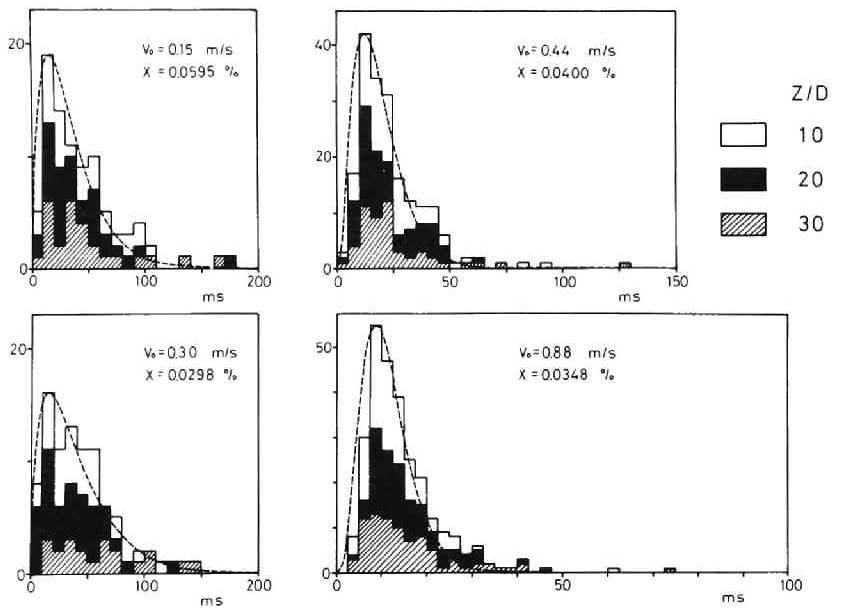

Fig. 4.29 Distribution of the time interval between bubble impingements on void probe (bubble flow : dotted lines represent Poisson distributions)

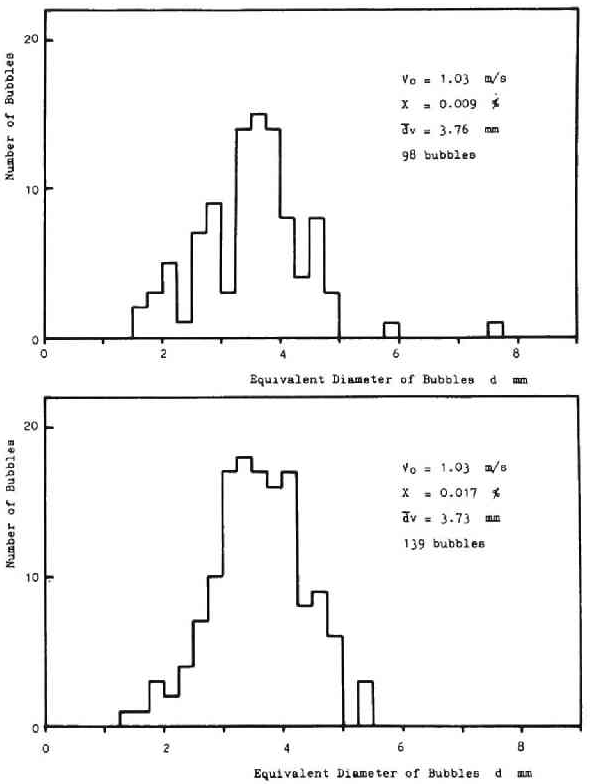

Fig. 4.30 Bubble size distribution

4.6 Profiles of Void Fraction and Bubble Impaction Rate

As cited earlier in Chapter III, a train of single bubbles introduced into a flowing stream tends to occupy the central position with minor deviation in all directions. As the number of bubbles increases, they may collide, adhere, and coalesce, and deviations may also increase. Therefore, an arrangement of bubbles may be expected to approach a regular order, depending upon their size relative to the pipe diameter and also depending upon the flow conditions or flow pattern. This process of flow arrangement has been already described in Section 4.4 in terms of the entrance effects on the distributions of the time average local void fraction and bubble velocity.

For the structural analysis of the flow or the cross sectional distribution of bubbles, our interests have been concentrated on describing the time average distribution of the local void fraction in fully-developed flow region rather than the arranging process of the flow. Practically, a number of experimental studies relating to this distribution across a pipe cross section have been carried out for various sets of gas-liquid two-phase flow. Nevertheless, almost no theoretical treatment has succeeded in accounting for the phenomena mainly for the lack of detailed information. Mere intuitive consideration follows that the local void fraction may be well defined by the local velocities of bubbles and liquid, and also by the number and the size of bubbles.

In this section, depending upon our experimental results, we will describe the distributions of the time-average local void fraction and the bubble number (in terms of the bubble impaction rate) for fully-developed two-phase flow.

4.6.1 Void Fraction Profile

Void fractions were measured by means of the void probe at the upper part of the test section Z/D = 30, where fully-developed flow was

already established. In order to clarify the characterizing properties of the void fraction profiles, traverses were made with various air and water flows in the bubble flow, the transition flow, and the slug flow regions.

Examples of the local void fraction distribution obtained are shown in Figs.4.31 to 4.35. In these figures, the distribution of the void fraction is shown to be a strong function of the flow pattern, and to change from saddle-shape distribution to parabolic-shape, as the gas flow or the quality increases for constant water velocity. (A saddle-shape distribution corresponds to bubble flow, and a parabolic-shape slug flow.) A similar trend in the void fraction profiles is reported to have been observed by Malnes[5], Kobayashi et al.[9], Aoki et al.[10], and Sekoguchi et al.[36] for air-water flow, by Kazin[12] for steam-water without heat addition, by Neal[14] for nitrogen-mercury, and also by Tamao[15](Figs.3.22 and 3.23 given in PART I of the present thesis) for argon-mercury flow.

The parabolic-shape distribution is perhaps due to the following reasons: that is, with increasing the quality, smaller bubbles tend to collide, adhere, and coalesce more violently to form larger bubbles (so called slugs or Taylor bubbles) which apt to ascend in the central core region of the pipe as stated in Paragraph 4.5.1. The trailing smaller bubbles, influenced by the wake of the leading slugs, tend towards the pipe axis. In addition, the bubbles are gradually concentrated in the central, high velocity region of the flow by the Bernoulli effect*. Thus, the void fraction distribution in slug flow shows a maximum concentration of gas bubbles towards the pipe center.

The peaking phenomenon of the local void fraction was observed in the vicinity of the pipe wall commonly in the low quality region (i.e., the bubble flow region). The effect of increasing the quality at con-

---

* The Bernoulli effect is a speeding up of the less dense phase relative to the more dense phase in an accelerating flow. Exposed to the same pressure gradient, the less dense phase attains a higher velocity than the more dense phase (by L.S.Tong[37]).

stant water velocity is to decrease the peak value of the void fraction near the wall relatively to the value at the pipe axis. A detailed inspection of the phenomenon reveals that the peak exists at the position away from the wall by a distance of nearly mean bubble radius. This result coincides with those obtained by Kobayashi et al. and also by Aoki et al. in air-water flow[9,10]. However, Kazin reported, in his paper, the similar peaking phenomenon existing nearly at r/R = o.6 for upward steam-water flow, and he tried to account for the phenomenon theoretically by introducing an equation of force balance acting on a single bubble[12]. (Neal showed experimentally the existence of the maximum gas fraction at the wall[14]. But this is slightly different from the above mentioned phenomenon, and, perhaps, it may be the result of the non-wetting character of mercury and, hence, the partial absence of a liquid film at the wall, just like his description.) This peaking phenomenon in the void fraction distribution may well be evaluated from the experimental peak of the bubble impaction rate near the wall (see Fig.4.37) and the lower velocity of bubbles there characterized, for instance, by a power-law type velocity distribution, as shown in Fig.4.60 (and, hence it may not be due to the Segre & Silberberg effect for dilute suspensions of neutrally buoyant rigid spherical particles in a Newtonian liquid moving in Poiseuille flow in tubes*).

Some comparisons were made between the experimental results of the present work and the empirical correlations proposed by Petrick & Kudirka[2] and Kobayashi et al.[9].

Petrick and Kudirka correlated their atomospheric air-water void fraction distribution data by assuming a power-law distribution between the local void fraction and the position in the channel:

$$\alpha_{loc} / \alpha_c = (1 - r/R)^m \quad ,$$

---

* Segre & Silberberg[38,39] showed, by means of a numerous series of experiments, that particles migrate, admittedly slowly, into a thin annular region concentric with the tube axis at a radius about 0.6 of the tube radius.

$$m = \{\ 0.024\ (V_l)^{3/2}\ \}\ /\ \bar{\alpha} \qquad (4.3)$$

where α_{loc}, α_c, $\bar{\alpha}$, and V_l are the local void fraction, the void fraction at the pipe centerline, the void fraction averaged over the cross-section, and the superficial water velocity (ft/sec), respectively.

Kobayashi et al. obtained the following empirical equations for vertical upward air-water flow, with an aim of accounting for the peaking phenomenon of the void fraction held in mind, which takes the effect of the bubble radius into consideration:

$$\frac{\alpha_{loc}}{\alpha_c} = \{y^{\dagger}\}^{(1/ay^{\dagger})} + n\ y^{\dagger}\ \exp(-1y^{\dagger}) \quad , \qquad (4.4.a)$$

$$\alpha_c = \frac{1.5\ (\log 100\ \frac{\beta}{1-\beta})^{2.7}}{1 + 0.75\ (\log 100\ \frac{\beta}{1-\beta})^{2.7}} \quad , \qquad (4.4.b)$$

$$\left.\begin{aligned} a &= 200\ \beta^{1.5} \quad , \quad 1 = 1.3\ (D/d), \\ n &= 0.01\ (D/10)^{3.3}\ \beta^{-1.8} \end{aligned}\right\} \qquad (4.4.c)$$

$$\text{for} \qquad \beta > 0.006\ (D - 15), \quad D > 15 \ , \qquad (4.4.d)$$

where $y\dagger = 1 - (r/R)$, and β, D, and d are the ratio of the volumetric gas flow rate to the total flow rate ($= Q_g/(Q_g + Q_l)$), pipe diameter (mm), and the major diameter of bubbles (mm), respectively.

As illustrated in Fig.4.36, Eq.(4.3) proposed by Petrick et al. is incapable of reflecting the peaking phenomenon, while the correlation of Kobayashi et al. seems to represent qualitatively well its characteristic trend, especially in the lower gas flow rate regions of bubble flow, but it does not always give a quantitatively satisfactory agreement with the experimental results even in the bubble flow region*.

---

* See footnote on next page.

4.6.2 Bubble Impaction Rate

The bubble number distribution (or the spatial distribution of the mean bubble frequency) is closely related to the void fraction distribution, as already mentioned. At the same time, interests as to the bubble migration process in turbulent bubble flow are intended to the measurement of the bubble number distribution across the pipe.

Several traverses were made of this quantity. Typical bubble number distributions are represented in Fig.4.37 in terms of the bubble impaction rate, of which trends are shown to be very similar to those of the void fraction distributions. Namely, the bubble number distribution is saddle-shape in the bubble flow region, whereas parabolic-shape in the slug flow region. The peaking phenomenon near the wall was observed also in the bubble number distribution correspondingly to that of the void fraction distributions. By means of a numerous series of experiments on the mean bubble frequency distribution, Lackme[6] has shown that a higher frequency in bubble passages near the wall is confined to the lower gas flow rate region. Sekoguchi et al.[40] carried out the measurements of the bubble distribution in an accelerated air-water flow in a vertical pipe, minicing a boiling flow by introducing air bubbles along the pipe axis through the porous wall of the test section. They observed two kinds of maximum bubble frequencies at the points corresponding to the maximum void fractions near the wall. First kind of the maximum is due to the wall bubbles, and the second due to just the same phenomenon as interested here.

This phenomenon of the bubble migration towards the wall may be qualitatively accounted for by the following reasons:

1) Magnus effect[41] due to the large gradient of the liquid velocity

---

* For D = 60 mm, Eq.(4.4.d) gives $\beta > 0.270$, while Figs.4.36(a), (b), and (c) correspond to β = 0.103, 0.261, and 0.236, respectively. Hence, the comparisons are merely for reference, although any theoretical or analytical validity for the limiting range defined by Eq.(4.4.d) cannot be found anywhere in the original paper.

near the wall,

2) Effect of the radially changing turbulent diffusivities of bubbles and liquid,
3) Interactions between bubbles and the wall (i.e., adherence or reflection of bubbles at the surface of the wall) which perhaps depend upon the colloidal contaminants at the interface between the gas bubbles and the liquid.

However, up to date, hydrodynamic forces acting on a gas bubble or a rigid spherical particle (for instance, Magnus force and Zhukovski force*[42]) have been often studied both theoretically and experimentally[42-45], the problems still remain unsolved for applying the results of those investigations to the analysis of the peaking phenomenon of the bubble distribution in two-phase bubble flow.

4.6.3 Summary and Conclusions

Measurements of the distributions of the void fraction and the bubble impaction rate across the pipe have revealed the followings:

1) The void fraction distribution is characterized by a saddle-shaped distribution for bubble flow, and by a parabolic-shaped for slug flow.
2) The peaking phenomenon of the void fraction distribution in the bubble flow region is found around the point away from the wall by a certain distance of nearly the mean bubble radius.
3) This peaking phenomenon is due to both the existence of the maximum bubble number and the low bubble velocity there.
4) The bubble number distribution (the distribution of the bubble impaction rate) is very similar, in its trend, to the void fraction distribution without regard of the flow pattern.

---

* Teletov has shown, a bubble of steam on the inner wall of a tube is considerably influenced by the Zhukovski force created by the circulation of the fluid along the bubble surface, due to the action of the main flow (quoted from Ref.[12]).

5) The phenomenon of the maximum bubble number near the wall may be mainly due to the effects of the hydrodynamic forces acting on a bubble, such as the Magnus force and the Zhukovski force, and partly due to the interaction between a bubble and the wall. But any quantitatively fruitful solutions could not be obtained to this phenomenon.
6) Both aforementioned hydrodynamic forces and the wall effect (adherence or reflection of bubbles) must be studied further.

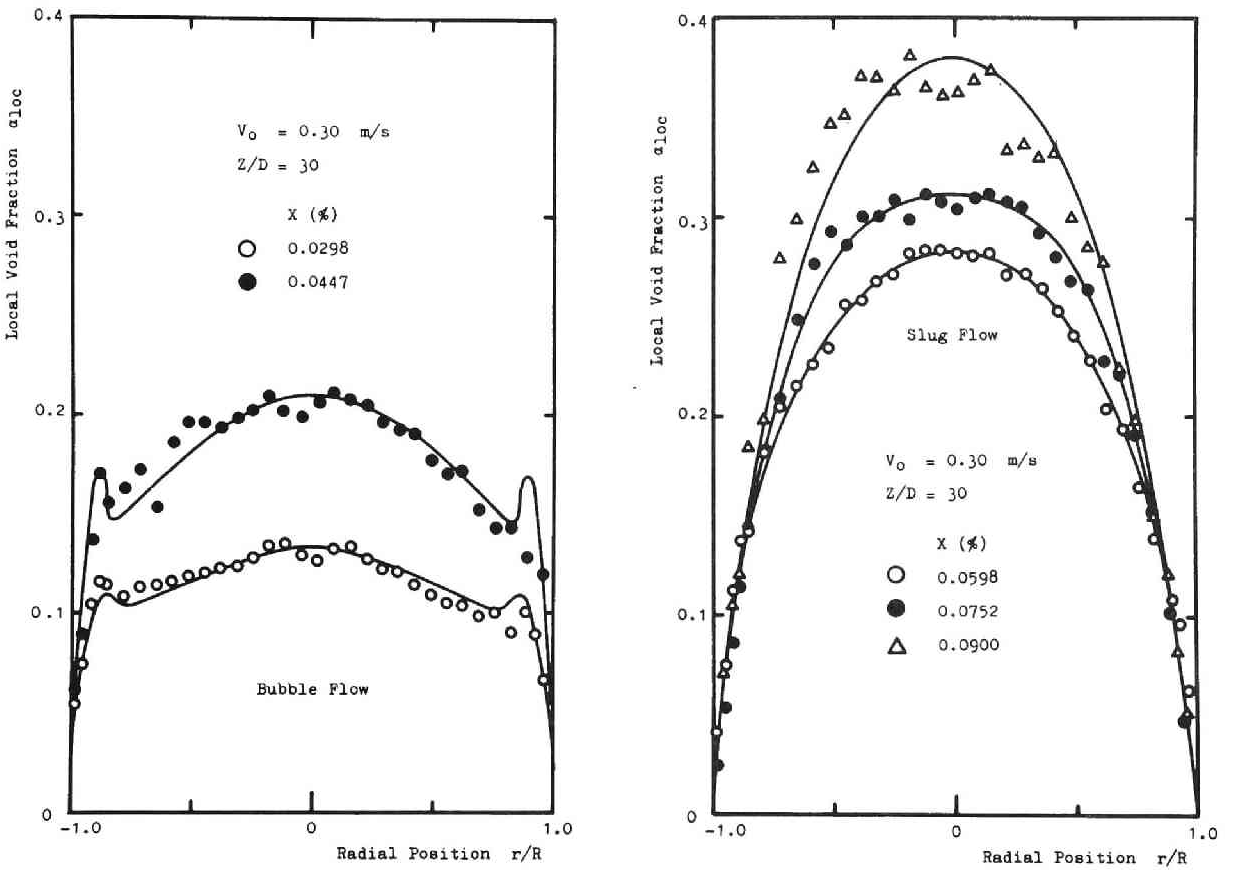

Fig. 4.31 Void fraction profiles

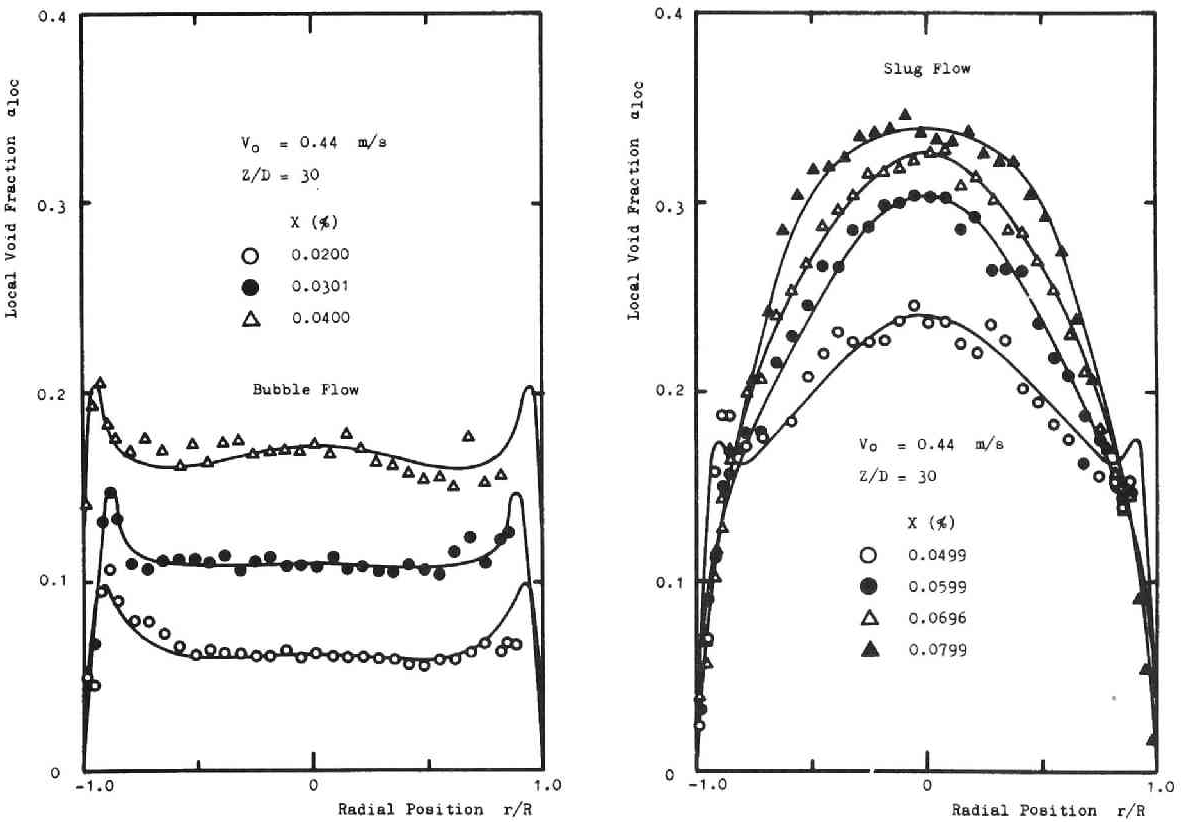

Fig. 4.32 Void fraction profiles

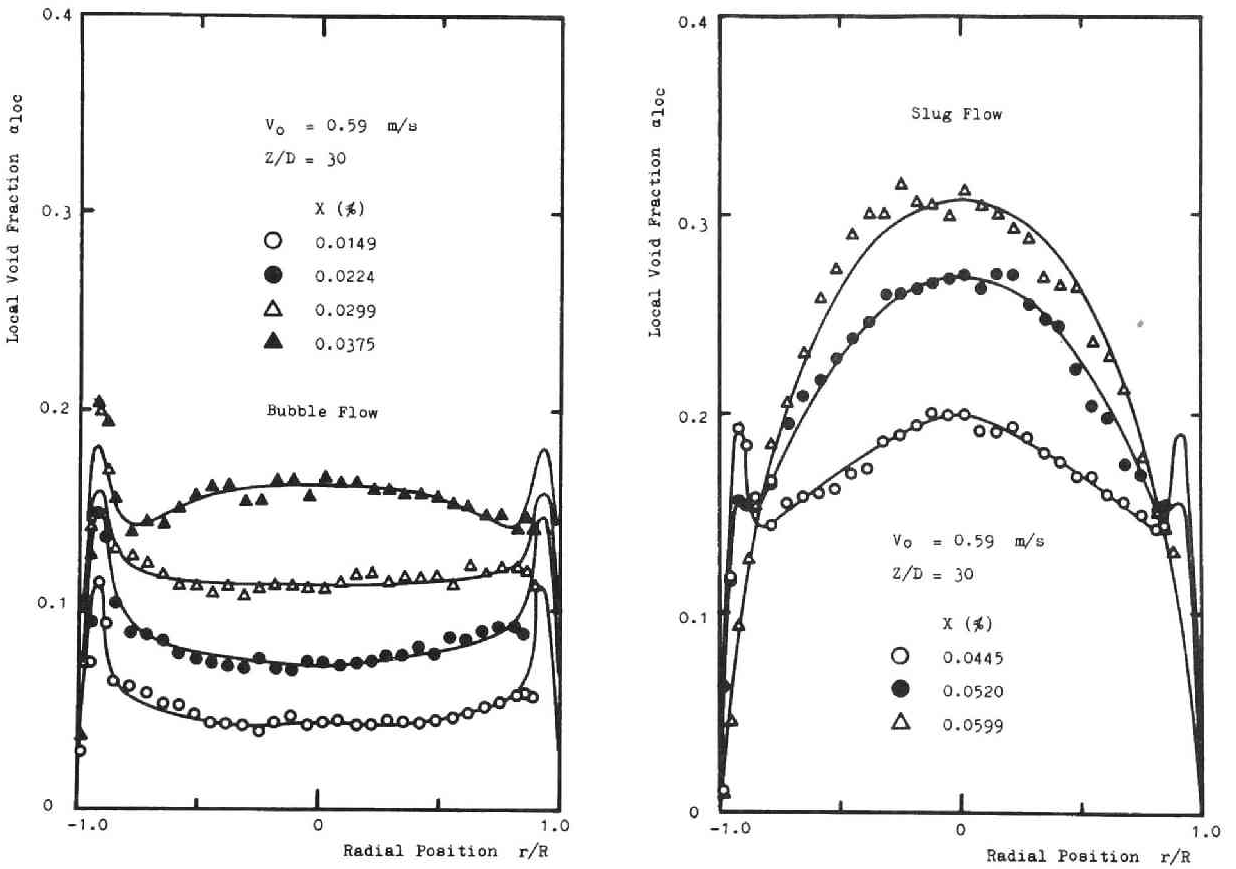

Fig. 4.33 Void fraction profiles

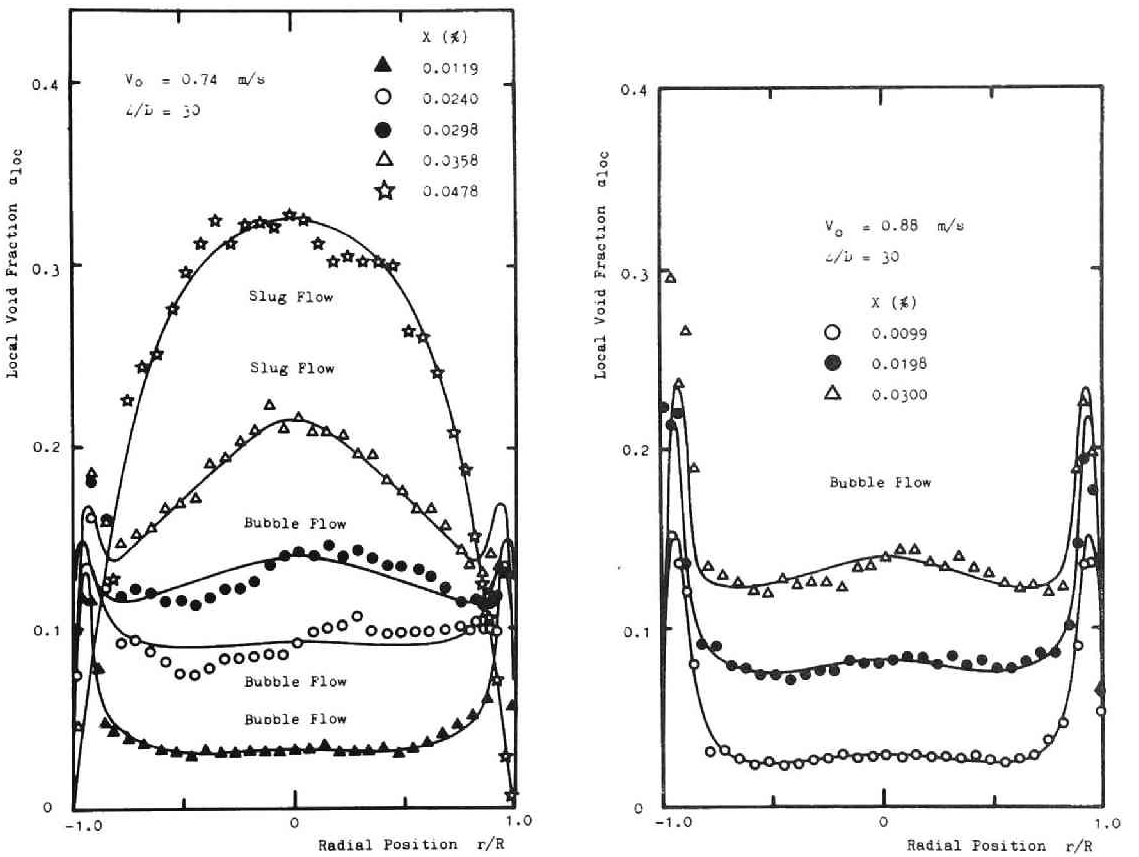

Fig. 4.34 Void fraction profiles

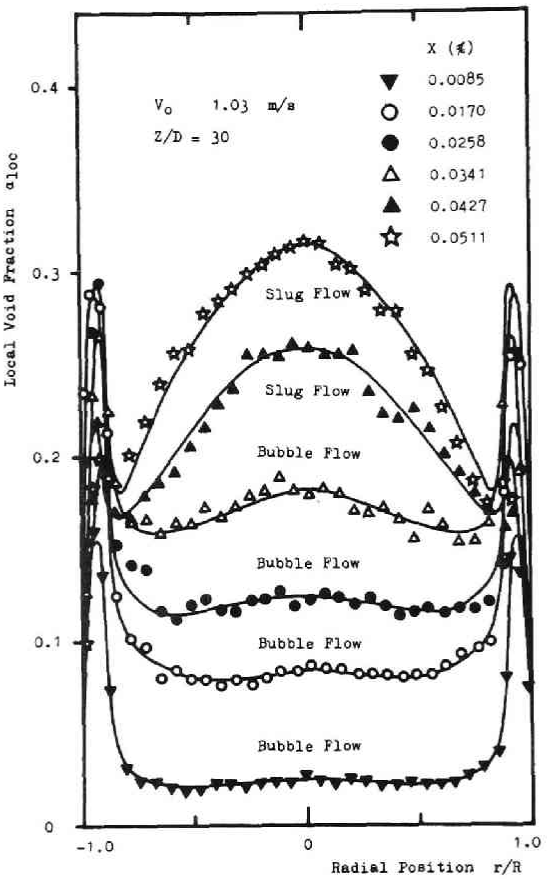

Fig. 4.35 Void fraction profiles

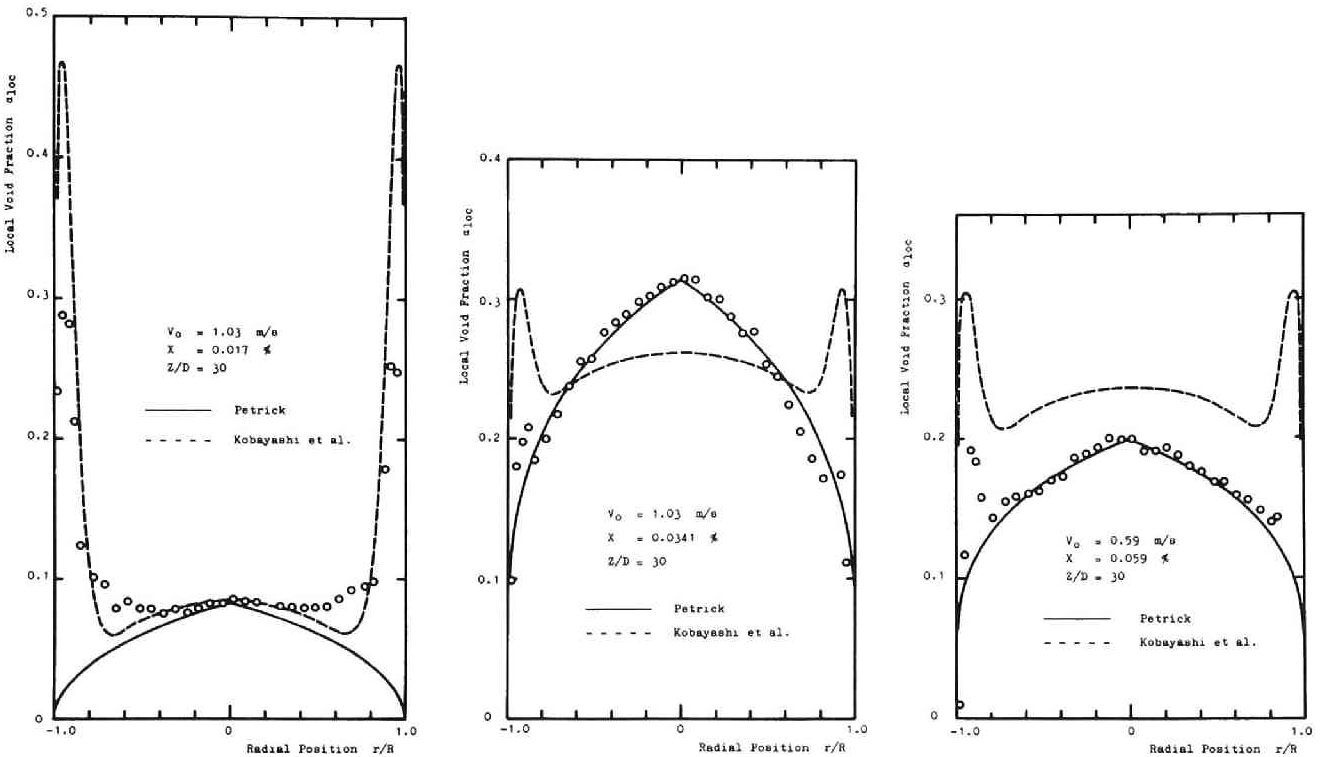

(a) (b) (c)

Fig. 4.36 Correlative representations of local void fraction

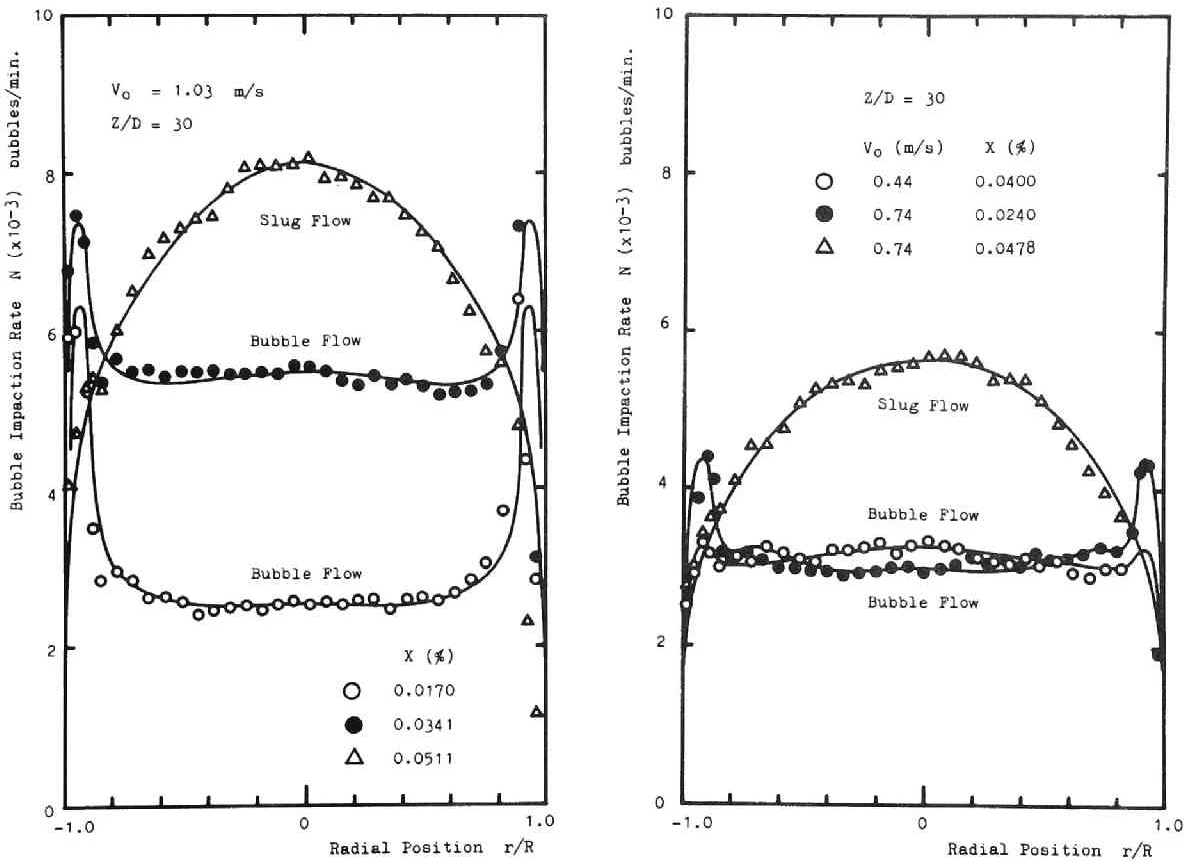

Fig. 4.37 Profiles of bubble impaction rate

4.7 Bubble Velocity and Its Spectrum

When a number of bubbles are flowing in the stream as suspended particles, their spatial distribution is affected by their velocity (or vice versa), as pointed out previously. The experimental relationship between the phase distribution and the bubble distribution was already described briefly, in respect to the peaking phenomenon of the bubble distribution near the wall.

The velocity profile of the flowing liquid, which plays an important role in the frictional pressure drop of the flow, is also influenced seriously by the velocity of the leading bubbles. And the wall pressure fluctuation, mainly due to the liquid velocity fluctuation, is affected indirectly by the fluctuating characteristic of the bubble velocity.

Inversely, the bubble velocity profile may be expected to be determined by the liquid velocity profile, the bubble distribution, the wall effects, and the interactions among bubbles, and all of these apt to influence each other. Therefore, we cannot but obtain the knowledge of the bubble velocity from the elaborated experimental works.

4.7.1 Bubble Velocity Spectrum

The bubble velocity spectrum was measured by Kitayama[46] and Kobayashi et al.[11] (by means of an electrical resistivity probe method) for vertical air-water flow in a pipe. But they merely presented the velocity histgrams for some tens or a few hundreds bubbles picked up and measured individually by random sampling method, and, hence, strictly speaking, their results can neither indicate the true bubble velocity spectrum nor offer any reliable information about it partly due to their poor counting statistics of the sampled bubbles and partly due to the discontinuous sampling methods.

The true bubble velocity spectrum was measured first by the author and others[20,47] with use of a double-probe by multi-channel technique. By this technique, we can easily obtain the bubble velocity

spectrum by measuring the velocities of all the bubbles that continuously pass over the measuring station during a given measuring time interval. In all experimental runs, 3 ~ 20 minutes was chosen for the measuring time interval according to the number of bubbles passing over that point, so that the results may have a statistical meaning.

Figures 4.38 to 4.44 represent the change of the bubble velocity spectrum along the flow direction measured at different radial positions for several flow conditions. In these figures, the major trend of the bubble velocity spectra is shown. Namely, those spectra are not seriously influenced by the entrance effect with the exception of this effect upon their standard deviations as already shown in Figs. 4.21 and 4.22.

Figures 4.45 to 4.58 represent the dependences of the bubble velocity spectrum both upon the flow rates of the gas and the liquid and upon the radial position, which were taken at the station Z/D = 30 in fully-developed flow region. They demonstrate the following two distinct characteristics:

1) bubble flow region; no significant spatial dependence can be seen directly from these figures,
2) slug flow region; the bubble velocity spectrum shows, for region near the wall, a similar trend to that observed in the bubble flow regime, and for the central core region of the flow a distorted curve due to the flowing slugs - this coincides clearly with the fact that a large slug tends to ascend rather in the central core region of the flow, as mentioned in Paragraph 4.5.1.

In order to speculate these two characteristics, typical spectra taken at the center of the pipe are given in Fig.4.59 for several qualities. Solid lines drawn for each spectrum represent the Poisson distribution functions fitted to each spectrum owing to the fitting procedure proposed by Petrick[1]. These correlative representations indicate that the bubble velocity spectrum at the pipe center line can be well approximated by the Poisson distribution function in the bubble

flow region, while in the slug flow region, it tends to deviate from that distribution due to the existence of slugs flowing at higher velocities than smaller bubbles.

4.7.2 Radial Profile of Bubble Velocity

Bubble velocity distribution across the pipe cross section was calculated from the aforementioned experimental results of the bubble velocity spectrum in conformity to the following relating equation:

$$V_b(r) = \sum_i N_i V_{bi}(r) \Big/ \sum_i N_i \quad . \tag{4.5}$$

Thus obtained bubble velocity distributions are presented in Fig. 4.60 to 4.62*, together with the corresponding relative standard deviations of the bubble velocity spectra defined as below:

$$s/V_b = \sqrt{\sum_i N_i (V_b - V_{bi})^2 / \sum_i N_i} \Big/ V_b \quad , \tag{4.6}$$

where s is the (absolute) standard deviation.
From these figures, it may be concluded to be expedient to approximate the bubble velocity distribution by the power law expression similar to the normal turbulent velocity profile, with regardless of the flow pattern or the peaking phenomenon of the bubble distribution near the wall**.

In consideration of the flow structure, the standard deviation of the bubble velocity spectrum is one of the most important variables,

---

* Bubble velocity profile for V_o = 1.03 m/sec, X = 0.0511 % shown in Fig.4.60 appears somewhat incomplete perhaps due to signal failure, as the case may be.

** Malnes (steam-water)[5] and Lackme (air-water)[6] obtained the similar results, using a double-probe by correlation technique. On the other hand, the work of Aoki et al.[10] shows that a slight peaking exists near the wall. But this peaking may be perhaps attributable to the inaccuracy involved in their measuring method.

which corresponds to the turbulent intensity (root mean square of the turbulent fluctuating velocity) of the liquid phase (in this sense, the standard deviation of the bubble velocity spectrum can be defined as the apparent mean fluctuating velocity of bubbles).

The distributions of the relative standard deviation of the bubble velocity spectrum are illustrated in Figs.4.60 ~ 4.62, together with the corresponding bubble velocity profiles. These experimental results indicate considerably larger values of the deviations in the region near the wall than those at the pipe axis, and also indicate uniform distributions over a large portion of the flow area. These trend are more remarkably seen especially in bubble flow of a higher superficial water velocity.

In the bubble flow region, the value s/V_b generally increases with increasing the quality for constant flow rate of water. This is partly due to the rated-up mixing actions by more densely concentrated bubbles, and is partly due to the rated-up interactions between bubbles. In the slug flow region, the distribution tends to be raised towards the pipe center owing to the fact that the trailing smaller bubbles, flowing up even along the wall at lower velocities, are influenced by the wake of the leading slugs to be concentrated towards the pipe axis and to be accelerated.

The effect of increasing the water velocity for constant quality is to decrease the bubble velocity fluctuation. This may be accounted for by a concept that, as the water velocity is increased, the fluctuating motions of bubbles suspended in the stream come to be relatively suppressed by the intensified inertia force of the water. As shown in Fig.4.62, a considerable peak, observed towards $r/R = -0.7$ in some cases of a lower flow rate of water ($V_o = 0.44$ m/sec), is perhaps related to the conflict between this effect (i.e., the effect of the inertia force of water) and the bubble-suction effect of the leading slugs.

4.7.3 Local Slip Velocity and Local Slip Ratio

Accurate and reliable information about the local slip velocity of bubbles and the local slip ratio between two phases are quite essential to two-phase flow investigations, and it gives us some basic insights into the surface conditions of bubbles or the degree of interactions between two phases.

For a circular channel of radius R, and rotationally symmetric flows, the local slip velocity $V_s(r)$ is defined by the equation,

$$V_s(r) = V_b(r) - V_l(r) \tag{4.7}$$

where $V_b(r)$ and $V_l(r)$ are the ensemble-average local bubble velocity and the time-average local liquid velocity, respectively. Slip ratio is defined in two ways. The first one is the local slip ratio $S_{loc}(r)$ caused by the true local slip velocity $V_s(r)$, whereas the other is an apparent slip ratio (or the overall slip ratio) S based upon the cross sectional average velocities of two phases.

$$S_{loc}(r) = V_b(r) \;/\; V_l(r) \tag{4.8}$$

$$S = \frac{\overline{V}_g}{\overline{V}_l} = \frac{X}{1 - X} \frac{1 - \overline{\alpha}}{\overline{\alpha}} \frac{\rho_l}{\rho_g} \tag{4.9}$$

where $\overline{V}_g$, $\overline{V}_l$, and $\overline{\alpha}$ are the cross sectional average velocities of the gas and the liquid phases, and the cross sectional average void fraction, defined respectively by the following corresponding equations.

$$\overline{V}_g = \int_o^R 2\pi r \, \alpha_{loc}(r) \, V_b(r) \, dr \;/\; \pi R^2 \, \overline{\alpha} \tag{4.10.a}$$

$$\overline{V}_l = \int_o^R 2\pi r \, (1 - \alpha_{loc}(r)) \, V_l(r) \, dr \;/\; \pi R^2 \, (1 - \overline{\alpha}) \tag{4.10.b}$$

$$\overline{\alpha} = \int_o^R 2\pi r \, \alpha_{loc}(r) \, dr \;/\; \pi R^2 \tag{4.10.c}$$

In earlier works on two-phase flow, original intention has been to measure the usual time and channel cross sectional averages, as already described in PART I. Some of the analytical models for predicting the average void fraction are based upon the assumptions concerning the local slip velocity or the local slip ratio. Bankoff[48] assumed the local slip velocity to be zero and further assumed power law distributions of $\alpha(r)$ and $V_l(r)$. Neal[14] introduced a local slip ratio which was assumed to be constant over the cross section. Nevertheless, to the present author's knowledge, the validity for those assumptions on local slip made by Bankoff and by Neal has never been discussed yet on the basis of the accurate measurements of such quantities. This may be due, to a large extent, to the limitations in measuring technique (irrespective of whether their analytical results may satisfactorily agree with experiments or not).

As a rule, the bubble slip velocity in axial direction is determined by the force balance among the hydrodynamic resistance (drag force), buoyant force, shear force of the stream, inertia force, and other forces induced by the complicated interactions between bubbles and their surrounding liquid or among bubbles. Therefore, it is quite important to provide accurate experimental data on the bubble slip, and, at the same time, to clarify the dependence of the bubble slip upon the flow condition.

Typical results of the present work are represented in Figs.4.63 ~ 4.65 in which both the local slip velocity and the local slip ratio are plotted against radial position with a parameter of the flow pattern (or the quality). The experiment shows nearly uniform distributions of the slip ratio for bubble flow* but the inflated of the slip velocity**.

Agreement between two cross sectional average slip ratios (one is

---

* The experimental work of Kobayashi et al.[11] will serve to confirm this observation.

** See footnote on page 312.

the overall slip ratio defined by Eq. (4.9), and the other is that calculated from the local slip ratio distribution according to Eq. (4.11)) is not usually satisfactory, since the variation of the local slip ratio exists especially towards the wall.

$$\bar{S} = \int_o^R 2\pi r\, \alpha_{loc}(r)\, S_{loc}(r)\, dr \;/\; \pi R^2 \bar{\alpha} \qquad (4.11)$$

As the quality is increased for constant water flow rate, the slip velocity generally increases and its profile becomes sharper (a lower slip velocity in the vicinity of the wall is the result of the wall effect which has been already mentioned in Paragraph4.6.2). The effect of the flow pattern seems to appear, but it is difficult to state it clearly.

4.7.4 Summary and Conclusions

On the basis of the experimental results, the followings are summarized:

1) The bubble velocity spectrum in bubble flow is well approximated by the Poisson distribution function.
2) The effect of slugs is to deviate this spectrum from Poisson distribution, especially in the central core region of the flow area.

** For reference, theoretical rise velocity of a single bubble in stagnant water has been proposed by Harmathy[49] in terms of the following expressions which take into consideration the effects of shape, properties, and the wall proximity.

$$V_s = 1.53 \{g(\rho_1 - \rho_g)\, \sigma/\rho_1^2\}^{1/4} K_2$$

$$K_2 = \frac{0.88 \{1 - (d/D)^2\}}{E_o^{1/4} \{1 + (d/D)^4\}^{1/2}} \left\{1 - \frac{2}{3}\left(\frac{E_o}{1 + E_o}\right)\left(\frac{d}{D}\right)^{3/2}\right\}$$

where $E_o = g(\rho_1 - \rho_g)\, d^2 / \sigma$ (Eotvos number).
For the present case, V_s is calculated to be 0.19 m/sec.

3) It is confirmed that the distribution of the ensemble average bubble rise velocity can be expressed by such a monotonous function as a power law expression. No significant peaking near the wall was observed in all experimental runs.
4) The effect of increasing the quality for constant water flow rate is to increase the bubble velocity. But the effect of the flow pattern was not observed.
5) Relative standard deviation of the bubble velocity spectrum generally increases towards the wall, and shows a considerable flattening over a large portion of the flow area, especially in the case of bubble flow.
6) Furthermore, this deviation increases with increasing the quality.
7) The local slip ratio is nearly uniformly distributed across the pipe cross section regardless of the flow pattern. But the local slip ratio does not always agree with the value of the overall slip ratio. This may be the result of the variation of the local slip ratio towards the wall.
8) The slip velocity profile becomes sharper with increasing the quality, and the wall effect upon this profile was seen.
9) The effect of the flow pattern upon the slip velocity of bubbles seems to exist, but details could not be clarified.

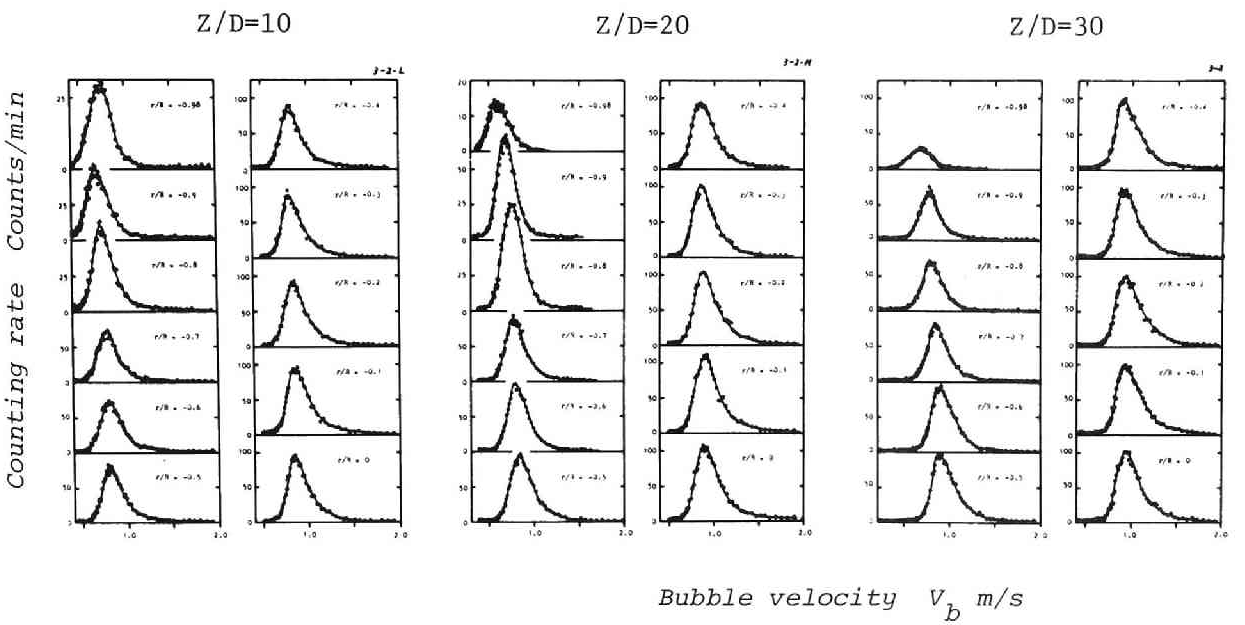

Fig. 4.38 Axial and radial variations of bubble velocity spectrum (V_o=0.44 m/sec, X=0.0200 % : bubble flow)

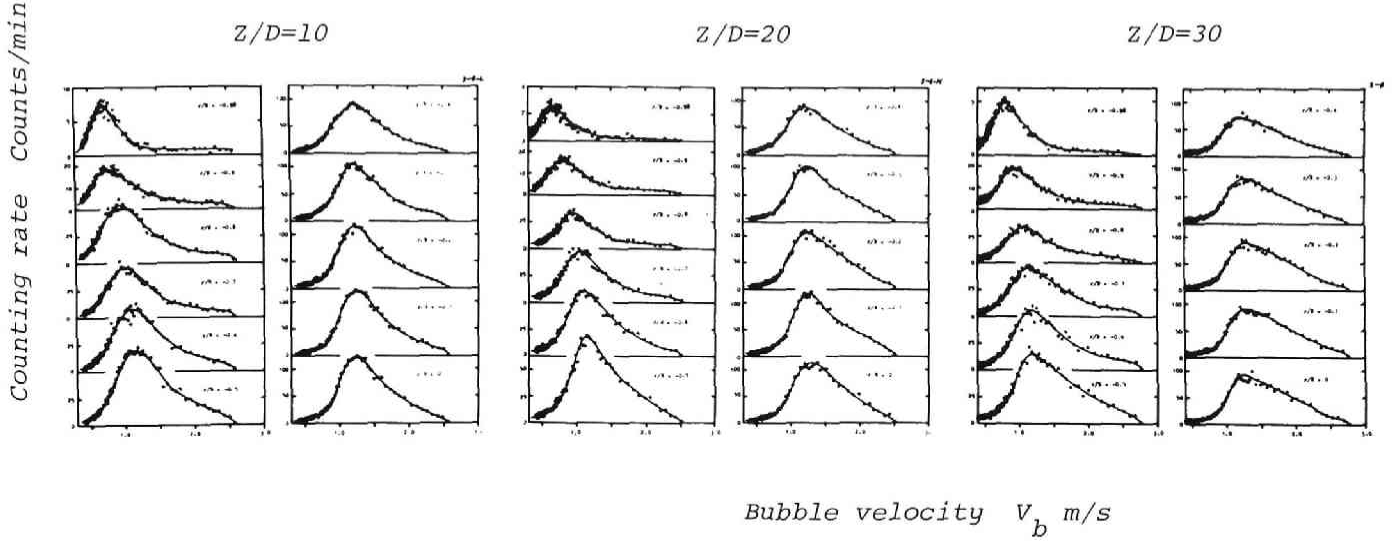

Fig. 4.39 Axial and radial variations of bubble velocity spectrum (V_o=0.44 m/sec, X=0.0599 % : slug flow)

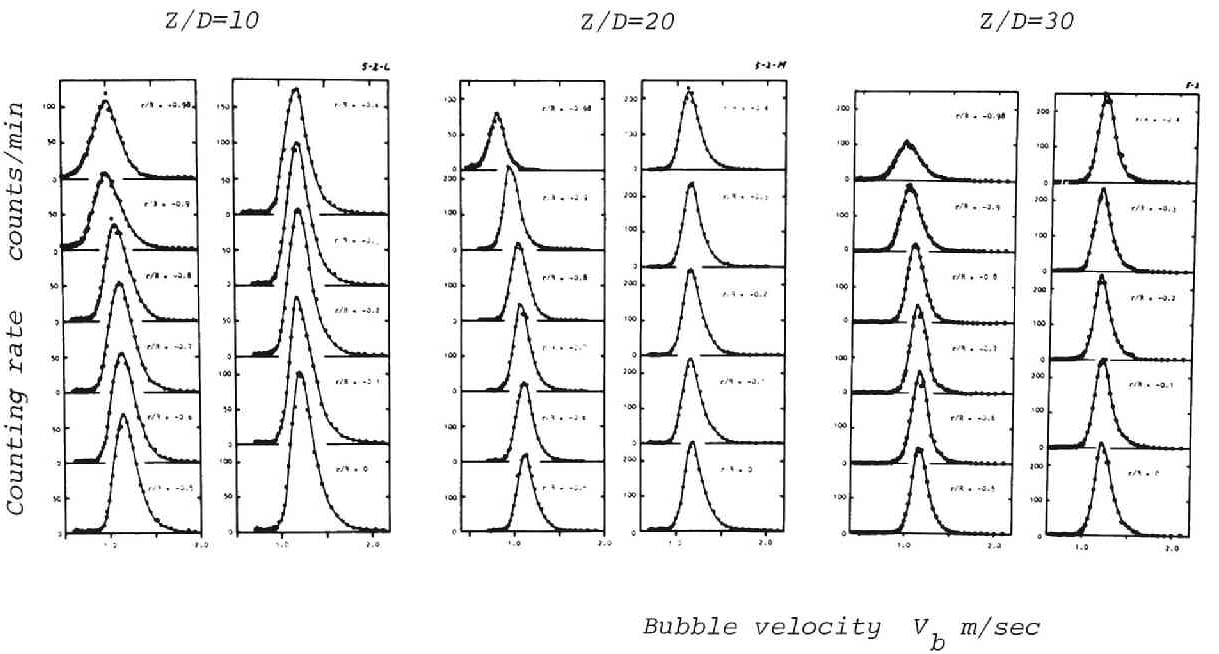

Fig. 4.40 Axial and radial variations of bubble velocity spectrum (V_o=0.74 m/sec, X=0.0240 % : bubble flow)

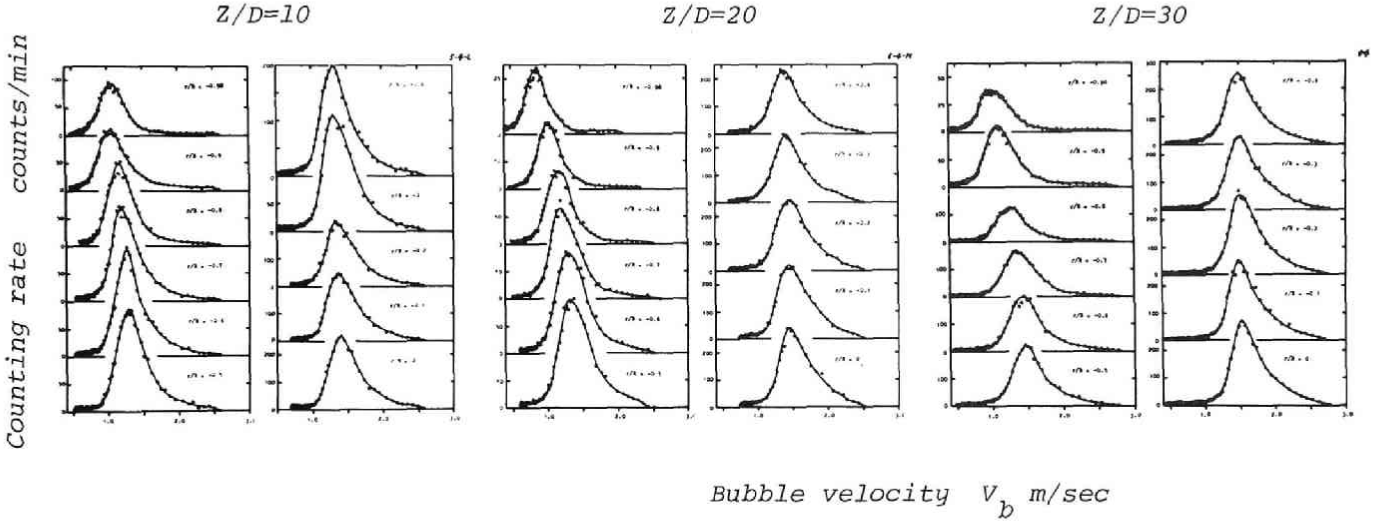

Fig. 4.41 Axial and radial variations of bubble velocity spectrum (V_o=0.74 m/sec, X=0.0478 % : transition flow)

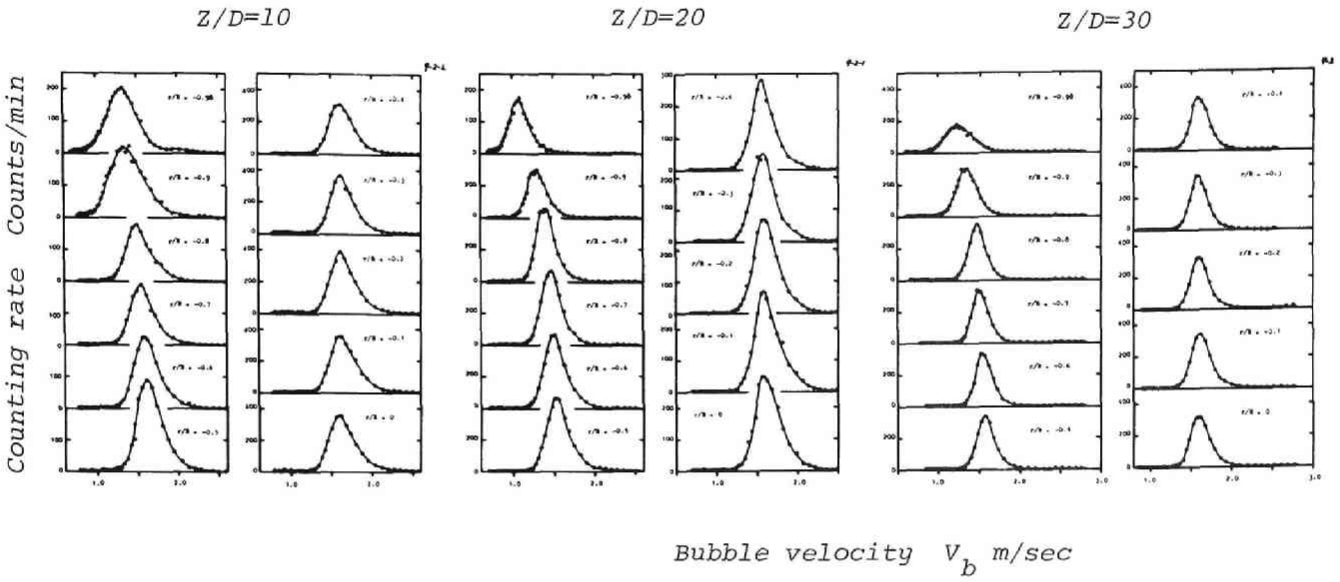

Fig. 4.42 Axial and radial variations of bubble velocity spectrum (V_o=1.03 m/sec, X=0.0170 % : bubble flow)

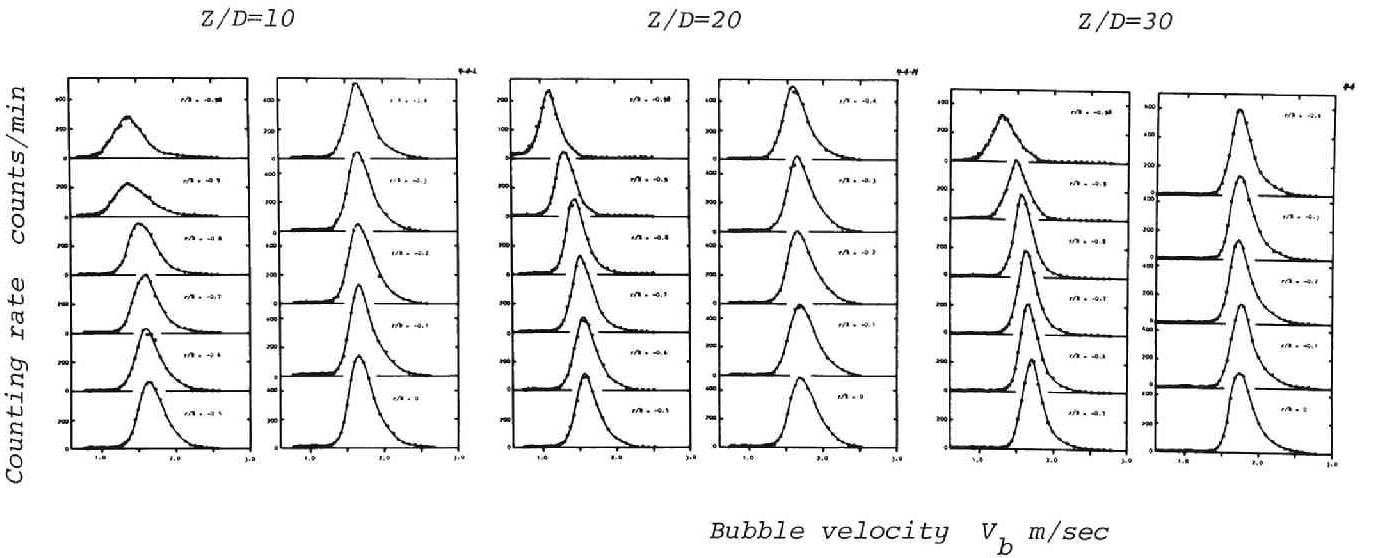

Fig. 4.43 Axial and radial variations of bubble velocity spectrum (V_o=1.03 m/sec, X=0.0341 % : bubble flow)

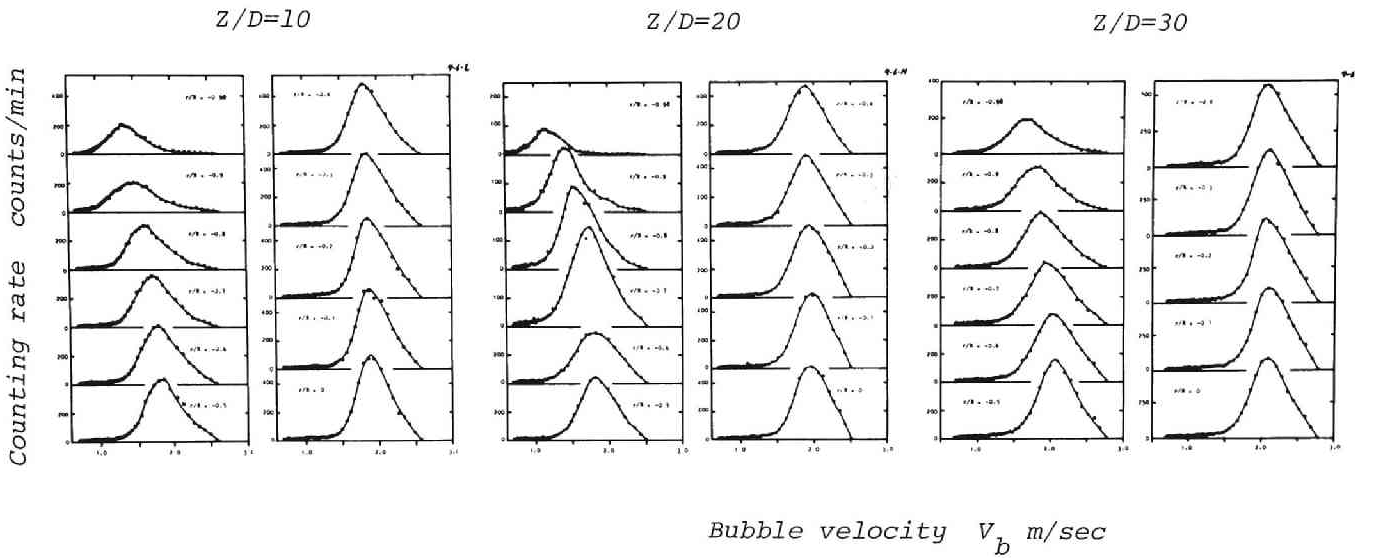

Fig. 4.44 Axial and radial variations of bubble velocity spectrum (V_o=1.03 m/sec, X=0.0511 % : slug flow)

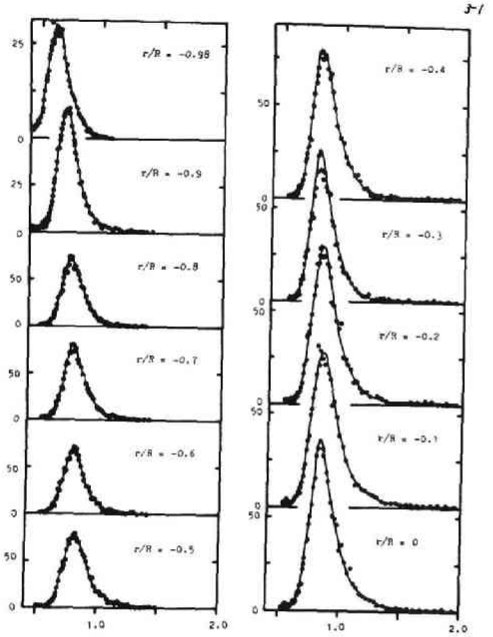

Fig. 4.45 Bubble velocity spectrum (Bubble flow : V_o=0.44 m/sec, X=0.0200 %, Z/D=30)

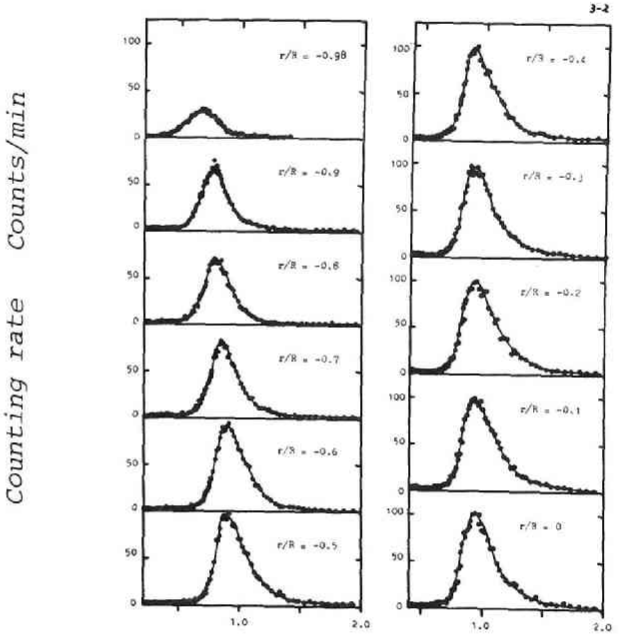

Counting rate Counts/min

Bubble velocity V_b m/s

Fig. 4.46 Bubble velocity spectrum (Bubble flow : V_o=0.44 m/sec, X=0.0400 %, Z/D=30)

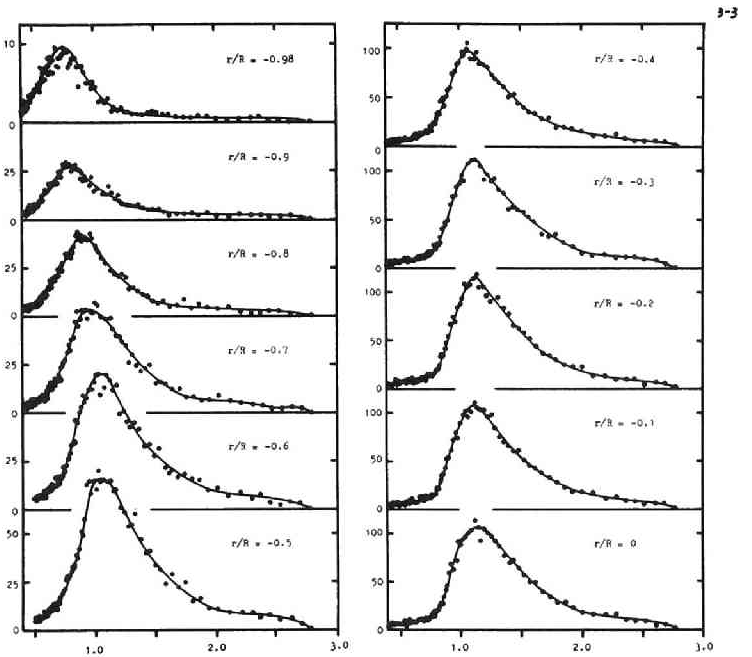

Fig. 4.47 Bubble velocity spectrum (Slug flow : V_o=0.44 m/sec, X=0.0599 %, Z/D=30)

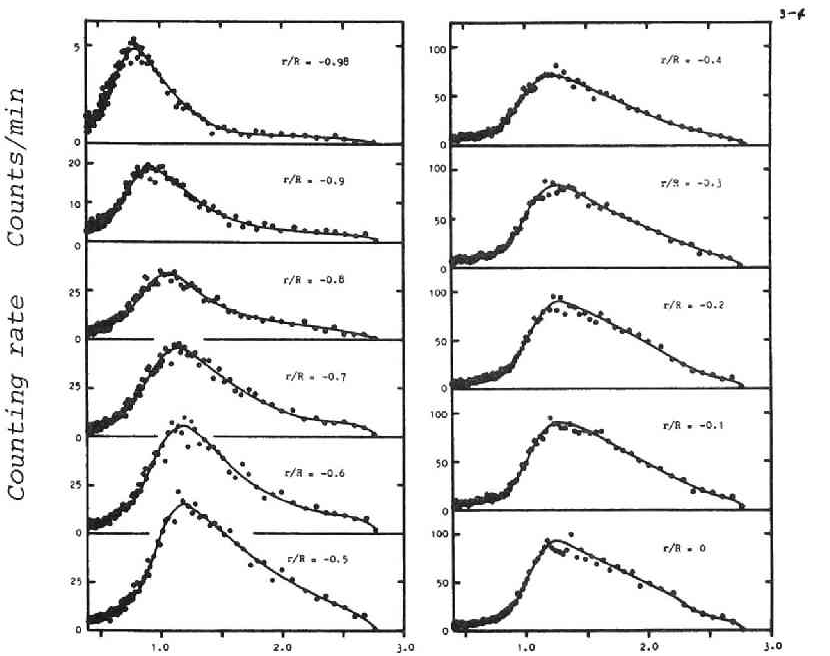

Fig. 4.48 Bubble velocity spectrum (Slug flow : V_o=0.44 m/sec, X=0.0799 %, Z/D=30)

Counting rate Counts/min

Bubble velocity V_b m/s

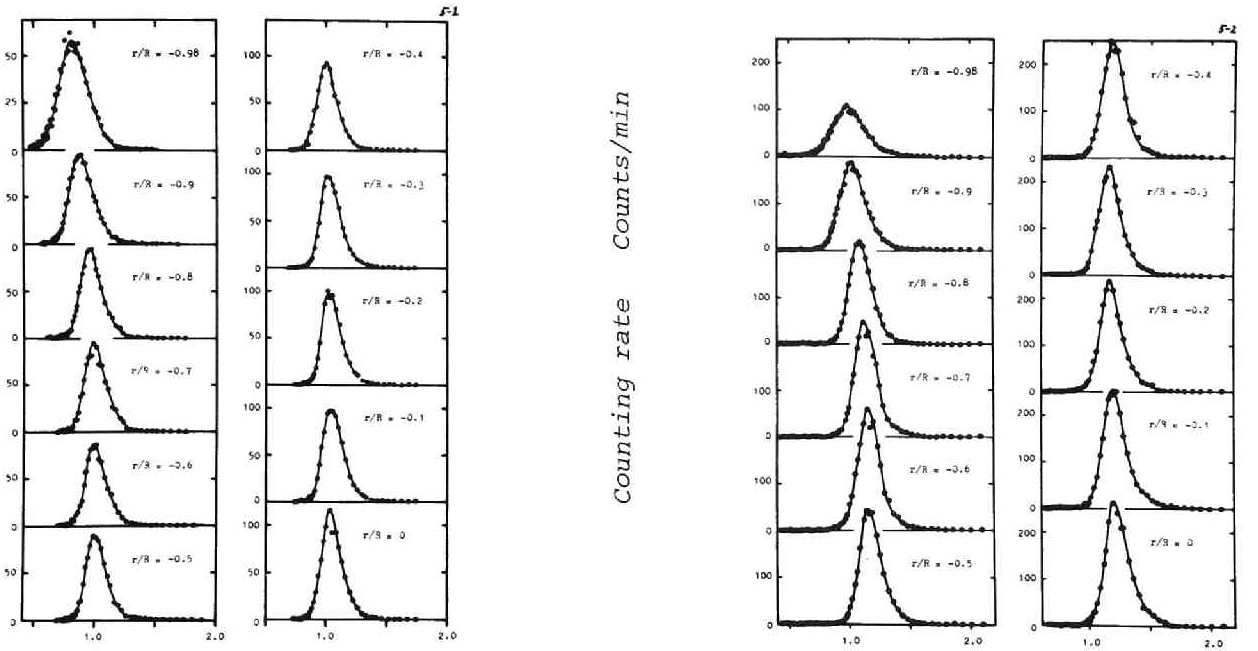

Fig. 4.49 Bubble velocity spectrum (Bubble flow : V_o=0.74 m/sec, X=0.0119 %, Z/D=30)

Fig. 4.50 Bubble velocity spectrum (Bubble flow : V_o=0.74 m/sec, X=0.0240 %, Z/D=30)

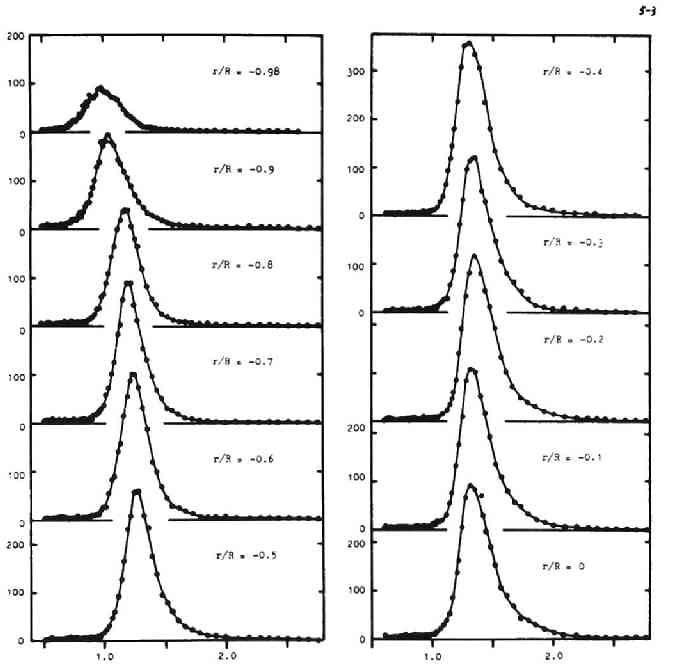

Fig. 4.51 Bubble velocity spectrum (Bubble flow : V_o=0.74 m/sec, X=0.0358 %, Z/D=30)

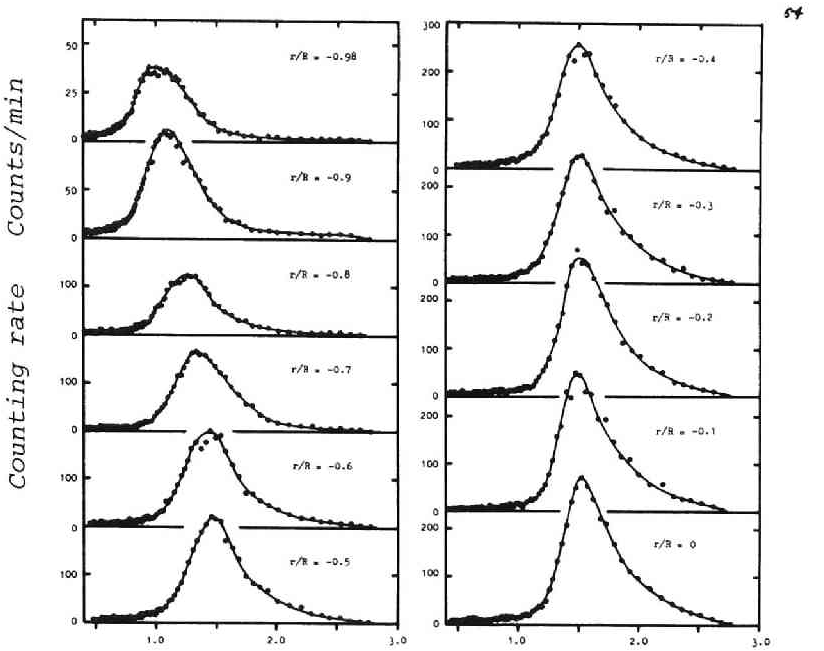

Fig. 4.52 Bubble velocity spectrum (Slug flow : V_o=0.74 m/sec, X=0.0478 %, Z/D=30)

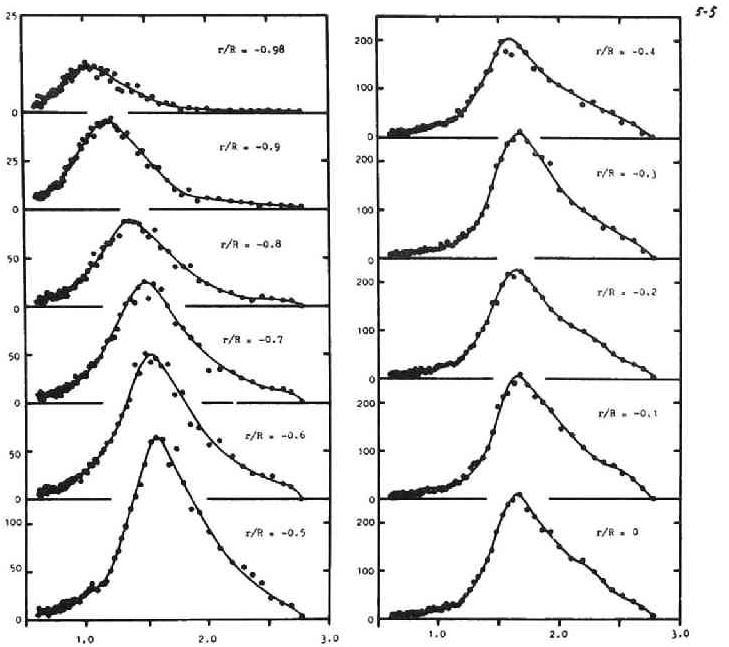

Fig. 4.53 Bubble velocity spectrum (Slug flow : V_o=0.74 m/sec, X=0.0598 %, Z/D=30)

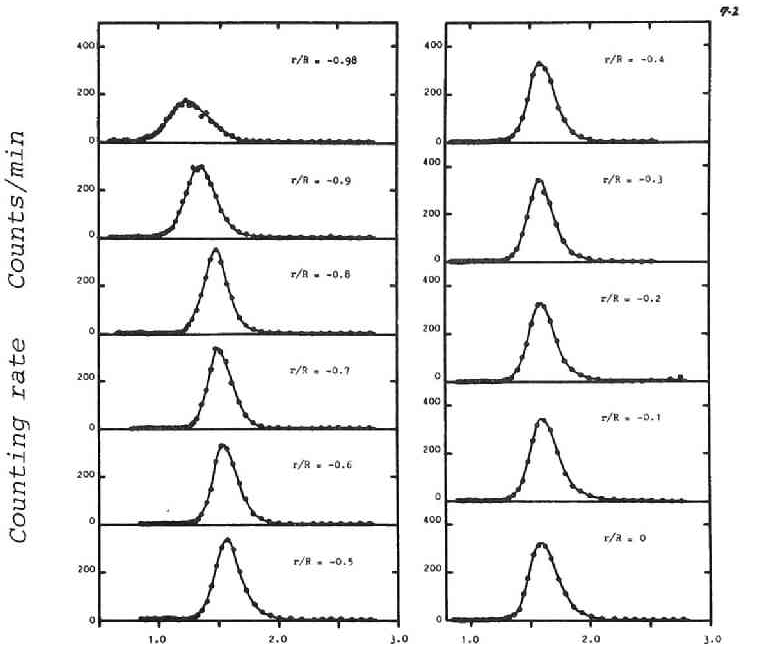

Fig. 4.54 Bubble velocity spectrum (Bubble flow : V_o=1.03 m/sec, X=0.0170 %, Z/D=30)

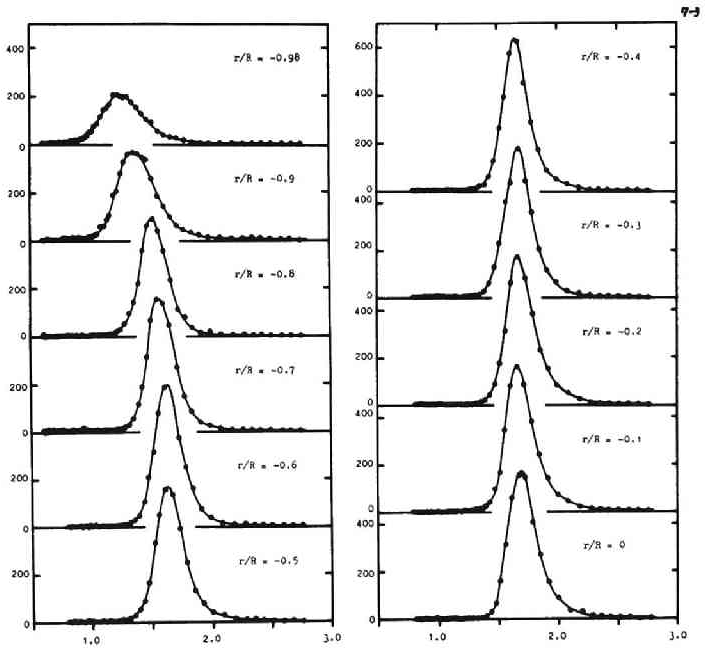

Fig. 4.55 Bubble velocity spectrum (Bubble flow : V_o=1.03 m/sec, X=0.0258 %, Z/D=30)

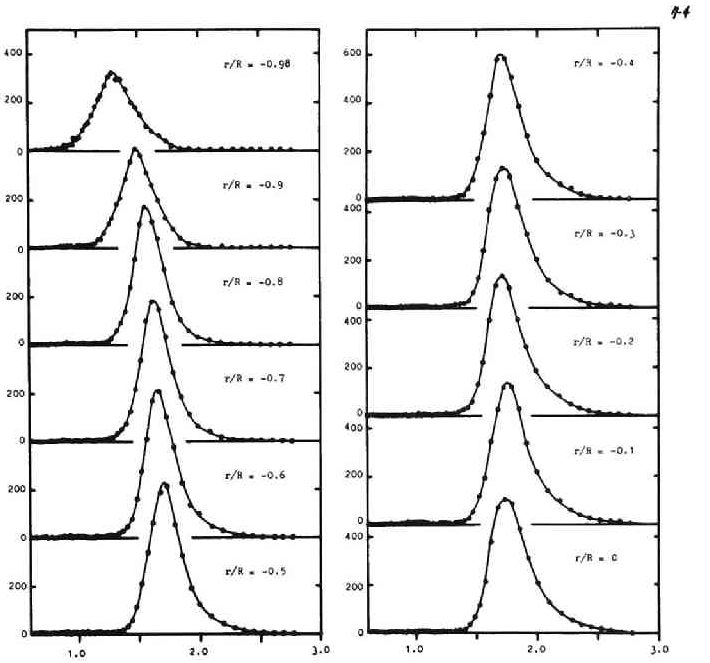

Counting rate Counts/min

Bubble velocity V_b m/s

Fig. 4.56 Bubble velocity spectrum (Bubble flow : V_o=1.03 m/sec, X=0.0341 %, Z/D=30)

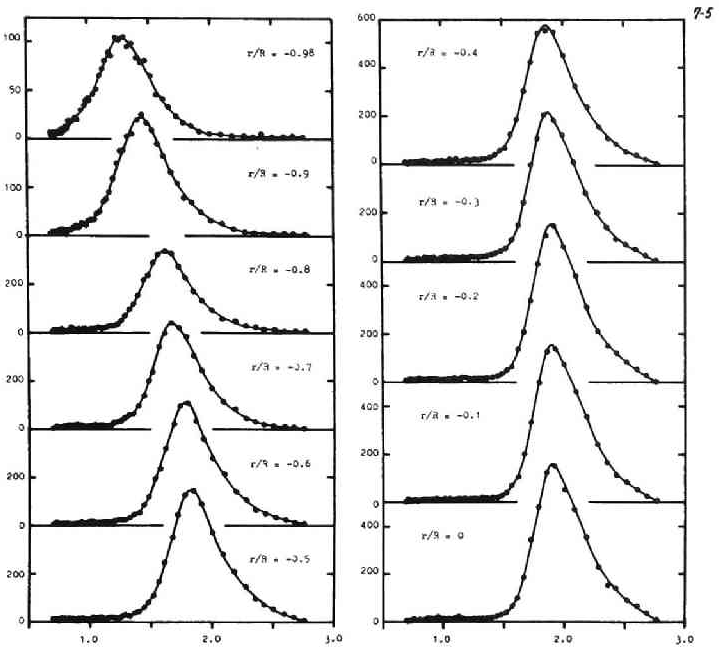

Fig. 4.57 Bubble velocity spectrum (Transition flow : V_o=1.03 m/sec, X= 0.0427 %, Z/D=30)

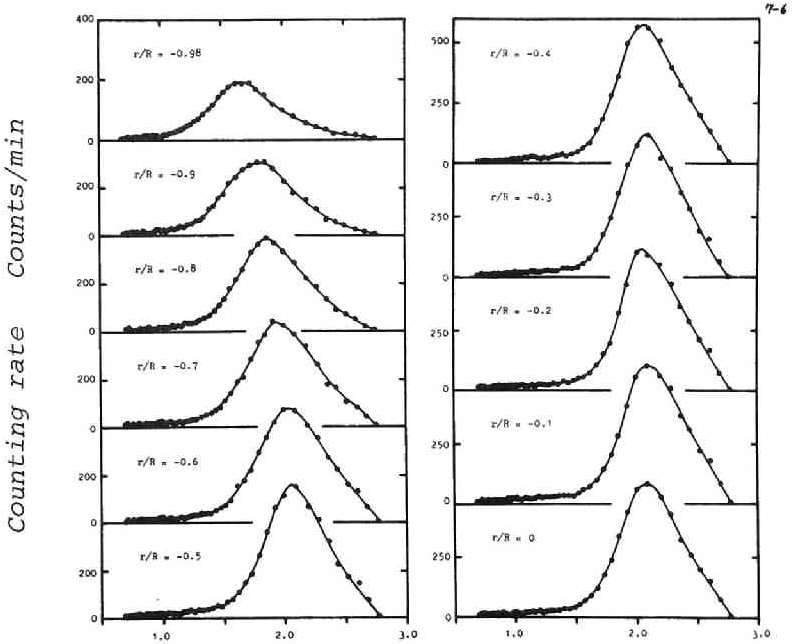

Fig. 4.58 Bubble velocity spectrum (Slug flow : V_o=1.03 m/sec, X=0.0511 %, Z/D=30)

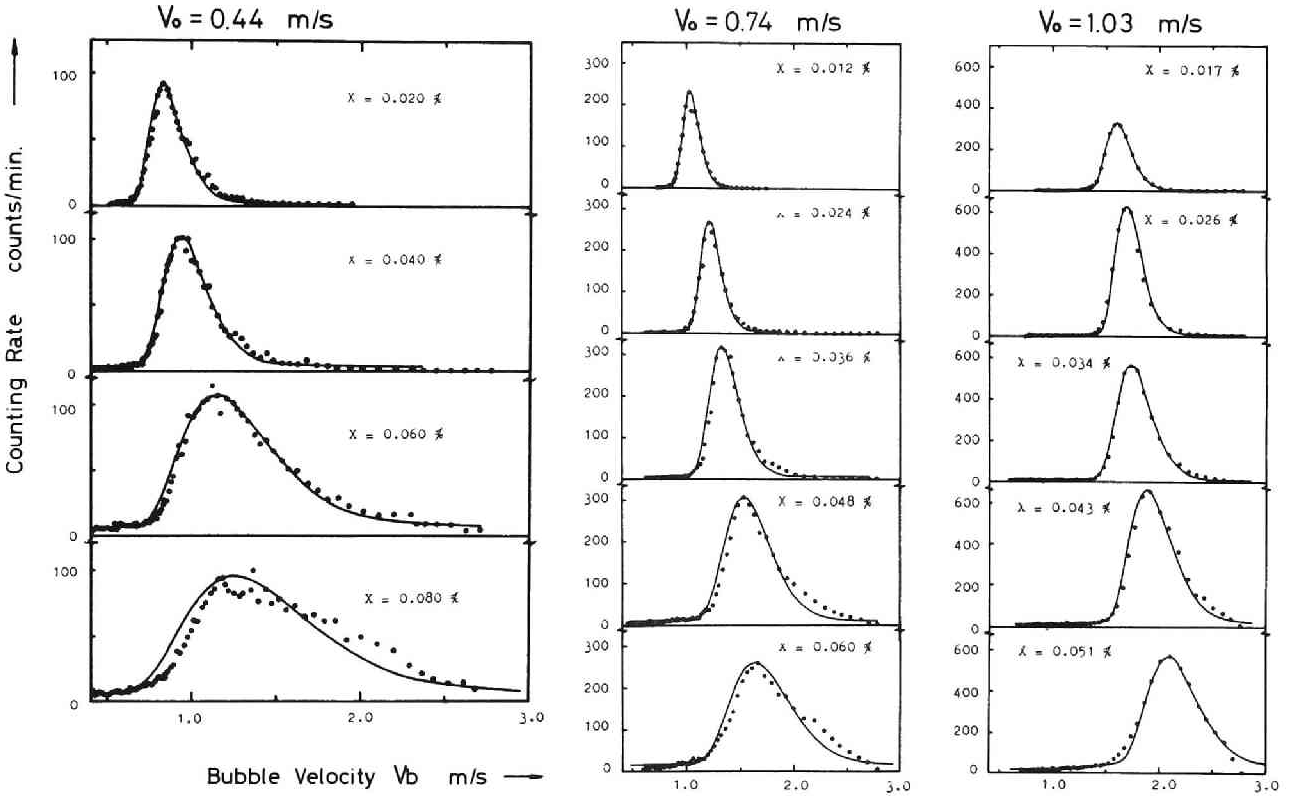

Fig. 4.59 Bubble velocity spectrum (at r/R=0) (solid lines : Poisson distribution)

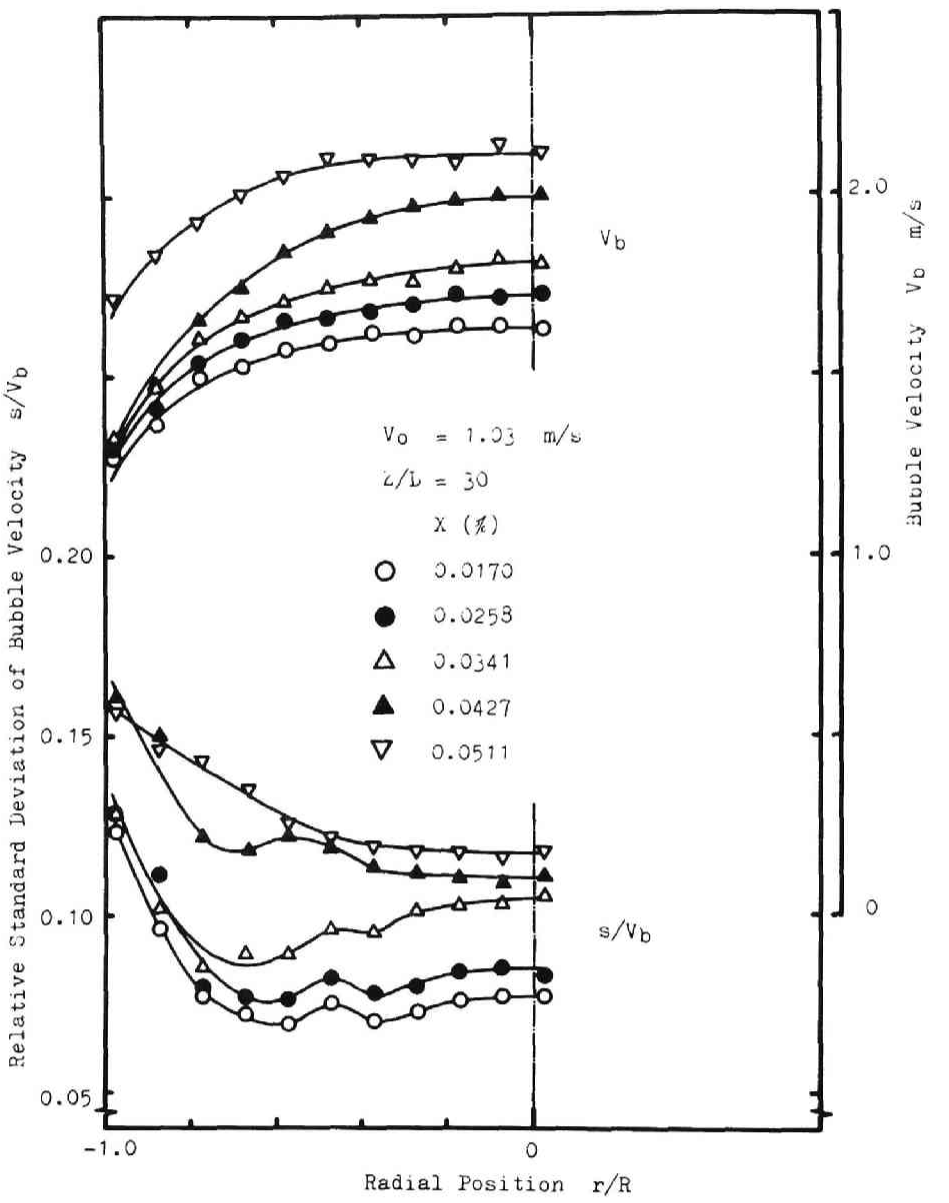

Fig. 4.60 Profiles of bubble velocity and relative standard deviation of its spectrum

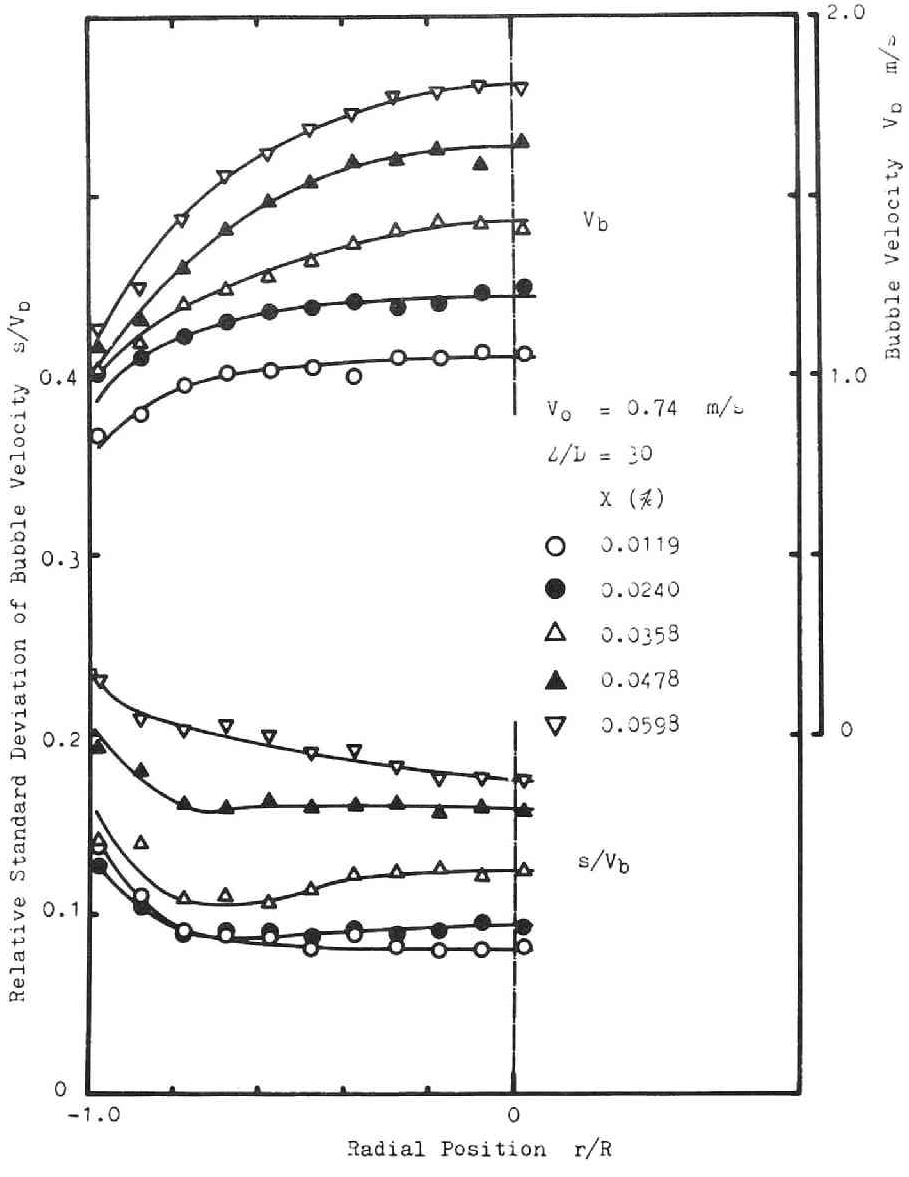

Fig. 4.61 Profiles of bubble velocity and relative standard deviation of its spectrum

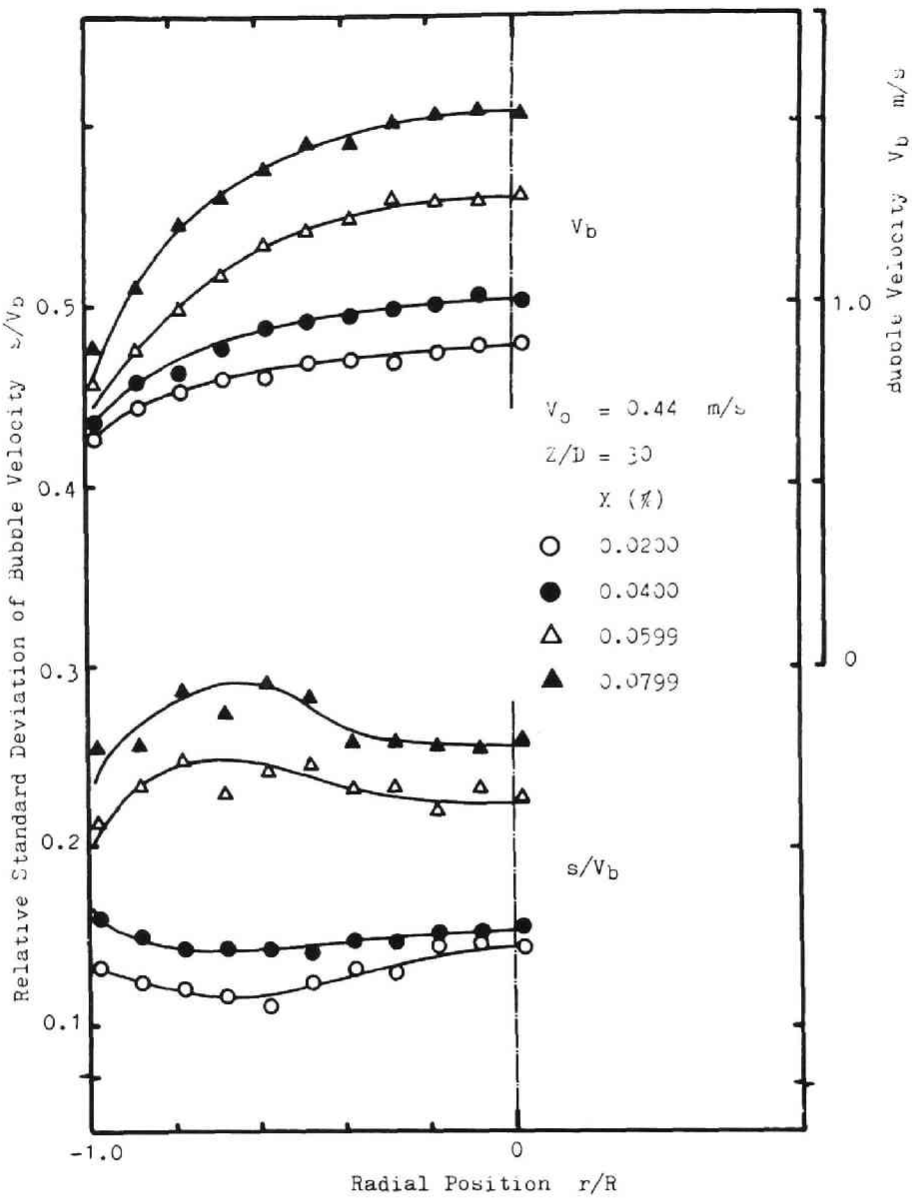

Fig. 4.62 Profiles of bubble velocity and relative standard deviation of its spectrum

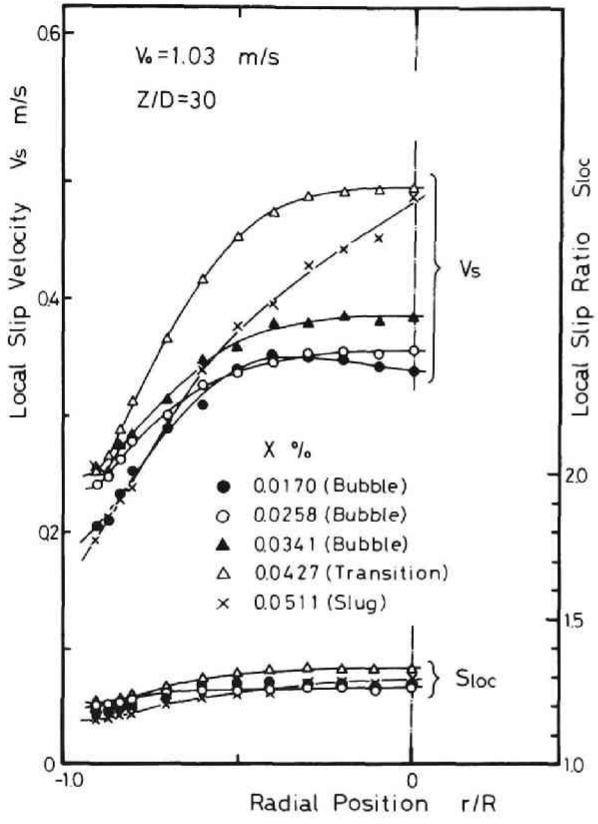

Fig. 4.63 Profiles of slip velocity and slip ratio

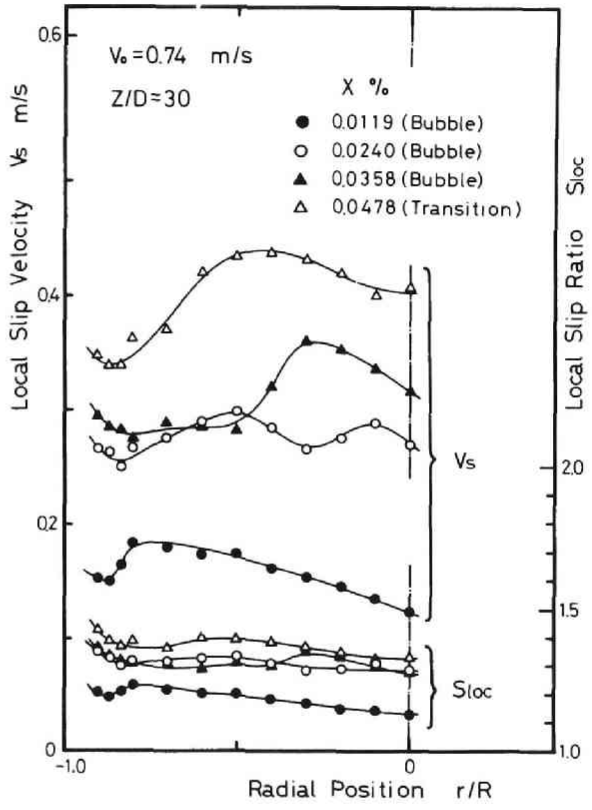

Fig. 4.64 Profiles of slip velocity and slip ratio

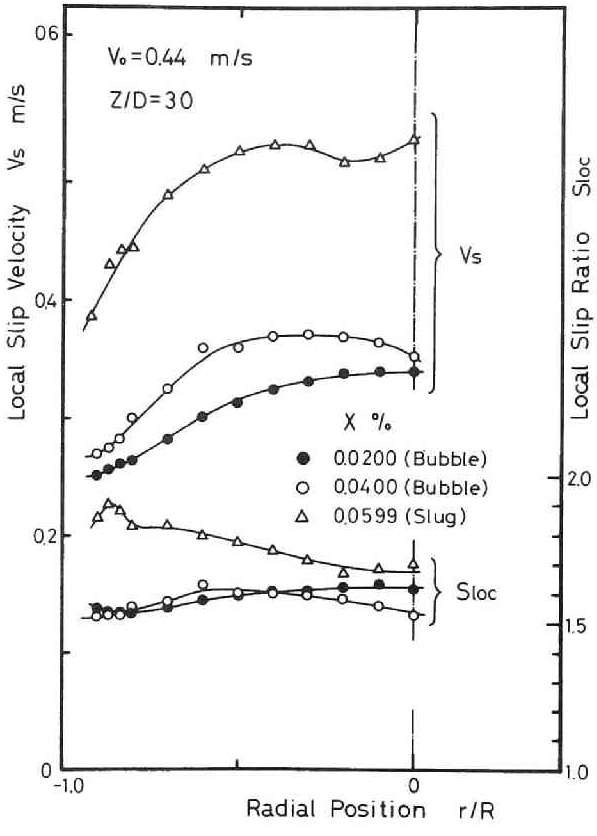

Fig. 4.65 Profiles of slip velocity and slip ratio

4.8 Water Velocity and Its Spectrum

The author has repeatedly described in this thesis the importance of the measurements of water velocity profile and its time-dependent fluctuating components in two-phase flow in pipes.

In respect to the enormous momentum of the liquid phase, bubbles are expected to be most strongly influenced in their motions or behaviors by the liquid velocity and its fluctuating characteristics. Therefore, the liquid velocity profile acts a decisively important role in characterizing the flow structure. In spite of this, accurate measurements of the liquid velocity profile and the turbulent intensity have been very scanty due to the difficulties involved in their measurements.

Neal[14], Malnes[5], and Aoki et al.[10] carried out the measurement of the liquid velocity profile by means of a Pitot tube. Despite of the detailed discussion made by Malnes on applying the Pitot tube for measurement of the liquid velocity, some doubts are still left behind as to their interpretation of the impact pressure in two-phase flow systems. Shires & Riley[4], and Brown & Kranich[8] used an isokinetic probe under some assumptions concerning the principle of measurements. Serizawa et al.[20] and Kobayashi et al.[11] have recently proposed independently a tracer technique for water velocity measurement. As a tracer, the former used lumps of the salt water or hot water injected into the stream, whereas the latter lumps of hot water generated by a special electronic circuit (thermal pulse generator). But, in order to get accurate information on the water velocity profile by these techniques, a number of measurements are required to be repeated at the same position under the same flow condition.

The most reliable work among those already published was carried out by Delhaye[50] with using an anemometry and a multi-channel pulse height analyzer. He obtained both the water velocity profiles and their corresponding turbulent intensities in an air-water flow. But he could not give us detailed and systematic information on such quantities for lack of the experimental data.

Like Delhaye, with using a hot-film probe anemometer and a 400-channel pulse height analyzer (see Chapter III), we measured the water velocity profiles and the corresponding turbulent intensity profiles.

At the start of a series of measurements, the single-phase water velocity and the turbulent intensity in single-phase flow were measured in order to check the accuracy of the anemometer technique.

The results are represented in Figs.4.66 and 4.67 for five different water velocities. Figure 4.66 is a correlative dimensionless expression of the experimental results with the universal velocity profile indicated by the following formula.

$$u^+ = 5.5 + 5.75 \log_{10} y^+ \tag{4.12}$$

where

$$u^+ = V_l(r)/u^* \quad , \quad y^+ = u^* (R - r)/\nu_l \quad , \quad u^* = \sqrt{\frac{\tau_w}{\rho_l}} \tag{4.13}$$

Figure 4.67 shows indications of the water velocity $V_l(r)$ and the turbulent intensity $I_l(r)$ (the solid lines for each water velocity profile are the corresponding 1/7 - power laws).

During these measurements, it turned out that the anemometer arrangement is very sensitive to the water temperature variation, and that the reliable measurement can be performed only by keeping the overheating ratio strictly constant (= 0.03) for every operation of the anemometer.

4.8.1 Water Velocity Spectrum

Results are given in Figs.4.68 ~ 4.85 for various flow conditions of two-phase flow. As stated in Chapter III, these figures merely indicate the apparent water velocity spectrum because of the opera-

tional principle of the anemometer in two-phase flow. The true spectrum will be obtained by subtracting the bubble-component (a background component) from the apparent spectrum according to the calculating procedure described in Paragraph 2.2.4 (a small peak towards zero velocity seen in figures corresponds to the bubble passages).

By taking such an additional background component due to bubbles into consideration, it may be concluded, from these figures, that the water velocity spectrum can be well expressed by the normal distribution function rather than the Poisson distribution, and that this tendency is more distinguished in bubble flow than in slug flow. The discrepancy in the distribution function between the bubble velocity spectrum (Poisson distributon) and the water velocity spectrum (normal distribution) may indicate that, due to the relatively small momentum of the bubble motion compared to that of the liquid motion and also due to the relatively weak effect of the backflow of water induced by the bubble slip compared to that of the bulk flow, the water velocity fluctuates independently of the velocity fluctuation of the leading or the following bubbles, and that, hence, it gives its own spectrum the normal distribution which is very familiar to the fluctuating characteristics in single-phase flow.

4.8.2 Radial Profile of Water Velocity

Figures 4.86 ~ 4.90 show the typical water velocity profiles at Z/D = 30 for increasing the quality which are calculated from the water velocity spectrum according to Eq.(2.4).

As seen from these figures, the water velocity profiles are slightly different from the bubble velocity profiles, and give an indication of a very interesting phenomenon. As the quality is increased in the low bubble density and high water flow rate region from zero up to below a certain value determined by the water flow rate, the water velocity profile changes from the normal turbulent velocity profile (i.e., 1/7 - power law) to a plug-shaped profile (nearly uniform

distribution)*, and the water velocity towards the pipe axis is sometimes lower than that in single-phase water flow (for example, the data denoted ▼ in Fig.4.86 and ● in Fig.4.87). The dominant flow pattern in this quality range is bubble flow of lower void fraction. And in the bubble flow region, no further remarkable change in shape of the water velocity profile occurs with further increasing the quality**.

When the gas flow rate is remarkably increased, the profile finally changes from the flat distribution to a dome-shaped one with a maximum at the pipe center, and the corresponding flow pattern changes from bubble to slug flow. No further change was observed to occur, even though the gas flow rate was increased within the range of flow variables of the present experiment.

It may be evaluated that the change of the water velocity profile does not parallel that of the void fraction but are susceptible to it. For a low void fraction (low bubble density) or a low quality, as shown in Section 4.4, the bubble number distribution or the void fraction distribution has a maximum towards the wall which surely serves to accelerate the water velocity there, and hence the water velocity profile tends to be flattened. As the bubble number or the quality increases, the void fraction also increases especially towatds the pipe axis and its profile changes to a dome-shaped one. This follows the acceleration of the water favorably in the center core region of the flow passage, and then the water velocity profile changes also to an inflated one. At this stage, the dominant flow pattern is transition or slug flow.

---

* However, for very small void fraction, the water velocity profile may be expected to approach that of single-phase flow.

** A large gradient of the water velocity at the wall resulting from the uniform water velocity distribution across the pipe is closely related to a large frictional pressure drop in the bubble flow region, as stated in PART I.

Neal[14], Malnes[5], and Aoki et al.[10] reported in their papers a saddle-shaped profile or a profile with a maximum point near the wall for the liquid velocity profiles which were measured commonly by means of the Pitot tubes. In the Pitot tube method, the liquid velocity should be, for convenience, assumed to be calculated by the following incomprehensible formulas:

$$\Delta P = \frac{1}{2} \rho_l \{1 - \alpha(r)\} \{V_l(r)\}^2 + \frac{1}{2} \rho_g \alpha(r) \{V_b(r)\}^2 \quad , \tag{4.14a}$$

or

$$V_l(r) = \sqrt{\frac{2 \Delta P}{\rho_l \{1 - \alpha(r)\}}} \quad , \tag{4.14b}$$

where ΔP is the impact pressure measured by the Pitot tube. In practical measurements, ΔP is substantially small, especially for the low density fluid, and, therefore, the variation of the pressure difference with radial position is also small. Hence, it is most probable that the liquid velocity obtained by virture of Eq.(4.14b), which is indeed very sensitive to the void fraction, may often give a maximum at the position corresponding to a maximum void fraction, depending upon the magnitude of the maximum void fraction. Actually, we can easily find in their reports that a maximum water velocity often corresponds to a maximum void fraction (for example, the data of Malnes shown in Fig.4.106).

On the other hand, the work of Kobayashi et al.[11] by tracer method indicates obviously the water velocity distribution of the same trend as that observed in the present work (i.e., nearly uniform and monotonous distribution). When we recall the rapid decrease of the bubble velocity towards the wall, and a nearly uniform distribution of the slip ratio across the pipe cross section, it is natural that the water velocity should also rapidly decrease there.

Then, as a whole, it may well be concluded that the water velocity profile can be approximated by a power-law expression and its exponent is a strong function of the flow rates of both phases.

4.8.3 Longitudinal Turbulent Intensity

In order to get an indication of the turbulent characteristics of the water, the longitudinal turbulent intensity was deduced from the true spectrum of the longitudinal (axial) water velocity (the spectrum supplemented for the background correction) in terms of the standard deviation of the spectrum which is equivalent to the root mean square value of the turbulent velocity of the liquid.

Profiles of the relative turbulent intensity*, often denoted by I_1 ($= \sqrt{\overline{u^2}}/V_1$), are represented together with the corresponding water velocity profiles in Figs.4.86 ~ 4.90.

As is expected, the value I_1 generally increases toward the wall and has a minimum at the pipe center in all experimental runs (it may be naturally expected to decrease rapidly in the very vicinity of the wall).

For bubble flow, a uniform distribution of the relative turbulent intensity was observed especially for a higher superficial water velocity as indicated in Figs.4.86 and 4.87. In such a case, the distributions of other quantities scuh as the void fraction, the bubble velocity, the bubble velocity fluctuation, and the water velocity are all nearly uniform over a large portion of the flow area. These facts imply the existence of the nearly homogeneous flow field can be assumed for such flow conditions.

The effects of increasing the quality for constant water flow rate are to increase the relative turbulent intensity over the whole range of the radial position, and to deviate the profile from uniform

---

* In respect to turbulence, the relative turbulent intensity is a measure for the similarity of the flow field.

distribution.

Even a mere comparison of the relative turbulent intensity I_l ($=\sqrt{\overline{u^2}}/V_l$) with the aforementioned relative standard deviation of the bubble velocity spectrum I_g ($= s/V_b$) will suggest some close relationship between them.

Profiles of the longitudinal turbulent velocity $\sqrt{\overline{u^2}}$ (or the longitudinal turbulent intensity) are indicated in Figs.4.91 ~ 4.96 (Figure 4.91 shows the results in single-phase water flows). These figures indicate two remarkable tendencies. The one is that the increasing rate of the turbulent velocity with the increase of the quality is generally slightly larger for a low superficial water velocity than for a higher one. For a higher water velocity, the inertia force of the liquid may overwhelm the mixing actions caused by the capricious bubble motions, and hence the increase of the quality may not lead directly to the remarkable increase of the turbulent velocity. On the other hand, for a low water velocity, the effect of the inertia force may be relatively weakened and the turbulent velocity of water may become very sensitive to the mixing actions and hence to the increase of the gas flow rate. (The turbulent velocity is of roughly the same order of magnitude as the corresponding friction velocity u* defined as $\sqrt{\tau_w/\rho_l}$.)

The other tendency is that, for bubble flows of low void fraction, the turbulent velocity is very uniformly distributed over almost whole cross sectional area of the pipe, and, in some cases of higher water velocity, it exhibits lower values than those obtained in single-phase water flow, as indicated in Figs.4.95 and 4.96. This is an interesting phenomenon which is contrary to our intuition that the flow should be more strongly disordered by introducing agitating bubbles into the stream. A similar effect of introducing particles of small size into the stream upon the turbulent intensity or its energy spectrum has been reported in detail by Hino[51] in his lecture on the microscopic structure of the solid-liquid two-phase flow. However it is a premature to apply his theoretical results to the present phenomenon observed

in air-water bubble flows, his description is very instructive for us to consider the case phenomenologically. Referring to his description, to some extent, and considering the flow characteristic of the present case, the phenomenon may be ascribed to the competition among the following effects and others*:

1) Decrease in the effective volume of the liquid phase for energy dissipation due to the volume occupied by the suspended bubbles - this effect is to increase the turbulent intensity.
2) Work done for floating the bubbles - some of the turbulent energy may be used for accelerating the velocity of bubbles up to more than a certain value determined by the buoyant force due to the density difference between the liquid and the bubbles (refer to Paragraph 4.7.3) - this effect is of service to the reduction of the turbulent intensity.
3) Energy dissipation associated with the lateral relative motions or rotations of bubbles - the turbulent intensity may be decreased for supplying this energy dissipation.
4) An energy absorbing characteristic of bubbles - bubbles may act as a kind of energy absorber. The turbulent energy obtained from the liquid may be dissipated by the circulating motions of the gas within bubbles or by the microscopic bubble motions. Many corrugations of various shapes observed on the surface of every bubble, as seen in Photos.4.1 and 4.2, are considered to give some experimental verification to this argument.

---

* The turbulent energy balance is given by
(Energy production transferred from the mean motion through the Reynolds shear stress) = (The convective diffusion by turbulence of the total turbulent energy) + (The work done by the viscous shear stress of the turbulent motion) + (The dissipation by the turbulent motion) + (The work done for the interactions between the liquid and the bubbles: the dissipation by the relative motions or the rotation of the bubbles).

More detailed and pertinent investigations are strongly needed for more accurate interpretations of this phenomenon of the turbulent intensity*.

4.8.4 Summary and Conclusions

Accurate measurements were made of the water velocity spectrum, and of the radial profiles of the water velocity and the turbulent intensity. From these measurements, one may summarize and conclude that:

1) The water velocity spectrum is well approximated by the normal distribution function both in the bubble, the transition, and the slug flow regions. This trend is analogous to that in single-phase water flow.
2) The water velocity profile can be expressed, analogously to the bubble velocity profile, by such a monotonous function as a power law expression (when the power law expression is assumed to the water velocity profile, the exponent of that function may be a strong function of the quality). No significant peaking near the wall was observed in all experimental runs. The profile shows nearly flat-shape for bubble flow, while dome-shape for slug flow.
3) The relative turbulent intensity generally increases towards the wall and has a minimum at the pipe center. In bubble flow a uniform distribution was observed especially for higher water flow

---

* Hino[51] suggested that the elongation of the mixing length might follow a decrease in energy production. However, Figs.4.112 and 4.113 cannot give any direct experimental evidences to the validity of his argument, in which the turbulent energy production has been deduced from the measured distributions of the liquid velocity and the local void fractions in bubble flow, with an aid of the corresponding mixing length evaluated by employing a mixing length concept (see Paragraph 4.9.2 and Figs.4.108 and 4.109).

rate.

4) In bubble flow with lower void fraction, the turbulent velocity is also uniformly distributed, and, in some cases of higher water velocity, it exhibits somewhat lower values than those obtained in single-phase water flow. This peculiar phenomenon could not be satisfactorily accounted for in respect to both its quantitative and qualitative characteristics. More pertinent discussions will be needed further.

5) The effects of increasing the quality for constant water flow rate are to increase both the relative turbulent intensity and the turbulent velocity over the whole range of the flow area, and to deviate their profiles from uniform distributions.

6) The ratio $s/\sqrt{\overline{u^2}}$ is approximately uniform across the pipe, and is order of magnitude 1 ~ 3, depending upon the flow variables.

7) Corrugated surface of a bubble appears to give some useful suggestions to understanding the physical picture of the flow turbulence in gas-liquid two-phase bubble flow.

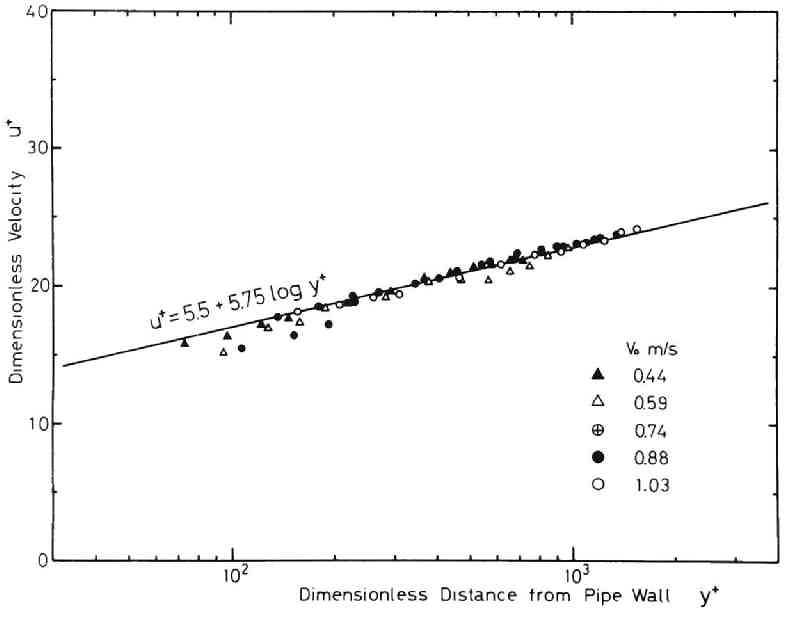

Fig. 4.66 Water velocity profile in single-phase flow

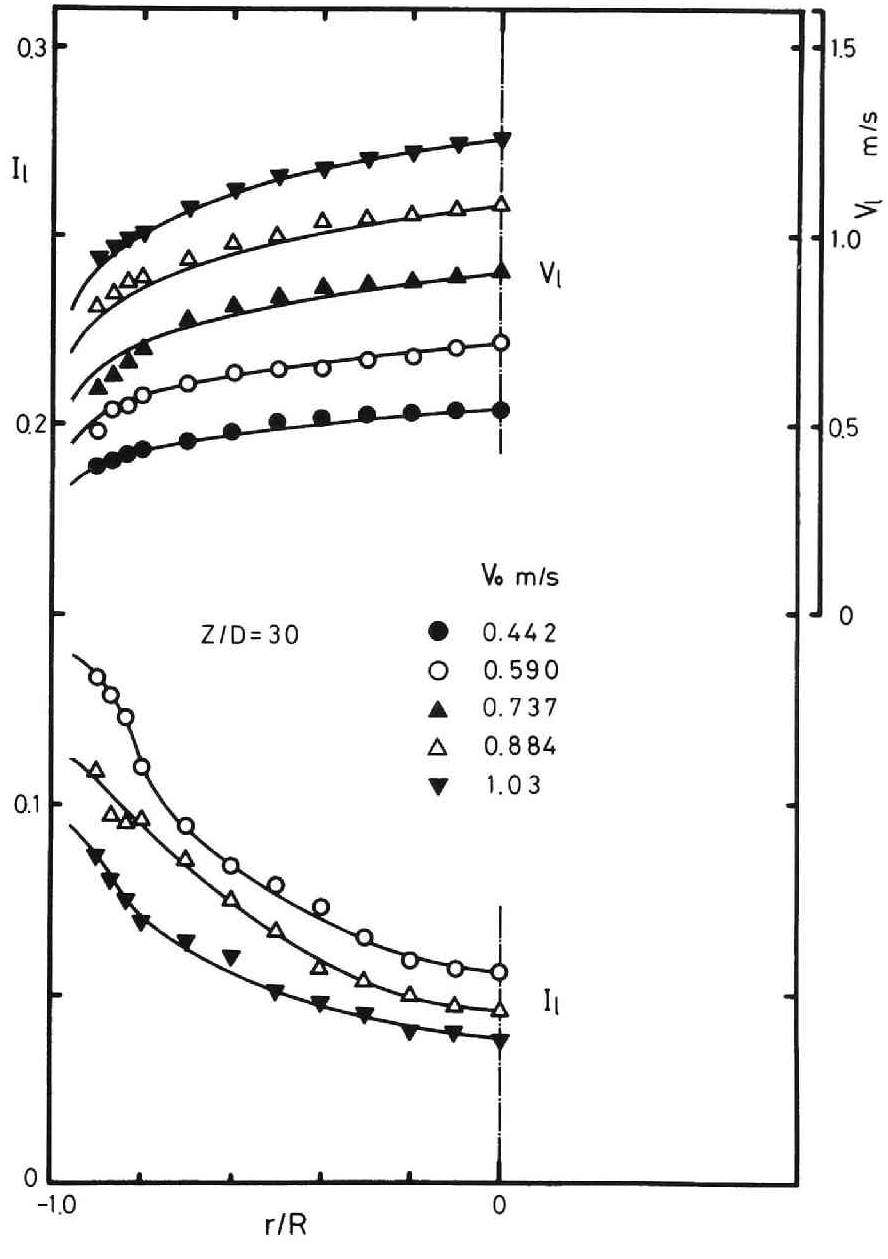

Fig. 4.67 Profiles of water velocity and relative turbulent intensity in single-phase flow

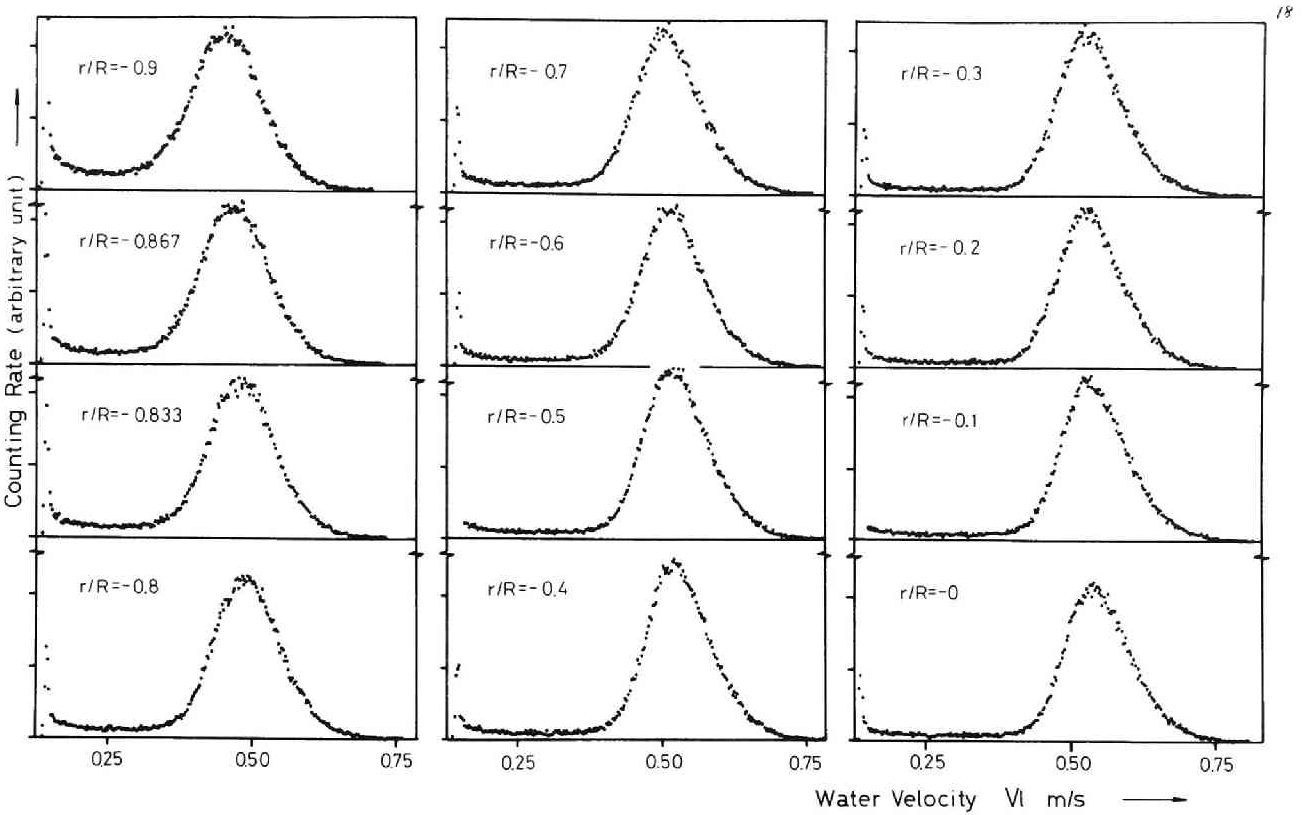

Fig. 4.68 Water velocity spectrum
(Bubble flow : V_o=0.44 m/sec, X=0.0200 %, Z/D=30)

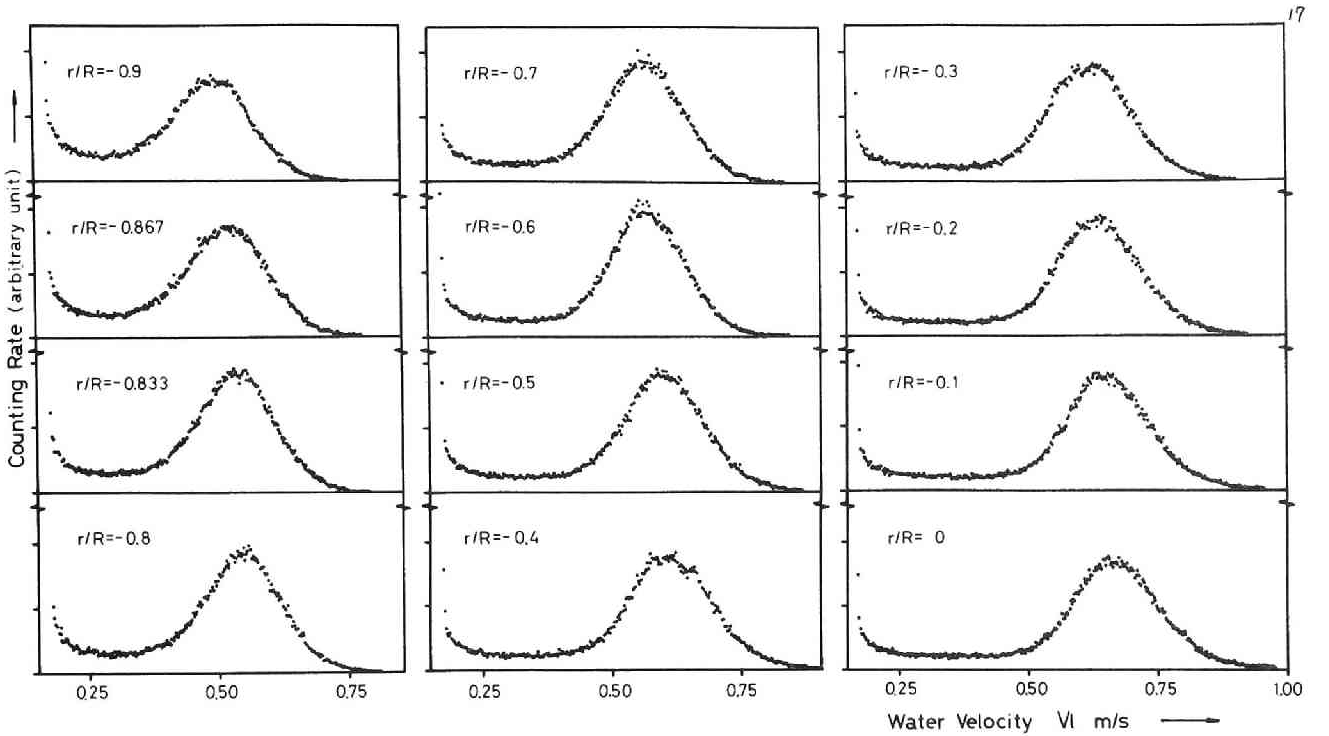

Fig. 4.69 Water velocity spectrum
(Bubble flow : V_o=0.44 m/sec, X=0.0400 %, Z/D=30)

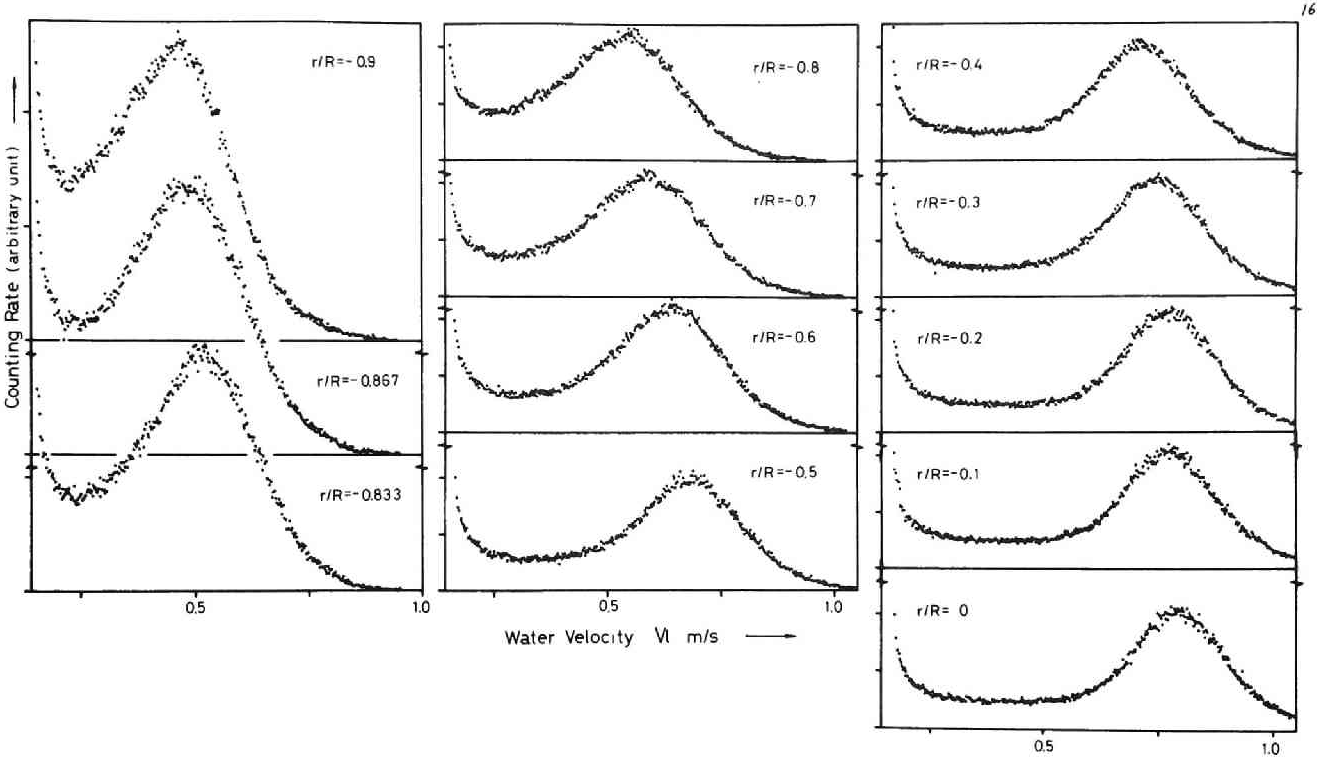

Fig. 4.70 Water velocity spectrum
(Slug flow : V_O=0.44 m/sec, X=0.0599 %, Z/D=30)

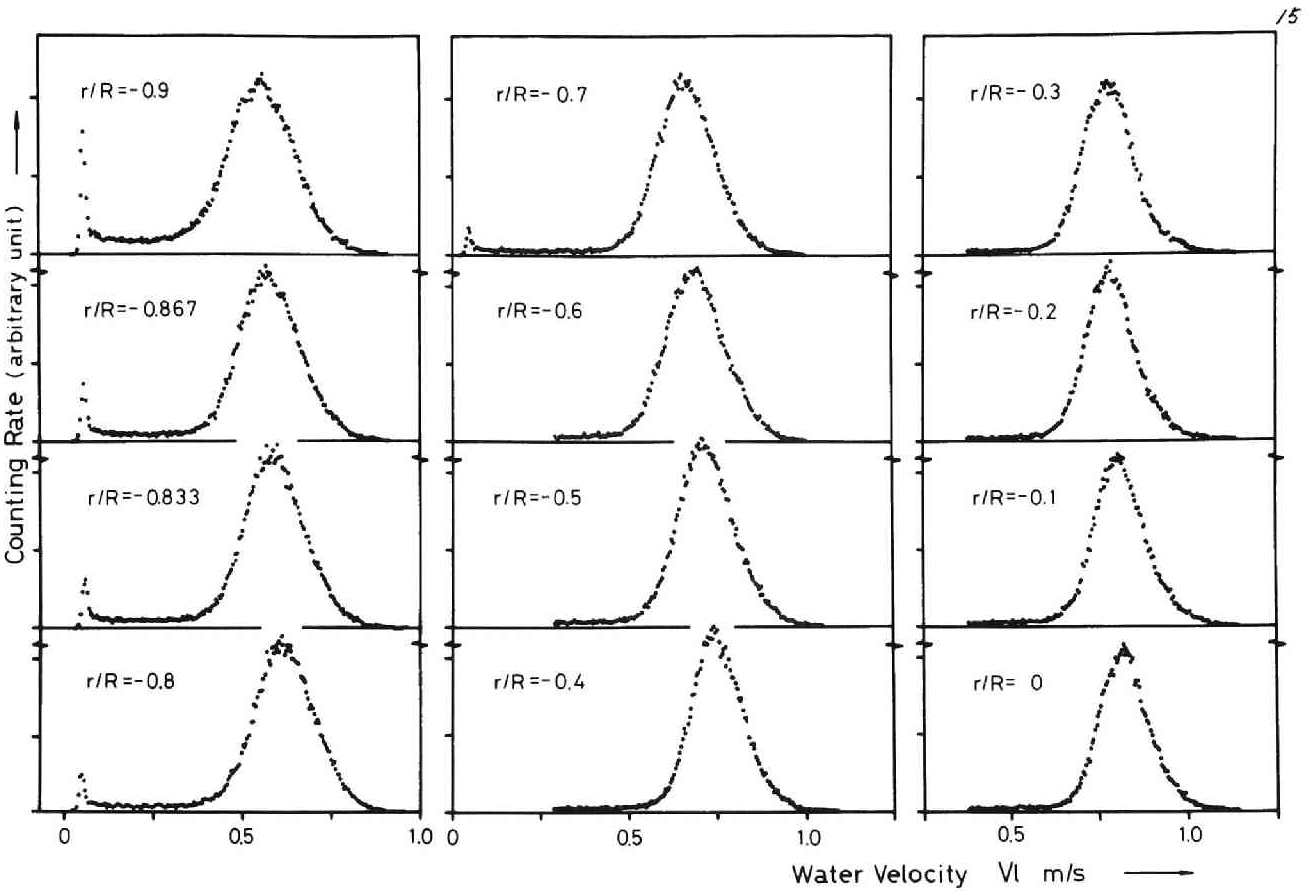

Fig. 4.71 Water velocity spectrum
(Bubble flow : V_o=0.59 m/sec, X=0.0149 %, Z/D=30)

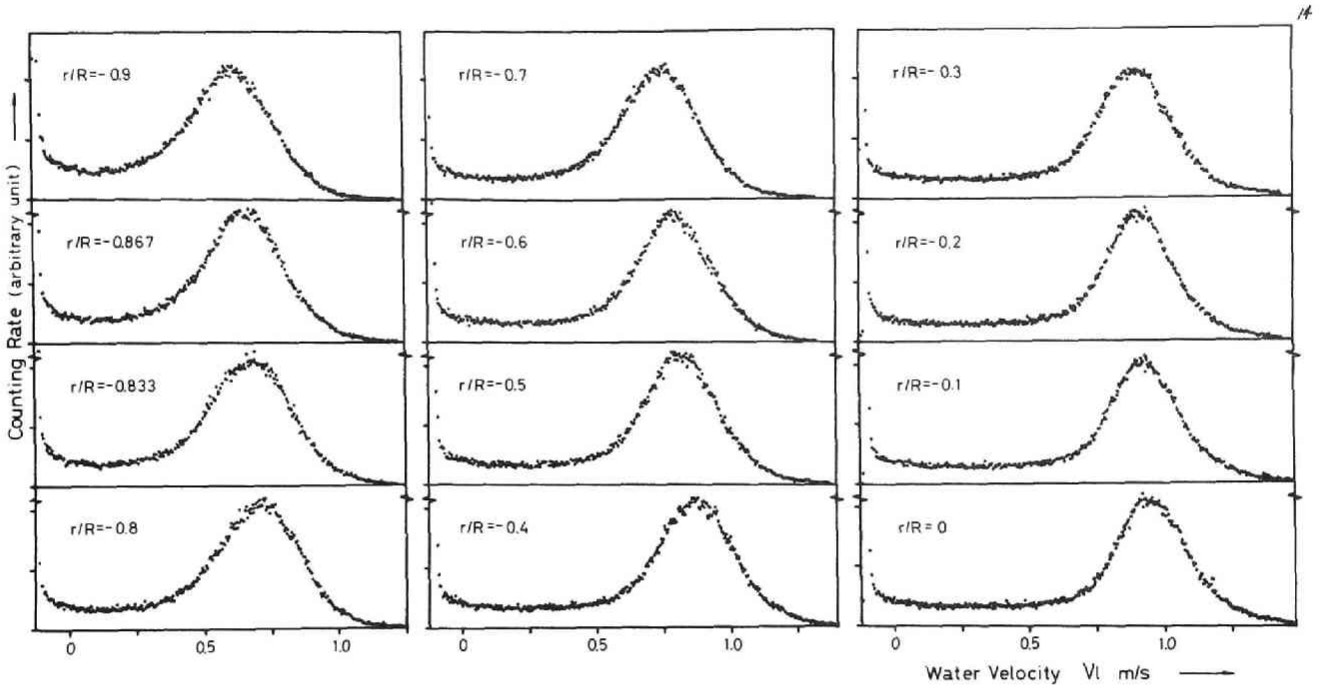

Fig. 4.72 Water velocity spectrum
(Transition flow : V_o=0.59 m/sec, X=0.0445 %, Z/D=30)

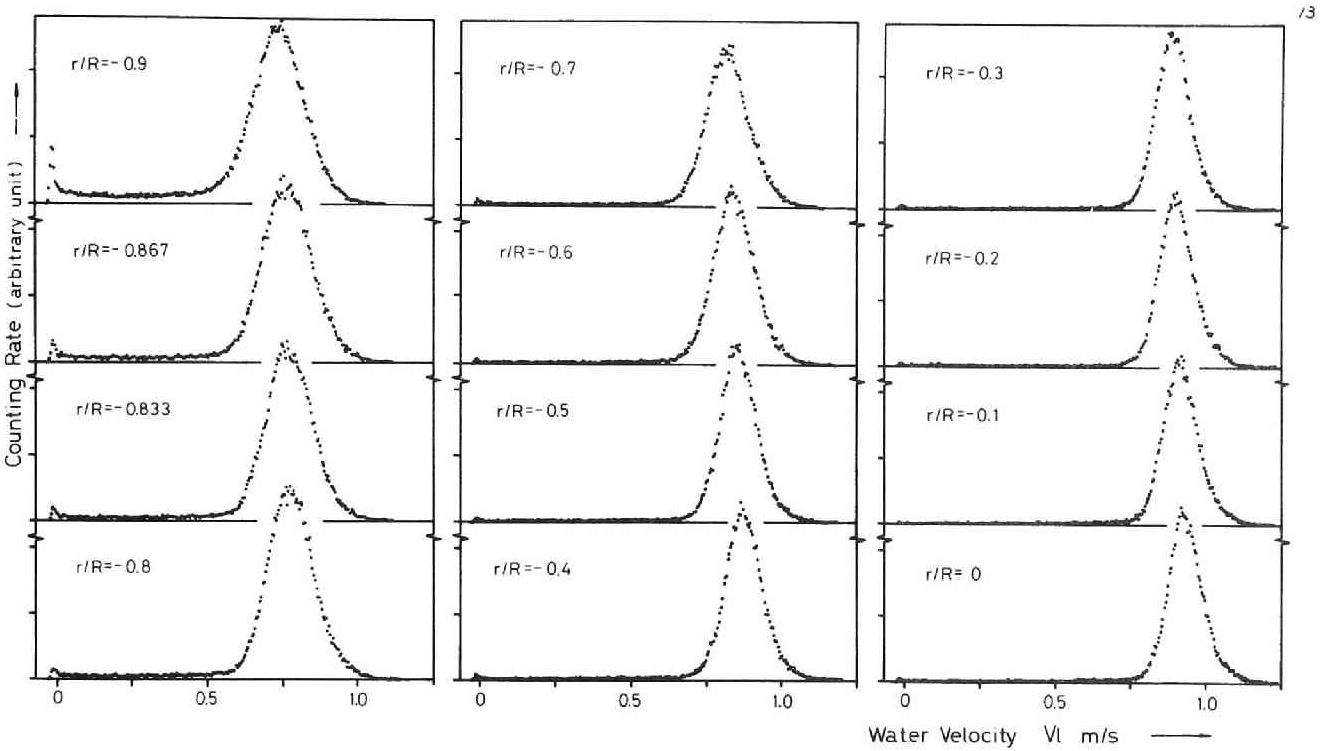

Fig. 4.73 Water velocity spectrum
(Bubble flow : V_o=0.74 m/sec, X=0.0119 %, Z/D=30)

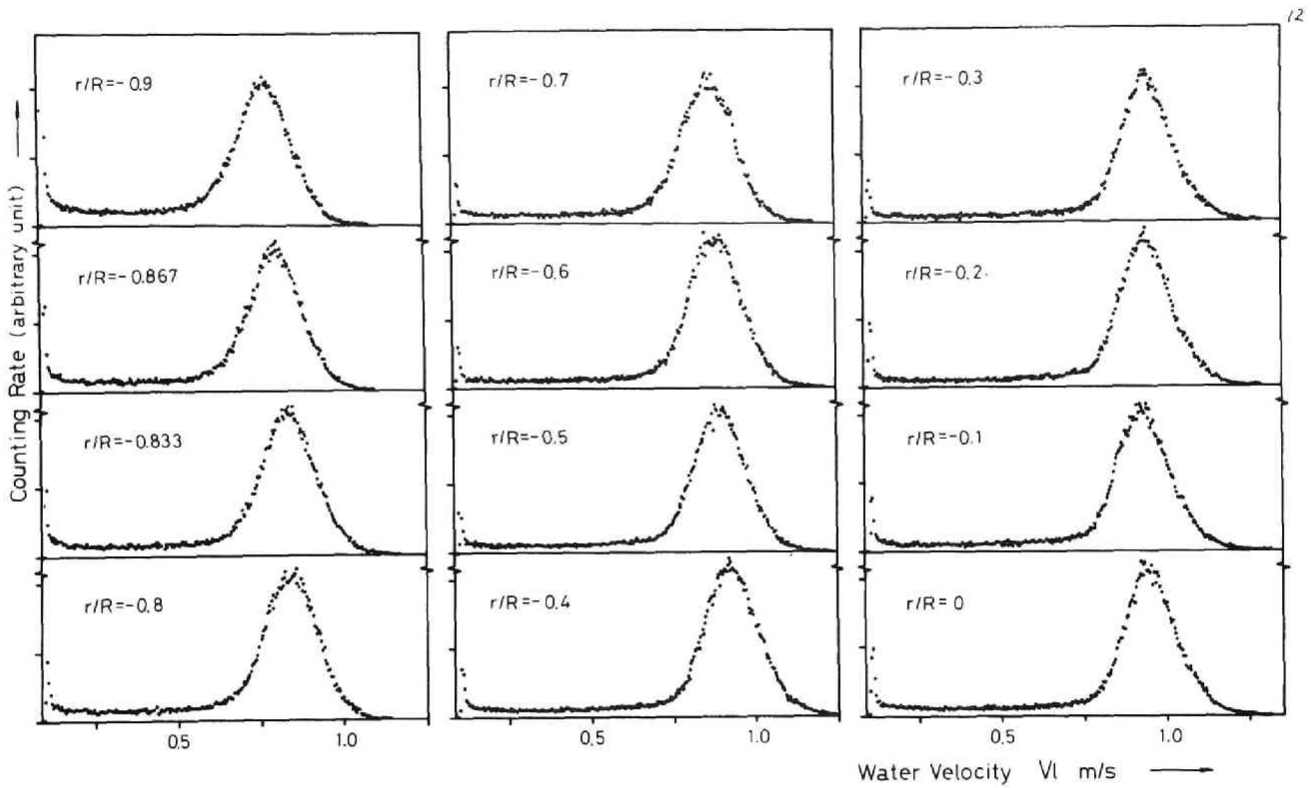

Fig. 4.74 Water velocity spectrum
(Bubble flow : V_o=0.74 m/sec, X=0.0240 %, Z/D=30)

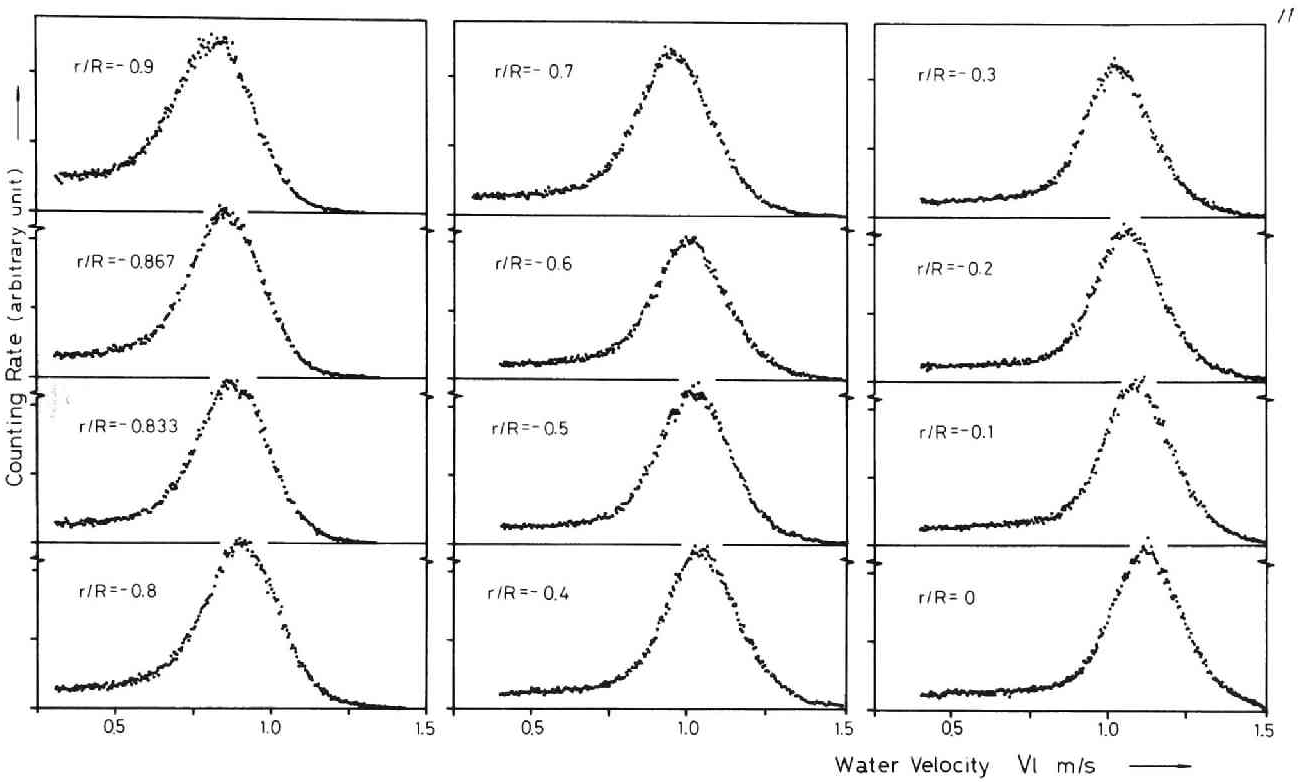

Fig. 4.75 Water velocity spectrum
(Bubble flow : V_o=0.74 m/sec, X=0.0358 %, Z/D=30)

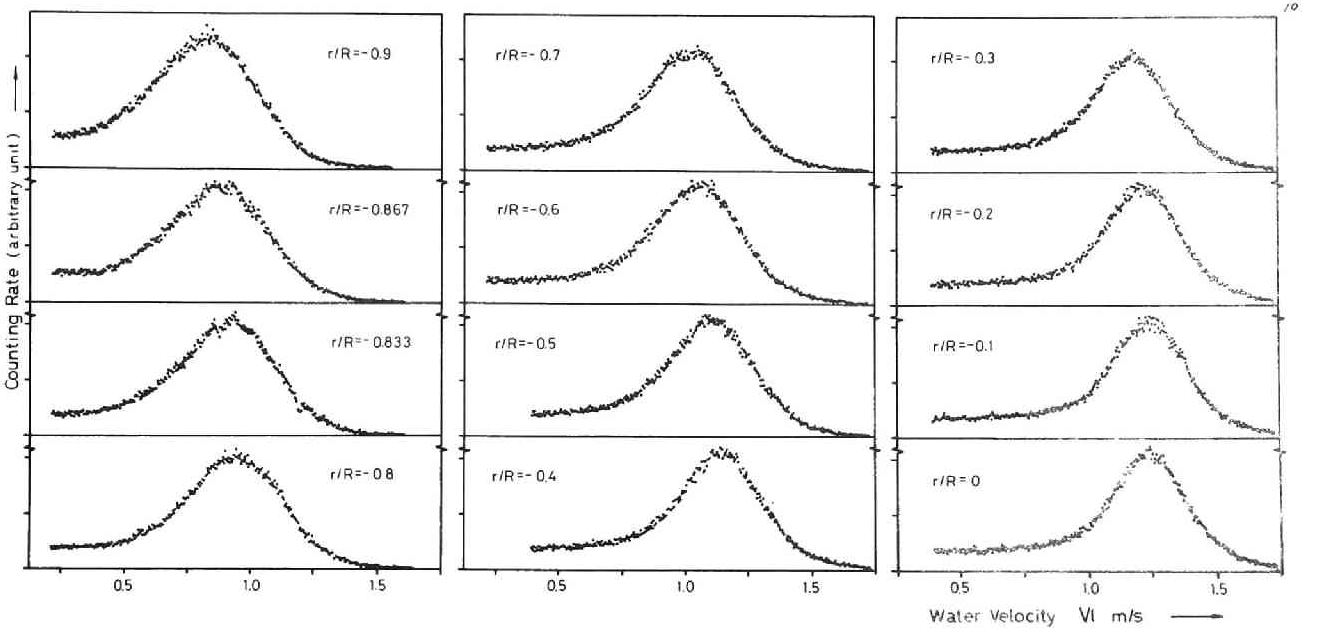

Fig. 4.76 Water velocity spectrum
(Transition flow : V_o=0.74 m/sec, X=0.0478 %, Z/D=30)

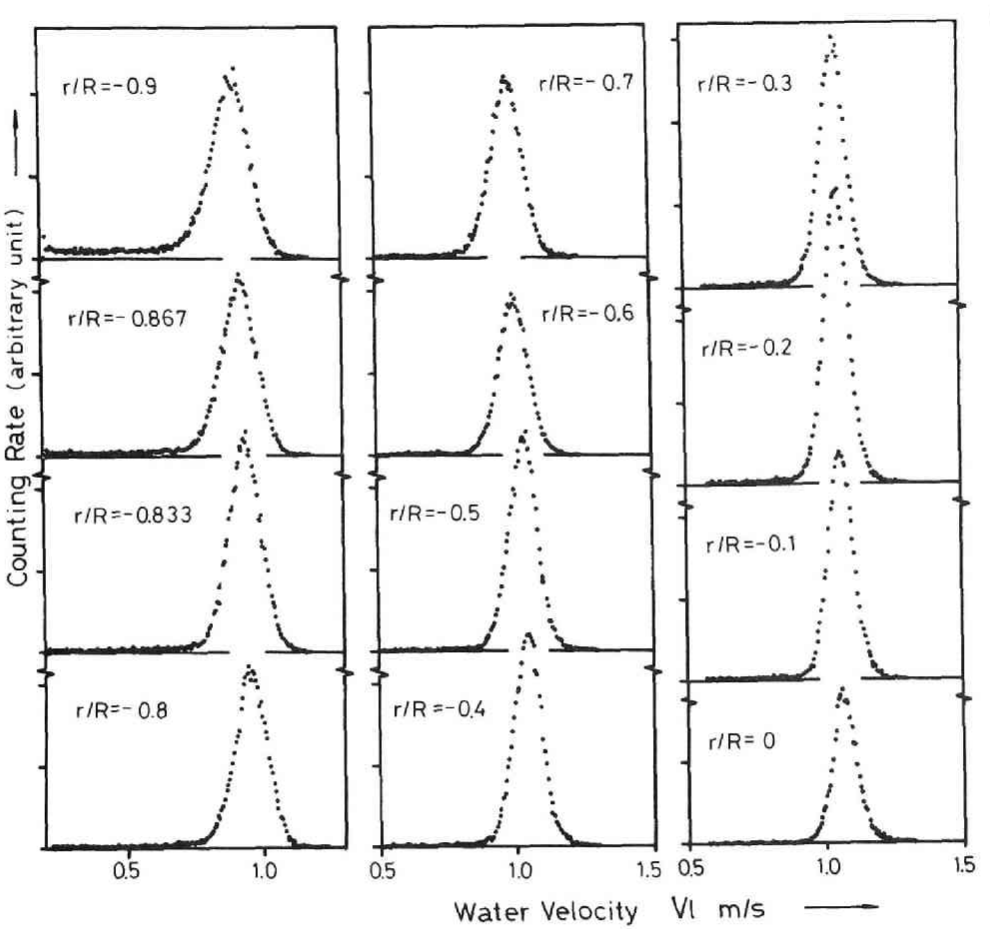

Fig. 4.77 Water velocity spectrum
(Bubble flow : V_o=0.88 m/sec, X=0.0099%, Z/D=30)

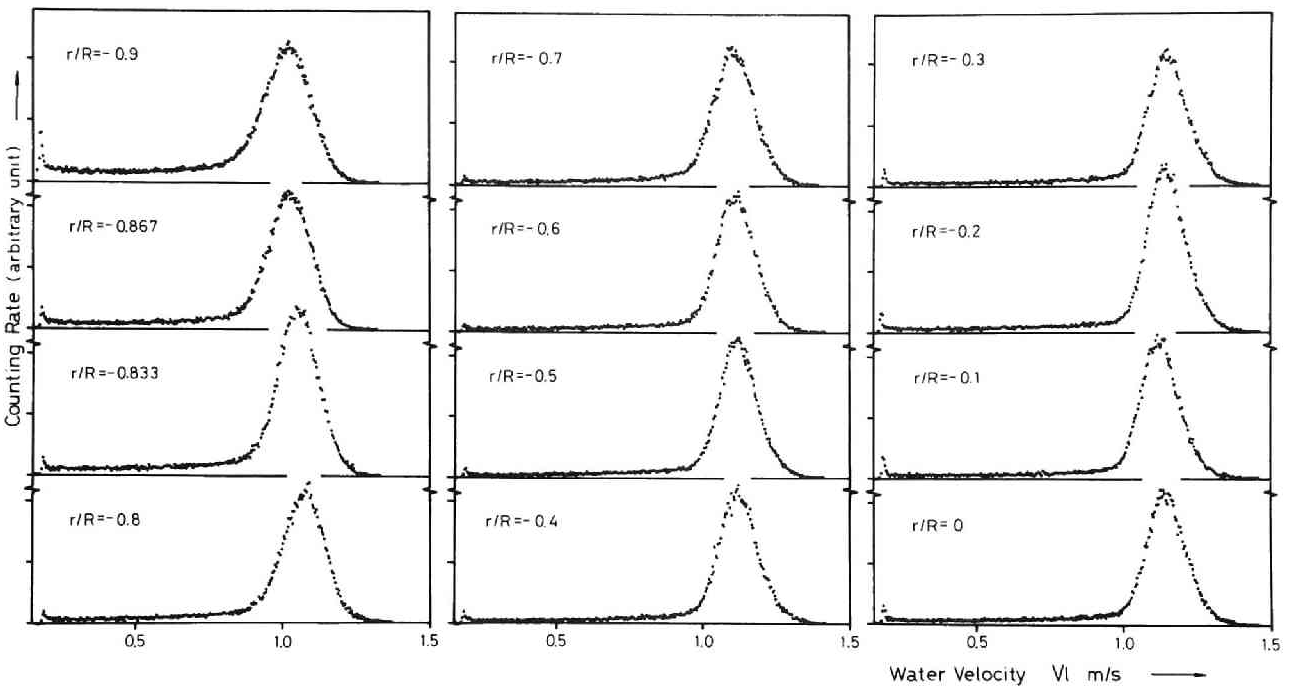

Fig. 4.78 Water velocity spectrum
(Bubble flow : V_o=0.88 m/sec, X=0.0198 %, Z/D=30)

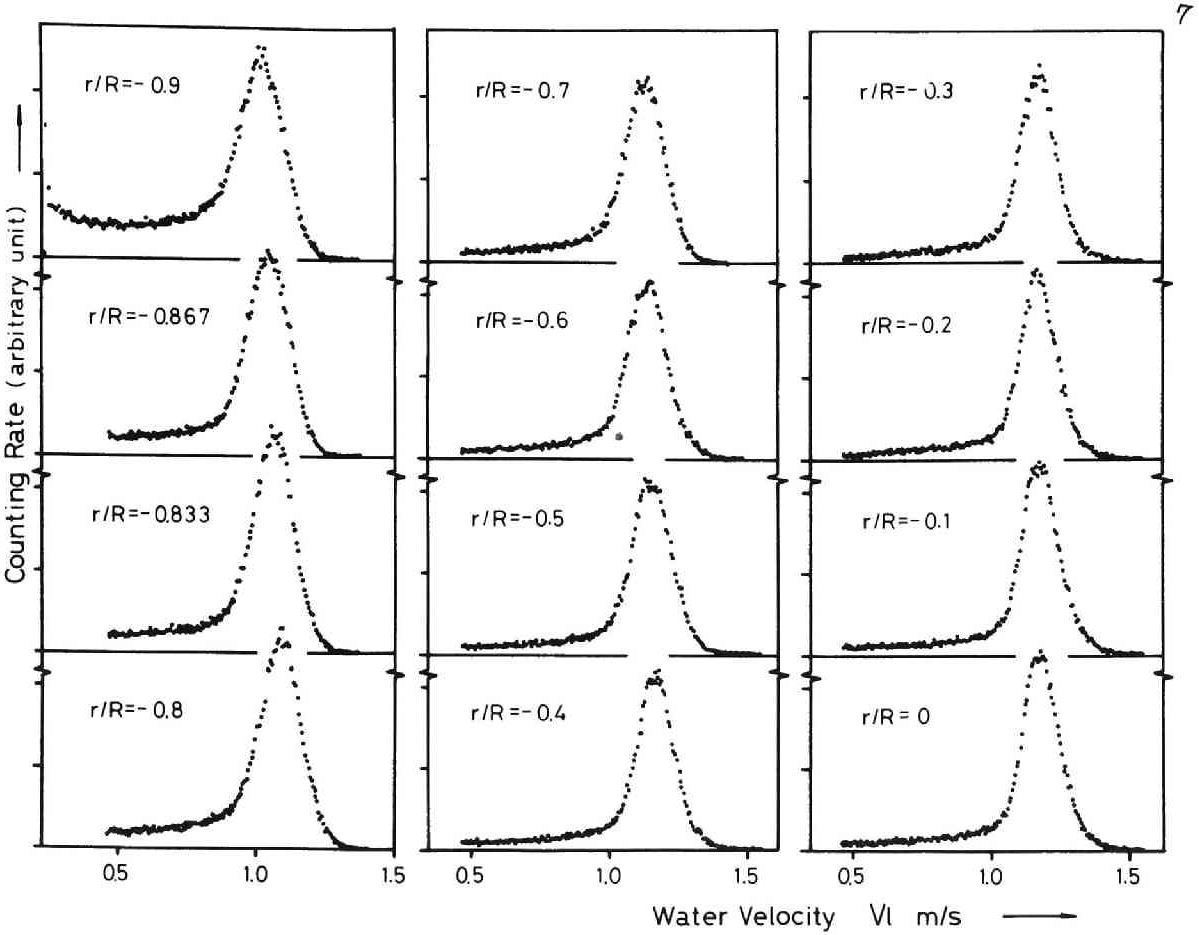

Fig. 4.79 Water velocity spectrum
(Bubble flow : V_o=0.88 m/sec, X=0.0300 %, Z/D=30)

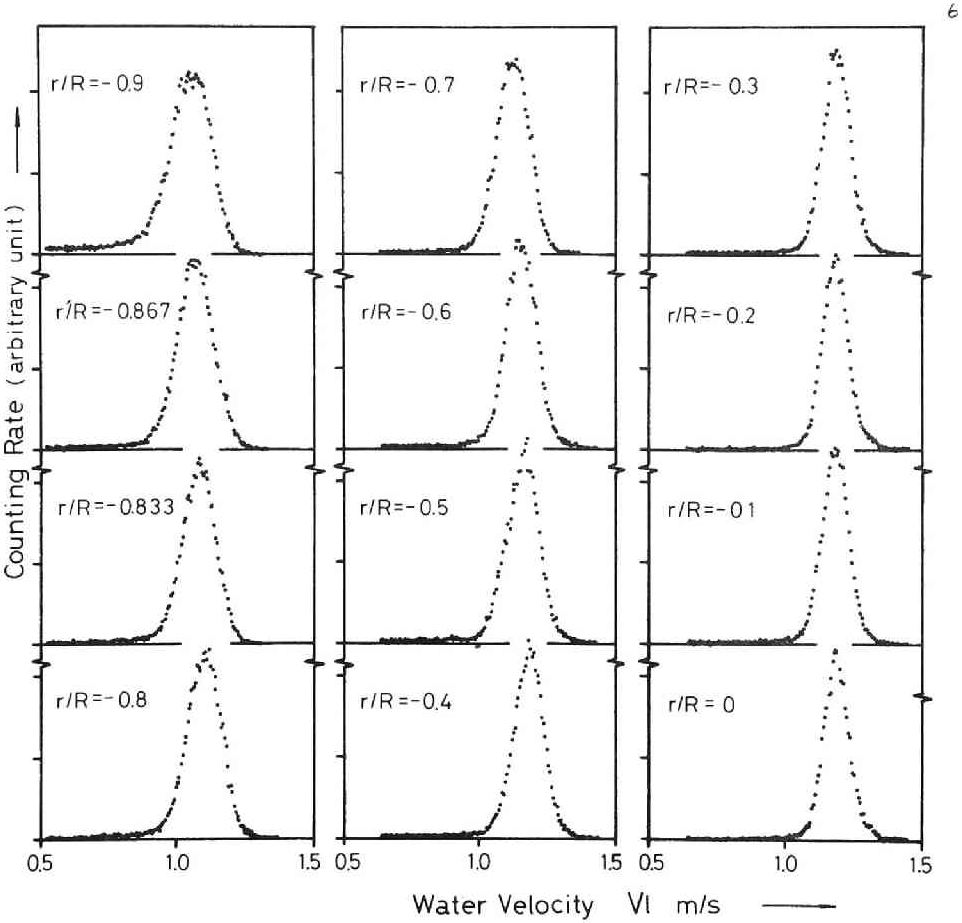

Fig. 4.80 Water velocity spectrum
(Bubble flow : V_o=1.03 m/sec, X=0.0085 %, Z/D=30)

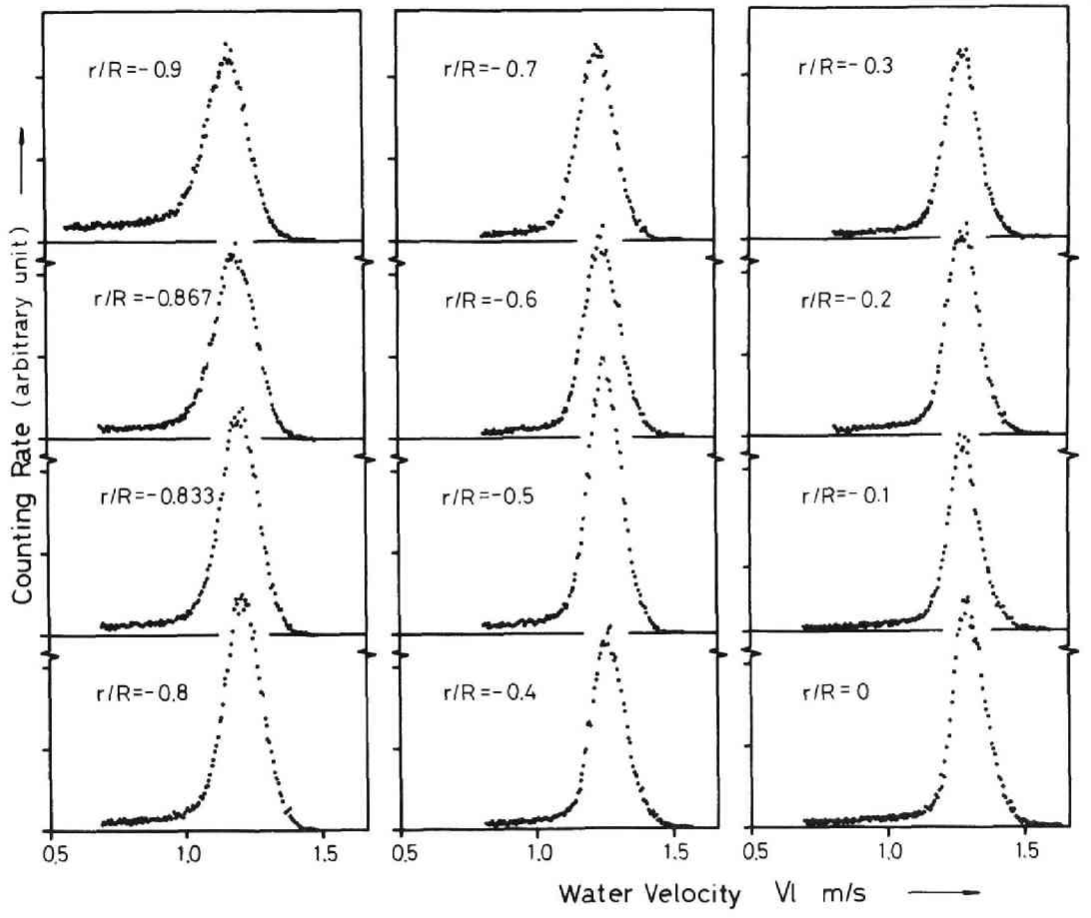

Fig. 4.81 Water velocity spectrum
(Bubble flow : V_o=1.03 m/sec, X=0.0170 %,Z/D=30)

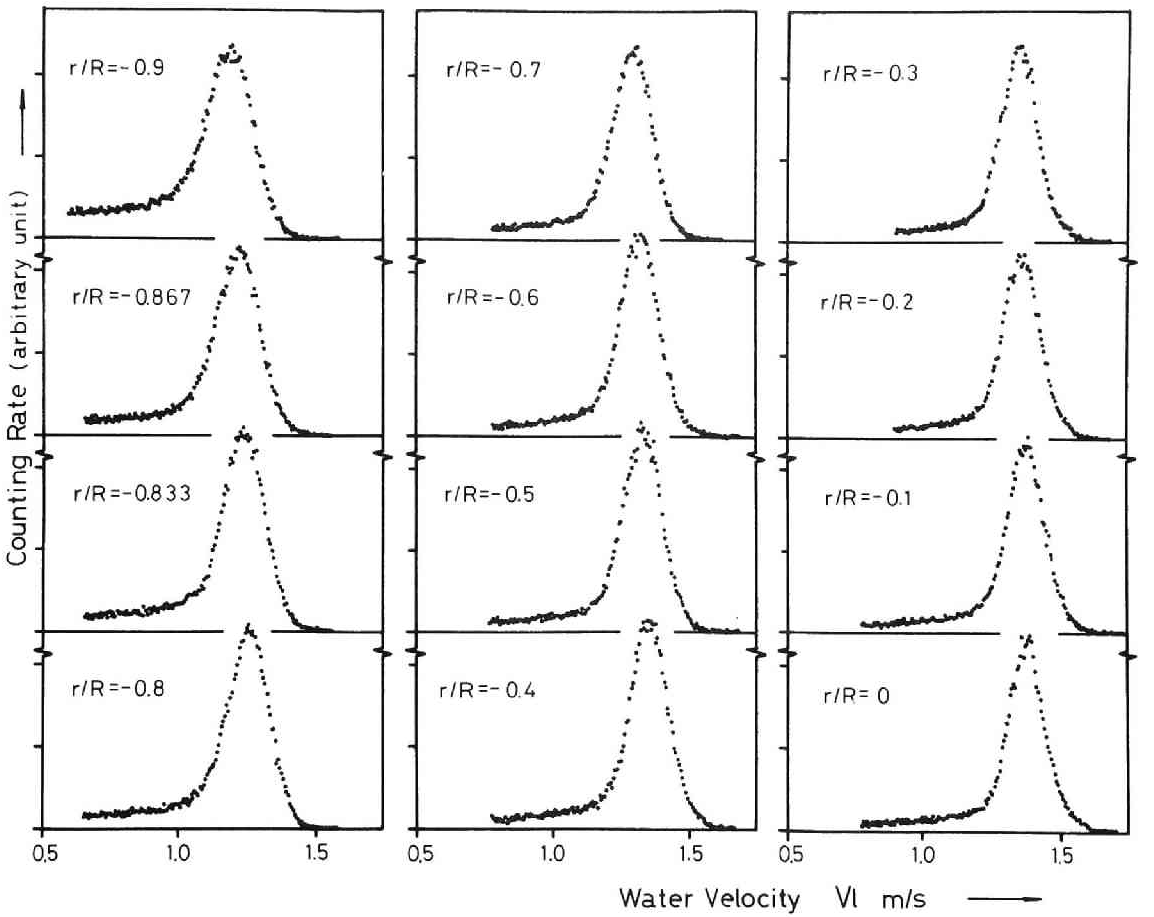

Fig. 4.82 Water velocity spectrum
(Bubble flow : V_o=1.03 m/sec, X=0.0258 %, Z/D=30)

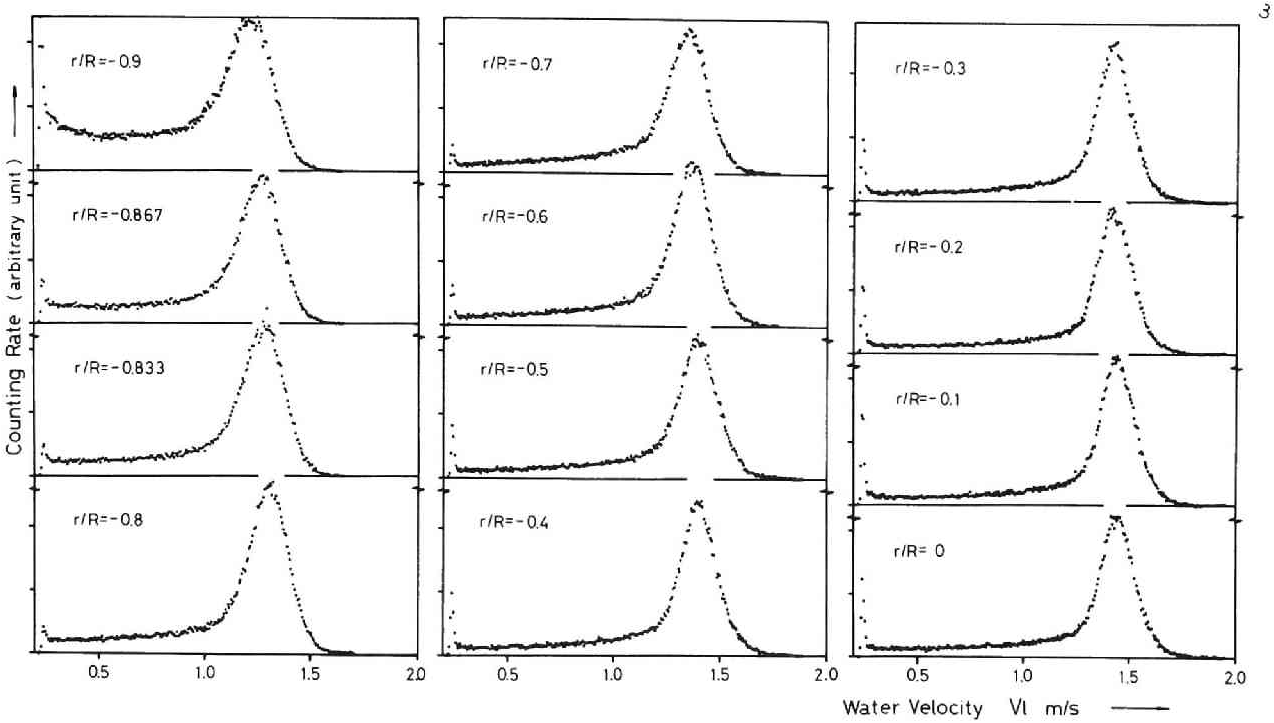

Fig. 4.83 Water velocity spectrum
(Bubble flow : V_o=1.03 m/sec, X=0.0341 %, Z/D=30)

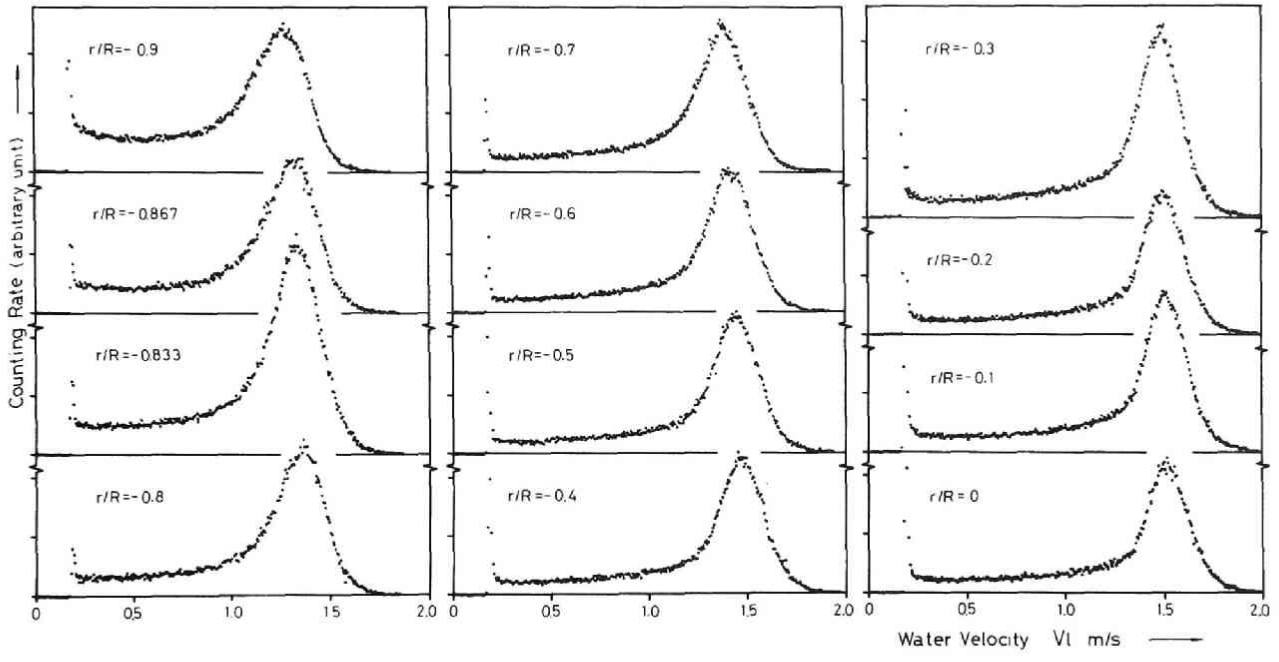

Fig. 4.84 Water velocity spectrum
(Transition flow : V_o=1.03 m/sec, X=0.0427 %, Z/D=30)

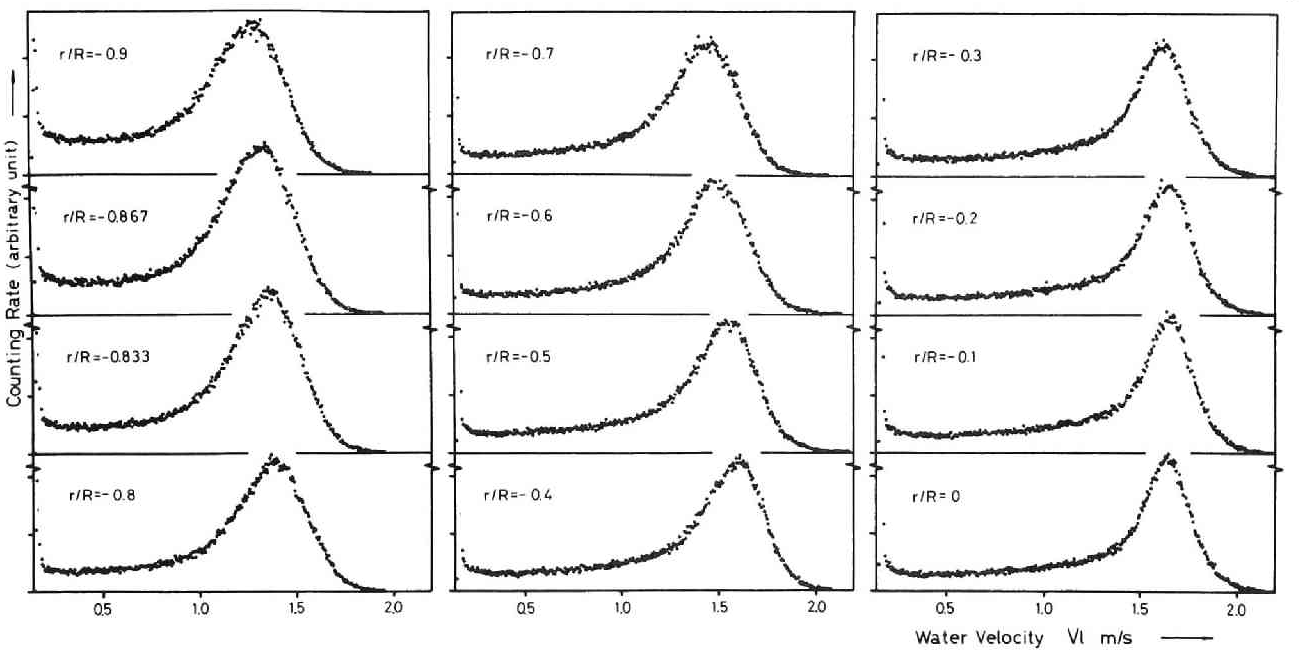

Fig. 4.85 Water velocity spectrum
(Slug flow : V_o=1.03 m/sec, X=0.0511 %, Z/D=30)

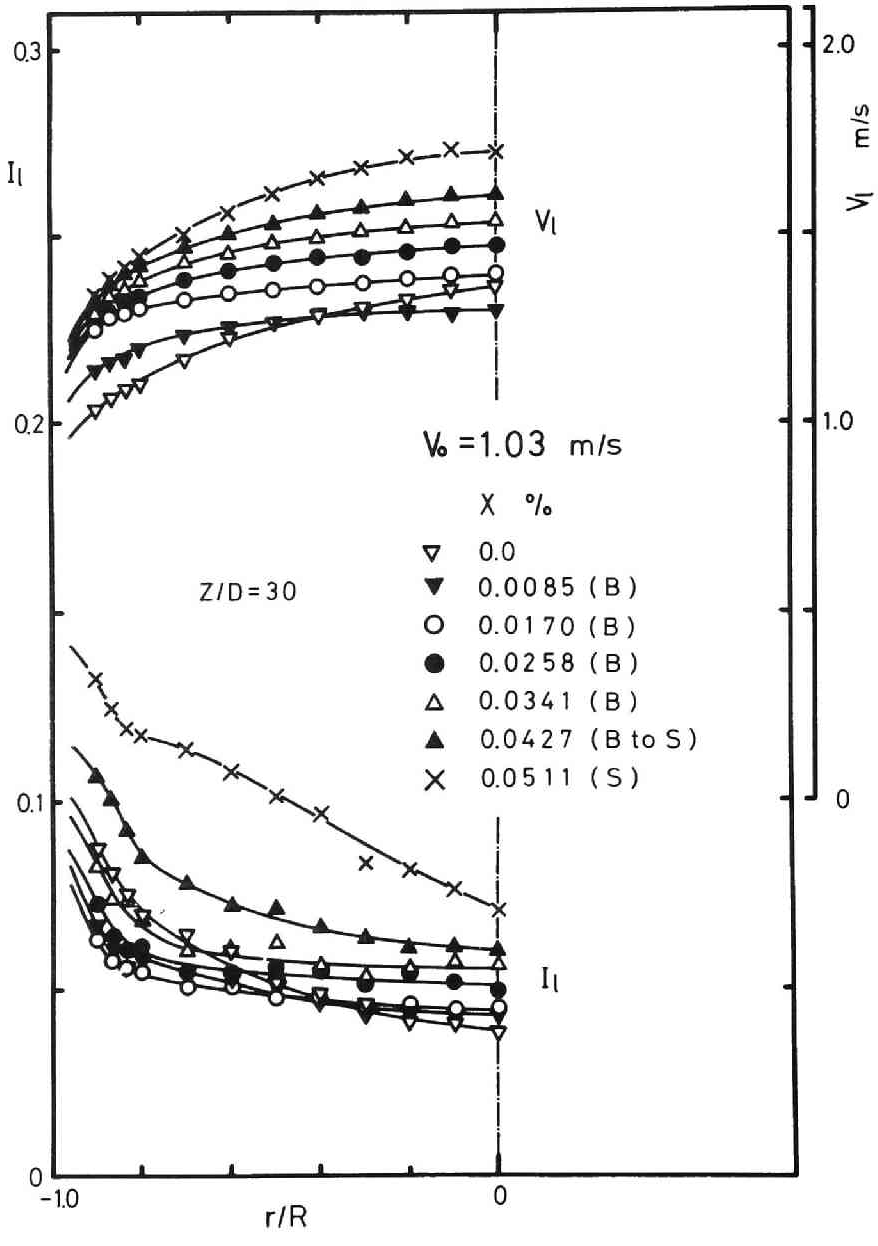

Fig. 4.86 Profiles of water velocity and relative turbulent intensity

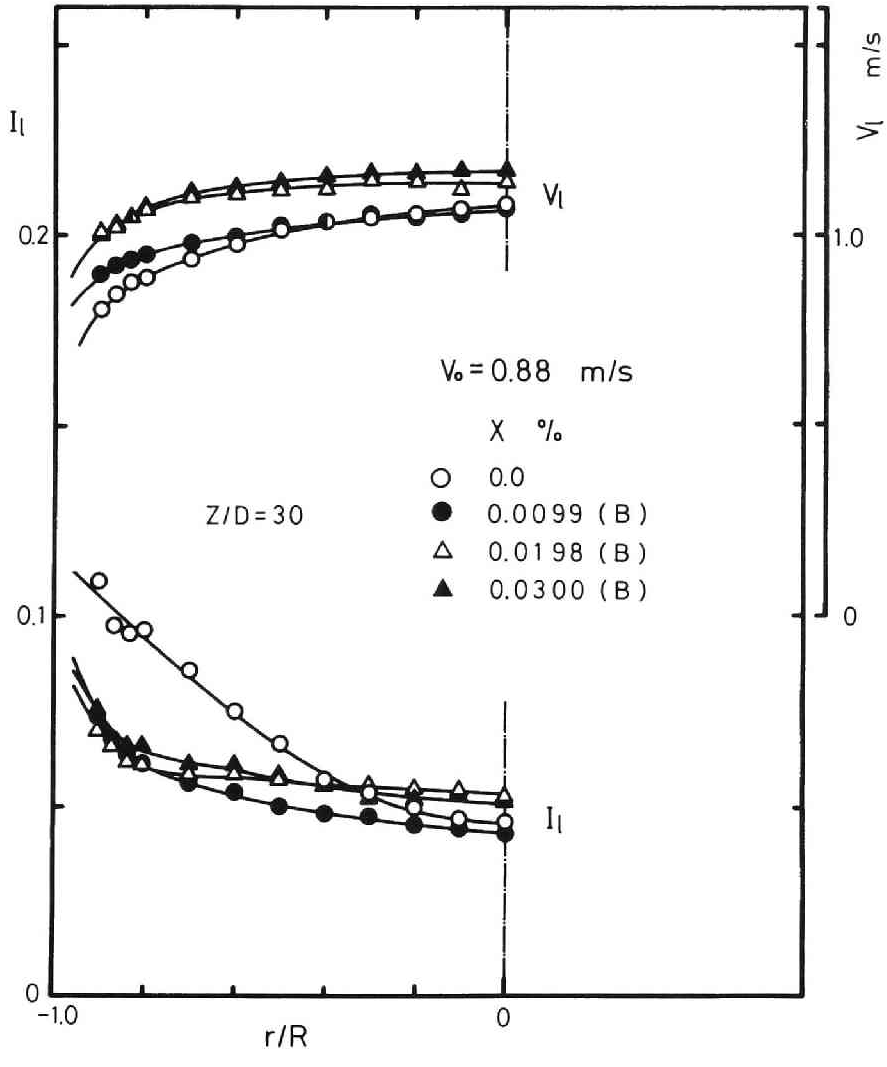

Fig. 4.87 Profiles of water velocity and relative turbulent intensity

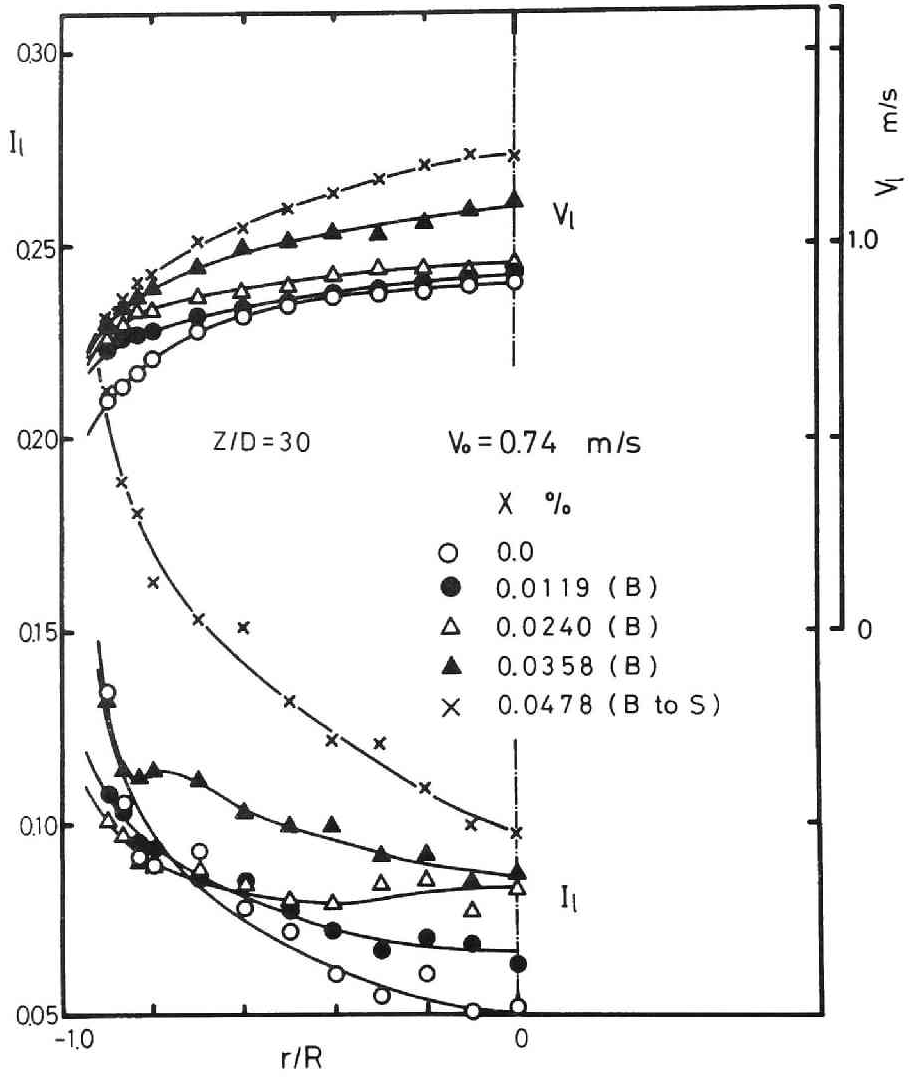

Fig. 4.88 Profiles of water velocity and relative turbulent intensity

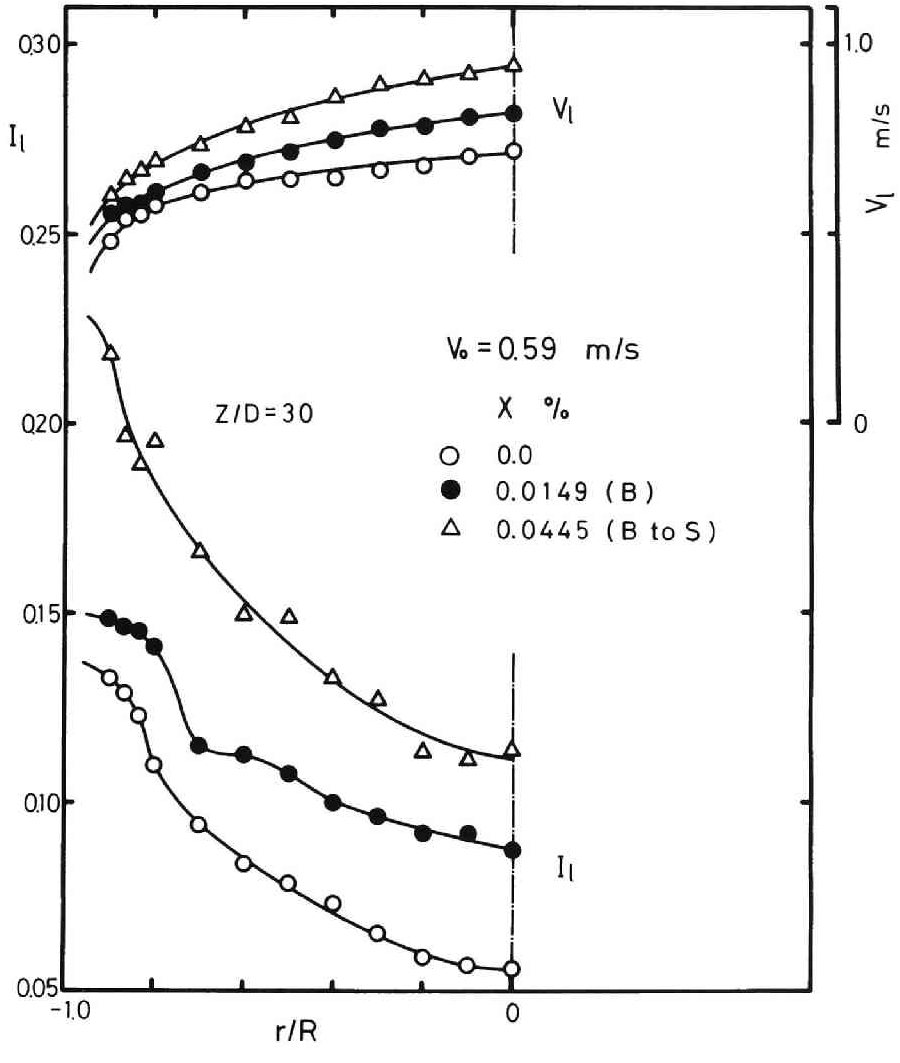

Fig. 4.89 Profiles of water velocity and relative turbulent intensity

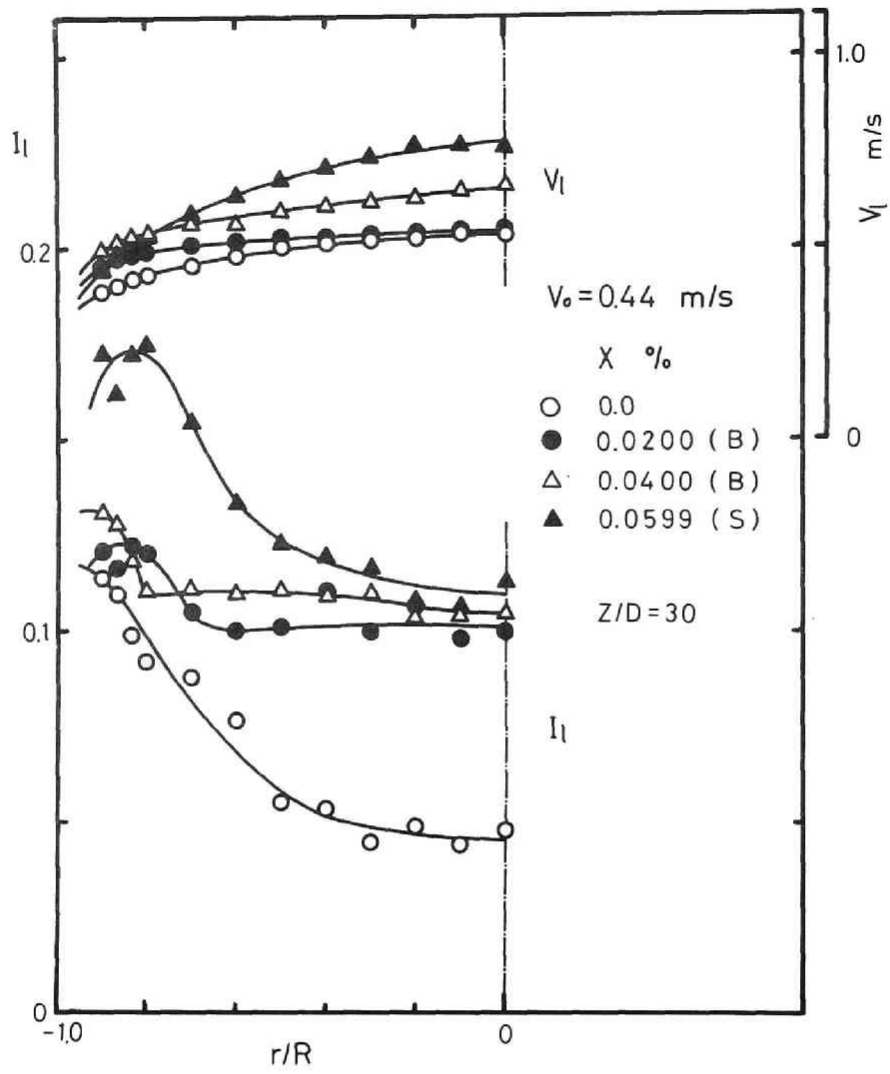

Fig. 4.90 Profiles of water velocity and relative turbulent intensity

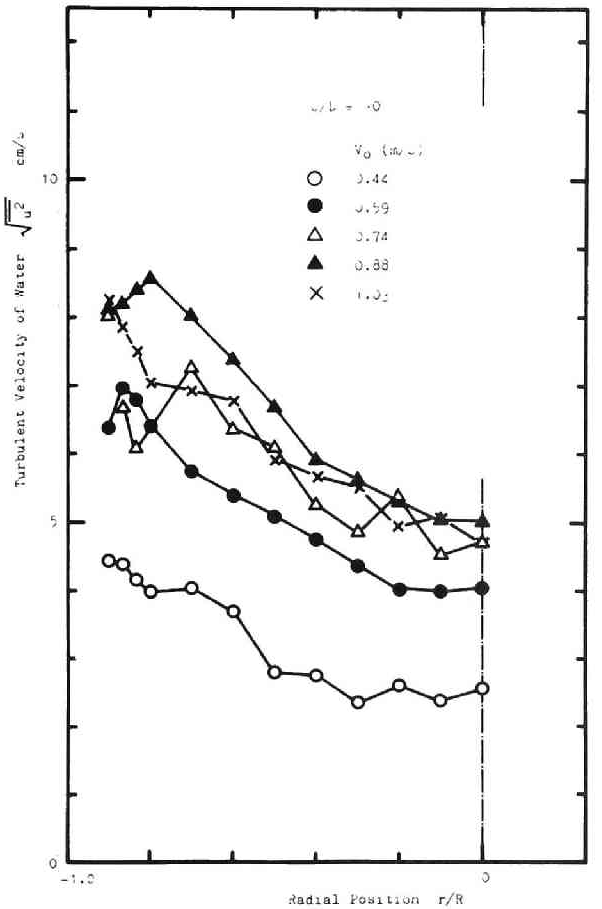

Fig. 4.91 Turbulent velocity of water (single-phase flow)

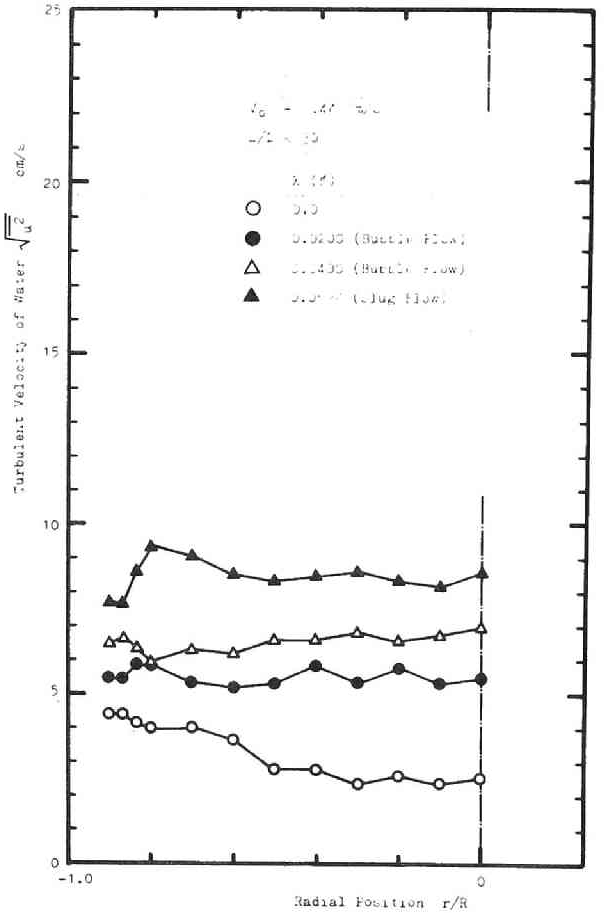

Fig. 4.92 Turbulent velocity of water (V_o=0.44 m/sec)

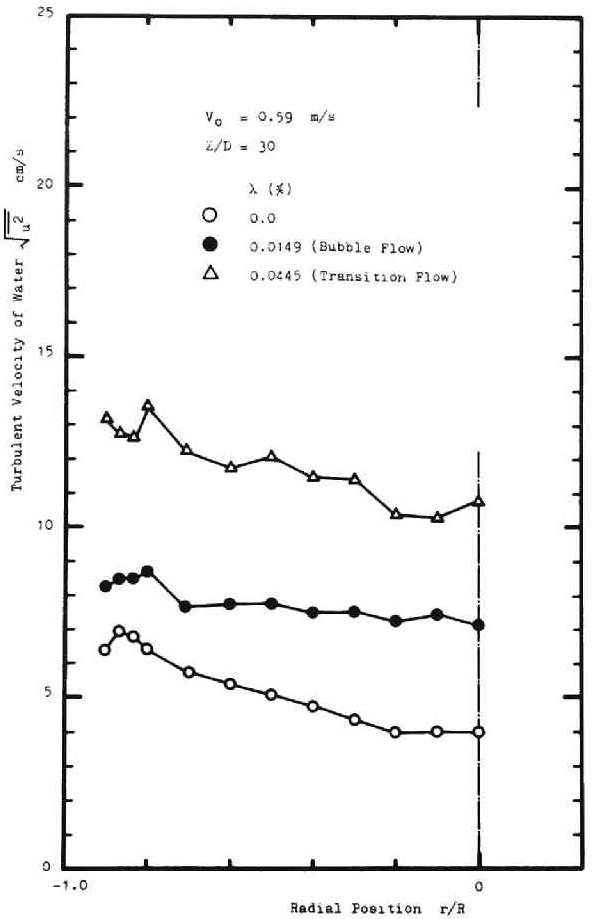

Fig. 4.93 Turbulent velocity of water (V_o=0.59 m/sec)

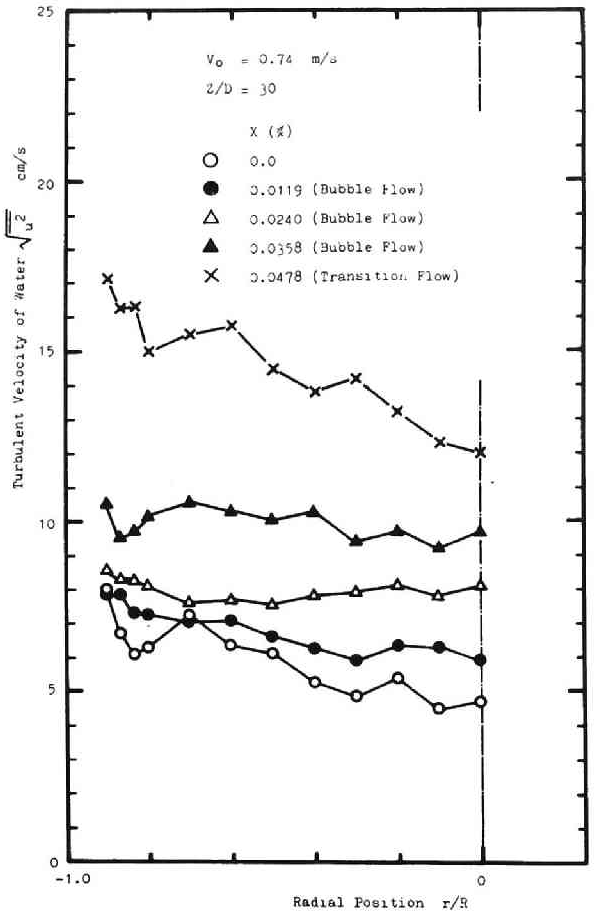

Fig. 4.94 Turbulent velocity of water (V_o=0.74 m/sec)

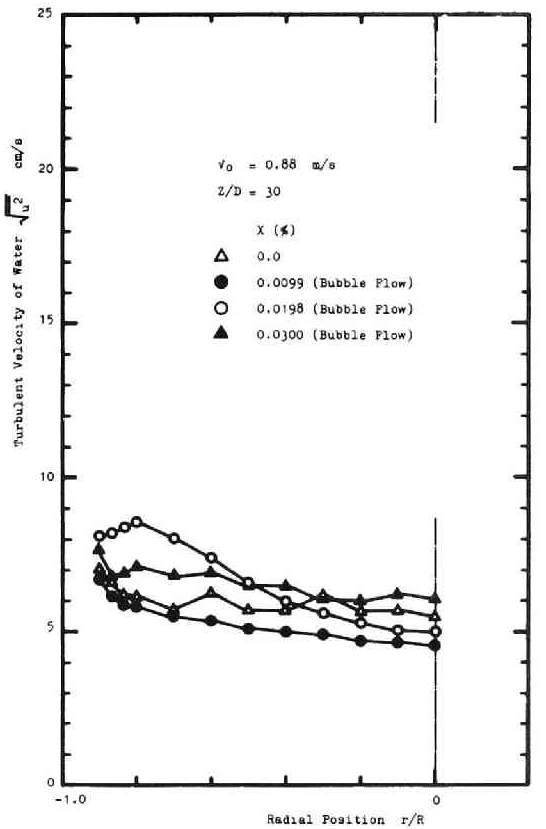

Fig. 4.95 Turbulent velocity of water (V_o=0.88 m/sec)

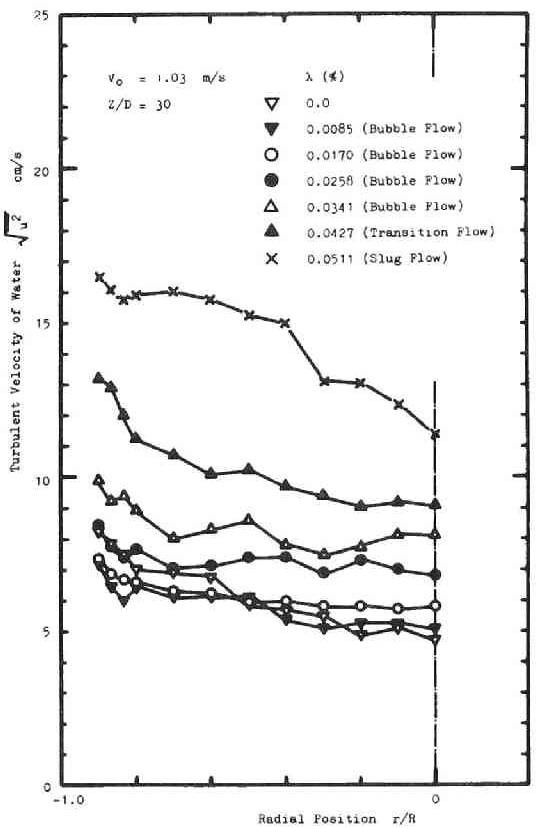

Fig. 4.96 Turbulent velocity of water (V_o=1.03 m/sec)

4.9 Some Additional Discussions

In the foregoing sections of this chapter, the important variables characterizing an air-water two-phase flow have been discussed individually, based upon the experimental results obtained. But all of those variables may influence each other very complicatedly, and hence, to summarize them and to make a broad inspection will be quite necessary for understanding or having sound insights into the physical picture of the flow mechanism.

First, we shall restrict ourselves to consider the relationships between those variables and to embody them.

Secondly, the mixing length concept will be applied for the analysis of the present problems in order to get an indication of the mechanism of the turbulent transport process in two-phase flow of which thema will be treated experimentally in next chapter. (Though it has been shown by many studies that the physical picture based upon the concept of a mixing length cannot be correct in all details, the mixing length theories still prove to be most useful in practice[52].)

4.9.1 Experimental Relationships between Various Local Parameters

Figures 4.97 ~ 4.105 are correlative representations of the experimental relationships between various local parameters already obtained for two different water flow rates. The work of Malnes[5] in air-water flow is shown in Fig.4.106 for reference.

From these figures, it may be confirmed again that there are strong functional relationships or similarities between the void fraction and the bubble number (bubble impaction rate), the bubble velocity and the water velocity, and between the relative standard deviation of the bubble velocity spectrum and the relative turbulent intensity of the liquid.

In bubble flow, most parameters are uniformly distributed over the central region of $|r/R| < 0.7 \sim 0.8$ where the turbulent transport

in radial direction is evaluated to be overwhelmingly predominant due to the continuous stirring effects of small bubbles. In the outer region of the flow where direct viscous effects are still negligibly small, almost all the parameters either increase or decrease rapidly with radius because of the wall effects.

4.9.2 Application of the Mixing Length Theory

Here, as elsewhere, it is the mechanism of the turbulence and of its transport process governing the two-phase bubble flow that we want to consider in detail, in so far as this is made possible by the available results obtained by the present experimental work.

If we can assume that the bubbles are small enough with respect to the smallest turbulence scale, then the mixing length concept analogous to that proposed by Levy[53] will serve to this purpose. Under the assumption of a homogeneous flow with radial variation of the fluid density, Levy applied Navier-Stokes equation to two-phase, steady-state, incompressible flow by introducing the turbulent components, and obtained an expression

$$\tau = \bar{\rho} \cdot \overline{uv} + \bar{V} \cdot \overline{\rho' v} \qquad (4.15)$$

where

τ = Time-average shear force,
$\bar{\rho}$ = Time-average density,
$\bar{V}$ = Time-average velocity along the pipe axis,
u = Turbulent velocity component along the pipe axis,
v = Turbulent velocity component in radial direction,
ρ' = Density fluctuation .

Brandt[54], who first applied a mixing length theory for two-phase flow analysis, obtained an expression identical to that of one-phase flow,

$$\tau = \bar{\rho} \cdot \overline{uv} \quad . \tag{4.16}$$

As cited in Ref.[5], Peterson pointed out in his paper[55] that the last term in Eq.(4.15) obtained by Levy should be zero, which could be deduced from Levy's own assumptions, and consequently Eq.(4.15) should become analogous to the aforementioned Brandt's equation (Eq. (4.16)). However, details are to be known about their arguments.

When the system is considered to be composed of the liquid and small suspended particles as it is, then the fluctuation of the mean fluid density averaged over the unit volume element of the fluid taken at any position of the channel is indeed the result of bubble-coming-in or out of that volume element. And the newly coming bubble may exclude the liquid of the same volume out of the fluid element, or the liquid may enter the element to fill the space which has been previously occupied by the coming-out bubble. As a result of this density variation, a change in radial velocity may occur instantaneously. For this case, $\overline{\rho' v} = 0$. (When $\rho' = 0$, $\overline{\rho' v}$ is of course zero whatever v may be.)

But in the above discussion, the flow has not been postulated to be homogenous, and hence the mixing length concept cannot be applied to the case from the beginning. Taking this the other way round, it seems more natural that, under the assumption of a homogenous fluid, the variation in radial velocity should not be always the result of the variation in density, and this may lead to $\overline{\rho' v} \neq 0$ (in mixing length theory, the flow is postulated to be composed of a single fluid of which local density is $\rho = \rho_l(1 - \alpha_{loc}) + \rho_g \alpha_{loc}$).

This problem associated with whether the term $\overline{\rho' v}$ is zero or not will be briefly commented later, based upon the experimental results on mixing length.

Now, in order to determine the mixing length experimentally from the measured distributions of the void fraction and the liquid velocity, the following additional assumptions are made:

1) Viscous effects are mainly due to the liquid,

2) The mixing length for the density distribution is equal to that for the velocity,

3) The local density of the flow is defined as

$$\rho = \rho_l(1 - \alpha_{loc}) + \rho_g\alpha_{loc}$$

With these assumptions, Levy's equation, Eq.(4.15), becomes Eq.(4.17) with the addition of viscous effects.

$$\tau = \bar{\rho}\cdot\overline{uv} + \bar{V}_l\cdot\overline{\rho'v} + \mu_l\bar{\alpha}_l\frac{d\bar{V}_l}{dy} \tag{4.17}$$

where

μ_l = Liquid viscosity

$\bar{\alpha}_l$ = Time-average local liquid fraction (= $1 - \alpha_{loc}$)

$\bar{\alpha}_{loc}$ = Time-average local void fraction

Equation (4.17) indicates that the momentum transport process can be divided into three contributions. The first term on the right hand side of Eq.(4.17) represents the exchange of momentum by the turbulent velocity components, the second that by the density variation, and the last that by the viscous force.

From accepted mixing length theory, the turbulent velocity components and the fluctuating component of density are written as below:

$$u = v = L_v\ (d\bar{V}_l/dy) \tag{4.18}$$

$$\rho' = L_d\ (d\bar{\rho}/dy) \tag{4.19}$$

Assumption (2) yields

$$L_v = L_d \equiv L_m \tag{4.20}$$

By substituting Eqs.(4.18) ~ (4.20) into Eq.(4.17), we obtain

$$\tau = L_m^2 (d\bar{V}_1/dy) \left| d(\bar{\rho}\bar{V}_1)/dy \right| + \mu_1 \bar{\alpha}_1 (d\bar{V}_1/dy)$$

$$\simeq \rho_1 L_m^2 (d\bar{V}_1/dy) \left| d(\bar{\alpha}_1 \bar{V}_1)/dy \right| + \mu_1 \bar{\alpha}_1 (d\bar{V}_1/dy) \quad . \qquad (4.21)$$

Hence,

$$L_m = \left[\left| \tau - \mu_1 \bar{\alpha}_1 (d\bar{V}_1/dy) \right| \; / \; \{ \rho_1 (d\bar{V}_1/dy) \left| d(\bar{\alpha}_1 \bar{V}_1)/dy \right| \} \right]^{1/2} \qquad (4.22)$$

Local shear stress $\tau(r)$ can be determined by the force balance in the following form of equation,

$$-\tau(r) = \frac{1}{r} \int_0^r \{ \bar{\rho} g + (d\bar{P}/dz)_t \} r \, dr$$

$$\simeq \frac{1}{r} \int_0^r \{ \rho_1 \bar{\alpha}_1 g + (d\bar{P}/dz)_t \} r \, dr \quad . \qquad (4.23)$$

Combination of Eqs.(4.22) and (4.23) makes it possible to calculate the mixing length for momentum transport from the experimental results on the velocity and the phase distributions.

The mixing length for velocity can be obtained in another way. According to Eq.(4.18), the longitudinal turbulent intensity of the liquid $\sqrt{\overline{u^2}}$ is then expressed in terms of the mixing length:

$$\sqrt{\overline{u^2}} = L_v \left| d\bar{V}_1/dy \right| \quad ,$$

and therefore

$$L_v = \sqrt{\overline{u^2}} \Big/ \left| \frac{d\bar{V}_1}{dy} \right| \quad . \qquad (4.24)$$

Thus, the mixing length L_v can be deduced also from the experimental

data on the distributions of the liquid velocity and the corresponding turbulent intensity.

Figure 4.107 represents comparison between the mixing lengths obtained in two different ways, the one calculated from Eq.(4.22) (denoted by L_m (calculated)), and the other from Eq.(4.24) (denoted by $\sqrt{\overline{u^2}}/|\frac{dV_1}{dr}|)_{meas.}$). A satisfactory agreement can be seen between them within the range $-0.85 < r/R < -0.25$. This implies or indirectly verifies the validity of Eqs.(4.17) and (4.20) (i.e., $\overline{\rho' v} \approx 0$). (For single-phase flow data, $\sqrt{\overline{u^2}}/|\frac{dV_1}{dr}|$ was somehow roughly two times larger than L_m.)

Values of the mixing length for momentum transport predicted by Eq.(4.22) are given in Figs.4.108 and 4.109 for two different water flow rates. Curves shown in both figures indicate the mixing length in single-phase flow:

$$\text{Curve (1)} \quad \frac{L_m}{R} = 0.14 - 0.08\left(\frac{r}{R}\right)^2 - 0.06\left(\frac{r}{R}\right)^4$$

$$\text{Curve (2)} \quad L_m = 0.4(R - r)$$

These figures indicate much larger values of mixing length in bubble flow than in single-phase water flow. This follows that the distributions of the water velocity and the density are more flattened in bubble flow than in single-phase flow. This tendency coincides completely with the experimental indications of both distributions.

As pointed out by Malnes[5], the mixing length is a strong function both of the void fraction and of the water velocity. Experimental results indicate that, as the void fraction or the quality increases, the mixing length first increases rapidly up to a certain value determined mainly by water velocity, and finally decreases towards the value for single-phase flow*. (Mixing length concept cannot be applied to slug flow, because the homogeneity of the flow can be no longer postulated for such a flow pattern.) This trend is

---

* See footnote on next page.

more remarkable for lower water velocities.

Here, it is of great interest to consider the relative effects of the momentum transport caused by three contributing terms. Let Γ_v, Γ_d and Γ_{vs} the momentum transports due to the velocity fluctuation, the density fluctuation and due to the viscous force, respectively, then

$$\Gamma_v = \rho_1 L_m^2 \bar{\alpha}_1 \left|\frac{d\bar{V}_1}{dy}\right| \left(\frac{d\bar{V}_1}{dy}\right) , \tag{4.25a}$$

$$\Gamma_d = \rho_1 L_m^2 \left|\frac{d(\bar{\alpha}_1\bar{V}_1)}{dy}\right| \left(\frac{d\bar{V}_1}{dy}\right) , \tag{4.25b}$$

$$\Gamma_{vs} = \mu_1 \bar{\alpha}_1 \frac{d\bar{V}_1}{dy} . \tag{4.25c}$$

Typical results are shown in Fig.4.110 where Γ_v/Γ_{vs} and Γ_d/Γ_{vs} are plotted as functions of radius. As is expected, it will be seen that both contributions due to the turbulent fluid motions (Γ_v and Γ_d) are thus two or three orders of magnitude higher than the viscous effect. It will be noted that the turbulent velocity contribution Γ_v is favorably higher than the density contribution Γ_d for two cases within the range $|r/R| < 0.8$ and, in the outer region, the latter is dominant. This observation means that, in the flow with low void fraction, momentum transport will be carried out mainly by the turbulent fluctuating velocities except near the wall, while towards the wall to which bubbles are apt to approach as seen in Fig.4.37, it will be carried out by the density fluctuation due to the voilent stirring effect of bubbles or due to the wall effect.

According to the mixing length theory, the eddy diffusivity for

---

* According to the descriptions by Malnes[5], Brandt[54] found that the mixing length in two-phase flow varies over the cross section in the same way as for single-phase flow, but its absolute value was 1.73 times higher.

momentum transport ε_M is normally defined as below*,

$$\varepsilon_M = L_m^2 \frac{d\bar{V}_l}{dy} \quad . \tag{4.26}$$

Combination of Eqs.(4.22) and (4.26) yields the experimental eddy diffusivity of momentum.

Typical results obtained are illustrated in Fig.4.111. It will be seen that the results for four respective gas flow rate are rather similar. However, the data is subjected to some error due to the graphical differentiations of $\bar{V}_l$ and $\bar{\alpha}_{loc}$, and the detailed differences between the curves for the respective gas velocities may not be too significant. However, it is apparent that the diffusivities are not affected very greatly by the change in gas flow rate, and that they pass through a maximum at a point intermediate between the wall and the pipe center (a point corresponding approximately to r/R = 0.4) which is of a qualitatively similar form to the results of the single-phase water flow obtained in the present work and also to the published data on diffusivity for single or two-phase flow (for instance, data of Page et al.[56], Corcoran & Sage[57], Schwarz & Hoelscher[58], Cousins & Hewitt[59], and others).

A general trend is that, for constant water flow rate, the diffusivity first increases rapidly with the quality, and, after the

---

* This eddy diffusivity is defined according to the turbulent velocities. Namely,

$$\varepsilon_M = - \overline{uv} \Big/ \frac{d\bar{V}_l}{dy} = L_m^2 \frac{d\bar{V}_l}{dy} \quad .$$

The alternate eddy diffusivity can be also defined based upon the density fluctuation,

$$\varepsilon_M' = - \overline{\rho' v} \Big/ \frac{d\bar{\rho}}{dy} = L_v L_m \frac{d\bar{V}_l}{dy} = L_m^2 \frac{d\bar{V}_l}{dy} \quad .$$

quality exceeds a certain value (for instance, this boundary quality is about 0.0170 % in the case V_o = 1.03 m/sec), it gradually decreases again. This is quite consistent with the data on the water velocity profile and the void fraction profile which indicate more uniform distributions for lower quality. Accordingly, it is confirmed again that the turbulent transport phenomena are made most active by introducing an appropriate quantity of the gas bubbles into the stream.

4.10 Conclusions

Accurate measurements were made of the various flow variables characterizing the turbulence structure of air-water two-phase flow, normally including earlier stages of the flow pattern (i.e., bubble flow, transition flow and slug flow), which is flowing upwards in a vertical pipe of 60 mm inside diameter.

The following remarks summarize the findings of this experimental study:

1) Entrance effects on development of two-phase flow were seen down to the axial position Z/D = 20, while in single-phase water flow fully-developed flow was already attained at Z/D = 20.
2) Bubbles suspended in the stream of bubble flow exhibit some statistical properties in respect to their size distribution, the transit frequency distribution and the rising velocity.
3) Slug flow can be successfully distinguished from bubble flow by taking into account the Eulerian auto-correlation function of the local density fluctuation measured by means of an electrical resistivity probe.
4) In bubble flow, many variables are almost uniformly distributed across the pipe cross section except near the wall. Non-uniformity of the flow due to the wall effects can be expected to be significant in the outer region of the flow area approximately $|r/R| > 0.7$. In slug flow, non-uniformity of the flow increases over the whole cross section of the pipe.
5) Void fraction and bubble number distributions show quite similar trends to each other. They change from a saddle-shaped distribution with a maximum at the position away from the wall by a distance of nearly bubble radius to a dome-shaped one with a maximum at the pipe center, as the quality is gradually increased or the flow pattern varies from bubble to slug flow for constant water flow rate.
6) Distributions of the ensemble-average bubble velocity and the

water velocity show monotonous decreasing functions with radius, and they may be approximated by an expression of the power law of which exponent is a strong function of the flow conditions.

7) Local slip ratio is nearly uniform across the pipe.

8) Spectra of the bubble velocity and the water velocity can be well approximated by the Poisson distribution function and the normal distribution, respectively. Deviation from the Poisson distribution in bubble velocity spectrum can be seen in accordance with the appearance of slugs in the stream.

9) Distributions of the relative standard deviation of the bubble velocity spectrum and the relative turbulent intensity of the liquid show fair uniformity for bubble flow, especially at higher water velocities.

10) Experimental results on the longitudinal turbulent velocity component indicate, in some cases of bubble flow with high water flow rate and low void fraction, lower values than those measured for single-phase water flow. Mechanism of this interesting phenomenon will have to be analyzed in more detail, however some brief discussions were made in relation to the energy dissipations.

11) Mixing length concept can be approximately applied to air-water bubble flow by assuming that the mixing length for velocity distribution is equal to that for the density. Results of the calculated mixing length and eddy diffusivity for momentum transport can successfully show good consistencies with qualitative tendencies of the uniform distributions of the transferable quantities already mentioned. The calculated mixing length for momentum has been confirmed to be a function of the flow variables, as pointed out by Malnes[5] and Aoki et al.[10].

12) According to the mixing length concept, there are three types of contributions to the momentum transport in two-phase flow, that is, the contributions due to the turbulent velocity components, the density fluctuation, and due to the viscous effects. It may be evaluated that the first type of contribution is the dominant

mechanism of the turbulent transport process in two-phase bubble flow, and that the viscous effects is negligibly small except in the very vicinity of the wall.

More detailed descriptions can be referred to concluding paragraphs of each section of this chapter.

REFERENCES

[1] Petrick, M.: ANL-6581, (1962).

[2] Petrick, M., Kudirka, A.A.: 3rd Int. Heat Trans. Conf., Chicago, p.184, (1966).

[3] Nassos, G.P.: ANL-6738, (1963).

[4] Shires, G.L., Riley, P.J.: AEEW-M-650, (19).

[5] Malnes, D.: KR-110, (1966).

[6] Lackme, C.: CEA-R-3203, (1967).

[7] Delhaye, J.M.: CEA-R-3465, (1968).

[8] Brown, F.C., Kranich, W.L.: Am. Inst. Chem. Engrs. J., 14[5], 750 (1968).

[9] Kobayashi, K., Iida, Y., Kanegae, N.: Trans. Japan Soc. Mech., Engrs., 35[280], 2365 (1969).

[10] Aoki, S., Inoue, A., Yaegaki, H.: 7th Japan Heat Trans. Symp., p.241 (1970).

[11] Kobayashi, K., Irino, Y.: 10th Japan Heat Trans. Symp., p.41 (1973).

[12] Kazin, I.V.: Teploenergetika, 11[1], 40 (1964).

[13] Iida, Y.: 7th Japan Heat Trans. Symp., p.217 (1970).

[14] Neal, L.G.: ANL-6625, (1963).

[15] Tamao, S.: M.S. thesis, Kyoto Univ., (1970).

[16] Vohr, J.: Am. Inst. Chem. Engrs. J., 8[2], 280 (1962).

[17] Lamb, D.E., White, J.L.: ibid., 8[2], 281 (1962).

[18] Van Deemter, J.J., Van der Laan: Appl. Sci. Res. Soc., A10, 102 (1961).

[19] Sekoguchi, K., Kawakami, Y., Nishikawa, K.: 9th Japan Heat Trans. Symp., p.21 (1972).

[20] Serizawa, A., Kataoka, I., Michiyoshi, I.: 1973 Annu. Meeting At. Energy Soc. Japan, E47 ~ 48 (1973).

[21] Govier, G.W., Aziz, K.: The Flow of Complex Mixtures in Pipes, Van Nostrand Reinhold Co., (1972).

[22] Pertick, M.: ANL-5787, (1958).

[23] Adachi, K., Segawa, M.: 3rd Japan Heat Trans. Symp., p.77 (1966).
[24] Kinoshita, T., Murazaki, H.: Trans. Japan Soc. Mech. Engrs., 34 [267], 2003 (1968).
[25] Nishikawa, K., Sekoguchi, K., Ikeda, H., Fukano, T.: ibid., 35 [271], (1969).
[26] Nishikawa, K., Sekoguchi, K., Fukano, T.: ibid., 35[271], 591 (1969).
[27] Hubbard, M.G., Dukler, A.E.: Proc. 1966 Heat Trans. Fluid Mech. Inst., (1966).
[28] Terano, T., et al.: 1962 National Nuclear Congress, Tokyo, Japan, (1962).
[29] Terano, T., et al.: Annu. Meeting At. Energy Soc. Japan, C54 (1963).
[30] Nishihara, H., Michiyoshi, I.: News of Heat Trans. Soc. Japan, 7[26], 11 (1968).
[31] Nakano, S.: B.S. thesis, Kyoto Univ., (1967).
[32] Yamaguchi, K.: M.S. thesis, Kyoto Univ., (1973).
[33] Eurola, A.T.: ANL-6369, (1961).
[34] Lackme, C.: Symposium on Two-Phase Flow, D2, Exeter, (1965).
[35] Sekoguchi, K., Fukui, H., Matsuoka, T., Nishikawa, K.: 9th Japan Heat Trans. Symp., p.435 (1972).
[36] Sekoguchi, K., Fukui, H., Tsutsui, M., Nishikawa, K.: ibid., p.439 (1972).
[37] Tong, L.S.: Boiling Heat Transfer and Two-Phase Flow, John Wiley & Sons, (1965).
[38] Segre, G., Silberberg, A.: Nature, Lond., Vol.189, 209 (1961).
[39] idem.: J. Fluid Mech., Vol.14, 115 (1962).
[40] Sekoguchi, K., Kawakami, Y., Nishikawa, K.: 9th Japan Heat Trans. Symp., p.21 (1972).
[41] Schlichting, D.H.: Boundary Layer Theory, McGraw-Hill, p.267 (1960).
[42] Teletov, S.G.: (Quoted from Ref.[12]).
[43] Hall, I.M.: J. Fluid Mech., Vol.1, 147 (1956).

[44] Saffman, P.G.: J. Fluid Mech., Vol.22, Part 2, 385 (1965).

[45] Jeffery, R.C., Pearson, J.R.A.: J. Fluid Mech., Vol.22, Part 4, 721 (1965).

[46] Kitayama, Y.: J. Nucl. Sci. Technol., 9[10], 613 (1972).

[47] Serizawa, A., Kataoka, I., Michiyoshi, I.: Bulletin Inst. Atom. Energy, Kyoto Univ., Vol.43, p.56, 57 (1973).

[48] Bankoff, S.G.: Trans. Am. Soc. Mech. Engrs., Ser.C, Vol.82, 265 (1960).

[49] Harmathy, T.Z.: Am. Inst. Chem. Engrs. J., Vol.6, 281 (1960).

[50] Delhaye, J.M.: Two-Phase Flow Instrumentation, p.58, 11th National ASME/AIChE Heat Trans. Conf., Minneapolis, Minnesota (1969).

[51] Hino, M.: Proc. Symp. on Multi-Phase Mixtures sponsored by Japan Science Academy, p.21 (1967).

[52] Hinze, J.O.: Turbulence, McGraw-Hill, (1959).

[53] Levy, S.: Trans. Am. Soc. Mech. Engrs., Ser.C, 85[2], 137 (1963).

[54] Brandt, F.: Dissertation, Darmstadt (1958).

[55] Peterson, E.N.: Diplom-Aufgabe, Reinisch-Westfälische Technische Hochscule Aachen (1964).

[56] Page, F., Corcoran, W.H., Schlinger, W.G., Sage, B.H.: Ind. Eng. Chem., Vol.44, 419 (1952).

[57] Corcoran, W.H., Sage, B.H.: Am. Inst. Chem. Engrs. J., 2[2], 251 (1956).

[58] Schwarz, W.H., Hoelscher, H.E.: ibid., 2[1], 101 (1956).

[59] Cousins, L.B., Hewitt, G.F.: AERE-R 5693 (1968).

NOMENCLATURE

d	bubble diameter
$\bar{d}_v$	mean equivalent-spherical diameter of bubbles defined by Eq.(4.2)
D	pipe diameter
E_o	Eotvos number (= $g(\rho_l - \rho_g)d^2/\sigma$)
f	frequency
F_{xx}	auto-correlation function of x(t)
g	gravitational constant
I_g	relative standard deviation of bubble velocity spectrum (s/V_b)
I_l	relative turbulent intensity (= $\sqrt{\overline{u^2}}/V_l$)
L	length of flow channel
L_d	mixing length for density variation
L_m	mixing length for momentum transport
L_v	mixing length for velocity variation
m	exponent
n	integer
n	number of bubbles
N	bubble impaction rate
N_i	counting rate
P	pressure
ΔP	pressure difference
$(\frac{d\bar{P}}{dz})_t$	time-average total pressure drop
Q_g	volumetric flow rate of gas
Q_l	volumetric flow rate of liquid
r	radial coordinate
R	pipe radius
s	standard deviation of bubble velocity spectrum
S	over-all slip ratio (= $\bar{V}_g/\bar{V}_l$)
$\bar{S}$	slip ratio defined by Eq.(4.11)
S_{loc}	local slip ratio (= V_b/V_l)

t	time
T	sampling time
T_l	liquid temperature
u	turbulent velocity component along pipe axis
$\sqrt{\overline{u^2}}$	turbulent intensity
u^*	friction velocity ($= \sqrt{\tau_w/\rho_l}$)
u^+	dimensionless velocity ($= V_l/u^*$)
v	turbulent velocity component in radial direction
$\bar{V}$	time-average velocity
V_b	bubble velocity
$\bar{V}_g$	cross-sectional average velocity of gas phase
V_l	liquid velocity
$\bar{V}_l$	cross-sectional average velocity of liquid phase
V_o	superficial liquid velocity
V_s	local slip velocity ($= V_b - V_l$)
$x(t)$	probe signal
X	quality
$y\dagger$	lateral coordinate
y^*	dimensionless distance ($= 1 - (r/R)$)
y^+	friction Reynolds number ($= u^*(R - r)/\nu_l$)
z	axial coordinate
Z	axial position
$\alpha(r)$	local void fraction
$\bar{\alpha}$	cross-sectional average void fraction
α_c	void fraction at pipe center
α_l	local liquid fraction ($= 1 - \alpha_{loc}$)
$\bar{\alpha}_l$	time-average local liquid fraction
α_{loc}	local void fraction
β	volumetric gas flow rate ratio ($= Q_g/(Q_g + Q_l)$)
Γ_d	momentum transport due to density fluctuation
Γ_v	momentum transport due to fluctuating velocity components
Γ_{vs}	momentum transport due to viscous force
ε_M	turbulent diffusivity for momentum transport

μ_l	viscosity of liquid
ν_l	kinematic viscosity of liquid
$\bar{\rho}$	time-average density
ρ'	density fluctuation
ρ_g	density of gas
ρ_l	density of liquid
σ	surface tension
τ	time lag
τ	shear stress
τ_w	wall shear stress

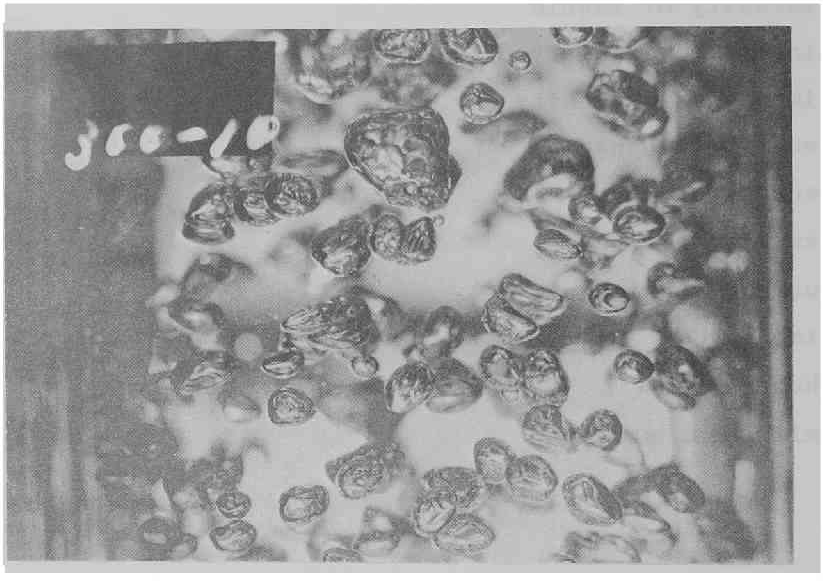

(a) Bubble flow
(V_o=0.44 m/sec, X=0.0200 %, Z/D=22.5)

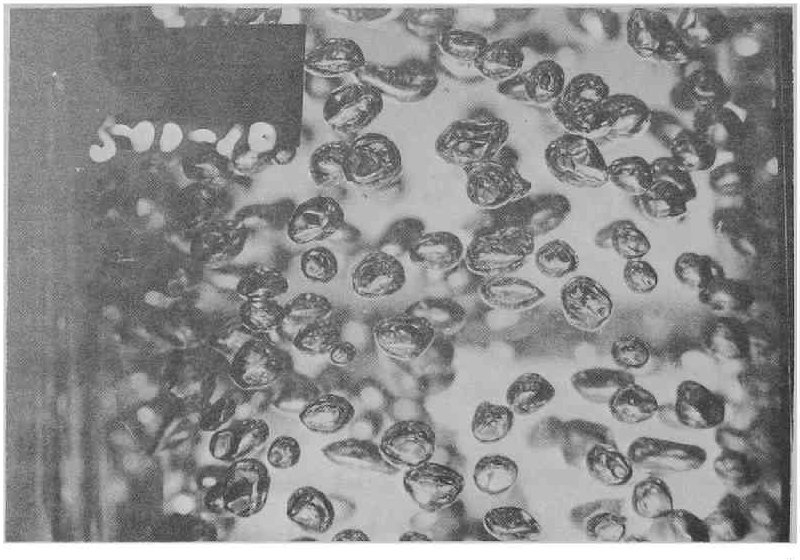

(b) Bubble flow
(V_o=0.74 m/sec, X=0.0119 %, Z/D=22.5)

Photo. 4.1 Typical bubble photograph

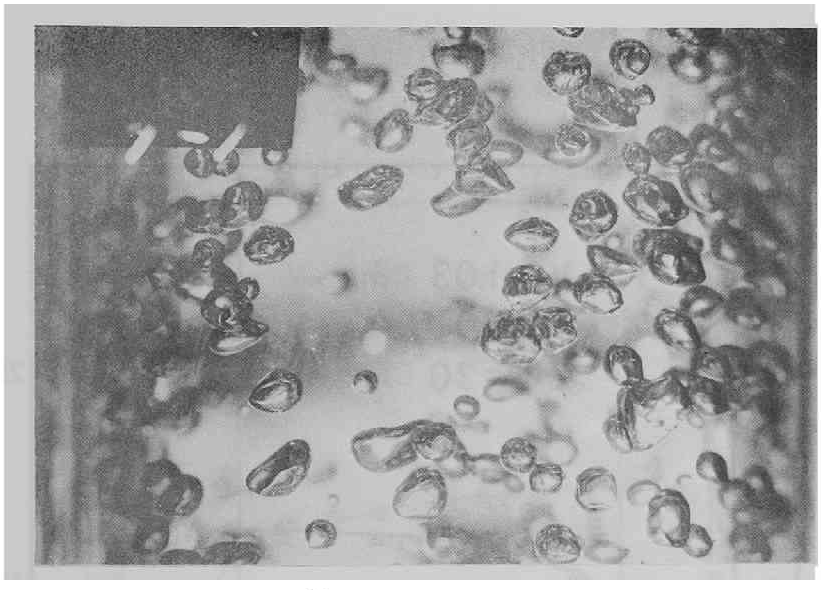

(a) Bubble flow
(V_o=1.03 m/sec, X=0.0085 %, Z/D=22.5)

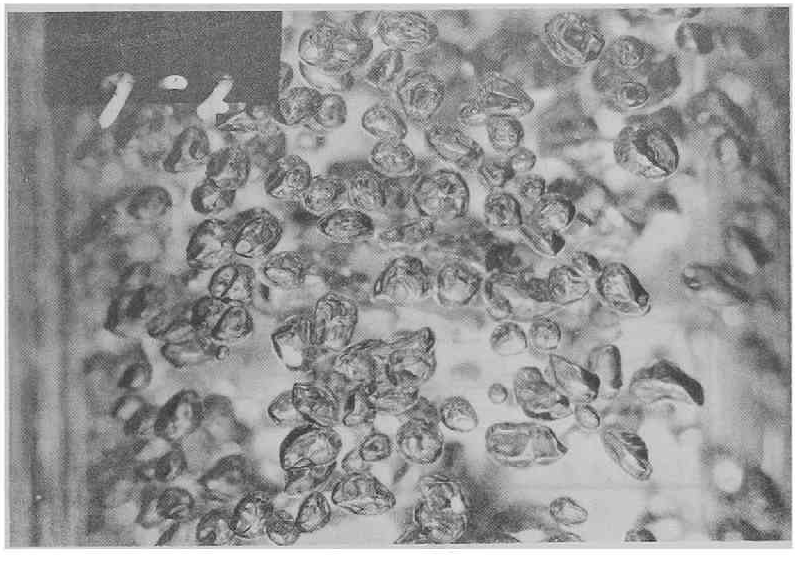

(b) Bubble flow
(V_o=1.03 m/sec, X=0.0170 %, Z/D=22.5)

Photo. 4.2 Typical bubble photograph

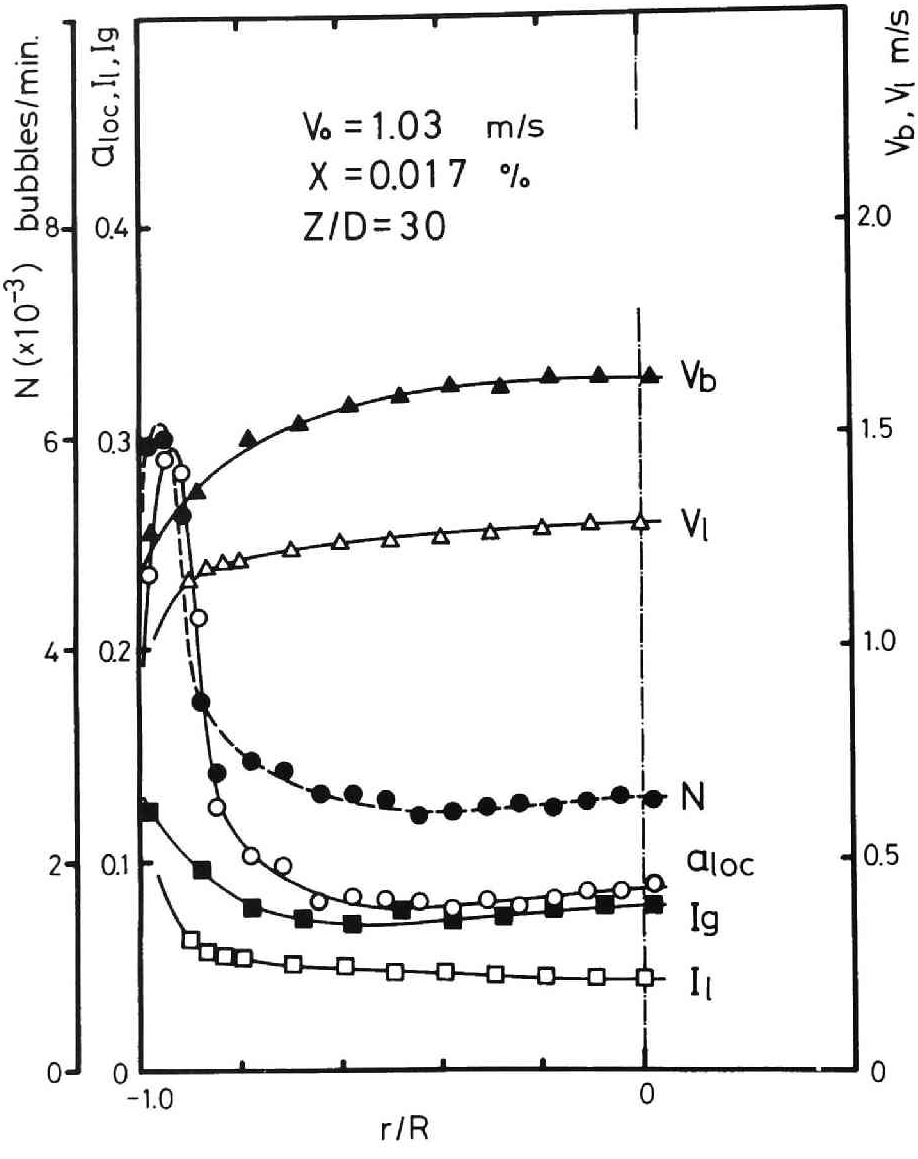

Fig. 4.97 Correlative representation of various local parameters for bubble flow

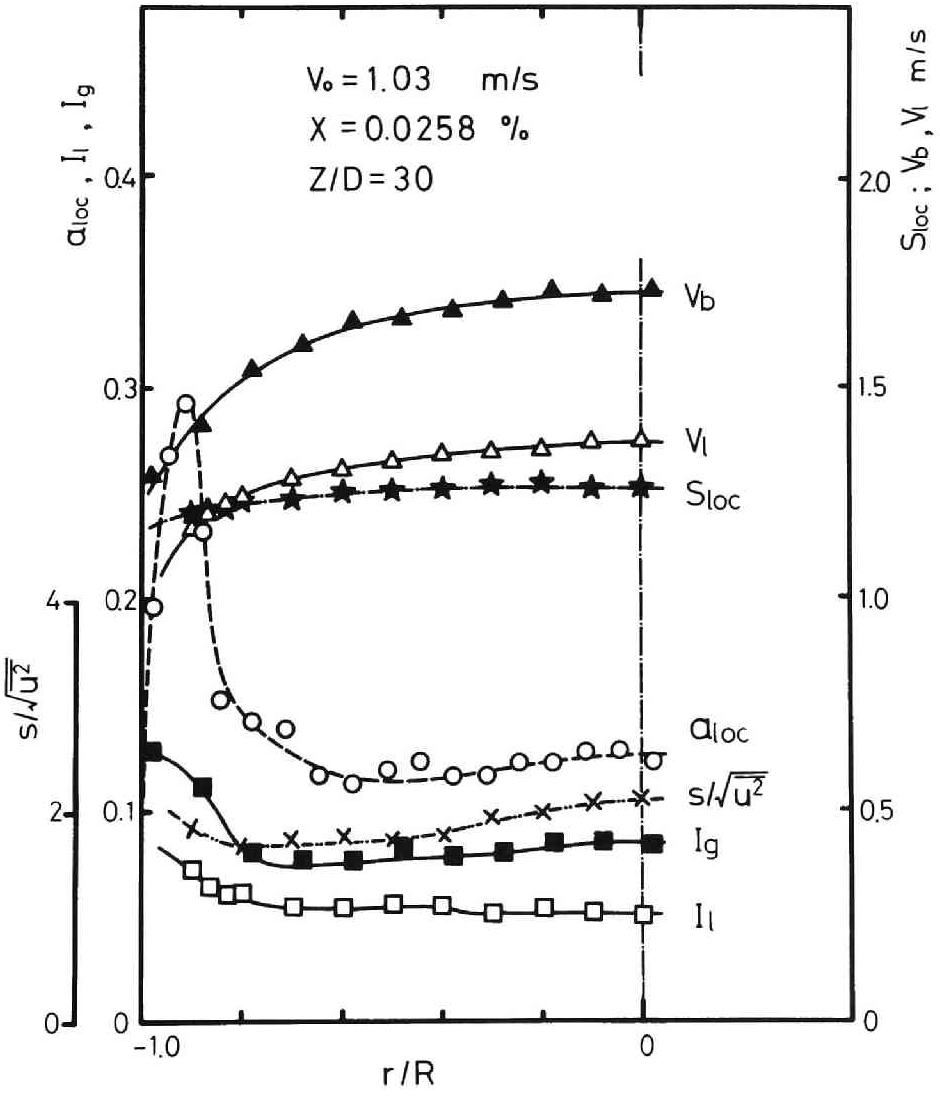

Fig. 4.98 Correlative representation of various local parameters for bubble flow

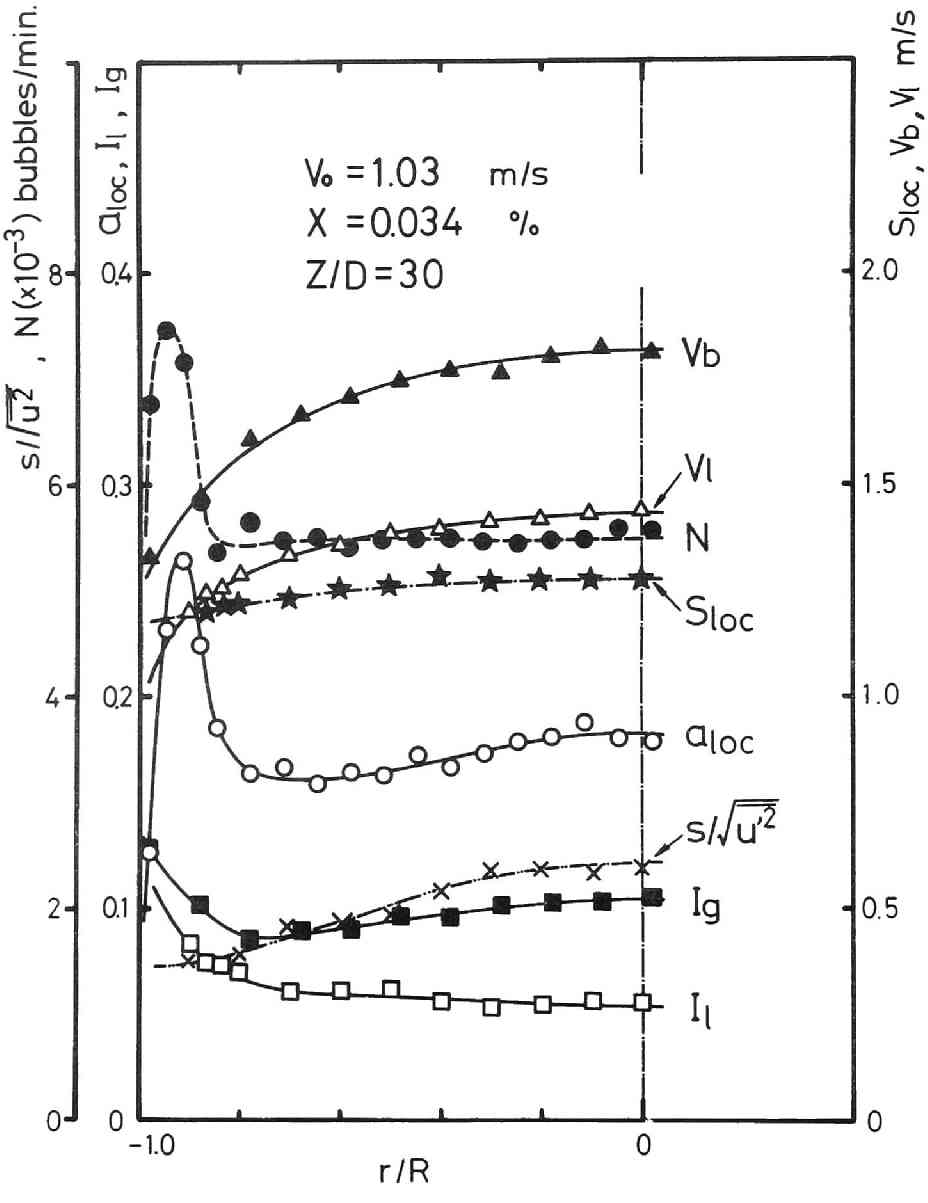

Fig. 4.99 Correlative representation of various local parameters for bubble flow

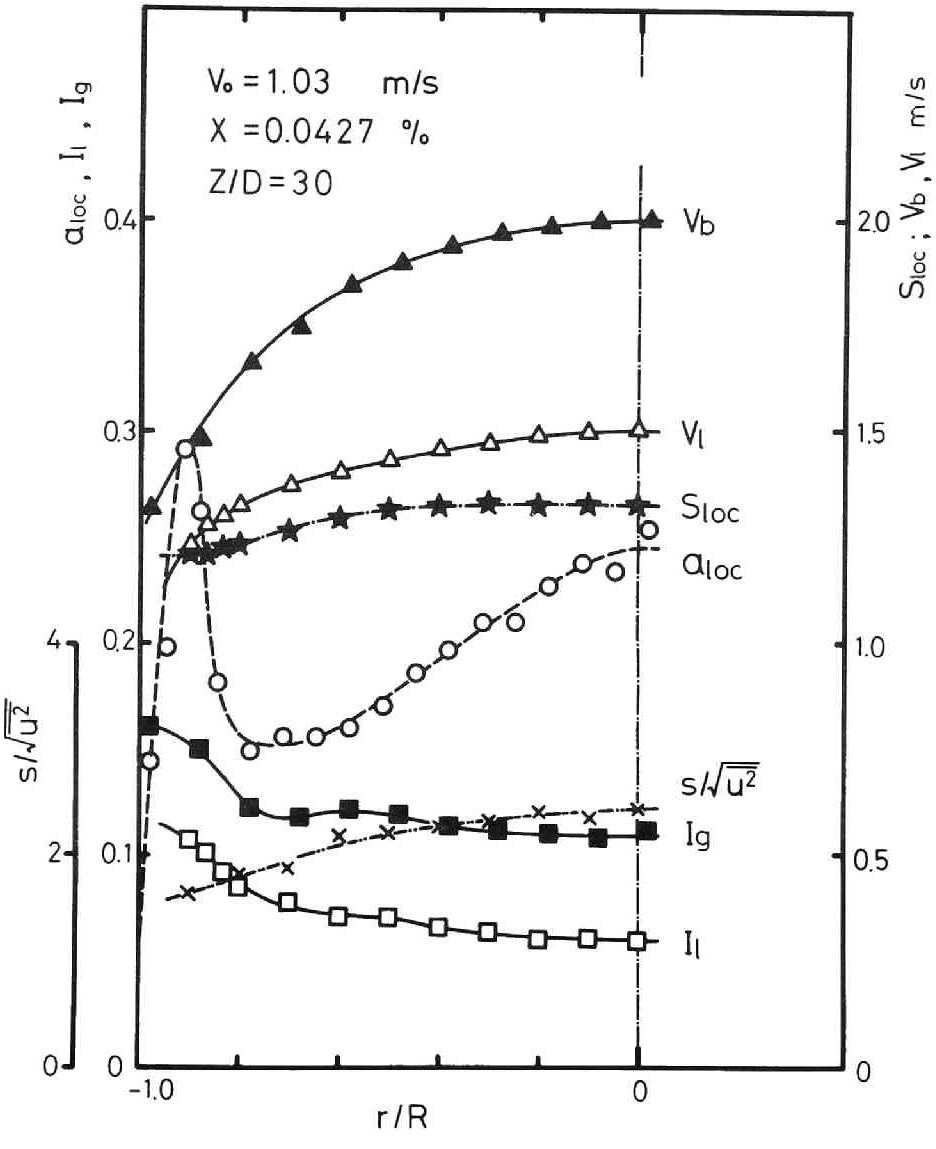

Fig. 4.100 Correlative representation of various local parameters for transition flow

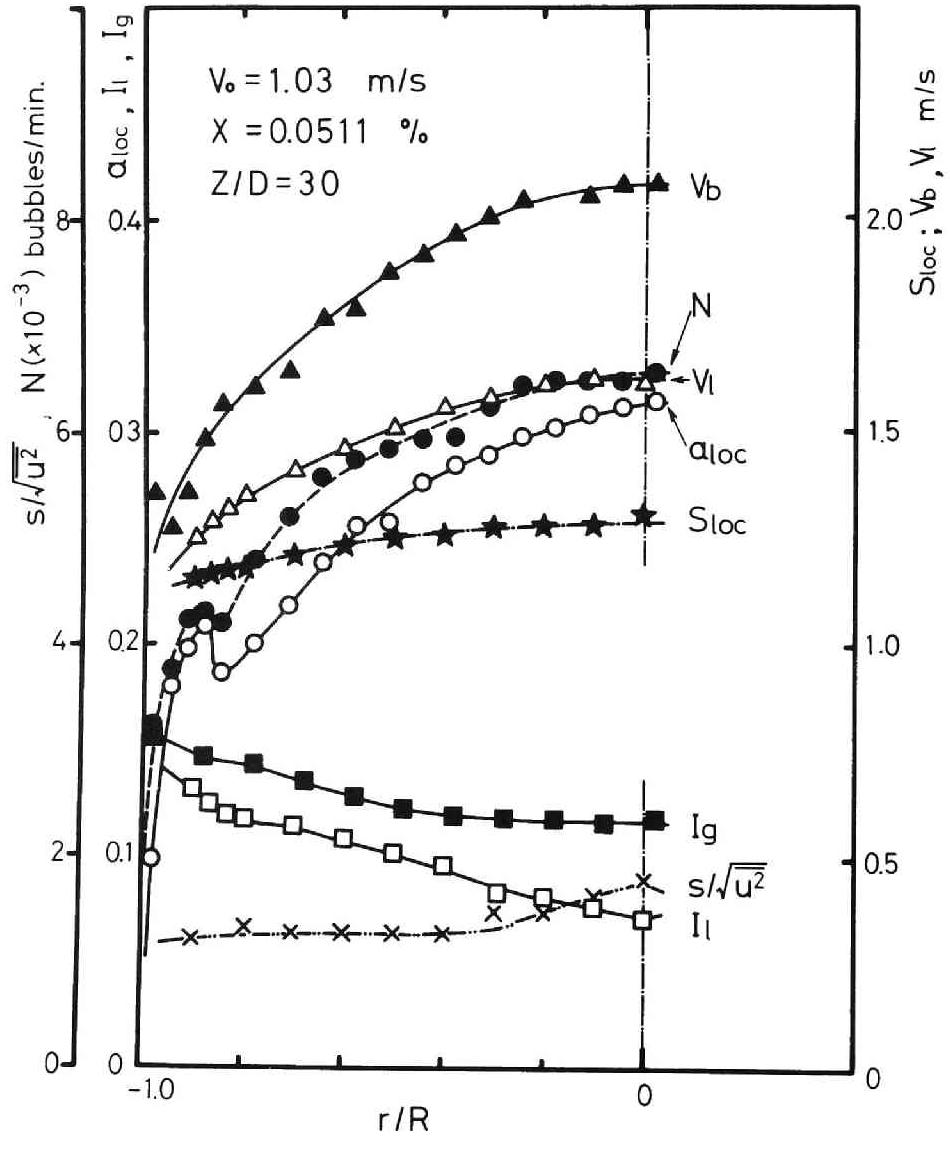

Fig.4.101 Correlative representation of various local parameters for slug flow

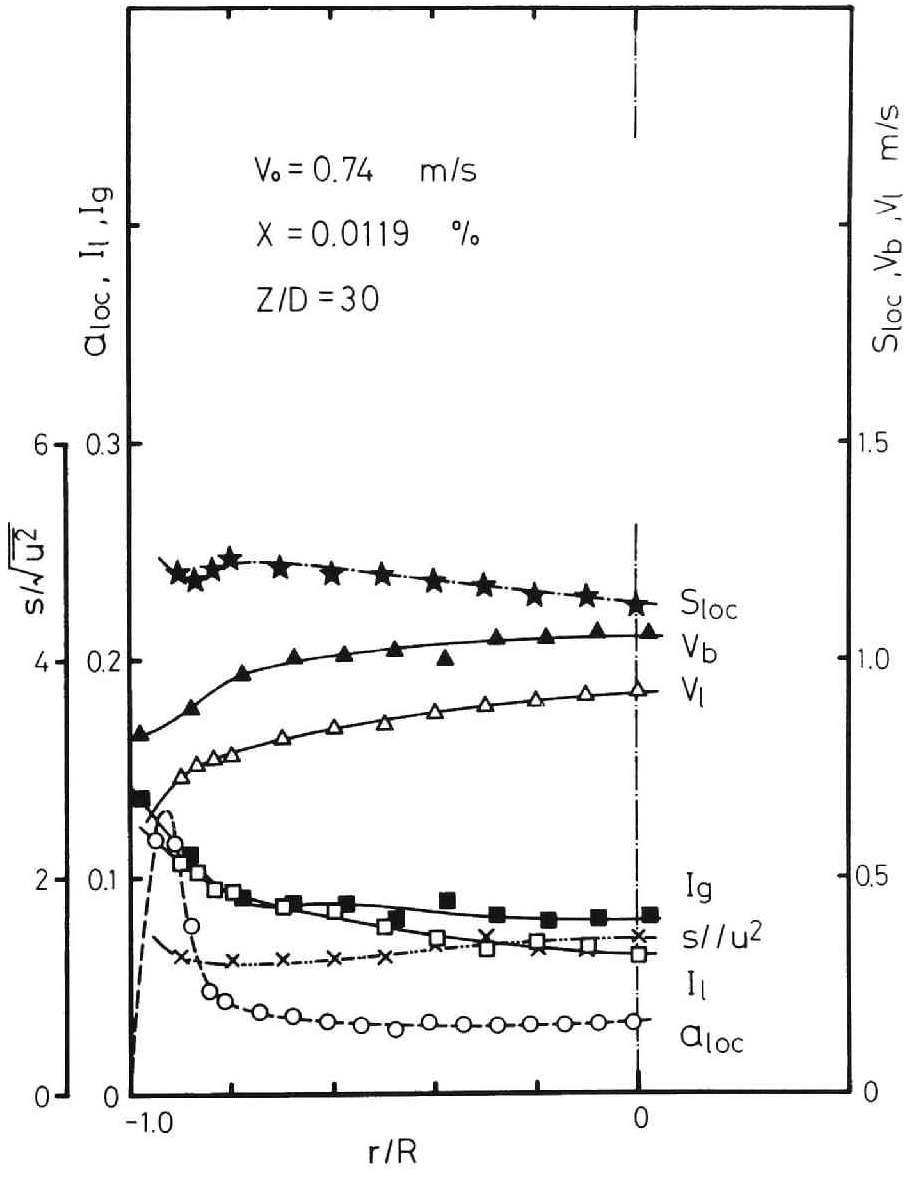

Fig. 4.102 Correlative representation of various local parameters for bubble flow

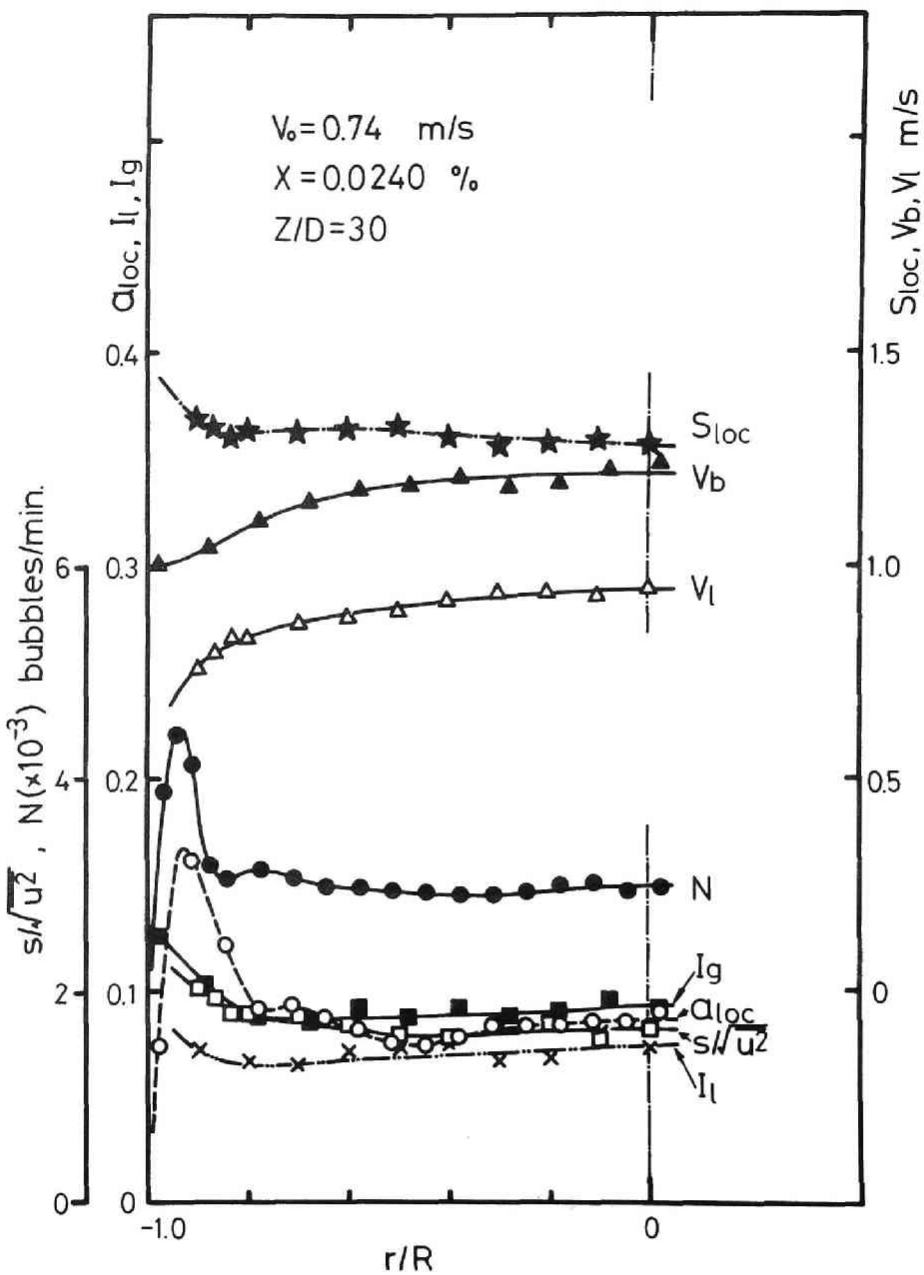

Fig. 4.103 Correlative representation of various local parameters for bubble flow

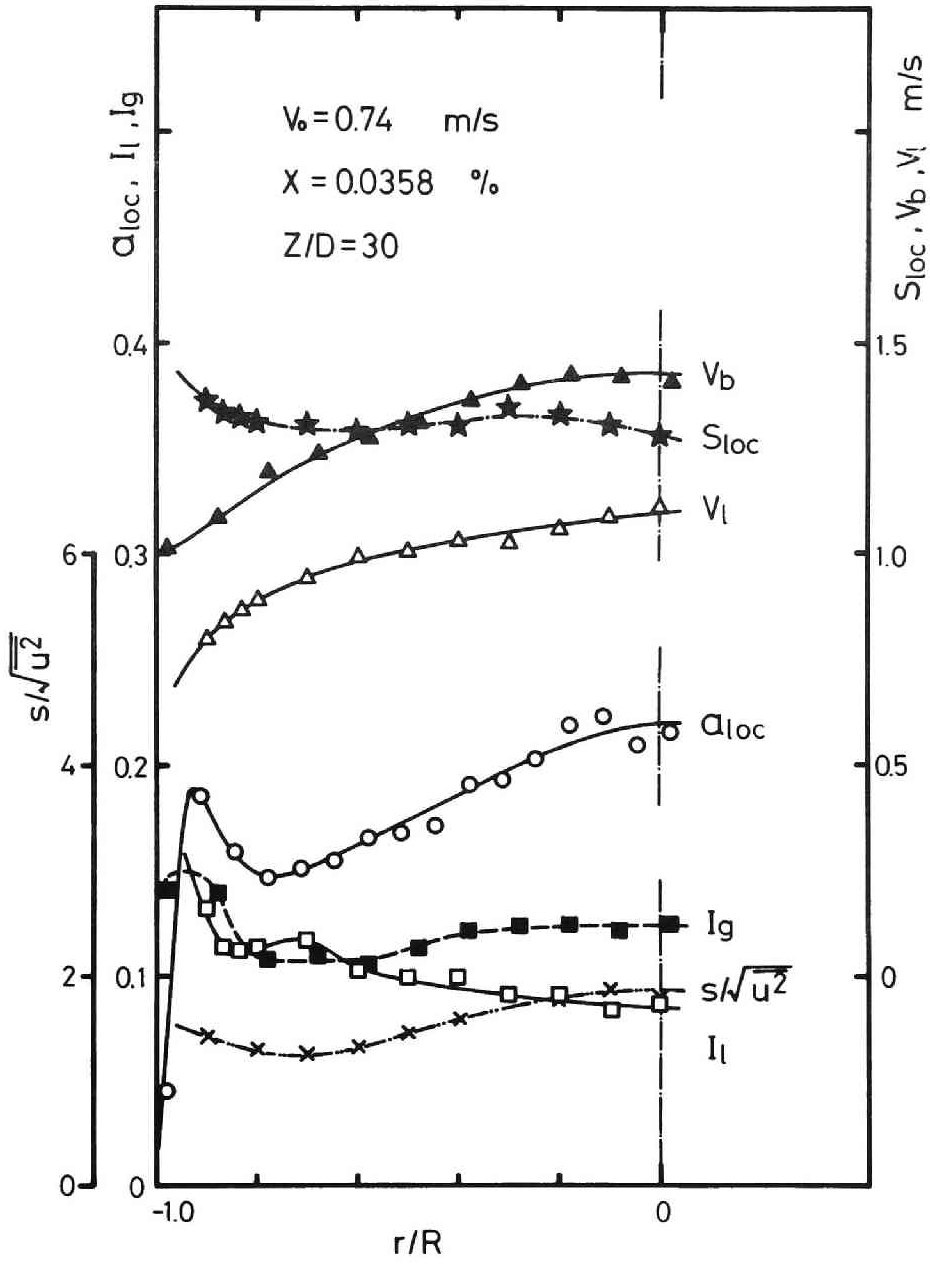

Fig. 4.104 Correlative representation of various local parameters for bubble flow

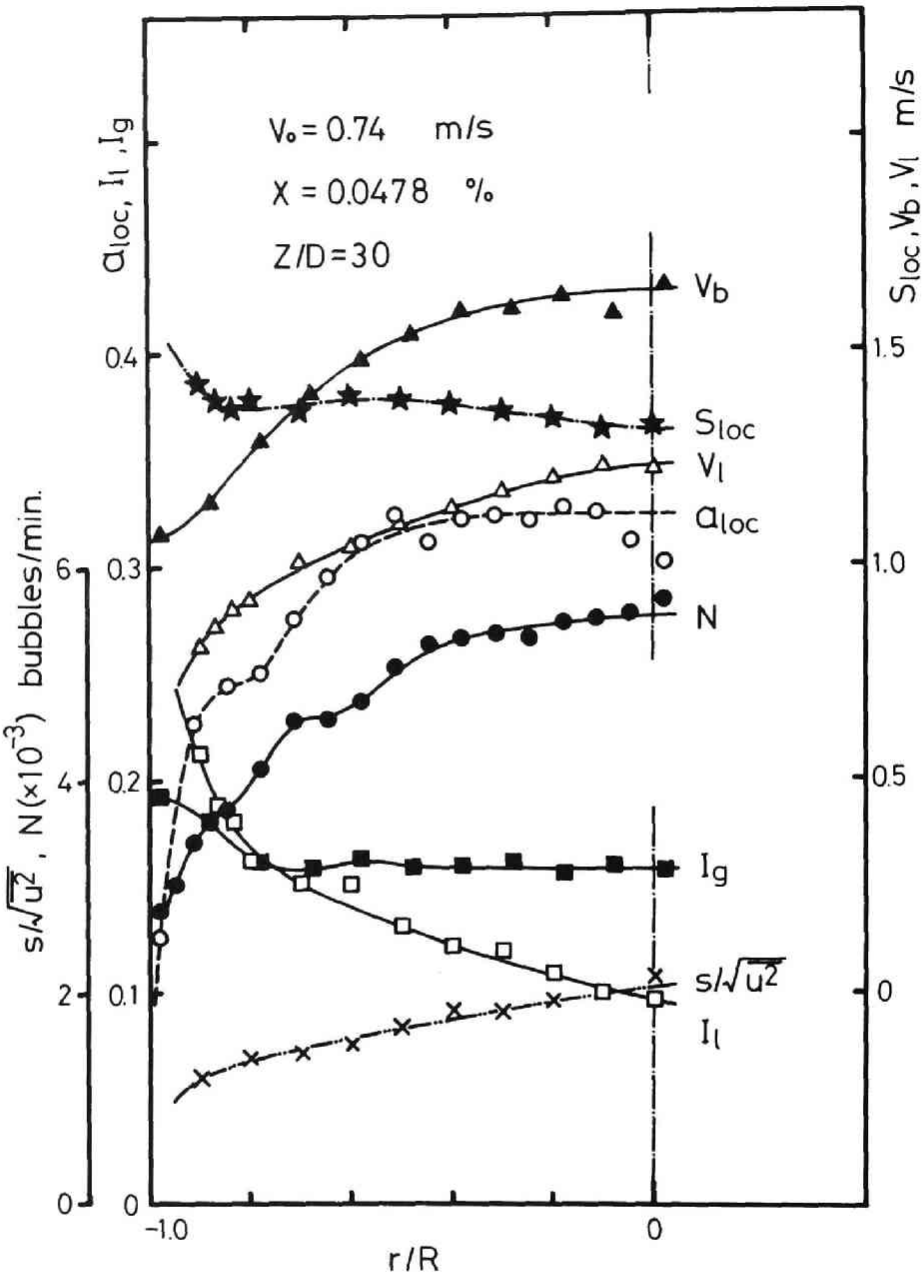

Fig. 4.105 Correlative representation of various local parameters for transition flow

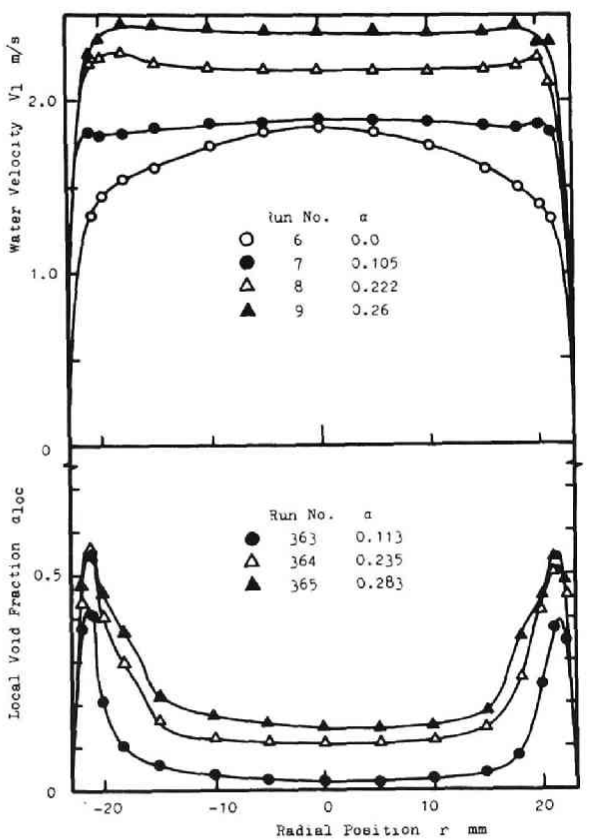

(a) V_o=1.5 m/sec (D_p=46 mm)

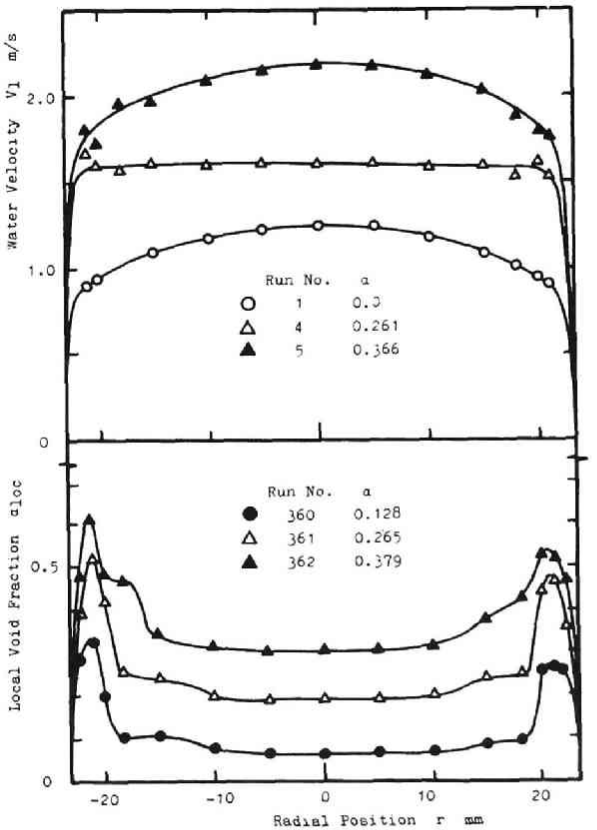

(b) V_o=1.0 m/sec (D_p=46 mm)

Fig. 4.106 Void fraction and water velocity (air-water data of Malnes[5])

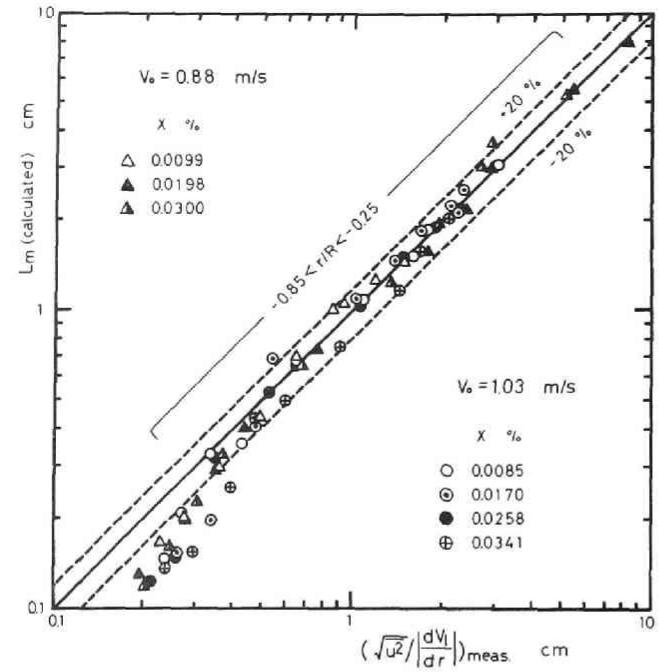

Fig. 4.107
Correlative representation between two mixing lengths calculated in different ways

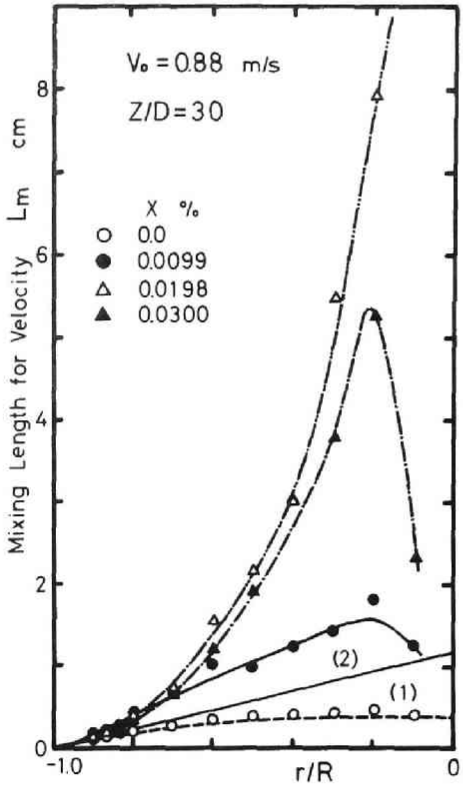

Fig. 4.108
Mixing length for velocity

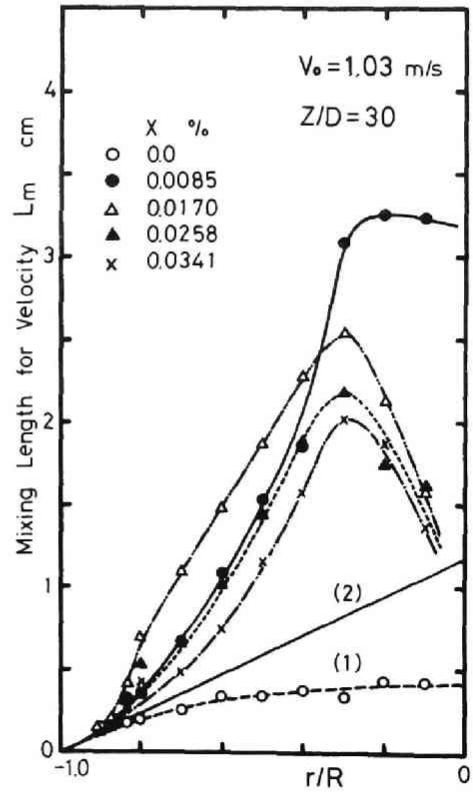

Fig. 4.109
Mixing length for velocity

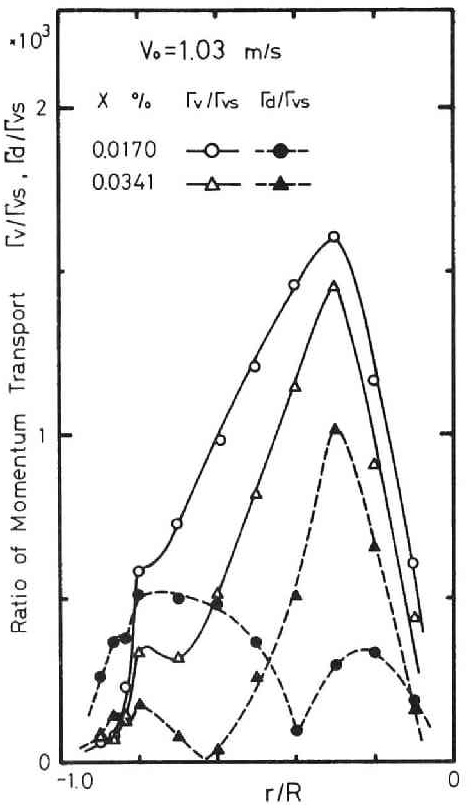

Fig. 4.110 Momentum transport ratio

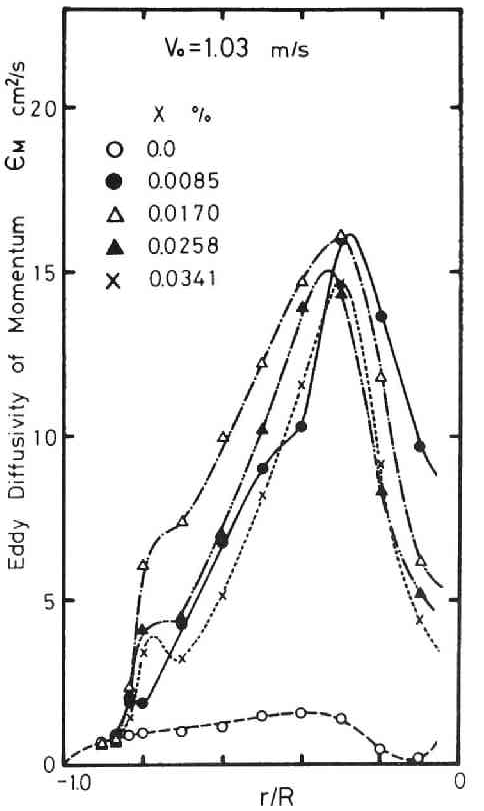

Fig. 4.111 Eddy diffusivity for momentum transport

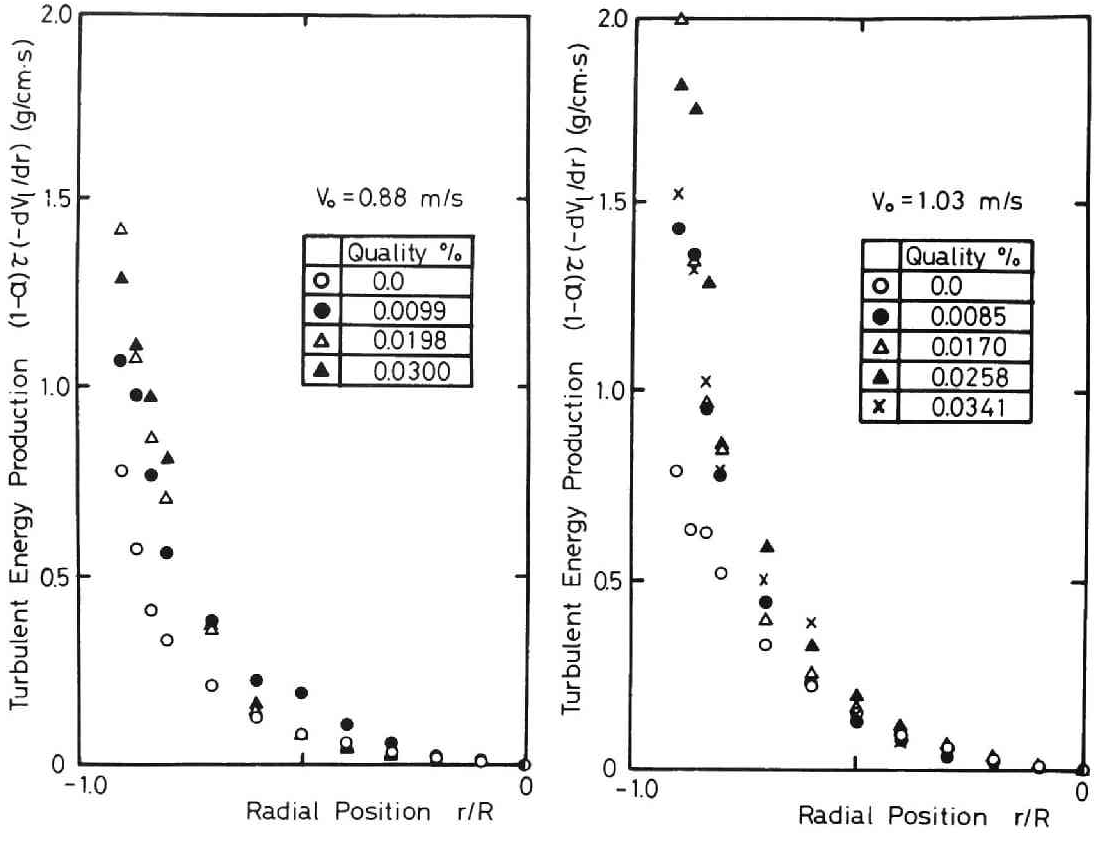

Fig. 4.112 Turbulent energy production

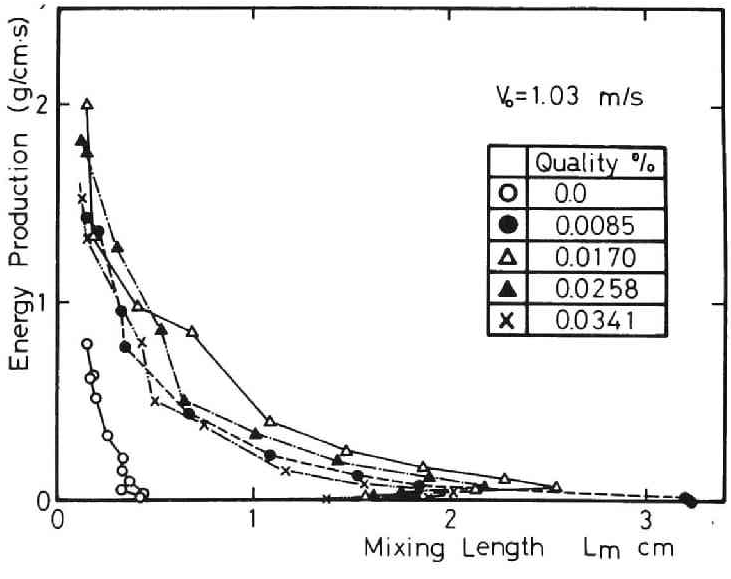

Fig. 4.113 Turbulent energy production vs. mixing length

V. MEASUREMENTS OF TURBULENT DIFFUSIVITIES OF HEAT AND BUBBLES IN THE CORE OF AIR-WATER TWO-PHASE BUBBLE FLOW IN PIPE

5.1 General

In Chapter III, it was shown that the bubble behavior in fully-developed turbulent pipe flow of water is diffusive in nature, and in Chapter IV, we showed that the distributions of the transferable quantities such as the void fraction and the velocities of both phases are very sensitive to the turbulent transport process which depends entirely on both random fluid motion and random bubble motions. The degree of uniformity in the distributions of those quantities is severely dependent on the competition between the inertia force and the random mixing actions of the liquid caused by the random bubble motions. Hence, a complete knowledge of the turbulent transport rates of transferable quantities is quite necessary to put a precise systematic and physical interpretation on the experimental results already obtained, and hence, to have a sound insight into the mechanism of two-phase turbulent flow. The more our knowledge of the two-phase turbulence increases, the greater will be the possibility of obtaining a correct and satisfactory solution to the phenomena.

In earlier days of turbulence investigations, measurements of the eddy diffusivities of momentum, mass, and heat have been intended for structural analysis of single-phase flow[1]. However, recently, many attempts have been carried out in order to get an indication of particle diffusivity in gas-solid systems[2-5], or gas-liquid droplet systems[6,7], a knowledge is still severely lacking for gas bubble-liquid system[8].

Thus, it seems useful to deal with the various turbulent transport rates in two-phase bubble flow extensively and in detail in this chapter. Possible turbulent transport rates here are the eddy diffusivities for momentum transport, mass (bubble) transport, and heat

transport. The eddy diffusivity for bubble transport is based upon an assumption of random motions of bubbles of which sizes are relatively small enough to the smallest turbulence scale. Experimental results obtained in Chapter III on the properties of bubble dispersion in single-phase flow and in Chapter IV on the statistical properties of bubbles in two-phase flow may indicate that the assumption of random bubble motions is valid also for two-phase bubble flow.

Experiments were conducted of the eddy diffusivities of heat and bubbles in the core region of air-water two-phase bubble flow. Experimental apparatus used here is the same one as shown in Fig.3.2.

5.2 Turbulent Transport of Heat

5.2.1 Experimental and Calculating Procedures

The radial turbulent or eddy diffusivity of heat was obtained by measuring radial temperature distributions at five different axial positions downstream of a line source located along the pipe diameter (see Fig.5.1).

Experimental procedures and relating techniques have been already mentioned in Chapter II.

In the present data reduction procedure, the following assumptions are made:

1) Azimuth-symmetric distributions of the velocity and the void fraction,
2) Steady-state conditions,
3) Infinite medium without wall effects,
4) Thermal equilibrium

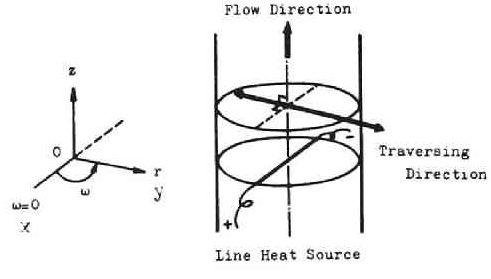

Fig. 5.1 Configuration and coordinate system

conditions between bubbles and surrounding liquid,

5) Heat transported by bubbles is negligibly small compared to that by the liquid,
6) Axial diffusion of heat can be relatively small to the heat transport due to the axial bulk motions,
7) Molecular effects (heat conduction) can be neglected,
8) Convective heat transports by bulk motions in radial and azimuth directions can be neglected.

Then, for a cylindrical polar coordinate system, the temperature Θ at any point (z, r, ω) in a fully-developed bubble flow in pipe is given by

$$\frac{\partial}{\partial z}(\alpha_1 V_{eff,z} \Theta) + \frac{1}{r}\frac{\partial}{\partial r}(r \alpha_1 V_{eff,r} \Theta) + \frac{1}{r}\frac{\partial}{\partial \omega}(\alpha_1 V_{eff,\omega} \Theta) = 0 \quad , \tag{5.1}$$

where $V_{eff,z}$, $V_{eff,r}$, and $V_{eff,\omega}$ (= radius × angular velocity: m/sec) are the axial, radial, and azimuth components of the liquid velocity, respectively, which, as pointed out by Houghton[9] in Eq.(3.2), take into account the effects of the backflow induced by the slip velocity between gas bubbles and the liquid. In the present case, they are given by

$$\begin{aligned} V_{eff,z} &= V_{l,z} - \alpha_{loc}(V_{b,z} - V_{l,z}) \\ &= V_{l,z}[1 - \alpha_{loc}(S_{loc} - 1)] \quad , \\ V_{eff,r} &= V_{l,r} \quad , \quad V_{eff,\omega} = V_{l,\omega} \quad . \end{aligned} \tag{5.2}$$

Let

$$\begin{aligned} V_{eff,z} &= \bar{V} + u \quad , \quad V_{eff,r} = v \quad , \quad V_{eff,\omega} = w \quad , \\ \Theta &= \bar{\Theta} + \theta \quad , \quad \alpha_1 = \bar{\alpha}_1 + \alpha' \quad , \end{aligned} \tag{5.3}$$

where $\bar{V}$, $\bar{\Theta}$, and $\bar{\alpha}_1$ are the time-average effective velocity in axial direction, fluid temperature, and liquid fraction, respectively, while u, v, w, and α' are the fluctuating terms of the velocity and the liquid fraction.

Insert Eq.(5.3) into Eq.(5.1) and average the result with respect to time, and then assume

$$\bar{V}\frac{\partial\bar{\Theta}}{\partial z} >> \frac{\partial\bar{\Theta}}{\partial z}(\overline{u\theta}) \quad , \quad \bar{\alpha}_1\frac{\partial\bar{\Theta}}{\partial z} >> \frac{\partial}{\partial z}(\overline{\alpha'\theta}) \quad , \quad \bar{\alpha}_1\bar{V}\frac{\partial\Theta}{\partial z} >> \frac{\partial}{\partial z}(\overline{\alpha'v\theta})$$

$$, \quad \bar{\Theta}\,\overline{\alpha'u} >> \overline{\alpha'u\theta} \quad , \quad \bar{\alpha}_1\bar{V} >> \overline{\alpha'u} \quad , \quad \bar{\alpha}_1\frac{\partial\bar{\Theta}}{\partial r} >> \frac{\partial}{\partial r}(\overline{\alpha'\theta}) \quad ,$$

$$\bar{\alpha}_1\frac{\partial^2\bar{\Theta}}{\partial\omega^2} >> \frac{\partial^2}{\partial\omega^2}(\overline{\alpha'\theta}) \quad .$$

The result obtained is given by

$$\bar{\alpha}_1\bar{V}\frac{\partial\bar{\Theta}}{\partial z} + \frac{1}{r}\frac{\partial}{\partial r}\left[r\left(\bar{\alpha}_1\overline{v\theta} + \bar{\Theta}\,\overline{\alpha'v}\right)\right]$$

$$+ \frac{1}{r}\frac{\partial}{\partial\omega}\left(\bar{\alpha}_1\overline{w\theta} + \bar{\Theta}\,\overline{w\alpha'}\right) = 0 \quad . \qquad (5.4)$$

The first and the second terms in the closure on the left hand side of Eq.(5.4) represent two contributions to the heat transport process due to the turbulent velocity components and the turbulent exchange of phases, respectively.

Here, the eddy diffusivities for heat and momentum transports are defined by the following equations:

$$\overline{v\theta} = -\varepsilon_{H,r}\frac{\partial\bar{\Theta}}{\partial r} \quad , \quad \overline{w\theta} = -\varepsilon_{H,\omega}\frac{1}{r}\frac{\partial\bar{\Theta}}{\partial\omega} \quad , \qquad (5.5a)$$

$$\overline{v\alpha'} = -\varepsilon_{M,r}\frac{\partial\bar{\alpha}_1}{\partial r} \quad , \quad \overline{w\alpha'} = -\varepsilon_{M,\omega}\frac{1}{r}\frac{\partial\bar{\alpha}_1}{\partial\omega} = 0 \quad . \qquad (5.5b)$$

Further assume,

$$\varepsilon_{H,r} = \varepsilon_{H,\omega} = \varepsilon_H(r) \quad , \quad \varepsilon_{M,r} = \varepsilon_M \quad . \qquad (5.5c)$$

Substitution of Eqs.(5.5a) ~ (5.5c) into Eq.(5.4) yields

$$\bar{\alpha}_1 \bar{V} \frac{\partial \bar{\Theta}}{\partial r} = \frac{1}{r} \frac{\partial}{\partial r} [r(\varepsilon_H \bar{\alpha}_1 \frac{\partial \bar{\Theta}}{\partial r} + \varepsilon_M \bar{\Theta} \frac{\partial \bar{\alpha}_1}{\partial r})] + \varepsilon_H \frac{1}{r^2} \frac{\partial^2}{\partial \omega^2} (\bar{\alpha}_1 \bar{\Theta}) \quad . \tag{5.6}$$

Hence, provided that the azimuth heat transport due to the turbulent actions can be neglected, Eqs.(5.2) and (5.6) will give the following equation for predicting the eddy diffusivity of heat,

$$\varepsilon_H = - \varepsilon_M \frac{\bar{\Theta} \frac{\partial \bar{\alpha}_1}{\partial r}}{\bar{\alpha}_1 \frac{\partial \bar{\Theta}}{\partial r}} + \frac{\int_0^r \bar{\alpha}_1 [\bar{V}_1 \{1 - \bar{\alpha}_{1oc} (S_{1oc} - 1)\} \frac{\partial \bar{\Theta}}{\partial z}] r \, dr}{r \bar{\alpha}_1 \frac{\partial \bar{\Theta}}{\partial r}} \quad . \tag{5.7}$$

Uniform distribution of the void fraction in the core region of bubble flow of low void fraction will make Eq.(5.7) more simplified form,

$$\varepsilon_H = \frac{\int_0^r \bar{\alpha}_1 \bar{V}_1 \frac{\partial \bar{\Theta}}{\partial z} r \, dr}{r \bar{\alpha}_1 \frac{\partial \bar{\Theta}}{\partial r}} \quad . \tag{5.8}$$

Radially changing diffusivity ε_H can be thus deduced from the experimental distributions of the void fraction, the liquid velocity, and the fluid temperature. However, as pointed out in Section 3.7, the results deduced from Eq.(5.7) or (5.8) are subjected to some error due to the graphical differentiations, $\frac{\partial \bar{\Theta}}{\partial r}$ and $\frac{\partial \bar{\Theta}}{\partial z}$ (it is quite difficult to get a correct value of $\frac{\partial \bar{\Theta}}{\partial z}$ to which $\varepsilon_H(z, r)$ is very sensitive, unless the radial temperature distribution is measured by a narrow margin in axial direction).

Therefore, another method was applied to the present measurement. For this purpose, the following assumptions are made additionally:

9) Radially uniform eddy diffusivity for temperature distribution,

10) In the central core region of bubble flow of low void fraction,

$\bar{\Theta} \frac{\partial \bar{\alpha}_1}{\partial r} / \bar{\alpha}_1 \frac{\partial \bar{\Theta}}{\partial r}$ can be neglected, and $\bar{\alpha}_{loc}$, S_{loc}, and $\bar{V}_1$ can be postulated to be uniform and equal to the values at the pipe center, $\bar{\alpha}_c$, S_{locc}, and $\bar{V}_c$, respectively.

The diffusion model based upon the assumption of radially independent diffusivity implies that the length scale of the process responsible for the transporting is much less than the characteristic dimensions of the fluid-medium boundaries. But, in actuality, this is not necessarily the case for turbulent transport in two-phase flow. However, the assumption of uniform diffusivity is made as has been done by Ginsberg in Ref.[7] for describing the liquid droplet diffusion, recognizing that the experiments must show how reasonable a description it represents of the transport process.

Then, Eq.(5.6) becomes

$$\bar{V} \frac{\partial \bar{\Theta}}{\partial z} = \varepsilon_H(z) \frac{1}{r} \left[\frac{\partial}{\partial r} \left(r \frac{\partial \bar{\Theta}}{\partial r}\right) + \frac{1}{r} \frac{\partial^2 \bar{\Theta}}{\partial \omega^2}\right] \quad , \tag{5.9}$$

or

$$\frac{\partial \bar{\Theta}}{\partial t} = \varepsilon_H(t) \frac{1}{r} \left[\frac{\partial}{\partial r} \left(r \frac{\partial \bar{\Theta}}{\partial r}\right) + \frac{1}{r} \frac{\partial^2 \bar{\Theta}}{\partial \omega^2}\right] \quad , \tag{5.10}$$

where diffusion time t is defined by

$$t = \frac{z}{\bar{V}} = \frac{z}{\left[\bar{V}_1 \{1 - \bar{\alpha}_{loc} (S_{loc} - 1)\}\right]_{r = 0}} \quad . \tag{5.11}$$

On writing

$$dT = \varepsilon_H(t)\, dt \quad ,$$

that is

$$T = \int_0^t \varepsilon_H(t')\, dt' \quad , \tag{5.12}$$

Eq.(5.10) for variable diffusivity reduces to

$$\frac{\partial\bar{\Theta}}{\partial T} = \frac{1}{r}\frac{\partial}{\partial r}\left(r\frac{\partial\bar{\Theta}}{\partial r}\right) + \frac{1}{r^2}\frac{\partial^2\bar{\Theta}}{\partial\omega^2} \quad \text{(for cylindrical coordinate)}, \tag{5.13a}$$

$$= \frac{\partial^2\bar{\Theta}}{\partial x^2} + \frac{\partial^2\bar{\Theta}}{\partial y^2} \quad \text{(for rectangular coordinate)} \quad . \tag{5.13b}$$

Thus, the diffusion equation has become a similar equation to that of two-dimensional heat conduction with unity diffusivity from a line source located along ω-axis in the plane $z = \int_0^t \bar{V}\, dt$.

For a line heat source of infinite length and of strength Q_o per unit length and along ω-axis (or x-axis) (corresponding coordinate systems are illustrated in Fig.5.1) in the plane $z = \int_0^t \bar{V}\, dt$, the solution to Eq.(5.13b) for initial condition

$$T = 0\ (t = 0): \quad \bar{\Theta} - \bar{\Theta}_o = Q_o/C_p\rho_1 \equiv Q^* \quad \text{(for } y = 0\text{)}$$

$$= 0 \quad \text{(for } y \neq 0\text{)} \quad ,$$

is

$$\bar{\Theta}\ (y, T) - \bar{\Theta}_o = \frac{Q^*}{\sqrt{4\pi T}} \exp\left(-\frac{y^2}{4T}\right) \quad , \tag{5.14}$$

where $\bar{\Theta}_o$, the reference temperature of the fluid, is the temperature at the point far away from the source.
Substitution of Eq.(5.12) into (5.14) yields

$$\bar{\Theta}\ (y, t) - \bar{\Theta}_o = \frac{Q^*}{\left[2\pi \int_0^t 2\varepsilon_H(t)\, dt\right]^{1/2}} \exp\left[-\frac{y^2}{2\int_0^t 2\varepsilon_H(t)\, dt}\right] \quad . \tag{5.15}$$

In the measurements, traversing was performed towards radial direction within a plane x = 0 which contains the origin of the coordinate and perpendicular to the x-axis. In this case, "y" can be replaced by "r" in the above equation for convenience sake. Then,

$$\bar{\Theta}\ (r,\ t) - \bar{\Theta}_o = \frac{Q^*}{[2\pi \int_0^t 2\varepsilon_H(t)\ dt]^{1/2}} \exp[-\frac{r^2}{2 \int_0^t 2\varepsilon_H(t)\ dt}] \quad , \tag{5.16a}$$

or

$$\frac{\bar{\Theta}\ (r,\ t) - \bar{\Theta}_o}{\bar{\Theta}\ (0,\ t) - \bar{\Theta}_o} = \exp[-\frac{r^2}{2 \int_0^t 2\varepsilon_H(t)\ dt}] \quad . \tag{5.16b}$$

The eddy diffusivity of heat can be given by

$$\varepsilon_H(t) = \frac{1}{2} \frac{d}{dt} \overline{y_\theta{}^2} \quad , \tag{5.17}$$

where

$$\overline{y_\theta{}^2} = \frac{\int_0^\infty (\bar{\Theta}\ (t,\ r) - \bar{\Theta}_o)\ r^2\ dr}{\int_0^\infty (\bar{\Theta}\ (t,\ r) - \bar{\Theta}_o)\ dr} \quad . \tag{5.18}$$

Eddy diffusivity $\varepsilon_H(t)$ is, therefore, directly calculable from Eqs. (5.17) and (5.18)*.

Measurements of the temperature distribution were conducted at five different positions downstream of the heat source (Z ≃ 3.5, 8.7,

---

* Strictly speaking, the total spread of the heat is determined by the molecular diffusion and by the action of turbulence. The mean square of the temperature distribution is determined by[1]

$$\overline{y_\theta{}^2} = \overline{y^2} + 2\ a\ t \quad .$$

Since, in two-phase turbulent flow of interest here, the molecular effect is considered to be negligibly small, $\overline{y_\theta{}^2}$ is approximated equal to $\overline{y^2}$, spread of heat due to the action of turbulence.

13.6, 20.9, and 26.4 cm), and were confined to the central two-thirds of the pipe over which $\bar{V}_l$, $\bar{\alpha}_{loc}$, and S_{loc} are considered to be approximately constant.

5.2.2 Results and Discussions

Typical experimental results appear in Figs.5.2 and 5.3 showing, respectively, fluid temperature distributions and plots of the variance $\overline{[y_\theta(t)]^2}$ versus diffusion time t. It is notable that a good agreement can be seen between the mean temperature profiles and the corresponding Gaussian approximation curves (solid lines for each profile shown in Fig.5.2).

The data reduction from the profiles to the desired eddy diffusivity ε_H is a straight-forward process. As indicated in Fig.5.3, the plot of the displacement variance $\overline{y_\theta^2}$ vs. diffusion time t shows a quite similar trend to that observed in the experiment on bubble dispersion already mentioned in Chapter III, and shows such a functional dependence as below:

$$\overline{y_\theta(t)^2} = 2\ \varepsilon_H\ t^*\ [\frac{t}{t^*} - \{1 - \exp(-\frac{t}{t^*})\}] \quad , \qquad (5.19)$$

where t* is the intersection of the asymptote to the curve with the t-axis[1] (see Fig.5.4). (For constant velocity, $z = \bar{V}\ t \propto t$.) A least squares procedure was used to fit the calculated variance $\overline{y_\theta^2}$ to Eq.(5.15) and to obtain the eddy diffusivity for heat transport ε_H.

Thus obtained results are given in Fig.5.5, showing the diffusivity ε_H as a function of the quality for constant water velocities. From this

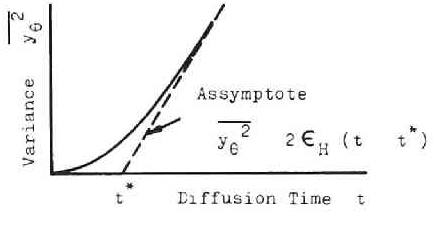

Fig. 5.4 Displacement variance vs. diffusion time

figure, it will be seen that the diffusivity, varying in the range of 0.4 ~ 1.5 cm^2/sec*, increases considerably with the quality and also with the water flow rate. This gross trend is qualitatively consistent with the concluded fact associated with the propelled momentum transport phenomena in two-phase bubble flow which have been already treated in Chapter IV. However, a doubt may arise as to why the eddy diffusivity ε_H for temperature distribution should be considerably small relative to the diffusivity for velocity ε_M deduced with using a mixing length theory (see Fig.4.111). In view of the fact that the major portions of the momentum and heat transported by the turbulent actions of the fluid are both due to the turbulent fluctuating velocity components of the liquid, the diffusivity of heat should be as large as the diffusivity of momentum. The quantitative difference between them should be then ascribed either to whether an analogy between the momentum and heat transports could not hold good for such a flow condition or not, or to some essential errors involved in the data reduction procedures for ε_M or ε_H.

From this viewpoint, it is useful to check the validity of the assumption of thermal equilibrium conditions between two phases, although the small heat capacity of bubbles is rationally considered to make much less contributions to the turbulent transport of heat than the liquid. An analysis of the power spectral density of temperature fluctuation of the mixture appears one of the most efficient and appropriate approaches to this objective. If the temperature of bubbles might be greatly different from that of the liquid, the power spectrum of the temperature fluctuation of the mixture measured at a fixed position in the stream should have a peak near at the frequency, f_n, corresponding to the mean bubble transit frequency at that position.

As the transducer for the measurement of the temperature fluctuation, a fast response thermocouple was fabricated. The alumel-chromel

---

* Thermal diffusivity of water a is 0.14×10^{-2} cm^2/sec, when the water temperature is 20^oC.

wire elements (0.25 mm$^{\phi}$) of a sheathed thermocouple were exposed by removing the stainless steel tubing for a few mm at the end. The stripped ends of the wire elements were joined by spot-welding, and, finally, a commercial resin solution was applied to the naked tip of the thermocouple for electrical insulation.

The detected temperature fluctuation was amplified approximately to 10,000 times, and then recorded on a magnetic tape (Teac R-400). For calculating the power spectral density in an analog manner, the played back signal was fed to a wave analizer (Hewlett Packard, Model 302A), and its output was squared and integrated by an analog computer (Hitachi, Model ALM-502T).

Figure 5.6 shows the results of the power spectral density of the temperature fluctuation for various flow conditions (for each experimental run, the measurement was carried out at the pipe center), where f_n is the bubble transit frequency. These plots indicate no distinguishable differences among them. This means that the assumption of thermal equilibrium between two phases is valid for such flows.

Other possible reasons for the difference between ε_M and ε_H are the assumption of the infinite medium made for obtaining ε_H, and a non-uniform distribution of the heat generation along the axis of the line heater. However, it is very difficult to evaluate these effects quantitatively. Details should be clarified further in future.

With a view to correlating the diffusivity ε_H with flow conditions by a simple equation, we will introduce for the data arrangement the flow modulus X_{tt} defined by Eq.(5.20) which represents a degree of the similarity of the flow field between the different flow conditions.

$$X_{tt} = \left(\frac{1 - X}{X}\right)^{0.9} \left(\frac{\rho_g}{\rho_l}\right)^{0.5} \left(\frac{\mu_l}{\mu_g}\right)^{0.1} \tag{5.20}$$

Figure 5.7 shows a plot of $\varepsilon_{H,TP}/\varepsilon_{H,SP}$ (the ratio of the eddy diffusivity of heat for two-phase flow $\varepsilon_{H,TP}$ to that for single-phase water flow $\varepsilon_{H,SP}$) in terms of the modulus X_{tt}. It will be seen that the ratio $\varepsilon_{H,TP}/\varepsilon_{H,SP}$ can be grossly correlated by a single curve

though some data scatter around it. Although the data shown in Fig. 5.7 have been obtained under rather limited range of conditions, it will serve as an approximate basis for the formulation of the phenomenon to get an empirical correlating equation for the diffusivity ε_H.

The empirical equation obtained for predicting the eddy diffusivity $\varepsilon_{H,TP}$ is given by

$$\varepsilon_{H,TP}/\varepsilon_{H,SP} = 1 + 462\ X_{tt}^{-1.27} \quad . \tag{5.21}$$

5.3 Turbulent Transport of Gas Bubbles

5.3.1 Experimental and Calculating Procedures

The radial eddy diffusivity (in more adequate term, bubble dispersion coefficient) of air bubbles was obtained by measuring radial concentration distributions of the tracer gas (helium) with use of an isokinetic sampling probe and a gas chromatograph, under the assumption that the hydrodynamic properties of helium bubbles, including the diffusivity, are all equal to the corresponding properties of air bubbles (tracer gas was introduced into the stream of air-water mixture from a point source located at the pipe center).

Detailed descriptions on measurement of the turbulent dispersion of bubbles by means of isokinetic sampling method have already appeared in Paragraph 2.2.6.

Consider the dispersion of tracer bubbles from a fixed point source, then the solution for predicting the concentration distribution of the tracer at the position downstream of the source is given by Eq. (3.17) for radially unchanging bubble dispersion coefficient and for the case of no wall effects.

$$C(r,\ t) = \frac{S_o}{2\pi[\int_0^t 2\phi(t)\ dt]} \exp[-\frac{r^2}{2\int_0^t 2\phi(t)\ dt}] \tag{3.17}$$

In this case, the uniform bubble dispersion coefficient $\phi(t)$ and the displacement variance $\overline{y(t)^2}$ are given by Eqs.(3.19) and (3.20), respectively.

$$\phi(t) = \frac{1}{2}\frac{d}{dt}\overline{y(t)^2} \quad , \tag{3.19}$$

$$\overline{y(t)^2} = \frac{\int_0^\infty r^3 C(r, t)\, dr}{\int_0^\infty r\, C(r, t)\, dr} \quad . \tag{3.20}$$

For radially changing bubble dispersion coefficient $\phi(r, z)$, Eq. (3.33) can be applied to the case with replacing the bubble impaction rate $N(r, z)$ by the concentration $C(r, z)$.

$$\phi(r, z) = \frac{\int_0^r V_b \frac{\partial C}{\partial z} r\, dr}{r \frac{\partial C}{\partial r}} \quad . \tag{5.22}$$

Except for special cases, the assumptions of the radially uniform dispersion of bubbles, and of Eqs.(3.17), (3.19), and (3.20) were used to evaluate the turbulent bubble dispersion coefficient.

5.3.2 Results and Discussions

Prior to the measurements, the dependence of the tracer bubble diffusivity upon the flow rate of helium tracer was examined at three different volumetric flow rates of the helium, i.e., 121, 214, and 462 cc/min. The result indicated no significant dependence upon such a variable, and therefore, the volumetric flow rate of helium tracer gas was chosen 462 cc/min in all experimental runs.

In Fig.5.8 is presented a typical record of the two peaks of the output signal of gas-chromatograph which correspond to the peak for the helium gas and that for the nitrogen, respectively. Thus, the tracer gas bubbles is clearly discriminated from air bubbles.

Figures 5.9 and 5.10 represent typical experimental results show-

ing, respectively, the mass concentration distributions of the helium tracer involved in the unit volume of air-water mixture, and plots of variance $\overline{y^2}$ against the dispersion time t.

The turbulent dispersion coefficient of bubbles at large dispersion times, ϕ, deduced from the plots of displacement variance according to Eq.(3.19), is presented in Fig.5.11 as a function of the quality and the water velocity. It will be seen from this figure that the bubble dispersion coefficient increases considerably with an increase in the quality for low water velocities, while only slightly for higher water velocities, however its dependence upon the water velocity is very obscure. It is notable that, in some cases of a small quality, the turbulent dispersion coefficient of bubbles ϕ is smaller in bubble flow than in single-phase water flow (see Fig.3.23). In single-phase water flow, bubble diffusivity is raised mainly by the turbulent velocity components of the water flow which increase monotonously, as a rule, with increasing the water velocity. While in two-phase flow, when the gas flow rate is increased, bubble diffusivity will be determined by the competition among the rated-up interactions between bubbles, the rated-up inertia force of the water accelerated by bubbles, and the resultant rated-up turbulent velocity components of the water flow. With recalling the experimental fact that, in some cases of higher water velocity and small quality, the turbulent intensity of the liquid exhibits a lower value in two-phase bubble flow than in single-phase water flow as already shown in Figs.4.95 and 4.96, we may notice a good coincidence in dependences upon the quality and the water velocity between those of the turbulent velocity $\sqrt{\overline{u^2}}$ and those of the turbulent dispersion coefficient of bubbles ϕ.

Figure 5.12 shows a representation of the Péclet number defined as $\phi/u_c'\bar{d}$ (where $u_c' = \sqrt{\overline{u^2}}$ is the turbulent intensity of the flow field at pipe center, and $\bar{d}$ the mean bubble diameter) as a function of the local void fraction at pipe center, α_c. From this figure,

Péclet number, $u_c'\bar{d}/\phi$, can be made approximately equal to 2.0 independently of the void fraction, despite of some scatters of the data.

A more detailed survey of the experimental results shown in this figure reveals a weak dependence of the Péclet number upon the void fraction, when the scattered data points denoted with a mark ↓ in the figure are ignored. This fact may follow an important conclusion that the direct major mechanism of bubble dispersion both in single-phase water flow and in two-phase bubble flow is the turbulent transport characteristic of the liquid phase, and the interaction between bubbles and the inertia force of the liquid phase are both additional mechanisms, and that the effects of the bubble interaction upon bubble diffusivity may be suppressed relatively by the inertia effects for higher water velocities.

Figure 5.13 represents the diffusivity ratio ϕ/ε_H between the diffusivity for bubble transport and that for heat transport in terms of the quality and the water velocity. This figure appears to present a trend for the diffusivity ratio ϕ/ε_H to approach unity as the quality and the water velocity become larger, though it strongly depends upon the water velocity. In consideration of the experimental fact that the turbulent diffusivity of heat is determined mainly by the turbulent characteristic of the liquid phase, and with recalling that $\phi/\varepsilon_H = 1$ means the same mechanism both in turbulent transport of heat and in that of bubbles, it is confirmed again that, for higher quality and higher water velocity region, the predominant mechanism in bubble transport process in turbulent pipe flow is the turbulent motions of the liquid phase, and the inertia force of the liquid phase will serve to reduce the bubble diffusivity by suppressing the lateral bubble motions caused by the interactions between bubbles.

5.4 Conclusions

Turbulent transports of heat and bubbles have been investigated in the core region of air-water two-phase bubble flow in pipe. The concentration (or temperature rise) distribution data reduction was carried out to determine the turbulent bubble dispersion coefficient

ϕ and the turbulent diffusivity for heat transport ε_H.

The following conclusions may be presented:

1) The turbulent velocity components of liquid phase play a predominantly important role in turbulent transport process of heat and bubbles in common.
2) A systematic variation of the diffusivity ε_H with the quality and the water velocity was observed with increasing tendencies.
3) The diffusivity ratio $\varepsilon_{H,TP}/\varepsilon_{H,SP}$, defined as the ratio of the diffusivity for heat transport between that in two-phase flow and that in single-phase water flow, is correlated with Martinelli modulus X_{tt} by the following empirical equation:

$$\varepsilon_{H,TP}/\varepsilon_{H,SP} = 1 + 462\ X_{tt}^{-1.27}$$

4) No systematic variation of bubble dispersion coefficient ϕ with the water velocity was observed, while ϕ increases, as a rule, with increasing the quality.
5) The Péclet number $u_c'd/\phi$ can be approximated 2.0 independently of the quality and the water velocity.
6) The diffusivity ratio ϕ/ε_H decreases till unity dependently upon the quality and the water velocity. A smaller value of ϕ/ε_H is related to a higher water velocity for constant quality.

REFERENCES

[1] Hinze, J.O.: Turbulence, McGraw-Hill, (1959).

[2] Goldschmidt, V.W., Householder, M.K., Ahmadi, G., Chuang, S.: Progress in Heat and Mass Transfer, Vol.6, 487 (1972).

[3] Briller, R., Robinson, M.: Am. Inst. Chem. Engrs. J., 15[5], 733 (1969).

[4] Suneja, S.K., Wasan, D.T.: Ind. Eng. Chem. Fundam., 11[1], 57 (1972).

[5] Hino, M.: Proc. Symp. on Multi-Phase Mixtures sponsored by Japan Science Academy, p.21 (1967).

[6] Cousins, L.B., Hewitt, G.F.: AERE-R 5693 (1968).

[7] Ginsberg, T.: ANL-7694 (1971).

[8] Reith, T. Renken, S., Israel, B.A.: Chem. Eng. Sci., Vol.23, 619 (1968).

[9] Houghton, G.: Nucl. Sci. Engr., Vol.11, 121 (1961).

NOMENCLATURE

a	thermal diffusivity of water
C	mass concentration of helium tracer involved in air-water mixture
C_p	specific heat at constant pressure
$\bar{d}$	mean bubble diameter
f_n	bubble transit frequency
N	bubble impaction rate
Q_o	strength of a line heat source per unit length
Q^*	reduced strength of a line heat source per unit length ($= Q_o/C_p\rho_l$)
r	radial position
R	pipe radius
S_o	strength of a point source of helium bubbles
S_{loc}	local slip ratio ($= V_b/V_l$)
t	diffusion time
u	turbulent velocity component in axial direction
u'	root mean square of fluctuating liquid velocity (turbulent intensity, $\sqrt{\overline{u^2}}$)
u'_c	turbulent intensity at pipe center
v	turbulent velocity component in radial direction
$\bar{V}$	time-average velocity
V_b	bubble velocity
$\bar{V}_c$	time-average liquid velocity at pipe center
$V_{eff,r}$	radial velocity component of liquid defined by Eq.(5.2)
$V_{eff,z}$	axial velocity component of liquid defined by Eq.(5.2)
$V_{eff,\omega}$	azimuth velocity component of liquid defined by Eq.(5.2)
V_l	liquid velocity
$\bar{V}_l$	time-average liquid velocity
$V_{l,r}$	radial velocity component of liquid
$V_{l,z}$	axial velocity component of liquid
$V_{l,\omega}$	azimuth velocity component of liquid (= radius angular velocity)

V_o	superficial liquid velocity
w	turbulent velocity component in azimuth direction
X	quality
X_{tt}	flow modulus defined by $(W_l/W_g)^{0.9}(\rho_g/\rho_l)^{0.5}(\mu_l/\mu_g)^{0.1}$
y	lateral coordinate
$\overline{y^2}$	displacement variance due to turbulent actions
$\overline{y_\theta^2}$	displacement variance of temperature distribution
z	axial coordinate
Z	downstream distance from heat or bubble source
(z,r,ω)	cylindrical coordinate system
(x,y,z)	Cartesian coordinate system
α'	fluctuating component of local liquid fraction
$\bar{\alpha}_c$	time-average void fraction at pipe center
α_l	local liquid fraction (= 1 - α_{loc})
$\bar{\alpha}_l$	time-average local liquid fraction
α_{loc}	local void fraction
$\bar{\alpha}_{loc}$	time-average local void fraction
ε_H	turbulent diffusivity of heat (in axial direction)
$\varepsilon_{H,r}$	turbulent diffusivity of heat in radial direction
$\varepsilon_{H,\omega}$	turbulent diffusivity of heat in azimuth direction
$\varepsilon_{H,TP}$	turbulent diffusivity of heat in two-phase flow
$\varepsilon_{H,SP}$	turbulent diffusivity of heat in single-phase flow
ε_M	turbulent diffusivity of momentum (in axial direction)
$\varepsilon_{M,r}$	turbulent diffusivity of momentum in radial direction
$\varepsilon_{M,\omega}$	turbulent diffusivity of momentum in azimuth direction
θ	temperature fluctuation
Θ	fluid temperature
$\bar{\Theta}$	time-average fluid temperature
Θ_o	time-average temperature of ambient fluid away from heat source
ρ_l	density of liquid
ϕ	turbulent dispersion coefficient of bubbles
ω	azimuth coordinate

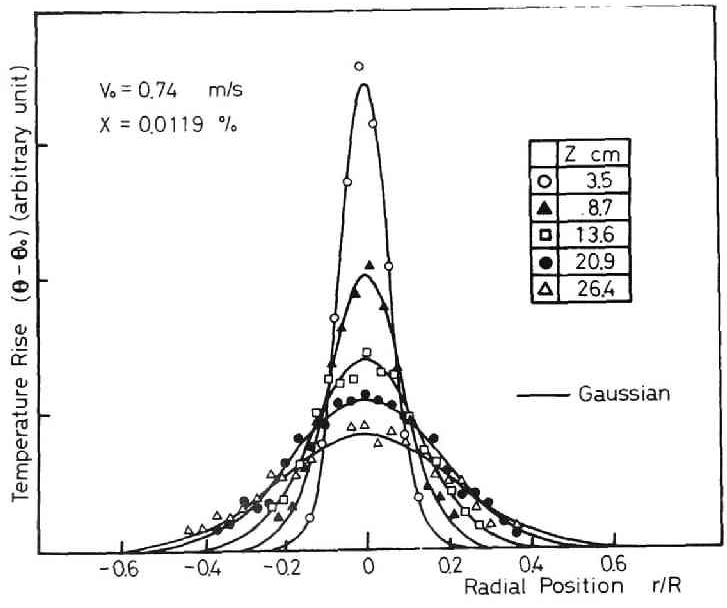

Fig. 5.2 Profile of temperature rise

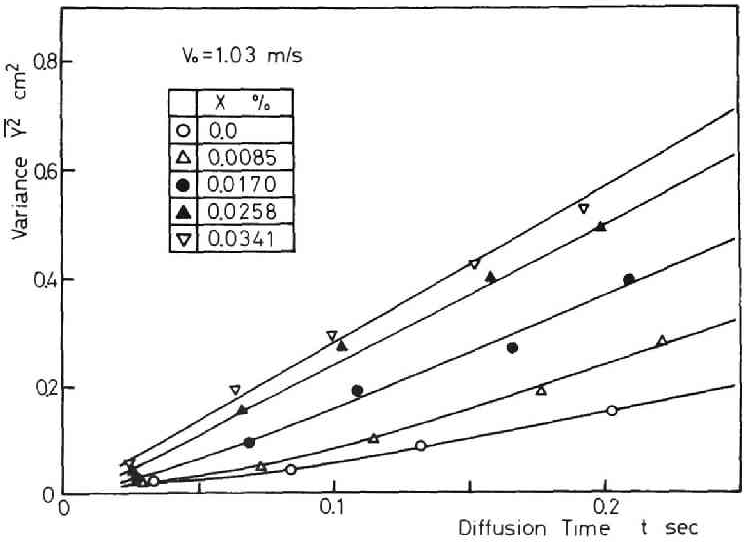

Fig. 5.3 Displacement variance vs. diffusion time

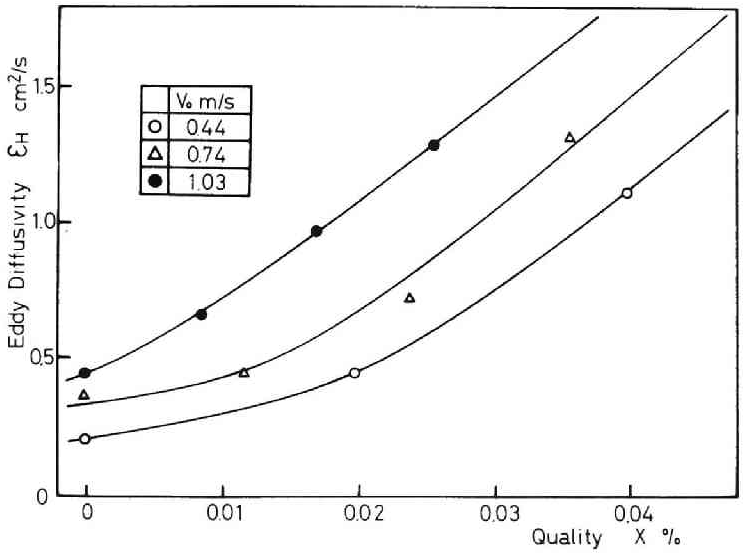

Fig. 5.5 Variation of turbulent diffusivity for heat transport

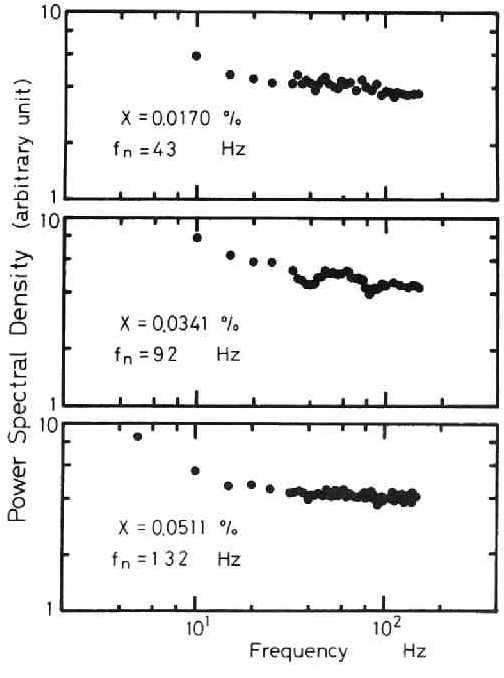

Fig. 5.6 Power spectral density of the temperature fluctuation

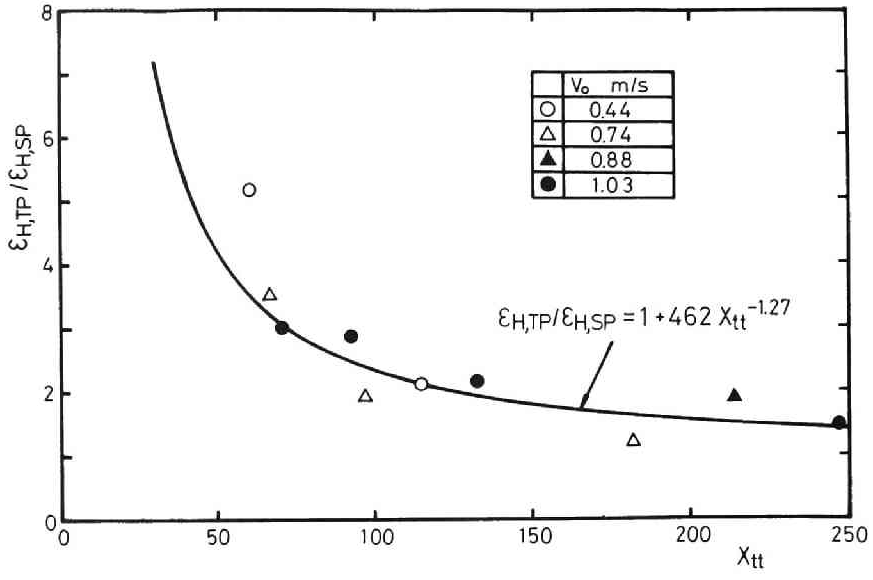

Fig. 5.7 Plots of $\varepsilon_{H,TP} / \varepsilon_{H,SP}$ *vs.* X_{tt}

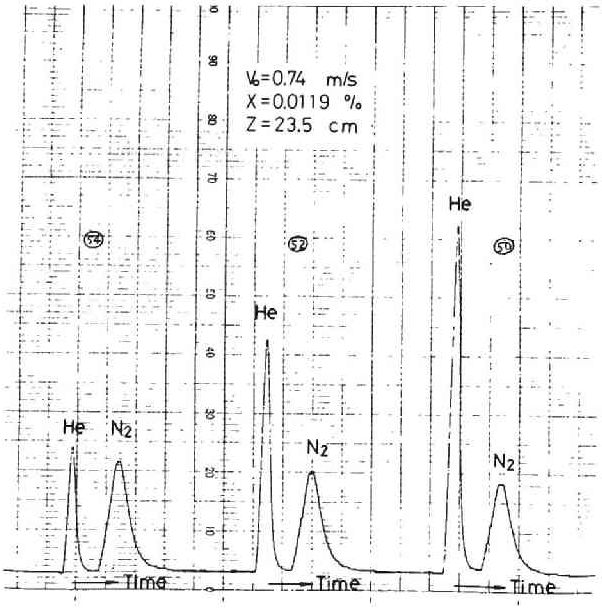

Fig. 5.8 Typical record of output signal of gas-chromatograph

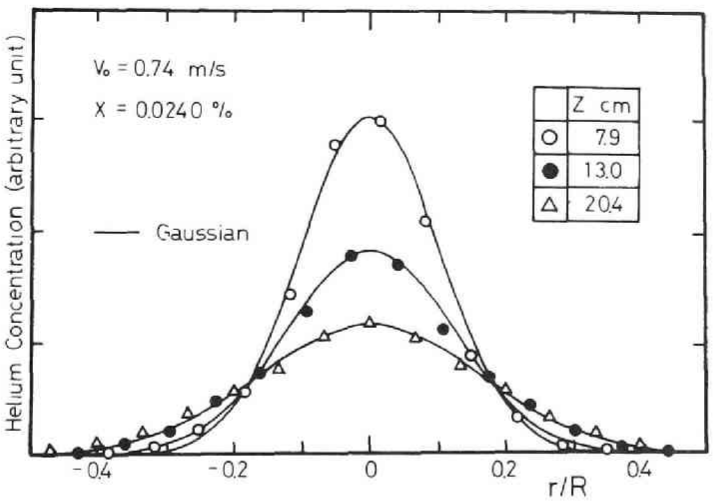

Fig. 5.9 Profile of mass concentration of helium tracer bubbles

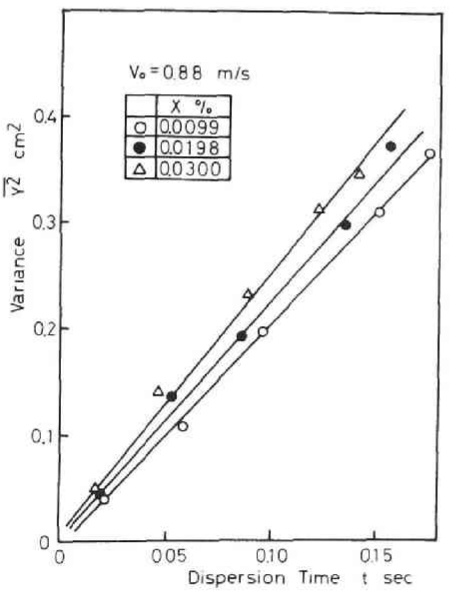

Fig. 5.10 Displacement variance vs. dispersion time

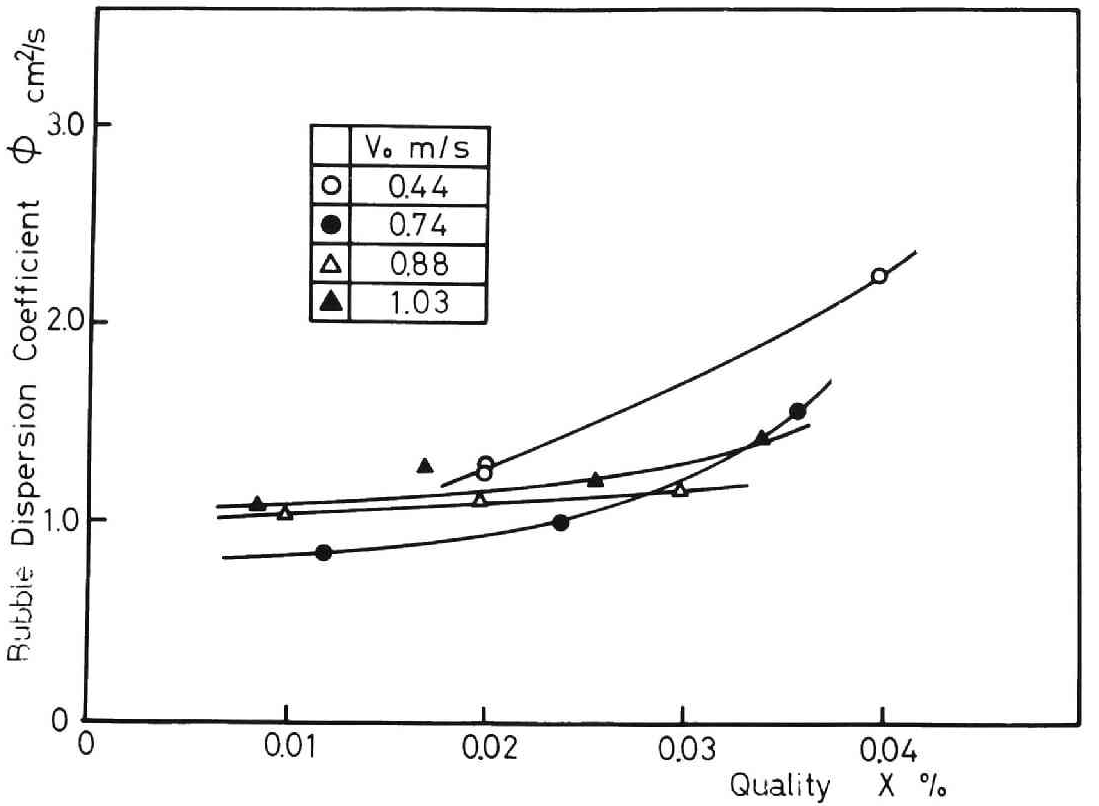

Fig. 5.11 Variation of bubble dispersion coefficient

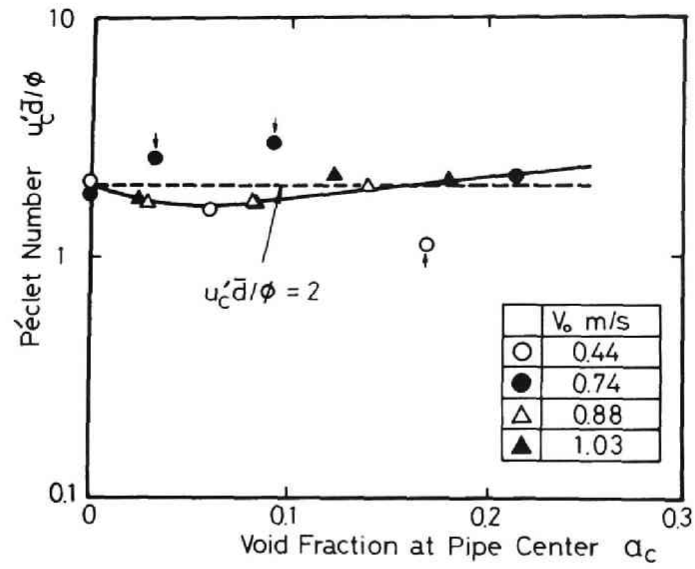

Fig. 5.12 Péclet number vs. void fraction at pipe center

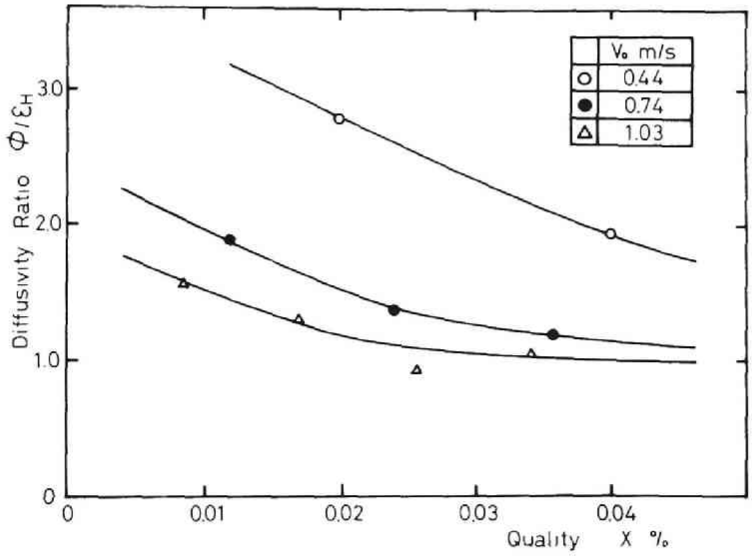

Fig. 5.13 Diffusivity ratio ϕ/ε_H vs. quality

VI. CONCLUDING REMARKS

Measuring techniques for various flow variables, applicable to the diabatic systems, have been developed.

A considerable amount of information have been obtained and many have been also clarified with respect to the turbulence structure of air-water two-phase bubble flow in pipe, which will give us a correct physical picture of the situation.

The experimental results indicate that, over a large portion of any cross-section in fully-developed bubble flow region, most of the various local parameters are uniformly distributed in radial direction, which may support the validity for applying a homogeneous flow field to an air-water bubble flow of small quality. Uniform distributions of the local parameters follow from the intensified turbulent transport of the transferable quantities, which was confirmed by employing a mixing length concept for such cases. On the other hand, in the outer region of the flow cross-section, the wall region, the wall effects appeared in maxima of the local void fraction and the bubble impaction rate near the wall. These wall effects are needed to be studied further.

Statistical character of the bubble rise velocity and the water velocity was studied. Spectra of the bubble velocity and the water velocity showed the Poisson distribution and the normal distribution functions respectively. A particularly important and interesting phenomenon was found about the turbulent intensity. The experimental evidence indicated a trend for the turbulent intensity to decrease first with increasing the gas flow rate for constant water velocity, and to increase again with a further increase in the gas flow rate. This phenomenon was more remarkable for a higher water velocity. Moreover, corrugated surface of bubbles observed by photograph appears to give some useful suggestions to understanding the physical picture of the flow turbulence in gas-liquid two-phase bubble flow.

Turbulent transport of heat and bubbles in air-water bubble flow was also investigated based upon a bubble diffusion model. It is expected from the experimental results that the turbulent velocity components of the liquid phase play a predominantly important role in turbulent transport process of heat and bubbles in common, and hence, the bubble-to-heat diffusivity ratio approaches unity with increasing the quality and the water velocity as was actually observed in experiments.

The next step in the development of a model of the bubble flow regime should be a more sound and systematic pertinent investigation of the mechanism itself of the turbulent transport process, and a mathematical description of the phenomena. The possibility of extending the bubble diffusion model to include a radially dependent bubble dispersion coefficient should be also considered. In addition, the boundary condition on the bubble diffusion equation for the case with wall effect should be investigated. An attempt should be also carried out to extend the results obtained by the present work to understand the over-all characteristics of gas-liquid two-phase flow.

Furthermore, the experiments described here should be extended to obtain the information about the thermohydrodynamics of the diabatic two-phase flow systems.

APPENDIX

Appendix I. THEORETICAL DERIVATION OF Eq.(4.4)

The relation described by Eq.(4.4) may be derived theoretically by considering a balance of energy fluxes of two-phase flow. The equation of energy flux is given by

$$\frac{1}{2} WV_o^2 + JLWX = \frac{1}{2} W_1 V_1^2 + \frac{1}{2} W_g V_g^2 + WgZ \quad , \tag{4.5}$$

where J and L are the mechanical equivalent of heat (or Joule's equivalent), and latent heat, respectively, and

$$W_g = WX, \quad V_g = V_o \frac{\rho_1}{\rho_g} \frac{X}{\alpha} \tag{4.6}$$

Substitution of Eqs.(4.2) and (4.6) into Eq.(4.5) yields

$$\frac{(1 - X)^3}{(1 - \alpha)^2} - 1 + \frac{X^3}{\alpha^2} \left(\frac{\rho_1}{\rho_g}\right)^2 = \frac{2}{V_o^2} (JLX - gZ) \quad . \tag{4.7}$$

For axially uniform heat addition, we have

$$WXL = \int_o^Z Q(z)dz = Q_o Z \quad , \tag{4.8}$$

where Q_o is an heat input through the heating surface per unit length and unit time. Hence, from Eqs.(4.7) and (4.8), we obtain

$$\frac{(1 - X)^3}{(1 - \alpha)^2} - 1 + \frac{X^3}{\alpha^2} \left(\frac{\rho_1}{\rho_g}\right)^2 = \frac{2L}{V_o^2} \left(J - \frac{Wg}{Q_o}\right) X \equiv KX \quad , \tag{4.9}$$

where

$$K = \frac{2L}{V_o^2} \left(J - \frac{Wg}{Q_o}\right) \quad . \tag{4.10}$$

Since L and Q_o are the unique function of the pressure and of the heat flux, respectively, the function K is a function of q, V_o, P, and also

the heating area.

The experimental evidence indicates that the additional term $(X^3/\alpha^2)(\rho_l/\rho_g)^2$ is usually very small relative to unity except in the higher quality region where the relative increment $(\frac{\partial\alpha}{\partial X}\Delta X) / \alpha$ is very small[3]. Then, Eq.(4.9) becomes approximately equal to Eq.(4.4).

Appendix II. DISCUSSIONS ON PROBE METHOD AND TRUE LOCAL VOID FRACTION

As stated in Chapter II (PART II), the probe method for measuring the local void fraction is associated with the ratio of the gas-contact time with the probe to the total sampling time. Hence, in using this method, it is quite necessary prior to measurements to speculate on the problem as to whether the true local void fraction α_{loc} is given by the time ratio $\Sigma_i\, t_{gi}/T$ or not.

Now, let us consider the configurations of the probe and bubbles illustrated in Fig.II-1. For the simplicity of the present analysis, it is assumed that the liquid and the gas phases are alternately passing over the measuring point, constituting a number of liquid-gas pairs. A liquid-gas pair, passing over that point in i-th turn from the beginning of the measurement at $\tau = 0$, is named "i-th pair". And, as illustrated in Fig.II-1, at $\tau = \tau_o$ the probe tip lies on the boundary between the liquid phase of the i-th pair and the gas phase of the (i-1)-th pair.

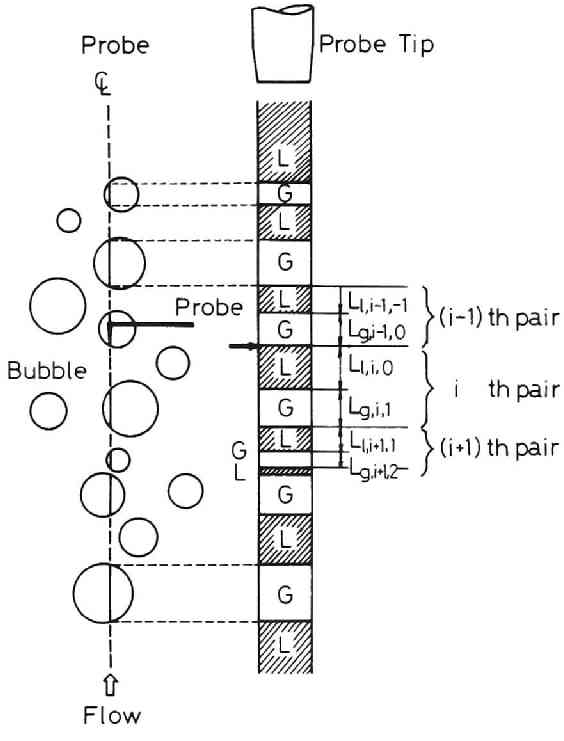

Fig. II-1 Configuration of the probe and bubbles

Let us denote the reduced lengths of the columns of the liquid and the gas phases of individual pairs by the terms, $L_{l,j,k}$ and $L_{g,j,k}$, respectively, where

the first subscript l or g = liquid and gas phase, respectively,

the second subscript j = j-th liquid-gas pair,

the last subscript k = location of the pair, for instance,

k=0 : a pair which is contact with the probe tip,

k<0 : a pair located downstream of the probe,

k>0 : a pair located upstream of the probe.

The time durations required for each component of the i-th pair to transit over the measuring station and their corresponding velocities are $t_{l,i}$ and $V_{l,i}$ for the liquid phase, and $t_{g,i}$ and $V_{g,i}$ for the gas, respectively (see Fig.II-2).

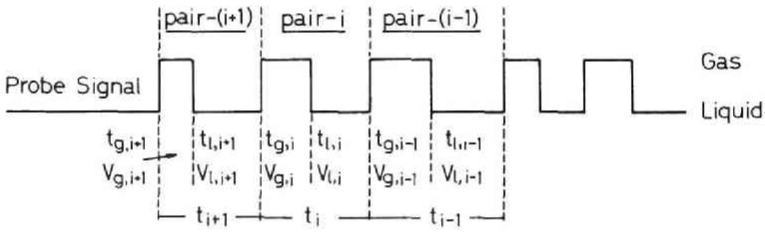

Fig. II-2 Modified signal of the void probe

Further assumptions are made for the present analysis :

1) Velocities for the i-th pair of two phases do not vary during their travels, however the fluid particles having composed the i-th pair at $\tau = \tau'$ are probably different from those constituting the same pair at $\tau = \tau_o$ ($\tau_o \neq \tau'$) because of the slip velocity between the two phases and because of the mixing actions due to turbulence. Velocities of the liquid and gas of the i-th pair, and the slip velocity are denoted by $V_{l,i}$, $V_{g,i}$, and $V_{s,i}$ ($= V_{g,i} - V_{l,i}$), respectively.

2) No volumetric change due to the expansion or compression occur in

the gas phase during its travelling process, e.g.,

$$L_{g,j,k+1} = L_{g,j,k} = \cdots\cdots\cdots = L_{g,j,0} \equiv L_{g,j} \qquad (1)$$

3) Imagine the column of the two-phase flow which runs parallel to the flow axis and includes the probe tip (the cross-sectional area of this column is taken to be equal to that of the probe tip). Then, it is postulated that there is no gas flow-in or -out of the column and the number of the liquid-gas pair is constant over the region considered here, i.e., agglomeration or extinction, or segmentation of bubbles is assumed not to occur.

Definitions of the Void Fraction and Reduced Lengths

Generally speaking, the void fraction is defined as the ratio of the volume occupied by the gas phase to the total volume of the two phases. In the case of no change in sizes of the bubbles during their travels along the flow direction, this definition may be extended or lead to the local void fraction defined as the ratio of the reduced length of the gas phase to that of the two-phase flow, and is given by the following equation with referring to Fig.II-1.

$$\alpha_{loc} = \frac{\sum_j L_{g,i+j,j+1}}{\sum_j (L_{l,i+j,j} + L_{g,i+j,j+1})} \qquad (2)$$

On the other hand, the time ratio T_R associated with the probe method is defined by

$$T_R = \frac{\sum_i t_{g,i}}{\sum_i (t_{l,i} + t_{g,i})} = \frac{\sum_i t_{g,i}}{\sum_i t_i} = \frac{\sum_i t_{g,i}}{T} \quad , \qquad (3)$$

where $t_{l,i}$, $t_{g,i}$, t_i, and T are the transit time durations for the liquid column, the gas column, and the liquid-gas of the i-th pair, and the total sampling time, respectively. Both $t_{l,i}$ and $t_{g,i}$ are closely related to the corresponding reduced lengths $L_{l,i,0}$ and $L_{g,i,0}$ through the velocities $V_{l,i}$ and $V_{g,i}$.

But, in general, the reduced lengths vary with time, that is, the reduced lengths for the i-th pair at $\tau = \tau_j$ are mostly different from those at $\tau = \tau_k$ ($\tau_j \neq \tau_k$), since the slip velocity between the two phases may exist for every pair. Consequently, a knowledge about the relationships between $L_{l,j,0}$ and $L_{l,j,k}$, and between $L_{g,j,0}$ and $L_{g,j,k}$ ($k \neq 0$) is much required to get an indication of the relationship between α_{loc} defined by Eq.(2) and T_R defined by Eq.(3). The former relationship will be deduced in the following manner with an aid of the illustrations shown in Fig.II-3.

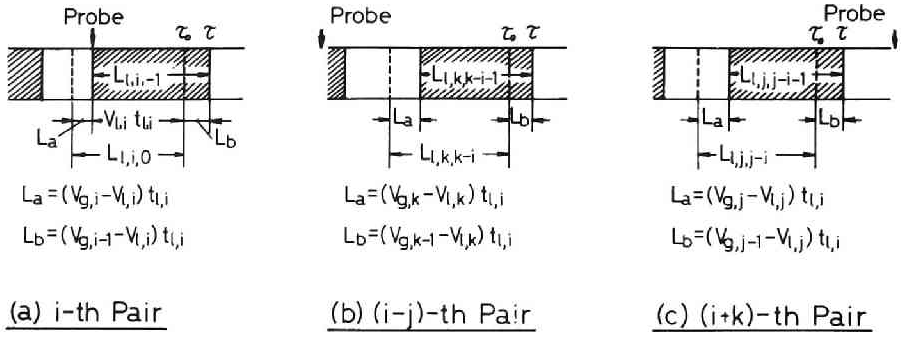

Fig. II-3 Illustration of reduced lengths

i-th pair

From Fig.II-3(a), we have

$$L_{l,i,0} = V_{l,i} \cdot t_{l,i} + (V_{g,i} - V_{l,i}) \cdot t_{l,i} = V_{g,i} \cdot t_{l,i} \quad , \tag{4}$$

$$L_{1,i,-1} = L_{1,i,0} - L_a + L_b$$

$$= L_{1,i,0} + (V_{g,i-1} - V_{g,i})\cdot t_{1,i} \quad , \qquad (5)$$

and from the assumption (1),

$$L_{g,i,-1} = L_{g,i,0} = L_{g,i} \quad . \qquad (6)$$

(i-j)-th pair ($i \geq j+1$)

Put $i - j = k$, and then, $L_{1,i-j,-j} = L_{1,k,k-i}$.

Therefore, referring to Fig.II-3(b), we have

$$L_{1,k,k-i-1} = L_{1,k,k-i} - L_a + L_b$$

$$= L_{1,k,k-i} - (V_{g,k} - V_{g,k-1})\cdot t_{1,i} \quad .$$

Hence

$$L_{1,k,k-i} = L_{1,k,k-i+1} - (V_{g,k} - V_{g,k-1})\cdot t_{1,i-1}$$

$$= L_{1,k,k-i+2} - (V_{g,k} - V_{g,k-1})(t_{1,i-1} + t_{1,i-2})$$

$$= \cdots\cdots\cdots$$

$$= L_{1,k,0} - (V_{g,k} - V_{g,k-1})(t_{1,i-1} + t_{1,i-2} + \cdots$$

$$\cdots\cdots + t_{1,k}) \quad .$$

Substitution of the relation $i - j = k$ into this result yields

$$L_{1,i-j,-j} = L_{1,i-j,0} - (V_{g,i-j} - V_{g,i-j-1}) \cdot \sum_{k=1}^{j} t_{1,i-k} \quad . \tag{7}$$

From the assumption (1), we have

$$L_{g,i-j,-j} = L_{g,i-j,0} = L_{g,i-j} \quad . \tag{8}$$

(i+k)-th pair ($k \geq 1$)

Put $i + k = j$, and then $L_{1,i+k,k} = L_{1,j,j-i}$.

Therefore, referring to Fig.II-3(c), we have

$$\begin{aligned} L_{1,j,j-i} &= L_{1,j,j-i-1} + L_a - L_b \\ &= L_{1,j,j-i-1} + (V_{g,j} - V_{g,j-1}) \cdot t_{1,i} \\ &= L_{1,j,j-i-2} + (V_{g,j} - V_{g,j-1})(t_{1,i} + t_{1,i+1}) \\ &= \cdots\cdots\cdots \\ &= L_{1,j,0} + (V_{g,j} - V_{g,j-1})(t_{1,i} + t_{1,i+1} + \cdots \\ &\qquad \cdots\cdots + t_{1,j-1}) \quad . \end{aligned}$$

Substitution of the relation $i + k = j$ into this result yields

$$L_{1,i+k,k} = L_{1,i+k,0} + (V_{g,i+k} - V_{g,i+k-1}) \cdot \sum_{j=1}^{k} t_{1,i+j-1} \quad . \tag{9}$$

From the assumption (1), we have

$$L_{g,i+k,k} = L_{g,i+k,0} = L_{g,i+k} \quad . \tag{10}$$

When we consider the column of the two-phase flow which is composed of (m + n) pairs of the liquid and gas phases as is shown in Fig.II-4 (i = m), the summation of the reduced lengths for the liquid column L_l, and for the gas column L_g will be expressed by the following formulas.

$$L_l = \sum_{j=1}^{m-1} L_{l,i-j,-j} + L_{l,i,0} + \sum_{k=1}^{n} L_{l,i+k,k} \quad , \tag{11}$$

$$L_g = \sum_{j=1}^{m-1} L_{g,i-j,-j} + L_{g,i,0} + \sum_{k=1}^{n} L_{g,i+k,k} \quad , \tag{12}$$

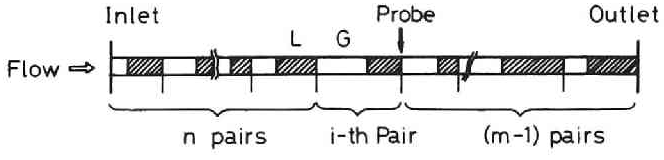

Fig. II-4 Arrangement of the columns of two-phase flow

Substituting Eqs.(5),(7), and (9) into Eq.(11), we can easily obtain the following expressions for L_l.

$$L_l = L_{l0} + \Delta_l \quad , \tag{13.a}$$

where

$$L_{l0} = \sum_{j=1}^{m+n} L_{l,j,0} = \sum_{j=1}^{m+n} (V_{g,j} \cdot t_{l,j}) \quad , \tag{13.b}$$

$$\Delta_1 = -\sum_{j=1}^{m-1}\{(V_{g,i-j} - V_{g,i-j-1})\cdot\sum_{k=1}^{j} t_{l,i-k}\}$$

$$+\sum_{k=1}^{n}\{(V_{g,i+k} - V_{g,i+k-1})\cdot\sum_{j=1}^{k} t_{l,i+j-1}\} \quad . \quad (13.c)$$

On the other hand, L_g can be obtained by substituting Eqs.(6),(8), and (10) into Eq.(12).

$$L_g = \sum_{j=1}^{m+n} L_{g,j} = \sum_{j=1}^{m+n} L_{g,j,0} = \sum_{j=1}^{m+n} (V_{g,j}\cdot t_{g,j}) \equiv L_{g0} \quad . \quad (14)$$

Hence, using Eqs.(13.a) to (14), we can rewrite Eq.(2) for local void fraction in the following form.

$$\alpha_{loc} = \frac{L_{g0}}{L_{l0} + L_{g0} + \Delta_1} = \frac{\sum_{j=1}^{m+n} (V_{g,j}\cdot t_{g,j})}{\sum_{j=1}^{m+n}\{V_{g,j}\cdot(t_{l,j} + t_{g,j})\} + \Delta_1}$$

$$= \frac{\sum_{j=1}^{m+n} (V_{g,j}\cdot t_{g,j})}{\sum_{j=1}^{m+n} (V_{g,j}\cdot t_j) + \Delta_1} \quad (15)$$

And the total sampling time T is given by

$$T = \sum_{j=1}^{m+n} t_j = \sum_{j=1}^{m+n} (t_{l,j} + t_{g,j}) \quad . \quad (16)$$

Relationship between α_{loc} and T_R

Provided that the total sampling time T is sufficiently large in a statistical sense, the approximation m = 1 (and sufficiently large value for n) should not give any serious disadvantages to the generality of the present analysis. Then, Eq.(13.c) becomes,

$$\Delta_1 = \sum_{k=1}^{n} (V_{g,1+k} - V_{g,k})(t_{1,1} + t_{1,2} + \cdots\cdots + t_{1,k})$$

$$= (V_{g,2} - V_{g,1})(t_{1,1} + t_{1,2})$$

$$+ (V_{g,3} - V_{g,2})(t_{1,1} + t_{1,2} + t_{1,3})$$

$$+ \cdots\cdots\cdots$$

$$+ (V_{g,n} - V_{g,n-1})(t_{1,1} + t_{1,2} + \cdots\cdots + t_{1,n-1})$$

$$+ (V_{g,n+1} - V_{g,n})(t_{1,1} + t_{1,2} + \cdots\cdots + t_{1,n-1} + t_{1,n})$$

$$= - \sum_{k=1}^{n} (V_{g,k} \cdot t_{1,k}) + V_{g,n+1} \cdot \sum_{k=1}^{n} t_{1,k}$$

$$= - \sum_{k=1}^{n} L_{1,k,0} + V_{g,n+1} \cdot \sum_{k=1}^{n} t_{1,k}$$

$$= - L_{10} + V_{g,n+1} \cdot \sum_{k=1}^{n} t_{1,k} \quad . \tag{17}$$

Hence,

$$L_1 = L_{10} + \Delta_1 = V_{g,n+1} \cdot \sum_{k=1}^{n} t_{1,k} \quad , \tag{18}$$

and

$$L_l + L_g = V_{g,n+1} \cdot \sum_{k=1}^{n} t_{l,k} + \sum_{k=1}^{n} (V_{g,k} \cdot t_{g,k}) \quad . \tag{19}$$

Now, we will introduce the ensemble average value V_g and the corresponding standard deviation s_i for rising velocity $V_{g,i}$ of the i-th gas phase. Here,

$$V_{g,i} = V_g + s_i \ , \text{ and } \sum_{i=1}^{n} s_i = 0 \quad . \tag{20}$$

Then, from Eqs.(14),(19), and (20) with putting $m = 1$, we have

$$L_g = \sum_{i=1}^{n} V_{g,i} \cdot t_{g,i} = (V_g \cdot \sum_{i=1}^{n} t_{g,i})(1 + \Delta_2) \quad , \tag{21}$$

and

$$L_l + L_g = V_g \cdot T \cdot (1 + \Delta_3) \quad , \tag{22}$$

where

$$\Delta_2 = \sum_{i=1}^{n} (s_i \cdot t_{g,i}) / \{V_g \cdot \sum_{i=1}^{n} t_{g,i}\} \quad ,$$

$$\Delta_3 = \{s_{n+1} \cdot \sum_{i=1}^{n} t_{l,i} + \sum_{i=1}^{n} (s_i \cdot t_{g,i})\} / (V_g \cdot T) \quad . \tag{23}$$

Substitution of Eqs.(21) to (23) into Eq.(15) yields

$$\alpha_{loc} = \{(V_g \cdot \sum_{i=1}^{n} t_{g,i})(1 + \Delta_2)\} / \{V_g \cdot T \cdot (1 + \Delta_3)\}$$

$$= \{\sum_{i=1}^{n} t_{g,i} / T\} \{(1 + \Delta_2) / (1 + \Delta_3)\}$$

$$= T_R \cdot \{(1 + \Delta_2)/(1 + \Delta_3)\} \quad . \tag{24}$$

Here, it is very rational to postulate that Δ_2 and Δ_3 should be sufficiently small relative to unity, and then

$$\alpha_{loc} = T_R(1 + \Delta_4) \quad , \tag{25}$$

where

$$\Delta_4 = \Delta_2 - \Delta_3$$

$$= [\sum_{i=1}^{n} (s_i \cdot t_{g,i})/\{V_g \cdot \sum_{i=1}^{n} t_{g,i}\}]$$

$$- \{s_{n+1} \cdot \sum_{i=1}^{n} t_{1,i} + \sum_{i=1}^{n} (s_i \cdot t_{g,i})\}/(V_g \cdot T)$$

$$= [\sum_{i=1}^{n} (t_{1,i} + t_{g,i}) \cdot \sum_{i=1}^{n} (s_i \cdot t_{g,i}) - \{s_{n+1} \cdot \sum_{i=1}^{n} t_{1,i}$$

$$+ \sum_{i=1}^{n} (s_i \cdot t_{g,i})\} \sum_{i=1}^{n} t_{g,i}]/\{V_g \cdot T \cdot \sum_{i=1}^{n} t_{g,i}\}$$

$$= \{\sum_{i=1}^{n} t_{1,i}/T\}[\sum_{i=1}^{n} \{(s_i - s_{n+1}) \cdot t_{g,i}\}/(V_g \cdot \sum_{i=1}^{n} t_{g,i}) << 1.$$

Consequently, it may well be concluded from Eq.(25) that T_R becomes approximately equal to α_{loc} for statistically sufficiently large sampling time.

Appendix III. EFFECT OF THE INITIAL CONDITION ON THE DYNAMICS OF BUBBLES INJECTED INTO THE STREAM THROUGH BUBBLE INJECTOR

In the study of the diffusivity of bubbles injected into the stream from a fixed point source, a knowledge is required for the time-dependent variations (or the variation along the flow direction) of the velocity, temperature, and diameter of bubbles. Especially, the bubble acceleration or deceleration may act an important role in the measurement of the bubble diffusivity.

Now, let us consider a single gas bubble which is introduced into the stream at time t_o through the bubble injector at initial conditions V_o, d_o, and T_o, and will be accelerated up to a certain terminal velocity V_∞; where V, d, and T are the bubble velocity, diameter, and temperature, respectively. During the travel, the bubble may undergo heat exchange with the ambient fluid, and consequently, its temperature and diameter also vary and approach to the fluid temperature and the corresponding thermal-equilibrium diameter, respectively.

Following assumptions are made for simplifying the analysis:

1) The fluid velocity V_1 is constant within the marked region of the flow field, which is the velocity of the fluid in the neighborhood of the bubble but sufficiently remote not to be disturbed by the relative motion of the bubble,
2) A spherical bubble under thermodynamic equilibrium conditions with the ambient fluid at any time of its travelling,
3) Uniform distributions of the concentration, the temperature, and the pressure within the gas bubble, and no mass transfer between the gas bubble and the fluid,
4) Temperature dependence of the physical properties of bubbles and the fluid can be neglected,
5) So-called Basset term can be neglected in the equation for bubble motion.

Equation for Bubble Motion

According to the force balance, we have the following equation (in an Eulerian description) for the motion of an accelerated single bubble.

$$\frac{\pi}{6}d^3\rho_g \frac{dV}{dt} = C_D \frac{\pi}{4} d^2 \frac{\rho_1}{2} (V_1 - V) |V_1 - V| - \frac{1}{2}\frac{\pi}{6} d^3 \rho_1 \frac{dV}{dt}$$

$$+ \frac{\pi}{6} d^3(\rho_1 - \rho_g)g \quad , \qquad (1)$$

where ρ_g, ρ_1, and C_D are the densities of the gas bubble and the fluid, and the drag coefficient of the flow resistance of the bubble.

According to Ref.[1], the drag coefficient C_D for a single spherical bubble-non-purified water system can be approximated by

$$C_D = 18.5 \; / \; Re_b^{3/5} \quad , \qquad (2)$$

where

$$Re_b = \frac{|V_1 - V| d}{\nu_1} \quad .$$

Substitution of Eq.(2) into Eq.(1) yields

$$\frac{dV}{dt} = \frac{111}{4} \frac{2\rho_1}{2\rho_g + \rho_1} \nu^{3/5} (V_1 - V) |V_1 - V|^{2/5} d^{-8/5}$$

$$+ \frac{2(\rho_1 + \rho_g)}{2\rho_1 + \rho_g} g \qquad (3)$$

Heat Transfer between the Bubble and the Ambient Fluid

$$\pi d^2 h(T - T_1) = - m_b C_{pg} \frac{dT}{dt} = - \frac{\pi}{6} d_o^3 \rho_g C_{pg} \frac{dT}{dt} \quad , \qquad (4)$$

where C_{pg}, m_b, and h are the specific heat of the gas bubble at constant pressure, the mass of the bubble and the heat transfer coefficient.

It is assumed that the heat transfer coefficient can be expressed by the correlation of Ranz-Marshall for convective heat transfer between a rigid sphere and the fluid.

Then,

$$Nu = 2 + 0.60\ Pr^{1/3}\ Re_b^{1/2} \qquad \text{for} \quad 0.6 < Pr < 380,\quad 1 < Re_b < 10^5 \qquad (5)$$

where

$$Nu = hd/\lambda$$

Relationships between T, P_b, and d

The pressure within a bubble of diameter d is given in terms of the pressure of the flow field P.

$$P_b - P = \frac{4\sigma}{d} \quad , \qquad (6)$$

where σ is the surface tension of the fluid.

Apply the assumption of the ideal gas for the present case, and then we have

$$(P + \frac{4\sigma}{d})\ \frac{\pi}{6}\ d^3 = R(T + 273) \quad , \qquad (7)$$

where R is the ideal gas constant.

When the origin of the coordinate is taken at the exit of the bubble injector, we have the following description for bubble dynamics.

$$t = 0 : z = 0,\quad d = d_o,\quad P = P_o,\quad \theta = T_o + 273 \quad ,$$

$$t = t : z = z,\quad d = d,\quad P = P,\quad \theta = T + 273 \quad .$$

Consequently, from Eq.(7) we obtain

$$\frac{T + 273}{T_o + 273} = (\frac{d}{d_o})^3\ (P + \frac{4\sigma}{d})/\ (P_o + \frac{4\sigma}{d_o}) \quad . \qquad (8)$$

The static pressure at z = z is given by

$$P = P_o - (\rho_l\alpha_l + \rho_g\alpha)z$$

$$\simeq P_o - \rho_l\alpha_l z$$

$$= P_o - \rho_1 \alpha_1 \int_o^t V \, dt \quad , \tag{9}$$

where α_1, and α are the cross sectional average liquid fraction and the void fraction, respectively.

Dimensionless Basic Equations

For known T_1, T_o, d_o, P_o, α_1, and V_1, V, T, and d can be calculated from Eqs.(3), (4), (5), (8), and (9). Following non-dimensional velocity V^*, temperature T^*, and diameter d^* are defined for simplicity;

$$V^* = \frac{V_1 - V}{V_1} \quad , \quad T^* = \frac{T - T_1}{T_o - T_o} \quad , \quad d^* = \frac{d}{d_o} \quad . \tag{10}$$

Then, the basic equations for velocity, temperature, and diameter of the bubble are rewriten and summarized here by the following expressions.

$$\frac{dV^*}{dt} = -A \, V^* |V^*|^{2/5} \, d^{*-8/5} - B \quad , \tag{11.a}$$

$$\frac{dT^*}{dt} = \frac{- d^* T^* (C + D|V^* d^*|^{1/2})}{T^*(T_o - T_1) + T_1 + 273} \quad , \tag{11.b}$$

$$\frac{dd^*}{dt} = \frac{d^{*2} \left[G d^{*2} (1 - V^*) - T^* \left\{ \frac{C + D|V^* d^*|^{1/2}}{T^*(T_o - T_1) + T_1 + 273} \right\} \right]}{3(T^* + E) - F \, d^{*2}} \quad , \tag{11.c}$$

where,

$$A = \frac{111}{4} \frac{2\rho_1}{2\rho_g + \rho_1} \left(\frac{V_1}{d_o}\right) (Re_{bo})^{-3/5} \qquad (1/\text{sec}),$$

$$B = \frac{2(\rho_l - \rho_g)}{2\rho_g + \rho_l} \frac{g}{V_l} \qquad (1/\text{sec}),$$

$$C = 6\lambda(T_o + 273) / \rho_g C_{pg} d_o^2 \qquad (^oC/\text{sec}),$$

$$D = 0.3CPr^{1/3} Re_{bo}^{1/2} \qquad (^oC/\text{sec}),$$

$$E = (T_l + 273)/(T_o - T_l) \qquad (\text{dimensionless}),$$

$$F = E \frac{4\sigma}{d_o} / (P_o + \frac{4\sigma}{d_o}) \qquad (\text{dimensionless}),$$

$$G = E \rho_l V_l \alpha_l / (P_o + \frac{4\sigma}{d_o}) \qquad (1/\text{sec}),$$

$$Re_{bo} = V_l d_o / \nu_l \qquad (\text{dimensionless}).$$

The solutions to Eqs.(11.a), (11.b), and (11.c) can be numerically obtained by Runge-Kutta-Gill method, for initial condition

$$t = 0 \; ; \; V^* \text{ (given)}, \quad T^* = 1, \quad d^* = 1 \; .$$

In actual calculating process, we used the physical properties of the gas and the fluid at the following temperatures.

ν_l, λ, σ, ρ_l: at $T = T_l$

ρ_g, C_{pg} : at $T = (T_o + T_l)/2$.

REFERENCES

(1) Kihō.Ekiteki Kōgaku (in Japanese): Kagaku Kōgaku Kyōkai (1969).

ERRATA

Page	Line	As printed	To read
vii	3	Effect of Channel	Effect of the Channel
viii	9	Accesories	Accessories
21	18	heat flux give	heat flux given
23	23 ~ 24	, indicates clearly	, indicate clearly
24	24	the product Fd	the product Fd_b
25	6	, d increases	, d_b increases
26	17	give an uniform	give a uniform
28	31	Z/D = 13.0, 27.7,	Z/D = 13.0, 27.8,
29	9	from an uniform to a dome-shpaed	from uniform to dome-shaped
32	2	Rouhani, S.G.	Rouhani, S.Z.
32	14	Atomenergi, Halde,	Atomenergi, Halden,
38	Fig.3.4	Martinelli-Nerson	Martinelli-Nelson
51	13	correlates neary	correlates nearly
68	26	normally writen as	normally written as
69	15	between that for	between those for
71	18	take a place	take place
72	13	aby putting	by putting
80	21	approximate eqation	approximate equation
87	9	[8] Serzawa, A.	[8] Serizawa, A.
87	14	Ph. D. these	Ph. D. thesis
100	14	an upward downward	an upward or downward
101	24	good agreemant with	good agreement with
124	18	due to the rate	due to the fact that the rate
127	15	● -marmed	● -marked
128	6	◐ -marked component in	◐ -marked components in
137	1	W_{fo} = 0)* and	W_{io} = 0) and
143	Fig.8.8	$\Gamma=(\rho_g V_{sg}^2 D/\sigma)($	$\Gamma=(\rho_g V_{go}^2 D_p/\sigma)($
146 ~ 147	29 ~ 1	are presented. These correlations ····· are presented. These ···	are presented. These
154	4	gas-contact periods	gas-contact period
156	Fig.2.1	Analizer	Analyzer

Page	Line	As printed	To read
165	Fig.2.7	Analizer	Analyzer
171	Fig.2.11	V_g	V_b
175	20	and Accesories	and Accessories
186	8	[8] Hyu, Y.Y., AL :	[8] Hsu, Y.Y., et al. :
200	18	the ssumptions, V_b	the assumptions, V_b
202	2	small downstream from	small downstream distance from
209	25	two mechanisma	two mechanisms
225	Fig.3.2	Analizer	Analyzer
248	30	a heat exchager	a heat exchanger
248	31	respectively contained	respectively were contained
281	25	afforementioned	aforementioned
281	footnote	on pase 280.	on page 280.
307	5	results may have	results might have
312	3	(4.11) is not	(4.11)) is not
312	9	Paragraph4.6.2).	Paragraph 4.6.2).
336	13	may indicates that	may indicate that
337	14	velocity profiles	velocity profile
342	10 ~ 11	and in the slug	and the slug
371	5	may influenced each	may influence each
405	18	in Chapter III.	in Chapter II.
414	9	a wave analizer	a wave analyzer
431	12	an heat input	a heat input
432	5	is very small(3).	is very small (see Ref.[3] in Chapter IV).
437	9	$= L_{1,k,k-1} - ($	$= L_{1,k,k-i} - ($
439	8	and (9) into Eq.(10),	and (9) into Eq.(11),
440	4	and (10) into Eq.(11).	and (10) into Eq.(12).
441	5	Then, Eq.(12.c)	Then, Eq.(13.c)
446	20	t = p : z = o,	t = 0 : z = 0,
447	7	V^*, and diameter	V^*, temperature T^*, and diameter
447	10	are rewriten and	and rewritten and